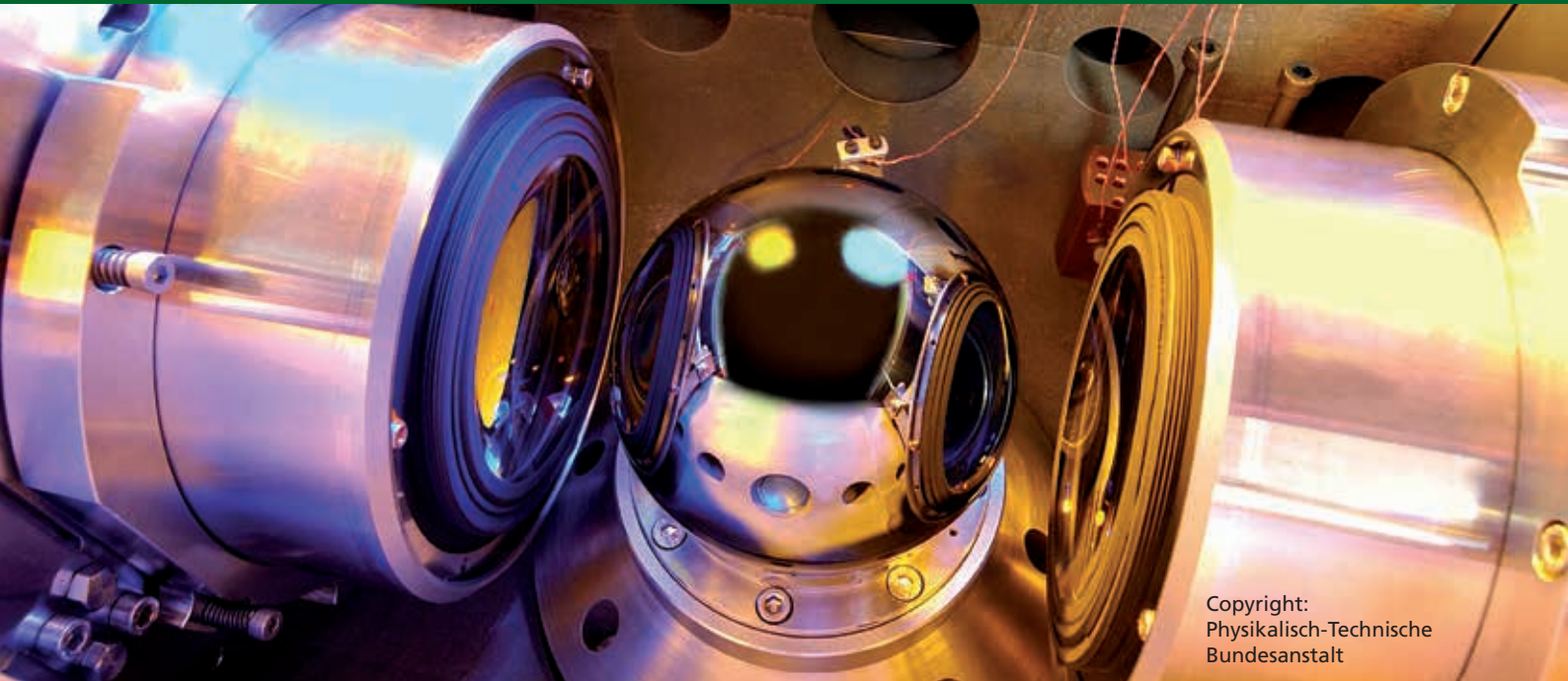


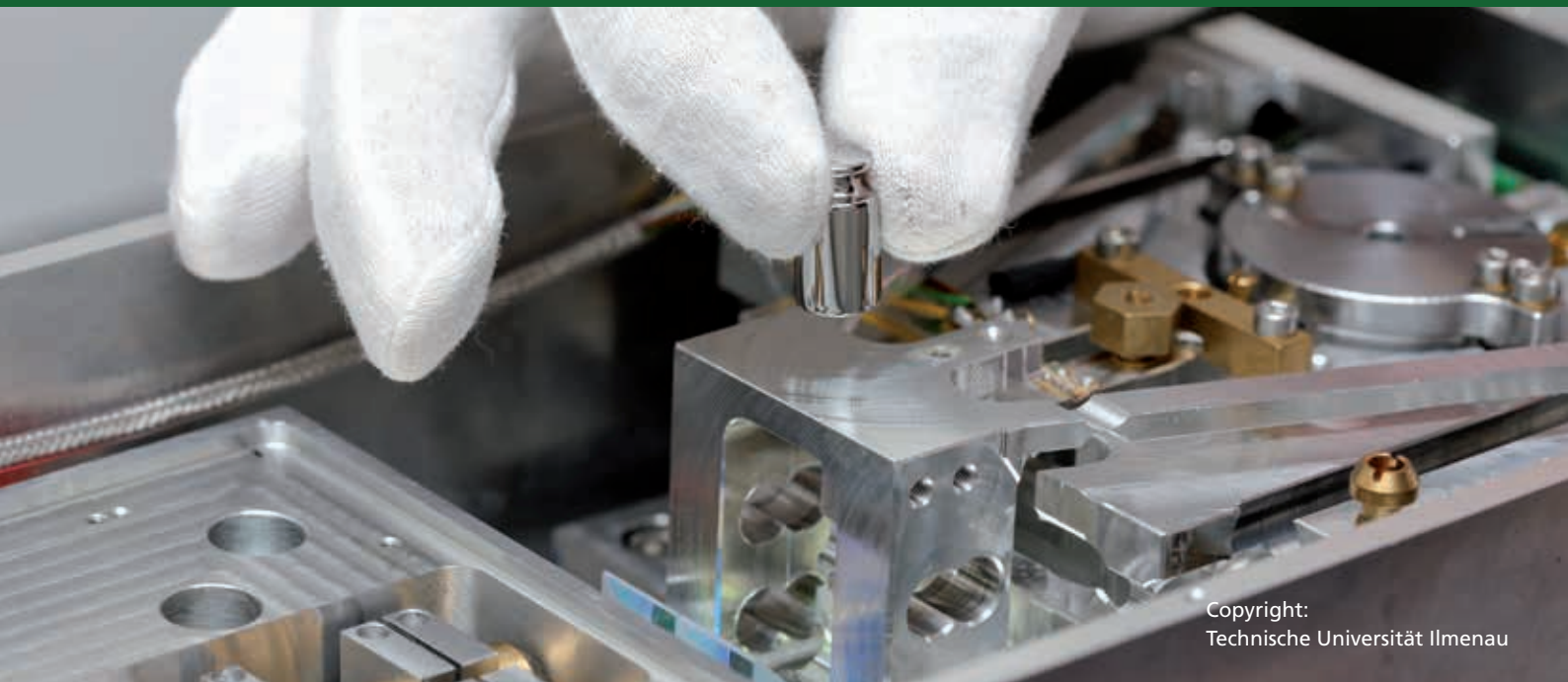
SMSI 2020

Sensor and Measurement
Science International



Copyright:
Physikalisch-Technische
Bundesanstalt

Proceedings



Copyright:
Technische Universität Ilmenau

www.smsi-conference.com



AMA Association for Sensors and Measurement

Proceedings

SMSI 2020 Conference

Sensor and Measurement Science International

This volume covers the elaborated proceedings of the SMSI 2020. Due to the covid-19 virus pandemic it was not possible to hold the SMSI 2020 Conference with the lectures and poster presentations as planned.

This volume comprises the short papers of the scheduled lectures and poster presentations.

The authors are responsible for form and content of the papers. AMA Service GmbH accepts no responsibility for the correctness and completeness of the details and the consideration of private rights of third parties.

Herausgeber / Publisher:

AMA Service GmbH
Von-Münchhausen-Str. 49
31515 Wunstorf / Germany
Tel. +49 5033 9639-0
info@ama-service.com
www.ama-service.com / www.sensor-test.com
www.ama-science.org / www.smsi-conference.com



ISBN 978-3-9819376-2-6

© AMA Service GmbH, 2020

SMSI 2020

Preface by the Conference Chairmen

Lord Kelvin is supposed to have said: “If you cannot measure it, you cannot improve it”. The more accurate and reliable measured data are the better is the opportunity to control and to advance the corresponding processes and products. Precise metrology regulations, sophisticated measurement theories and highly developed sensors for the instrumentation of every possible process for monitoring our health and our environment are essential for relevant ideas of today, such as the Industrial Internet and the Internet of Things.

The well-known AMA Conferences in Nuremberg, organized by AMA Association for Sensors and Measurement, parallel to the SENSOR+TEST, the world’s largest trade fair in this industry, have so far been the annual highlights in the field of sensor technology in Germany and Europe for more than 30 years. The purpose of the AMA Conferences was and is to provide scientists from universities, research institutes, and industry an opportunity to exchange ideas and, thus, to promote cooperation in the highly multidisciplinary areas of sensors and measurement technology.

Feeling the need to concentrate the power of the long-lasting experiences from several conferences, symposia and expert sessions in one common event with international visibility, the idea of the SMSI – Sensor and Measurement Science International was born two years ago. It is the central idea of this new conference to extend the previous AMA Conferences by a much broader scope comprising the following Conference Pillars:

- **Sensors and Instrumentation:** Sensor principles and quantities, Sensor materials and technology, Sensor interface electronics, Applications, Satellite Conference IRS² - Infrared Sensors and Systems,
- **Measurement Science:** Measurement foundations, Advanced methods and measurement systems, Networked and IoT-related measurement systems, AI approaches in measurement, Applications,
- **System of Units and Metrological Infrastructure:** Revised SI and its opportunities, Metrology and traceability, Calibration methods, Advance testing methods, Regulations, and standards in metrology.

Our joint planning until March 2020 was that this new format of the conference would take place in Nuremberg, Germany, from 22-25 June 2020. However, the recent development and increasingly critical risks inherent in the Covid-19 pandemic have led to further injunctions against major public events in Bavaria, Germany. Consequently, it was no longer possible to hold the SMSI 2020 as we have planned it so enthusiastically. We deeply regret this, especially because the SMSI was to take place in this form for the very first time. But the health of our participants and visitors had to have our highest priority.

To keep the conference idea alive and to acknowledge the preparatory work already done we have decided that all evaluated and accepted short papers for SMSI 2020 should be compiled and published as a Conference Proceedings. We are incredibly pleased that you can now hold the result in your hands! Our special thanks go to the Topical Chairmen of the Conference Pillars, the session chairs, and the authors. We really appreciate their commitment in bringing up this new Conference!

Meanwhile, the Program Committee as well as the AMA Association for Sensors and Measurement and the AMA Service GmbH as organizers have decided to hold the real first SMSI conference right next year. SMSI 2021 – Sensor and Measurement Science International – Conference now will take place from **3rd to 6th May 2021** in Nuremberg, Germany, parallel to the SENSOR+TEST Exhibition. We are looking forward to seeing you there!



Gerald Gerlach



Klaus-Dieter Sommer

Gerald Gerlach

Technische Universität Dresden
General Chair

Klaus-Dieter Sommer

Technische Universität Ilmenau
General Co-Chair

SMSI 2020 Conference Committee

General Chair

G. Gerlach Technische Universität Dresden (Germany)

General-Co-Chair

K.-D. Sommer Technische Universität Ilmenau (Germany)

Sensors and Instrumentation - Including Satellite Conference IRS²

Topical Chairs

G. Gerlach Technische Universität Dresden (Germany)
 R. Lerch Friedrich-Alexander-Universität Erlangen (Germany)
 U. Schmid Technische Universität Wien (Austria)

Members

J. Auge Hochschule Magdeburg-Stendal (Germany)
 C. Cavalloni Kistler Instrumente AG (Germany)
 J. Czarske Technische Universität Dresden (Germany)
 C. Corleto STIL SAS (France)
 M. da Silva Federal University of Technology Parana (Brazil)
 M. Deilmann KROHNE Messtechnik GmbH (Germany)
 G. Fischerauer Universität Bayreuth (Germany)
 M. Fleischer Siemens AG, Corporate Technology (Germany)
 J. Hollandt Physikalisch-Technische Bundesanstalt (Germany)
 B. Jakoby Johannes-Kepler-Universität Linz (Austria)
 U. Kaiser Endress+Hauser Management AG (Switzerland)
 U. Kienitz Optris GmbH (Germany)
 R. Kirchner Technische Universität Dresden (Germany)
 A. König Technische Universität Kaiserslautern (Germany)
 M. Kraft University of Liege (Belgium)
 P. A. Lieberzeit Universität Wien (Austria)

Members

A. Lloyd Spetz	University of Linköping (Sweden)
W. A. Minkina	Czestochowa University of Technology (Poland)
R. Moos	Universität Bayreuth (Germany)
M. Penza	Italian National Agency for New Technology, Energy and Sustainable Economic (Italy)
L. Reindl	Albert-Ludwigs-Universität Freiburg (Germany)
S. J. Rupitsch	Friedrich-Alexander-Universität Erlangen (Germany)
V. Schauer	HENSOLDT Optronics GmbH (Germany)
J. Schieferdecker	Heimann Sensor GmbH (Germany)
A. Schütze	Universität des Saarlandes (Germany)
S. Semancik	National Institute of Standards and Technology -NIST- (USA)
E. Starke	SICK Engineering GmbH (Germany)
H. K. Trieu	Technische Universität Hamburg-Harburg (Germany)
G. Urban	Albert-Ludwigs-Universität Freiburg (Germany)
M. Vellekoop	Universität Bremen (Germany)
M. Walther	Fraunhofer-Institut - IAF – (Germany)
J. Wöllenstein	Fraunhofer-Institut - IPM – (Germany)
S. Zimmermann	Leibniz Universität Hannover (Germany)
J. Zosel	Kurt-Schwabe-Institut für Mess- und Sensortechnik e.V. Meinsberg (Germany)

Measurement Science

Topical Chairs

K.-D. Sommer	Technische Universität Ilmenau (Germany)
L. Mari	University Carlo Cattaneo (Italy)
F. Puente	León Karlsruher Institut für Technologie KIT (Germany)

Members

Y. Aloimonos	University of Maryland (USA)
E. Benoit	Université Savoie Mont Blanc (France)
A. Chunovkina	VNIIMS D.I.Mendeleev Institute for Metrology (Russia)
A. Fischer	Universität Bremen (Germany)
C. Franklin	Measurement Science Conference (USA)
T. Fröhlich	Technische Universität Ilmenau (Germany)
C. Gulka	NCSL International Inc (USA)
E. Hazarian	California State University (USA)
B. Jeckelmann	Eidgenössisches Institut für Metrologie (Switzerland)
M. Heizmann	Karlsruher Institut für Technologie KIT (Germany)
W. Jian	National Institute of Metrology (China)
B. Henning	Universität Paderborn (Germany)
R. N. Kacker	National Institute of Standards (USA)
D. Knopf	Physikalisch-Technische Bundesanstalt (Germany)
A. König	Technische Universität Kaiserslautern (Germany)
R. Leach	University of Nottingham (Ireland)
L. Pendrill	SP Technical Research Institute of Sweden (Sweden)
A. Schäfer	Hottinger Baldwin Messtechnik GmbH (Germany)
A. Schütze	Universität des Saarlandes (Germany)
R. Tutsch	Technische Universität Braunschweig (Germany)
J. Valdés	INTI - Instituto Nacional de Tecnología Industrial (Argentina)
B. Zagar	Johannes-Kepler-Universität Linz (Austria)

System of Units and Metrological Infrastructure

Topical Chairs

B. Jeckelmann	Eidgenössisches Institut für Metrologie (Switzerland)
M. Bartholmai	BAM Bundesanstalt für Materialforschung (Germany)
P. Ulbig	Physikalisch-Technische Bundesanstalt (Germany)

Members

T. Bulygin	VNIIMS All-Russian scientific research institute for metrological service (Russia)
C. Corleto	STIL SAS (France)
A. Ganesh	CEN-CENELEC (Belgium)
E. Georgin	CETIAT - Centre Technique des Industries Aérauliques et Thermiques (France)
J. H. Hendricks	National Institute of Standards (USA)
J. Hollandt	Physikalisch-Technische Bundesanstalt (Germany)
A. Kuzin	VNIIMS All-Russian scientific research institute for metrological service (Russia)
P. Neyeshmakov	COOMET (Ukraine)
F. Ogheard	CETIAT - Centre Technique des Industries Aérauliques et Thermiques (France)
G. Rietveld	VSL - Dutch Metrology Institute (Netherlands)
C. Tiebe	BAM Bundesanstalt für Materialforschung (Germany)
J. Unger	BAM Bundesanstalt für Materialforschung (Germany)
J. Zosel	Kurt-Schwabe-Institut für Mess- und Sensortechnik e.V. Meinsberg (Germany)

SMSI 2020: Plenary Talks

1.	Measurement and Sensor Technology in the Digital Transformation Process	28
	U. Kaiser, Endress+Hauser Group Services AG, Reinach (Switzerland)	
2.	NIST on a Chip: Revolutionizing Metrology through Deployable, Quantum-Based Sensors	30
	B. Goldstein, NIST - National Institute of Standards and Technology, Gaithersburg (USA)	
3.	Realising the Redefined Kelvin	32
	G. Machin, National Physical Laboratory (NPL), Teddington (Great Britain)	
4.	NIST on a Chip: Photonic and Quantum-Based Sensors for Measurements of Pressure, Vacuum, Temperature and Beyond!	34
	J. Hendricks, Z. Ahmed, D. Barker, K. Douglass, S. Eckel, J. Fedchak, N. Klimov, J. Ricker, J. Scherschligt, NIST – National Institute of Standards and Technology, Gaithersburg (USA)	
5.	Measurements Beyond the SI: On the Longstanding Existence of Metrology-ready Precision Quantities in Psychology and the Social Sciences	38
	W. P. Fisher, University of California, Berkeley (USA)	

Sensors and Instrumentation

A1: Magnetic Sensors

Chair: R. Lerch, Friedrich-Alexander-Universität Erlangen, Erlangen (Germany)

A1.1	Analytic Method for Magnetic System Calibration	41
	M. Ortner, P. Malagò, S. Lumetti, Silicon Austria Labs, Villach (Austria), D. Spitzer, Infineon Technologies Austria, Villach (Austria), S. Zaruba, Infineon Technologies AG, Neubiberg (Germany)	
A1.2	Noise-free Inspection of Rotary Encoder Magnets	43
	K. Vervaeke, Magcam NV, Leuven (Belgium)	
A1.3	Multichannel Heterodyning-Based Eddy Current Testing with Magnetoresistive Sensors	45
	H. Ehlers, M. Pelkner, Federal Institute for Materials Research and Testing (BAM), Berlin (Germany), R. Thewes, Institute of Technology Berlin, Berlin (Germany)	
A1.4	Highly Sensitive Compact Room Temperature Quantum Scalar Magnetometer	47
	L. Horsthemke, C. Bischoff, P. Glösekötter, FH Münster - University of Applied Sciences, Steinfurt (Germany), B. Burchard, Elmos Semiconductor AG, Dortmund (Germany), R. Staacke, J. Meijer, Leipzig University, Leipzig (Germany)	

A2: Piezoelectric High-temperature Sensors

Chair: Y. Suhak, Technische Universität Clausthal, Goslar (Germany)

- A2.1 Contributions to Acoustic Loss in Langasite, Langatate, and Catangasite Resonators at High Temperatures** 49
W. L. Johnson, National Institute of Standards and Technology, Boulder (USA)
- A2.2 CTGS: Advanced Piezoelectric Single Crystal for Sensor Applications over Extremely Wide Temperature Range** 51
A. Sotnikov, R. Weser, H. Schmid, Leibniz IFW Dresden, Dresden (Germany), B. P. Sorokin, Technological Institute for Superhard and Novel Carbon Materials, Moscow (Russia), Y. Suhak, H. Fritze, Clausthal University of Technology, Goslar (Germany)
- A2.3 High-Temperature Acoustic Loss in Bulk AlN Piezoelectric Resonators** 53
H. Fritze, I. Kogut, Clausthal University of Technology, Goslar (Germany), I. Gamov, K. Irmscher, M. Bickermann, Leibniz-Institut für Kristallzüchtung, Berlin (Germany)
- A2.4 Investigations of the Actuator Based on Lithium Niobate Diffuse Bonded Bimorph Structure** ... 55
U. Yakhnevych, O. Buryy, S. Ubizskii, D. Sugak, Lviv Polytechnic National University, Lviv (Ukraine), Y. Suhak, H. Fritze, Clausthal University of Technology, Goslar (Germany), I. I. Syvorotka, Scientific Research Company "Electron-Carat", Lviv (Ukraine)
- A2.5 Electrical and Electromechanical Properties of Single Crystalline Li(Nb,Ta)O₃ Solid Solutions for High-Temperature Actuator Applications** 57
Y. Suhak, B. Jerliu, H. Fritze, Clausthal University of Technology, Goslar (Germany), S. Ganschow, Leibniz-Institut für Kristallzüchtung, Berlin (Germany), D. Roshchupkin, B. Red'kin, Institute of Microelectronics Technology and High Purity Materials, Chernogolovka (Russia), S. Sanna, Justus Liebig University Gießen, Gießen (Germany)

A3: Low-power Sensing and Energy Harvesting

Chair: E. Starke, SICK Engineering GmbH, Ottendorf-Okrilla (Germany)

- A3.1 System Design for Low Power Applications with Digital MEMS Sensors** 59
P. Stukjunger, STMicroelectronics, Prague (Czech Republic)
- A3.2 Flexible Equivalent Circuit Modeling for Piezoelectric Vibration Energy Harvesters** 61
D. Gedeon, S. J. Rupitsch, University Erlangen-Nuremberg, Erlangen (Germany)
- A3.3 A Self-Sustained Microcontroller Regulated Energy Extraction Network for Piezoelectric Energy Harvesters** 63
P. Dorsch, S. Götz, F. Hubert, S. Rupitsch, Friedrich-Alexander-University Erlangen-Nuremberg, Erlangen (Germany)
- A3.4 Universal Energy Harvesting Topology Used for Small Variable Temperature Gradients** 65
M. Lenzhofer, Silicon Austria Labs GmbH, Villach (Austria)

A4: Measurement of Force, Pressure, and Strain

Chair: T. Fröhlich, Technische Universität Ilmenau, Ilmenau (Germany)

- A4.1 Measuring Considerations for Jitter Characterization on Small Satellite Reaction Wheels** 67
C. Cavalloni, M. Dumont, Institution Kistler Instrumente AG, Winterthur (Switzerland),
B. Zwolinski, Kistler Instrument Corp., Amherst (USA)
- A4.2 New Reference Force Transducer for Compressive Forces Based on the Radially Symmetric Shear-beam Principle** 69
T. Kleckers, Hottinger Baldwin Messtechnik GmbH, Darmstadt (Germany)
- A4.3 Development and Calibration of Dynamic Pressure Sensor for Motor Pressure Range** 71
J. Salminen, R. Högström, S. Saxholm, J. Hämäläinen,
VTT Technical Research Centre of Finland Ltd., Espoo (Finland)
- A4.4 Measuring Load on Linear Guides in Different Load Scenarios Using an Integrated DLC Based Sensor System** 73
D. Krampert, S. Unsleber, Bosch Rexroth AG, Schweinfurt (Germany), L. Reindl,
Albert-Ludwigs-University Freiburg, IMTEK, Freiburg (Germany)
- A4.5 Influence of Temporal Strain Evolution on Distributed Strain Sensing with OTDR in Polymer Optical Fibers** 75
S. A. Dengler, N. Schmidt, M. Lubber, J. Fischer, O. Ziemann, R. Engelbrecht,
Technische Hochschule Nürnberg Georg Simon Ohm, Nuremberg (Germany),
H. Hangen, HUESKER Synthetic GmbH, Gescher (Germany)

A5: Sensor Materials and Technologies

Chair: H. K. Trieu, Technische Universität Hamburg-Harburg, Hamburg (Germany)

- A5.1 Development of a 3D-integrated Thermocatalytic Sensor for Combustible Gas Detection** 77
F. M. Münchenberger, S. Dreiner, H. Kappert, R. M. Neubieser, H. Vogt, Fraunhofer Institute for
Microelectronic Circuits and Systems, Duisburg (Germany)
- A5.2 Inline Quality Monitoring of Diesel Exhaust Fluid (AdBlue) by Using the 3w-Method** 79
R. E. Bernhardsgrütter, C. J. Hepp, Innovative Sensor Technology IST AG,
Ebnat-Kappel (Switzerland), M. Jäggle, H.-F. Pernau, K. Schmitt, J. Wöllenstein, University of Freiburg,
Freiburg (Germany)
- A5.3 Single Cell Immobilization at High Flow Rates Using 2PP-Traps in a Microfluidic Channel** 81
S. Reede, M. J. Vellekoop, University of Bremen, Bremen (Germany), H. Müller-Landau,
N. Matscheko, U. Rant, Dynamic Biosensors, Martinsried/ Planegg (Germany), F. Lucklum,
Technical University of Denmark, Kgs. Lyngby (Denmark)
- A5.4 Development of a New Measurement System for Electrical Conductivity and Hall Constant** 83
R. Werner, J. Kita, R. Moos, University Bayreuth, Bayreuth (Germany), M. Gollner, F. Linseis,
Linseis Thermal Analysis, Selb (Germany)

A6: MEMS Sensors

Chair: R. Tutsch, Technische Universität Braunschweig, Braunschweig (Germany)

A6.1 Design, Simulation, Fabrication and Characterization of Piezoelectric MEMS Cantilever for Gas Density and Viscosity Sensors Applications	85
A. Mehdaoui, C. Huber, J. Becker, F. Schraner, TrueDyne Sensors AG, Reinach BL (Switzerland)	
L. G. Villanueva, Ecole Polytechnique Fédérale de Lausanne, Lausanne (Switzerland)	
A6.2 Applications of Tactile Microprobes for Surface Metrology	87
C. Reuter, M. Holz, A. Reum, nano analytik GmbH, Ilmenau (Germany), M. Fahrbach, E. Peiner, Technische Universität Braunschweig, Braunschweig (Germany), U. Brand, Physikalisch-Technische Bundesanstalt, Braunschweig (Germany), M. Hofmann, I. Rangelow, Technische Universität Ilmenau, Ilmenau (Germany)	
A6.3 Higher-Mode Contact Resonance Operation of a High-Aspect-Ratio Piezoresistive Cantilever Microprobe	89
M. Fahrbach, E. Peiner, Technische Universität Braunschweig, Braunschweig (Germany)	
A6.4 A MEMS Micromachined Detector Platform for kW Power Radiation in a Wide Spectral Range	91
A. Laades, S. Görlandt, C. Heinze, F. Machalet, T. Ortlepp, CiS Forschungsinstitut für Mikrosensorik GmbH, Erfurt (Germany)	

B1: Hydrogen Sensors (Special Session)

Chair: J. Zosel, Kurt-Schwabe-Institut für Mess- und Sensortechnik e.V. Meinsberg, Waldheim (Germany)

B1.1 Hydrogen-Sensors for Selected Fuel Cell Applications	93
O. Kiesewetter, UST Umweltsensortechnik GmbH, Geschwenda (Germany)	
B1.2 Sensitivity and Selectivity of Pd based Thin Film Hydrogen Sensors	95
M. Wienecke, L. Godenrath, M. Hoffmann, Materion GmbH, Wismar (Germany), J. Heeg, Hochschule Wismar, Wismar (Germany)	
B1.3 Development and Characterization of a Miniaturized Hydrogen Gas Sensor System for Safety Monitoring	97
P. Sood, M. Mertig, Kurt-Schwabe-Institut für Mess- und Sensortechnik Meinsberg e.V., Waldheim (Germany), J. Zosel, Technische Universität Dresden, Dresden (Germany), O. Herrmann, M. Woratz, ACI Analytical Control Instruments GmbH, Berlin (Germany)	
B1.4 Microstructural Investigations of Blackening in YSZ Sensors for Hydrogen Coulometry	99
A. Graff, W. Münchgesang, F. Altmann, Fraunhofer Institute for Microstructure of Materials and Systems, Halle (Germany), C. Himcinschi, T. Köhler, Technische Universität Bergakademie Freiberg, Freiberg (Germany), P. Sood, J. Zosel, M. Mertig, Kurt-Schwabe-Institut für Mess- und Sensortechnik Meinsberg e.V., Waldheim (Germany)	

B2: Flow Measurement

Chair: S. J. Rupitsch, Friedrich-Alexander-Universität Erlangen, Erlangen (Germany)

B2.1	Monitoring of Pumps and Valves in Fluidic Systems with Electro-Magnetic Flowmeters	101
	J. Förster, T. Fritsch, J. Friderich, KROHNE Innovation GmbH, Duisburg (Germany), R. Gentemann, R. Vonnahme, WILO SE, Dortmund (Germany)	
B2.2	A Hermetic Sensor Concept for Measuring Fluid Flows	103
	P. Radler, J. Ringkamp, P. Lehardt, J. Langejürgen, Fraunhofer IPA, Mannheim (Germany)	
B2.3	Development of a Capacitive Sensor System for Gas-Liquid Flow Monitoring and Application in Hazardous Areas	105
	M. J. da Silva, E. Nunes dos Santos, D. Bertoldi, A. do Nascimento Wrasse, R. E. M. Morales, Federal University of Technology - Paraná (UTFPR), Curitiba (Brazil), D. C. dos Reis, R. da Fonseca Jr., Petrobras Research and Development Center (CENPES), Rio de Janeiro (Brazil)	
B2.4	Microwave Mass Flow Sensor for Online Measurements of Pure Liquids and Mixtures	107
	M. E. Euken, A. Penirschke, Technische Hochschule Mittelhessen, Friedberg (Germany)	
B2.5	Modeling the Fluid-Structure Interaction of Non-conventional Vibrational Modes for MEMS Fluid Sensing	109
	D. Platz, A. Gesing, U. Schmid, TU Wien, Vienna (Austria)	

B3: Biosensors and Sensors for Biology

Chair: U. Schmid, Technische Universität Wien, Vienna (Austria)

B3.1	Integrated Intelligent Sensor Systems for In-Hive Varroa Infestation Control in Digital Bee Keeping	111
	A. König, TU Kaiserslautern, Kaiserslautern (Germany)	
B3.2	Adaptive Soft Sensor for Bioprocess Monitoring	113
	M. Siegl, V. Brunner, D. Geier, T. Becker, Technische Universität München, Freising (Germany)	
B3.4	Synthesis of MIP Nanoparticles for Selective Sensing of Penicillin V	115
	M. Bagheri, P. A. Lieberzeit, University of Vienna, Vienna (Austria)	

B4: Gas Sensors for Safety and Security

Chair: R. Moos, Universität Bayreuth (BERC), Bayreuth (Germany)

B4.1	Fluorescence Multi-Sensor System for the Simultaneous Detection of Various Types of Explosives in Gas-Phase	117
	B. Heller, M. Biyikal, R. Noske, K. Rurack, Federal Institute for Materials Research and Testing (BAM), Berlin (Germany)	
B4.2	Percolation Networks of Polypyrrole for Vapour Sensing of Improvised Explosive Devices	119
	M. Lefferts, B. Armitage, K. Murugappan, M. Castell, University of Oxford, Oxford (United Kingdom)	
B4.3	Wireless Low-power Warning System for the Detection of Flammable Gases	121
	B. Bierer, J. Wöllenstein, O. Yurchenko, L. Engel, H.-F. Pernau, Fraunhofer Institute IPM, Freiburg (Germany), L. Reindl, D. Grgic, University of Freiburg, Freiburg (Germany)	
B4.4	Ultra-fast Gas Spectroscopy with a Dual-Comb Spectrometer	123
	L. Nitzsche, J. Kießling, S. Wolf, F. Kühnemann, J. Wöllenstein, Fraunhofer Institute for Physical Measurement Techniques IPM, Freiburg (Germany)	
B4.5	Sensory Options for Earthquake Victim Recovery	125
	R. Jha, Vishvachi, W. Lang, R. Jedermann, University of Bremen, Bremen (Germany)	

B5: Air Quality Monitoring

Chair: M. Bartholmai, BAM Bundesanstalt für Materialforschung und -prüfung, Berlin (Germany)

- B5.1 Evaluation of Commercial Metal Oxide Gas Sensors for Indoor Aeration Control** 127
J. Zosel, M. Mertig, Kurt-Schwabe-Institut für Mess- und Sensortechnik Meinsberg e.V., Waldheim (Germany), D. Deininger, Renesas Electronics America Inc., Longmont (USA), R. Schreiber, C. Meyer, Renesas Germany GmbH, Dresden (Germany)
- B5.2 Metal Oxide Nanolayer Decorated Epitaxial Graphene Gas Sensors for Air Quality Monitoring** 129
M. Rodner, A. Icardi, J. Eriksson, Linköping University, Linköping (Sweden), M. Kodu, R. Jaaniso, University of Tartu, Tartu (Estonia)
- B5.3 Evaluation of Indoor Air Quality by High School Students** 131
S. Höfner, A. Schütze, Saarland University, Saarbrücken (Germany), M. Hirth, J. Kuhn, Technical University Kaiserslautern, Kaiserslautern (Germany), B. Brück, Student Research Center, Saarlouis (Germany)
- B5.4 Semi-automatic Measurement Device for Long-Term Monitoring of Ammonia in Gas Phase** ... 133
K. Gawlitza, S. Johann, M. Mansurova, H. Kohlhoff, C. Tiebe, J. Bell, M. Bartholmai, K. Rurack, Federal Institute for Materials Research and Testing (BAM), Berlin (Germany)

B6: Chemical Sensors for Water Analysis

Chair: J. Zosel, Kurt-Schwabe-Institut für Mess- und Sensortechnik e.V. Meinsberg, Waldheim (Germany)

- B6.1 Glass Electrode Half-cells for Measuring Unified pH in Water-organic Solvent Mixtures** 135
A. Heering, F. Bastkowski, S. Seitz, Physikalisch-Technische Bundesanstalt, Braunschweig (Germany)
- B6.2 Development of an Universal Measuring Instrument for Quality Monitoring of Ultrapure Water** 137
S. Schäfer, J. Warmer, P. Kaul, Bonn-Rhine-Sieg University, Rheinbach (Germany), K. van Dyk, D. Schulze, Innovatec Gerätetechnik GmbH, Rheinbach (Germany), T. C. Schmidt, University of Duisburg-Essen, Essen (Germany)
- B6.3 HTCC Multilayer Based Ion Sensitive Sensors For Water Analysis** 139
C. Feller, U. Partsch, S. Körner, Fraunhofer Institute for Ceramic Technologies and Systems (IKTS), Dresden (Germany)
- B6.4 Development of a Glass-Fiber-Based Spectrometer for the Determination of Drug Residues in Groundwater** 141
E. Melekhov, V. Abb, T. Weidauer, A. Lechner, M. Kammler, Regensburg University of Applied Sciences, Regensburg (Germany)

C1: IRS² Satellite Conference: Infrared Detectors

Chair: G. Gerlach, Technische Universität Dresden, Dresden (Germany)

- C1.1 Thermal-electrical Design Improvements of a New CMOS Compatible Pyroelectric Infrared Sensor Based on HfO₂** 143
 R. Lehmkau, M. Ebemann, D. Mutschall, N. Neumann, InfraTec GmbH, Dresden (Germany),
 J. Lienig, TU Dresden, Institute of Electromechanical and Electronic Design, Dresden (Germany)
- C1.2 A Radiation Thermometer based on an InGaAs-Photodiode at 1.6 μm for Temperatures down to 80 °C** 145
 J. Bories, I. Mueller, B. Gutschwager, J. Hollandt, Physikalisch-Technische Bundesanstalt, Berlin (Germany)
- C1.3 Absolute Calibration of the Spectral Responsivity of Detectors in the MIR at the PTB** 147
 T. Pohl, P. Meindl, U. Johannsen, L. Werner, J. Hollandt, Physikalisch-Technische Bundesanstalt (PTB), Berlin (Germany)
- C1.4 Multi-spectral mid-IR Temperature Measurement Using Tuneable Detectors** 149
 M. Gillott, F. Turner, P. Droegmoeller, Ametek Land, Dronfield (United Kingdom)

C2: IRS² Satellite Conference: Infrared Spectroscopic Gas Sensing

Chair: F. J. M. Harren, Radboud University Institute of Molecules and Materials, Nijmegen (Netherlands)

- C2.1 FLAIR Airborne System for Multi-Species Atmospheric Gas Spectroscopy in the mid-IR** 151
 L. Balet, S. Chin, T. Herr, F. Lütolf, P. Renevey, J. Van Zaen, S. Dasen, J. Gouman, G. Buchs, S. Lecomte, CSEM SA, Neuchâtel (Switzerland), G. Vergara, New Infrared Technologies S.L., Madrid (Spain), H. Martin, SenseAir AB, Delsbo (Sweden), P. M. Moselun, NKT Photonic A/S, Birkerød (Denmark), F. J. M. Harren, Radboud University, Nijmegen (The Netherlands), C. Hüglin, EMPA, Dübendorf (Switzerland)
- C2.2 New Coherent Sources for mid infrared Spectroscopic Applications** 153
 F. J. M. Harren, Radboud University, Nijmegen (The Netherlands)
- C2.3 Uncooled High Speed MWIR Cameras Applied to Advanced Apectrometers** 155
 G. Vergara, R. Linares, R. Gutiérrez, C. Fernández, S. de la Fuente, A. Baldasano, New Infrared Technologies, Boadilla del Monte-Madrid (Spain)
- C2.4 Highly Compact Laser Spectrometers for Mobile Trace Gas Sensing Applications** 157
 M. Graf, B. Tuzson, P. Scheidegger, H. Looser, A. Kupferschmid, J. Ravelid, L. Emmenegger, Empa Swiss Federal Laboratorues for Materials Testing and Research, Dübendorf (Switzerland)
- C2.5 Multispecies Trace Gas Sensor for Real-time Quality Control of Stored Fruits** 159
 A. Khodabakhsh, K. E. Jahromi, Q. Pan, M. Nematollahi, F. J. M. Harren, Radboud University, Nijmegen (The Netherlands)

C3: IRS² Satellite Conference: Infrared Cameras and Thermal Imaging

Chair: J. Schieferdecker, Heimann Sensor GmbH, Dresden (Germany)

- C3.1 Metrological Characterization and Calibration of Thermographic Cameras in the Temperature Range from 50 °C to 960 °C** 161
S. König, B. Gutschwager, I. Müller, R. D. Taubert, J. Hollandt, Physikalisch-Technische Bundesanstalt, Berlin (Germany), F. Nagel, DIAS Infrared GmbH, Dresden (Germany)
- C3.2 Evaluation of Cryogenic Preamplifiers for Infrared Focal Plane Array Detectors** 163
C. Mandla, M. Plattner, Max-Planck-Institute for Extraterrestrial Physics, Garching (Germany), M. Engelhardt, N. Bezawada, D. Ives, European Southern Observatory, Garching (Germany)
- C3.3 Development of a Scalable Nanotube-Microbolometer Technology** 165
M. Michel, S. Weyers, D. Weiler, T. Geruschke, S. Blaeser, E. Zakizade, F. Hochschulz, H. Vogt, Fraunhofer Institute for Microelectronic Circuits and Systems, Duisburg (Germany)
- C3.4 New High Resolution 120x84 Thermopile Arrays for IR Imaging Applications** 167
J. Schieferdecker, M. Schnorr, B. Forg, F. Herrmann, C. Schmidt, W. Leneke, M. Simon, Heimann Sensor GmbH, Dresden (Germany)

C4: IRS² Satellite Conference: Infrared Sensor Applications: Non-destructiv

Chair: J. Hollandt, Physikalisch-Technische Bundesanstalt (PTB) , Berlin (Germany)

- C4.1 New Techniques in Super Resolution Photothermal Imaging for Nondestructive Testing** 169
S. Ahmadi, P. Hirsch, J. Lecompanion, C. Hassenstein, M. Ziegler, Bundesanstalt für Materialforschung und -prüfung, Berlin (Germany), P. Jung, G. Caire, Technical University of Berlin, Berlin (Germany)
- C4.2 Detection of Initial Subsurface Defects on Coated Glass-Fiber Reinforced Composite Components by Means of Active Micro-thermography** 171
F. Jensen, M. Sorg, A. Fischer, University of Bremen, Bremen (Germany)
- C4.3 Emissivity Measurement of Semitransparent Samples** 173
J. Gieseler, A. Adibekyan, C. Monte, J. Hollandt, Physikalisch-Technische Bundesanstalt (PTB), Braunschweig (Germany)
- C4.4 Measurement of ¹³C and ¹⁸O Ratio in CO₂ using Quantum Cascade Laser based Tunable Absorption Spectroscopy** 175
P. Nitzsche, C. Dinc, J. Wöllenstein, K. Schmitt, University of Freiburg, Freiburg (Germany)
- C4.5 FT-IR Coupled Goniometer Setup for Characterization of the Spatial and Spectral Emission of IR-Sources** 177
A. Eberhardt, C. Weber, M.-L. Bauersfeld, J. Wöllenstein, Fraunhofer Institute for Physical Measurement Techniques IPM, Freiburg (Germany)

C5: Thermometry and Thermal Imaging

Chair: G. Fischerauer, Universität Bayreuth, Bayreuth (Germany)

- C5.1 Using Spatial and Temporal Shaping for Laser-induced Diffuse Thermal Wave Fields in Thermography** 179
S. Ahmadi, M. Ziegler, P. Hirsch, J. Lecompanion, C. Hassenstein, E. Thiel, N. W. Pech-May, Bundesanstalt für Materialforschung und -prüfung, Berlin (Germany)
- C5.2 Application of Microwave based Electrical Read-Out of Fiber Bragg Gratings in Thermometry** 181
U. Nordmeyer, N. Neumann, X. Wang, D. Plettemeier, TU Dresden, Dresden (Germany), T. Thiel, AOS GmbH, Dresden (Germany), K. Kojucharow, KMDC, Dresden (Germany)
- C5.3 Thermographic Monitoring of Electrical Assets by Enhanced Thermal Images for Feature Extraction** 183
A. Boyaci, S. Wildermuth, ABB AG, Ladenburg (Germany)
- C5.4 Thermowells with Improved Response Time** 185
M. Schalles, Technische Universität Ilmenau, Ilmenau (Germany), P. Vrdoljak, C. Peuker, Endress+Hauser Temperature and System Products, Nesselwang (Germany)

C6: Optical Sensors and Measuring Systems

Chair: R. Tutsch, Technische Universität Braunschweig, Braunschweig (Germany)

- C6.1 Computational Laser Metrology using In Situ Calibration for Lensless Fiber Endoscopy** 187
J. Czarske, E. Scharf, R. Kuszmierz, TU Dresden, Dresden (Germany)
- C6.2 Microsecond Optical Frequency Tuning of DFB Laser Diodes for Coherent Optical Frequency Domain Reflectometry** 189
G. Saur, R. Kruglov, S. Schroll, R. Engelbrecht, Technische Hochschule Nürnberg Georg Simon Ohm, Nuremberg (Germany)
- C6.3 Investigation of a Metrological Atomic Force Microscope System with a Combined Cantilever Position, Bending and Torsion Detection System** 191
Y. Wu, E. Wirthmann, U. Klöpzig, T. Hausotte, Friedrich-Alexander-Universität Erlangen-Nürnberg, Erlangen (Germany)
- C6.4 Optical Multi-Distance Measurements of Spur Gears** 193
M. Pillarz, A. von Freyberg, A. Fischer, University of Bremen, Bremen (Germany)

Poster Session

P1: Chemical Sensors

- P1.1 Multi-Sensor System for Selective Methane Measurements in Harsh Environments** 195
H. Lensch, T. Sauerwald, A. Schütze, Saarland University, Saarbrücken (Germany), M. Müller, F. Braunecker, T. Dudziak, 3S GmbH - Sensors, Signal Processing, Systems, Saarbrücken (Germany), H. Brünnet, Schaller Automation Industrielle Automationstechnik GmbH&Co. KG, Blieskastel (Germany)
- P1.2 Compensation of Siloxane Poisoning of Metal Oxide Semi-Conductor Gas Sensors in Temperature Cycled Operation** 197
C. Schultealbert, T. Baur, T. Sauerwald, A. Schütze, Saarland University, Saarbrücken (Germany)
- P1.3 Smart Gas Sensor Systems can help to reduce Food Waste** 199
M. S. Marschibois, T. Sauerwald, A. Schütze, Saarland University, Saarbrücken (Germany), M. Leidinger, T. Conrad, 3S GmbH, Saarbrücken (Germany)
- P1.4 Systematic Investigations on the Reaction Potential of Catalytic Sensor Materials** 201
O. Yurchenko, H.-F. Pernau, L. Engel, B. Bierer, M. Jäggle, J. Wöllenstein, Fraunhofer Institute IPM, Freiburg (Germany)
- P1.5 The Optimization of a Photoacoustic Refrigerant Sensor System Using a Three-Chamber Concept** 203
M. El-Safoury, C. Weber, J. Wöllenstein, Fraunhofer Institute for Physical Measurement Techniques, Freiburg (Germany), O. Kiesewetter, UST Umweltsensortechnik GmbH, Geratal (Germany)
- P1.6 Multispectral Readout System for Detecting Tiny Color Changes of Gas Sensitive Colorimetric Dyes** 205
C. Weber, M. El-Safoury, C. Pannek, L. Engel, A. Eberhardt, M.-L. Bauersfeld, J. Wöllenstein, Fraunhofer IPM, Freiburg (Germany)
- P1.7 NO Detection by Pulsed Polarization with Pt interdigital Electrodes on Yttria Stabilized Zirconia** 207
N. Donker, M. Müller, D. Schönauer-Kamin, R. Moos, University of Bayreuth, Bayreuth (Germany), J. Zosel, A. Ruchets, Kurt-Schwabe-Institut für Mess- und Sensortechnik e.V. Meinsberg, Waldheim (Germany), U. Guth, Dresden University of Technology, Dresden (Germany)
- P1.8 Selective and Reliable Amperometric H₂O₂ Sensor Based on Au-ZnO Heterostructure Electrode** 209
S. Zhuiykov, M. Karbalaee Akbari, Gent University Global Campus, Incheon (South Korea)
- P1.9 Resonant Sensor for In-Situ Gas Detection in Heat Treatment Processes** 211
S. Schroeder, H. Fritze, Clausthal University of Technology, Goslar (Germany), A. Strauß, P. Quadbeck, Fraunhofer Institute for Manufacturing Technology and Advanced Materials, Dresden (Germany)
- P1.10 Errors in Relative Humidity Measurements Due to Slow Temperature Response** 213
H. Sairanen, Vaisala Oyj, Vantaa (Finland)
- P1.11 PVDF-SPEEK Blend Based Resistive Humidity Sensors** 215
Z. Ahmad, S. A. Mallick, F. Touati, Qatar University, Doha (Qatar)
- P1.12 Cure Monitoring using Single-Sided NMR** 218
N. Halmen, L. Mittelberg, E. Kraus, B. Baudrit, T. Hochrein, M. Bastian, SKZ – German Plastics Center, Würzburg (Germany)
- P1.13 Development of Disposable Antibiotic Drug Sensor Based on Screen-printed Electrode Modified with Magnetic Nanocomposites** 220
R. P. Poo-arporn, King Mongkut's University of Technology Thonburi, Bangkok (Thailand), Y. Poo-arporn, Synchrotron Light Research Institute, Nakhon Ratchasima (Thailand), S. Pakapongpan, Thailand Organic and Printed Electronics Innovation Center, Pathum Thani (Thailand)

P1.14 Fiber Optical Sensing System for Simultaneous Manometry, pH-metry and Bilimetry in Oesophagus	222
K. Schroeder, T. Habisreuther, M. Zeisberger, M. Becker, M. Rothhardt, Leibniz IPHT, Jena (Germany), F. Chiavaioli, F. Baldini, CNR, Institute of Applied Physics, Sesto Fiorentino (Italy), M. Hahn, O.-M. Rados, F. Mönkediek, OSCOMED GmbH, Sonneberg (Germany), S. Goerlich, J. Gäbler, JETI Technische Instrumente GmbH, Jena (Germany), A. Taddei, M. N. Ringressi, I. Bartolini, Careggi University Hospital, Firenze (Italy), P. Cecchi, Cecchi S.R.L., Firenze (Italy)	
P1.15 Mimiking Biological Sensorimotor Systems by Opto-electronic Artificial Neurobotics	224
S. Zhuiykov, M. Karbalaei Akbari, Gent University Global Campus, Yeonsu-gu, Incheon (South Korea)	
 P2: Sensors and Measurement Systems for Physical Quantities	
P2.1 Explosion Pressure Measurement and Thermal Shock	226
T. Krause, D. Markus, Physikalisch-Technische Bundesanstalt, Braunschweig (Germany), M. Meier, Kistler Instrumente AG, Winterthur (Switzerland)	
P2.2 Redundant Pressure Sensor Based on Steel and Ultra-Thin Glass Strain Gauges	228
D. Wachter, ZeMA gGmbH, Saarbrücken (Germany), G. Schultes, Hochschule für Technik und Wirtschaft des Saarlandes, Saarbrücken (Germany)	
P2.3 Miniaturized System for Vapor Pressure Measurement using a Combination of Knudsen Cell and Nanobalance	230
M. Schulz, H. Fritze, Clausthal University of Technology, Goslar (Germany)	
P2.4 Multifunctional Stick-Slip Sensor	232
K. Gintner, M. Weber, B. Beck, University of Applied Sciences Karlsruhe, Karlsruhe (Germany)	
P2.5 Investigations to Determine the Clamping Force of Screw Connections	234
T. Frank, A. Grün, H. Jayaprakash, M. Kermann, S. Jagomast, A. Cyriax, C. Maier, T. Ortlepp, Forschungsinstitut für Mikrosensorik GmbH, Erfurt (Germany)	
P2.6 Simulation of the Temperature Influence of an Inductive Sensor for the Geometry Detection of Rotating Components	236
C. Lehmann, M. Rogowski, S. Fisahn, H. Garbe, Leibniz Universität Hannover, Hannover (Germany)	
P2.7 Mode Analysis for Long, Undamped Cantilevers with Added Diamond Tips of Varying Length for Fast Roughness Measurements	238
H. Behle, U. Brand, Physikalisch-Technische Bundesanstalt, Braunschweig (Germany)	
P2.8 Smart Ratchet Tie-Down Straps for Monitoring Cargo Safety	240
Y. Wu, Z. Yan, BCM SENSOR TECHNOLOGIES bvba, Schoten (Belgium)	
P2.9 Packaging Concepts and Development Progress of Ceramic Thermocouples for up to > 1800 °C	242
P. Gierth, L. Rebenklau, B. Feng, H.-P. Martin, Fraunhofer IKTS, Dresden (Germany)	
P2.10 Validation of High-Temperature Stable Sensor Packaging Materials and Methods	244
P. Gierth, L. Rebenklau, H. Barth, Fraunhofer IKTS, Dresden (Germany)	
P2.11 Multiphysics Electro-Thermal Simulation of Pt Microheater Structures for Gas Sensing Application	246
F. O. V. Gomes, S. Linke, TE Connectivity Sensors Germany GmbH, Dortmund (Germany), P. Wafo, V. Leger, TE Sensor Solutions, Toulouse (France)	
P2.12 Equivalent Circuit Model and Evaluation of Inductive Conductivity Sensors	248
J. Förster, M. Mallach, T. Lange, KROHNE Innovation GmbH, Duisburg (Germany), M. Vogt, KROHNE Messtechnik GmbH, Duisburg (Germany)	
P2.13 Design of Planar Capacitive Transducers for the Detection of Road Surface Wetness	250
J. Döring, D. Lepke, K.-L. Krieger, University of Bremen, Bremen (Germany)	

P2.14 Resistance Wire Thermometers for Temperature Pulse Measurements on Internal Combustion Engines	252
V. Venkataraman, O. Stenlaas, A. Cronhjort, Y. Murai, M. Liverts, R. Örlü, J.H.M. Fransson, KTH Royal Institute of Technology, Stockholm (Sweden)	
P2.15 Power over POF – A Short Overview	254
S. A. Dengler, J. Fischer, M. Luber ¹ , O. Ziemann, H. Lenkowski, C. Schüßler, K. Carruth, P. Urbanek, Technische Hochschule Nürnberg Georg Simon Ohm, Nuremberg (Germany)	

Measurement Science

D1: Model-based Measurement

Chairs: E. Benoit, Université Savoie Mont Blanc, Chambéry (France),
F. Puente León, Karlsruhe Institut für Technologie, Karlsruhe (Germany)

D1.1 Minimal Model Selection for Calibrating a Hall-Stress- Temperature Multisensor System Using LASSO Regression	257
M. Berger, O. Paul, University of Freiburg, Freiburg (Germany), S. Huber, C. Schott, Melexis Technologies SA., Bevaix (Switzerland)	
D1.2 Precision Measuring Chain out of Reference Strain Gauge Sensor and Inductive-Voltage-Divider-Based Digital Amplifier	259
A. Schäfer, Hottinger Baldwin Messtechnik - HBM, Darmstadt (Germany)	
D1.3 Increasing the Sensitivity in the Determination of Material Parameters by Using Arbitrary Loads in Ultrasonic Transmission Measurements	261
D. Dreiling, N. Feldmann, B. Henning, Paderborn University, Paderborn (Germany), D. Itner, H. Gravenkamp, University of Duisburg-Essen, Essen (Germany)	
D1.4 Measurements at Laser Materials Processing Machines: Spectrum Deconvolution, Including Uncertainties and Model Selection	263
R. Behrens, B. Pullner, M. Reginatto, Physikalisch-Technische Bundesanstalt (PTB), Braunschweig (Germany)	

D2: AI-Approaches in Measurement

Chairs: A. König, Technische Universität Kaiserslautern, Kaiserslautern (Germany),
K.-D. Sommer, Technische Universität Ilmenau, Ilmenau (Germany)

D2.1 Artificial Intelligence with Neural Networks in Optical Measurement and Inspection Systems – Opportunities and Challenges	265
M. Heizmann, M. Ulrich, Karlsruhe Institute of Technology, Karlsruhe (Germany), A. Braun, University of Applied Sciences, Düsseldorf (Germany), M. Hüttel, Fraunhofer IPA, Stuttgart (Germany), C. Klüver, University of Duisburg-Essen, Essen (Germany), Erik Marquardt, VDI e. V., Düsseldorf (Germany), M. Overdick, SICK AG, Waldkirch (Germany)	
D2.2 Visualizing Neural Network Decisions for Industrial Sound Analysis	267
D. Johnson, J. Liebetrau, Fraunhofer Institute IDMT, Ilmenau (Germany), S. Grollmisch, University of Technology, Ilmenau (Germany)	
D2.3 Adaptive Algorithms for Linear Position Measurement Applications	269
A. Voss, A. Bartos, TE Connectivity Sensors Germany GmbH, Dortmund (Germany)	
D2.4 Lean Data with Edge Analytics: Decentralized Current Profile Analysis on Embedded Systems Using Neural Networks	271
T. Kufner, University Bayreuth, Bayreuth (Germany), A. G. Trenz, Fraunhofer IPA, Bayreuth (Germany), S. Schöning, Maxsyma GmbH & Co. KG, Floss (Germany)	
D2.5 Application of Machine Learning Algorithms for the Analysis of an Optical Fiber Sensor for Use in Endovascular Coiling of Intracranial Aneurysms	273
S. Shojaei Khatouni, J. C. E. Ewald, H. K. Trieu, Hamburg University of Technology, Hamburg (Germany)	

D3: Novel Measurement Approaches & Measurement Uncertainty

Chair: T. Fröhlich, Technische Universität Ilmenau, Ilmenau (Germany), Leslie Pendrill, SP Technical Research Institute of Sweden, Boras (Sweden)

- D3.1 Operational Measurement Uncertainty and Bayesian Probability Distribution** 275
 R. N. Kacker, National Institute of Standards and Technology, Gaithersburg, (USA), R. Kessel, Metrodata, Braunschweig (Germany), K.-D. Sommer, Technical University of Ilmenau, Ilmenau (Germany)
- D3.2 Light Stimulation of Gas Sensors with an LED Array in a Compact Setup** 277
 R. Falkowski, J. Joppich, T. Baur, T. Sauerwald, A. Schütze, Saarland University, Saarbrücken (Germany)
- D3.3 Analysis of Accuracy Requirements to the Meteorological Sensors used to Compensate for the Influence of the Earth's Atmosphere in High Precision Length Measurement** 279
 P. Neyezhnikov, V. Kupko, T. Panasenko, A. Prokopov, V. Skliarov, A. Shloma, National Scientific Centre "Institute of Metrology", Kharkiv (Ukraine)
- D3.4 Difficulties in Understanding and Teaching the Definition of the Kilogram in the Revised SI** 281
 J. Valdés, Universidad Nacional de San Martín, Buenos Aires (Argentina)

D4: Condition Monitoring

Chairs: G. Fischerauer, Universität Bayreuth, Bayreuth (Germany), A. Schütze, Universität des Saarlandes, Saarbrücken (Germany)

- D4.1 Optical Microphone-based Acoustic Response Analysis for Non-contact Non-destructive Testing** 283
 W. Rohringer, G. Kaniak, F. Lücking, N. Panzer, B. Fischer, XARION Laser Acoustics GmbH, Vienna (Austria)
- D4.2 Condition Monitoring of Machine Elements using Magneto-resistive Sensors** 285
 R. Slatter, Sensitec GmbH, Lahnau (Germany)
- D4.3 Inline Inspection of Ceramic Tape Casting Processes by Means of Optical and Eddy Current Methods** 287
 T. Härtling, M. Heymann, S. Münch, M. Schulze, Fraunhofer Institute for Ceramic Technologies and Systems IKTS, Dresden (Germany), B. Capraro, D. Schabbel, A. Vogel, Fraunhofer Institute for Ceramic Technologies and Systems IKTS, Hermsdorf (Germany)
- D4.4 Characterization of Sand and Sand-Binder Systems from the Foundry Industry with Impedance Spectroscopy** 289
 L. Bifano, A. Fischerauer, G. Fischerauer, Universität Bayreuth (Germany), A. Liedtke, Michenfelder Elektrotechnik, Mainz (Germany)
- D4.5 Non-destructive Validation Method for Understanding Water Uptake Processes of Moldings in Electronic Packaging** 291
 P. Gierth, L. Rebenklau, U. Gierth, U. Langklotz, M. Schneider, Fraunhofer IKTS, Dresden (Germany)

D5: Advanced Methods & Measurement Systems

Chair: E. Benoit, Université Savoie Mont Blanc, Chambéry (France)

- D5.1 An Approach for Feature Interpolation Between Classes to Simplify Calibration of Sensor Systems for Odour Monitoring** 293
J. Joppich, M. Bastuck, A. Schütze, T. Sauerwald, Saarland University, Saarbrücken (Germany)
- D5.2 Robust Optimization of Self-x Sensory Electronics in Presences of Environmental Variations for Industry 4.0** 295
Q. Zaman, S. Alraho, A. König, TU Kaiserslautern, Kaiserslautern (Germany)
- D5.3 Three-directional Drift Correction Method Based on Iterative Closest Point (ICP) Algorithm** ... 297
J. Degenhardt, G. Dai, Physikalisch-Technische Bundesanstalt, Braunschweig (Germany),
R. Tutsch, Technische Universität Braunschweig, Braunschweig (Germany)
- D5.4 Compensation of Strong Aberrations with a Time Reversal Virtual Array for Ultrasound Imaging** 299
L. Grüter, R. Nauber, C. Kupsch, J. Czarske, TU Dresden, Dresden (Germany)

D6: Inverse Problems in Measuring Technology

Chairs: B. Henning, Universität Paderborn, Paderborn (Germany),
B. Zagar, Johannes-Kepler-Universität Linz, Linz (Austria)

- D6.1 Determination of Murnaghan Constants of Plate-Shaped Polymers under Uniaxial Tensile Load** 301
S. Johannesmann, S. Becker, B. Henning, M. Webersen, Paderborn University, Paderborn (Germany)
- D6.2 Model-based Acoustic Identification of Hidden Layers** 303
S. Wöckel, H. Arndt, Institut für Automation und Kommunikation e.V., Magdeburg (Germany)
- D6.3 Guided Wave Based Characterization of Mechanical Parameters and Wall Thickness of Metal Tubes** 305
M. Ponschab, L. Petzold, D. A. Kiefer, S. J. Rupitsch, Friedrich-Alexander-University
Erlangen-Nürnberg, Erlangen (Germany)
- D6.4 Fundamentals of Dynamic Sensor Positioning with Nanoscale Accuracy by an Inverse Kinematic Concept** 307
G. Straube, S. J. Fischer Calderón, I. Ortlepp, E. Manske, Technische Universität Ilmenau,
Ilmenau (Germany)

E6: Applied Measurement Science

Chair: M. J. da Silva, Federal University of Technology Parana, Curitiba-PR (Brazil),
J. Valdés, Instituto Nacional de Tecnología Industrial, Buenos Aires (Argentina)

- E6.1 Towards 3D-Motion Tracking of Instrumented Flow Follow-ers in Large Vessels** 309
L. Buntkiel, S. Reinecke, U. Hampel, Helmholtz-Zentrum, Dresden-Rossendorf (HZDR),
Dresden (Germany)
- E6.2 Unmanned Aircraft Based Gamma Spectrometry System for Radiological Surveillance** 311
M. Luchkov, S. Neumaier, Physikalisch-Technische Bundesanstalt (PTB),
Braunschweig (Germany), A. Vargas, Technical University of Catalonia, Barcelona (Spain)
- E6.3 An Advanced Multi-Parameter Condition Monitoring System for Lubricants and Hydraulic Fluids** 313
T. Voglhuber-Brunnmaier, Johannes Kepler University, Linz (Austria), A. O. Niedermayer,
Micro Resonant Technologies, Linz (Austria)
- E6.4 Electro-magnetic Sensors for Online Condition Monitoring of Medium Voltage Cables** 315
M. Shafiq, K. Kauhaniemi, University of Vaasa, Vaasa (Finland), A. Hussain,
American University of Kuwait, Salmiya (Kuwait), L. Kutt, Tallinn University of Technology, Tallinn (Estonia)

Poster Session

P3: Advanced Methods and Approaches in Measurement

- P3.1 Blockchain Platforms as Solution for a Secure Data Transfer and a Secure Payment System From Sensor Supplier to Service Provider** 317
M. Haid, I. Boyaci, J. Biswas, N. Berezowski, CCASS University Darmstadt, Darmstadt (Germany)
- P3.2 Adaptable System for Diagnosing Sensor Faults for Application on Engine Test Benches** 319
M. Wohlthan, G. Pirker, LEC GmbH, Graz (Austria), A. Wimmer, Graz University of Technology, Graz (Austria)
- P3.3 Safety Sensor Applications with Graphical Programming** 321
N. Berezowski, M. Haid, J. Biswas, I. Boyaci, University of Applied Science Darmstadt, Darmstadt (Germany)
- P3.4 Fracture Detection of Bearings in Long-Term Measurements Using a Feature-Based CUSUM Algorithm** 323
A. Beering, A. Zitnikov, K.-L. Krieger, University of Bremen, Bremen (Germany)
- P3.5 Inductive Communication and Localization of Wireless Sensors in Photoreactors** 325
D. Demetz, A. Sutor, Institute of Measurement and Sensor Technology, UMIT – Private University, Hall in Tirol (Austria)
- P3.6 Indirect Geometry Measurement Method for In situ Application in Laser Chemical Machining** 327
M. Mikulewitsch, D. Stöbener, A. Fischer, University of Bremen, Bremen (Germany)
- P3.7 Experimental Set-up for Sensors Evaluation in a Controlled Environment** 329
A. Bescond, F. Gaie-Levrel, L. Bregonzio-Rozier, T. Macé, Laboratoire National de Métrologie et des Essais, Paris Cedex (France)
- P3.8 Form and Mid-Spatial-Frequency Measurement of Unknown Freeform Surfaces** 331
T. Binkele, D. Hilbig, M. Essameldin, T. Henning, F. Fleischmann, University of Applied Sciences Bremen, Bremen (Germany)
- P3.9 FEM Model of a Tactile Sensor Based on Inductance Measurements and Magnetosensitive Elastomer** 333
S. Gast, K. Zimmermann, University of Technology, Ilmenau (Germany)
- P3.10 Photonic Measurement System for Load Detection in a Neuro Interventional Training Model** .. 335
S. Shojaei Khatouni, L. Rennpferdt, H. K. Trieu, Hamburg University of Technology, Hamburg (Germany)
- P3.11 Plastic Material Classification Using Neural Network Based Audio Signal Analysis** 337
D. Johnson, T. Krüger, J. Liebetrau, Fraunhofer Institute IDMT, Ilmenau (Germany), S. Grollmisch, University of Technology, Ilmenau (Germany)

P4: Measurement Uncertainty and Mathematical Strategies

P4.1 Measurement Uncertainty Assessment for Virtual Assembly	339
M. Kaufmann, I. Effenberger, M. Huber, Fraunhofer Institute for Manufacturing Engineering and Automation IPA, Stuttgart (Germany)	
P4.2 Signal-to-Noise-Ratio Optimized Design of Rotating-Coil Magnetometers	341
P. Rogacki, L. Fiscarelli, S. Russenschuck, CERN, Meyrin (Switzerland), K. Hameyer, RWTH Aachen University, Aachen (Germany)	
P4.3 6 DoF Pose Estimation with im/irad Accuracy Based on Laser Multilateration	343
J. Nitsche, M. Franke, D. Heißelmann, Physikalisch-Technische Bundesanstalt, Braunschweig (Germany), N. Haverkamp, Carl Zeiss Industrielle Messtechnik, Oberkochen (Germany)	
P4.4 Estimate the Error of Offset Issue and Amplitude Mismatch of Atan2 Function	345
J. Zhou, M. Dietrich, P. Walden, Schaeffler Automotive Buehl GmbH & Co. KG, Bühl (Germany), J. Kolb, Schaeffler Technologies AG & Co. KG, Karlsruhe, (Germany), Martin Doppelbauer, Karlsruhe Institute of Technology, Karlsruhe (Germany)	
P4.5 Linear Regression Method for Measuring Characteristics of the ADC on Harmonic Test Signals	347
S. V. Sherstobitov, M. V. Karpova, All-Russian Scientific Research Institute of Physicotechnical and Radio Engineering Measurements(VNIIFTRI), Moscow (Russia)	
P4.6 Mathematical Measures for Calibration and Evaluation of Gas Sensor Data	349
R. Seifert, HybridSensorNet, Karlsruhe (Germany), H. Keller, Karlsruhe Institute of Technology, Eggenstein-Leopoldshafen (Germany)	
P4.7 Expanded Uncertainty Evaluation Taking into Account the Correlation Between Estimates of Input Quantities	351
P. Neyezhnikov, I. Zakharov, National Scientific Centre "Institute of Metrology", Kharkiv (Ukraine), O. Botsiura, Kharkiv National University of Radioelectronics, Kharkiv (Ukraine)	

System of Units and Metrological Infrastructure

E1: Traditional and Quantum-based Measurement Standards

Chair: J. H. Hendricks, National Institute of Standards and Technology, Gaithersburg, (USA)

- E1.1 Innovative Mass Standards for the Worldwide Transfer of the Redefined Unit Kilogram** 354
K. Lehmann, D. Knopf, F. Härtig, Physikalisch-Technische Bundesanstalt (PTB), Braunschweig (Germany)
- E1.2 SI Realization of the farad at LNE** 356
A. Imanaliev, O. Thevenot, K. Dougdag, F. Piquemal, LNE, Trappes (France)
- E1.3 Studies on the Use of Bandgap References as a Voltage Standard** 358
B. Schumacher, C. Rohrig, Physikalisch-Technische Bundesanstalt, Braunschweig (Germany), G. Weckwerth, wekomm engineering GmbH, Planegg (Germany)
- E1.4 Photonic Thermometry at PTB – Challenges and Perspectives for Contact Temperature Metrology Utilizing Optical Sensors** 360
S. Krenek, R. Eisermann, S. Rudtsch, Physikalisch-Technische Bundesanstalt, Berlin (Germany), G. Winzer, Leibniz-Institut für innovative Mikroelektronik, Frankfurt an der Oder (Germany), T. Habisreuther, Leibniz-Institut für Photonische Technologien, Jena (Germany)

E2: Future Topics in Metrology

Chairs: S. Eichstädt, Physikalisch-Technische Bundesanstalt, Berlin (Germany), P. Ulbig, Physikalisch-Technische Bundesanstalt, Braunschweig (Germany)

- E2.1 Intriduction “Future Topics in Metrology”** 362
S. Eichstädt, Physikalisch-Technische Bundesanstalt, Berlin (Germany)
- E2.2 Isemantic Information in Sensor Networks** 364
M. Gruber, Physikalisch-Technische Bundesanstalt, Berlin (Germany), B. Seeger, Physikalisch-Technische Bundesanstalt, Braunschweig (Germany)
- E2.3 Propagation of Uncertainty for an Adaptive Linear Approximation algorithm** 366
T. Dorst, S. Eichstädt, Physikalisch-Technische Bundesanstalt, Braunschweig and Berlin (Germany), T. Schneider, ZeMA – Center for Mechatronics and Automation Technology gGmbH, Saarbruecken, (Germany), A. Schütze, Saarland University, Saarbruecken (Germany)
- E2.4 Deep Neural Networks for Optical Form Measurements** 368
L. Hoffmann, C. Elster, Physikalisch-Technische Bundesanstalt, Berlin, (Germany)

E3: Traceability, New Calibration and Testing Methods

Chair: P. Neyezhnikov, National Scientific Centre, Kharkiv (Ukraine)

- E3.1 Metrological Support of VNIIFTRI for Air Ions Measurements** 370
P. N. Zubkov, N. G. Oganyan, All-Russian Scientific Research Institute of Physicotechnical and Radio Engineering Measurements (VNIIFTRI), Moscow (Russia)
- E3.2 Traceable Measurements of Harmonic (2 – 150 kHz) Emissions in Smart Grids** 372
D. Istrate, D. Amaripadath, LNE, Trappes (France), E. Toutain, EDF, Moret-sur-Loing (France), R. Roche, F. Gao, Univ. Bourgogne Franche-Comté, Belfort (France)
- E3.3 Calibration Service as a Gateway to Sustainable Research and Development** 374
M. Melzer, M. Fischer, M. Thomas, A. Subaric-Leitis, M. Bartholmai, Bundesanstalt für Materialforschung und -prüfung (BAM), Berlin (Germany)
- E3.4 Calibration of Digital Dynamic Pressure Sensors** 376
R. Yilmaz, Y. Durgut, A. Hamarat, TUBITAK UME, Kocaeli (Turkey)

E4: Advanced Measurement and Testing, Regulations

Chair: M. Bartholmai, BAM Bundesanstalt für Materialforschung und -prüfung, Berlin (Germany)

E4.1	Statistical Analysis of Nonlinear Time Series Based on Bearing Dynamic Response	378
	N. Meier, A. Georgiadis, Leuphana University of Lüneburg, Lüneburg (Germany), B. Ambrozkiwicz, G. Litak, Lublin University of Technology, Lublin (Poland)	
E4.2	Outline for a Radiometric Unit of Measure to Characterize SWIR illumination	380
	M. Hübner, HENSOLDT Optronics GmbH, Oberkochen (Germany), A. Richards, FLIR Systems Inc., Wilsonville (USA)	
E4.3	Measurement Uncertainty Consideration of Electric Field Meters	382
	C. Schierding, M. Thedens, M. Beyer, Physikalisch-Technische Bundesanstalt, Braunschweig (Germany)	
E4.4	Higher Accuracy for Absolute Magnetic Position Measurement	384
	T. Becker, BOGEN Electronic GmbH, Berlin (Germany)	
E4.5	Study the Co-C/Re-C Eutectics Fixed Point Measurements For High Temperature Radiation Thermometer	386
	H. Ko, J. Liu, S. Liao, C. Yeh, C. Chen, Industrial Technology Research Institute, Hsinchu (Taiwan)	

E5: Creative Metrology: From Research to Industry 4.0Chairs: B. Jeckelmann, Eidgenössisches Institut für Metrologie METAS, Bern-Wabern (Switzerland),
Sandrine Gazal, CIM, Villeurbanne Cedex (France)

E5.4	Design and Implementation of Smart Multisensor Monitoring System for Safe Workplaces with LoRaWAN	388
	S. Johann, A. Lapalus, C. Tiebe, M. Bartholmai, Bundesanstalt für Materialforschung und -prüfung, Berlin (Germany)	

Keywords	390
-----------------------	------------

Plenary Talks

Measurement and Sensor Technology in the Digital Transformation Process

Ulrich Kaiser¹, Klaus-Dieter Sommer²

¹ *Endress+Hauser AG, Kägenstr. 2, 4153 Reinach, Switzerland,*

² *TU Ilmenau, Ehrenbergstraße 29, 98693 Ilmenau, Germany*
ulrich.kaiser@endress.com, klaus-dieter.sommer@tu-ilmenau.de

Summary:

The use of digital technologies can also lead to an increase in productivity and functionality for measurement and sensor technology. The prerequisite is that sensors are made "smart" and become components of the "Internet of Things" in an IoT ecosystem. Then optimizations are possible in many ways.

Keywords: Internet of Things, IoT Ecosystem, Calibration, Soft Sensors, Information security

Industry 4.0 is the use of digital technologies, including especially the Internet technologies, in industrial automation. This transformation is expected to lead to enormous gains in productivity and flexibility. Measurement and sensor technology are an essential component of automation and is therefore doomed to participate in this transformation. Because of this late entry, however, it can rely on already existing, mature technologies and infrastructures, such as powerful hardware controllers, networks and cloud architectures from the IT and consumer world.

Smart sensors in an IoT Ecosystem

In order to be able to use and benefit from the methods of digitization, a number of important prerequisites must be met: the essential elements of a technical system, the sensors, but also the actuators must become "smart" [1]. They must have connectivity and communication capabilities to be part of the Internet of Things (IoT). And they must be capable of self-diagnosis and - as a goal - also be capable of their own maintenance, such as self-validation or even self-calibration. Then, an adapted architecture of the control system and a platform for the execution of the methods, the IoT ecosystem, is needed. For new technical systems to be created, this ecosystem can include the control system. However, the majority of today's implementations are based on the existing architecture of the automation pyramid and connect the IoT ecosystem via a separate communication channel at the field level.

Diagnostics and predictive maintenance

Digitization offers the potential to move from preventive maintenance to predictive maintenance, thus reducing maintenance costs and increasing the technical health of the system too. There are two different approaches. On the one hand, statistical methods, with which maintenance events can be predicted from a large amount of other information, and on the other hand - in knowledge of the underlying physical and chemical interrelationships - the recording of suitable indicators for maintenance requirements using sensors. In [2] the requirements for these sensors for condition monitoring and predictive maintenance for use in chemical process plants are described.

Calibration

To maintain its metrological quality, a sensor needs regular calibration, where its measured value must be traceable to a reliable reference and thus ultimately to the SI. In many cases, today, this requires the sensor to be removed from the system, which is costly and disadvantageous for operation. This traditional requirement is opposed to the necessary sharp increase in the use and application of measuring and sensor systems in automated and partially autonomous production. Desirable here would be sensors that either ideally no longer need to be calibrated or having very long calibration intervals that are in line with the maintenance cycles of the respective technical system. One approach to the solution is sensor-internal verification. This involves subjecting all or most of the components relevant to the metrological

quality of a sensor to ongoing internal sensor verification based on the available sensor internal and also external information, including the use of redundant information of the system under consideration. This therefore allows to reduce the probability of erroneous measurements combined with a reduction of the calibration effort. Of course, it would be ideal if a reference directly traceable to the SI were part of a sensor and calibration could be performed anywhere and anytime without external intervention. Such developments are already underway in some large metrology laboratories. There are interesting developments such as the NIST on a Chip [3] The NIST-on-a-Chip project [3] appears to be particularly advanced with micro-technologically realized traceable quantum-based reference standards built into the sensor [3].

Soft Sensors

Soft sensors are measuring systems where difficult to measure variables are determined from a number of more easily to measure variables (measurands). Either because the measurand cannot be measured directly, the measurement location is not accessible or a value to be measured in the future is required. The relationship of the measured quantities to the target quantity is either known, i.e. model-driven, or must be learned, i.e. data-driven. The latter is more appropriate, because it allows the mapping of complex dependencies with many input variables that are no longer easy to model [4]. However, there are also combinations of both methods in place. For the data-driven methods, the technique of machine learning comes into play. Machine learning has been booming in recent years. However, the necessary completeness and quality of training data

is still a challenge. IoT Ecosystems are ideal platforms for implementing such Soft Sensors.

Information security for measurement and sensor technology

Smart sensors in IoT ecosystems are more vulnerable to cyberattacks than in isolated, proprietary systems because of their principle greater openness. Sensor data can be manipulated or unauthorized "overheard"; communication connections can be interrupted. Here too, measurement and sensor technology can build on the experience already acquired in information technology. A large arsenal of procedures and techniques is available for the information security of technical systems [5].

References

- [1] Maiwald, Michael. Die Technologie-Roadmap „Prozess-Sensoren 4.0“ – Chancen für neue Automatisierungskonzepte und neue Geschäftsmodelle. ATP Plus - Das Magazin der Automatisierungstechnik (2016)
- [2] U. Hampel et al. Sensorik für die Digitalisierung chemischer Produktionsanlagen. ProcessNet Fachgesellschaft, Dechema e.V. (2020)
- [3] National Institute of Standards and Technology (NIST) (2018)
<https://www.nist.gov/pml/productservices/nist-chip-portal/nist-chip-overview>
- [4] Michael Heizmann, Klaus-Dieter Sommer. Expertenforum Trends in der industriellen Mess- und Automatisierungstechnik – Von der Messung zur Information. tm – Technisches Messen 2019; 86(11): 619-622
- [5] IEC 62443 Industrial communication networks

NIST on a Chip: Revolutionizing Metrology through Deployable, Quantum-Based Sensors

Barbara Goldstein¹

¹ National Institute of Standards and Technology, Physical Measurement Laboratory, 100 Bureau Drive, Gaithersburg, MD 20899, barbara.goldstein@nist.gov

Summary:

This talk provides an overview of the NIST on a Chip program, which is transforming how precision measurements are delivered through a suite of fit-for-purpose, quantum-based, traceable sensors. A brief history of the program will be provided, and examples from the program will be used to highlight how the redefinition of the SI, nanofabrication and integrated photonics, and the quantum revolutions have enabled this completely new approach to metrology, which in turn is enabling the fourth industrial revolution. The talk will include a discussion of sensors versus standards, and the importance of public-private partnerships.

Keywords: Quantum Revolution, Metrology, Redefinition of the SI, Industry 4.0, Technology Readiness

NIST on a Chip Vision

NIST has embarked on a sweeping program called “NIST on a Chip” (NOAC) that will revolutionize measurement services and metrology by bringing them out of the lab and directly to the user. To that end, NIST is developing a suite of intrinsically accurate, quantum-based measurement technologies intended to be deployed nearly anywhere and anytime, performing uninterrupted without the need for NIST’s traditional measurement services.

These quantum-based measurement technologies will enable users to make precision measurements referenced to the International System of Units (SI) on factory floors, in hospital diagnostic centers, in commercial and military aircraft, in research labs, and ultimately in homes, automobiles, personal electronic devices, and more. NOAC thus provides an opportunity for the “democratization” of measurement technology, where affordable devices drastically reduce the cost and increase the availability of precise measurements that could previously only be delivered at the world’s best metrology institutes.

NOAC will meet those goals by creating prototypes for a new generation of ultra-compact, inexpensive, low-power measurement tools for quantities including time and frequency, distance, mass and force, temperature and pressure, electrical and magnetic fields, current and voltage, and fluid volume and flow. The program envisions eventually combining multiple measurement capabilities onto an integrated

platform to enable, for example, a single, embeddable chip that senses absolute temperature, pressure, and humidity to immediately detect any excursions in safe storage conditions of sensitive goods, such as vaccines or food. Other applications will leverage inexpensive mass fabrication, leading to applications such as a chip-scale radiation monitor that could be embedded in every driver’s license or other ID card to serve as a ubiquitous monitor or early-warning system for radiation exposure.

These NIST-pioneered technologies will be manufactured and distributed by the private sector, opening new technology transfer and lab-to-market opportunities in accordance with NIST’s goal of strengthening U.S. economic competitiveness by supporting advanced manufacturing.

Defining Criteria for NOAC Devices

The integrated NOAC program will develop and deploy practical quantum-based standards and sensors, traceable to the new international system of units (SI), that are:

Deployable to where customers need them, such as on the factory floor, embedded into products, in a laboratory environment, in space or at home.

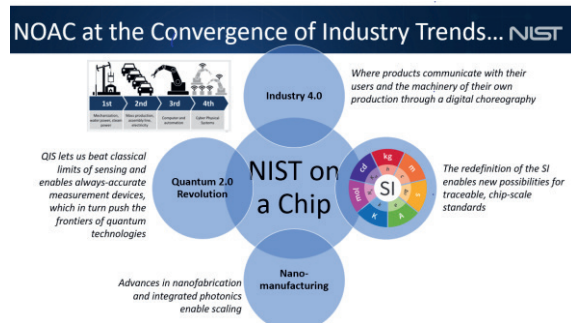
Flexible, providing a broad range of “zero chain” SI-traceable measurements and standards that are configurable into a single small-form package and adaptable to customers’ requirements.

Manufacturable, with production costs that scale appropriately for applications, such as low-cost/high-volume for broad deployment.

Reliable, providing either the right value of a measurement or no value at all.

Fit-to-Function, tending towards small size, low power consumption, rugged, easily integrated and operated, with an operating range and uncertainty required by the application.

Propitious Timing



NOAC innovations will be increasingly valuable to industry, medicine, defense, and science because of the current convergence of major trends in technology advancement. For example, Industry 4.0 is an optimization strategy in which the machinery of industrial production no longer simply “processes” the product, but the product communicates with that machinery in a digital choreography of production.

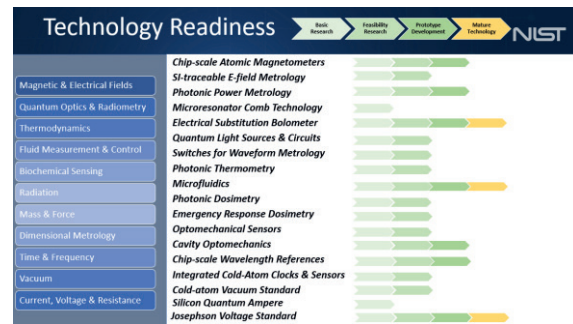
This approach will come to redefine the consumer-manufacturer relationship, as products in the field (i.e., in the Internet of Things) communicate back to the manufacturing ecosystem that produced them (the Industrial Internet of Things) to influence everything from next-generation product design, supply chain management, peer-to-peer consumer networking, product maintenance and end-of-life. This new paradigm won't be possible without accurate sensors both in the field and in the plant to provide reliable information to drive automated, machine-to-machine communication and decision making.

At the same time, the emergence of the second quantum revolution – which depends on the control and manipulation of matter at the most fundamental levels – will spur a new generation of technologies based on phenomena such as entanglement and superposition. The preservation and manipulation of these very fragile quantum states will require reliable, in-situ sensors and measurements, a NOAC goal. In addition, advances in quantum information science will enable unprecedented advances in measurement precision and thus fuel a new

generation of quantum-accurate standards and measurements.

Finally, the explosive demand for high-speed transfer of ever-larger volumes of data will benefit directly from NOAC's pioneering work in miniaturized photonic channels, novel signal transduction schemes, and accurate calibration standards for devices that must operate at unprecedented frequencies.

Portfolio at a Glance



NOAC technologies are at varying stages of technology readiness. NIST is actively building partnerships with industry, both domestically and globally, to bring these innovations from lab to market.

Realising the Redefined Kelvin

*Graham Machin*¹, *M. Sadli*², *A. Peruzzi*³, *J. Pearce*¹, *J. Engert*⁴, *R. Gavioso*⁵

¹*National Physical Laboratory (NPL), Teddington, TW11 0LW, UK*

²*LNE-CNAM, Laboratoire commun de métrologie, 93210 Saint-Denis, France*

³*VSL, Thijssseweg 11, 2629 JA Delft, Netherlands*

⁴*Physikalisch-Technische Bundesanstalt (PTB), Abbestr. 2-12, 10587 Berlin, DE*

⁵*Instituto Nazionale di Ricerca Metrologica (INRIM), 91 Strada delle Cacce, 10135, Torino, Italy*

Corresponding Author's e-mail address: graham.machin@npl.co.uk

Summary:

The redefinition of the SI unit the kelvin in May 2019 has opened new possibilities for the realization, dissemination and measurement of temperature. Besides the two practical scales that were in place before the redefinition, now, through the mechanism of the *mise en pratique* for the definition of the kelvin, temperature can be realized and disseminated through primary thermometry approaches with direct traceability to the redefined kelvin. In the medium to long term practical primary thermometry approaches could be developed allowing for in-process driftless thermometry.

Keywords: kelvin redefinition, primary thermometry, temperature scales, ITS-90, PLTS-2000

Introduction

The redefinition of the kelvin resulted from co-ordinated global activity by the thermometry community [1-4]. The redefinition, in terms of a defined value of the Boltzmann constant [1], has opened new possibilities for realizing and disseminating temperature. Instead of the two defined scales, the International Temperature Scale of 1990 (ITS-90, [5]) and the Provisional Low Temperature Scale of 2000 (PLTS-2000, [6]), being the accepted means of attaining traceability, now a more flexible approach, by the *mise en pratique* for the definition of the kelvin (*MeP-K-19*) [7, 8] is possible. The *MeP-K-19* details how to attain temperature traceability by means of primary thermometry without recourse to any defined scale.

In this paper the possibilities for temperature realization and dissemination, linked to the redefined kelvin, are discussed, mainly in the context of the European Metrology Programme for Innovation and Research (EMPIR) project "realising the redefined kelvin" (Real-K) [9].

An outlook of the impact of the kelvin redefinition on the practice of thermometry in the short, medium and longer term, including on the practice of practical thermometry, is given.

Required progress and challenges

To turn the *MeP-K-19* into a reality requires substantial research effort. The aim of the EMPIR Real-K project is to begin this process through the following research activities:

At high temperatures >1235 K indirect primary radiometry will be used to directly link to the redefined kelvin, via known temperature high temperature fixed points (HTFPs) [2, 10]. Low uncertainty thermodynamic temperatures of Fe-C (1426 K), Pd-C (1765 K), Ru-C (2226 K) and WC-C (3020 K); will be determined. Both realisation *and* dissemination of thermodynamic temperatures >1300 K with uncertainties like the ITS-90 ($U < 0.05\%$) will be demonstrated.

At temperatures <25 K the ITS-90 is complex to establish and disseminate and hardly ever realised in practice. Primary thermometry techniques will be established for the realisation and dissemination of thermodynamic temperature from 1 K and 25 K to provide a direct link to the redefined kelvin, as well as ensuring a smooth transition to the PLTS-2000 range (i.e. <1 K).

To give time for primary thermometry techniques to become established in the intermediate temperature region (25 K - 1235 K) life extension research addressing two of the ITS-90's most pressing problems will be performed; namely reducing non-uniqueness uncertainty by 30% in calibration of platinum resistance thermometers and preparing a suitable fixed-point replacement for the mercury triple point (e.g. CO₂ or SF₆) including addressing integration of a replacement fixed point within ITS-90.

To facilitate the uptake of primary thermometry in the intermediate temperature region (>25 K) thermophysical properties of gases (e.g. He, Ne, Ar) are required over a wide range of condi-

tions. These will be determined by *ab initio* calculations and experiment. These values will be used to reduce the attainable uncertainties by primary thermometry, which are, with a few exceptions, currently uncompetitive with the ITS-90.

These are only the first steps towards realising the redefined kelvin. Progress will be monitored closely by the CIPM Consultative Committee of Thermometry, especially its Strategy Group, to ensure on-going fitness of realisation and dissemination of the temperature unit.

Impact of the kelvin redefinition

Here the impact of the kelvin redefinition both the short to long term implications and the potential impact on the practice of thermometry in the wider user community will be discussed.

In the *short term* the current temperature scales will be used to provide temperature traceability. For those requiring thermodynamic temperature, the $T - T_{90}$ and $T - T_{2000}$ data available in the *MeP-K-19* annexes will allow users to access thermodynamic values.

In the *medium to long term* primary thermometry, directly linked to the redefined kelvin, could supplant the defined scales for realisation and dissemination of the unit. Primary thermometry may do this when similar uncertainties can be attained to the current defined scales. These developments may by the mid-2020s, lead to the ITS-90 (>1235 K) being superseded by relative primary radiometry. On a similar time-scale, for temperatures <25 K, different approaches to primary thermometry (variants of Johnson Noise <1 K, or acoustic gas or polarising gas thermometry <25 K) may provide sufficiently reliable low uncertainty thermodynamic temperatures so that the PLTS-2000 the ITS-90 (<25 K) could be superseded by low temperature primary thermometry.

For a time primary thermometry, the ITS-90, and the PLTS-2000 will co-exist. But in the long-term (2030s+) progressive elimination of the defined scales may be possible as primary thermometry for temperature realisation and dissemination becomes increasingly adopted. The ITS-90 may become the last defined temperature scale, though a restricted-range scale may be needed at intermediate temperatures (the so-called ITS-20XX [11]). Nevertheless, the redefinition of the kelvin has opened the way for improvements in thermometry that can be introduced through the *MeP-K-19* with no disruption to the user community.

Implications for science and industry

The redefinition of the kelvin, may lead to *practical* primary thermometry. Thermometers where there is a direct link to the redefined kelvin will become available. Advances in practical Johnson Noise thermometry [12] is an early version of this. In fact if *in-situ* practical primary thermometry were to become a reality then the need to calibrate temperature sensors would ultimately be un-necessary. These new sensing methods are essential if autonomous production is to be a reality.

Summary

The kelvin redefinition has ushered in a paradigm change in the field of thermometry. Temperature realization and dissemination will increasingly be based on direct linkage to primary thermometry and in the long-term users will turn to self-calibrating practical primary thermometry to address their thermometry needs.

References

- [1] Fischer, J., *et. al.* "The Boltzmann Project", *Metrologia*, **55**, R1-R20 (2018)
- [2] Machin, G., *et. al.* "Summary of achievements of the EMRP project implementing the new kelvin (InK)", *Measurement*, **94**, 149-156 (2016)
- [3] Machin, G., "Towards implementing the new kelvin" *Phil. Trans R. Soc. A.* **374**: 20150053, (2016)
- [4] Machin, G., Engert, J., Gianfrani, L., H McEvoy, H., Sparasci, F., "The European Metrology Programme for Innovation and Research project: Implementing the new kelvin 2 (InK2)", *XXII World Congress of the International Measurement Confederation (IMEKO 2018) IOP Conf. Series: Journal of Physics: Conf. Series* **1065** (2018) 122002
- [5] Preston-Thomas, H., "The international temperature scale of 1990", *Metrologia*, **27**, 3-10 (1990)
- [6] Rusby, R.L., *et. al.* "The provisional low temperature scale from 0.9 mK to 1 K the PLTS-2000", *J. Low. Temp., Phys.* **126**, 633-42 (2002)
- [7] Fellmuth, B., *et. al.* "The kelvin redefinition and its *mise en pratique*", *Phil. Trans R. Soc. A.* **374**: 20150037 (2016)
- [8] <https://www.bipm.org/utis/en/pdf/si-mep/SI-App2-kelvin.pdf>
- [9] <https://real-k.aalto.fi/>
- [10] Machin, G., "Twelve years of high temperature fixed point research: a review", *AIP Conf. Proc.* **1552**, 305 (2013)
- [11] Machin, G., "The Kelvin redefined", *Meas. Sci. Technol.*, **29**, 022001 (11pp) (2018)
- [12] Bramley, P., Cruickshank, D., Pearce, J., "The development of a practical, drift-free, Johnson-Noise Thermometer for industrial applications", *Int. J. Thermophys.*, **38**, 25 (2017)

NIST on a Chip: Photonic and Quantum-Based Sensors for Measurements of Pressure, Vacuum, Temperature and Beyond!

J Hendricks, Z Ahmed, D Barker, K Douglass, S Eckel, J Fedchak, N Klimov, J Ricker, J Scherschligt

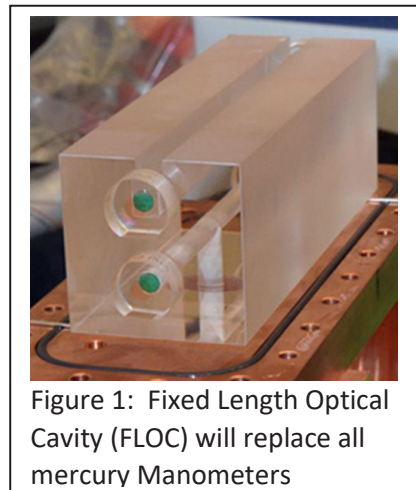
National Institute of Standards and Technology, Physical Measurement Laboratory, ¹Sensor Science Division, Thermodynamic Metrology Group, 100 Bureau Drive, Gaithersburg, MD 20899-8363
E-mail: jayh@nist.gov

Abstract At the core of the NIST on a Chip (NoAC) program is the idea that measurement technology can be developed to enable metrology to be done “outside the National Metrology Institute” by virtue of deployed and often miniaturized standards (that can also serve as sensors) that are based on fundamental properties of nature and are therefore directly traceable to the international system of units known as the SI. Nested within this idea is the development of quantum-based standards for SI traceability, what NIST is now calling, QSI, or Quantum based International System of units. More specifically, this paper will cover NIST efforts in the area of thermodynamic metrology relating to pressure, vacuum and temperature measurements.

Introduction: For pressure measurements, this paper will cover NIST efforts to eliminate mercury manometers with a photonic based measurement based on ultra-precise measurements of gas refractive index. For vacuum measurements, this paper covers NIST efforts to develop a new a vacuum standard for measuring and understanding the pascal at the lowest pressures through the development of a cold atom vacuum standard. For temperature measurements, this paper covers NIST efforts to develop a method of measuring temperature using a photonic-based method.

The unifying theme is that all these efforts are aimed at the development of standards and sensors that are small, deployable, and based on fundamental physics, or are quantum-based. This has been embodied within the “NIST on a Chip” or NOAC program. The core the idea of NOAC is that quantum-based measurements are fundamental and when employed in sensors will not require re-calibration. In this embodiment, the standards lab, or in this case “NIST”, is “on a chip” and is powerful to industry and society as it means that large networks sensors (or sensors “integrated” into a product or device) can be deployed and trusted to provide accurate measurements without costly re-calibration.

Pressure: Moving forward, the next generation of pressure standards will provide a new route of SI traceability for the pascal. By taking advantage of both the properties of light interacting with a gas and that the pressure dependent refractive index of helium can be precisely predicted from fundamental, first-principles quantum-chemistry calculations, a new route of realizing the pascal has been demonstrated. This technique is very different from classical methods of realizing pressure that have served the metrology community well for the past 375 years. The new photonic-based pressure standards that will enable the elimination of mercury manometers, replacing them with a smaller, lighter, faster, and higher precision standard. From a metrology standpoint, the new quantum-based SI pascal will move us from the classical force/area definition, to an energy density (joules per unit volume) definition. Should the technique be further



miniaturized, it will lead to a revolution in pressure metrology, enabling a photonics-based device that serves both a gas pressure sensor and a portable gas pressure standard all in one. In the future, the mercury barometer will be replaced with a new standard based on quantum chemistry calculations.

The new method relies on a pair of optical cavities, each consisting of a set of mirrors on a spacer with the gas/vacuum filling the space between the mirrors. To improve upon this design, the reference cavity is always kept at vacuum to help eliminate noise and other systematic errors. This device, referred to as a Fixed Length Optical Cavity (FLOC), is shown in Figure 1. The FLOC made out of a glass with Ultra-Low thermal Expansion (ULE) to prevent changes in interferometer length with temperature. The upper cavity consists of a slot to allow gas to easily flow in and out whereas the reference cavity is a hole drilled through the glass block and sealed at either end via mirrors. [1-4]

Additionally, a vertical tube allows one to pump out the reference cavity through a vacuum pump. The glass cavity is placed inside a chamber to improve temperature stability and to ensure that the gas species is known, and therefore has a known refractivity. For gasses such as helium with simple electron structure and limited number of isotopes, the refractivity and density virial coefficients can be calculated through quantum mechanics [2]. This calculation can provide refractivity to an uncertainty better than 1 parts in 10^6 . For other gasses, the values must be measured or will be calculated but with significantly larger uncertainties. Because the calculation of pressure is only dependant on refractivity and temperature, we can define the FLOC as a primary realization of pressure.

The FLOC is primary but does requires corrections be carefully accounted for when making a high accuracy pressure measurement with the lowest possible uncertainties. The first correction is the distortion of the glass when pressure is applied. The glass experiences a bulk compression when forces to the outside surfaces occur. In addition to the bulk compression, the glass experiences a non-uniform bending due to the reference cavity being at a different pressure. While these distortion corrections are different for each glass cavity; the value can be determined experimentally and corrected with high accuracy. The second correction that must be accounted for is that helium can absorb into glass causing the glass to change its dimensions. By collection interferometer data the absorption can be traced over time and extrapolated back to zero, with high accuracy.

Overall a FLOC standard can achieve an uncertainty of 9 parts in 10^6 in nitrogen [4]. It is anticipated that a better determination of this index will soon allow this to be drastically reduced. Additionally, the best method to measure pressure distortions is to use several gasses of known refractive index at the same pressure. The distortions will be independent of gas species and can be solved to determine the magnitude of the error and even lower uncertainties. This means that as lower and lower uncertainty refractivity measurements are made by independent labs, the lower the uncertainty the FLOC method becomes world-wide. This is the power of quantum-based measurements.

Vacuum: For vacuum measurements, NIST efforts to develop a new vacuum standard for measuring and understanding the pascal at the lowest pressures is underway. To achieve this, the Cold- Atom Vacuum Standard (CAVS) has been developed which uses a cold atom trap to sense pressure. [5] Since the earliest days of neutral atom trapping, it has been known that the background gas in the vacuum limits the trap lifetime (the characteristic time that atoms remain trapped). NIST is inverting this problem to create a quantum-based standard and sensor. Because the measured loss-rate of ultra- cold atoms from the trap depends on a fundamental atomic property (the loss-rate coefficient, related to the thermalized cross section) such atoms can be used as an absolute sensor and primary vacuum standard. Researchers have often observed that the relationship between the trap lifetime and background gas can be an indication of the vacuum level, and several research groups have pursued using cold atom traps as vacuum sensors. [6,7] However, an absolute vacuum standard, sufficient for use as an international quality standard, has not yet been realized. To do this requires rigorous attention to all potential error sources, from both the atomic perspective and the vacuum perspective. Moreover, a primary CAVS requires the collision cross section between trapped ultra-cold atoms and the background gas to be traceable to an ab initio theoretical determination. NIST has built a laboratory-scale CAVS apparatus, developed the measurement scheme, and done preliminary theoretical calculations, all of which show promising early results. In addition, NIST is developing a small, portable version that uses a grating-based trap (shown in the Figure 2) that will eventually enable users to realize and measure vacuum pressures in their lab without relying on calibrated sensor artifacts. [8]

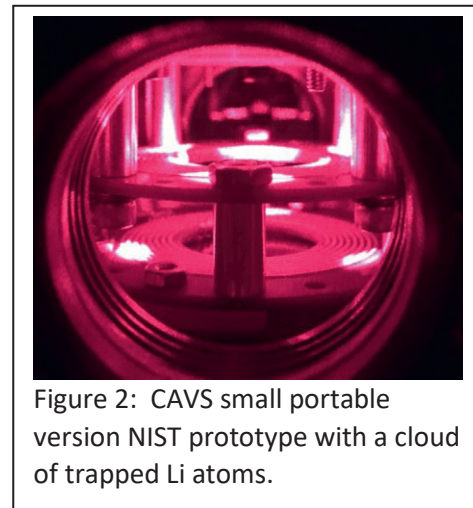


Figure 2: CAVS small portable version NIST prototype with a cloud of trapped Li atoms.

Temperature: For temperature measurements, NIST efforts to develop a method of measuring temperature using a photonic-based method are underway. Temperature measurements and sensors play a crucial role in various aspects of modern technology ranging from medicine and manufacturing process control, to environmental and oil-and-gas industry. Among various temperature measurement solutions, resistance-based thermometry is a time-tested method of disseminating temperature standards. [9] Although industrial resistance thermometers can routinely measure temperatures with uncertainties of 10 mK, their performance is sensitive to multiple environmental variables such as mechanical shock, thermal stress and humidity. These fundamental limitations of resistance thermometry, as well as the desire to reduce sensor ownership cost have ignited a substantial interest in the development of alternative temperature measurement solutions such as photonics-based temperature sensors [10,11]. NIST is developing novel on-chip integrated silicon photonic temperature sensors with nanoscale footprint and ultra-high resolution as an alternative solution to legacy-based resistance thermometers. These sensors are Fabry-Perrot cavity type silicon photonic devices that are based on Photonic Crystal nanobeam Cavity (PhCC), whose high-Q resonant frequency mode is highly sensitive to even ultra-small temperature variations.

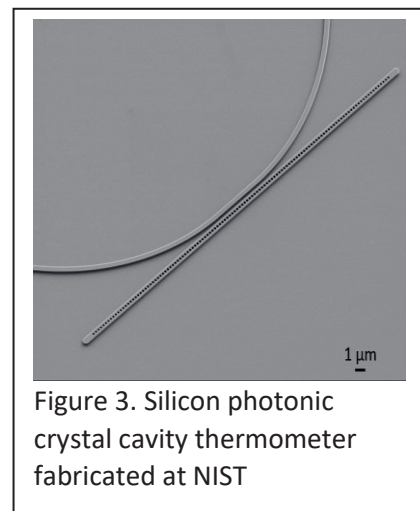


Figure 3. Silicon photonic crystal cavity thermometer fabricated at NIST

NIST has performed the first direct comparison of our photonic thermometers to Standard Platinum Resistance Thermometers, the best in class resistance temperature sensors used to disseminate the International Temperature Scale of 1990. The preliminary results indicate that our PhCC nanothermometers can detect changes of temperature as small as sub-10 μK and can achieve measurement capabilities that are on-par or even better than the state-of-the-art resistance thermometry.

References

- [1] P. Egan, J. Stone, J. Hendricks, J. Ricker, G. Scace, G. Strouse, "Performance of a dual Fabry–Perot cavity refractometer," *Opt. Letters*, Vol. 40, No. 17, August 2015
- [2] M. Puchalski, K. Piszczatowski, J. Komasa, B. Jeziorski, K. Szalewicz, 2016, "Theoretical determination of the polarizability dispersion and the refractive index of helium," *Amer. Phys. Soc., Phys. Rev. A*
- [3] P. Egan, J. Stone, J. Ricker, J. Hendricks, 2016, "Metrology for comparison of displacements at the picometer level," *Amer. Inst. of Phys., Rev. of Sci. Inst.* 87, 053113
- [4] J. Stone, P. Egan, J. Hendricks, G. Strouse, D. Olson, J. Ricker, G. Scace, D. Gerty, 2015 "Metrology for comparison of displacements at the picometer level," *Key Eng. Mat.* Vol. 625 p 79-84
- [5] J. Scherschligt, J. A. Fedchak, D.S. Barker, S. Eckel, N. Klimov, C. Makrides, and E. Tiesinga, *Metrologia* 54, S125 (2017).
- [6] D.E. Fagnan, J. Wang, C. Zhu, P. Djuricanin, B.G. Klappauf, J.L. Booth, and K.W. Madison, *Phys. Rev. A - At. Mol. Opt. Phys.* 80, 1 (2009).
- [7] T. Arpornthip, C.A. Sackett, and K.J. Hughes, *Phys. Rev. A - At. Mol. Opt. Phys.* 85, 1 (2012).
- [8] S. Eckel, D. Barker, J. Fedchak, N. Klimov, E. Norrgard and J. Scherschligt, *Metrologia* (submitted 2018).
- [9] Strouse, *NIST Spec. Publ.* 250, 81 (2008).
- [10] Kim et al., *Opt. Express* 18, 22215 (2010).
- [11] Klimov et al., *Proc. SPIE* 9486, 948609 (2015).
- [12] Douglass, K.O. and D.A. Olson 2016 Towards a standard for the dynamic measurement of pressure based on laser absorption spectroscopy. *Metrologia*. 53(3): p. S96-S106.
- [13] Ahmed, Z., D. Olson, and K.O. Douglass 2016 Precision Spectroscopy to Enable Traceable Dynamic Measurements of Pressure. *CLEO*: p. ATu1J.1.
- [14] Hanson, E., et al. 2018 Towards traceable transient pressure metrology. *Metrologia*.

Measurements Toward a Future SI: On the Longstanding Existence of Metrology-Ready Precision Quantities in Psychology and the Social Sciences

William P. Fisher, Jr¹

¹ BEAR Center, Graduate School of Education, University of California, Berkeley, USA,
Senior Scientist, Research Institute of Sweden, & Living Capital Metrics LLC, Sausalito CA USA

wfisher@berkeley.edu, wfisherjr@livingcapitalmetrics.com

Summary:

Pressing needs for improved information quality are emerging from every sector of life in the world today. Urgent calls for new kinds of thinking, however, almost always change only the content of thinking, not its processes. To obtain higher quality information, humanity must do two things commonly assumed impossible: (1) measure human abilities and attitudes using instruments calibrated to unit standards, and (2) do so without homogenizing, smothering, or ignoring individual differences. Neither of these tasks is impossible, they both have been accomplished and in use for decades.

Keywords: measurement, modeling, metrology, statistics, uncertainty

Circumstances Demanding the Impossible

Urgent calls for sustainable approaches to human suffering, social discontent, and environmental degradation often note these problems cannot be solved using the same kind of thinking that created them [1]. But instead of new ways of thinking, these proposals typically change only the content of the thinking, not the kind of thinking that is itself the problem. How we conceptualize problems is the problem.

We have to stop defining problems from the outside-in and top-down, and we have to stop defining solutions in terms of applied will power. We need to start to think and act on problems from the inside-out and bottom-up. Instead of assuming we need to persuade and educate individuals to change how they live, we have to supply interoperable, networked tools that meet the demand for change. Instead of informing policy and practice from the top-down in centrally designed command-and-control systems, we need populations of individuals to collectively structure coherent and manageable expressions informing policy and practice from the bottom up. Instead of assuming solutions require methodical applications of systematic processes we need to imagine them in terms of spontaneous self-organized processes of uncoerced individual decision making, as analogies to existing socioeconomic systems [2].

The way we formulate problems and solutions is itself the problem. A truly different way of thinking conceives problems and solutions together as complex, multilevel, unified wholes [3]. The stories told by these problem/solution monads must be articulated in concrete local terms for individuals, communicated in abstract global terms via instruments measuring in common metrics, and explained in the formal terms of heuristic fictions by predictive theories.

Each more complex level contextualizes the simpler levels below it. Formal theory's explanatory model reproducibility sets up quality improvement communications employing comparable abstract metrics. Individuals focus on patterns of concrete responses informing them what comes next, and where their special strengths and weaknesses are [4].

Individual vs Collective Problem Definitions

It is commonly assumed that true quantification of living human, social, and environmental relations and processes is impossible. This assumption is an artefactual by-product of the Western Cartesian worldview and clockwork universe paradigm. As long as wholes are understood to be the sums of parts that are best studied by mechanically disassembling them, the complex aggregation of stochastic patterns will remain elusive. Living human, social, and natural systems are wholes greater than the

sums of their parts, and are more aptly seen as processes of relational development [3].

Numbers are often assumed to be inherently quantitative, even when nothing is done to model or estimate a repeatedly identifiable interval unit. But mathematical models, experimental results, calibrated instruments, and practical applications of rigorously defined and estimated quantities and associated uncertainties have been in use for decades. In his measurement work in the 1920s at the University of Chicago, Thurstone, for instance, "stole fire from the gods" [5]. The concept of the identified model was worked out with Thurstone's participation at that same university in 1947 [6]. Another participant in those conversations in Chicago was Rasch, who, along with Wright, Professor of Education and Psychology at the University of Chicago, developed the practical formulations of model mathematics, estimation algorithms, data quality assessments, software, instrument designs, construct validation methods, research applications, and professional associations in wide use today [2, 4, 7-8].

Instead of merely counting up events or ratings and calling the sum a measure, Rasch begins from a model of an open system. Where the meaning of sum scores changes depending on the items and persons included, Rasch modeled measures retain their meaning no matter which items or persons are involved, within the limits of individually estimated uncertainties.

Doing the Impossible:

Rasch's models "embody the essential principles of measurement itself, the principles on which objectivity and reproducibility, indeed all scientific knowledge, are based" (Wright, in 7, p. xix). Metrologists concur. A past chair of the European Association of National Metrology Institutes wrote, "The Rasch approach...is not simply a mathematical or statistical approach, but instead [is] a specifically metrological approach to human-based measurement" [9]. Similarly, a member of a BIPM working group co-authored an article saying "Rasch models belong to the same class that metrologists consider paradigmatic of measurement" [10].

Given the longstanding existence and use of these models, why exactly is their value not more widely appreciated and leveraged?

One problem is that applications of the models are conceived, designed, implemented, and interpreted in the analytic terms associated with the Western Cartesian prioritization of individual subjectivity. The fact that these models facilitate collectively determined stochastic expressions of invariant constructs cannot itself alone be sufficient to the task of trans-

forming a culture and its institutions. The focus on data analytic solutions informing homogeneous policy treats all models as equivalent.

In this context, models for measurement are often taken to be just one kind of descriptive statistical approach among others. This mindset fails to distinguish explanatory scientific models from descriptive statistical models. The advantages of quality-assured unit quantities are luxuries that can be traded off because there is no comprehension or imagination of the value to be created by supporting meaningful end user applications and communications.

As long as the statistical mindset continues to dominate measurement thinking, today's sustainability problems will remain insoluble. Collectively created problems demand collectively created solutions. An alternative paradigm for imagining new possibilities is as readily available as it is urgently needed.

References

- [1] E. Laininen, Transforming our worldview towards a sustainable future. In J. W. Cook (Ed.), *Sustainability, human well-being, and the future of education* (pp. 161-200). Cham, Switzerland: Palgrave Macmillan (2019).
- [2] W. P. Fisher, Jr, What the world needs now: A bold plan for new standards, *Standards Engineering*, 64, 1-5 (2012); ssrn.com/abstract=2083975
- [3] M. Commons, E. Goodheart, Cultural progress is the result of developmental level of support, *World Futures* 64, 406-415 (2008); doi: 10.1080/02604020802301360
- [4] W. Fisher, A. Stenner, Theory-based metrological traceability in education: A reading measurement network, *Measurement*, 92, 489-496 (2016); doi: 10.1016/j.measurement.2016.06.036
- [5] J. Lumsden, Variations on a theme by Thurstone, *Applied Psychological Measurement* 4, 1-7 (1980); doi: 10.1177/014662168000400101
- [6] T. Koopmans, O. Reiersøl, The identification of structural characteristics, *The Annals of Mathematical Statistics*, XXI, 165-181 (1950); www.jstor.org/stable/2236899
- [7] G. Rasch, *Probabilistic models*, Chicago: University of Chicago Press, (1980)
- [8] B. Wright, A history of social science measurement, *Educational Measurement: Issues and Practice*, 16, 33-52 (1997); doi: 10.1111/j.1745-3992.1997.tb00606.x
- [9] L. Pendrill, Man as a measurement instrument, *NCSLI Measure*, 9, 22-33 (2014); doi: 10.1080/19315775.2014.11721702
- [10] L. Mari, M. Wilson, An introduction to the Rasch measurement approach for metrologists, *Measurement*, 51, 315-327 (2014); doi: 10.1016/j.measurement.2014.02.014

Pillar

Sensors and Instrumentation

Analytic Method for Magnetic Position System Calibration

Michael Ortner¹, Perla Malagò¹, Stefano Lumetti¹, Dietmar Spitzer², Sigmund Zaruba³

¹ Silicon Austria Labs, Europastraße 12, 9500 Villach, Austria

² Infineon Technologies Austria, Siemensstraße 2, 9500 Villach, Austria

³ Infineon Technologies AG, Am Campeon 1-15, 85579 Neubiberg, Deutschland

michael.ortner@silicon-austria.com

Summary:

The greatest shortcoming of magnetic position sensor systems is their sensitivity to fabrication tolerances. In this work, we propose a novel calibration scheme based on evolutionary optimization and the analytic solution for the magnetic field. This method allows us to calibrate more than 10 degrees of freedom in the course of seconds with little computation requirements, and realize a complex, novel position system by simple means.

Keywords: Magnetic system design, analytic method, magnetic position sensor systems

Introduction and Background

Magnetic position sensor systems are based on the relative motion of a permanent magnet with respect to a magnetic field sensor. Such systems are widely used for industrial applications due to their excellent properties [1]. In the automotive sector alone there are more than 100 applications that include gear position, steering wheel, gas- and brake pedals, wheel speed, window lifter and many others [2].

Recently, a novel magnetic system was proposed for the detection of the motion of a 3-axis joystick by means of a single sensor and a single magnet only [3]. This highly cost-efficient implementation is now called "MJ113". A realization with 5 discrete tilt states is displayed in Fig.1(a). In Fig.1(b) the magnetic field at the sensor position is shown for a 360° rotation for each tilt. In this implementation, the circular paths in the magnetic space are well-separated from each other by >10 mT.

Problem and Motivation

The major drawback of all magnetic position systems is their difficulty to deal with fabrication tolerances. In this respect the MJ113 is no exception as revealed by the experimental analysis shown in Fig.2, where the sensor outputs of 15 similar systems (colored dots) are displayed together with the corresponding theoretical predictions (solid lines).

A precision fabrication of the MJ113 would nullify the cost-efficiency which is its main advantage. In this work we show that it is possible to realize such a system by relying on simple

experimental means and on a novel calibration scheme based on analytical methods.

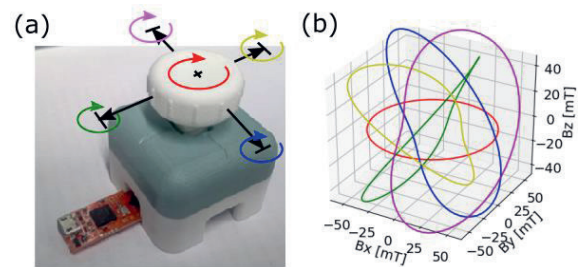


Fig. 1. Mechanical 3-axis motion and resulting field at the sensor.

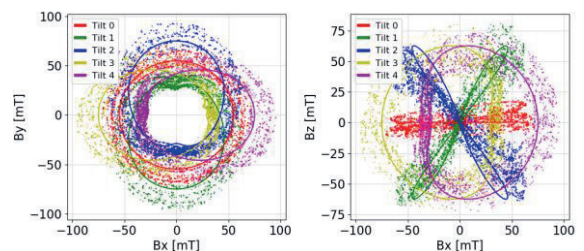


Fig. 2. Experimental analysis of 15 similar systems.

Experimental Setup

The experimental implementation is based on cost-efficient 3D-printing technology. The final device, shown in Fig.1(a), includes a test board of the Infineon XMC 2Go type endowed with a TLE493D 3D-magnetic field sensor. In our implementation choice, a Neodymium ($B_r \sim 1\text{T}$) cubical permanent magnet with 4-mm sides is embedded at the bottom of the joystick's rod. The airgap is 2 mm, the distance from the center of tilt is 7 mm and the magnet sideways displacement is 2 mm in accordance with [3].

The experimental data in Fig.2 is obtained by tracking the sensor output while rotating the joystick knob in the five discrete tilt positions, as indicated in Fig.1(a).

Calibration Scheme

State-of-the-art systems approximate the field in a simple manner, e.g. by an arctangent function, and compensate for the tolerances in an end-of-the-line process. This method is limited by the simple form of the field approximation and cannot account for multiple tolerances in a complex system like the MJ113.

Instead, we propose to use the full solution for the magnetic field and perform the calibration as a multivariate optimization problem which includes all relevant system tolerances. Such an optimization is impossible when slow numerical methods are used for field computation.

We have shown that the analytic solution provides an excellent approximation in this case, with errors below 0.1 % [4]. Specifically, for special geometries like cuboids the formulas are simple and compute in microseconds on common CPUs [5].

For the computation of the magnetic field we use the Magpylib package [5] and for the optimization we apply a differential evolution algorithm [6]. This combination is very synergetic as the vectorized code of Magpylib employs SIMD operations while the differential evolution algorithm parallelizes the computation of each generation. Thereby, 13 co-dependent calibration variables can be determined in only a few seconds on a mobile CPU (i5-8365U). The chosen tolerances include the sensor position, the magnet position and magnetization as well as the individual tilt end-point angles.

As input data of the calibration procedure we use only four points on each circle and minimize the square of their distance to the theoretical circles by variation of the tolerances. The calibration points can be obtained experimentally by a user with little effort.

Results and Discussion

The result of the calibration procedure is shown in Fig.3. For each tilt, 50 random positions on the circles are chosen, and their distance to the designated theoretical values are displayed in units of LSB ($\sim 0.1\text{mT}$). The circular markers show the calibrated states while the crosses correspond to the uncalibrated ones. The orange region outlines the nearest false tilt states, while the gray region corresponds to the best possible result from a full calibration which includes all 5x50 experimental data points.

Clearly, the system is unusable in its uncalibrated state (bad tilt circles are closer than the designated ones) while the 4-point calibration makes an identification of the correct tilt state possible. Still it seems that the calibrated states can be quite far from their designated circles, see e.g. yellow peaks. However, this is a result of the cheap mechanics and the user moving the joystick by hand to collect the data, as can also be seen by looking at the full calibration where all data points are used in the calibration. From that point of view, the 4-point calibration is surprisingly efficient as the best possible result is mostly achieved.

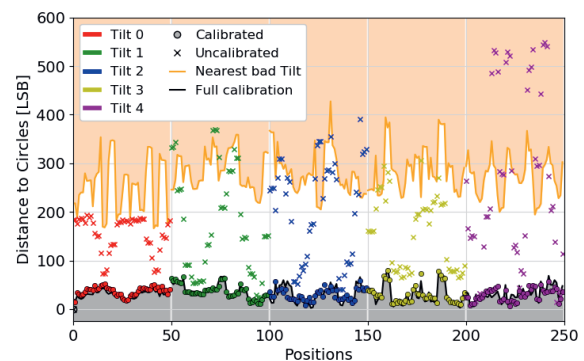


Fig. 3. Results of the 4-point calibration procedure.

Conclusion and Outlook

We have proposed a novel calibration method that makes it possible to deal with multiple fabrication tolerances in magnetic systems within short time frames and with little computation effort. For demonstration, the algorithm was applied for the calibration of a novel magnetic joystick realized by cost-efficient 3D printing.

Ongoing work is dedicated to study the potential of this method for calibration and design of arbitrary magnetic systems.

References

- [1] Treutler, C. P. O. "Magnetic sensors for automotive applications." *Sensors and Actuators A: Physical* 91.1-2 (2001): 2-6.
- [2] Infineon Technologies AG, "XENSIV – Sensing the world", Product catalog, B142-I0675-V2-7600-EU-EC-P, 06, (2019)
- [3] Ermakova, A. et al. "Analytical Development of a Four-Axis Magnetic Multimedia Control Element." *IEEE Sensors Journal* 18.19 (2018): 7819-7825.
- [4] Malagò, P. et al. "Magnetic system design by analytic computation", in preparation, 2020.
- [5] Ortner, M. et al. "Magpylib – A free Python package for computation of magnetic fields", submitted to SoftwareX, Elsevier, 01/2020.
- [6] Storn, R. "On the usage of differential evolution for function optimization." *Proceedings of North American Fuzzy Information Processing*. IEEE, 1996.

Noise-free Inspection of Rotary Encoder Magnets

Dr. Koen Vervaeke
Magcam NV, Romeinse straat 18, B-3001 Leuven, Belgium
koen.vervaeke@magcam.com

Summary:

We report on a method to measure a noise-free magnetic field distribution of rotary encoder sensor magnets, based on Magcam's established 3-axis magnetic field camera technology. This method involves measuring the 3-axis magnetic field distribution in a 2D plane at close distance above the magnet and extrapolating this field distribution into a 3D volume using a patented 'Distance Filter' algorithm that yields virtually noise-free data at larger distances. This powerful method allows to evaluate the magnetic field distribution and the magnet's intrinsic angular error, with a resolution better than the measurement resolution of the originally measured plane.

Keywords: sensor magnet, magnet inspection, magnetic field camera, magnetic field mapping, magnet

Background, Motivation and Objective

A method is presented for magnetically characterizing 2-pole rotary encoder magnets, which are widely used in angular encoders in e.g. electric motors and rotary positioning systems. The method uses a proprietary 'Distance Filter' algorithm, which allows to extrapolate a magnetic field distribution recorded at one certain (close) distance above a magnet or magnet assembly to another (larger) distance in a very fast way and with a strong suppression of measurement noise. This allows very fast and at the same time highly accurate measurements, making the method suitable for production quality control.

Description of the Distance Filter Method

The Distance Filter algorithm is used in combination with Magcam's magnetic field camera systems. When the extrapolation is in the direction away from the magnet, there is a strong suppression of noise, resulting in μ Tesla magnetic field resolutions. This makes the Distance Filter algorithm very powerful for determining magnetic field distributions far away from a magnet, since a direct measurement at the farther distance would suffer from a poorer signal-to-noise ratio.

For accurate results with the Distance Filter, the recorded magnetic field distribution must contain the full magnetic field of the measured magnet or magnet assembly, meaning that at all edges of the measured magnetic field image the magnetic field should be monotonically decreasing towards zero when going outwards towards the image edges. In practice, this

means that a sufficiently large area should be measured, including extra space around the magnet.

Results

Consider a cylindrical axially magnetized 2-pole rotary encoder magnet, with the cylindrical symmetry axis pointing in the Z direction. The original measurement is in the XY plane at a certain height Z_0 above the magnet surface. The magnetic field distribution at a different height Z_1 is obtained by the Distance Filter method by supplying one single input parameter Delta, namely the distance between the original measurement plane and the desired plane: $\Delta = Z_1 - Z_0$. When $\Delta > 0$ the extrapolation takes place in the direction away from the magnet. When $\Delta < 0$, the extrapolation is in the direction towards the sample. When $\Delta = 0$ the original data is retained.

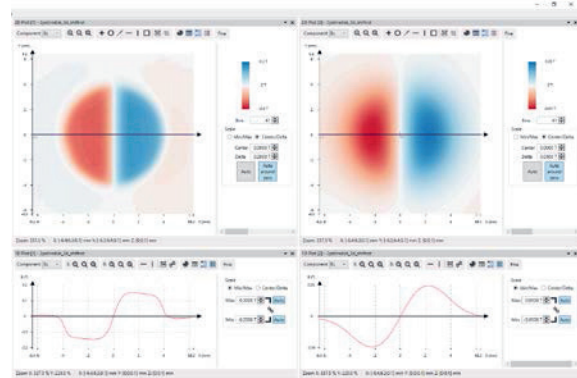


Fig. 1. Measured B_z magnetic field distribution and cross section along the X direction at $Z_0 = 0.3\text{mm}$ (left) and Distance Filter result at $Z_1 = 2\text{mm}$ (right).

Fig. 1 shows the measured B_z magnetic field distribution and cross section along the X direction at $Z_0 = 0.3\text{mm}$ (left) and Distance Filter result at $Z_1 = 2\text{mm}$ (right). Hereby the value for Delta is: $\Delta = 2\text{mm} - 0.3\text{mm} = 1.7\text{mm}$.

Analyzing B_{xy} and azimuthal angle error in 2-pole rotary encoder magnets

In a typical end application a B_x, B_y sensor is positioned on the symmetry axis of the rotary encoder magnet at a certain distance from the magnet surface, which is typically several mm. At such distance the B_{xy} magnetic field is typically of the order of 50mT. The B_x, B_y sensor then measures B_x and B_y and from those calculates the in-plane angle of the magnetic field using $\text{atan2}(B_y, B_x)$. Due to inhomogeneities of the magnetic field distribution, there is a certain error on this measured angle value. During quality control on such magnets, this angle error needs to be determined with high accuracy, typically in the order of 0.1° or better. By using a magnetic field camera in combination with the Distance Filter this can be achieved in a superior way as is shown below.

A magnetic field distribution measurement directly at the working distance of the B_x, B_y sensor in the above application would result in a poorer signal-to-noise ratio than a measurement very close to the magnet (typically 0.3-0.5mm). The Distance Filter makes it possible to 'preserve' the signal-to-noise ratio at close distance to remote distances, resulting in virtually noise-free magnetic field distributions.



Fig. 2. 2-pole axially magnetized cylinder magnet measured with MiniCube3D magnetic field camera.

The 3D magnetic field distribution is measured at a close distance above the magnet surface using a Magcam MiniCube3D magnetic field camera (see Fig. 2).

As mentioned higher, the relevant magnetic field components for this application are the in-plane (B_{xy}) magnetic field and the in-plane direction (azimuthal angle) of the field in a region in the center of the magnet. These components can be analyzed as explained below.

B_{xy} component and azimuthal angle

The B_{xy} component is readily obtained from the B_x and B_y components of the magnetic field (Fig. 3). A circle is interpolated centered on the magnet center and with a certain radius, taken to be 0.25mm in this example (see Figure 8), typically determined by the tolerance region where the B_x, B_y sensor will be located in the end application. In the obtained line plot, the maximum and minimum values can be automatically detected, which can be directly used in a pass/fail test to check if they are within the tolerance window.

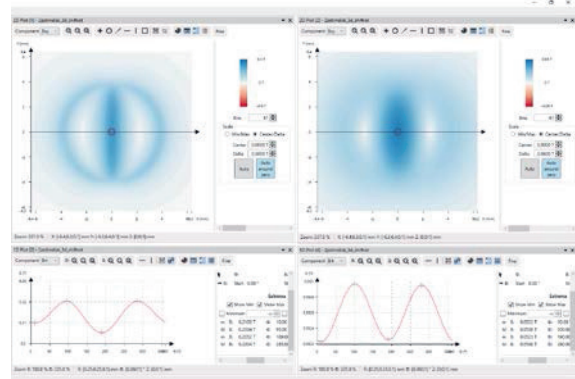


Fig. 3. B_{xy} (in-plane) magnetic field distribution with a circle section in the middle of the magnet for $Z = 0.3\text{mm}$ (left) and $Z = 2\text{mm}$ (right). In the 1D Plots the minimum and maximum values are automatically detected.

The second important quantity of the magnetic field distribution is the in-plane direction (azimuthal angle) distribution of the magnetic field. This quantity is also readily calculated from the B_x and B_y components of the magnetic field by using $\text{atan2}(B_y, B_x)$. By analyzing the extreme values of the azimuthal angle on the same circle section as before, the angle error is directly obtained, as shown in Fig. 4.

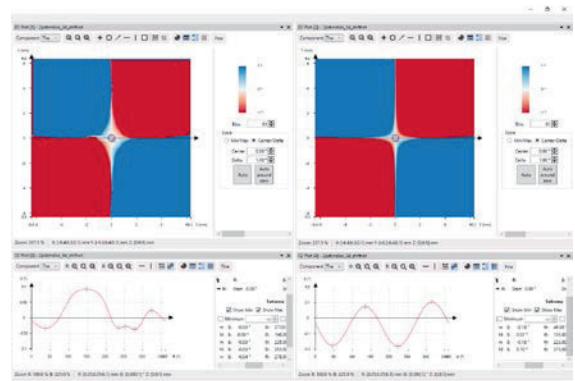


Fig. 4. Azimuthal (in-plane) angle distribution with a circle section in the middle of the magnet for $Z = 0.3\text{mm}$ (left) and $Z = 2\text{mm}$ (right). In the 1D Plots the minimum and maximum values are automatically detected and give a direct measure of the angle error of the B_{xy} magnetic field distribution on the circle.

Multichannel Heterodyning-Based Eddy Current Testing with Magnetoresistive Sensors

Henrik Ehlers^{1,2}, Matthias Pelkner¹, Roland Thewes²

¹ Federal Institute for Materials Research and Testing (BAM), 12205 Berlin, Germany,

² Institute of Technology Berlin, Chair of Sensor and Actuator Systems,
Faculty of EECS, 10623 Berlin, Germany
henrik.ehlers@bam.de

Summary:

High spatial resolution magnetoresistive arrays are utilized for eddy current testing in combination with a single wire excitation and a heterodyne principle to minimize metrology efforts. A discrete frontend with FPGA-based data acquisition makes use of a 128-element eddy current probe to test 440 μm artificial surface defects with an SNR of 24 dB.

Keywords: Eddy Current Testing, Magnetoresistance, Heterodyning, Additive Manufacturing.

Background, Motivation and Objective

The most common question when discussing NDT methods is always: “*What is the smallest defect size that can be detected?*” For eddy current testing (ET) this is not any different. Unfortunately, there is not a simple answer to this question. Since magnetoresistive (MR) sensors based on giant, anisotropic or tunnel magnetoresistive effect (GMR, AMR or TMR) became available, it has not only been shown, that MR-based ET is possible [1][2], but also that MR elements can easily be miniaturized and parallelized while maintaining high sensitivity and, therefore, pushing the limit of smallest detectable defect sizes. Combined with precise excitation of magnetic fields a spatial resolution down to some μm can be achieved [3][4].

In the past, approaches based on integrated or discrete electronics have been made to utilize MR-based high element count ET probes and applying a heterodyne principle to reduce inductive coupling and carrier frequency. [5][6][7][8].

However, utilizing the MR arrays full potential is often not possible due to either ET probes not being widely available or the lack of suitable hardware for amplification and data acquisition. Furthermore, parallelization of the ET probes is often not possible simply because of geometric limitations.

Description of the New Method or System

In this work approaches are made to overcome those limitations. A convenient method is proposed to manufacture MR-based ET probes

with 128 single MR elements and a single wire as inducer made from a rigid-flex PCB (see Fig. 1) with a testing width of 16 mm that can be extended to any desired testing width.

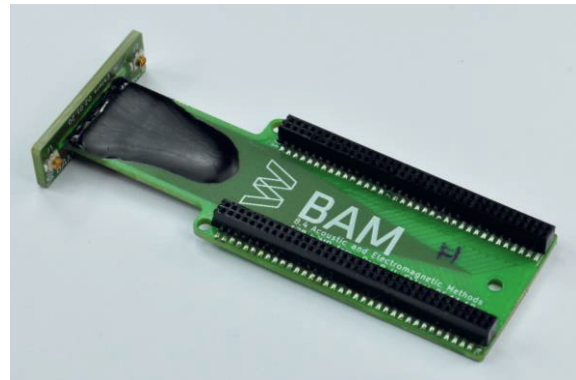


Fig. 1. 128x MR-based ET probe with a single wire on rigid-flex PCB as inducer.

Furthermore, to utilize this ET probes a compact system is set up.

A heterodyning-based frontend with discrete amplification and multiplexing (see Fig. 2) in combination with FPGA-based data acquisition results in a minimum of expensive laboratory scale equipment needed while still being able to achieve similar signal-to-noise ratios (SNR).

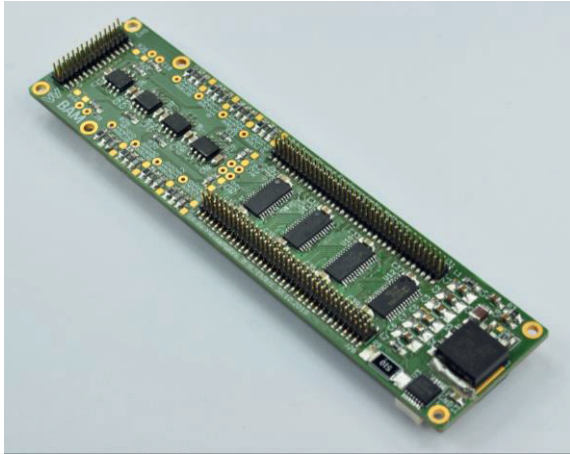


Fig. 2. Heterodyning-based sensor frontend with multiplexing and amplification for 128 MR elements.

Results

The proposed system is used to measure an artificial surface defect of five boreholes each with a diameter of $440\ \mu\text{m}$. The data of 32 MR Elements are used to create a normalized amplitude image (see Fig. 3) showing the defect information with a SNR of 24 dB. The testing time is 1,7 s

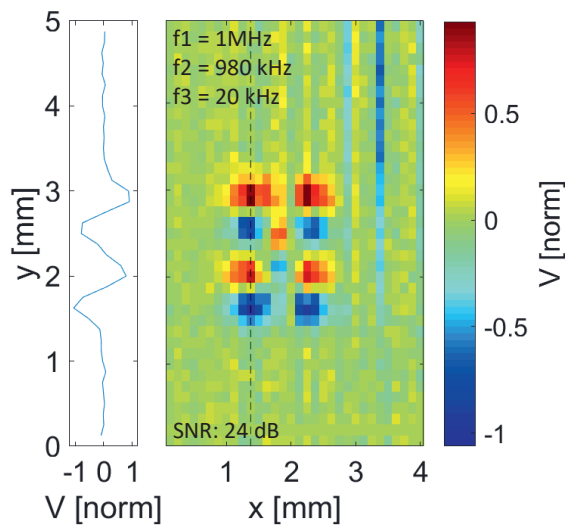


Fig. 3. Amplitude image of $5 \times \varnothing 440\ \mu\text{m}$ artificial defect in AL-FN-22 specimen

Outlook

In the future, one of the target applications of this system will be online monitoring of additive-

ly manufactured parts. During laser powder bed fusion (LPBF) each manufactured layer will be tested. Helping to understand the LPBF process, the formation of defects and gathering geometric information of the manufactured parts.

References

- [1] Dogaru, T.; Smith, S. T. Giant Magneto-resistance-Based Eddy-Current Sensor. **2001**, 37 (5), 3831–3838.
- [2] Nair, N. V.; Melapudi, V. R.; Jimenez, H. R.; Liu, X.; Deng, Y.; Zeng, Z.; Udpa, L.; Udpa, S. S.; Moran, T. J. A GMR-Based Eddy Current System for NDE of Aircraft Structures. *IEEE Trans. Magn.* **2006**, 42 (10), 3312–3314. <https://doi.org/10.1109/TMAG.2006.879820>.
- [3] Allweins, K.; Von Kreutzbruck, M.; Gierelt, G. Defect Detection in Aluminum Laser Welds Using an Anisotropic Magneto-resistive Sensor Array. *J. Appl. Phys.* **2005**, 97 (10). <https://doi.org/10.1063/1.1852391>.
- [4] Vacher, F.; Decitre, J. M.; Fermon, C.; Pannetier, M. Non Destructive Testing with GMR Magnetic Sensor Arrays. **2006**, 1–8.
- [5] Caetano, D. M.; Piedade, M.; Graça, J. A CMOS ASIC for Precise Reading of a Magneto-resistive Sensor Array for NDT. *11th Eur. Conf. Non-Destructive Test.* **2014**, No. Ecnedt, 1–10.
- [6] Rosado, L. S.; Cardoso, F. A.; Cardoso, S.; Ramos, P. M.; Freitas, P. P.; Piedade, M. Eddy Currents Testing Probe with Magneto-Resistive Sensors and Differential Measurement. *Sensors Actuators, A Phys.* **2014**, 212, 58–67. <https://doi.org/10.1016/j.sna.2014.03.021>.
- [7] Pelkner, M.; Pohl, R.; Erthner, T.; Stegemann, R.; Kreutzbruck, M.; Sergeeva-Chollet, N.; Cardoso, F. A.; Freitas, S.; Freitas, P. P.; Caetano, D. M.; et al. Eddy Current Testing With High-Spatial Resolution Probes Using Mr Arrays As Receiver. In *7th International Symposium on NDT in Aerospace*; Bremen, 2015.
- [8] Caetano, D. M.; Rabuske, T.; Fernandes, J.; Pelkner, M.; Fermon, C.; Cardoso de Freitas, S.; Ribez, B.; Franco, F.; Paul, J.; Piedade, M.; et al. High-Resolution Non-Destructive Test Probes Based on Magneto-resistive Sensors. *IEEE Trans. Ind. Electron.* **2018**, 46 (c). <https://doi.org/10.1109/TIE.2018.2879306>.

Highly Sensitive Compact Room Temperature Quantum Scalar Magnetometer

Ludwig Horsthemke¹, Robert Staacke³, Bernd Burchard², Jan Meijer³, Christian Bischoff¹, Peter Glösekötter¹

¹ FH Münster – University of Applied Sciences, Stegerwaldstraße 39, 48565 Steinfurt, Germany

² Elmos Semiconductor AG, Heinrich-Hertz-Straße 1, 44227 Dortmund, Germany

³ Applied Quantum Systems, Felix-Bloch Institute for Solid-State Physics, Leipzig University, Linnéstraße 5, 04103 Leipzig, Germany
l.horsthemke@fh-muenster.de

Summary:

A new detection scheme for all optical magnetometry using nitrogen-vacancies in diamond is proposed.

Keywords: Nitrogen vacancy, room temperature, quantum, scalar, magnetometer

Motivation

Magnetometry with nitrogen–vacancy (NV) defects in diamond has been extensively studied in the past [1]. While most approaches include the use of microwaves (MW) for the detection of electron spin resonance, only few investigate the sensitivity of the photoluminescence (PL) from NV centers to an external magnetic field without MW [2, 3, 4]. This work aims to utilize this effect to build a highly sensitive and compact room temperature magnetometer. The avoidance of MW serves the reduction of production costs and allows a commercialization at the current patent situation.

Description of the System

The proposed system is based on the magnetic field dependent red fluorescence of NV-diamonds. The luminescence occurs when optically pumped by green light and is attenuated by magnetic fields between 10 mT and 50 mT because of the magnetic-field-induced mixing of NV spin states [5]. Recently some of us published a new methodology to create NV-centers by ion implantation into diamond [6].

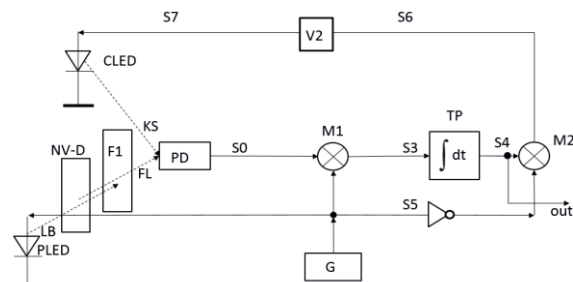


Figure 2: Transmission measurement system schematic.

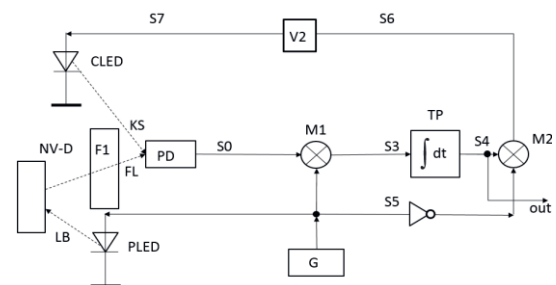


Figure 1: Reflection measurement system schematic.

This allows to create arrays of NV centers and the fabrication of quantum computer becomes possible. However, for magnetic sensing diamonds with a high density of NVs (so called red diamonds) are necessary. Electron irradiation of HPHT diamonds enables to create these diamonds with a high NV content with regard to carbon atoms. In these “red” diamonds, we observe a magnetic flux density dependent red fluorescence.

Figure 1 and 2 show schematics of the measurement systems in reflection and transmission mode, respectively. Exemplarily, Figure 3 reflects a compact working prototype realization of our room temperature quantum transmission magnetometer. Anyhow, the following functional principal holds true for both modes: A generator G produces a square wave signal S5 with frequency ω to drive a 520 nm laser. This laser optically pumps the NV-diamond through a collimating lens. The luminescent light passes through a longpass filter with a cut on wavelength of 600 nm onto a silicon PIN photodiode. After appropriate amplification and high pass filtering to remove the DC bias the multiplier M1

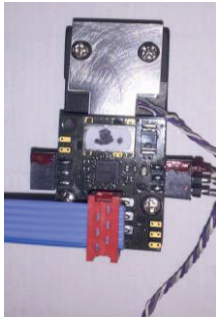


Figure 3: room temperature quantum transmission magnetometer.

multiplies the resulting signal S1 and the signal S5. Subsequent integration of the resulting signal S3 suppresses the $\sin(2\omega)$ term because of the low pass filter property. A second multiplier M2 multiplies the integrator output with the generator signal, phase shifted by 180° . An amplifier V2 amplifies the resulting signal S6 and drives a compensating LED using the signal S7. The compensating red LED irradiates directly into the photodiode. This ensures, once the integrator has settled to a constant value for the photodetector to stay in the same operating point independent of the generator signal. This avoids negative effects of non-linear photodetector behavior. Thus, only the difference of fluorescence and compensation light is amplified by the phase sensitive detection and becomes zero once the control system has settled to its operating point. So the integrator value which is proportional to the photoluminescence is also the measurement output. An Elmos HALIOS[®] gesture recognition device performs the described measurement procedure.

Results

Figure 4 shows the circuits measurement value C in reflection mode, which is proportional to the photoluminescence as a function of the external magnetic flux density B. It is non-monotonic due to a reproducible rise at about 6 mT which has not been reported before. Figure 5 shows the responsivity $\partial C/\partial B$, with a peak value of $\partial C/\partial B \approx -31$ counts/mT in the range of 15 mT to 25 mT. Figure 6 shows the noise spectral density of 20 minutes sampling time at the systems maximum sampling frequency $f_s = 53.3$ Hz and an applied bias field of 20 mT. The integrated noise spectral density equates

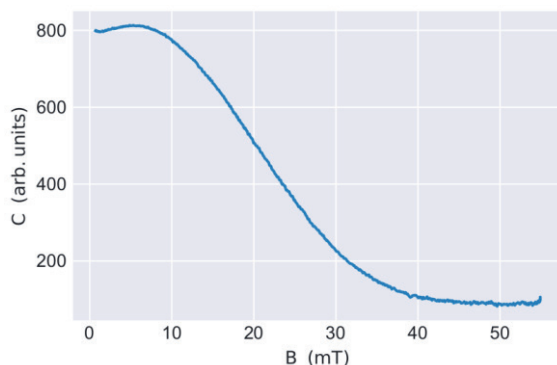


Figure 4: Reported value C of the sensor as a function of the external magnetic field (in reflection mode).

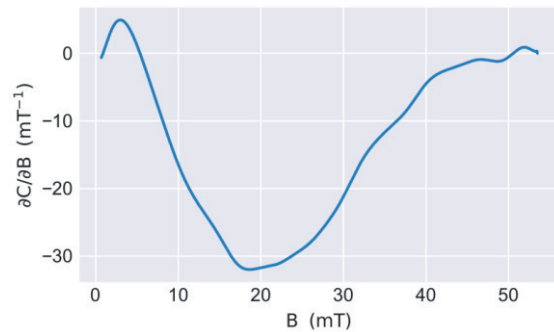


Figure 5: Derivative of measured value $\partial C/\partial B$ as a function of the external magnetic field. (in reflection mode)

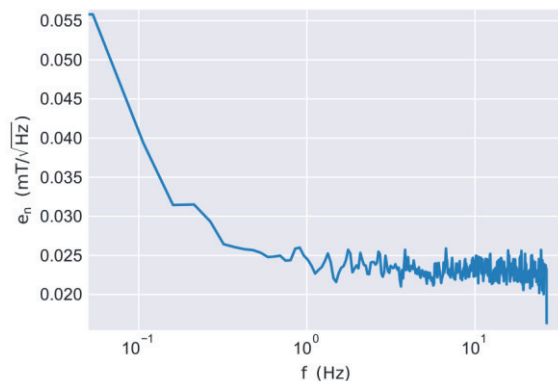


Figure 6: Noise spectral density at a bias field of 20 mT (in reflection mode).

to $32 \mu\text{T}/\sqrt{\text{Hz}}$; which is slightly lower than the setup of Fedotov et al. [4] with $50 \mu\text{T}/\sqrt{\text{Hz}}$.

References

- [1] Lee, M.; Yoon, J. and Lee, D. (2019). In: (Ed.), Atomic Scale Magnetic Sensing and Imaging Based on Diamond NV Centers.
- [2] Tetienne, J.-P.; Rondin, L.; Spinicelli, P.; Chipaux, M.; Debuisschert, T.; Roch, J.-F. and Jacques, V. (2012). Magnetic-field-dependent photodynamics of single NV defects in diamond: an application to qualitative all-optical magnetic imaging, *New Journal of Physics* 14: 103033.
- [3] Wickenbrock, A.; Zheng, H.; Bougas, L.; Leefer, N.; Afach, S.; Jarmola, A.; Acosta, V. M. and Budker, D. (2016). Microwave-free magnetometry with nitrogen-vacancy centers in diamond, *Applied Physics Letters* 109: 053505.
- [4] Fedotov, I.; Amitonova, L.; Sidorov-Biryukov, D.; Safronov, N.; Blakley, S.; Levchenko, A.; Zibrov, S.; Fedotov, A.; Kilin, S.; Scully, M.; Velichansky, V. and Zheltikov, A. (2014). Fiber-optic magnetic-field imaging, *Optics Letters* 39.
- [5] Epstein, R. J.; Mendoza, F. M.; Kato, Y. K. and Awschalom, D. D. (2005). Anisotropic interactions of a single spin and dark-spin spectroscopy in diamond, *Nature Physics* 1: 94-98.
- [6] Lühmann, T.; John, R.; Wunderlich, R.; Meijer, J. and Pezzagna, S. (2019). Coulomb-driven single defect engineering for scalable qubits and spin sensors in diamond, *Nature Communications* 10 4956.

Contributions to Acoustic Loss in Langasite, Langatate, and Catangasite Resonators at High Temperatures

Ward L. Johnson

Applied Chemicals and Materials Division, National Institute of Standards and Technology, 325
Broadway St., MS 647, Boulder, CO 80305, USA
wjohnson@boulder.nist.gov

Summary:

Piezoelectric crystals in the langasite family can serve as a basis for resonant acoustic sensors that operate at temperatures exceeding the range of conventional piezoelectric resonators, but their performance is limited by acoustic loss at elevated temperatures. This paper presents an overview of what is currently known and not known about physical contributions to temperature-dependent acoustic loss in langasite, langatate, and catangasite [1].

Keywords: acoustic loss, attenuation, high temperature, langasite, langatate, catangasite, piezoelectric resonators

Background

Applications of resonant piezoelectric sensors have traditionally been limited to temperatures below several hundred degrees Celsius, because phase transitions and/or material degradation occur at higher temperatures in common commercially available piezoelectric materials [2]. However, over the past four decades, substantial research has focused on growing, characterizing, and optimizing innovative piezoelectric crystals that can be used in resonant sensors at temperatures exceeding 1000 K [3]. These piezoelectrics include crystals with the structure of langasite ($\text{La}_3\text{Ga}_5\text{SiO}_{14}$, LGS).

A critical factor in the performance of resonators is the quality factor Q and corresponding acoustic loss Q^{-1} . This paper is focused on contributions to Q^{-1} in LGS and two piezoelectrics with similar crystal structure, langatate ($\text{La}_3\text{Ga}_{5.5}\text{Ta}_{0.5}\text{O}_{14}$, LGT) and catangasite ($\text{Ca}_3\text{TaGa}_3\text{Si}_2\text{O}_{14}$, CTGS).

LGS

Figure 1 shows measurements of Q^{-1} acquired at the National Institute of Standards and Technology (NIST, U.S.A.) and Clausthal University of Technology (TUC, Germany) on two Y-cut crystals grown by different manufacturers [2,4]. The combined data in this figure extend over an exceptionally broad temperature range and thereby provide a unique illustration of typical contributions to the temperature-dependent loss in LGS and other crystals in the langasite family. The NIST measurements were performed with noncontacting electrodes in vacuum, and

the TUC measurements were performed with Pt surface electrodes in air.

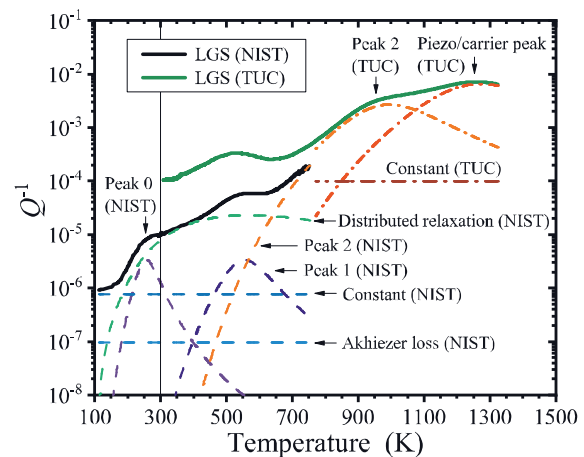


Fig. 1. Acoustic loss Q^{-1} of two LGS crystals measured at NIST and TUC. Resonant frequencies were 6.05 MHz (NIST) and 5.0 MHz (TUC) at ambient temperature. Dashed and dashed-dotted lines are contributions to Q^{-1} of the NIST and TUC crystals, respectively, determined from least-squares fits.

The three peaks below 1100 K in Fig. 1 are consistent with anelastic point-defect relaxations with a characteristic Debye dependence on temperature T and angular frequency ω [5]:

$$Q^{-1} = (\Delta/T)\omega\tau/(1+\omega^2\tau^2), \quad (1)$$

where the relaxation strength Δ is proportional to defect concentration. The relaxation time τ has an Arrhenius dependence on T ,

$$\tau = \gamma\exp(U/kT), \quad (2)$$

where U is an activation energy on the order of an electron volt and k is Boltzman's constant.

Another peak appears in the TUC data near 1260 K, and this is associated with piezoelectric/carrier relaxation, involving the motion of charge carriers in acoustically generated piezoelectric fields [2,4]. In LGS, this peak is expected to have Debye form, but without T in the pre-factor [4]. An additional contribution in all crystals is intrinsic loss from phonon-phonon interactions (Akhiezer loss) [6], which is expected to be proportional to ω and weakly dependent on T above 100 K [4].

The data from NIST in Fig. 1 (112 K to 752 K) were fit to a function that includes three point-defect relaxations, Akhiezer loss approximated as independent of T , a constant background, and a broad relaxation consisting of a continuous set of Debye functions with a log-normal distribution of activation energies. The last term was found necessary to accurately fit the data [4]. Piezoelectric/carrier loss was not included, because initial analysis indicated it to be a minor contribution at all measured temperatures. The results of this fit at 6 MHz, simultaneously performed on data from two additional harmonics, are shown in the figure.

A fit of the TUC data (Fig. 1) accurately matches the data without including a distributed relaxation term. To simplify the figure, contributions to this fit are only plotted above the range of the NIST data and Peak 1 is not included. The piezoelectric peak position is consistent with predictions based on the measured temperature-dependent conductivity and dielectric constant [7]. The constant term in the fit is 1.0×10^{-4} , two orders of magnitude greater than the constant in the fit of the NIST data. This difference may be due to greater mechanical contact and/or anelasticity in the Pt electrodes.

LGT and CTGS

Similar point-defect and piezoelectric/carrier contributions have been reported in LGT and CTGS at resonant frequencies in the low megahertz range [4,7,8]. Two point-defect peaks are typically observed between 300 K and 1000 K. Lower conductivity and corresponding τ_c of CTGS, relative to LGS, lead to lower piezoelectric carrier loss over the measured ranges of temperature, since the peak maximum is shifted to higher temperatures [7].

In an LGT crystal measured at NIST, no broad temperature-dependent contribution similar to that observed in LGS (NIST, Fig. 1) was detected [4]. The fact that dislocation density was much lower in this LGT crystal supports the hypothesis that the physical mechanism re-

sponsible for this contribution in LGS involves anelastic motion of kinks in dislocations [4].

Suhak *et al.* [7] found evidence for a broadly temperature-dependent background loss in Y-cut CTGS and employed a simpler Arrhenius form to fit this background. They also found the constant term in the fitting function to be much greater for a CTGS crystal with Pt electrodes than for a different CTGS crystal without electrodes.

Conclusions

LGS, LGT, and CTGS display similar features in the temperature dependence of acoustic loss, although the magnitudes and peak positions of loss contributions vary. The general form of the piezoelectric/carrier contribution and its dependence on electrical conductivity is well understood. However, specific defects responsible for point-defect peaks have not been identified. Such identification may be less than straightforward because correlations of peaks with impurity concentrations can be indirect. In particular, defect symmetries and associated relaxations can depend on charge states that change with dopant levels. The physical mechanisms responsible for observed contributions with broad temperature dependence are also not established. The combination of results from multiple crystals suggests that these mechanisms include effects that are both internal and external to the piezoelectric material.

- [1] This manuscript is a contribution of the National Institute of Standards and Technology and is not subject to copyright in the United States.
- [2] Fritze, H., High-temperature piezoelectric crystals and devices, *J. Electroceram.* 26, 122-161 (2011); doi: 10.1007/s10832-011-9639-6
- [3] Johnson, W., Acoustic and Electrical Properties of Piezoelectric Materials for High-Temperature Sensing Applications, *Proc. SENSOR 2015*, 384-389 (2015); doi: 10.5162/sensor2015/C3.1
- [4] Johnson, W., Kim, S. A., Uda, S., and Rivenbark, C. F., Contributions to anelasticity in langasite and langatate, *J. Appl. Phys.* 110, 123528 (2011); doi: 10.1063/1.3672443
- [5] A. S. Nowick and B. S. Berry, *Anelastic Relaxation in Crystalline Solids* (Academic, NY, 1972).
- [6] Akhiezer, A., On the absorption of sound in solids, *J. Phys. USSR* 1, 277-287 (1939).
- [7] Suhak et al., Electromechanical properties and charge transport of $\text{Ca}_3\text{TaGa}_3\text{Si}_2\text{O}_{14}$, *Solid State Ionics* 317, 221-228 (2018); doi: 10.1016/j.ssi.2018.01.032
- [8] Johnson, W. L., High-Temperature Electroacoustic Characterization of Y-Cut and Singly-Rotated $\text{Ca}_3\text{TaGa}_3\text{Si}_2\text{O}_{14}$ Resonators, *IEEE T. Ultrason. Ferr.* 61, 1433-1441 (2014); doi: 10.1109/TUFFC.2014.3052

CTGS: advanced piezoelectric single crystal for sensor applications over extremely wide temperature range.

A.Sotnikov¹, R.Weser¹, B.P.Sorokin², Yu.Suhak³, H.Fritze³, H.Schmidt¹

¹*Leibniz IFW Dresden, SAWLab Saxony, Helmholtzstr. 20, 01069 Dresden, Germany*

²*Technological Institute for Superhard and Novel Carbon Materials, Tsentral'naya 7a, 108840 Troitsk, Moscow, Russia*

³*Institute of Energy Research and Physical Technologies, Clausthal University of Technology, Am Stollen 19 B, 38640 Goslar, Germany
a.sotnikov@ifw-dresden.de*

Summary:

Material parameters of CTGS piezoelectric single crystal were derived in extremely wide temperature range from cryogenic temperature to 1173 K. Temperature sensor on the base of Y-cut CTGS SAW resonator was demonstrated.

Keywords: piezoelectric crystal, bulk acoustic wave, SAW, langasite family, catangasite, temperature sensors

Introduction

Piezoelectric single crystals are key materials for microacoustic devices and sensors of various physical quantities. Of particular interest are crystals which possess a reasonable piezoelectric response i.e. high electromechanical coupling over extremely wide temperature ranges from cryogenic to very high temperatures up to 1000°C and higher. Materials for application under such harsh conditions should maintain their material parameters over this temperature range without noticeable deterioration. Among potential candidates, piezoelectric crystals of the langasite (LGS, $\text{La}_3\text{Ga}_5\text{SiO}_{14}$) family are very promising. For example, catangasite (CTGS, $\text{Ca}_3\text{TaGa}_3\text{Si}_2\text{O}_{14}$) crystal, a member of LGS family with ordered structure, demonstrates a combination of very attractive properties like relatively high electromechanical coupling, moderate dielectric constant, low acoustic loss and the absence of a structural phase transition in the entire considered temperature range. In this communication, we present CTGS material parameters measured at 4.2 and 1173 K, estimation of sound attenuation including measurements in the GHz range as well as the characteristics of a SAW temperature sensor based on Y-cut CTGS crystal.

Crystal growth and sample preparation

CTGS single crystals were grown by the Czochralski technique by FOMOS Materials, Moscow, Russia and Leibniz Institute for Crystal Growth, Berlin, Germany. For the ultrasonic wave velocity measurements of CTGS, cube-

like samples were prepared. Attenuation measurements were carried out on the thin plates of 10 mm diameter and 0.5 mm thickness. For GHz frequencies, AlScN thin film piezoelectric transducers were deposited on the samples to realize High overtone Bulk Acoustic Resonator (HBAR). Finally, a demonstrator of SAW-based temperature sensor was realized by a one-port resonator chip comprising CTGS Y-cut crystal and advanced temperature stable electrode metallization system on top.

Experimental procedure

Measurements of the bulk acoustic wave velocities propagating along certain directions were carried out by means of a RITEC RAM-5000 System and UT340 Pulser Receiver. Results at GHz frequencies were obtained using Agilent E5071C Network Analyzer in combination with AlScN thin film transducer. All temperature measurements were carried out using a continuous flow cryostat, a Carbolite tube furnace and a Linkam HFS600E temperature stage, respectively.

Results and discussion

The elastic C_{ij} and piezoelectric e_{ij} constants were derived using a system of relations between bulk velocities of different characteristic modes propagating along certain crystallographic directions. As a result, elastic, piezoelectric and dielectric constants of CTGS single crystal at 4.2 K [1] and 1173 K are presented in Tab.1. Notice strong piezoelectric response of the crystal in a very wide temperature range

including both cryogenic and high temperatures. Sound attenuation in GHz range is an important parameter, especially for SAW sensors usually operating at high frequencies.

Tab. 1: Material parameters of CTGS single crystal at 4.2 and 1173 K.

Material constant	4.2 K	1173 K
C_{11} (GPa)	159.8	136.2
C_{12} (GPa)	83.15	57.9
C_{13} (GPa)	70.6	68.5
C_{14} (GPa)	1.2	0.52
C_{33} (GPa)	218.3	180.7
C_{44} (GPa)	39.02	42.9
C_{66} (GPa)	38.3	39.15
e_{11} (C/m ²)	-0.36	-0.435
e_{14} (C/m ²)	0.62	0.646
$\varepsilon_{11}/\varepsilon_0$	19.7	17.2
$\varepsilon_{33}/\varepsilon_0$	34.4	22.9

Fig. 1 shows as an example obtained attenuation coefficient α as a function of frequency for longitudinal mode on Y-cut CTGS measured at room temperature.

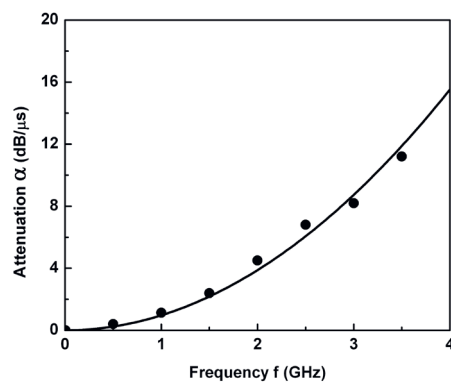


Fig. 1. Sound attenuation versus frequency for Y-cut CTGS (L-mode). Symbols: experiment, solid line: function $\sim f^2$ for comparison.

Note the well-defined square dependence of the attenuation versus frequency, which is also valid for X and Z crystal cuts. As for sound attenuation as a function of temperature, it was found to be low at 4.2 K while still reasonable at high temperature. Fig. 2 shows as an example ultrasonic pulse-echo patterns for Y-cut CTGS sample at 298 and 1195 K, resp. The results were obtained using very short ultrasonic pulses (5 ns); sound excitation and receiving here were done using the intrinsic piezoelectric effect of the crystal.

The temperature dependence of the resonance frequency of a SAW one-port resonator operated as temperature sensor in the range between 25°C and 600°C is depicted in Fig. 3. Note the very good linear frequency vs. temperature characteristics of the SAW device.

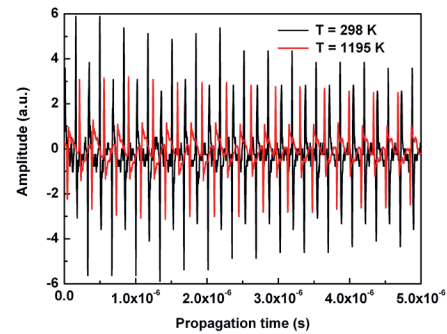


Fig. 2. Pulse-echo pattern for Y-cut CTGS single crystal at 298 K (black line) and 1195 K (red line).

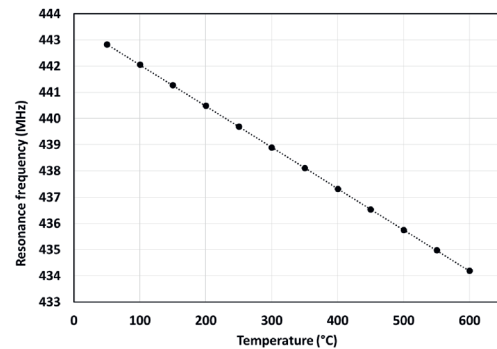


Fig. 3. Resonance frequency vs. temperature for SAW one-port resonator as temperature sensor.

Conclusion

Material parameters of CTGS single crystals were derived over extremely wide temperature range up to 1173 K. Strong piezoelectric response as well as reasonable sound attenuation even in GHz frequency range predetermine catangasite crystal as promising material for sensors capable of operating in a very wide temperature range. Temperature sensor behavior on the base of Y-cut CTGS SAW resonator was successfully demonstrated.

Acknowledgements

Financial support from the German Research Foundation (DFG grants SO 1085/2-2 and FR 1301/21-2) are gratefully acknowledged.

References

- [1] A. Sotnikov, H. Schmidt, M.H. Haghghi, M. Gorev, Yu. Suhak, H. Fritze, S. Sakharov, Material parameters of $\text{Ca}_3\text{TaGa}_3\text{Si}_2\text{O}_{14}$ (CTGS) piezoelectric single crystal at extreme temperatures, *Proc. Joint Conf. Europ. Freq. and Time Forum and IEEE Int. Freq. Contr. Symp.*, 193-197 (2017); doi: 10.1109/FCS.2017.8088844.

High-Temperature Acoustic Loss in Bulk AlN Piezoelectric Resonators

Iurii Kogut¹, Ivan Gamov², Klaus Irmscher², Matthias Bickermann², Holger Fritze¹

¹ Clausthal University of Technology, Am Stollen 19B, 38640 Goslar, Germany,

² Leibniz-Institut für Kristallzüchtung, Max-Born-Str. 2, 12489, Berlin, Germany

Corresponding Author's e-mail address: iurii.kogut@tu-clausthal.de

Summary:

Aluminum nitride (AlN) single crystals are grown by physical vapor transport under varying conditions to achieve samples that exhibit a wide range of doping concentrations for carbon, oxygen and silicon. Accordingly, properties such as electrical conductivity and acoustic loss vary significantly. Beside structural quality and essential point defects, the electrical conductivity, thermal expansion, elastic constants and acoustic losses are determined up to 900°C. Special attention is paid to the correlation of acoustic losses and electrical conductivity, as they are crucial application-relevant parameters. For example, the losses in crystals with low dopant concentration ratios of oxygen to carbon ($[O]/[C] \leq 1$) are found to be determined by the electrical conductivity above about 650°C. The lowest overall losses are observed in AlN with lowest concentration of oxygen impurities.

Keywords: aluminum nitride, high temperature, piezoelectric resonator, acoustic loss.

Motivation

Single crystalline aluminum nitride (AlN) shows attractive properties if used for piezoelectric sensors at temperatures above 500°C. The predominant covalent bonds in the material result in high thermal stability and low losses of piezoelectric resonators thereby enabling new applications like resonant pressure and temperature sensors for turbines and engines.

To take advantage of these properties, high quality bulk crystals are required. Presently, they are provided by a very low number of commercial suppliers which limits the options for users to get crystals with tailored materials properties. Therefore, (1) the growth of crystals that exhibit a wide range of properties such as electrical conductivity, (2) the determination of electrical and acoustic properties and (3) their correlations are the focus of this work.

Samples and methods

AlN single crystals are grown by physical vapor transport under varying conditions resulting, in particular, in dopant concentration ratios of oxygen to carbon ranging from $[O]/[C] = 0.4$ to 4.0. Differently oriented crystal plates are cut and polished to enable piezoelectrically excitation of length-thickness extension, thickness extension and thickness-shear vibrations. The resonance spectra are acquired by resonant piezoelectric spectroscopy [1]. Details on the

AlN growth, sample preparation and electrode deposition can be found in [2,3].

Results

The electrical conductivity of the AlN samples at 900°C ranges from 10^{-5} to 10^{-2} S/m and shows activation energies of about 2 eV in the temperature range from 650 to 900°C. The highest value of about 2.2 eV results for $[O]/[C] = 1$.

The resonance spectra show the expected pattern and are clearly evident even at 900 °C (Fig. 1). A nearly linear decrease of the resonance frequency f is observed with increasing temperature (Fig. 2).

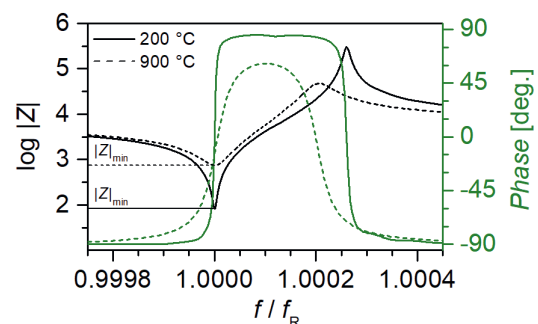


Fig. 1. Resonance spectra of a *m*-cut sample operated in thickness-shear mode at 200 and 900°C (f_R : f at room temperature).

The acoustic losses, as expressed e.g. by the inverse Q-factor, are of particular importance for piezoelectric resonators since they determine the accuracy of the frequency measure-

ment. The overall loss results from the following contributions (Fig. 3):

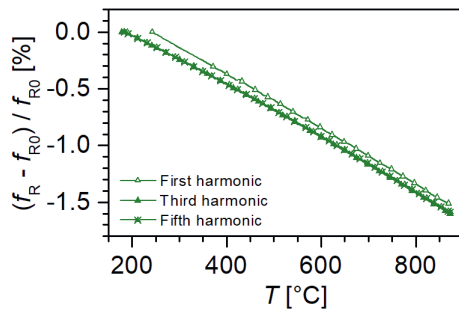


Fig. 2. Resonance frequency of a *m*-cut sample operated in thickness-shear mode as a function of temperature.

- Intrinsic phonon-phonon interaction
In the temperature range of interest, i.e. well above room temperature, this loss mechanism shows a low temperature dependence [4]. Since the intrinsic phonon-phonon interaction is generally low and the total losses increase strongly with temperature, this contribution is practically negligible in the present samples.
- Anelastic relaxation of point defects
At low and medium temperatures, high contributions are observed in oxygen dominated AlN samples (Q_{a1}^{-1} and Q_{a2}^{-1} in Fig. 3).

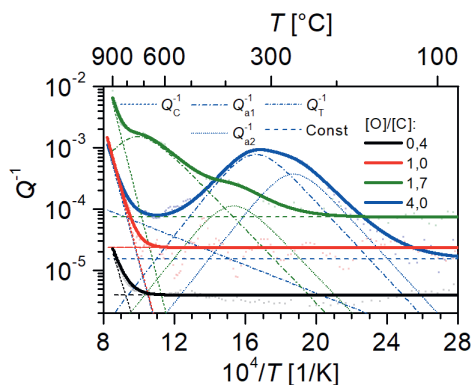


Fig. 3. Contributions to the electromechanical losses in AlN single crystals with different dopant concentrations (details see text).

- Electrical conductivity
The piezoelectric effect couples the mechanical and electrical systems on a microscopic level. The corresponding mechanical losses is caused by the relaxation of charge carriers and dominates in AlN with high C- or O-concentrations at temperatures of about 650-900°C (Q_C^{-1} in Fig. 3). This statement results directly from the conversion of the electrical conductivity into mechanical losses [3].
- Temperature dependent background and contributions from sample support
For AlN samples with higher oxygen content ($[O]/[C] = 4.0$ and 1.7) the background is

relatively high and determines the total losses below about 250°C. For AlN with low oxygen content ($[O]/[C] = 1.0$ and 0.4) the losses are very low ($< 3 \times 10^{-5}$) [3].

Further, the long-term stability of ALN at high temperatures (900°C) and low oxygen partial pressures (10^{-17} bar) is investigated. Within 22 days, the resonance frequency decreases by only 0.36%. The losses are low and remain virtually unchanged.

Finally, the losses in AlN are compared with those of other high temperature stable piezoelectric crystals using the product of Q-factor and resonance frequency. Above about 500°C, AlN exhibit lower losses than LGS ($\text{La}_3\text{Ga}_5\text{SiO}_{14}$). In contrast, AlN generally shows slightly higher losses than CTGS ($\text{Ca}_3\text{TaGa}_3\text{Si}_2\text{O}_{14}$) [5].

Conclusions

The modeling of the temperature dependent acoustic losses in the AlN crystals allows an assignment of dominating loss contributions. In AlN with an oxygen content lower or comparable to that of carbon, the electrical conductivity is the main loss contribution at temperatures above 650°C.

Acknowledgment

The authors gratefully acknowledge financial support from the Deutsche Forschungsgemeinschaft with the funding IDs BI 781/11 and FR 1301/26-1. Further, the authors from TUC acknowledge the support of the Energie-Forschungszentrum Niedersachsen, Goslar, Germany.

References

- [1] H. Fritze, High-temperature bulk acoustic wave sensors, *Meas. Sci. Technol.*, 22 (2011) 12002.
- [2] C. Hartmann, J. Wollweber, S. Sintonen, A. Dittmar, L. Kirste, S. Kollowa, K. Irmischer, M. Bickermann, Preparation of deep UV transparent AlN substrates with high structural perfection for optoelectronic devices, *CrystEngComm* 18 (2016) 348.
- [3] I. Kogut, C. Hartmann, I. Gamov, Y. Suhak, M. Schulz, S. Schröder, J. Wollweber, A. Dittmar, K. Irmischer, T. Straubinger, M. Bickermann, H. Fritze, Electromechanical losses in carbon- and oxygen-containing bulk AlN single crystals, *Solid State Ionics* 343 (2019) 115072.
- [4] W. P. Mason, *Physical Acoustics, Principles and Methods*, Academic Press, New York, 1965.
- [5] Y. Suhak, M. Schulz, W. L. Johnson, A. Sotnikov, H. Schmidt, H. Fritze, Electromechanical Properties and Charge Transport of $\text{Ca}_3\text{TaGa}_3\text{Si}_2\text{O}_{14}$ (CTGS) Single Crystals at Elevated Temperatures, *Solid State Ionics* 317 (2018) 221.

Investigations of the Actuator Based on Lithium Niobate Diffuse Bonded Bimorph Structure

Uliana Yakhnevych¹, Oleh Buryy¹, Yuriy Suhak², Ihor I. Syvorotka³, Dmytro Sugak^{1,3}, Sergii Ubizskii¹, Holger Fritze²

¹ Lviv Polytechnic National University, 12, Bandera Str., 79013 Lviv, Ukraine

² Institute for Energy Research and Physical Technologies, Clausthal University of Technology, 19B Am Stollen, 38640 Goslar, Germany

³ Scientific Research Company "Electron-Carat", 202, Stryjska Str., 79031 Lviv, Ukraine
Corresponding Author's e-mail address: yakhnevych.u@gmail.com

Summary:

The simulation of the actuator based on lithium niobate bimorph (bidomain) structure was carried out by the finite elements method. The calculated value of the displacement of the actuator was about 17.8 μm at the voltage of 300 V. Based on results of simulation, an actuator was manufactured from the oppositely polarized plates of congruent lithium niobate bonded by diffusion of copper from the film placed between the plates. It was found that the displacement of this actuator is equal to 9 nm upon the applied voltage of 1 V, and to 26.5 nm upon 3 V.

Keywords: positioning devices, bidomain structure, lithium niobate, diffusion bonding method, Doppler interferometer

Introduction

The systems of precise positioning are widely used in the areas of science and technique where the small movements should be realized with high precision, linearity, reproducibility and thermal stability. Particularly, such systems are used for precise positioning of the probe in the devices of scanning probe microscopy, precision engineering devices, micro-electromechanical systems, micro-dispensers, micro-motors for surgery, laser gyroscopes, mechanisms of laser resonator adjusting, piezo-drives of regulating systems of car suspensions and lamps, etc. [1]. One of the most frequently used materials for electromechanical actuators is the lead zirconate-titanate ($\text{PbZr}_x\text{Ti}_{1-x}\text{O}_3$, PZT) piezo-ceramics. However, in accordance with the decision of EU, the lead containing compounds must be removed from technical devices [2]. Thus the piezoelectric crystals, particularly lithium niobate (LiNbO_3 , LN) and lithium tantalate (LT) are considered as an alternative to PZT. These crystals almost do not have shortcomings of PZT, however the values of their piezoelectric moduli are significantly (approximately an order) lower than the ones of PZT. To increase the possible deformation under the influence of the electric field the bimorph structures can be used. Such structures are formed by two bonded plates of piezoelectric crystals, at that the vectors of

polarization of both parts are anti-parallel and perpendicular to the interface between them. In other words, such a construction is a bidomain structure functioning in accordance with bimorph principle. Thus, the purpose of this work is a simulation, preparation and testing of the actuator of precise positioning based on lithium niobate diffuse bonded bimorph structure.

The actuator simulation

The simulation of an actuator is carried out by the finite elements method. The parameters of LN crystal used in our calculations are indicated in Tab. 1 (in accordance with the data given in Ref. [3]). The orientation of the plates was (Y + 127°) in accordance with data given in [4].

Tab. 1: The parameters of LiNbO_3 crystal used in our calculations

Parameter	Value
Density, kg/m^3	4700
Dielectric permittivity	$\epsilon_{11} = \epsilon_{22} = 43.6$; $\epsilon_{33} = 29.16$
Elastic constants, 10^{10} Pa	$C_{11} = C_{22} = 20.3$; $C_{33} = 24.3$; $C_{44} = C_{55} = 6.0$; $C_{66} = 7.5$; $C_{12} = 5.3$; $C_{13} = C_{23} = 7.5$; $C_{14} = -C_{24} = C_{56} = 0.9$
Piezoelectric coefficients, C/m^2	$e_{15} = e_{24} = 3.7$; $e_{22} = -e_{16} = -e_{21} = 2.5$; $e_{31} = e_{32} = 0.2$; $e_{33} = 1.3$

The obtained results are in good agreement in the entire investigated range ($-300...300$ V) with the experimental data (see [4]). Particularly, in accordance with [4], the displacement of the actuator is about $17 \mu\text{m}$ at the voltage of 300 V, whereas the calculated value of the displacement is equal to $17.8 \mu\text{m}$.

Formation of bidomain structure of LiNbO_3 crystal

One option to obtain the bimorph structures from single-crystal materials is the diffusion bonding method, which, for example, has been used to obtain lithium niobate-tantalate plates [5]. In our case, the 0.5 mm thick oppositely polarized LN plates were bonded by copper films of different thickness (700 , 600 and 350 nm) deposited on both negatively and positively charged lithium niobate plates.

The XY surfaces of the crystals were mechanically processed till the flatness degree of $\lambda/8$ (for the wavelength λ of 633 nm). The deposition was performed by thermal method on the equipment of Torr International, Inc. (USA). The film thickness control was carried out by the sensor based on the quartz microbalance. The plates were connected by annealing in air during 24 hours at 800 °C under the load about 3 kg/cm² applied to the connected surfaces. Investigations of the bonding interface between the plates were carried out by polarizing microscope ECLIPSE LV100 POL (Nikon, Japan) in the direction perpendicular to the surface of connection through the polished XY side. Based on the obtained results, we conclude that the best bonding was obtained for two negatively charged surfaces with 350 -nm thick copper film deposited on only one plate.

Testing of the actuator of precise positioning

The active element of the actuator was manufactured from LN plates in accordance with the technological scheme described above. The gold electrodes were deposited on the surfaces of the active element (the area of 5×30 mm²) by sputter coating. One edge of the actuator was rigidly fastened in the special holder between two copper electrodes used to apply the voltage (Fig. 1). The measurements of the actuator displacements upon applied voltage were performed by laser Doppler interferometer Polytec OFV 505. The interferometer design allows to use the alternating voltages in the range of $1...10$ V. This study revealed that applying of the voltage of 1 V leads to the displacement of 9 nm at the actuator length of 23 mm (the distance from the holder to the center of the light spot). At the

applied voltage of 3 V the displacement is equal to 26.5 nm.

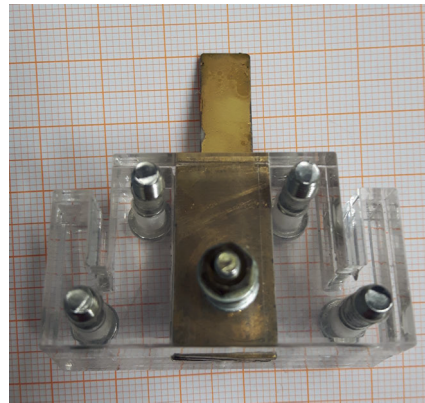


Fig. 1. The actuator of precise positioning based on lithium niobate diffuse bonded bimorph structure.

Conclusions

Based on the results of the simulation, an actuator was manufactured on the basis of oppositely polarized plates of congruent lithium niobate, connected by diffusion of copper from the film placed between the plates. It was found that the displacement of the actuator is equal to 9 nm for the applied voltage of 1 V, and to 26.5 nm at the voltage of 3 V.

Acknowledgements. The work is carried out in the frames of the project DB/MEZHA of the Ministry of Education and Science of Ukraine.

References

- [1] M. S. Vijaya, Piezoelectric Materials and Devices. Applications in Engineering and Medical Science, CRC Press, 186 (2017); <https://doi.org/10.1201/b12709>
- [2] P.K. Panda, Review: environmental friendly lead-free piezoelectric materials, *Journal of Material Science*, 44:19, 5049 – 5062 (2009); <https://doi.org/10.1007/s10853-009-3643-0>
- [3] A.A. Blistanov, V.S. Bondarenko, N.V. Perelomova, F.N. Strizhevskaya, V.V. Chkalova, M.P. Shaskolskaya, Acoustic Crystals: Handbook [in Russian], Nauka, Moscow, 632 (1982); <https://ui.adsabs.harvard.edu/#abs/1982MolZn...S...B/abstract>.
- [4] I.V. Kubasov, M.D. Malinkovich, R.N. Zhukov, D.A. Kiselev, S.V. Ksenich, A.S. Bykov, N.G. Timushkin, A.A. Temirov, Yu.N. Parkhomenko, Precision hysteresis-free actuators of micro- and nano-range displacements based on lithium niobate [in Russian], *Proc. of Intern. Scientific and Technical Conf. INTERMATIC*, part 4, 45 – 48 (2014).
- [5] L.A. Skvortzov, E.S. Stepantsov, Laser strength of the bicrystal system of lithium niobate – tantalate [in Russian], *Quantum Electronics*, 23:11, 981–982 (1993); <https://doi.org/10.1070/QE1993v023n11ABEH003238>

Electrical and Electromechanical Properties of Single Crystalline Li(Nb,Ta)O₃ Solid Solutions for High-Temperature Actuator Applications

Yuriy Suhak¹, Bujar Jerliu¹, Steffen Ganschow², Dmitry Roshchupkin³, Boris Red'kin³, Simone Sanna⁴, Holger Fritze¹

¹ *Clausthal University of Technology, Am Stollen 19B, 38640, Goslar, Germany.*

² *Leibniz-Institut für Kristallzüchtung, Max-Born-Str. 2, 12489, Berlin, Germany.*

³ *Institute of Microelectronics Technology and High Purity Materials, RAS, Academician Ossipyan str. 6, 142432, Chernogolovka, Russia.*

⁴ *Justus Liebig University Gießen, Heinrich-Buff-Ring 16, 35392, Gießen, Germany
yuriy.suhak@tu-clausthal.de*

Summary:

The electrical conductivity, resonance frequency and acoustic loss are determined for piezoelectric resonators which are based on Czochralski grown Li(Nb,Ta)O₃ solid solutions with different Nb/Ta ratios up to 700 °C. Experimental methods include impedance spectroscopy and resonance ultrasound spectroscopy. Further, the long-term behaviour of resonant properties is examined at high-temperatures. After about 400 hours at 700 °C a LiNb_{0.5}Ta_{0.5}O₃ resonator shows an increase in resonance frequency only by 0.1%.

Keywords: Piezoelectricity, high temperature, lithium niobate-tantalate, actuator, sensor.

Background, Motivation and Objective

High-temperature stable piezoelectric actuators whose displacement can be adjusted easily by an applied voltage are required for e.g. energy conversion, aerospace or automotive industrial applications. For such materials, excellent thermal stability and large piezoelectric coefficients are required. However, common piezoelectric materials are limited by their application temperature or suffer from low piezoelectric coefficients. For example, polycrystalline ceramics show thermal instability above about 300°C [1]. Quartz type crystals from langasite (La₃Ga₅SiO₁₄) family are not suitable for actuators due to their low piezoelectric coefficients [2]. Lithium niobate (LiNbO₃, LN) and lithium tantalate (LiTaO₃, LT) attract substantial scientific and industrial interest because of their excellent electro-optical, piezoelectric and acoustic properties. However, their high-temperature usage is limited by thermal instability of LN and low Curie temperature of LT. Recently, attention has been attracted by Li(Nb,Ta)O₃ (LNT) solid solutions that combine potentially the advantages of the end members of the material system [3]. The current work explores electrical conductivity, resonant frequency and loss of LNT resonators with different Nb/Ta ratios as a function of temperature and time and in a wide oxygen partial pressure (p_{O_2}) range.

Specimens and Measuring Techniques

The crystals, used in this study were grown by Czochralski technique at the Institute of Microelectronics Technology and High Purity Materials, Russian Academy of Sciences, Moscow, and at the Institute for Crystal Growth, Berlin. The high-temperature experiments are performed on platinum-electroded Y-cut and Z-cut samples in a gas-tight tube furnace, which allows working temperatures up to 1000 °C. The adjustment of p_{O_2} is realized using an oxygen ion pump in the range from 10⁻¹⁸ to 10⁻³ bar by adjusting the oxygen content in Ar/H₂ gas mixtures [4].

The electrical conductivity σ is determined by impedance spectroscopy in the frequency range from 1 Hz to 1 MHz using an impedance/gain-phase analyzer (Solartron 1260). The investigations of acoustic losses are performed by means of resonant ultrasound spectroscopy on Y-cut and Z-cut LNT resonators, operated in the thickness-shear mode and in the thickness mode, respectively, using a high-speed network analyzer (Agilent E5100A). Detailed description of measuring techniques is given elsewhere [5].

Results and Discussion

Electrical conductivity of LiNb_{0.88}Ta_{0.12}O₃ and LiNb_{0.5}Ta_{0.5}O₃ samples, measured in air in the temperature range from about 400 °C to 700 °C

is shown in Fig. 1 and compared to that of pure LN and LT. As seen from the figure, the samples exhibit similar conductivity that increases linearly in the Arrhenius presentation, indicating that it is governed by a single thermally activated process in the measured temperature range. The activation energies vary between 1.2 eV and 1.3 eV for LN and LT, respectively. The observation follows the general trend of similar conduction mechanisms in LN and LT at temperatures below 700 °C [6]. Earlier, it was shown in [7] that the electrical conductivity of congruent LiTaO₃ shows an activation energy of 1.2 eV in the temperature range of 350–800 °C. The authors concluded that the conductivity is governed by mobile lithium vacancies. Similarly to LiTaO₃, our previous study shows that the lithium ion migration via lithium vacancies is the main transport mechanism in LiNbO₃ and the activation energy, determined for the congruent LiNbO₃ is equal to 1.3 eV [8].

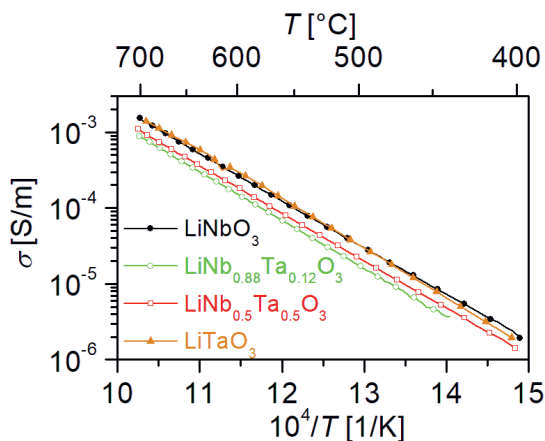


Fig. 1. Conductivity of Li(Nb,Ta)O₃ samples as a function of temperature.

Further, the measurements of electrical conductivity as a function of p_{O_2} revealed, that the decrease of p_{O_2} leads to the conductivity increase in all measured samples. However Ta-rich samples show much smaller increase, comparing to LN indicating that increased Ta content improves the stability of Li(Nb,Ta)O₃ at low p_{O_2} .

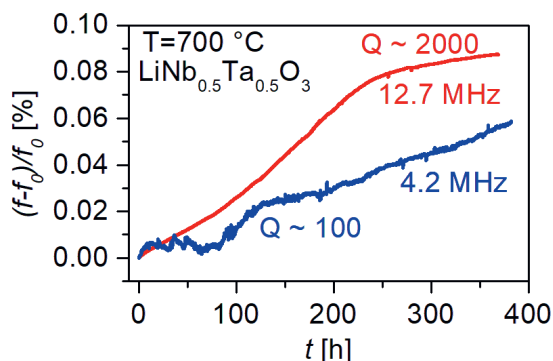


Fig. 2. Time-dependent relative change of the frequency of a LiNb_{0.5}Ta_{0.5}O₃ resonator.

Finally, in order to determine the stability of the resonant properties of LNT, the change of the resonance frequency (f_R) of the LiNb_{0.5}Ta_{0.5}O₃ specimen is examined at 700 °C in air as a function of time. Fig. 2 shows the change of the f_R for the 1st and 3rd harmonics, relative to initial values measured when 700 °C was reached (f_0). As seen from the figure, f_R steadily increases, showing however a shift of less than 0.1% only relative to f_0 . The Q-factor equals 100 and 2000 for the 1st and the 3rd harmonics, respectively.

Conclusions

In summary, the electrical and electromechanical properties of LNT were investigated at high temperatures and low oxygen partial pressures. The conductivity measurements reveal similar magnitudes and activation energies for all measured samples that suggests similar conduction mechanisms. At low p_{O_2} , Ta-rich samples show improved stability compared to LN. The change of resonance frequency of the LiNb_{0.5}Ta_{0.5}O₃ specimen after about 400 operating hours at 700 °C in air is less than 0.1 %.

References

- [1] V. Segouin, B. Kaeswurm, K.G. Webber, L. Daniel, Temperature-dependent anhysteretic behavior of co-doped PZT, *J. Appl. Phys.* 124, 104103 (2018); doi: 10.1063/1.5040556.
- [2] K. Shimamura, H. Takeda, T. Kohno, T. Fukuda, Growth and characterization of lanthanum gallium silicate La₃Ga₅SiO₁₄ single crystals for piezoelectric applications, *J. Cryst. Growth* 163, 388-392 (1996); doi: 10.1016/0022-0248(95)01002-5.
- [3] I. G. Wood, P. Daniels, R. H. Brown, A. M. Glazer, Optical birefringence study of the ferroelectric phase transition in lithium niobate tantalate mixed crystals: LiNb_{1-x}Ta_xO₃, *J. Phys.: Condens. Matter* 20, 235237 (2008); doi: 10.1088/0953-8984/20/23/235237.
- [4] M. Schulz, H. Fritze, C. Stenzel, Measurement and control of oxygen partial pressure at elevated temperatures, *Sensors and Actuators B* 187, 503-508 (2013); doi: 10.1016/j.snb.2013.02.115.
- [5] H. Fritze, High-temperature bulk acoustic wave sensors, *Meas. Sci. Technol.*, 22, 12002 (2011); doi: 10.1088/0957-0233/22/1/012002.
- [6] A. Krampf, M. Imlau, Yu. Suhak, H. Fritze, S. Sanna, LiNbO₃: Model ferroelectric oxide or unique compound?, *In press*.
- [7] A. Huanosta and A. R. West, The electrical properties of ferroelectric LiTaO₃ and its solid solutions, *J. Appl. Phys.* 61, 5386-5391 (1987); doi: 10.1063/1.338279.
- [8] A. Weidenfelder, J. Shi, P. Fielitz, G. Borchardt, K. D. Becker, H. Fritze, Electrical and Electromechanical Properties of Stoichiometric Lithium Niobate at High-Temperatures, *Solid State Ionics* 225, 26-29 (2012); doi: 10.1016/j.ssi.2012.02.026

System Design for Low Power Applications with Digital MEMS Sensors

Petr Stukjunger
STMicroelectronics, Pobrezni 620/3, Prague, Czech Republic,
petr.stukjunger@st.com

Summary:

System design for low power applications has been significantly simplified by the introduction of new digital MEMS sensors. Engineers can employ several methods at sensor and at system level to optimize power consumption without sacrificing the performance of their applications.

Keywords: low power, MEMS sensor, application, system design, machine learning

Motivation

With continuously increasing number of applications that are utilizing MEMS sensors to measure environmental, motion and other types of data, system engineers need to deal with tradeoffs every day. The applications require more and more features and functionalities, but at the same time they demand to decrease overall system power consumption.

Features of digital MEMS sensors and system level techniques that designers may exploit in order to minimize power consumption are discussed in this paper.

Low Power Sensor

Wide popularity of battery-operated nodes motivated manufactures of MEMS sensors to develop devices with ultra-low current consumption. The newest accelerometers can measure movements while consuming less than one microamp. Even larger improvements have been done in the design of gyroscopes, where we have seen nearly 10times drop in their current consumption just over last couple of years.

Digital MEMS sensors are very flexible in their configuration offering variety of operating modes with associated output resolution and wide range of applicable data rates. Designers can therefore select the most suitable configuration for each application case. Some sensors are even capable to switch their operating mode and data rate autonomously based on an external motion event.

Even though these improvements are of substantial help in low power system design, the newest MEMS sensors bring more features that can help.

Standard Embedded Features

Motion detection features like wake-up (for system activation based on a motion), free fall (detection of device falling on the ground), orientation detection (used daily in our mobile phones), single & double tap (for enhanced user interface) became almost industry standard. More and more common are also features like step counter or pedometer, tilt detection etc.

The above-mentioned features allow the system to offload the microcontroller from continuous acquisition and evaluation of sensor data bringing a substantial decrease in system power consumption. It is simply achieved by the utilization of interrupt signals routed from the sensor to the microcontroller. The microcontroller is not involved in data acquisition, instead it is solely waiting for a signal from the sensor raised just in the moment when there is a new event to be handled by the system.

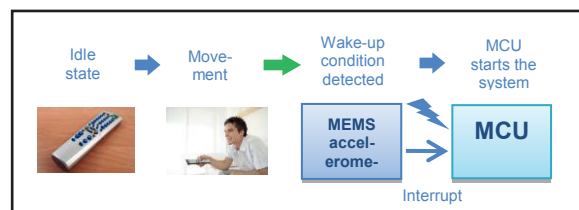


Fig. 1. System wake up utilizing embedded feature and interrupt of MEMS accelerometer.

Advanced Embedded Features

The latest six axis inertial measurement units (IMUs) from STMicroelectronics bring system power reduction to a next level as discussed in [1]. Thanks to Finite State Machine and Machine Learning Core blocks it is possible to move medium complex algorithms from microcontroller inside the sensor itself and consequently reduce not just microcontroller's current

consumption and load, but also traffic on communication bus.

Finite State Machine

Finite State Machine (FSM) provides to designer possibility to create his own state program, where in each state two conditions may be evaluated, or a command executed. The conditions can be evaluation of sensor output data with respect to a user-defined threshold or time-related condition based on an internal timer. FSM is well suited for implementation of gesture recognition algorithms.

Machine Learning Core with AI

Machine Learning Core (MLC) is a hardware implementation of decision trees inside IMU sensor. The sensor can run motion classification algorithms by its own and take the advantage of machine learning techniques well known from the field of artificial intelligence.

The utilization of MLC follows common machine learning process. It starts with data collection and labeling followed by identification and extraction of the features that characterize the movements to be recognized. Then any conventional machine learning tool is executed to generate decision tree. Finally, the decision tree is converted into set of values, which shall be loaded into the sensor's configuration registers to run the decision tree algorithm.

The overall system current consumption is dramatically reduced as can be seen from the following example. We took human activity recognition algorithm and compared its implementation as microcontroller library vs. MLC algorithm.

Tab. 1: Current consumption of ST's MEMS sensor when running activity recognition algorithm

Sensor	MCU library implementation	MLC implementation
Core	15 μ A	15 μ A
MLC	0 μ A	4 μ A

As shown in Tab 1. in both cases the sensor needs 15 μ A to sample data. Running algorithm inside MLC adds just few extra micro amps.

Tab. 2: Current consumption of microcontroller when running activity recognition library

MCU	Wake up rate	Consumption
STM32L476 (Cortex-M4)	63 ms (1/16 Hz)	51 μ A

As shown in Tab 2. when the microcontroller is running activity recognition library, it needs to collect sensor data at certain rate (16Hz in this case) and run the classification algorithm.

Tab. 3: Current consumption of microcontroller when running activity recognition algorithm in MLC

MCU	Wake up rate	Consumption
STM32L476 (Cortex-M4)	1 s	2.8 μ A
	30 s	0.7 μ A
	100 s	0.6 μ A

When MLC is running activity recognition, the microcontroller can be left for most of the time in a very low power mode and wakes-up only upon notification from the sensor that a new motion class has been detected, see Tab 3.

From Low Power Sensor to Low Power System

We have seen that sensors offer many options to optimize overall system current consumption. There are several methods how to save current also at the system level as discussed in [2].

The output data shall be read from the sensor using so-called data ready interrupt instead of continuously polling status register to check whether new data has been sampled.

Communication on the serial bus between the sensor and the microcontroller is another contributor to the overall system power consumption. SPI interface is therefore preferred over I²C. Brand new sensors are equipped with MIPI I3CSM bus that combines benefits of SPI, i.e. speed, and I²C, i.e. number of wires.

Power supply level shall be as low as possible, because it decreases the current consumed by the sensor. Some applications can benefit from power cycling, mechanism where the sensor is powered only for necessarily short period of time and remains unpowered for the rest. For this purpose, the sensor can be even powered directly from a pin of microcontroller.

Conclusion

Low power system design can benefit from the ultra-low current consumption of modern digital MEMS sensors and utilization of their standard and advanced embedded features like FSM and MLC. By employing optimizations also at the system level, the overall power consumption can be reduced multiple times.

References

- [1] M. Castellano, R. Bassoli, M. Bianco, A. Cagidiaco, C. Crippa, M. Ferraina, M. Leo, S.P. Rivolta, Embedded Algorithms for Motion Detection and Processing, proceedings of embedded world 2018 exhibition&conference
- [2] Vladimir Janousek, Petr Stukjunger, Low-power application design with ST's MEMS accelerometers, design tip, Rev 1, February 2019

Flexible Equivalent Circuit Modeling for Piezoelectric Vibration Energy Harvesters

Dominik Gedeon¹, Stefan J. Rupitsch¹

¹ Chair of Sensor Technology, University Erlangen-Nuremberg,
Paul-Gordan-Str. 3/5, 91052 Erlangen, Germany
dominik.gedeon@fau.de

Summary:

We present a parameter extraction method for piezoelectrically coupled equivalent circuit models. We describe a method for modeling multi electrode configurations, that can be configured as needed by introducing additional coupled capacitors.

Keywords: Piezoelectric Energy Harvesting, Electromechanical Modeling, Finite Element Method, Equivalent Circuit Models, Multi Electrode Configurations

Introduction

When designing Vibration Energy Harvesting devices (VEHs), both the electromechanical structure as well as the electronic circuit have to be optimized. A common approach in describing piezoelectric VEHs is a multi-modal electromechanical model, incorporating coupling between mechanical eigenmodes and an electric capacitance, and vice-versa. When pursuing a system simulation approach, a modal model may be implemented as an Equivalent Circuit Model (ECM) in an electrical circuit simulator. In [1] such multi-modal models are examined in detail and the importance of distributed mechanical parameters, as well as proper electromechanical coupling is underlined. Moreover, we have proposed a modal reduction technique, based on Finite Element (FE) modal analysis, resulting in a reduced order coupled system [2]. In [3], a FE based approach is presented to extract the Parameters for an ECM from various frequency-resolved simulations of the electric admittance of a VEH.

In this work, we extend our approach [2] to parameter extraction for electrical equivalent circuit models and propose a circuit structure for multi-electrode harvesters.

Methods

The basic structure of our ECM is depicted in Fig. 1. The non-greyed part is a coupled model as used by, e.g., [4], [3]. The equivalent elements L_n, C_n, R_n represent a mechanical mode, the current is a mechanical displacement in generalized coordinates. The ideal transformer with winding-ratio N_n couples mechanical displacement with electric current through the static capacitance C_0 and vice-versa.

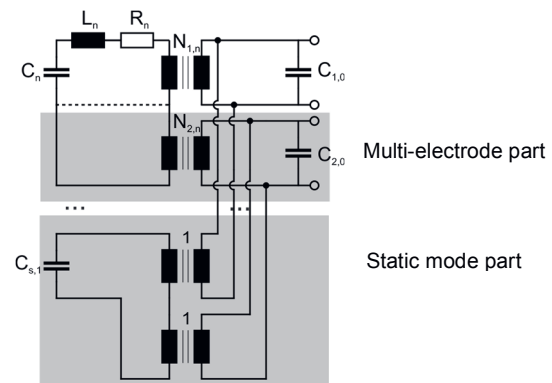


Fig. 1. Structure of the equivalent circuit model.

Considering multi-electrode structures, we add additional transformers and static capacitors. As an example we use two configurations of a trimorph cantilever, depicted in Fig. 2. One configuration is completely symmetrical. In a second configuration the lower piezoelectric layer is shorter than the upper layer.

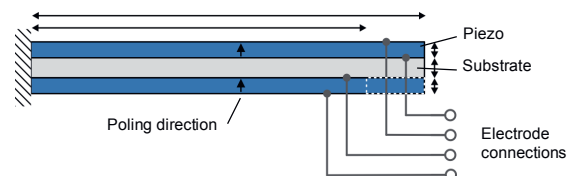


Fig. 2. Trimorph Energy Harvester, used here as an example.

Parameters R_n, L_n, C_n are derived by solving a generalized eigenvalue problem for a number of M eigenmodes, for a FE model with all electrodes in short circuit condition and subsequent diagonalization of the FE matrices. As we pointed out in [2], it is important to include the piezoelectric effect already at this stage of the

mechanical eigenmode calculation, as the electromechanical coupling exerts material stresses even in external short circuit conditions. The coupling (i.e., winding ratios N_n) are computed by imposing the eigenvectors (i.e., mode shapes and corresponding electric potentials) onto the original FE stiffness matrix. The static Capacitances C_0 are derived from static computations, yielding the unclamped capacitances C^t . As the electromechanical capacitors C_n will transform to the electrode through the ideal transformers by $C_{el} = N^2 C_n$, the capacitances from all considered modes must be subtracted [3]

$$C_0 = C^t - \sum C_{el} \quad (1)$$

The static capacitance of each of the electrodes therefore coincides with the result from a static computation of the original FE model, regardless of the number of modes considered. If we, however, want to investigate different interconnections between electrodes, e.g., series or parallel connections, the different static bending shapes in different electrical configurations will change the static capacitances that are being observed. As an example, the static, unclamped capacitance of the symmetrical trimorph from Fig. 2 in parallel configuration was 6% larger than the sum of the two single capacitances. This effect can be captured by considering a sufficiently large number of electromechanical mode shapes, that may well exceed the frequency range of interest. Neglecting this effect, however, will result in deviations in both resonance frequency as well as in magnitude of the electrical impedance.

With a view to resolving this trade-off between necessary number modes and precision, we propose the introduction of *static modes* that are represented in the ECM by capacitors that couple via ideal transformers to the static capacitances (cf. Fig. 1). Each additional capacitance is derived from a static computation of a possible electric configuration. In case of the two-electrode example (cf. Fig. 2), the static modes are “bending” when operated in anti-parallel or anti-serial configuration, and “elongation” when operated in parallel or serial configuration. Additionally, each electrode capacitance C_0 is now computed as the clamped capacitance C^s . The coupled capacitors are then calculated similarly to (1), depending on the sign of the respective winding ratios. In doing so, effects on the static capacitance and therefore the overall electric impedance are captured without considering an unnecessarily high number of eigenmodes.

Results

Figure 3 shows the electric impedance around the first bending mode frequency of the symmet-

rical trimorph model with anti-parallel configuration. The 4 mode ECM shows a considerable deviation due to an incorrect static capacitance. When considering 20 eigenmodes, the ECM coincides perfectly with the original FE model. The same is achieved, however, if the 4 mode ECM is extended by the static mode circuits as proposed here.

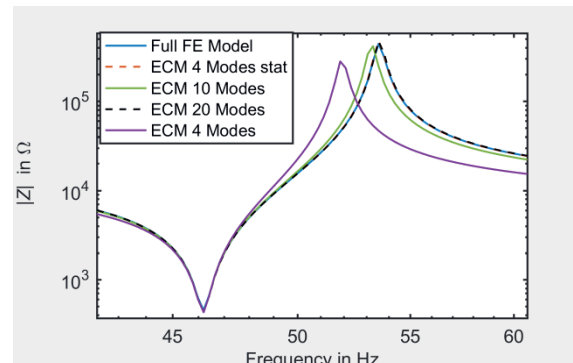


Fig. 3 Anti-parallel configuration, 1st bending mode.

For the unsymmetrical variation from Fig. 2, a parallel connection of the electrodes is shown in Fig. 5. The uncompensated 4 mode ECM shows a much lower effective capacitance, resulting in considerable deviations from the original model.

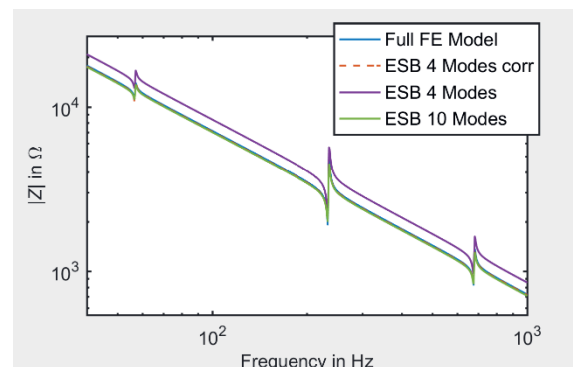


Fig. 5 Non-symmetrical trimorph (Fig. 2) in parallel-configuration.

References

- [1] A. Erturk, D.J. Inman, Issues in mathematical modeling of piezoelectric energy harvesters, *Smart Materials and Structures* 17, 065016 (2008), doi: 10.1088/0964-1726/17/6/065016
- [2] D. Gedeon, S.J. Rupitsch, Finite element based system simulation for piezoelectric vibration energy harvesters, *Intelligent Material Systems and Structures* 29, 1333–1347, doi: 10.1177/1045389X17733328
- [3] Y. Yang, L. Tang, Equivalent circuit modeling of piezoelectric energy harvesters, *Intelligent Material Systems and Structures* 20, 2223–2235 (2009); doi: 10.1177/1045389X09351757
- [4] N.G. Elvin, A.A. Elvin, A general equivalent circuit model for piezoelectric generators, *Intelligent Material Systems and Structures* 20, 3–9, doi: 10.1177/1045389X08089957

A Self-Sustained Microcontroller Regulated Energy Extraction Network for Piezoelectric Energy Harvesters

Philipp Dorsch¹, Stefan Götz¹, Florian Hubert¹, Stefan J. Rupitsch¹

¹ Chair of Sensor Technology, Friedrich-Alexander-University Erlangen-Nuremberg,
Paul-Gordan-Straße 3/5, 91052 Erlangen, Germany
Philipp.dorsch@fau.de

Summary:

The presented energy extraction network regulates the output voltage of a rectifier in order to meet the point of maximum power extraction. This point depends on the mechanical excitation of a piezoelectric energy harvester. The obtained results are compared to an unregulated approach. Though the proposed solution requires a higher supply current, the overall power output remained comparable. Additionally, the option of managing the harvested energy was gained. This leads to a promising feature for various self-sustained applications.

Keywords: Piezoelectricity, Internet of Things, Asset-Tracking, Energy-Autarchic, Low-Power and Harvesting

Background, Motivation and Objective

Wireless sensor systems are widely used in industrial, consumer and medical applications. Most of those sensor systems are powered by batteries, which have to be replaced, recharged and disposed after their lifetime. This results in operational expenses and is harmful for the environment. Consequently, there is a great demand for self-sustained systems.

The key-technology for the development of such systems is energy harvesting. In [1], a cantilever based piezoelectric energy harvester (PEH) was used to convert the mechanical power from the movement of an asset into electrical power. This obtained electrical energy was used to send radio-transmissions that allow to track an asset. The piezoelectric principle was chosen for several reasons: Firstly, it delivers excellent conversion rates from mechanical into electrical power [2]. Secondly, it can be implemented in simple and scalable structures. And finally, it can not only serve as a source of energy, but also as a sensor that detects the movement of the asset.

The piezoelectric conversion is based on the coupling between the mechanical and the electrical domain of the harvesting structure. Therefore, it naturally inherits a resonant behavior, which acquires the most ambient power for sinusoidal excitation at its resonance frequency. Consequently, the eigen frequency of the harvesting structure must coincide with the most

powerful spectral component of the excitation for maximum power output.

Additionally, a proper electrical network is needed to extract and provide the harvested energy. A lot effort has been made to design synchronized energy extraction circuits for PEHs (SSHI, SSHC, SECE). However, it has been shown in [3] that such energy extraction networks (EEN) do not perform better than a conventional rectifier for PEHs with strong coupling which are excited referenced to acceleration. Nonetheless, the full-bridge rectifier also has drawbacks. The amount of extractable energy depends on the ratio of the voltage V_{C1} of the storage capacitor to the open-circuit voltage $V_{PEH,OC}$ of the PEH, because the energy extraction is based on a capacitive-capacitive discharge.

In [1], a two-stage EEN, which regulates the voltage V_{C1} to a predefined value, was proposed. If the excitation scenario deviated from the expected one, a decrease in the amount of extractable power was observed. To overcome this undesired behavior, we introduce a completely self-sustained, microcontroller regulated EEN for PEH. The proposed EEN regulates V_{C1} to meet the point of maximum extractable power for each excitation scenario dynamically.

Energy Extraction Network

The EEN is displayed in Fig. 1. The top part shows the power path and the bottom part describes the generation of the supply voltage V_{DD} for the microcontroller (MCU), which regulates

the network. The power path consists of a full-bridge rectifier connected to the input capacitance C_1 of a flyback converter. The switching signal V_G is deduced from a comparison of the input voltage V_{C1} to the internal voltage V_{DAC} of the MCU. By varying V_{DAC} , V_{C1} is adjusted to meet the maximum power-point. At this point, V_{C1} is half of the open circuit voltage of the PEH $V_{PEH,OC}$.

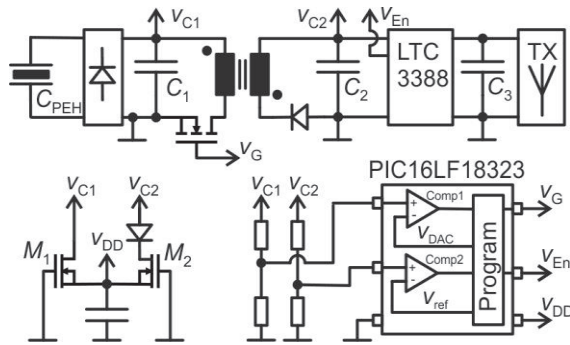


Fig. 1. Schematic of the proposed EEN.

Since $V_{PEH,OC}$ is not available to measure it directly, it is calculated in the software of the MCU according to

$$V_{PEH,OC} = \frac{n_s}{t_{eval}} \frac{1}{2f_r} \frac{C_{PEH} + C_1}{C_{PEH}} V_H + V_{C1,pre} \quad (1)$$

Thereby, n_s is the number of switching events of the signal V_G in the evaluation time t_{eval} . The capacitance and the resonance frequency of the used PEH are given by C_{PEH} and f_r , respectively. Furthermore, the hysteresis voltage V_H of comparator 1 and the DAC-voltage $V_{C1,pre}$ of the previous step are necessary. Needless to say, all of those values can be easily adjusted according to the used PEH.

Peripheral units of the MCU like counters, timers and internal voltages can be used in its sleep mode and are activated solely on demand. So, the MCU only has to wake up to evaluate (1) and check if there is enough energy in the storage capacitance C_2 to activate the buck converter LTC3388 and the application. This results in a low average current consumption of $20 \mu A$ at $2.2 V$, which accounts for less than 8 % of the harvested power for excitation scenarios with $RMS(V_{PEH,OC}) > 30 V$.

Results and Discussion

In order to test the capabilities of the proposed network, we excited the PEH on a vibration test system with respect to acceleration, applying noise signals with different amplitudes. This simulates different excitation scenarios with different $V_{PEH,OC}$. For each of those, the harvested mean output power was measured. We compare the proposed regulated approach with the previous analog solution from [1]. The

measurements were obtained with completely self-sustained EENs and are depicted in Fig. 2.

As the results revealed, the overall power output for the regulated EEN is comparable to the power output for the constant V_{C1} approach in [1]. For excitation scenarios that produce a $V_{PEH,OC} < 30 V$, the proposed solution is inferior to the approach with constant V_{C1} . This is so because the previous analog solution requires less current to supply itself ($4 \mu A$) since it does not need a MCU to function.

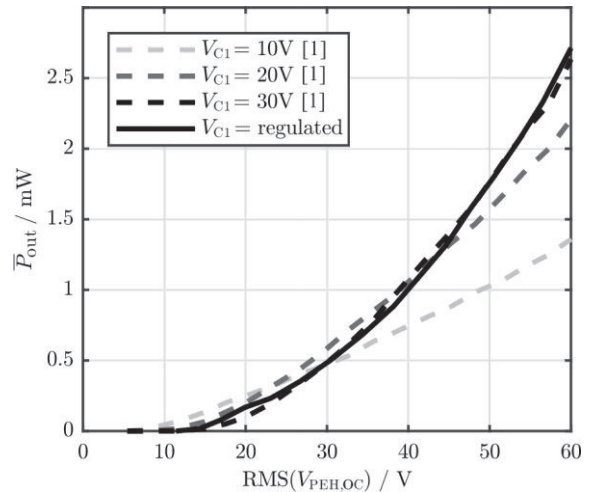


Fig. 2. Comparison of the mean output power \bar{P}_{out} for different excitation scenarios ($V_{PEH,OC}$). Dashed lines: output power for analog solution [1]. Solid line: output power for regulated V_{C1} .

For use-cases that provide higher $V_{PEH,OC}$, the proposed regulated EEN adapts V_{C1} automatically and delivers a higher power output compared to low predefined values V_{C1} .

The proposed EEN delivers another major advantage for the asset-tracking application: While the previous approach always sent a transmission, when there was just enough energy stored to do so, the novel approach can manage the harvested energy. This gives the possibility to gather the energy when the asset is moving and to send the transmission for position update after the movement of the asset.

References

- [1] P. Dorsch, T. Bartsch, F. Hubert, H. Milosiu, S.J. Rupitsch, Implementation and Validation of a Two-Stage Energy Extraction Circuit for a Self Sustained Asset-Tracking System, *Sensors* 19(6), 1330 (2019); doi: 10.3390/s19061330
- [2] S.J. Rupitsch, Piezoelectric Sensors and Actuators - Fundamentals and Applications, *Springer*, (2019); ISBN: 978-3-662-57534-5
- [3] D. Guyomar, M. Lallart, Recent Progress in Piezoelectric Conversion and Energy, *Micromachines* 2011, 2, 274-294;doi:10.3390/mi2020274

Universal Energy Harvesting Topology Used for Small Variable Temperature Gradients

Martin Lenzhofer

*Silicon Austria Labs GmbH, Europastraße 12, 9524 Villach, Austria
martin.lenzhofer@silicon-austria.com*

Summary:

This paper presents a thermo-electric energy harvesting circuit that starts up at very low input voltages, harvests the very little energy contained in small variable temperature gradients and bases on a commercially available converter chip. To guarantee a safe system start and stable operation over a certain time, external components are added that realize the topology developed within a modified block diagram. As a result, it turns out that beside optimal load matching also the power distribution and sequencing within the system is essential to deal with such low energy levels.

Keywords: harvester topology, harvesting circuit, thermo-electric generator, LTC3108

Introduction

Due to the rapid growing number of wireless sensor systems favored by the IoT and industry 4.0 applications also the demand for low power electronics increases. Many systems are powered by battery, but their drawbacks are an increase in dimensions and costs. Additionally, there is a need for replacement or recharging. To overcome these problems and to develop systems that are even able to be used in harsh environments, methods are introduced to harvest energy from present energy sources in the environment of the sensor. Since their quantities are quite small, sophisticated circuits must be developed to convert this low energy into useful supply levels for electronic circuits. Possible energy sources to be converted are - light emissions, radio frequency transmissions, vibrations and heat as it is used in the presented work. There are many publications dealing with harvesting circuits working under stable conditions, but there are rarely few dealing with temperature gradients [1], [2].

Modified Block Diagram for an Energy Harvesting System

Generally an energy harvesting system is built up by a detector unit that converts the physical quantity into an electrical signal, an energy converter, to boost the signal amplitude to a proper one for supplying an electronic circuit, an energy storage module for charging up with not instantly used energy and at last the energy consumption module represented by the electronic circuit of the sensor, refer to Fig. 1.

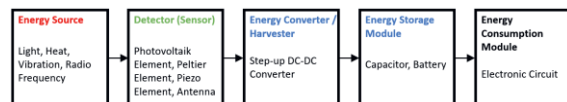


Fig. 1. General valid block diagram for a harvester unit working under stable environmental conditions.

If dealing with temperature gradients, which may additionally vary in time, this simple block diagram must be modified and extended to a configuration shown in Fig. 2.

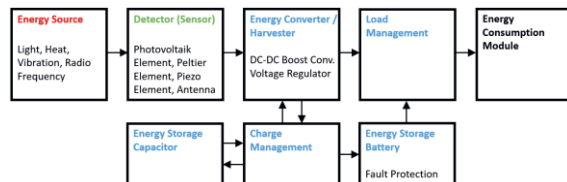


Fig. 2. Modified block diagram for a general harvester unit, dealing with not stable environmental conditions.

There are two main differences between the block diagram in Fig. 1 and the modified one in Fig. 2. First, the energy storage block is separated and split for both storage technologies - a capacitor and a battery, which additionally may need a fault protection. Furthermore, the constant voltage level enables a direct connection to the so important load management block, which represents the second main modification. This block is essential, especially if dealing with very low energy of temperature gradients. In this case first the energy must be harvested, before switching on the power supply for the electronics, which requires, even if using low power components a few milli amperes to start-up and run for a certain time.

Thermal Harvester Circuit Development

Thermal energy harvesting systems require optimizations on the thermal and on the electrical circuit level. In particular, the thermo-electric device must be sized appropriately for the available heat and the electrical load. To maximize the converted power a perfect matching condition of the thermo-electric generator (TEG) and the input impedance of the DC-DC converter circuit is aimed. In the presented use case of exploiting the energy from thermal gradients the LTC3108 from Linear Technologies seemed to be the best fitting one. As it is already pointed out, also the suggested circuit schematic in the datasheet of the chip (see Fig. 3, [3]) bases on the simple block diagram shown in Fig. 1.

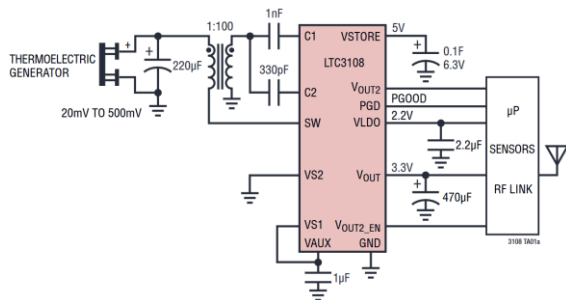


Fig. 3. Wireless remote sensor application powered from a Peltier cell recommended in the datasheet.

The implemented start-up sequence in the LTC3108 requires constant input levels. As this is not given with transient gradients, the switching scheme must be influenced, which is just possible by applying external components. Fig. 4 illustrates the developed circuit and its modifications realizing a circuit based on the adopted block diagram shown in Fig. 2.

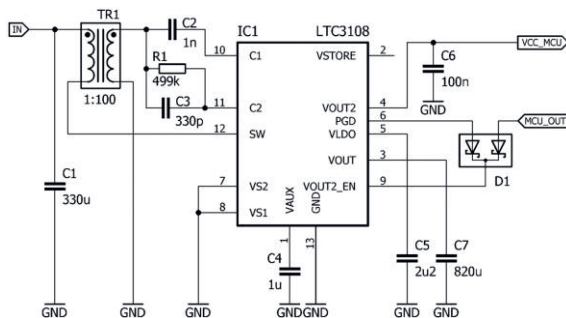


Fig. 4. Developed circuit with improved power-up sequence influenced by external components.

The first key modification is the connection of just a capacitor C7 to VOUT of the LTC3108, which represents a high impedance load. Therefore, all available energy at the input is stored in C7, right after start-up of the DC-DC converter. If the programmed output level of 2.35 V, set via VS1 and VS2, is reached, the power good PGD signal enables VOUT2, where

the low power microcontroller is connected. However quite a high start-up current is necessary, leading to a voltage drop at VOUT, because the current flows from the input and additionally from C7 via VOUT2 to the MCU. Due to the fixed internal hysteresis, this drop causes the chip to deactivate PGD again, resulting in a shutdown of VOUT2 and therefore deactivation of the electronics again. Now just C7 represents the load again, and after reaching the valid level PGD is activated once more. To overcome this kind of ringing phenomena, which would never allow the circuit to start-up properly, an external OR-gate is realized by D1. If PGD is deactivated again by the LTC3108, one output of the controller switches on in the meantime, which leads the power supply to remain at the desired level. So, this configuration represents a self-locking circuit mechanism, which is the second important feature of the circuit. The value of C7 must be carefully chosen according to either provide enough stored energy to start-up the electronics or to charge up in time to reach the valid output level at VOUT according to the given thermal gradient at the input.

Results

Measurements show the functionality of the circuit and demonstrate how the switching sequence of the LT3108 is influenced by external components to deal with the little energy of thermal gradients.

Acknowledgement

The COMET Centre ASSIC Austrian Smart Systems Integration Research Center is funded by BMVIT, BMDW, and the Austrian provinces of Carinthia and Styria, within the framework of COMET - Competence Centres for Excellent Technologies. The COMET programme is run by FFG.

References

- [1] Y. Meydbray, R. Singh, and A. Shakouri, "Thermoelectric module construction for low temperature gradient power generation", Proc. 24th Int. Conference on Thermoelectrics, pp. 348-351, 2005
- [2] P. Woias, "Thermoelectric Energy Harvesting from small variable Temperature Gradients", Proc. 12. Dresdener Sensor-Symposium, pp. 83-88, DOI 10.5162/12dss2015/5.6, 2015
- [3] Linear Technology Corp., datasheet LTC3108. [Online]. Available from: <https://www.analog.com/media/en/technical-documentation/data-sheets/LTC3108.pdf>

Measuring Considerations for Jitter Characterization on Small Satellite Reaction Wheels

Bill Zwolinski¹, Claudio Cavalloni², Marine Dumont²

¹ Kistler Instrument Corp., 75 John Glenn Drive, Amherst NY 14228-2171, USA,
² Institution Kistler Instrumente AG, Eulachstrasse 22, 8408 Winterthur, Switzerland
 Marine.dumont@kistler.com

Summary:

Reaction wheels are used for attitude control of satellites without the need to use thrusters. Characterizing the unwanted vibration or jitter during reaction wheel operation supports balancing operations to optimize the unwanted disturbances. Usage of 6-Component Piezoelectric measurement chains was investigated and optimized to measure low level jitter with the highest precision.

Keywords: Reaction Wheel, Jitter, Microvibration, Piezoelectric Dynamometer

Small satellites, Reaction Wheels and Jitter

Recent years have seen advances in terrestrial observation accompanied by an increase in the need to measure Earth's surface and atmosphere with greater precision. For example, cameras on the latest Earth observation satellites feature resolution on the order of 0.5m.

Reaction wheels are used for attitude control of satellites without the need to use thrusters and propellant, which is in limited supply. The operation of a reaction wheel uses an electrical motor to rotate a flywheel at various rotational speeds, causing the satellite to counterrotate proportionately due to the conservation of angular momentum. As the flywheels rotate there are small fluctuations, called jitter, that are directly coupled into the satellite and can affect imaging precision as illustrated in Figure 1.

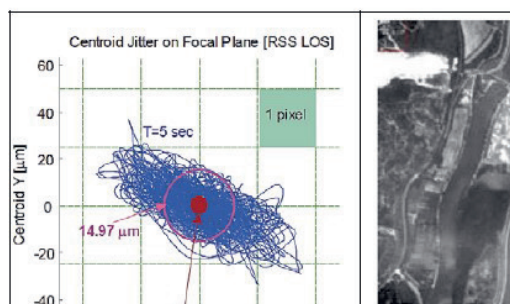


Fig. 1. Satellite Pointing (blue line), which is worse than requirement (red dot), resulting in image distortion (b); image without distortion (c). [1]

Characterizing the unwanted vibration or jitter during reaction wheel operation supports bal-

ancing operations to optimize the unwanted disturbances. It is then increasingly common for satellite manufacturers to request jitter characterization.

Satellites with low mass and size, usually under 500kg are becoming more common for cost and convenience reasons. For small satellites, resolution of forces and moments lower than 5mN and 0.5mNm can be significant to the mission.

Piezoelectric Technology for High resolution and High frequency measurement

A 6-component Piezoelectric sensor is ideally suited for jitter characterization of small reaction wheels. Such a solution provides very high measurement resolution as well as direct measurement forces and moments. This makes it possible to measure dynamic force changes greater than 0.5mN, and moments changes greater than 0.02mNm, depending on the signal bandwidth and assuming optimal measuring configurations with optimal charge amplifier. In addition, a static weight can be "eliminated" by resetting the charge amplifier (like a tare function). This allows the measurement range to be based on the magnitude of the dynamic signals of interest – while increasing the signal to noise ratio. Such piezoelectric sensors deliver a rigid measurement platform achieving very high natural frequencies of 6.9kHz in force and 6.3kHz once mounted. Such a 6-component piezoelectric sensor uses 6 pairs of quartz disk, cut in different orientations. The sensor output must be combined to a laboratory grade low noise quasi-static charge amplifier delivering the high

resolution previously mentioned and converting the signal into voltage.

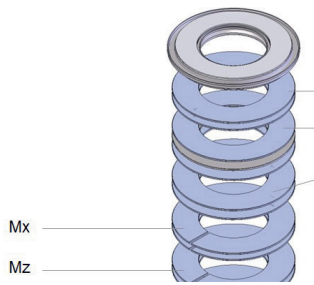


Fig. 2. Internal design of a Piezoelectric 6 Component Force sensor

The voltage output is then input to a 6 Channel DAQ with a noise level that must be at least as good as the charge amplifier in order to allow for the lowest possible measured signal.

Low background Noise

To measure low-level, high-resolution forces and moments, the test environment should be constructed to minimize environmental noise from sources such as airflow and seismic inputs. Typical considerations include a vibration isolation table (see Figure 3) with resonances outside the frequency of interest. This will isolate the force sensor from external vibration sources such as compressors, machinery, people walking and road traffic. Even airflow from an air-conditioning system can create unwanted input to the sensor and may require the use of a box over the test article. Electrical noise from the signal-conditioning system can sometimes be improved by using battery power instead of AC mains power.



Fig. 3. Small satellite reaction wheel jitter investigations using 9306A 6 Component Force sensor conducted onto a vibration isolation table and using an airflow insulation box.

High Frequency Response

A piezoelectric sensor can be modelled as a lightly damped second order system illustrated in Figure 4. As such the natural frequency can be used to estimate the amplitude response tolerance at different frequencies.

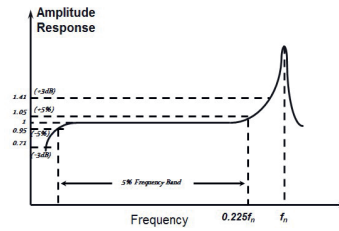


Fig. 4. Lightly damped second order system

Most piezoelectric sensors follow then the high frequency response rule shown in eq (1) :

$$f_{+5\%} = f_n/5; f_{+10\%} = f_n/3; f_{+3dB} \quad (1)$$

The test engineer should decide on the amplitude response tolerance and the frequency range of interest based on the lightly damped second order approximation. For a natural frequency of 6.9kHz, the 5% amplitude response is up to 6.9kHz/5, or 1.4kHz.

In addition, as mass acting upon the sensor affect natural frequency, a basic tap test, using a very small screwdriver or a small impact hammer can be used to determine the FRF and related f_n of the complete system.

Rangeability and Resolution considerations

Piezoelectric measurement chains permit adjustment of the full-scale measurement range using the charge amplifier. By using a lower full-scale range, the broadband noise can be improved as illustrated in table 1.

	Case 1	Case 2
Full Scale Range	10V = 10N; Therefore 1N/V	10V = 2N Therefore 0.2N/V
Broadband Noise (V)	1mVrms=0.001Vrms	1mVrms=0.001Vrms
Broadband Noise (N)	1N/V*0.0025Vrms =2.5mNrms	0.2N/V*0.0025Vrms =0.5mNrms

Table 1. Broadband noise vs full scale range

Signal Synchronization

It is crucial that measurement signals are synchronized, or results may be interpreted completely incorrectly. Synchronization can be performed in two ways. The classic solution is to have a separate line, where a system clock is routed to each device to ensure that the measured values are recorded at the same time. The other option is to equip each device with a precise clock and periodically adjust it as is used in the precision time protocol (PTP). This last one solution is highly recommended in case of dynamic events such as in Jitter testing.

References

[1] Le, M.P. (2017). Micro-disturbances in reaction wheels Eindhoven, TU Eindhoven

New reference force transducer for compressive forces based on the radially symmetric shear-beam principle

Thomas Kleckers

Hottinger Baldwin Messtechnik GmbH; Im Tiefen See 45; 64293 Darmstadt, Germany; E-mail: Thomas.Kleckers@HBKworld.com

Summary:

Shear beam type force sensors are very common in the world of experimental mechanics, testing machines and in advanced production lines. High stiffness, high output signal and good robustness are the proven advantages of this technology. The principle has been increasingly used for reference sensors in the last years. A new sensor design shows an even higher accuracy for compressive forces.

Keywords: Force transducer, force reference standards, force calibration, radial symmetric force transducer

Introduction

Radial symmetric shear type sensors are available with capacities from 1.25 kN to 5 MN. A spring body of such a sensor is shown in figure 1. The force is introduced in a central thread in the middle of the transducer, the outer flange allows the connection to the components below of the sensor.

Strain gauges are placed on the bars in a way so that they measure the strain under 45 degrees to the sensor axis. Those strains are shear strains- this is also the reason for the naming of the sensors. [1]



Fig.1: A spring body of a radially symmetric shear-force transducer. The strain gauges are glued on the bars in a way that there is always one strain gauge picking up the negative strain and another one picking up the positive strain. The Wheatstone bridge circuit compensates the temperature influence on every single bar so that the sensor has an excellent behavior under temperature gradients.

The sensors are available with and without a load base, shown in figure 2. As the mounting of the sensor to its load base is of high importance for the many of the sensor characteristics, in the world of reference force transducers all sensors are coming along with a mounted load base.



Fig.2: Radial symmetric shear types without (left) and with (right) load base: Picture: HBM

Radial symmetric shear type load cells are available with Chrome – Nickel strain gauges which offer a higher sensitivity [2] and a design with a constant strain field. Because of both facts the output signal is 4 mV/V and more at full load. This is twice the value of other mechanical principles for reference force transducers.

The hysteresis is the limiting point with the shear type load cells. The reason is given by the mechanical characteristic of the bolting between sensor and load base. In case of tensile forces, the stresses between the load base and the sensors decreasing at this point so that

very little movements are possible. Those movements lead to changes in the stress state of the sensor and therefore finally to differences between increasing and decreasing loads [1]-monolithic sensors have a clear advantage with this characteristic.

The hysteresis effect is not of importance for compressive forces as those loads increase the stresses between sensor and load base. Therefore, the new design is for compressive forces only.

New design for compressive force (Type designation: C15)

Hysteresis effects

A higher torque is applied to the bolts that connect the load cell to the base. (Fig. 3). Therefore, the contact of both parts is better than with tension/compression force transducers with a similar design. This makes the connection more stable and optimized the hysteresis characteristics of the transducer.

Repeatability

The load bases for radial shear types for experimental tasks are massive- for highest stiffness and easy mounting. The disadvantage is that those load bases introduce bending moments in the sensor so that the repeatability in different mounting positions is not on the level of a high-end sensor. A new load base has been designed in order to provide a good stiffness in the direction of the load, but less stiffness for bending moments. (Figure 3)

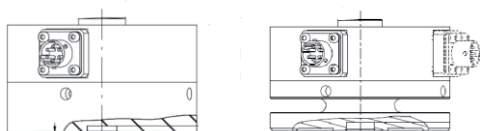


Fig.3: Load base for experimental tasks (left) and for reference tasks (right).

Results are shown in figure 4. Depending on the load base mounted the uncertainty of the sensor changing as well. With the new design it is possible to achieve a repeatability in different mounting position of less than 0.01 %.

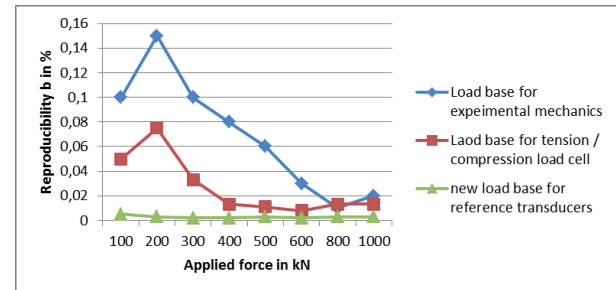


Fig 4: Comparison of the same sensor but with different load bases. The new load base shows by far best results.

1. Conclusion

Radial shear type load cells fulfil class 00 according the ISO376 standard for compressive forces. By optimizing the stiffness of the load base, the results are on reference level in a measurement range from 10 % to 100 %. The advantages of high output and general robust design stay also with this new sensor.

References

- [1] Thomas Kleckers, "Radial Shear Beams used as high precision transfer transducers", IMEKO 2010 TC3, TC5 and TC22 Conferences Metrology in Modern Context, November 22-25, 2010, Pattaya, Chonburi, Thailand
- [2] Karl Hoffmann, "Eine Einführung in die Technik des Messens mit Dehnungsmessstreifen" Hottinger Bladwin Messtechnik GmbH, Darmstadt, 1987; Page 62

Development and calibration of dynamic pressure sensor for motor pressure range

J. Salminen¹, R. Högström¹, S. Saxholm¹, J. Hämäläinen¹

¹VTT Technical Research Centre of Finland Ltd, National Metrology Institute VTT MIKES, Espoo, Finland

Summary:

Reliable dynamic pressure measurements are essential in control and optimization of modern combustion engines. To ensure reliability of dynamic pressure measurements, dynamic pressure sensors should be calibrated using dynamic pressure calibration methods. VTT has developed solutions to improve reliability of dynamic pressure measurements: A new dynamic pressure sensor for harsh engine environments, a secondary dynamic pressure calibrator for industry use and an option to heat dynamic pressure sensors during calibration.

Keywords: Dynamic pressure, Dynamic pressure sensor, Pressure calibration, Traceability, Pressure sensor

Introduction

To ensure reliable performance of dynamic pressure sensors, they need to be calibrated using dynamic calibration methods that are traceable to the International System of Units (SI). Despite of this, dynamic pressure sensors are usually calibrated using static pressure calibration methods, because traceable dynamic pressure calibrations are not readily available. Currently, only two National Metrology Institutes offer traceable dynamic pressure calibration services: VTT MIKES from Finland and LNE/ENSAM from France.

VTT Dynamic pressure sensor and developments in dynamic pressure calibration

Recently, VTT has further developed solutions to improve the reliability of dynamic pressure measurements. These solutions include a new dynamic pressure sensor for harsh engine environments, a secondary dynamic pressure calibrator and an option to heat sensors during calibration.

The VTT dynamic pressure sensor is based on a remote reading of the bending membrane. The sensing element is not in direct contact with the bending membrane, which makes the sensor very durable. Besides durability, a major advantage of the sensor is its unique patented capacitive sensing technology. This innovation

enables reliable static calibrations of sensor even though the sensor is used under dynamic pressures. This in turn makes the calibration of the sensor cost-effective, because unlike dynamic calibrations, static calibrations can be carried out using existing pressure calibration instrumentation. As shown in results, a static calibration of the VTT pressure sensor gives comparable results with the dynamic calibration.



Fig. 1. VTT Dynamic Pressure Sensor

Unlike VTT dynamic pressure sensor, typical commercial dynamic pressure sensors cannot be calibrated reliably using static calibration techniques. Primary dynamic pressure calibration techniques are laborious and require high-level of expertise. Therefore, VTT MIKES has developed the secondary dynamic pressure calibrator, which is easy to use, compact and

relatively simple to manufacture. The calibrator creates a few millisecond long half-sinewave shaped pressure pulses. These pulses are typically repeated once a few seconds. Traceability of this calibrator to SI is based on a reference sensor calibrated using the VTT MIKES dynamic pressure primary standard.

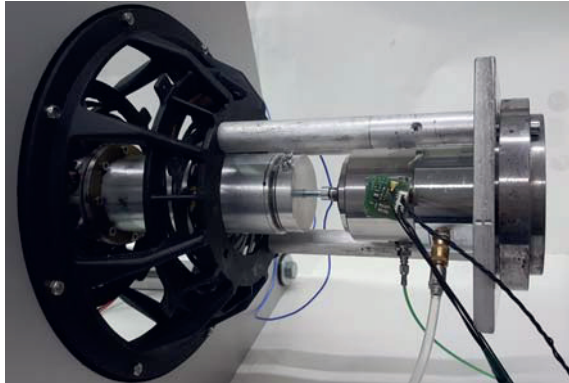


Fig. 2. VTT MIKES secondary dynamic pressure calibrator

Dynamic pressure sensors are typically used in high temperature environments. Therefore, in order to calibrate them at temperatures that corresponds to the environment they are used in, a heating option for sensors under calibration has been developed.

Results

In figure 3, static and dynamic calibrations of VTT Dynamic Pressure Sensor are compared with each other. Uncertainty of comparison is around 2% and difference between static and dynamic calibrations is around 0.5%. It can be assumed that VTT dynamic pressure sensors can be calibrated both dynamically and statically.

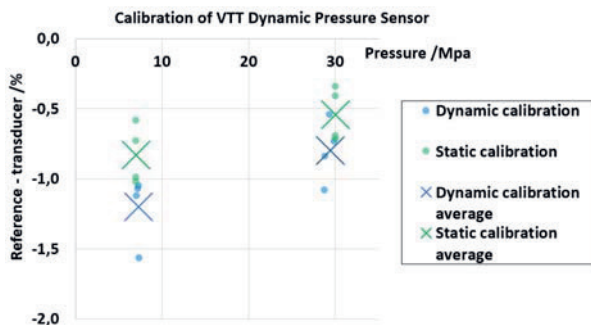


Fig. 3. Calibration of VTT MIKES Dynamic pressure sensor in with dynamic and static calibration

Calibration results in temperatures 20, 120 and 180 °C for VTT dynamic pressure sensor are

shown in Figure 4. Sensor has sensitivity change of around 1 %/100 °C when heated.

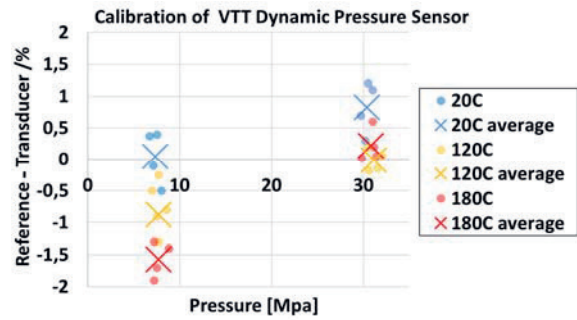


Fig. 4. Calibration of VTT MIKES Dynamic pressure sensor in different temperatures

Conclusions

VTT has developed solutions to improve reliability of dynamic pressure measurements. These solutions include a new dynamic pressure sensor for harsh engine environments, a secondary dynamic pressure calibrator for industry use and an option to heat dynamic pressure sensors during calibration. Based on initial calibration measurements, it is concluded that VTT dynamic pressure sensors can be calibrated both dynamically and statically. When heated, sensitivity of VTT dynamic pressure sensor changes around around 1 %/100 °C.

Measuring Load on Linear Guides in Different Load Scenarios Using an Integrated DLC Based Sensor System

David Krampert^{1,2}, Sebastian Unsleber¹, Leonhard Reindl²

¹ Bosch Rexroth AG, Ernst-Sachs-Straße 100, 97421 Schweinfurt, Germany,

² Albert-Ludwigs-University Freiburg, IMTEK, Georges-Köhler-Allee 106, 79110 Freiburg, Germany
david.krampert@boschrexroth.de

Summary:

The integration of a load measurement system into a linear guide is both a challenging and promising topic. This work focuses on evaluating a model for the load distribution in linear guide bearings for establishing a sensor system using a direct strain measurement method based on a piezoresistive Diamond Like Carbon (DLC) layer, capable of determining the up to five degrees of freedom load state of the bearing. We observe good matching between the theoretical model and the measured sensor data, demonstrating the capability of the sensor system in different load scenarios.

Keywords: Load Determination, Linear Guide Bearings, Industry 4.0, Piezoresistive DLC, Load Distribution Model

Background, Motivation and Objective

Linear guides are standard machine parts that constrain movement of connected machine parts to a linear, translational one. For machine tools, profiled rail guide cylindrical roller bearings are heavily employed. Integrating a sensor system that is able to determine the load vector acting on the linear guide, without affecting its mechanical characteristics, would allow both for better remaining lifetime predictions as well as improving accuracy in manufacturing. In [1] we presented a load measurement system based on local strain measurement using piezoresistive, DLC based sensors. The sensors are placed in a group of three sensors on each of the four raceways of the runner block and measure the strain introduced by loading the rolling elements above the sensor elements.

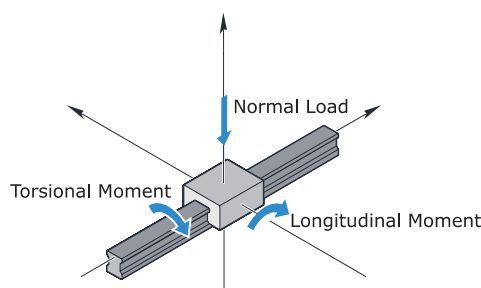


Fig. 1. Linear Guide with Load Modes (based on [2])

Until now, we have only shown principal functionality by comparing to a normal load in one direction and uniform local load distribution and mainly focused on addressing non-idealities for measuring the local load. The objective of this work is to show compliance to a simplified

model for mapping the different external loads (fig. 1) to local loads. This enables the sensor system to capture the load scenarios accurately. Additionally, **direct** empirical evaluation of the model assumptions is possible for the first time. This is valuable insight for different research areas in mechanical engineering.

Description of the New Method or System

In order to reduce complexity, the most foundational assumption made is that the **runner block and the rail are rigid**, i.e. all deformation occurs at the rolling element contact, [3] calls this the classical model. For the non-linear load-deflection relationship of the rolling elements, a profiled, **slice based model** with 41 slices has been used with a profile as defined in the DIN 26281 norm [4] where each slice is assumed to act like proposed in [5]. This nonlinearity also prohibits linear superposition of the local loads introduced by different external load components. Therefore, an iterative procedure, based on the one described in [3], is employed until local loads agree with external defined loads. Preload is introduced in linear guides by design using oversized rolling elements and changes when loading the bearing [2]. This effect is modelled as part of the iteration process. Since the sensors measure strain, rolling element load has to be converted into **resulting strain** at the sensor position. For this, the method in [1] based on a partial Fourier transformation, has been extended to cover torque, i.e. differently loaded neighboring rolling elements. The solving procedure remains the same. This model allows the sensor system to relate measured sensor data to the external load state, as shown below.

Results

Experiments have been performed loading two runner blocks type SNS size 45 from Bosch Rexroth, equipped with the sensor system. Normal loads are ranging from 0 kN to 100 kN, torsional moments from 0 Nm to 1900 Nm and longitudinal moments from 0 Nm to 1150 Nm, each applied in both directions. The sensor signal is dependent on the relative position of rolling elements, so the runner blocks have been moved 1 mm between repeating measurements. The amplitude can be defined as the difference between maximum positive and negative signal at a certain load over the positions. The shape of the load dependent signal is of more interest than absolute values. Therefore, amplitude curves have been normalized to their maximum value.

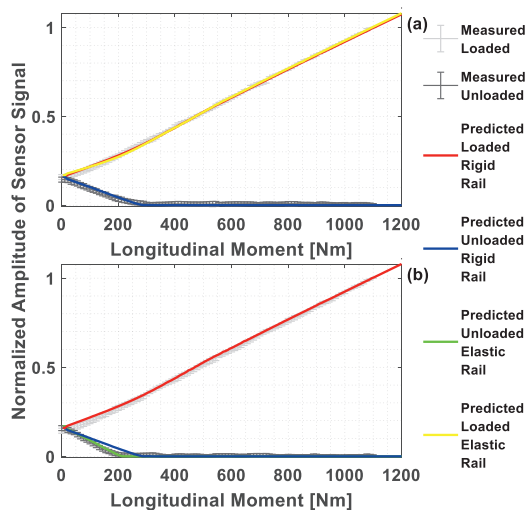


Fig. 2. Sensor Amplitude vs. Longitudinal Moment. (a) Upper Raceways, (b) Lower Raceways

Error bars represent three standard deviations calculated from the obtained curves. For longitudinal moments, fig. 2 shows good agreement of model predictions with measured values, especially when loading the lower raceways. The preload liftoff point, after which the unloaded raceways do not carry any load, happens at lower moment when loading the upper raceways. This could be explained by increased elastic yield of the rail, which is more flexible at the upper raceways. Modelling this linearly shows good improvement, as seen for the elastic rail curve. Fig. 3 shows torsional moment, where the variation of the preload liftoff point is found to be less significant, and the curves match well in both cases. Fig. 4 shows normal loading. Here variation in preload liftoff occurs, but the model fits well for loading the upper raceways. The variation again can be explained by elastic behavior of the rail, but has to be combined with further modeling that shifts the preload liftoff to higher loads, which is left open

for further research. One possibility is the inclusion of changing contact angles with an elastic runner block.

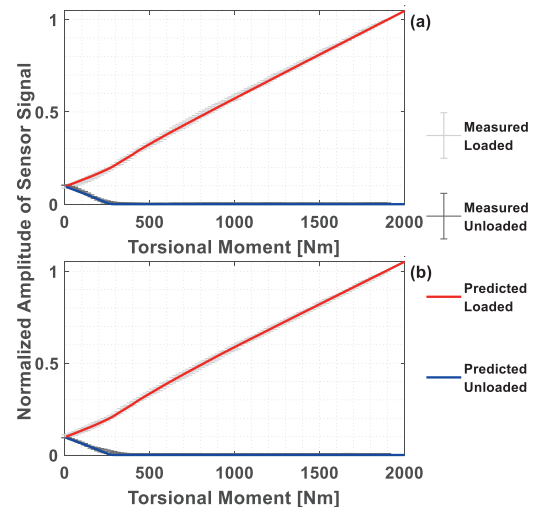


Fig. 3. Sensor Amplitude vs. Torsional Moment. (a) Lower Raceways (b) Upper Raceways

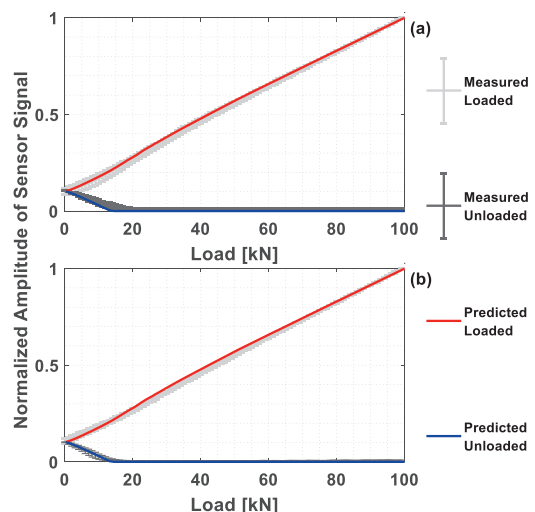


Fig. 4. Sensor Amplitude vs. Normal Load. (a) Upper Raceways (b) Lower Raceways

References

- [1] D. Krampert, S. Unsleber, C. Janssen und L. Reindl, „Load Measurement in Linear Guides for Machine Tools,“ *Sensors*, Vol. 19, No. 3411, 2019. doi: 10.3390/s19153411
- [2] Bosch Rexroth AG, *Handbook Linear Motion Technology*, Schweinfurt, 2007.
- [3] S. Lenssen und J. Sarfert, „Berechnung wälzgelagerter Linearführungen“ *Konstruktion*, Vol. 46, pp. 209-214, 1994.
- [4] DIN, *DIN 26281 - Wälzlager - Berechnung der modifizierten nominellen Referenz-Lebensdauer für Wälzlager*, 2010.
- [5] K. Kunert, „Spannungsverteilung im Halbraum bei elliptischer Flächenpressungsverteilung über einer rechteckigen Druckfläche,“ *Forschung auf dem Gebiete des Ingenieurwesens*, Vol. 27, pp. 165-174, 1961. doi: 10.1007/BF02561354

Influence of Temporal Strain Evolution on Distributed Strain Sensing with OTDR in Polymer Optical Fibers

S. A. Dengler¹, N. Schmidt¹, M. Luber¹, J. Fischer¹, H. Hangen², O. Ziemann¹; R. Engelbrecht¹

¹ *Polymer Optical Fiber Application Center (POF-AC), Technische Hochschule Nürnberg Georg Simon Ohm, Wassertorstraße 10, 90489 Nuremberg, Germany,*

² *HUESKER Synthetic GmbH, Fabrikstraße 13-15, 48712 Gescher, Germany.
simon.dengler@pofac.th-nuernberg.de*

Summary:

To measure strain in ground and earthworks, polymer optical fibers (POF) applied to geotextiles can be used. In case of an optical time domain reflectometry (OTDR) measurement, the backscattered intensity increases in strained areas. The increase of backscattering (IOB) has been characterized by gradual elongation of the fiber up to 5% with different elongation levels and holding times. A dynamic behavior of the IOB has been proved. It could be shown that for the tested elongation patterns the IOB varies around 0.3% up to 0.9% for absolute strain less than 2.2% and up to 5%, respectively.

Keywords: optical time domain reflectometry, structural health monitoring, strain sensing, geotextiles, polymer optical fiber

Background

Condition monitoring of critical earthworks as for example dams, dikes and disposal sites is a challenging yet not satisfactorily solved measuring task. A possible sensor consists of a polymer optical fiber (POF) applied to a geotextile [1]. Geotextiles are fabrics made of polymer fibers, which are used to absorb stress within the soil and therefore, are ideal to provide friction.

When straining the POF, the level of optical backscattering within the fiber increases along strained sections [2, 3], as shown at the Insert in Fig. 1. Therefore, a spatially resolved measurement of strain by OTDR is in principle possible. The increase of backscatter (IOB) is also affected by side effects like temperature and humidity [4].

However, a more dominant side effect is the relaxation processes that may result from adaptation of the POF material to external force. Hence, IOB is not stable over time, even at constant strain. Therefore, different strain profiles over time may result in varying IOB, even at the same amount of strain applied to the POF. In this work, this effect is characterized to quantify resulting uncertainties and potentially diminish them in field measurements of strain by OTDR in POF.

Method

An automated measurement program strained a standard PMMA-POF with 1 mm diameter (Mitsubishi GH-4001-P) and a total length of 15 m. Afterwards, at constant time steps OTDR

measurements were taken using a commercially available POF OTDR (Luciol LOR-220) at 520 nm wavelength. In order to transfer the strain to the fiber, two rods were stucked to it using a two-component epoxy glue, were motorized linear drives apply the elongation.

Three fibers were treated identically besides the strain to time pattern. Strain was applied at the position 10 m - 11 m increasing over time from 0% to 5% in steps of 0.1%. For fiber 1 each 0.1% step was maintained for 10 minutes, for fiber 2 for 1 hour and for fiber 3 for 10 hours, respectively.

To check whether the relaxation takes place within one strain step and if the total testing time does compromise the results, two more fibers were tested. The fibers were strained at the position 40 m – 41 m. Both fibers were elongated from 0% to 5%. The step size of fiber 4 was 0.1%, maintained for 1 hour, each. In contrast, the step size of fiber 5 was 1% maintained for 10 hours, each. The total measurement time was the same, for fiber 4 and 5.

The IOB is calculated for each fiber at the center of the elongated length, as shown at the Insert in Fig. 1. Therefore, an average over a range of measurement points at the center is compared to two equally spaced areas before and after the elongation.

Results

Fig. 1. compares the IOB to strain dependence of fiber 1, fiber 2 and fiber 3. It is noticeable that

faster strained fibers reach a higher IOB above a level of 2.2% total strain. However, the overall plot looks similar. Up to 2.2% the IOB remains almost the same and all measurements are reaching a similar slope between 3% and 5% strain.

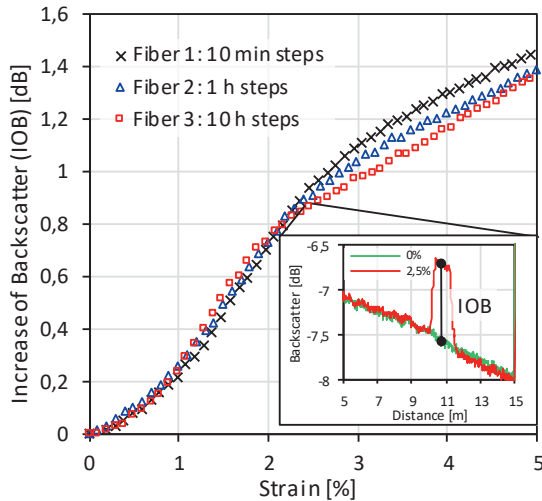


Fig. 1. Strain to IOB dependence of three fibers elongated in steps of 0.1% with different holding times. Insert: Example of an OTDR reflectogram at 2.5% strain and visualisation of increase of backscatter (IOB)

Strain for fiber 4 and fiber 5 was increased at the same rate. However, the step size has changed. Interestingly, at any particular strain step, the IOB is identical as shown in Fig. 2.

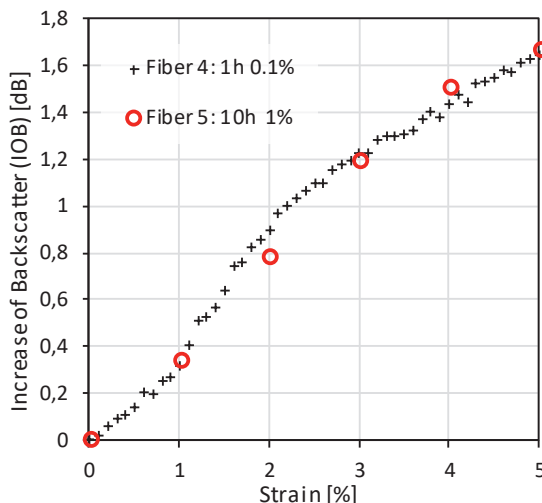


Fig. 2. Strain to IOB dependence of two fibers elongated with identical total testing time and different elongation step sizes and hold times.

A quick comparison of Fig. 1 and Fig. 2 shows a greater IOB at maximum strain in Fig. 2. This is caused by pulse dispersion over length in POF and the two measurements are therefore not comparable.

Conclusion

On the observed time scale from min 10 minutes to max 10 hours, the specific course of increase in strain up to 2.2% has no influence on the measured IOB. The temporal slope of the strain increase IOB for further measurements above 2.2%.

Due to the high linearity of fiber 3 above 2.2% strain, we assume it is close to the IOB after relaxation. The nonlinearity of fiber 2 and fiber 1 above 2.2% strain would then be a side effect of the underlying relaxation process. One way to test this hypotheses is to investigate on the hysteresis of IOB by strain above and beyond 2.2% strain.

The alteration due to different elongation speeds and levels is 0.3% in the IOB for strain less than 2.2% and 0.9% alteration between 2.2% and 5% strain.

Furthermore, Fig 2 shows that the step size does not affect IOB for identical overall relaxation times.

In our future work, we will improve our IOB calculation for better cross comparability through fiber length. Therefore, we will investigate on using puls energy instead of IOB.

Acknowledgements

This work has been funded by the Federal Ministry of Education and Research, funding program Forschung an Fachhochschulen (FHprofUnt) under contract number 13FH137PX6, "Optische Sensoren zur Überwachung von Erdstrukturen (SmartOSE)."

References

- [1] S. Liehr, P. Lenke, K. Krebber, M. Seeger, E. Thiele, H. Metschies, B. Gebreselassie, J. Ch. München and L. Stempniewski, Distributed strain measurement with polymer optical fibers integrated into multifunctional geotextiles, Proc. SPIE 7003, 7003-02–7003-15 (2008).
- [2] I. R. Husdi, K. Nakamura and S. Ueha, Sensing characteristics of plastic optical fibres measured by optical time domain reflectometry, Meas. Sci. Techn. 15 (8), 1553-1559 (2004)
- [3] S. Liehr, Ph. Lenke, M. Wendt, K. Krebber, M. Seeger, E. Thiele, H. Metschies, B. Gebreselassie and J. Ch. München; Polymer Optical Fiber Sensors for Distributed Strain Measurement and Application in Structural Health Monitoring, IEEE Sensors J. 9 (11), 1330 – 1338 (2009).
- [4] S. Liehr, M. Breithaupt, and K. Krebber; Distributed humidity sensing in PMMA optical fibers at 500 nm and 650 nm wavelengths; Sensors 17.4 (2017): 738.

Development of a 3D-integrated Thermocatalytic Sensor for Combustible Gas Detection

Finja M. Münchenberger¹, Stefan Dreiner¹, Holger Kappert¹, Rahel M. Neubieser¹, Holger Vogt^{1,2}

¹ *Fraunhofer Institute for Microelectronic Circuits and Systems, Finkenstraße 61, 47057 Duisburg, Germany,*

² *University Duisburg Essen, Forsthausweg 2, Duisburg, Germany
finja.marina.muenchenberger@ims.fraunhofer.de*

Summary:

A process to integrate a thermocatalytic sensor on top of a CMOS circuitry is presented. Therefore, COMSOL Multiphysics® simulations are performed to evaluate a heater with an optimized temperature uniformity and a suspended design of the sensor element to achieve thermal decoupling from the substrate. The steps for fabrication are shortly described using ALD materials and a sacrificial layer. An example for a released heater structure is shown.

Keywords: thermocatalytic sensor, 3D-integration, ALD, post-CMOS, pellistor

Introduction

Pellistors are thermocatalytic sensors that are used to detect combustible gases. A realization of a pellistor as a MEMS sensor has already been achieved (micro pellistor) [1]. This reduces the size of the sensor element, decreases the power consumption and increases the mechanical stability compared to the classic pellistor [2]. When mounting the micro pellistors on silicon substrate they have to be manufactured on membranes for thermal decoupling. If a readout circuit for the sensor is to be manufactured, it must either be processed separately or the chip area spared for the sensor in the case of monolithic integration causes high costs.

In order to save chip area and still achieve a monolithic assembly of readout circuit and sensor, the Fraunhofer IMS developed a concept to create free-standing electrically contacted structures by means of a sacrificial layer process combined with ALD deposition, which can be operated on top of a CMOS circuit [3]. Therefore, the concept of pellistors is to be adopted and further developed into a 3D integrated thermocatalytic sensor, which is applied on top of the readout circuit.

Design of the Sensor

The sensors produced by ALD materials are based on the components of a classic pellistor: a heater, an insulating material around the heater and a catalyst layer on the isolating material. Since the structures are smaller than those of micro pellistors, it is necessary to ensure that the heater is dimensioned reasonably

to achieve the most homogeneous temperature profile possible. Therefore, simulations with COMSOL Multiphysics® using the “Joule Heating” interface were performed.

Based on [4] a square shaped heater shows the highest temperature uniformity compared to other heater shapes. Instead of fabricating the heater structure directly on pillars resulting in a non-negligible substrate heating along the pillars, a design is chosen where a suspension via legs provides a thermal decoupling to the substrate, as the main temperature drop occurs over the legs. According to the simulations, at a maximum temperature of the heater of 513°C, the temperature drop at the heater itself is only 26°C, while the maximum temperature at the substrate directly below the pillars is 34°C.

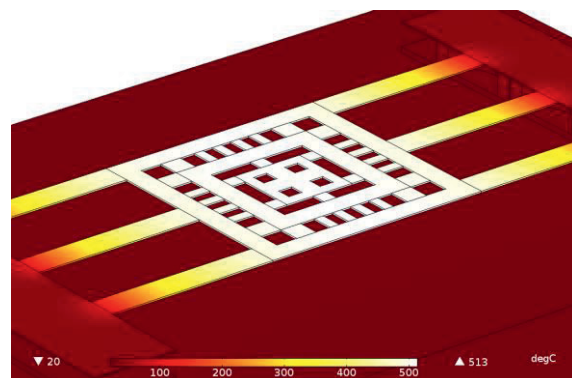


Fig. 1. Simulations with square shaped heater suspended by legs for main temperature drop. Height of pillars defines the distance between the free-standing sensor and the substrate.

Ruthenium as Heater and Catalytic Material

Ruthenium is used as both the catalytic layer and the heater material. Like platinum, ruthenium is a transition metal and shows catalytic activity towards combustible gases. According to [5] ruthenium is even better suited as a catalyst chosen for a pellistor (examined on the basis of CO). Although the material is liable to form a thin oxide layer especially at higher temperatures the catalytic activity still remains.

As the heater is also used to measure the temperature change caused by reaction at the catalysts surface a high and linear temperature coefficient is beneficial for a reliable measurement. According to tests the sheet resistance of ruthenium is nearly linear up to 400°C. This gives a temperature coefficient of approximately $2 \cdot 10^{-3} \text{ K}^{-1}$ (in comparison $3,92 \cdot 10^{-3} \text{ K}^{-1}$ for platinum) which makes ruthenium suitable for temperature measurement.

Fabrication of the Sensor

To fabricate a thermocatalytic sensor as a free-standing element, a sacrificial layer to set the distance between sensor and substrate with the circuitry has to be deposited first. After that holes or trenches are etched with a stop at the contact pads for electrical supply. The highly conformal deposition of an ALD layer provides the sensor with its heater material which can be structured. The sacrificial layer can then be etched so that the sensor structure is released. A released structure of a square shaped heater can be seen in Fig. 2.

To transform the sensor element to a pellistor like structure an Al_2O_3 layer can be deposited before etching the trenches into the sacrificial layer and another Al_2O_3 layer above the heater material encapsulates the heater. Eventually, a catalyst layer on top of the upper Al_2O_3 layer must be deposited.

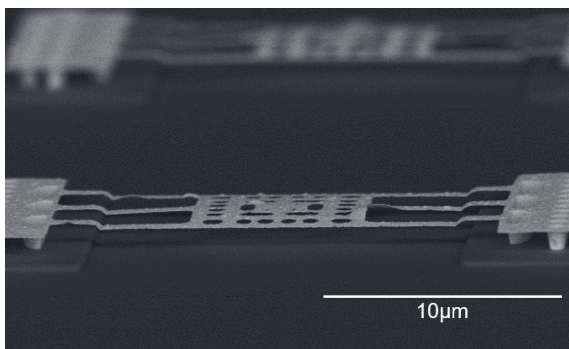


Fig. 2. SEM image of a released ruthenium square shaped heater with a distance of $1 \mu\text{m}$ to the substrate.

Conclusion and Outlook

A possibility to fabricate a free-standing gas sensor in a post-CMOS process was introduced. Therefore, an optimized square shaped structure was presented to achieve a high temperature uniformity and a design of a heater held by suspension legs was shown as a way to realize a thermal decoupling from the substrate without etching a membrane. Process flows to fabricate an unencapsulated heater as a thermocatalytic sensor and an encapsulated pellistor like element were described and actual structures were shown.

In future work the fabricated structures will be measured and characterized in terms of its properties. The encapsulated versions of the sensor will be completed and characterized as well.

Acknowledgements

This work was supported by the Fraunhofer Internal Programs under Grant No. MAVO 836931.

This publication is partly funded by the Federal Ministry of Education and Research under the project reference numbers 16FMD01K, 16FMD02 and 16FMD03.

References

- [1] M. Gall, The Si planar pellistor: a low-power pellistor sensor in Si thin-film technology, *Sensors and Actuators B: Chemical*, 4 (1991), 533-538
- [2] N. Setter, Electroceramic-Based MEMS: Fabrication-Technology and Applications, *Electronic Materials: Science & Technology*, 9 (2005), ISBN: 978-0-387-23310-9
- [3] A. Goehlich, A. Jupe, H. Vogt, Device and method for producing a device with microstructures or nanostructures, patent: DE102014213390A1
- [4] L. Sujatha, V. S. Selvakumar, S. Aravind, R. Padamapriya, B. Preethi, Design and Analysis of Micro-Heaters for Temperature Optimisation Using COMSOL Multiphysics for MEMS Based Gas Sensor, COMSOL Conference in Bangalore (2012)
- [5] F. Gao, D. W. Goodman, CO oxidation over ruthenium: identification of the catalytically active phases at near-atmospheric pressures, *Phy.Chem.*, 14 (2012), doi: 10.1039/c2cp40121

Inline Quality Monitoring of Diesel Exhaust Fluid (AdBlue) by Using the 3ω -Method

Ralf E. Bernhardsgrütter^{1,2}, Christoph J. Hepp¹, Martin Jäggle², Hans-Fridtjof Pernau², Katrin Schmitt^{2,3}, Jürgen Wöllenstein^{2,3}

¹ Innovative Sensor Technology IST AG, Ebnet-Kappel, Switzerland,

² Department of Microsystems Engineering IMTEK, University of Freiburg, Freiburg, Germany

³ Fraunhofer Institute for Physical Measurement Technique IPM, Freiburg, Germany

ralf.bernhardsgruetter@ist-ag.com

Summary:

Quality monitoring of diesel exhaust fluid is crucial for optimal selective catalytic reduction in diesel combustion processes. This article presents a platinum thin film sensor using the 3ω -method to characterize the diesel exhaust fluid. The results show that this sensor can determine the urea content with in 1 % by weight. An inline measurement is well applicable because the same structure can be used for both concentration and flow measurement.

Keywords: Diesel exhaust fluid, AdBlue, 3ω -method, quality monitoring, platinum thin film

Motivation and Background

The reduction and the control of pollutants produced by burning fossil fuels are a focus of governments and health organizations. The selective catalytic reduction (SCR) is an after-treatment method in diesel combustion processes to convert harmful detrimental nitrous oxides (NO_x) into nitrogen and water. Diesel exhaust fluid (DEF), also known as the registered trademark “AdBlue”, is needed for the SCR process and consists of 32.5 % by weight of urea and 67.5 % by weight of deionized water. The concentration of the urea is crucial for an optimal SCR. Inappropriate DEF brakes the SCR or breaks it down and the emission reduction fails.

Reported DEF quality sensors are based on optical principles [1], electrical [2] and pulsed heating measurements [3]. The sensor presented in this article uses the 3ω -method to determine the concentration of urea in DEF.

Method

The claims of this paper are: (1) The 3ω -method is used to determine the concentration or urea in DEF. (2) The resolution of the sensor is 1 % by weight. (3) The sensor is suitable for inline measurements e.g. in vehicles.

The 3ω -method is a well-known method to measure thermal conductivity and heat capacity [4]. This principle uses a metallic resistor which is driven by an AC-current with angular frequency ω . The resistor heats up by Joule heating and has an AC-component at frequency 2ω

which acts as a thermal wave. The propagation of this thermal wave depends on the thermal characteristics of the surrounding. If the resistor has a defined temperature-to-resistance behavior, the resistor is then also modulated with 2ω . Therefore, the voltage across the resistor has a term $V_{3\omega}$ at frequency 3ω and is dependent on the thermal characteristics of the surrounding.

Experiment and Results

The used sensor (shown in figure 1) bases on platinum thin film technology. The platinum thin film element is processed on a zirconia substrate by standard MEMS processes. The resistor is designed as a 45Ω at 0°C resistance with a temperature-to-resistance coefficient of 3900 ppm/K.

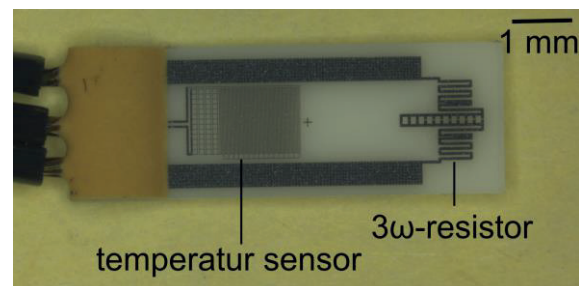


Figure 1: Sensor design: Platinum thin film element on a zirconia substrate. The 3ω -resistor has a resistance of 45 Ohm at 0°C with a temperature-to-resistance coefficient of 3900 ppm/K. A temperature sensor is also located on the element for further investigations.

The setup of the measurement is designed as a digital lock-in amplifier and allows phase sensi-

tive measurements. A current amplitude of 30 mA is applied for the presented measurements.

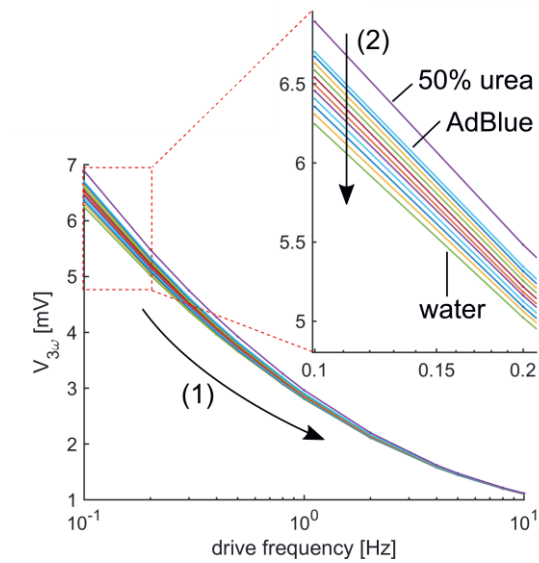


Figure 2: Voltage amplitude $V_{3\omega}$ as function of drive frequency for different urea-water concentrations. (1) The amplitude $V_{3\omega}$ decreases for increasing frequency. (2) The amplitude $V_{3\omega}$ increases for increasing urea amount.

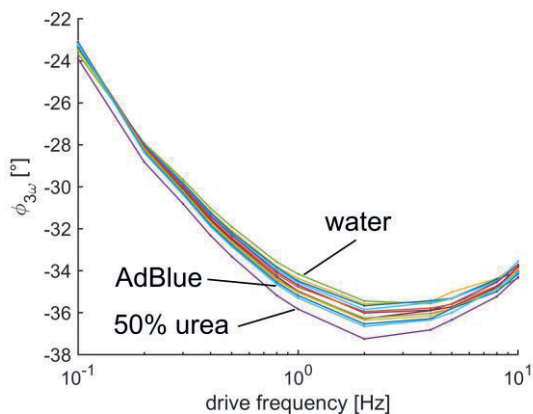


Figure 3: Phase $\Phi_{3\omega}$ as function of drive frequency. The urea concentration is mainly resolvable at a frequency range between 0.2 Hz and 3 Hz.

The 3ω -method is used to characterize mixtures with different urea-water concentration between 0 % by weight and 50 % by weight with respect to urea for frequencies between 0.1 Hz and 10 Hz.

Figure 2 shows the voltage amplitude $V_{3\omega}$ as function of drive frequency. First, the amplitude decreases for increasing frequency. The reason is the smaller penetration depth of the thermal wave ($\sim 1/\sqrt{\omega}$) [4] and a smaller thermal response result. Second, the amplitude increases for increasing amount of urea. Mixtures of different urea amount are clearly distinguishable for frequencies below 1 Hz. The best resolution is at a drive frequency of 0.1 Hz.

Figure 3 shows the corresponding phase of the 3ω -signal. The urea concentration is best resolvable at frequency of 2 Hz which is different compared to the amplitude. Further investigations have to be done to find the reason. The lock-in amplification may need some adjustments. However, an advantage is that the phase is in first order independent of the current amplitude and the temperature-to-resistance coefficient. This point can be important for applications because it can simplify fabrication processes and calibration procedures.

The amplitude $V_{3\omega}$ as function of urea concentration at 0.1 Hz is shown in figure 4. It is clearly visible that the amplitude increases for increasing urea concentration. Pure deionized water has the smallest amplitude whereas the amplitude at 50 % by weight has the highest amplitude. The reason is in first order the decrease of the thermal conductivity. The concentration resolution is at 1 % by weight. The measurement error is evaluated by multiple measurements. Therefore, the 3ω -method is suitable to monitor the quality of the DEF in a diesel combustion process.

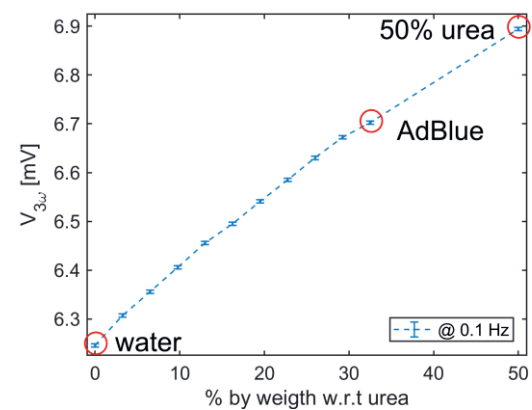


Figure 4: Voltage amplitude $V_{3\omega}$ as function urea with respect to weight.

References

- [1] N. Kumawat, et al., Quality monitoring of diesel exhaust fluid in vehicles using diffractive interference sensors, *SENSORS IEEE*, 1676-1678 (2014); doi: 10.1109/ICSENS.2014.6985343
- [2] A. Fendri et al., AdBlue Quality Control using Impedance Spectroscopy, *AMA Conferences*, 830-832 (2015), doi: 10.5162/sensor2015/P7.3
- [3] B. Schmitt, et al., Microthermal sensors for determining fluid composition and flow rate in fluidic systems, *Microsyst. Technol.* 20, 641-652 (2014); doi: 10.1007/s00542-013-2001-y
- [4] D. G. Cahill et al., Thermal conductivity of α -Si:H thin films, *Phys. Rev. B* 50 (9), 6077-6081 (1994), doi: 10.1103/PhysRevB.50.6077

Single Cell Immobilization at High Flow Rates Using 2PP-Traps in a Microfluidic Channel

S. Reede^{1, 2}, *H. Müller-Landau*³, *N. Matscheko*³, *U. Rant*³, *F. Lucklum*⁴, *M. J. Vellekoop*^{1, 2}

¹ *Institute for Microsensors, -actuators and -systems (IMSAS), University of Bremen, Otto-Hahn-Allee 1, 28359 Bremen, Germany,*

² *Microsystems Center Bremen (MCB), 28359 Bremen, Germany*

³ *Dynamic Biosensors, Lochhamer Straße 15, 82152 Martinsried/ Planegg, Germany,*

⁴ *Center for Acoustic-Mechanical Microsystems (CAMM), Technical University of Denmark, Ørstedss Plads 352, 2800 Kgs. Lyngby, Denmark
sreede@imsas.uni-bremen.de*

Summary:

This paper presents robust single cell traps fabricated in a microfluidic channel by two-photon polymerization (2PP) that withstand a very high average flow velocity of 1 m/s. The traps consist of a direct laser written thin grid structure allowing a good flow around the captured cells as well as optical measurements. Therefore, they enable the characterization of binding kinetics between active substances and cells. The traps have the shape of half a circular cylinder and capture the cells hydrodynamically. Jurkat cells with a diameter of 15 μm are captured in every trap within the first seconds of sample injection.

Keywords: 2PP, two-photon polymerization, additive manufacturing, cell trap, cell capturing

Background, Motivation and Objective

To characterize the binding behavior and cell specificity of active substances in an early stage of development, for instance in novel cancer drugs, the immobilization of cells in a flow with a flow rate between 40 $\mu\text{l}/\text{min}$ and 3 ml/min is crucial. The high flow rate around the cell ensures the immediate removal of e.g. antibodies as soon as an unbinding event is taking place. The current concentration of antibodies on the cell surface can be determined by measuring a fluorescent label. Therefore, in order to realize the cell immobilization, traps are required that withstand high flow rates and enable a sufficient flow around the cell. For this reason, grid structures realized using 2PP are advantageous, because they allow the liquid to flow through the structure. With soft lithography, by which most single cell traps have been fabricated, thin grid structures are not possible. Consequently, 2.5D polydimethyl-siloxane (PDMS) traps [1][2] block the fluid more, resulting in maximum flow velocities of only 50 $\mu\text{m}/\text{s}$ [1]. 3D grids have been used in multi cell sorting structures [3] reducing the flow around each cell as well as in cell cages for droplet deposition from the top applying no flow [4].

Description of the New Method or System

The novel 3D grid cell traps, shown in Fig. 1, are designed for cells that have a diameter of

about 15 μm , e.g. Jurkat cells, and have a height of 35 μm . The diameter of each strut of the grid is set to 1.8 μm , which is as thin as possible avoiding deformations. The meshes have a size of 6 μm by 8 μm preventing the cells from passing through the trap. In order to observe the capturing success with an optical microscope, there is no polymer covering the top. The cell traps are laser written in IP-Dip resin by 2PP (Photonic Professional GT, Nanoscribe GmbH) on top of a gold electrode, which is structured on a glass chip. The gold improves the adhesion of the 2PP structure and simplifies the interface finding in the Photonic Professional GT.

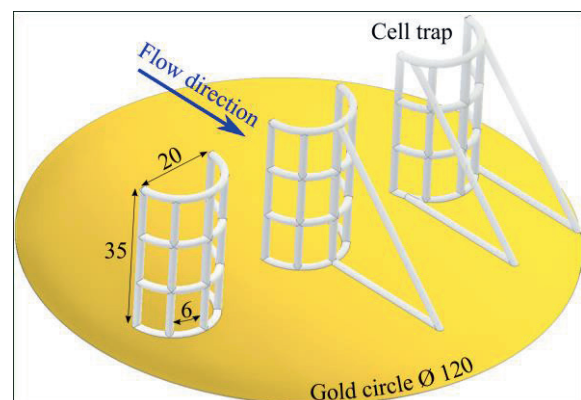


Fig. 1. Sketch of the cell traps with different support structures. The unit of all numbers is μm .

In order to test the stability of the traps with different support structures in a water flow, the chips are sealed with an 800 μm wide and 75 μm high PDMS channel on top of a second glass chip. Thus, the highest flow velocity in the middle of the channel hits the top of the trap. Two chips with 24 traps each are tested increasing the flow rate in steps of 100 $\mu\text{l}/\text{min}$ until the traps break. The trapping success is tested with Jurkat cells in a DRX Biosensors system. For this, the channel height is set to 30 μm clamping the traps between the two chips to avoid cells flowing over the traps.

Results

The SEM image shows the 2PP fabricated traps protruding from the chip as designed (see Fig. 2). A slight shrinkage can be noticed at the upper part of the left and middle trap.

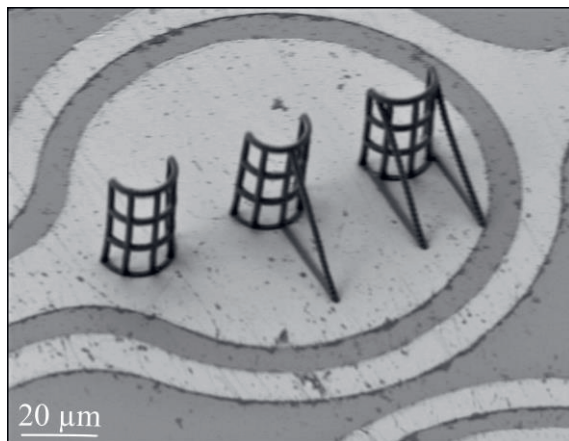


Fig. 2. SEM image of the different traps on a re-used chip. Residue on the surface is due to multiple reuse of the chip.

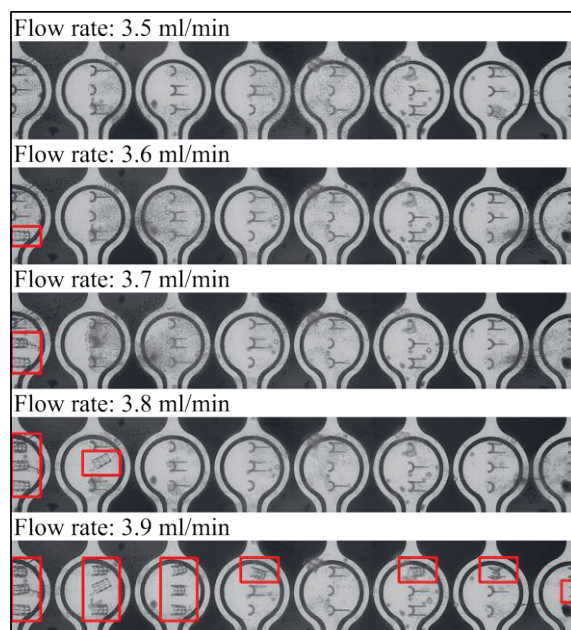


Fig. 3. Photographs of 24 cell traps in one 75 μm high channel from the top at increasing flow rates.

The broken traps are marked red. Up to a flow rate of 3.5 ml/min all traps are intact. At higher flow rates the first traps start breaking. At a flow rate of 3.9 ml/min half of the traps are broken.

Fig. 3 illustrates the traps at different flow rates. Up to a flow rate of 3.5 ml/min, which is equivalent to an average flow velocity of 1 m/s, all traps in both chips withstand the flow, proving a very high stability and a very good adhesion between gold and IP-Dip. At higher flow rates the traps start breaking (marked red in the figure). Nearly all traps are broken at a flow rate of 4 ml/min. There is no apparent effect of the different support structures on the stability. Instead, mostly the first traps in the flow (on the left side) break, probably because they are exposed to the highest flow velocity.

Fig. 4 depicts the successful capturing of Jurkat cells 16 s after sample injection. The concentration of Jurkat cells in the sample is 10^6 cells/ml.

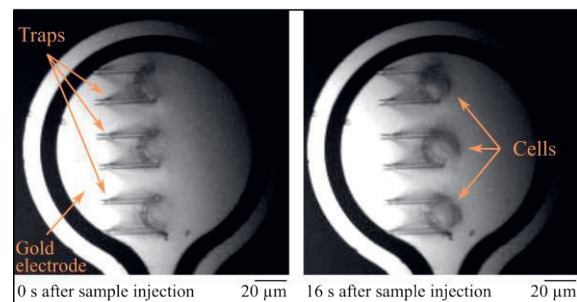


Fig. 4. Photographs of three cell traps before and 16 s after sample injection in a 30 μm high channel. After 16 s all traps are filled with Jurkat cells.

The presented results verify the ability of the novel 2PP traps to capture cells and their robustness at very high flow rates.

References

- [1] J. Xu et al, A Microfluidic Chip with Double-Slit Arrays for Enhanced Capture of Single Cells. *Micromachines* 9(4), 157 (2018); doi: 10.3390/mi9040157
- [2] D. H. Lee, X. Li, A. Jiang, A. P. Lee, An integrated microfluidic platform for size-selective single-cell trapping of monocytes from blood. *Biomicrofluidics* 12(5), 054104 (2018); doi: 10.1063/1.5049149
- [3] B. Xu et al, Arch-like microsorters with multimodal and clogging-improved filtering functions by using femtosecond laser multifocal parallel microfabrication. *Optics express* 25(14), 16739-16753 (2017); doi: 10.1364/OE.25.016739
- [4] C. Wang et al, Femtosecond mathieu beams for rapid controllable fabrication of complex microcages and application in trapping microobjects. *ACS nano* 13(4), 4667-4676 (2019); doi: 10.1021/acsnano.9b00893

Development of a new Measurement System for Electrical Conductivity and Hall Constant

Robin Werner¹, Jaroslaw Kita¹, Michael Gollner², Florian Linseis², Ralf Moos¹

¹ *Department of Functional Materials, University Bayreuth, 95440 Bayreuth, Germany*

² *Linseis Thermal Analysis, 95100 Selb, Germany*
functional.materials@uni-bayreuth.de

Summary:

A new system to measure the electrical conductivity and the Hall constant for high temperature characterization is presented here. A new sample holder with a screen-printed platinum heater and four moveable electrodes allow measurements of any geometry according to van der Pauw's method up to 600 °C. The new design also enables the use of low-cost permanent magnets. Measurements of a gold thin-film and a boron-doped silicon-wafer demonstrate the functionality of the measurement system. Further developments will add the possibility to measure the Seebeck coefficient.

Keywords: measurement system, Hall constant, electrical conductivity, high temperature, low-cost

Motivation

The electrical conductivity, the Hall constant, and the Seebeck coefficient are among the important electrical parameters of material characterization. There is no existing measurement setup yet that combines all measurements in one apparatus. To the best of our knowledge, commercial measuring instruments can only measure either Hall constant and conductivity or Seebeck coefficient and conductivity. Usually these measurement systems are complex, expensive and they require very careful sample contacting. Oftentimes, expensive furnaces and electromagnets are required combined with a low flexibility in terms of sample geometry.

This contribution describes a new measurement setup that makes passive heating superfluous due to a directly heated sample holder in thick-film technology and allows the use of permanent magnets. A further advantage are the flexible, very small electrical contact points, which allow measurements of any lateral geometry with homogeneous layer thickness using van der Pauw's method. [1]

Description of the New System

The sample holder, shown in Fig. 1, consists of a 635 µm thick alumina substrate. A sample of any geometry with overall dimensions between 5 and 12.7 mm can be contacted by four moveable electrodes on the front side allowing Hall and conductivity measurements according to van der Pauw's method. On the reverse side, a screen-printed platinum structure is used to

heat the sample area and the sample. The temperature on the upper side of the sample holder is controlled by the temperature-dependent resistance of the platinum heater structure.

The heater was designed by FEM analysis and validated by thermal imaging to guarantee a homogenous temperature distribution within the sample.

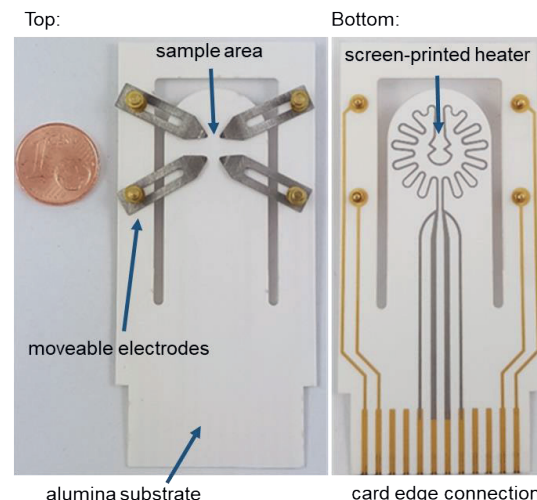


Fig. 1. Sample holder for Hall and conductivity measurements with a screen-printed heater

The four movable electrodes and the card edge connection allow a user-friendly exchange of the sample and sample holder and thus an easy installation and removal in the fixed gas floated measurement chamber. For Hall measurements, two counter-pole, moveable perma-

ment magnetic yoke systems have been added. The measurement setup is shown in Fig. 2.

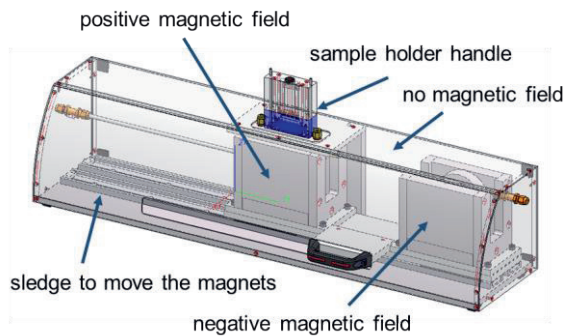


Fig. 2. Measurement setup with two moveable permanent magnetic yoke systems with ± 760 mT

The magnets with a diameter of 90 mm and a distance of 20 mm ensure a homogeneous magnetic flux density of $+760$ mT or -760 mT within the sample area. This new measurement setup allows to do conductivity and Hall measurements according to van der Pauw's method.

Results and Discussion

In order to test the functionality of the new measurement system, a gold thin-film and a boron-doped silicon-wafer were measured at temperatures up to 600 °C. The results are shown in Fig. 3. All measurements are performed according to the guidelines of the ASTM International standard (F76-08). [2]

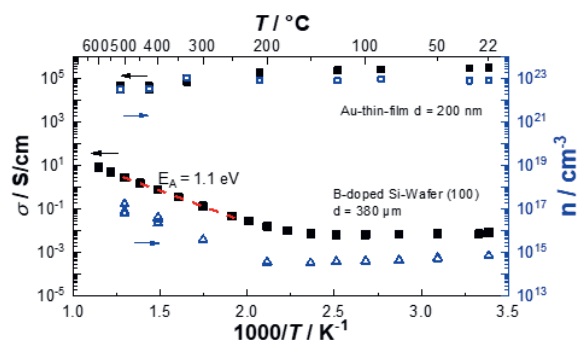


Fig. 3. Electrical conductivity and charge carrier concentration of a B-doped Si-Wafer and an Au-thin-film up to 600 °C

The measurements of a gold thin-film show a continuous decrease of the electrical conductivity while the charge carrier density remains nearly constant at increasing temperatures. This corresponds to a typical behavior of metals. It can be explained by the decrease of the mobility of the free electrons due to increased lattice vibrations with rising temperature. In contrast, the silicon wafer initially shows a slight decrease in conductivity up to a temperature of about 200 °C. After that, the conductivity increases by several decades, which can be ex-

plained by the typical formation of electron-hole pairs in the intrinsic region of a semiconductor. The charge carrier density in the intrinsic region above 200 °C also increases over several decades. The activation energy can be determined from these gradients. The calculated activation energy is 1.1 eV, which corresponds well to the band gap of silicon [3,4].

The measurements shown in Fig.3 can be seen as an evidence of the functionality of the new measurement system.

Conclusion and Outlook

The new measurement system allows measurements of the electrical conductivity and Hall constant up to 600 °C. The new sample holder with the screen-printed platinum heating structure can replace a furnace and enables the usage of permanent magnets even at high measurement temperatures.

In the future thermocouples and a second screen-printed heater for an additional temperature gradient for Seebeck measurements will be added. Furthermore, higher temperatures than 600 °C are envisaged.

References

- [1] L.J. van der Pauw, A Method of Measuring Specific Resistivity and Hall Effect of Discs of Arbitrary Shape, *Semiconductor Devices: Pioneering Papers*, 174-182 (1991); doi: 10.1142/9789814503464_0017
- [2] ASTM International, Test Methods for Measuring Resistivity and Hall Coefficient and Determining Hall Mobility in Single-Crystal Semiconductors, F76-08; doi: 10.1520/F0076-08
- [3] C. Kittel, Introduction to solid state physics, Wiley, (2018), ISBN 978-1119454168
- [4] G. Fasching, Werkstoffe für die Elektrotechnik: Mikrophysik, Struktur, Eigenschaften, Springer (2005); ISBN 3-211-22133-6

Design, Simulation, Fabrication and Characterization of Piezoelectric MEMS Cantilever for Gas Density and Viscosity Sensors Applications

A. Mehdaoui¹, C. Huber¹, J. Becker¹, F. Schraner¹, L. G. Villanueva²

¹ TrueDyne Sensors AG, Reinach BL, Switzerland

² Ecole Polytechnique Fédérale de Lausanne, Advanced NEMS Laboratory, Lausanne, Switzerland
alexandre.mehdaoui@truedyne.com

Summary:

A MEMS cantilever based resonant device for gas monitoring actuated and sensed piezoelectrically, has been designed, simulated, fabricated and tested. Aluminum Nitride (AlN) has been used as active material to implement the piezoelectric actuator and sensor. Simulation performed using COMSOL and measurements show a very good agreement. The final system, the full sensor for gas monitoring, allows the measurement of gas density and viscosity at temperatures between 0 and 60 °C and pressures between 1 and 10 bar abs. with accuracies of <math><0.03 \text{ kg/m}^3</math> and 6% respectively. A second technological run that aims to improve the viscosity accuracy is ongoing.

Keywords: MEMS, resonator, cantilever, piezoelectric actuation, piezoelectric sensing, density, viscosity, gas monitoring

Background, Motivation and Objective

Micromachined sensors are widely used to meet the increasing demand for miniaturized sensors for measuring physical parameters of gases, such as the density and viscosity. Also the realisation of ultra-precise scales in the field of inert gases e.g. welding gas or modified atmospheric packaging gas mixing application is of high interest. The use of standard silicon technology allows miniaturization at reduced costs, thus pushing the entry into new sensor markets such as low-power handheld systems [1]. The core of the sensor is an oscillating micro-cantilever which is fabricated at the Center of MicroNanotechnology (EPFL). The peak resonance response frequency f_r and the quality factor Q of a microcantilever are the two main dynamic characteristics that are very sensitive to the density and viscosity of the surrounding fluid [2]. Therefore, the viscosity and density of a fluid can be determined by analyzing the frequency response of a cantilever immersed in the fluid [3,4].

Description of the System: Design&Process

In this paper, a MEMS cantilever resonator (the core of the sensor), actuated and sensed piezoelectrically, has been designed, simulated, fabricated and tested. A piezoelectric transduction, Aluminum Nitride (AlN), is integrated on top of the cantilever to enable actuation and detection of devices (resonance frequency and

Q factor). Platinum (Pt) has been used as top and bottom metal contacts between which AlN has been sandwiched to form the actuating and sensing electrodes and also the temperature sensor. Indeed, as the temperature has to be well measured and controlled during the evaluation of the gas thermophysical properties, we need to define the temperature sensor as close as possible of the density and viscosity sensors. The cantilever investigated in this paper was fabricated on a SOI wafer with a 10 μm thick device layer and with a length of $L=600 \mu\text{m}$ and a width of $W=202 \mu\text{m}$. Fig. 1 shows the detailed process flow.

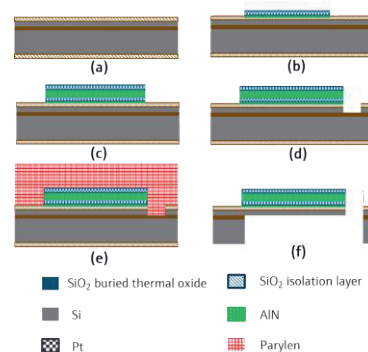


Fig. 1. AlN cantilever fabrication process: (a) thermal oxidation isolation layer, (b) adhesion AlN layer and bottom Pt metal deposition and patterned by lift-off, (c) active AlN layer and top Pt metal deposition by sputtering and patterned by Cl_2/Ar dry etch, (d) cantilever shape patterning by CF_4 and Cl_2 dry etch,

(e) Parylen deposition for the front side protection during the deep back side etching, (f) cavity patterning by dry Si and wet SiO₂ etching, cantilever release by plasma O₂

Results

Fig. 2a shows the SEM image of the fabricated AlN cantilever. Fig. 2b shows the MEMS chip bonded on a PCB, following by the glob-top encapsulation.

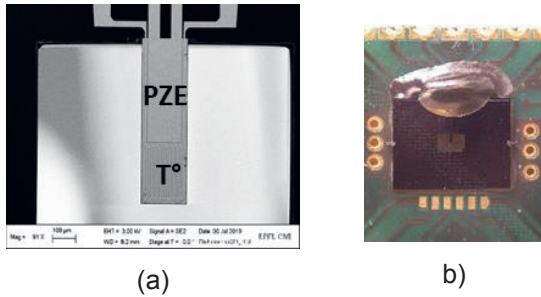
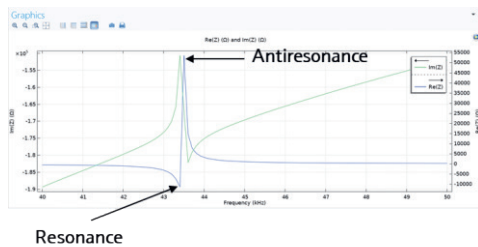
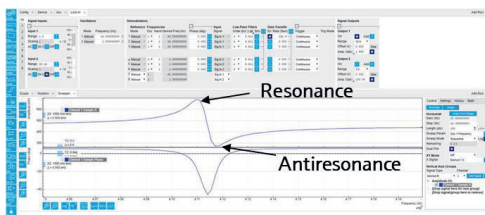


Fig. 2. MEMS Piezoelectric cantilever: (a) SEM image: Temperature sensor (T°) and Piezoelectric transducer (PZE), (b) MEMS sample + PCB

Fig. 3 a and b show respectively the simulated impedance real and imaginary parts performed in COMSOL and the measured frequency response, both amplitude and phase of the signal. We can see a good agreement between the simulation ($f_r = 43.7$ kHz, $Q = 882$) and measurement results ($f_r = 41.1$ kHz, $Q = 724$).



(a)



(b)

Fig. 3. Piezoelectric resonance and Q factor in Air: (a) simulated impedance in COMSOL, (b) Measured frequency response using lock-in amplifier

For the measurement in gases, we have manufactured a special PCB containing a MEMS chip, a pressure and temperature sensors. This PCB can be screwed into a gas tight metal cylinder that serves as a gas cell, see Fig. 4. For a standard density and viscosity calibration, 4

different gases (N₂, CO₂, Ar and He) are measured at temperatures between 0 and 60 °C and pressures between 1 and 10 bar abs. The measuring performance of the sensor is shown in Fig. 5. We can measure the gas density with an abs. accuracy <0.03 kg/m³ and the dynamic viscosity with a relative accuracy of 6%. In order to optimize the viscosity accuracy, we have decided to change the Si device layer from 10 μm to 5 μm and 3 μm. A second technological run is ongoing.

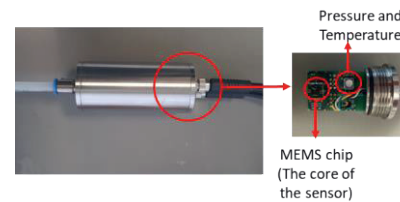
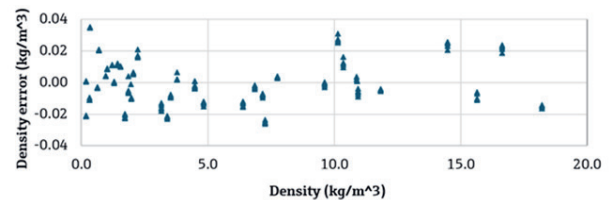
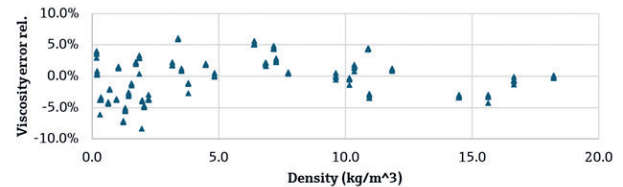


Fig. 4. Sensor PCB mounted in a pressure tight gas cell with electric connections on the right and fluidic connections on the left



(a)



(b)

Fig. 5. (a) Density and (b) viscosity measuring accuracy

References

- [1] M. Kucera and all, Characterization of multi roof tile-shaped out of plane vibrational modes in aluminum nitride actuated self sensing micro-resonators in liquid media, *Applied Physics Letters* 107, 053506 053506 (2015), doi: 10.1063/1.4928429
- [2] H. Qiu et al., Hydrodynamic analysis of piezoelectric microcantilevers vibrating in viscous compressible gases, *Sensors and Actuators A*, 238 (2016), 299-306
- [3] A. Badarlis et al., Measurement and evaluation of the gas density and viscosity of pure gases and mixtures using a micro-cantilever beam, *Sensors*, 15 (2016), doi: 10.3390/s150924318
- [4] C. Huber et al., Gas density and viscosity measurement with a micro-cantilever for online combustion gas monitoring, 19. GMA/ITG-Fachtagung Sensoren und Messsysteme, 2018

Applications of Tactile Microprobes for Surface Metrology

*Christoph Reuter*¹, *Mathias Holz*¹, *Alexander Reum*¹, *Michael Fahrbach*^{2,3}, *Erwin Peiner*^{2,3}, *Uwe Brand*⁴,
*Martin Hofmann*⁵, *Ivo Rangelow*⁵

¹ *nano analytik GmbH, Ehrenbergstraße 1, 98693 Ilmenau, Germany,*

² *Technische Universität Braunschweig, Institute of Semiconductor Technology (IHT), Hans-Sommer-Straße 66, 38106 Braunschweig, Germany,*

³ *Technische Universität Braunschweig, Laboratory for Emerging Nanometrology (LENA), Langer Kamp 6, 38106 Braunschweig, Germany,*

⁴ *Physikalisch-Technische Bundesanstalt (PTB), Bundesallee 100, 38116 Braunschweig, Germany*

⁵ *Technische Universität Ilmenau, Institute of Micro- and Nanoelectronics, Gustav-Kirchhoff-Straße 1, 98693 Ilmenau, Germany
c.reuter@nanoanalytik.net*

Summary:

In this paper we discuss the capabilities of micromachined piezoresistive silicon cantilevers regarding their application for surface metrology [1]. Measurements were performed using contact-mode Atomic Force Microscopy (AFM) and contact-resonance mode, respectively [2]. The contact-mode AFM measurements were carried out inside a Scanning Electron Microscope (SEM) vacuum chamber enabling correlative scanning probe and electron microscopy [4].

Keywords: piezoresistive cantilever, MEMS, atomic force microscopy, contact resonance, surface roughness

Microprobe Sensor

Piezoresistive cantilever sensors have become a versatile tool for measuring the mechanical properties, the topography and the surface roughness of various materials [1,2]. A SEM image of the probe used within this paper is shown in Figure 1.

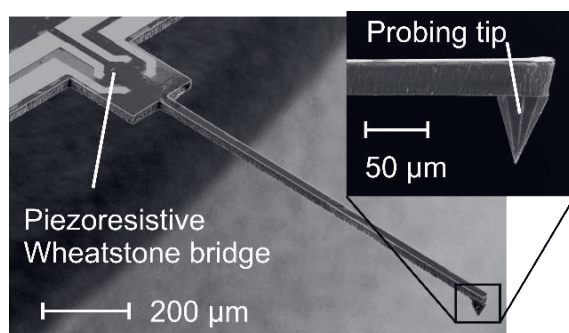


Fig.1. SEM image of a 1.5mm-long microprobe [1].

The probe is commercially available (CAN series, CiS Forschungsinstitut für Mikrosensorik GmbH, Erfurt/Germany) in different lengths ranging from 1.5mm up to 5mm. The slender structure of the cantilever allows to inspect surfaces inside cavities and narrow milling grooves which aren't accessible with other tools [1,2]. The probe features a height sensitivity of

$50\text{pm}/\sqrt{\text{Hz}}$ which leads to an achievable imaging resolution below 10nm [3].

Correlative AFM and SEM Measurements

Combining the AFM-based topography and roughness measurements of the microprobe with a SEM offers several advantages. Not only can the SEM be used for wide range coarse navigation on the sample, it also allows to simultaneously monitor the tip-sample interactions during the AFM scanning process.

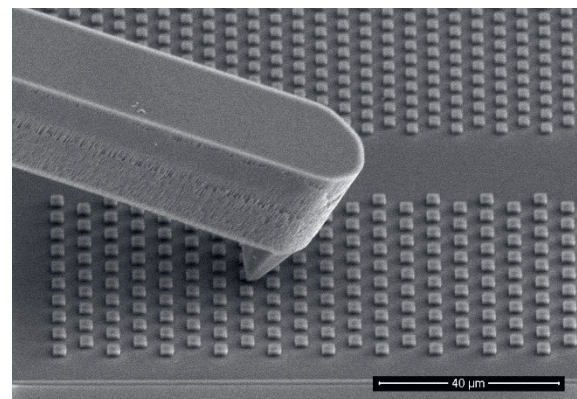


Fig.2. Contact-mode AFM imaging combined with SEM imaging.

Moreover is it possible to constantly observe the tip-wear of the probe, which is especially for high accuracy surface roughness measurements beneficial. The vacuum-compatible AFM (AFMinSEM, nano analytik GmbH) we used for measurements features a coarse positioning unit for moving the probe in an area of interest of 18mm x 18mm. Additionally, a capacitive closed loop scanner for high resolution imaging is used as a sample nanopositioning stage with a scanning range of up to 60 μ m x 60 μ m x 20 μ m in X-, Y-, Z-direction.

Contact Resonance Spectroscopy (CRS)

Contact Resonance Spectroscopy (CRS) is an operation mode of AFMs where the amplitude and phase response of a resonant-excited cantilever probe is recorded to detect sub-surface features of materials via its contact stiffness and damping. Using the piezoresistive CAN sensor, the range of work pieces to be characterized using CRS could be extended to high-aspect-ratio (HAR) geometries [5]. Here a chip-size piezo actuator (PL055.30 by Physik Instrumente) is mounted below the CAN chip corresponding to the configuration of ultrasonic atomic force microscopy (UAFM) operation mode in AFMs. It was shown that CAN-sensor-based CRS is sensitive enough to show a contrast of ~ 15-nm-thick layers of PEDOT on silicon [6]. For further performance evaluation a modified probe- holder and interface printed circuit board (PCB) was designed and fabricated for operation of the CAN-sensor-based CRS in a Cypher AFM (Asylum Research) (Fig. 3).

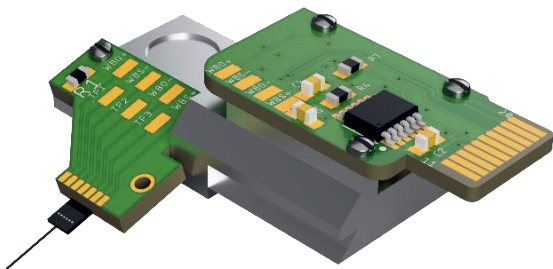


Fig.3. Schematic of a CAN50-2-5 probe holder with pre-amplifier and interface PCB for operation in a Cypher AFM.

Results

Within this work we presented the capabilities of the microprobe integrated in two different setups

each with unique functionalities. The integration into the AFMinSEM in enhancing its functionalities with standardized roughness measurements and allowing measurements to be taken in areas that standard cantilevers are normally withheld.

Acknowledgements

The authors gratefully acknowledge financial support through the European Union's European Metrology Programme for Innovation and Research (EMPIR), Grant no. 17IND05 MicroProbes.

References

- [1]E. Peiner, M. Balke, L. Doering, Slender Tactile Sensor for Contour and Roughness Measurements Within Deep and Narrow Holes, *IEEE Sens. J.* 8, 1960-1967 (2008); <https://doi.org/10.1109/JSEN.2008.2006701>
- [2]U. Brand et al., Long Slender Piezo-Resistive Silicon Microprobes for Fast Measurements of Roughness and Mechanical Properties inside Micro-Holes with Diameters below 100 μ m, *Sensors* 19(6), 1410 (2019); <https://doi.org/10.3390/s19061410>
- [3]U. Brand et al., Smart sensors and calibration standards for high precision metrology, *Proc. SPIE* 9517, 95170V (2015); <https://doi.org/10.1117/12.2179455>
- [4]I.W. Rangelow et al., Atomic force microscope integrated with a scanning electron microscope for correlative nanofabrication and microscopy, *Journal of Vacuum Science and Technology B* 36, 06J102 (2018); <https://doi.org/10.1116/1.5048524>
- [5]M. Bertke et al., Contact Resonance Spectroscopy for On-The-Machine Manufactory Monitoring, *Sens. Actuat. A Phys.* 279, 501–508 (2018); <https://doi.org/10.1016/j.sna.2018.06.012>
- [1]M. Fahrbach et al., Optimizing a Cantilever Measurement System towards High Speed, Nonreactive Contact-Resonance-Profilometry. *Proceedings*, 2, 889 (2018); <https://doi.org/10.3390/proceedings2130889>

Higher-Mode Contact Resonance Operation of a High-Aspect-Ratio Piezoresistive Cantilever Microprobe

Michael Fahrbach and Erwin Peiner

Technische Universität Braunschweig, Institute of Semiconductor Technology (IHT), Hans-Sommer-Straße 66, 38106 Braunschweig, Germany

*Technische Universität Braunschweig, Laboratory for Emerging Nanometrology (LENA), Langer Kamp 6A/B, 38106 Braunschweig, Germany
m.fahrbach@tu-bs.de*

Summary:

In this work, a long slender MEMS cantilever sensor for higher-order contact resonance tactile-sensing applications is described. The design is focused on enabling high-speed measurements on large work-pieces. To excite high-order out-of-plane bending modes of the cantilever, heating resistors integrated into the sensor are used as actuators. Their positions are optimized to allow for an efficient resonant excitation of the sensor, as confirmed by finite-element modelling (FEM).

Keywords: MEMS, microprobe, thermal actuator, piezoresistive cantilever, contact resonance

Motivation

The continuing digitalization of industrial production causes a need for high-speed methods to measure form, roughness and mechanical properties on-the-machine [1]. Tactile microcantilevers, such as depicted in Fig. 1, have been shown to be able to measure at velocities up to 15 mm/s and are, thus, promising for this application [2].

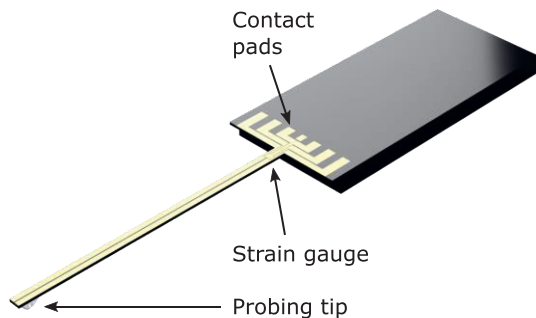


Fig. 1. Render of the microprobe design.

To further develop such microprobes, a European EMPIR project is being funded [3]. One of the aims of this project is to design new sensors which are optimized to efficiently measure mechanical properties of samples using contact resonance (CR) techniques. These sensors shall then be calibrated on reference samples.

Evaluation of different vibration modes

To evaluate the performance of different CR modes, first measurements were conducted using a commercial CAN50-2-5 probe (CiS Forschungsinstitut für Mikrosensorik GmbH, Erfurt,

Germany) which was mounted on a PL055.30 chip-size piezoactuator (Physik Instrumente (PI) GmbH und Co KG) [4]. The resulting data is analyzed to determine the resonance mode that results in the best compromise between measurement speed and resolution.

Design of the microprobe

The design is based on previous work [5] that is extended by implanted heating resistors. The outer dimensions remain unchanged and are listed in Tab. 1. An overview of the design is shown in Fig. 2.

Tab. 1. Geometrical and material properties of the microprobe.

Parameter	Symbol	Value
Length	L	5 mm
Tip position	L_1	4.95 mm
Strain gauge position	L_{WB}	185 μm
Width	w	200 μm
Thickness	b	50 μm
Density	ρ	2330 kg/m ³
Young's modulus [6]	E	169 GPa

Similar to the design described by Yu et al. [7], we utilize one heating resistor at the clamped end of the cantilever and an additional one at L_{HR2} , near the center of the cantilever.

Additionally, a probing tip is located at L_1 , near the free end of the cantilever.

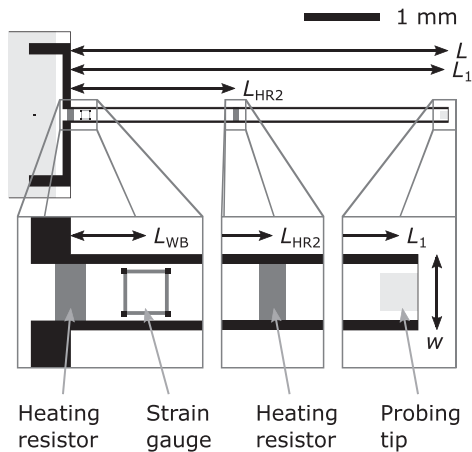


Fig. 2. Overview of the sensor design. The metal contact lines are not shown to maintain visibility.

To counteract thermal coupling described in [8], the distance between the first heating resistor and the strain gauge is increased to $100\ \mu\text{m}$ compared to approximately $30\ \mu\text{m}$ used in [8].

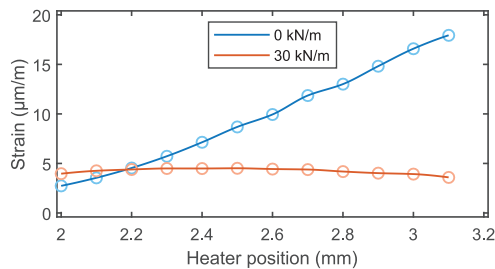


Fig. 3. FEM amplitude of strain at L_{WB} upon resonant actuation depending on the position of the second heating resistor L_{HR2} for $k_c^* = 0$ and $k_c^* = 30\ \text{kN/m}$.

As shown in Fig. 3, the optimal distance of the second heating resistor from the clamped end of the cantilever is $L_{HR2} = 2.2\ \text{mm}$, which will ensure uniform signal amplitudes for a range of materials (contact stiffness up to $k_c^* = 30\ \text{kN/m}$) when using third-mode CR.

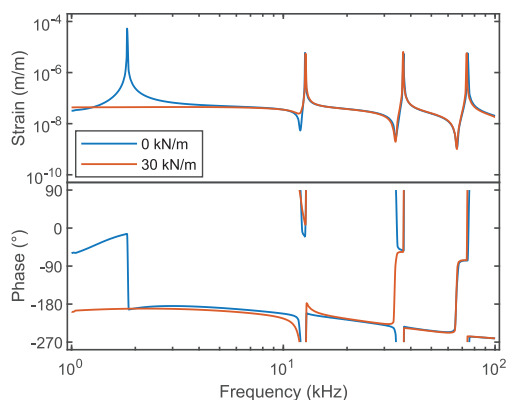


Fig. 4. FEM frequency response of strain at L_{WB} for $k_c^* = 0$ and $k_c^* = 30\ \text{kN/m}$.

As depicted in Fig. 4, the CR spectra of the probe are simulated showing similar amplitudes of the modes at $k_c^* = 0$ and $30\ \text{kN/m}$. The frequency

range for third-mode CR is found to be 37 kHz to 74 kHz for the accessible measuring range of k_c^* .

Fabrication and Test

For comparison with the FEM results, sensor samples are fabricated using our in-house bulk-silicon micromachining process. This process uses seven lithography masks to realize the novel cantilevers. The behavior of the sensor in CR mode during scanning operation will be measured and compared with FEM.

Acknowledgements

This project has received funding from the EM-PIR programme co-financed by the Participating States and from the European Union's Horizon 2020 research and innovation programme under no. 17IND05 MicroProbes.

References

- [1] E. Hofmann, M. Rüscher, Industry 4.0 and the current status as well as future prospects on logistics, *Computers in Industry* 89, 23-34 (2017); doi:10.1016/j.compind.2017.04.002
- [2] H. S. Wasisto et al., Ultra-high-speed cantilever tactile probe for high-aspect-ratio micro metrology, *2015 Transducers - 2015 18th International Conference on Solid-State Sensors, Actuators and Microsystems (TRANSDUCERS)*. IEEE. (2015); doi:10.1109/transducers.2015.7181109
- [3] 17IND05 MicroProbes Multifunctional ultrafast microprobes for on-the-machine measurements. (2018). Retrieved from <https://www.ptb.de/em-pir2018/microprobes/>
- [4] M. Fahrbach, E. Peiner, P2.10 Entwicklung eines taktilen Mikrotaster-Messsystems für Hochgeschwindigkeitsmessung von Form, Rauheit und mechanischen Eigenschaften, *20. GMA/ITG-Fachtagung Sensoren und Messsysteme 2019*, (2019); doi:10.5162/SENSOREN2019/P2.10
- [5] E. Peiner et al., Slender Tactile Sensor for Contour and Roughness Measurements Within Deep and Narrow Holes, *IEEE Sensors Journal* 8, 1960-1967 (2008); doi:10.1109/jksen.2008.2006701
- [6] M. A. Hopcroft et al., What is the Young's Modulus of Silicon?, *Journal of Microelectromechanical Systems* 19, 229-238 (2010); doi:10.1109/jmems.2009.2039697
- [7] H. Yu et al., Resonant-cantilever bio/chemical sensors with an integrated heater for both resonance exciting optimization and sensing repeatability enhancement, *Journal of Micromechanics and Microengineering* 19, 04502 (2009); doi:10.1088/0960-1317/19/4/045023
- [8] A. Setiono et al., Phase optimization of thermally actuated piezoresistive resonant MEMS cantilever sensors. *Journal of Sensors and Sensor Systems*, 8, 37-48 (2019); doi:10.5194/jsss-8-37-2019

A MEMS micromachined detector platform for kW power radiation in a wide spectral range

A. Laades¹, S. Görlandt¹, C. Heinze¹, F. Machalet¹ and T. Ortlepp¹
¹CiS Forschungsinstitut für Mikrosensorik GmbH Erfurt

Summary:

The focus of the development is on a silicon membrane based thermal detector for radiation extending from the infrared to the extreme ultraviolet (XUV) featuring very high powers in the range 100 W to 5 kW. The thermal radiation detector is equipped with a sensor platform chip consisting of an appropriate absorber and a silicon-based temperature sensor unit. This approach allows the radiation to be efficiently absorbed and converted into heat in the absorber leading to a local increase in temperature and a detectable temperature difference in the silicon unit.

Keywords: MEMS, Membrane, sensor responsivity, response time, microbolometer

Introduction

There is an increasing need for low cost radiation sensors for very high or total power radiation ranging from 100 W to 5 kW. These sensors find applications in e.g., fusion reactors [1], EUV lithography steppers or ultraviolet water treatments. MEMS (microelectromechanical sensors) micromachined CMOS compatible detectors with medium performance offer a viable solution to these needs.

In terms of the evaluated concepts for EUVL steppers requiring an area as large as possible, The sensors developed in this work are based on a chip size of at least 7x7 mm² with a membrane size of at least 5x5 mm².

Sensor fabrication and measurements

We have developed a sensor platform based on a microbridge bolometer using standard processing steps, regularly used to manufacture piezoresistive pressure sensors. Their sensing unit consists of an anisotropically etched cavity in a silicon wafer to form the supporting membrane. A Wheatstone bridge configuration has been formed by ion implantation. The sensor was packaged and then characterized electrically and optically in terms of response behavior and responsivity.

Results

In Fig. 1 the packaged sensor and the bridge based readout circuit can be seen. The sensors were mounted on circuit boards using wire bonding and die attach technology, provided with additional heat-dissipating aluminum plates and attached to other circuit boards to connect the devices using SMA/BNC cables.

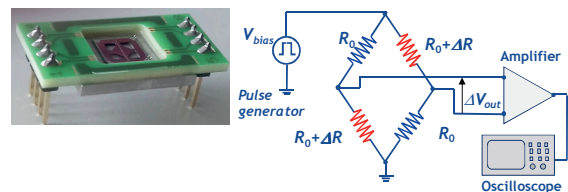


Fig. 1. Left: Sensor assembly. In the middle of the package the sensor with released membrane can be seen. Right: schematic drawing of the setup with Wheatstone bridge.

The suitability of the bridge based microbolometer as a thermal sensor was tested by means of electrical measurements by heating the bridge applying electrical power. Since the sensor does not have its own calibration heating resistor, the heating power was coupled-in via the bridge operating DC voltage.

The variation of the output offset voltage as a function of the bias voltage for one of the investigated devices is displayed in Fig. 2(a). This shows that the sensor responds to the electrical power by generating a bridge output signal and varying non-linearly with the bias voltage.

The changing sign of the slope in the characteristic curve demonstrates the increasing bridge unbalance (offset) of the sensor with the DC bias voltage and thus quadratic increasing power loss. The characteristic curve was fitted with a third degree polynomial function and corrected by subtracting all loss components with the exception of the quadratic part. The latter corresponds to the electrical power that was actually used to thermally change the resistance. This procedure was exploited to determine the responsivity (defined as output voltage/input power in V/W), as shown in Fig. 2

(b). The characteristic $\Delta V_{out} = f(V_{bias})$ was recorded directly on various sensors without absorber, and with membrane thicknesses of 10 to 20 μm .

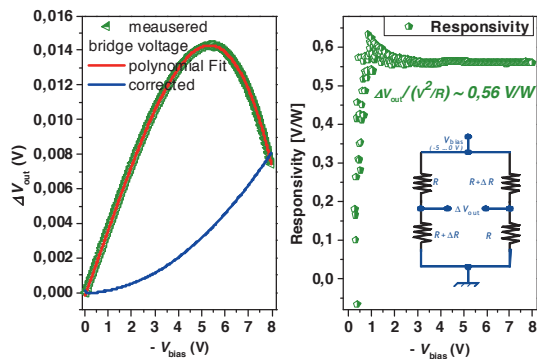


Fig. 2. Output voltage (left) and responsivity (right) of the sensor as functions of the applied bias voltage.

The (responsivity) of the sensors tested using this method varies between 0.5 and 1 V/W. Similarly, the sensor was further analyzed in terms of temporal response behavior electrically as well as optically. For this purpose, a precise voltage source was used to generate pulsed voltages. In Fig 3(a) the temporal response of the device to voltage pulses directly applied to the bridge are displayed. With a pulsed laser source, it is possible to analyze the response of the sensor to radiation absorbed in the membrane. A typical result for an excitation with a wavelength of 450 nm is displayed in Fig. 3 (b)

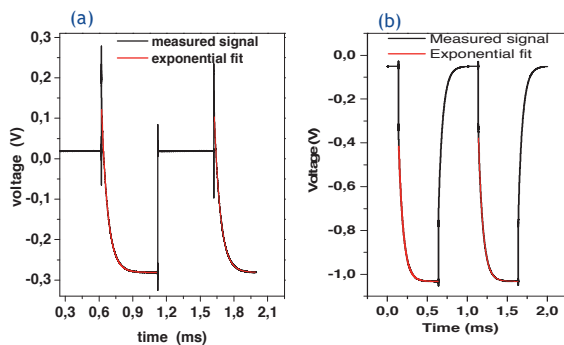


Fig. 3. Time response of electrically and optically excited sensor.

The exponential part of the response behavior results from thermal coupling. The graph with optical excitation ($f = 1$ Hz) also shows photo-sensitive behavior, which is added to the actual measurement signal. The exponential part could be fitted by an exponential function according to the procedure applied in [2].

Accordingly, we could determine the time constant τ_{th} , thermal conductivity (G_{th}) and heat capacity (C_{th}) of the sensor platform. For the

different sensors analyzed in this work τ_{th} ranges from 10 to 60 ms. G_{th} and C_{th} amount to 10^6 bis 10^7 W/K and von 10^{-7} J/K, respectively.

Finally we analyzed the temporal response of the sensor by EUV excitation using an XUV source.

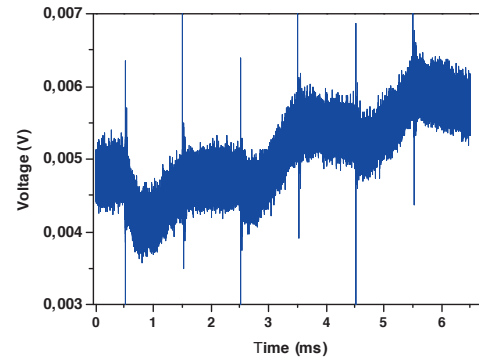


Fig. 4. Time response to XUV radiation.

The XUV source which was available features an output power of 100 μW maximum, such that the absorbed power was much less than that. Nevertheless an output signal upon XUV excitation could be recorded, though overwhelmed by the background noise. However, it can be predicted that for high powers from 100 W to 5 kW, the sensor solution is highly scalable and is well suited for detecting radiation in the EUV / XUV spectral range with high power.

Conclusion and outlook

It is demonstrated that using the cost effective MEMS technology, it is possible to fabricate thermal Sensors for a wide range of radiations. The developed bridge based bolometric sensors have a good response to photons in different spectral ranges (blue, green, XUV) with a thermal time constant in the range of 10 to 60 ms. The responsivity is approx. 1V/W. Thus, radiation with power over 100 W to 5 kW can be measured, which is the aim of the development. Since the approach is based on purely thermal excitation of absorber, the temperature sensor unit is less prone to XUV radiation damage.

References

- [1] H. Meister H. Langer, S. Schmitt, "An alternative geometry for bolometer sensors for use at high operating temperatures", Fusion Eng. Des. **120**, (2017) 21
- [5] X. Gu, G. Karunasiri, and G. Chen, "Determination of Thermal Parameters of Microbolometers Using a Single Electrical Measurement", App. Phys. Lett. **72**(1998) 15,

H₂-Sensors for Automotive Fuel Cell Application

*Olaf Kieseewetter¹, Alexander Krauß¹, Nils Kieseewetter¹, Jürgen Müller¹, Marcus Bose¹,
Stefan Schenk¹, Matthias May¹*

¹ UST Umweltsensortechnik GmbH, Dieselstr. 2 und 4, 99331 Geratal OT Geschwenda
o.kieseewetter@umweltsensortechnik.de

Summary:

For the measurement of H₂ concentrations in the exhaust gas of automotive fuel cells and in its vehicle environment the development of an active diversified-redundant hydrogen gas sensor system has been started. The combination of a selective metal oxide semiconductor gas sensor and a thermal conductivity detector as well as suitable signal preprocessing enables an application-specific H₂ sensor system with high sensitivity, selectivity, stability and safety. Work status and current results of the development will be presented.

Keywords: H₂-sensor, fuel cell, ambient, exhaust, automotive, diversified-redundant

Sensor principles for H₂ measurement

Typical fields of application of H₂ sensors in automotive fuel cells are the measurement of H₂ concentrations in the exhaust gas of the fuel cell and in its vehicle ambient. For the measurement of hydrogen different functional methods depending on application are used. Known and proven methods include e.g. sensors based on catalytic, electrochemical, thermal conductivity, resistive, optical functional principles and combinations of these.

Application specific requirements

The application-specific automotive requirements for functionalities, safety, life-time and reliability of H₂ sensors necessitate accordingly ambitious target parameters of such sensors to be developed: e.g. H₂ measuring range from 1ppm to 10Vol%, accuracy values from measured value $\pm 30\%$ ($\leq 1\%$ H₂) and $\pm 10\%$ ($> 1\%$ H₂), short time from 3s after switching on until operational readiness is reached (operational readiness after icing max. 5s), at least 45,000 on/off cycles, operating temperature range from -40°C up to $+85^{\circ}\text{C}/+125^{\circ}\text{C}$, resistance to a large number of chemical substances e.g. CO, C₆H₆, C₇H₈, NH₃, NO, NO₂, O₃, SO₂, HMDS, etc. as well as min. 8.000h operating hours, lifetime of at least 15 years, mileage of at least 300.000km.

Metal oxide (MOX) semiconductor gas sensors (resistive functional principle) are characterized by their high sensitivity in the ppm range and the very high selectivity for hydrogen when using specific filter-coated gas-sensitive layers.

The functional principle of a thermal conductivity detector (TCD) is based on different thermal conductivities of the gases. It is therefore particularly suitable for the detection of higher gas concentrations. Gas sensors, based on these functional principles have long been successfully used in vehicles for various applications.

H₂ sensor based on the Semicon[®] principle

To achieve the above mentioned objectives, a sensor system based on the Semicon[®] principle [1] was designed for H₂ measurement in the exhaust gas as well as in the environment. The H₂-Sensorsystem combines a thermal conductivity detector (TCD) and a metal-oxide semiconductor gas sensor (MOX). A TCD detects temperature changes resulting from the different thermal conductivities of individual gases and their concentrations. The functionality of a MOX gas sensor is based on the conductivity-change of the gas-sensitive MOX semiconductor layer/s at gas exposure, which can be externally measured and analysed. A specific MOX gas-sensitive layer reacts to oxidizing gases with increasing of the layer resistance and to reducing gases with decreasing of the layer resistance. Tab. 1 shows selected advantages and disadvantages of the TCD- and MOX-gas sensor principles [1] [2].

Tab. 1: Selected advantages and disadvantages of TCD- and MOX-gas sensors

Thermal conductivity detector (TCD)	MOX gas sensor
+ high linearity	+ high sensitivity

+ high accuracy	+ short response time
+ high stability	+ wide measuring range
+ pollution resistant	- low accuracy
- low selectivity	- low selectivity (depending on gas type)
- temperature sensitive	- pollution-sensitive

The innovative combination of a TCD and a MOX gas sensor combines the advantages and compensates the disadvantages of the two functional principles - Semicon[®] principle [1] [2].

Laboratory sample of the H₂ sensor

Fig.1 shows the block diagram of the H₂ sensor system for exhaust gas monitoring. The sensor system consists of the parts sensor head, currently with integrated H₂ MOX duo gas sensor element, TCD element, two platinum thin-film temperature sensor elements as reference elements and a separate sensor electronics module for sensor control, signal preprocessing, communication, interface and power supply. In a later development phase the MOX duo gas sensor element will be substituted by a new MOX gas sensor element with a multi-electrodes structure furthermore sensor head and electronics are to be integrated.

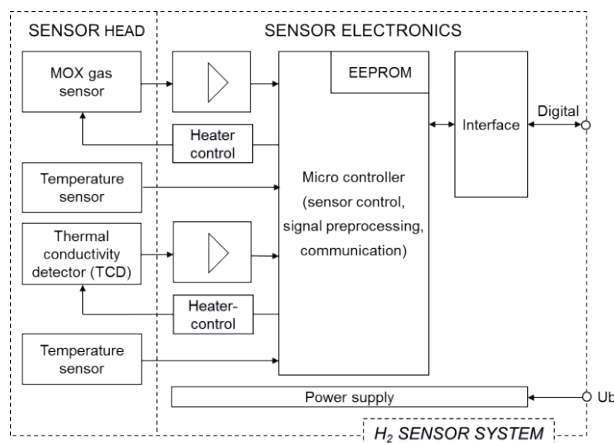


Fig. 1 Block diagram of the H₂ Semicon[®] sensor system for exhaust gas monitoring of an automotive fuel cell

Fig. 2 shows sensor elements, used for the first laboratory sample of the H₂ sensor for exhaust gas measurement.



Fig. 2 Ceramic TCD element 1,5x1,5mm (left) and MOX gas sensor element 2x2,3mm (right)

These MOX and TCD gas sensor elements are realized in hybrid-technology: ceramic carrier substrate (Al₂O₃) with a micro-structured platinum thin-film layer, covered with a passivation layer, specific layers for contacts and locking as well as a gas-sensitive metal oxide (MOX) layer for the MOX gas sensor element [3]. The H₂ sensor for the ambient monitoring will be realized with MOX gas sensor and the TCD element on one ceramic chip.

During a monitoring measurement in the laboratory test environment, a H₂ sensor system was exposed to various H₂ concentrations. c_{H2} shows the H₂ concentration, c_{sensor H2} the output by the sensor. The deviations between c_{H2} and c_{sensor H2} are within the specification (see Fig.3)

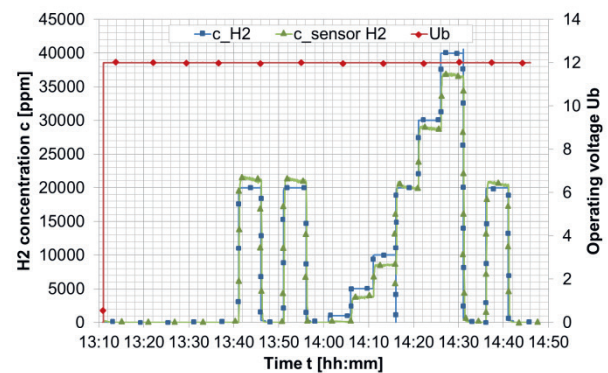


Fig. 3 Measurement of a H₂-Semicon[®] sensor system after use in the application

Results and outlook

The results show that the realized sensor system and its components in connection with a suitable sensor head design and integrated electronics provide realistic basics for a successful continuation of the development work with the aim of future development of application-specific and customized H₂ sensors for automotive fuel cell applications.

References

- [1] Ewert, A., Kiesewetter, O., Kittelmann, S., Melchert, V., „Verfahren zur Erfassung brennbarer Gase, insbesondere zur Erfassung von Wasserstoff / Method for detecting combustible gases, in particular hydrogen“, European Patent, No. EP000001621882B1, 02.06.2005.
- [2] Kiesewetter, O., Kraußner, A., May, M., Innovative H₂ sensor platform for customized applications, Lecture Sensor 2017, Nuremberg, 01.06.2017
- [3] Kiesewetter, O., Kohl, C.-D., Melchert, V., Bauersfeld, D., May, M., „Innovative Plattform für keramische Sensoren als Basis für automotive Applikationen“, In: Tille, T., et al., Sensoren im Automobil IV, 236-259, Haus der Technik Fachbuch Band 119, ISBN 978-3-8169-3066-2, Expert-Verlag, 2011.

Sensitivity und Selectivity of Pd-based Thin Film Hydrogen Sensors

Marion Wienecke^{1,2}, Laura Godenrath¹, Max Hoffmann¹, Jan Heeg²
¹*Materion GmbH, Alter Holzhafen 15, 23966 Wismar, Deutschland*
²*Hochschule Wismar, Institut für Oberflächen- und Dünnschichttechnik, PF1210, 23952 Wismar, Deutschland*

Abstract

Pd-based thin film hydrogen sensors are available on the market since several years. They run due to different physical mechanisms, such as optical switching, changing resistance or capacity of thin film structures. This article describes the capabilities of Pd-thin film optical sensors (POS) and of new micro-electromechanical systems (MEMS). MEMS Pd-based sensors utilise the volume change of Pd due to the hydrogenation, thus they switch mechanically. Both systems detect hydrogen concentrations between 100 vol.-ppm and 100 vol.-% hydrogen in any gas mixtures. They show low cross sensitivities and particularly no cross sensitivity to methane (CH₄) since the switching mechanism is a physical one. The response time (t_{90}) for POS and MEMS sensors is about 20 s and 5 s, respectively. Thus, both sensor types fulfil the requirements of ISO 26142 for control and explosion protection of stationary facilities.

Paper present laboratory investigations of sensory switching of Pd and Pd-alloy thin films deposited by magnetron sputtering. Investigations were conducted on optical transparency for POS and the change in resistance of piezo-electric Si-MEMS structures coated with Pd-thin films. The results show, that the sensory properties can be well explained by the physical properties of the Pd-H System. The absorption of hydrogen in Pd is reversible; it follows the outer partial pressure (Sievert law). The hydrogen initially adsorbed at the Pd-surface diffuse into the metal lattice, an equilibrium concentration of H-atoms in the metal lattice is adjusted. The transparency of Pd and Pd-alloy thin films appears when the solubility of hydrogen in the metallic α phase is depleted and a PdH β -phase occurs. This phase transition in pure Pd occurs at 1,68 at.-% H in Pdⁱ. Experimental results revealed that optical sensors with pure Pd-thin films as well as also Pd/Au alloys cannot detect very small H-concentrations, they show the lower detection limit of about 0,1 vol.-%, because the metallic phase is opaque. The transition between the metallic α phase and hydride β phase can be shifted due to intrinsic stress within the ultra-thin Pd – or Pd/Au films^{i,ii}. However, the results show that Pd/Y thin films reveal a lower detection limit of about 100 vol.-ppm.

Since the lattice constant in Pd is increasing due to the H-incorporation, the volume change of the Pd-thin films can also be used for sensor switching. The lattice distance within the metallic α phase from pure Pd to 2 at.-% hydrogen is increasing to 3,895 Å and within the β -phase with up to 37,6 at.-% hydrogen it is 4,025 Åⁱⁱ. This volume change is used for MEMS-hydrogen sensors. Investigations revealed a reversible switching of MEMS-Pd-sensors without any drift and fast response for hydrogen concentrations between some 100 vol.-ppm and 100 vol.-% hydrogen. For hydrogen concentrations between 1 vol.-% and 100 vol.-% the t_{90} response time is about 5 s. This volume change also occurs within the metallic α phase and thus MEMS-hydrogen sensors with Pd/Au thin films also detect minimum hydrogen concentrations of about 100 vol.-ppm. The response time for small concentrations is larger, it is about some minutes; however, this is in agreement with data from literature, which report response time increases at lower hydrogen concentrationsⁱⁱⁱ.

These results show new potentials for hydrogen sensor applications: new application fields for in-situ control of hydrogen concentrations; thus for processes working in high hydrogen concentrations of up to 100 vol.-%, such as in metallurgy, for fuel cells, or chemical process engineering. For low hydrogen concentrations, below the explosive limit, the new sensor concepts particularly show potentials because of their low cross sensitivity. E.g. for breathing gas sensors in medicine technique no cross sensitivity against ethanol or other disinfection liquids are required. Hydrogen concentrations below 150 vol.-ppm in breathing gas have to be detected. Since this concentration range is far away from explosive concentrations, the longer response time could be acceptable. The most promising and innovative application field for POS and particular for the MEMS hydrogen sensor is the injection of regeneratively produced hydrogen into the natural gas system, as it was demonstrated, that the

sensors have no cross sensitivity to methane and MEMS sensors can be produced in a low cost mass production by silicon technology.

Keywords: Palladium optical hydrogen sensor, MEMS hydrogen sensor, detection limits, response time, cross sensitivity

ⁱ Astrid Pundt, *Nanoskalige Metall-Wasserstoff-Systeme*. Universitätsverlag Göttingen; 2005.

ⁱⁱ F.D. Manchester, A.San-Martin, and J.M. Pitre, *The H-Pd (Hydrogen-Palladium) System*, *Journal of Phase Equilibria* 15, 62–83 (1994).

ⁱⁱⁱ J.-S. Noh, J. M. Lee, W. Lee, *Low-dimensional palladium nanostructures for fast and reliable hydrogen gas detection*, *Sensors (Basel, Switzerland)* 11, 825–851

Development and characterization of a miniaturized hydrogen gas sensor system for safety monitoring

P. Sood^{1,2}, J. Zosel², M. Mertig^{1,2}, O. Herrmann³, M. Woratz³

¹ Kurt-Schwabe-Institut für Mess- und Sensortechnik Meinsberg e.V., Kurt-Schwabe-Straße 4, 04736 Waldheim, Germany

² Technische Universität Dresden, Professur für Physikalische Chemie, Mess- und Sensortechnik, 01062 Dresden, Germany

³ ACI Analytical Control Instruments GmbH, 12489 Berlin, Germany

Summary:

This work reports on recent advances in the development and characterization of a miniaturized hydrogen sensor system based on the combination of an yttria-stabilized zirconia (YSZ) solid electrolyte coulometric (SEC) detector and a gas chromatographic (GC) separation process. A commercial oxygen-pumping cell was characterized for its sensitivity, long-term stability and accuracy under different operational conditions. The resulting insights were used to define appropriate boundary conditions and construction guidelines for miniaturizing different components such as the sample injection system, the GC column heating/cooling module and the SEC detector.

Keywords: Yttria-stabilized zirconia (YSZ), coulometry, gas chromatography, trace gas analysis

Background, Motivation and Objective

Scientific studies indicate that the ever-increasing energy demand and concern over greenhouse gas emissions has to be resolved using an environment friendly mixed energy infrastructure [1]. For hydrogen (H₂) to be widely accepted as a potential alternative energy carrier in the diverse and distributed energy infrastructure of the future, more sensitive, selective, long-term stable and standalone H₂ sensors are needed covering the whole supply chain. The ability to reliably detect trace concentrations < 10 Vol.-ppm in oxygen containing gaseous mixtures is essential in safety monitoring and quality management [2].

In the presented work, a Pt/YSZ/Pt-based SEC gas sensor is used as a GC detector. The system enables selective and calibration-free detection of oxidizable (H₂, CH₄) and/or reducible gas components in the vol.-ppb range [3]. This contribution is directed towards the miniaturization of such a sensor system and its characterization under varying GC and detector parameters, and thus, enabling a systematic and insight-driven miniaturization process.

Description of the New Method or System

For the characterization of sensor properties, a commercial oxygen-pumping cell was coupled with a table top GC [3]. The results were used to optimize operational parameters for reaching both the required lower limit of detection (LLOD) with minimum error and widest possible concentration measurement range. Fig 1 shows the some of the measured H₂ –peaks.

Miniaturization was carried out for the three main components of the sensor system, i.e. the sample injection unit, the GC column oven and the SEC detector. A miniaturized sample injection unit was realized using miniaturized solenoid valves mounted upon a hydraulic manifold. In comparison to the currently used 10-port rotational valve, it offers an increased control autonomy for establishing tailored injection procedures, higher long-term stability and a compact, rugged design without redundant tubing. The manifold was first constructed using stainless steel 3D printing, and further, was optimized using precision drilling of a stainless steel block. The new design exhibits reduced inter-canal leakage, no need of post processing for gas tightness, and minimized dead volumes [4]. In [4], also the basic concept for a miniaturized GC column oven was introduced using resistive heating of a cylindrical aluminum fixture. An optimized construction consists of packed GC columns coiled over a 3D-printed aluminum structure with embedded cooling fins as shown in Fig. 2A. In comparison to the conventional air bath oven, the miniaturized element enables rapid heating/cooling rates with reduced power consumption and increased compactness. Fig. 3 shows the optimized laboratory prototype of a miniaturized SEC detector using an YSZ (3 mol-% Y₂O₃ stabilized ZrO₂) tube with sintered Pt electrodes on the outer and inner side, and mantled in a heated quartz glass tube. The new detector has a reduced size and a working electrode, which is sintered on the outer side of the YSZ tube, thus increasing the total surface

area of the available triple phase boundary (TPB) sites. This enhances the intensity of electrochemical titration of incoming hydrogen in the sample, further decreasing LLOD.

Results

The analysis of hydrogen peaks in Fig. 1 showed that reducing the column length by half, resulted in hydrogen peak areas according with the amount calculated by Faraday's law with an error < 5 %, down to the trace concentration range (~0.2 vol.-ppm) at 600 °C.

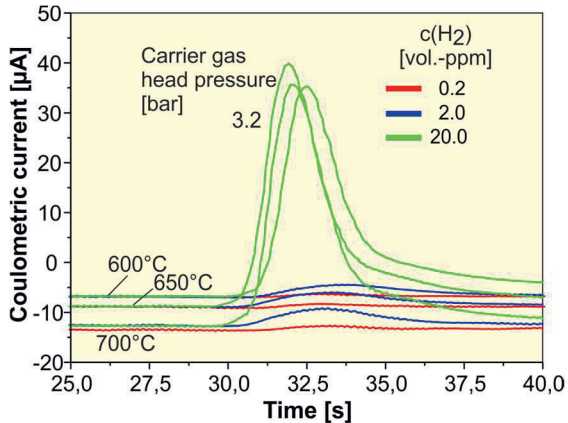


Fig. 1 H₂-Peaks for 1 m mol. sieve 13X + 1 m silica gel-Gel packed GC columns, carrier gas flowrate: 31,5 mL/min, detector temperature: 600-700 °C, injected H₂ concentration: 0.2-20 vol.-ppm.

The first prototype of the miniaturized column oven already meets the required heating (10 K/min) and cooling (30 K/min) rates but with an undesired large power consumption > 100 W [4]. Fig. 2B shows that the improved prototype offers clear advantages in terms of decreased heating power consumption (< 80 W), much faster heating rates (~ 15 K/min) due to the reduced thermal mass and rapid cooling rates (~80 K/min) due to the efficient heat dissipation from the rough surface of the 3D-printed structure. More linear temperature ramps and higher end- point temperatures were observed for stepwise increase in heating power (~ 5 W/min) in comparison to constant heating. The miniaturized SEC detector is being tested for gas tightness and initial potentiometric characterization in laboratory.

References

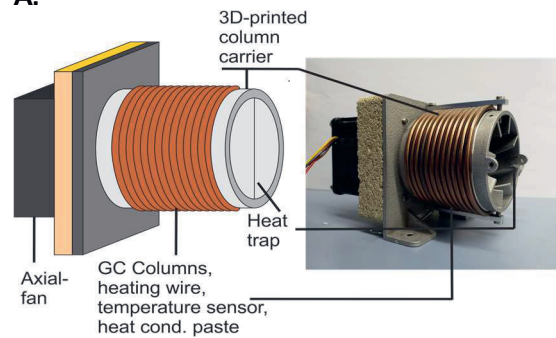
- [1] P.P Edwards, V.L Kuznetsov, W.I.F David, Hydrogen Energy, *Phil. Trans. R. Soc. A* 365, 1043–1056 (2007); doi: 10.1098/rsta.2006.1965.
- [2] T. Hübert, L. Boon-Brett, V. Palmisano, M.A. Bader, Developments in gas sensor technology for hydrogen safety, *International Journal of Hydrogen Energy* 39 (35), 20474-20483 (2014); doi: 10.1016/j.ijhydene.2014.05.042.

[3] M. Schelter, J. Zosel, W. Oelssner, U. Guth, M. Mertig, A solid electrolyte sensor for trace gas analysis, *Sensors and Actuators B: Chemical* 187, 209-214(2013); doi: 10.1016/j.snb.2012.10.111.

[4] P. Sood, J. Zosel, M. Mertig, W. Oelßner, Entwicklung und Erprobung eines hochsensitiven und miniaturisierten Wasserstoffmesssystems, 14. *Dresdner Sensor Symposium*, 23 - 29 (2019); doi: 10.5162/14dss2019/2.1.

Illustrations, Graphs, and Photographs

A.



B.

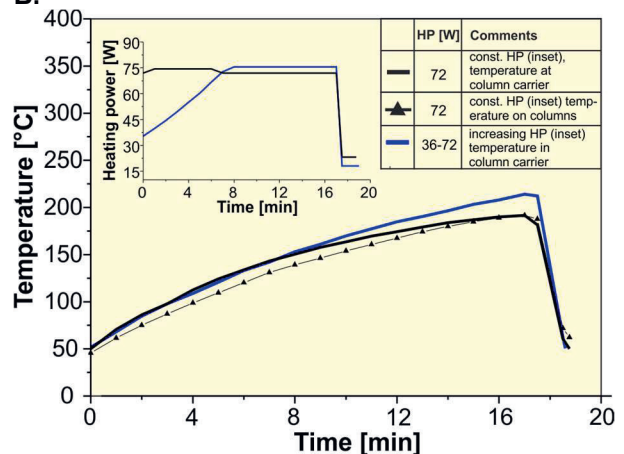


Fig. 2. **A.** Improved prototype of a miniaturized GC column oven. **B.** Heating/cooling ramps for the improved prototype. Heating power (HP) and resp. experimental conditions are listed in the inset table.

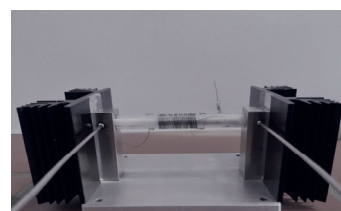
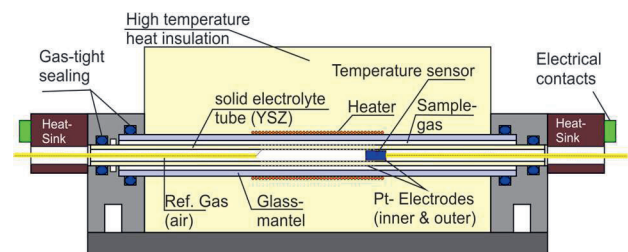


Fig. 3.

Schematic (above) and picture (below) of miniaturized SEC detector laboratory prototype

Microstructural investigations of blackening in YSZ sensors for hydrogen coulometry

*Andreas Graff*¹, *Wolfram Münchgesang*^{1,2}, *Frank Altmann*¹, *Cameliu Himcinschi*², *Thomas Köhler*², *Pramit Sood*³, *Jens Zosel*³ and *Michael Mertig*³

¹*Fraunhofer Institute for Microstructure of Materials and Systems (IMWS), 06120 Halle, Germany*

²*Technische Universität Bergakademie Freiberg, 09599 Freiberg, Germany*

³*Kurt-Schwabe-Institut für Mess- und Sensortechnik Meinsberg e.V., Kurt-Schwabe-Straße 4, 04736 Waldheim, Germany*

Summary:

A detailed microstructural analysis of a coulometric hydrogen sensor after operation at high electrical load is presented. The sensor is based on YSZ ceramic tube with outer and inner electrodes. Oxygen diffusion at grain boundaries under chemical and electrical potential leads to color changes (blackening), crack formation at the grain boundaries and phase transitions in the YSZ ceramic from cubic to monocline. These findings can explain an irreversible degradation mechanism of the solid electrolyte sensor.

Keywords: hydrogen sensor; Ytria-stabilized zirconia (YSZ), coulometry, gas chromatography, trace gas analysis

Background, Motivation and Objective

Using hydrogen produced by green electricity helps to satisfy the demand for fuel without using non-renewable fossil sources. The key component for producing hydrogen by electricity is the electrolyzer splitting water into hydrogen and oxygen. To ensure the safety during the production and storage of hydrogen gas sensors are mandatory. For the electrolyzer, hydrogen sensors must have a sensitivity of 100 Vol.-ppm up to a concentration of 4 Vol.-% hydrogen at pressures up to 30 bar and temperatures up to 90 °C. Coulometric solid electrolyte sensors for hydrogen are sufficient for these operation conditions and provide the required sensitivity. To suppress the cross sensitivity against other gases the substances can be separated in advance by gas chromatography. Such sensors have to sustain under harsh environment and high electrical fields causing degradation of the sensor materials and limiting the life time. This study focusses on the solid electrolyte YSZ in the coulometric measurement cell and its structural changes during extreme load conditions.

Description of the Methods

For the experiments a coulometric sensor was used based on a commercial sensor set up (Zirox GmbH). The main component is a YSZ ceramic gas-tight tube (Friatec, 8 mol% Y) inside a furnace with two pairs of Pt (99,99% pure) electrodes. One pair is used for the measurement and the other one as a reference. The YSZ tube is used to transport oxygen and to measure the difference of the chemical potential

between inside and outside the tube. The microstructure of the ceramic was determined by electron microscopy (SEM Zeiss Supra, TEM FEI Titan) combined with diffraction and analytical methods (Trident EBSD-EDX, EDAX). Additional structural information was obtained by Raman spectroscopy.

Results

The electrical load experiments started with oxygen transport from outside air to a reforming gas (50 Vol.-ppm H₂ in N₂) inside the tube for 60 s at 750 °C. The transport was forced by a voltage of 11 V and the current was limited to 0.6 A. During the conditioning the tube was damaged by elevated local current densities and developed several micro cracks which enable remarkable oxygen gas diffusion through the tube wall. After conditioning the voltage at the electrodes was reversed automatically to establish a low oxygen partial pressure inside the tube. Due to the unnoticed gas leakage, a high pumping current was established for more than 60 min. The structural changes caused by this experiment were investigated in detail.

3.1. Blackening

In reduction atmosphere the color of the YSZ changes from opaque to black known as blackening-effect [1]. The blackening is a local phenomenon and could indicate the sites of the morphological and electrical failure of the sensor. Microstructural investigations were performed at sites of visible blackening (Fig.3). The localized areas were separated by sawing to get cross sections of the YSZ tube. Blackening

Monitoring of Pumps and Valves in Fluidic Systems with Electro-Magnetic Flowmeters

Jan Förster¹, Thomas Fritsch¹, Jochen Friderich¹, Roland Gentemann², Roland Vonnahme²

¹ KROHNE Innovation GmbH, Ludwig-Krohne-Str.5, 47058 Duisburg, Germany,

² WILO SE, Nortkirchenstr. 100, 44263 Dortmund, Germany

j.foerster@krohne.com

Summary:

A standard electro-magnetic flowmeter has been enhanced by dedicated electronics to allow access to the measured raw data. These unfiltered raw data contain further information on the fluidic system in addition to the volume flow. Analysis of these raw data reveals that important information such as pump rotation speeds or disadvantageous valve settings are clearly visible. Thus, this study enables future work to improve the control of fluidic systems by electro-magnetic flowmeters.

Keywords: Electro-Magnetic Flowmeter, Predictive Maintenance, Condition Monitoring

Introduction

Several devices to measure the volume flow of liquids are available. Due to its reasonable price, good accuracy, and sustainability the electro-magnetic flowmeter (EMF) is a very popular type of these measurement devices [1]. Basically, charge carriers of the liquid flowing through the EMF are redirected by a magnetic field perpendicular to the flow direction. These redirected charge carriers result in an electric voltage between two electrodes perpendicular to the magnetic field. By measuring this voltage, the volume flow can be derived eventually. Although several disturbing electro-chemical potentials superpose this voltage, it is possible to obtain precise volume flow information by filtering the raw measurement data. A common practice is to derive the mean value over a constant period [2].

However, the eliminated electro-chemical potentials origin in changes of the temperature and pressure of the liquid, as well as of its conductivity. These eliminated information on the aforementioned parameters are of interest for the user and might prove to be valuable for many applications. Therefore, this work aims on enabling EMFs to not only provide the accurate value of the volume flow but to allow parallel access to the information hidden in the electro-chemical potentials.

Technical Solution

In this work a standard EMF of type OPTIFLUX 3300C from KROHNE was used. As in all common EMFs this device samples and digitizes the voltage between the two electrodes with

an analog-to-digital converter (ADC). The raw data values of the ADC are then processed by a microcontroller (μC) to obtain the precise volume flow. As the electronics of this device are optimized for this procedure, they do not offer the possibility to access raw data values directly for additional processing. Therefore, additional electronics have been implemented which allow direct access to the raw data of the ADC. Thus, the unfiltered raw data can be processed externally.

The additional electronics mainly consists of three components: a small single-board computer, a microcontroller, and the necessary power-supply. As single-board computer a Raspberry Pi 3B+ was chosen because it comes with a multi-core processor and enough computing power to allow for most experimental online data processing methods. Furthermore, lots of software is readily available for this component which significantly shortens development time. However, in the context of this work dedicated software had to be developed which accesses the raw data, prepares it for further analysis, and provides the data via a TCP/IP interface to the out-side world. Unfortunately, the Raspberry Pi as well as all other available small single-board computers do not come with the necessary hardware interface to directly access the raw data of the ADC. Therefore, a common ARM-core based μC was introduced between the ADC and the Raspberry Pi to perform fast recording of the ADC data and to provide these data to the Raspberry as a serial data stream.

Experimental Setup

The standard EMF with the additional electronics was integrated in an experimental setup to allow for recording of the raw data in a controlled environment. As experimental setup a basic pump circuit consisting of an impeller pump of type Stratos Giga 50/1-14 from WILO, a valve and the EMF was chosen. A schematic drawing of this setup is given in Fig. 1. The pump can be set to any rotational speed between 500 rpm and 3300 rpm. With the given pipe diameter of 100 mm this maximum rotational speed correlates to a maximum volume flow of approximately $30 \text{ m}^3\text{h}^{-1}$. The valve can be set to any value between fully opened and fully closed. For this experimental setup tap water was used as liquid. In addition, the static pressure of the liquid can be changed by adding water to or releasing water from the pipe system. With this setup various experiments with varying pump rotational speeds, varying valve settings, and different static pressures have been performed. The raw data were recorded using the attached computer. Afterwards, the raw data was analyzed what information on the fluidic system can be extracted from the raw data.

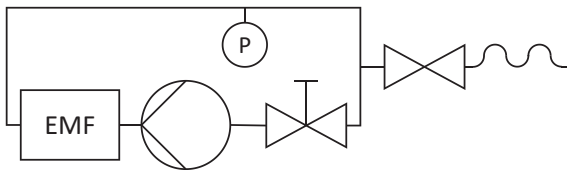


Fig. 1. Schematic drawing of the experimental setup

Results

The first analysis of the recorded data revealed that it contains a lot of noise as expected. However, in earlier work it was shown that some of this noise originates from periodic sources such as the impeller rotation of the pump [3]. Thus, analysis of the raw data was mainly performed in the frequency domain using a Fast Fourier Transformation (FFT).

In the spectral representation of the measured raw data the expected periodic signals are clearly visible. Fig. 2 shows the spectral results of measurements for pump rotational speeds of 3000 rpm and 3100 rpm at a constant static pressure of 2.4 bar and a constant volume flow of $5 \text{ m}^3\text{h}^{-1}$. Both curves show a clear peak at the frequency which correlates to the blade passing frequency at the pump outlet. As the pump has six impeller blades the frequency of 300 Hz correlates to the rotation speed of 3000 rpm and the frequency of 310 Hz correlates to the rotation speed of 3100 rpm. Furthermore, there are also peaks present at multiples of these

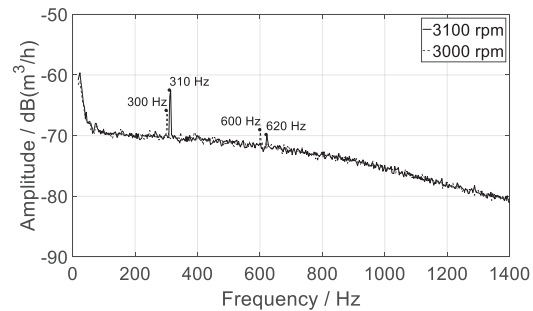


Fig. 2. FFT results derived from raw data of measurements with different pump rotation speeds

frequencies, because the impeller blades do not produce a pure sinusoidal flow fluctuation.

Repetitions of these experiments at different static pressures did not reveal any noticeable changes in the results. Thus, the static pressure can be neglected for future experiments.

However, valve settings at low static pressure causing cavitation are also clearly visible in the spectral representation of the raw data. They cause a drastic increase of the curve for lower frequencies. Therefore, disadvantageous valve settings can be detected by monitoring the raw data.

Conclusion and Outlook

The enhancement of an EMF by additional functionality to access the raw data has successfully been demonstrated. The first results prove, that impeller pumps and valve settings can be monitored by analysis of the raw data. Future work will deal with damaged pumps and valves to evaluate the use of such an EMF for predictive maintenance of fluidic systems.

Acknowledgment

Part of this work has been supported by the federal state of North Rhine-Westphalia and the European Regional Development Fund (EFRE) 2014-2020 in the course of the IKT.NRW project under grant number EFRE-0800890

References

- [1] F. Hofmann, Fundamental principles of Electromagnetic Flow Measurement, KROHNE Messtechnik GmbH, 2003, 7.02338.22.00
- [2] F Hofmann, Principles of Electromagnetic Flow Measurement, KROHNE Messtechnik GmbH, 2011, http://instrumentationandcontrol.net/wp-content/uploads/2016/04/KROHNE-2011-Principles-of-Electromagnetic-Flow-Measurement_.pdf
- [3] S. Melzer, P. Munsch, J. Förster, J. Friderich, R. Skoda, A system for time-fluctuating flow rate measurements in a single-blade pump circuit, Journal of Flow Measurement and Instrumentation 71, 2019, 101675

A hermetic sensor concept for measuring fluid flows

Philipp Radler^{1,2}, Jan Ringkamp^{1,2}, Dr. Philipp Lehardt¹, Dr. Jens Langejürgen¹

¹ Fraunhofer IPA, Project Group for Automation in Medicine and Biotechnology, Group for Biomedical Sensors and Microsystems, Theodor-Kutzer-Ufer 1-3 (Cubex41), 68167 Mannheim, Germany

² Medical Faculty Mannheim, Heidelberg University, Theodor-Kutzer-Ufer 1-3, 68167 Mannheim, Germany

Summary:

We present a novel, fully encapsulated sensor concept, which is especially suitable for the measurement of condensing gas flows. The sensor concept is based on the Magnus forces working on a magnetically levitated and rotated cylinder at high speeds. Our first experimental results have successfully shown the feasibility of this sensor concept.

Keywords: Magnus effect, flow sensor, condensing gas flow, high humidity, hermetic sensor

Introduction

Robust gas and liquid flow measurement is a crucial requirement for the production-related industries as well as in medical applications. Despite the wide range of available sensors, in applications where condensing or corrosive gas flows are to be measured, the range of available sensors narrows down significantly. Water droplets that accumulate on a sensor element i.e. of MEMS or dP-Sensors often negatively affect accuracy or lead to complete malfunction of the sensor. In this paper, we present a novel flow sensor concept based on the Magnus effect. A major advantage of this approach is that the sensor element is in constant rotation and thus robust against influences of a condensation on the sensor surface. In addition, it allows a fully encapsulate construction of the sensor with a single-use sensor element with magnetically coupled driver and read-out. With this features, the sensor concept is suitable for medical applications and for the use in corrosive media.

Materials and Methods

Measurement principle:

Figure 1 illustrates a gas flow from bottom to top through a tube and around a cylinder, which is rotating at an angular velocity ω . This results in the two forces F_D and F_M that work on the cylinder. The first is in the direction of the flow caused by drag. The second is due to the Magnus effect that acts orthogonally to the flow velocity vector and can be described as:

$$F_M = S(\omega \times v)$$

S is the air resistance coefficient across the surface of the cylinder. Both forces would lead to a displacement of the cylinder off its rotating axis. The aim is to drive the cylinder and measure these forces with our proposed sensor concept.

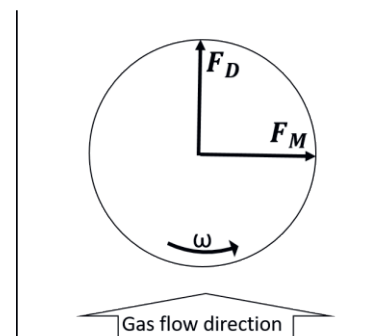


Fig. 1. Magnus (F_M) and drag (F_D) forces on a rotating cylinder with angular velocity ω

Sensor concept:

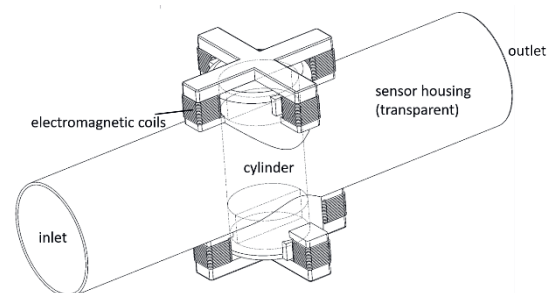


Fig. 2. Magnus sensor concept (overview)

Figure 2 and 3 illustrate the sensor concept. The sensor element consists of a cylinder that has

two magnets integrated on either ends. This cylinder is fully encapsulated by a sensor housing, which guides the gas flow from the inlet around the cylinder to the outlet. The cylinder is being levitated and rotated by multiple electromagnetic coils that are placed around the poles of the cylinders permanent magnets. Additional sensors measure the current angle and displacement of the cylinder. The individual coil currents are controlled such that the cylinder is levitated in the center and driven at a variable angular velocity.

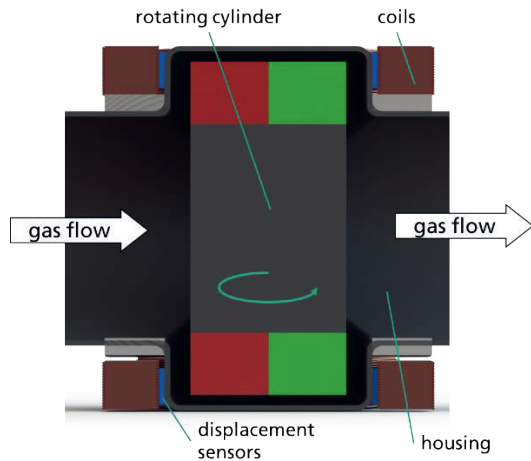


Fig. 3. Magnus sensor concept (cross-section)

Experimental Setup:

We used an existing medical rotary pump with displacement sensors and electromagnetic coils. We replaced the pump impeller by a 3D-printed cylinder and pump housing accordingly. We built a custom electromagnetic driver and implemented a custom PID-controller on an embedded microcontroller (TI, TMS320F28379D). This system controls the levitation and rotation of the cylinder. The inlet of the Magnus sensor was connected through a reference flow meter (Sensirion, SFM3000) to a gas source (pressurized air). The sensor signal is derived from the force that is necessary to counteract the respective Magnus and drag forces.

Results

First results in Figure 4 show the forces at two rotational speeds of the cylinder at 2500RPM

and 5000RPM for varying volume flows. As expected, due to the Magnus effect, there is a clear dependency on rotational speed for the measured forces.

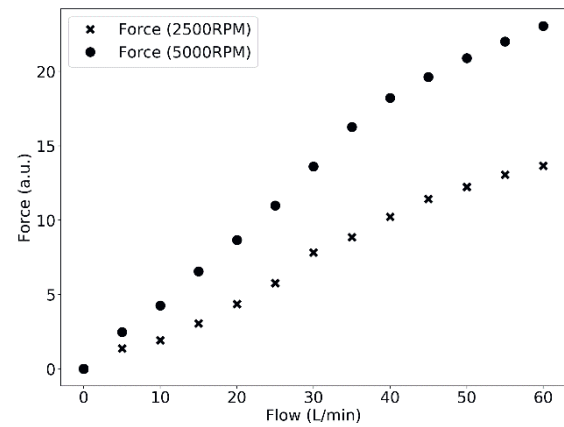


Fig. 4. Force signal for varying volume flows of 0-60 L/min

Discussion

Our first experiments have successfully shown that it is possible to measure the forces imposed on a cylinder by a gas flow with the proposed setup. The achievable sensitivity and resolution of the sensor is currently limited because of the relatively large dimensions of the setup. A dedicated coil geometry is expected to increase resolution and linearity significantly.

The presented sensor can be constructed as two separate parts. The more expensive driver electronics can be reused and have no parts prone to failure because none of them are mechanically moving or in contact with the fluid. The second unit is a low cost, fully encapsulated, single-use unit consisting of the rotating cylinder and housing. This enables the elimination of any possible cross contamination and maximizes sterility. Many applications like biological and chemical processes as well as the measurement of respiration gases of ventilated patients would benefit from such a sensor.

Development of a capacitive sensor system for gas-liquid flow monitoring and application in hazardous areas

Eduardo Nunes dos Santos¹, Dalton Bertoldi¹, Aluísio do Nascimento Wrasse¹,
 Diogo C. dos Reis², Roberto da Fonseca Jr.², Rigoberto E. M. Morales¹, Marco J. da Silva¹
¹ Multiphase Flow Research Center (NUEM), Federal University of Technology – Paraná (UTFPR),
 Curitiba, Brazil,
² Petrobras Research and Development Center (CENPES), Rio de Janeiro, Brazil
 mdasilva@utfpr.edu.br

Summary:

Sensors for the measurement of advanced two-phase flow parameters (besides temperature and/or pressure) in production and transportation of oil and gas are required for monitoring and control purposes of plant and equipment. This requirement is also pushed by the current digitalization trend in industry, where sensors play a pivotal role as reliable source of data. This work presents a capacitive sensor system which can be applied in industrial environment at hazardous areas. The sensor was designed to comply with explosion safety standards whilst its electronics was developed in order to support network connections. Three pair of sensors were successfully installed in different positions of a 6-inch test facility of an oil company to monitor crude oil and natural gas two-phase flow evolution along the pipe.

Keywords: Oil and Gas, Two-phase flow, Resonant Frequency, Capacitive Sensor, Explosion safety

Introduction

The simultaneous flow of oil and gas in pipelines is a common occurrence in the petroleum industry [1, 2]. Due the recent increase of oil offshore exploration and production, sensing technologies have been widely developed in order to monitor various processes in petroleum production, such as phase fractions and phase velocities for the effective operation of its equipment and pipelines [2, 3]. Several measuring techniques to investigate two-phase flows have been proposed and tested in the past [4, 5]. However, most of them have been only applied to laboratory test conditions using model fluids. The use of real fluids in industrial environment requires that the sensing solutions are able to safely operate in potential explosive atmosphere. In this paper, we introduce a capacitive sensor which was deployed and tested in an industrial test facility running real fluids, i.e. natural gas and crude oil.

Sensor

In this work, the sensing principle is based on the interaction of the flowing media and the electric field between the sensing rod and the grounded metallic sensor body (Fig. 1) which changes the measured electrical capacitance of the equivalent circuit. Once both gas and liquid are non-conducting materials, the equivalent circuit of flowing media can be represented as a capacitor

from the sensing rod to the grounded pipe wall. The resonant effect of LC circuits is used to determine the unknown capacitance given by

$$f_{\text{sensor}} = \frac{1}{2\pi\sqrt{L \cdot (C + C_{\text{sensor}})}} \quad (1)$$

The circuitry is based on FDC2214 (capacitive sensing IC) and MCP430 (microcontroller). The electronics is mounted inside an explosion-protected enclosure (Fig. 1), providing reliable protection for flammable environment. Furthermore, typical Zener barrier is deployed for feeding the excitation electrode (metallic rod) in order to comply with intrinsic safety of electrical installations (Fig. 2).

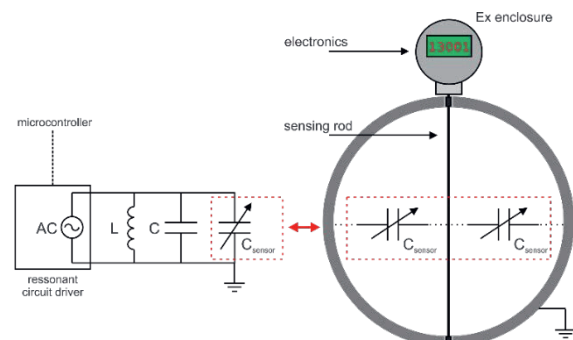


Fig. 1. Measurement schema for LC resonant circuit driver.

System Evaluation

The system was deployed at the Núcleo Experimental de Atalaia (NEAT), located in Aracaju, Sergipe, Brazil, which is an experimental test center and part of Petrobras Research and Development Center (CENPES). NEAT employs crude oil (156 cP at 40°C) and natural gas as working fluids. A simplified diagram of the test site is shown in Fig. 2. The gas line is supplied from a compression unit and the oil from tanks. The multiphase test flow loop consists of approximately 200 meters (in form of a “U” with 100 m in which segment) and six sensor nodes are disposed in pairs in order to further extraction of parameters such as bubbles translational velocity. Fig. 3 depicts a picture of the installed twin sensor with a pressure/temperature meter. Three different locations were chosen to monitor the flow evolution along the pipe.

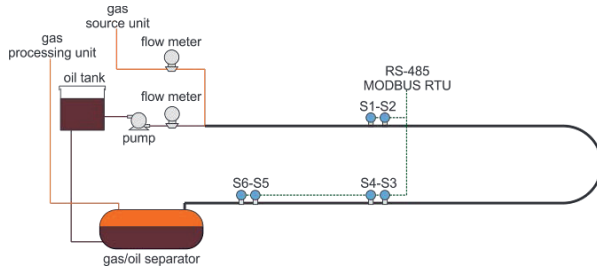


Fig. 2. Simplified overview of NEAT-Petrobras experimental facility and main components.



Fig. 3. Pair of sensors installed at 6" pipe flanges (ANSI B16.5 Class 300#) at NEAT-Petrobras.

Results and Discussion

Several experimental conditions were investigated. Here we report only one experiment with superficial velocities of 0.5 m/s for both gas and liquid phases. The superficial gas velocity was corrected by the pressure difference between reference measurement (at Coriolis) and the experimental point. In Fig. 4 one can observe the typical unit cell structures on the signal (liquid slugs and elongated gas bubbles) of the so-called slug flow. The study of unit cell parameters is directly related with the development of low-order models, which in turn are applied by engineers for design and during operation of flow lines. Hence, detailed analysis of flow behavior

is pivotal to better description of flow which in turn will be applied in better flow models and predictions.

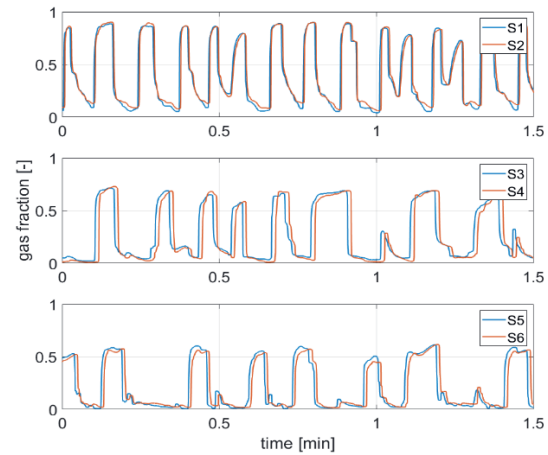


Fig. 4. Evolution of time series for an experimental gas and liquid superficial velocities of 0.5 m/s and 0.5 m/s respectively.

Conclusion

A capacitive sensor was developed and applied for two-phase flow investigation in industrial experimental facility with hazardous areas. Preliminary results have shown the capability of the sensor to investigate two-phase flow at high temporal resolution with minimum intrusiveness in an industrial environment running with real fluids (crude oil and natural gas). The development of sensor design to comply with a potentially explosive atmosphere was successfully tested. Hence, the developed measuring system may be applied to systematic flow studies at experimental conditions similar to real applications.

References

- [1] R.V.A. Oliemans and B.F.M. Pots, "Gas-Liquid Transport in Ducts" in *Multiphase flow handbook*, 1st ed., vol. 1, Boca Raton, FL, USA: CRC/Taylor & Francis, 2006, chapter 2, pp. 1–40.
- [2] G. Falcone, "Heavy Oil Metering Applications" in *Multiphase Flow Metering: Principles and Applications*, 1st ed., vol. 54, Elsevier Science, 2009, pp. 251–266.
- [3] V. Bertola, "Two-phase flow measurement techniques," in *Modelling and Experimentation in Two-Phase Flow*. New York, NY, USA: Springer-Verlag, 2003, pp. 281–323.
- [4] E.A. Hammer, T. Dyakowski, G.A. Johansen, "Advanced Experimental Techniques" in *Multiphase flow handbook*, 1st ed., vol. 1, Boca Raton, FL, USA: CRC/Taylor & Francis, 2006, chapter 14, pp. 1–125.
- [5] E. N. Dos Santos et al., "Sensing Platform for Two-Phase Flow Studies," in *IEEE Access*, vol. 7, pp. 5374–5382, 2019. doi: 10.1109/ACCESS.2018.2887309

Microwave Mass Flow Sensor for Online Measurements of Pure Liquids and Mixtures

Maria Elena Euken¹, Andreas Penirschke¹

¹Technische Hochschule Mittelhessen, Wilhelm-Leuschner-Straße 13, 61169 Friedberg, Germany
Email: maria.elena.euken@iem.thm.de

Summary:

This work reports on the design and measurement results of a circular waveguide sensor filled with dielectrics tuned at 5.6 GHz for online process monitoring applications of low loss liquids and mixtures of liquids with liquids or air. Connecting the sensor to a Universal Software Radio Peripheral (USRP), an online mass flow meter is realized, that can simultaneously detects the concentration and velocity for liquid/air mixtures.

Keywords: circular waveguide sensor, cavity perturbation technique, low dielectric materials, concentration measurements, velocity measurements, online measurement

Introduction

Real-Time Monitoring of liquids using microwave signals became a growing interest recently. Applications can be found in food, oil and pharmaceutical industries, especially when a non-invasive technology is mandatory [1]. For permittivity extraction, the cavity perturbation method was applied [2]. Changing the material inside the sensor causes a shift in the resonant frequency that is directly related to the dielectric constant of the liquid or liquid/air concentration. Additionally, the velocity of the liquid can be detected by applying the spatial microwave velocimetry [3]. The sensor is attached to a Universal Software Radio Peripheral Ettus B210 [4] to enable online measurements at microwave frequencies.

Sensor Design

The microwave sensor, shown in Fig. 1, consists of a resonant configuration of two cavities made of Rogers RT/duroid 5880 substrates and a PTFE pipeline.

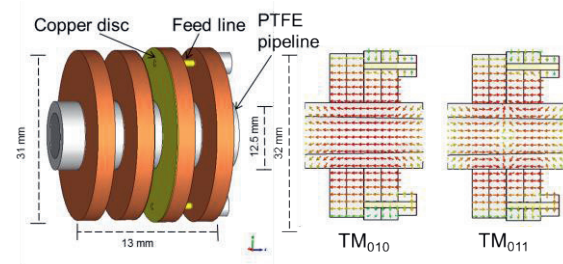


Fig.1. Microwave sensor exploded drawing and Transversal Magnetic (TM) modes

The coupling of the microwave sensor to an external circuitry is applied using two H-field

probes that are located parallel to the material flow. Transversal Magnetic (TM) modes are excited in the flow direction in the measure section. To obtain two symmetrical transmission maxima inside the pipeline only one fully copper disc is used in the middle of the sensor.

Concentration measurement

A change in the permittivity or the concentration of liquids or liquid/air mixtures in the measurement section causes a change in the resonant frequency. Due to the fact that liquid/air mixtures absorb energy from the sensor, attenuation of the transmitted signal occurs. This effect can be measured by the complex transmission type S-parameter S_{21} .

In order to extract the value of the dielectric constant, a sensor prototype was operated by the two-port vector network analyser HP 8722.

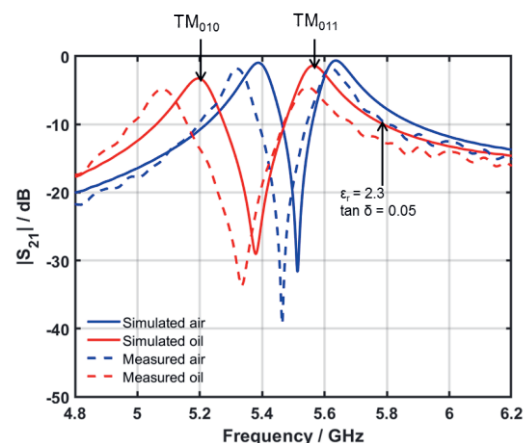


Fig.2. Simulated and measured results of the transmission $|S_{21}|$ with air/sunflower oil dielectric (preliminary results)

RF-simulations using CST Microwave were conducted using sunflower oil with a permittivity of 2.3 and low losses at 5.6 GHz.

Two transmission maxima (TM_{010} and TM_{011}) were measured with this sensor configuration as shown in Fig. 1 and Fig. 2. The comparison of the empty sensor and the oil-filled sensor at the fundamental TM_{011} mode shows a frequency shift of nearly 73 MHz for measurement and simulation. The observed frequency deviation between simulation and measurement for the TM_{010} mode is related to the assembly of the sensor and tolerance of the parts. Additionally, the oil measurement shows a higher attenuation, compared to the simulated results. The results of frequency shift air/oil are summarized in Tab.1.

Tab. 1. Frequency shift air/oil

	TM_{010}	TM_{011}
	Δf / MHz	Δf / MHz
Sim.	192	73
Meas.	290	76

Velocity measurement

In order to extract the velocity of liquids or liquid/air mixtures particles with the microwave sensor, measurement results versus time are analysed [3]. If a dielectric droplet enters in the measurement section the phase of the transmitted RF signal S_{21} describes a squared sinusoidal signal.

Fig. 3 shows the time depending amplitude and phase when a water droplet travels through the sensor. There are two sinusoidal half-waves. The amplitude of the half-waves depends on the position of the droplet inside the sensor measured section.

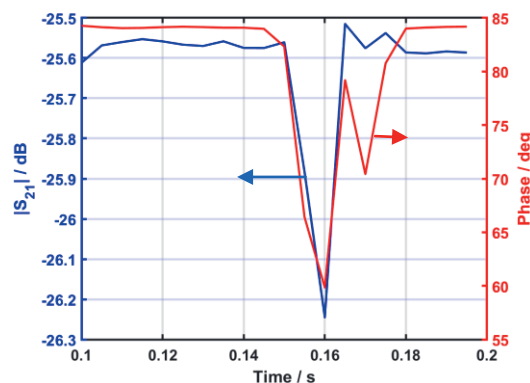


Fig. 3. Influence of a water droplet to the phase and magnitude of $S_{21}(t)$ for CW measurements at the sensors resonance frequency for the TM_{011} mode

Online Measurements

Fig. 4 depicts the fabricated microwave sensor and a block diagram of the USRP Module.

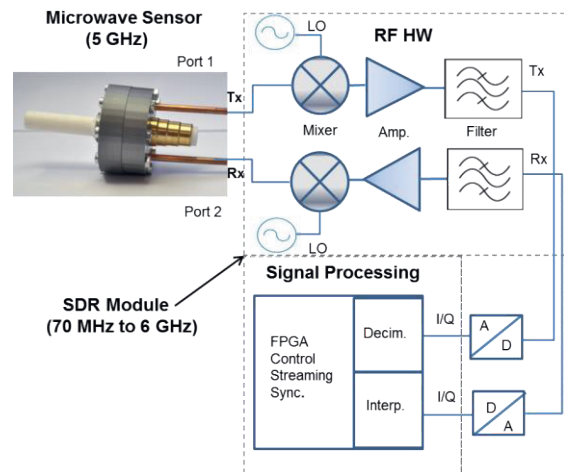


Fig. 4. Fabricated microwave sensor and USRP

A USRP transceiver B210 [4] is a software defined radio module that consists of a flexible RF hardware and a baseband platform for signal processing applications. In the USRP device, some of the key hardware functions can be implemented with MATLAB. Applying the Graphical User Interface, Real-Time Monitoring of the microwave sensor signals and extracting the concentration and velocity of liquid particles are possible.

Conclusion

The implementation of a microwave dielectric mass flow sensor for online monitoring without disturbance of the flow distribution was shown. The first prototype exhibits promising results for precise simultaneous concentration and velocity detection of low dielectric liquids and liquid/air mixtures.

References

- [1] G. Gennarelli, S. Romeo, M. R. Scarfi, and F. Soldovieri, "A Microwave Resonant Sensor for Concentration Measurements of Liquids Solutions", *IEEE Sensor Journal*, vol 13, 1857-1864 (2013); doi: 10.1109/JSEN.2013.2244035
- [2] A. Penirschke, S. Müller, P. Scheele, C. Weil, M. Wittek, C. Hock, and R. Jakoby, "Cavity perturbation method for characterization of liquid crystal up to 35 GHz", *IEEE, 34th European Conference*, (2004)
- [3] A. Penirschke and R. Jakoby, "Microwave Mass Flow Detector for Particulate Solids Based on Spatial Filtering Velocimetry", *IEEE Transactions on Microwave Theory and Techniques*, Vol 56, 3193-3199 (2008); doi: 10.1109/TMTT.2008.2007142
- [4] <https://www.ettus.com/all-products/ub210-kit/> (last visit 10.02.2020)

Modeling the fluid-structure interaction of non-conventional vibrational modes for MEMS fluid sensing

Daniel Platz¹, André Gesing¹ and Ulrich Schmid¹

*¹TU Wien, Institute of Sensor and Actuator Systems, Gußhausstraße 27-29, 1040 Vienna, Austria
daniel.platz@tuwien.ac.at*

Summary:

Understanding of the fluid-structure interaction between a mechanical resonator and a surrounding fluid is key for understanding and predicting the performance of MEMS fluid property sensors. Here, we present a novel method for modelling the fluid-structure interaction between a viscous fluid and vibrational eigenmodes of a plate-like MEMS resonator. The elastic dynamics of the MEMS resonator numerically determined by a finite element method while the fluid flow is obtained from a boundary integral formulation. With this method we compute the spectral response of MEMS plate resonators in fluids.

Keywords: fluid sensing, MEMS resonators, plates, fluid-structure interaction, simulation

Background, Motivation and Objective

The characterization of fluid properties like density or viscosity is a focal area in fluid sensing. Fluid sensors based on micromechanical systems (MEMS) have the potential for widespread use in various applications, like the monitoring of technical fluids like motor oil or medical diagnosis in lab-on-chip systems, due to their low-production cost and high integrability in complex sensor systems. In all applications, the measurement of fluid properties requires an interaction between the sensor and the fluid environment. Such an interaction is established by exciting a vibrational eigenmode of a MEMS resonator. Often, sensors have simple geometries like cantilever beam structures. Such resonators are relatively simple to fabricate and their vibrational eigenmodes are readily modeled with Euler Bernoulli beam theory. A typical vibrational eigenmode of a beam resonator is shown in figure 1a. However, the quality factor of beam-like MEMS resonators is usually very low in liquids which implies that reliable measurements of fluid properties is often difficult or even not feasible, especially in highly viscous fluids. A possible solution to this problem is the use of vibrational modes which have are commonly not considered for fluid sensing. An example of such a non-conventional mode is depicted in figure 1b. These non-conventional vibrational modes exhibit extraordinary high quality factors even in highly viscous fluids [1, 2] which allows for measurements in highly viscous fluids. However, the physical reason for the high quality factors of non-conventional modes in fluids remains elusive. Here, we introduce a novel method for

modelling the fluid-structure interaction between a fluid and plate-like MEMS resonators.

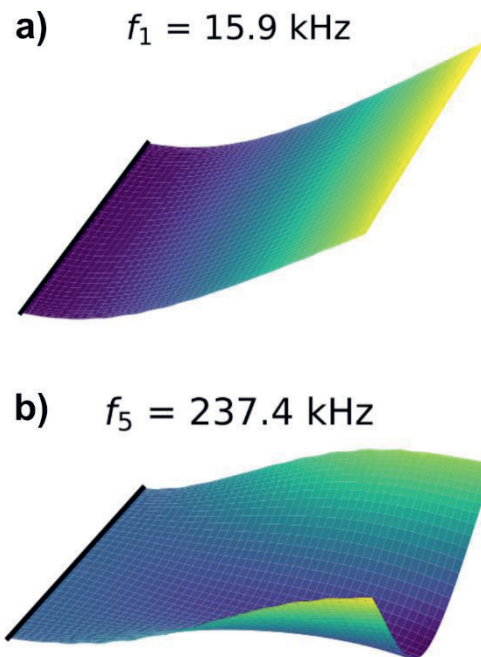


Fig. 1. Numerical simulation of vibrational eigenmodes of a cantilevered plate resonator clamped at the right edge (marked by thick black line). The mode in (a) is also observed in one-dimensional beam structures whereas the mode in (b) can only be found in two-dimensional plate structures.

Description of the Method

Two components are required for modelling the fluid-structure interaction between a fluid and plate resonator: the elastic dynamics of plate and the fluid flow. While beam resonators are readily

described by the Euler Bernoulli equation, modelling the dynamics of plate resonators is based on the Kirchhoff Love equation. In contrast to the Euler Bernoulli equation, analytic solutions for the Kirchhoff Love equation exist only for special cases. Therefore, we use a finite element method to obtain numerical solutions of the plate dynamics. The method weakly imposes the physical continuity requirements to the solution by introducing a penalty term which allows for the use of standard Lagrange-type elements.

We focus on MEMS resonators for which the characteristic length scale of the fluid flow is given by the width of the clamped side. This side has a typical width of 100 to 1000 μm . With this assumption the fluid flow can be modelled with the Stokes equation for an incompressible viscous fluid. We employ a stream function description of the flow and express the problem as a boundary integral equation which we solve numerically. From the resulting fluid flow as depicted in figure 2 we determine the hydrodynamic force on the plate resonator.

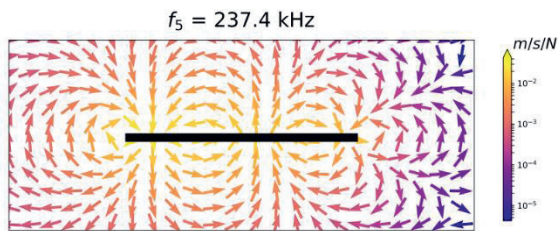


Fig. 2. Fluid flow around the cross section of the resonator for the mode shown in figure 1b. The flow velocity is normalized to the applied drive force.

Using this approach, we are able to determine for the first time the spectral response of two-dimensional MEMS resonators which has not been possible before with established theory for one-dimensional beam-like resonators [3].

Results

We apply the proposed method to a cantilevered plate resonator with a size of $300 \times 300 \times 5 \mu\text{m}^3$ immersed in water. The plate is excited at one of

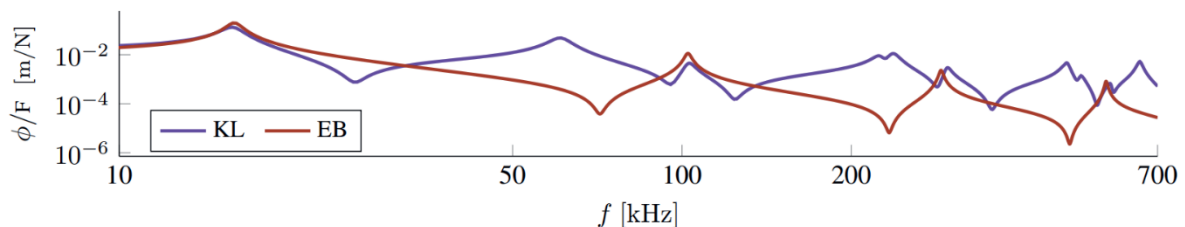


Fig. 3. Simulated spectral response of a plate resonator immerse in water. The blue line is based on Kirchhoff Love plate theory while the red line is based on Euler Bernoulli beam theory. While both theories predict the resonances of modes that can be found both in beams and in plates. The Euler Bernoulli based theory fails to predict resonance of modes which can only be found in plates.

its free corners and we solve for the spectrum directly in the Fourier domain. The resulting spectral response is shown in figure 3 (blue line). To compare our results with existing theory we also plot the corresponding results based on Euler Bernoulli beam theory. The peak at the lowest frequency corresponds to a flexural mode which can also be found in one-dimensional beam resonators. Therefore, both curves coincide. The second peak is a torsional mode not described by Euler Bernoulli beam theory. The peak at 100 kHz corresponds to the second beam mode and consequently both theories agree with each other. The mode at 237 kHz is the mode shown in figure 1b and its response can only be predicted with the proposed method.

Conclusion

We present a method for modelling the fluid-structure interaction of MEMS plate resonators. With this method we are able to predict the spectral response of plate resonators in liquids. These spectra pave the way for quantitative measurements of fluid properties and novel designs of fluid sensors which go beyond one-dimensional geometries.

References

- [1] Kucera, M. et al. Characterisation of multi roof tile-shaped out-of-plane vibrational modes in aluminium-nitride-actuated self-sensing micro-resonators in liquid media. *Appl. Phys. Lett.* 107, 053506 (2015).
- [2] Pfusterschmied, G. et al. Temperature dependent performance of piezoelectric MEMS resonators for viscosity and density determination of liquids. *J. Micromechanics Microengineering* 25, 105014 (2015).
- [3] Sader, J. E. Frequency response of cantilever beams immersed in viscous fluids with applications to the atomic force microscope. *J. Appl. Phys.* 84, 64–76 (1998).

Integrated Intelligent Sensor Systems for In-Hive Varroa Infestation Control in Digital Bee Keeping

Andreas König¹

¹ *Institute of Integrated Sensor Systems, TU Kaiserslautern, Kaiserslautern, Germany
koenig@eit.uni-kl.de*

Summary:

Bees are recognized as an indispensable link in the human food chain and general ecological system. Numerous threats, from pesticides to parasites, endanger bees and frequently lead to hive collapse. The varroa destructor mite is a key threat to bee keeping and the monitoring of hive infestation level is of major concern for effective treatment. Sensors and automation, e.g., as in condition-monitoring and Industry 4.0 with machine learning offer help. Here, integrated in-hive gas sensing system for infestation level estimation and emerging novel in-hive optical approach for varroa counting are presented.

Keywords: Gas sensing, varroa infestation level, digital bee keeping, in-hive measurement

Introduction

Major issues from environmental pollution to invasive species are threatening our ecological system and the human food supply. Insects, and honey bees in particular, play a decisive role, e.g., for pollination. The varroa mite parasite is a major threat to bee keeping and the cause of many bee colony losses. The monitoring of the varroa infestation level is one important task of conventionally operating bee keepers. Though there is a community practicing treatment free bee keeping [1], the majority of bee keepers follows standard treatment practice, e.g., by formic acid, which needs to know the right time to start treatment based on the hive infestation level. Sensors and automation, like in home automation, condition-monitoring and Industry 4.0, can both alleviate hive keeping and also make it much more effective. Thus, in the last 10-15 years numerous approaches to digital bee keeping can be observed [1]. In our IndusBee4.0 project, in-hive integrated sensor systems and machine learning based data analysis is pursued. Here, options for in-hive gas sensing and in-hive vision-based varroa counting are investigated to achieve small, effective, and affordable intelligent integrated sensor systems for continuous in-hive-monitoring and state estimation, e.g., monitoring and reporting the desired infestation level.

Conventional Varroa Monitoring Methods

There are several standard methods available for conventional varroa infestation level assess-

ment. They all have in common, that they imply substantial effort for the bee keeper and deliver results only at larger time steps. The analysis of hive debris including mites, dropping from the hive bottom and collected on a slider or tray, is most common. Usually, three days are expended until a manual, or more recently (semi) automated vision-based analysis, of the debris for the number of varroa can be conducted. The hive infestation level can be estimated from this count [1]. Another common approach, also denoted as flotation method, extracts a bee sample from the hive and drowns them to separate bees and varroa. The powder sugar and the CO₂-based sedation are two alternative more bee-friendly variants. Again, hive infestation level can be estimated from the count. Sample adequateness will probably depend on the location of extraction in the hive. A more recent principle approach tries to scrutinize in and out going bees at the flight hole for varroa mites clinging to them, e.g., [3, 1]. The advantage is the availability of continuous monitoring at the hive, but the computational effort and real-time requirement is substantial and same bees will be counted several times, going on multiple missions a day. Thus, alternative simple and quasi continuous in-hive monitoring methods less are of interest.

Indirect Sensor Based Infestation-Level Estimation

Basic investigations in the past have revealed, that both the sound patterns emitted by bees as

well as the air composition inside the hive host information, that correlates with the varroa infestation level, as determined by the conventional methods from the previous section. Hive sound patterns also allow to detect hints on 'missing queen', advent of 'swarming mood' etc. Thus, in our and many others previous work, microphones and signal processing and analysis have been applied, see e.g., [1]. MEMS microphones deliver in our Pi Zero W based **SmartComb** in-hive measurement system [1] the acoustical information on hive state, including continuous cues on varroa infestation.

Further, there are also early investigations on correlations of hive air composition and varroa infestation level. One recent intriguing work, based on a set of Figaro gas sensors and an external measurement system confirmed the existence and usefulness of such a correlation [2]. The availability of highly integrated gas sensing systems promote the improvement of the concept to cheap in-hive measurement systems, non-obtrusive to the bees, and continuously delivering registrations at any desirable rate. For instance, the Sensirion SGP30 multipixel sensor system [1] or the BOSCH Sensortec BME680 are candidates for this analysis. The latter sensor has the advantage, that the sensor heating temperature basically can be controlled and modulated for temperature cycles in measurement (virtual sensors).

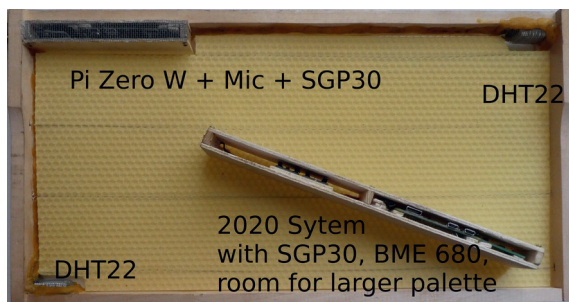


Fig. 1. **SmartComb** with SGP30 from 2019 ready for hive insertion and the extendable 2020 version with SGP30, BME680 et al..

The approach requires knowledge of true hive infestation level, which is not known. Estimates can be obtained by techniques of Section 2 or by an emerging novel alternative:

In-Hive Bee and Varroa Counting System

For honey harvest, there are two approaches: swapping the bees off with a bee brush or installing an intermediate floor equipped with bee escapes a day before. As illustrated in Fig. 2., the bees will move one by one through the narrow channel of the bee escape to rejoin with colony and queen. The vacated honey combs can be peacefully harvested. Additional ex-

ploitation option is to record and inspect the bees, as in flight hole inspection, by an embedded camera system., e.g., a cheap Pi Zero node and camera employing active illumination above 580 nm invisible to bees.

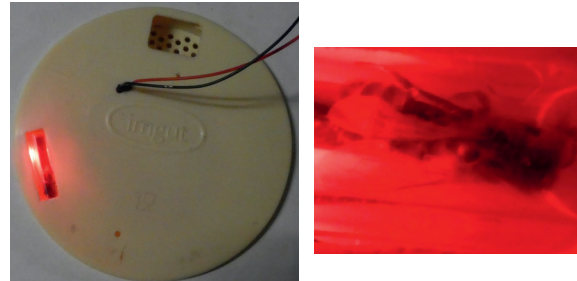


Fig. 2. *Extended bee escape for varroa counting*

Thus, a large unique bee sample could be drawn and bee and varroa counts determined. Processing could be done on host *post-mortem*.

Results

A low-cost, small, and unobtrusive in-hive monitoring system has been achieved [1] and extended with integrated E-nose capability. Fig. 3 shows a short campaign from a hive bottom in late winter 2020 as proof of functionality.

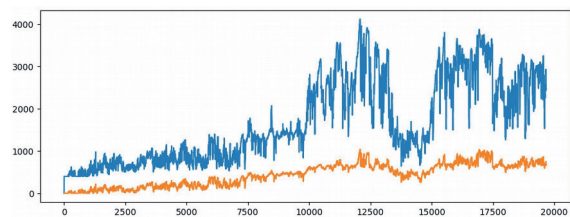


Fig. 3. *eCO₂ (blue) and TVOC (orange) SPG30 data from hive varroa floor for 12 h from 10:30 am.*

In contrast to similar E-nose projects, the measurement data obtained close to the brood nest in from April to August campaign first has to be correlated with conventionally determined infestation levels. Machine learning will help to create a virtual varroa infestation level sensor, potentially generalizable to foulbrood etc.

References

- [1] A. König, IndusBee4.0 – Integrated Intelligent Sensory Systems for Advanced Bee Hive Instrumentation and Hive Keeper's Assistance Systems, *Sensors & Transducers Journal*, 237.9-10, 109-121 (2019)
- [2] A. Szczurek, M. Maciejewska, B. Bąk, J. Wilk, J. Wilde, M. Siuda, Detection Level of Honeybee Disease: Varroosis Using a Gas Sensor Array, *SEIA'2019, Tenerife*, 25-27 Sep. 255-256 (2019).
- [3] L. Chazette, M. Becker and H. Szczerbicka, Basic algorithms for bee hive monitoring and laser-based mite control, *2016 IEEE SSCI, Athens*, 1-8 (2016)

Adaptive Soft Sensor for Bioprocess Monitoring

Manuel Siegl, Vincent Brunner, Dominik Geier, Thomas Becker
 Chair of Brewing and Beverage Technology, Weihenstephaner Steig 20, 85354 Freising, Germany
 Corresponding Author's e-mail address: dominik.geier@tum.de

Summary:

Soft sensors can be used to predict variables that cannot be measured directly. However, even these soft sensors are subject to errors that reduce the accuracy of the prediction. One way to overcome this is to predict a target quantity redundantly using independent measurement systems for the input variables. This study reports on the development of an algorithmic system for combining the redundant submodels to one reliable soft sensor. The proof of concept was conducted with a *Pichia pastoris* bioprocess.

Keywords: bioprocess monitoring, soft sensor, fault detection, model maintenance

Background, Motivation, and Objective

In biotechnological processes, process variables exist that cannot be measured directly in real-time and therefore have to be determined offline in tedious laboratory analyses. To determine these variables online, a so-called soft sensor can be utilized. However, the sensors contributing inputs to the soft sensors are often subject to interference and measurement errors. The typical error types of sensors can be classified as follows: bias (intermittent, step-wise, drift-wise or cyclic deviation), a reduction in precision, and a temporary or complete failure of sensors [1, 2]. The reasons can be attributed to damaged sensors, connection problems and inadequate calibration [3]. In order to be able to calculate an accurate prediction despite these limitations, more complex systems are required. One way to identify these individual sensor errors is to combine the information from the entire sensor network [4].

In addition to the identification of the errors, automated recalibration is also desirable for some error types (e.g., drift). One possibility to maintain soft sensors is to use selected historical data points [5]. Another option is the direct implementation of new laboratory measurements for the maintenance of the soft sensors [5, 6]. However, especially in bioprocesses, laboratory measurements are often very time-consuming and cannot be integrated into the running process using these methods. For example, in the bioprocess investigated in this work, the cultivation of the yeast *P. pastoris*, the target value (dry cell weight concentration, hereinafter referred to as X) cannot be deter-

mined in less than 2 days. This study aims to predict the target value X using several separate submodels and then to statistically interconnect the prediction of the submodels. In addition, it was examined whether incorrect submodels can be identified and directly maintained.

Generation of the process data

Five cultivations were carried out in a Biostat[®] Cplus bioreactor with a working volume of 15 L at 30 °C and 500 mbar. The dissolved oxygen was maintained at 40 %. As cultivation medium FM22 with an initial glycerol concentration of 40 g L⁻¹ was used. The pH of the batch cultivation was controlled to 5 with ammonium hydroxide, which additionally served as a nitrogen source. Data pre-processing and modeling were performed in MATLAB R2019a.

Development of the Adaptive Soft Sensor

Three different submodels were used to predict the biomass concentration X . The first submodel was used to predict the target value using a model based on the pH correction agents (*base submodel*). The second submodel is based on the exhaust gas measurements and includes the calculation of the carbon dioxide emissions rate (*CER submodel*). The third prediction is based on the measurement of a mid-infrared sensor (*MIR submodel*). To predict X using the mid infrared spectrum, a Savitzky-Golay filter was first applied and then the biomass was predicted using partial least squares regression (PLSR).

The sampling interval of the sensors made it possible to predict X every 30 s. For the subse-

quent interconnection, the three predictions were averaged within 5-minute intervals and their standard deviations were calculated ($n = 10$). A system based on a t-test with a subsequent minimum variance estimator was used to combine the submodel predictions to an adaptive soft sensor for biomass concentration (*mixed model*).

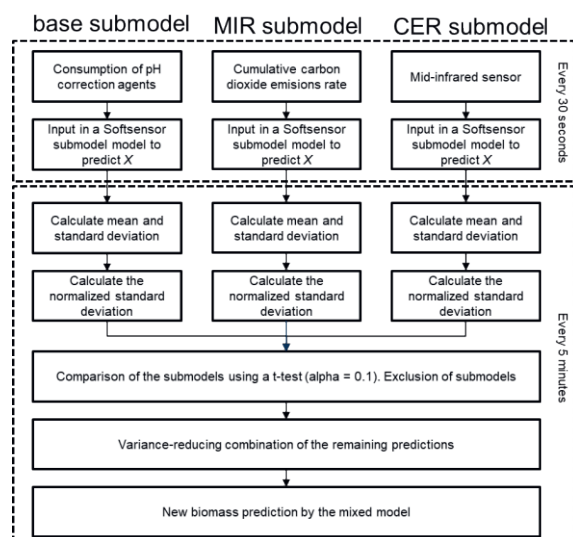


Figure 1: Structure of the adaptive soft sensor.

Performance of the Adaptive Soft Sensor

Three datasets were used to calibrate and validate the single submodels. The validation of the mixed soft sensor model was performed in two ways: on the one hand with the already used data with additional artificial errors and on the other hand with the remaining two data sets.

Figure 2 shows the validation of the system for artificially generated errors. Three errors were added: the intermittent malfunction of the logging of the pH correction agent (I); the intermittent increase of the measuring noise of the mid-infrared sensor (II) and a stepwise increase of the CER based submodel (III).

In all three cases, the algorithm of the mixed model was able to compensate for the sensor errors delivering a robust final prediction for X . In case of the fault type of stepwise increase (bias), recalibration would theoretically be possible using the two correct soft sensors or historical measurements. With the two datasets not used for calibration, malfunctions occurred mainly at the MIR measurement, which could be compensated for by the developed system (data not shown).

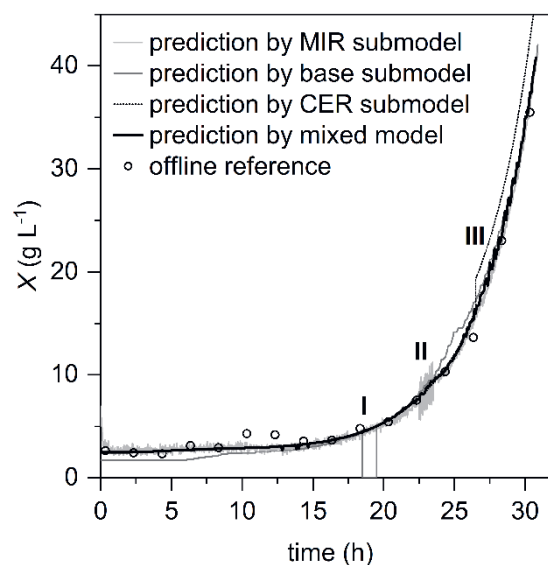


Figure 2: Comparison of the individual submodels with the adaptive soft sensor. Artificial errors were added to the underlying sensor data (I,II,III).

In the future, besides the automated recalibration due to stepwise biases, the behaviour of the system in case of multiple errors will be investigated and improved.

References

- [1] Mehranbod, Nasir; Soroush, Masoud; Piovoso, Michael; Ogunnaike, Babatunde A. (2003): Probabilistic model for sensor fault detection and identification. In: *AIChE J.* 49 (7), S. 1787–1802. DOI: 10.1002/aic.690490716.
- [2] Isermann, R. (2006). *Fault-diagnosis systems: an introduction from fault detection to fault tolerance*. Springer Science & Business Media. DOI: 10.1007/3-540-30368-5.
- [3] Sharma, Abhishek B.; Golubchik, Leana; Govindan, Ramesh (2010): Sensor faults. In: *ACM Trans. Sen. Netw.* 6 (3), S. 1–39. DOI: 10.1145/1754414.1754419.
- [4] Brunner, Vincent; Klöckner, Lukas; Kerpel, Roland; Geier, Dominik Ulrich; Becker, Thomas (2019): Online sensor validation in sensor networks for bioprocess monitoring using swarm intelligence. In: *Analytical and bioanalytical chemistry*. DOI: 10.1007/s00216-019-01927-7.
- [5] Yuan, Xiaofeng; Ge, Zhiqiang; Song, Zhihuan (2016): Spatio-temporal adaptive soft sensor for nonlinear time-varying and variable drifting processes based on moving window LWPLS and time difference model. In: *Asia-Pac. J. Chem. Eng.* 11 (2), S. 209–219. DOI: 10.1002/apj.1957.
- [6] Chen, Kuilin; Castillo, Ivan; Chiang, Leo H.; Yu, Jie (2015): Soft Sensor Model Maintenance: A Case Study in Industrial Processes*. In: *IFAC-PapersOnLine* 48 (8), S. 427–432. DOI: 10.1016/j.ifacol.2015.09.005.

Synthesis of MIP Nanoparticles for Selective Sensing of Penicillin V

M. Bagheri, P. A. Lieberzeit

University of Vienna, Faculty for Chemistry, Department of Physical Chemistry, Vienna, Austria
Peter.lieberzeit@univie.ac.at

Summary:

Molecularly imprinted polymers (MIP) based on an acrylic system have proven useful for sensing Penicillin V in aqueous solvents by the means of quartz crystal microbalances (QCM). Herein we carry that concept further by synthesizing MIP nanoparticles as sensitive matrices. This preliminary study discusses the effects of different parameters, namely solvent type and cross-linker amount, on the morphology of nanoparticles, i.e. particle size, polymer agglomeration and porosity. Overall, this resulted in particles with 300 nm diameter synthesized with trimethylolpropane trimethacrylate (TRIM) in both acetonitrile and methanol. The results indicate narrower size distribution in acetonitrile.

Keywords: Penicillin V, Molecularly Imprinted Polymer, Quartz Crystal Microbalance, Polymer Nanoparticles

Introduction

Most pharmaceuticals are deposited in the environment through human consumption and excretion, and are often filtered ineffectively by municipal sewage treatment. Persistence of pharmaceuticals and active drugs in wastewater are detrimental, because they are not only potential environmental pollutants, but are also pharmaceutically active. They also have the potential to accumulate in soil and plants that have been irrigated with wastewater and reclaimed water. Especially antibiotics are considered harmful for promoting the development of the antibiotic-resistant bacteria in nature. Various analytical techniques can be utilized for measuring concentrations of antibiotics in wastewater effluent. Molecular imprinting is a comparably recent method for generating artificial recognition matrices toward both biological and synthetic species. Combined with suitable transducers, e.g. QCM, they allow for rapid and reproducible measurement [1]. The project underlying this presentation aims at sensing the antibiotic Penicillin V (Pen V) with both MIP nanoparticles and bulk MIP via QCM measurements. During the first stage, we studied corresponding MIP thin films based on radical polymerization of acrylic monomers. QCM sensor characteristics revealed limit of detection at 0.02 mg/ml. Selectivity was investigated against Penicillin G and Amoxicillin, which have similar chemical structures [2].

The second step involving preparation of polymer Nanoparticles (NPs). The advantages of MIP NPs compared to bulk polymer is to enhance sensing efficiency due to their

increased surface-to-volume ratio: it provides larger number of accessible binding sites for molecular recognition. This study reports on synthesis methods for improving the recognition properties of MIP NPs.

Preparing Penicillin V MIP NPs

Herein, we used the initial bulk polymer recipe as a starting point to obtain nanoparticles in range of 200 nm by precipitation polymerization in MeOH and Acetonitrile (ACN). The other optimization parameter was employing Ethylene glycol dimethacrylate (EGDMA) and trimethylolpropane trimethacrylate (TRIM), respectively, as cross-linkers, as well as different ratios of monomer to cross-linker, type of solvent and type of cross-linker.

Results

Using TRIM instead of EGDMA for preparing MIP nanoparticles led to uniform size distribution, where type of cross-linker strongly influences the final size and yield of MIP nanoparticles. Varying the fractions of TRIM or EGDMA, respectively, in the polymer allowed us to control particle diameters (Table. 1).

Tab. 1: Nanoparticle size corresponding to the monomer to cross-linker ratios of TRIM and EGDMA

Ps	MAA:TRIM	MAA:EDGMA	NPs size (nm)
MIP	1:1	–	360
MIP	1:2	–	540
MIP	1:6	–	1.170
MIP	–	1:6	570
MIP	–	1:3	1.400

This data clearly shows that the TRIM structure provides more polymerizable groups – namely three per molecule, than EGDMA. Therefore, one can choose lower cross-linker:monomer ratios to obtain smaller particles.

The precipitation solvent also has substantial influence on the particles. For instance, Fig. 1 shows SEM images of MIP NP precipitated from ACN. As one can see, this leads to very appreciable, clearly defined, globular NP with a smooth surface.

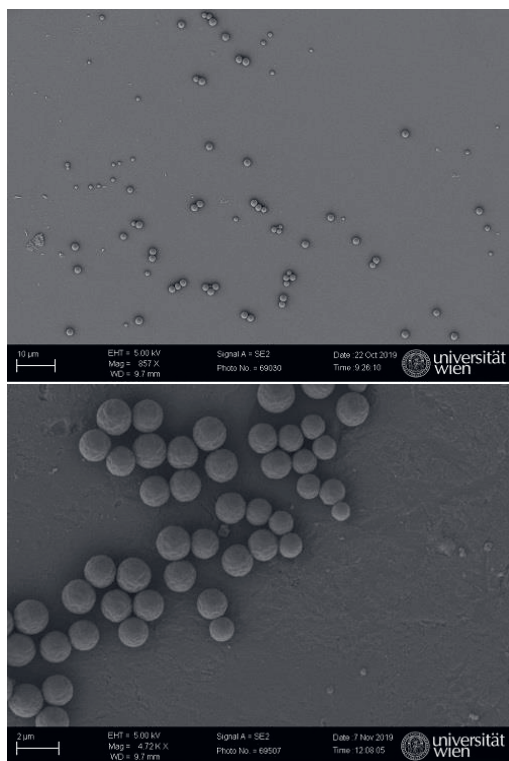


Fig.1. the SEM images of a. NPs synthesized in ACN

However, ACN is a bad solvent for the potassium salt of Pen V. Therefore, we decided to change to MeOH. This allows us to increase amount of template to achieve maximum Pen V binding sites in synthesized MIP NP.

Figure 2, shows how using MeOH - this solvent is protic - influences the aggregation of NPs. Moreover, in terms of using high amount of template in MIP particle shape increased roughness compared to NIP NPs (see Fig. 2b).

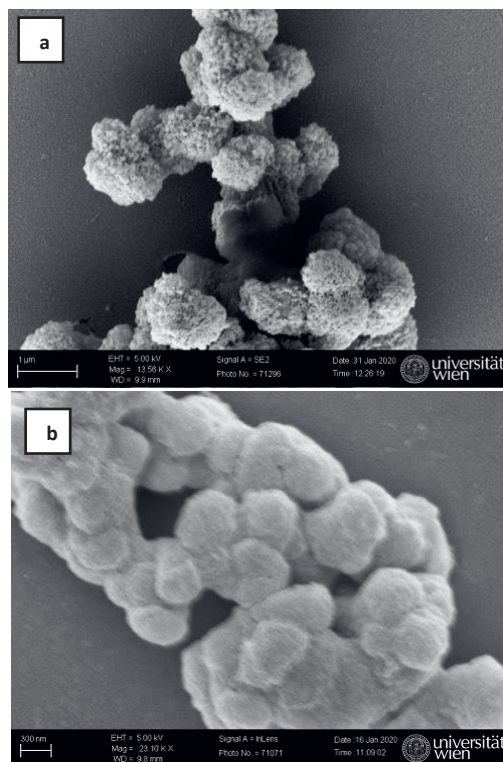


Fig. 2. SEM images illustrate the prickly shape of MIP particles synthesized in MeOH (b) compare to smooth surface of NIP particles synthesized in MeOH (a).

Acknowledgement

Authors gratefully acknowledge funding of this work by the Austrian Research Promotion Agency (FFG) through project AquaNOSE (Grant agreement no. 864893)

References

1. Vasapollo, G., Sole, R. D., Mergola, L., Lazzoi, M. R., Scardino, A., Scorrano, S., & Mele, G. (2011). Molecularly imprinted polymers: present and future prospective. *International journal of molecular sciences*, 12(9), 5908–5945. doi:10.3390/ijms12095908
2. S. Haghdoust and P. Lieberzeit, Molecularly Imprinted Thin Films for Detecting Penicillin V, 10th International Congress Nanotechnology in Biology & Medicine, Graz, Austria. (2019)

Fluorescence Multi-Sensor System for the Simultaneous Detection of Various Types of Explosives in Gas-Phase

Benedikt Heller¹, Mustafa Biyikal¹, Reinhard Noske¹, Knut Rurack¹

*¹ Federal Institute for Materials Research and Testing (BAM),
Richard-Willstätter-Street 11, 12489 Berlin, Germany
benedikt.heller@bam.de*

Abstract

The world is facing an increasing threat from improvised explosive devices (IEDs) used in terrorist attacks all around the world. Accordingly, the possibility for a fast and straightforward detection is of high importance. Therefore, a highly sensitive and selective handheld sensor system has been developed for the simultaneous detection of various types of explosives in gas-phase, using a combination of fluorescent sensor layers in a Lab-on-a-Chip system.

Keywords: Multi-sensor, fluorescence, detection, explosives, gas-phase

Introduction

IEDs have been used in various terroristic attacks within the last decades throughout the world. The type of explosive(s) used in such bombs can vary strongly, including nitro-based-explosives like TNT (Rijeka bombing), nitrate-esters like PETN and nitramines like RDX (Semtex; Pan Am 103 Bombing), peroxide-based explosives like TATP (Manchester Arena bombing) or ammonium nitrate (Breivik bombing). Thus, it is of utmost importance to develop a handheld sensor for the simultaneous detection of these kinds of explosives in gas-phase.

To achieve a simultaneous analysis of an unknown sample, a Lab-on-a-Chip (LoaC) system has been developed. To enable detection of low volatile explosives, the sample is heated in order to be transferred into gas-phase. The LoaC represents a microfluidic system in which this gas-phase is passed over various sensor layers. The combination and positioning of these films enable the simultaneous detection of various explosives. Using an optical system involving UV-irradiation and PMT, the signals can directly be analyzed. Inclusion of a customized software ensures high sensitivity and selectivity as well as a very good identification of false positive/negative measurements.

Merging all of the separately developed systems we were able to assemble a handheld prototype which is shown in Fig. 1.



Fig. 1. Handheld prototype (20 x 10 cm) for simultaneous detection of explosives in gas-phase.

Results and Discussion

A swipe sample, e.g. a Teflon strip, is wetted with a predetermined amount of analyte and dried. The sample is then heated to transfer the analyte into gas-phase. Using a pump, the gas stream is carried over the separate sensor layers of the LoaC. The speed is set to an average of 50 mL/min. It is a critical setting since it will determine the time of interaction between the sensor layer and the analyte. The principle of detection is hereby either a decrease or increase in fluorescence intensity upon reaction with the analyte. Nitro- and nitrate-based explosives as well as 2,3-dimethyl-2,3-dinitrobutane (DMDNB), which is a common additive to industrially synthesized TNT, lead to a strong decrease in fluorescence intensity. The mechanism for this quenching is caused by the electron deficient property of e.g. TNT. Thus, an electron can be transferred from the implemented dye in the sensor layer, resulting in a decrease in fluorescence. Peroxide-based explosives on the other hand induce a fluorescence decrease. This mechanism is based on

two consecutive steps. Due to an acidic catalyst, TATP is decomposed to hydrogen peroxide. The dye induced into the sensor layer was prior selected to show an enhancement in fluorescence upon oxidation. The positioning of the acidic catalyst in the LoAC also allows a very good distinction between a peroxide-based explosive like TATP or HMTD and hydrogen peroxide.

The exemplary results of the gas-phase experiments are shown in Fig. 2 and Fig. 3.

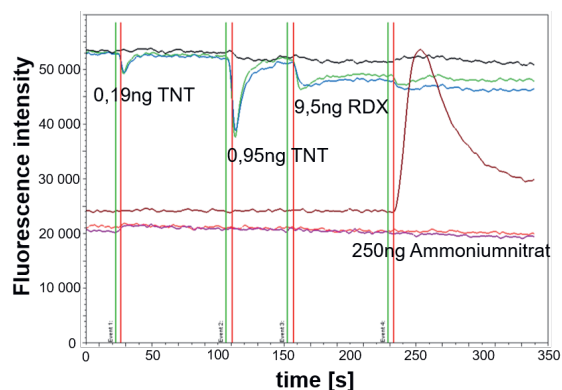


Fig. 2. Measurement various explosives with the handheld prototype.

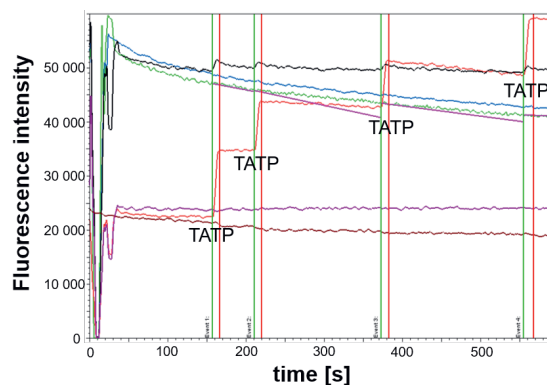


Fig. 3. Measurement of 155 ng TATP (4x) with the handheld prototype.

The combination of a handheld device with a LoAC, containing a series of separate sensor layers enables a straightforward and fast detection of various types of explosives in gas-phase with high sensitivity and selectivity. This prototype, due to its low weight and portability, shows promising performance for use in field experiments. The Limits of Detection (LoD) are shown in Tab. 1.

Tab. 1: Explosives with LoD

Explosive	LoD
TNT	0.2 ng
DMDNB	6.0 ng
TATP	10 ng
Ammonium nitrate	60 ng

This work presents the development of a handheld prototype for the simultaneous detection of various explosives. Due to the combination of fluorescent sensor layers and elaborated optical and microfluidic systems high sensitivity and selectivity could be achieved. Inclusion of a customized software allows a fast and user-friendly readout of the measurements. The high operator convenience shows a promising application in field experiments.

References

- [1] A. K. Singh, N. G. Ditkofsky, J. D. York, H. H. Abujudeh, L. A. Avery, J. F. Brunner, A. D. Sodickson, M. H. Lev, Blast Injuries: From Improvised Explosive Device Blasts to the Boston Marathon Bombing, *Radiographics*, 36, 1, 295-307 (2016); doi: 10.1148/rg.2016150114
- [2] J. V. Prata, A. I. Costa, C. M. Teixeira, A Solid-state Fluorescence Sensor for Nitroaromatics and Nitroanilines Based on a Conjugated Calix[4]arene Polymer, *Journal of Fluorescence* (2019); doi: <https://doi.org/10.1007/s10895-019-02466-1>
- [3] S. Fan, J. Lai, P. L. Burn, P. E. Shaw, Solid-State Fluorescence-based Sensing of TATP via Hydrogen Peroxide Detection, *American Chemical Society Sensors*, 4, 134-142 (2019); doi: 10.1021/acssensors.8b01029

Percolation Networks of Polypyrrole for Vapour Sensing of Improvised Explosive Devices

Merel J. Lefferts¹, Ben I. Armitage, Krishnan Murugappan, Martin R. Castell

¹ Department of Materials, University of Oxford, Parks Road, Oxford, OX1 3PH, UK

Merel.Lefferts@materials.ox.ac.uk

Summary:

Using chemiresistive vapour sensors based on a percolation network of polypyrrole (PPy) significantly increases the sensitivity compared to more traditional PPy thin film based sensors. At the optimum, close to the percolation threshold, an LOD of 18 ± 2 ppb ammonia was achieved. The sensors are also highly sensitive to vapour emitted by the ammonium nitrate/fuel oil (ANFO) mixture, which is commonly used in improvised explosive devices (IEDs).

Keywords: Chemiresistor, vapour sensing, conductive polymer, percolation network, ammonium nitrate/fuel oil (ANFO)

Introduction

Vapour sensing plays an important role in many safety, security, and healthcare applications. Therefore, it is perhaps surprising that despite modern technologies sniffer dogs are still considered the gold standard in vapour sensing. Achieving high sensitivities often remains challenging. Furthermore, existing technological solutions often require relatively large pieces of equipment, or pre-concentration steps [1].

Especially for the detection of improvised explosive devices (IEDs) small sensors with a fast response time are of high importance. Furthermore, they have to be easy to use and if possible be made on flexible or wearable substrates. Conductive polymer (CP) based chemiresistive vapour sensors offer an interesting solution because of the large range of materials available. Furthermore, they are relatively cheap and easy to process, and their small scale makes it possible to use them in small scale devices.

Concept and methods

Traditional conductive polymer based chemiresistors tend to make use of a conductive polymer thin film. Here we demonstrate that by using a percolation network of conductive polymers we can significantly improve the sensitivity compared to a more traditional thin film based sensor. When a sensor is operated close to the percolation threshold, a small number of chemical interactions causes a large change in the resistance of the sensor. This allows for a much higher sensitivity than thin film based sensors that by definition operate in the flatter region of the percolation curve.

The sensors consist of glass substrates with Pt interdigitated electrodes (IDEs). Au nanoparticles (NPs), created between the IDEs by dewetting an Au thin film, are used as nodes in the electrochemically grown PPy network [2][3]. Sensors consisting of various PPy coverages, corresponding to various points along the percolation curve, were created and exposed to 100-700 ppb ammonia. Furthermore, the optimized sensors were exposed to unknown concentrations of vapour emitted by ammonium nitrate/fuel oil (ANFO) samples.

Results

Upon exposure to ammonia the sensors displayed an instantaneous and reversible increase in resistance, where the magnitude of the resistance change is dependent on the ammonia concentration (fig 1a). A comparison of the limits of detection (LODs) of sensors with different polymer coverages shows that there is an optimum at resistances corresponding to the steep part of the percolation curve, close to the percolation threshold. At lower resistances, corresponding to thin film sensors, the LOD is higher. At resistances higher than the optimum the absolute sensor response is higher as well, but due to an increase in noise the sensitivity decreases when the sensor is too close to the percolation threshold. At the optimum we've achieved a LOD of 18 ± 2 ppb.

The optimized sensors were also exposed to unknown concentrations of vapour emitted by various ANFO samples, based on different types of fertilizer. The sensing responses to the fertilizer and ANFO samples were similar to the responses to ammonia, which is consistent with

the sensor response being caused by ammonia emitted by the fertilizer. The sensors do not respond to diesel. By comparing the sensor response to a calibration curve created with the ammonia sensing experiments the ammonia concentration detected as a result of the exposure to ANFO could be deduced. For example, 160 ppb ammonia resulting from an ANFO sample was easily detected. Furthermore, it was found that different fertilisers give different sensing responses.

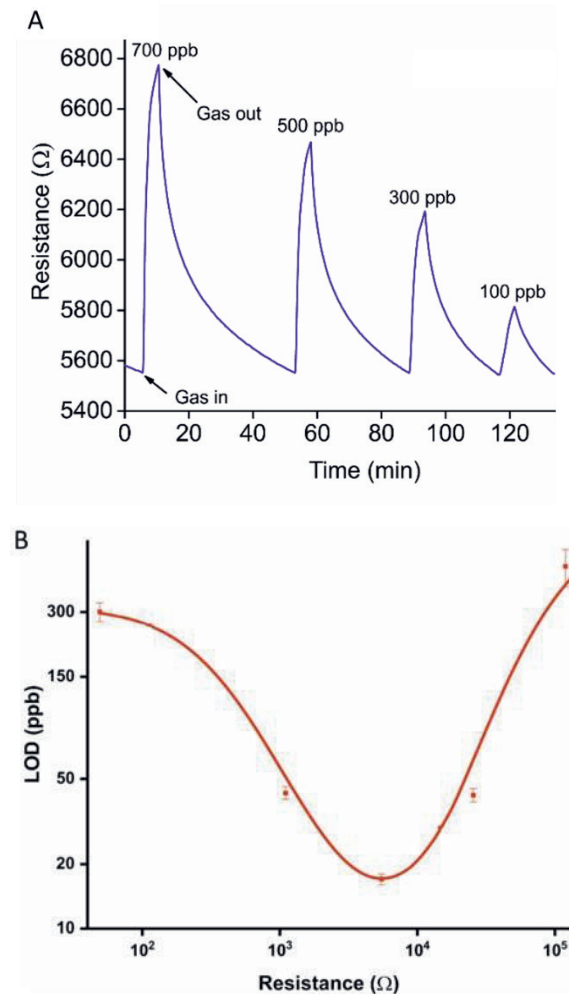


Fig. 1. A) Resistance change as a function of time upon exposing a sensor based on a percolation network of PPy to 700, 500, 300, and 100 ppb of ammonia. The sensor response is instantaneous and reversible. B) The limit of detection (LOD) for sensors with different starting resistances, corresponding to different points along the percolation curve. A LOD of 18 ± 2 ppb was achieved at the optimum, which is found at a resistance value corresponding to the steep part of the percolation curve.

Summary and outlook

By using a percolation network of ammonia the sensitivity was significantly improved compared to more traditional thin film based sensors. Sensors operating this way can achieve ppb

level sensitivity, making them especially interesting for the detection of IEDs. We have also successfully used sensors based on a percolation network of PPy to detect vapour emitted by ANFO, which is commonly used in IEDs.

Further work includes extending this work to different sensor materials and analyte vapours. And, to improve the potential for practical implementation of these sensors, the development of an integrated device and the development of these sensors on flexible substrates.

References

- [1] Lefferts, M. J. & Castell, M. R. Vapour sensing of explosive materials. *Analytical Methods* 7, 9005-9017 (2015); doi: 10.1039/C5AY02262B
- [2] Lefferts, M. J., Murugappan, K., Wu, C. & Castell, M. R. Electrical percolation through a discontinuous Au nanoparticle film. *Appl. Phys. Lett.* 112, 251602 (2018); doi:10.1063/1.5023163
- [3] Murugappan, K. & Castell, M. R. Bridging electrode gaps with conducting polymers around the electrical percolation threshold. *Electrochem. Commun.* 87, 40-43 (2018); doi:10.1016/j.elecom.2017.12.019

Wireless low-power warning system for the detection of flammable gases

Benedikt Bierer¹, Dario Grgić², Olena Yurchenko^{1,2}, Laura Engel¹, Hans-Fridtjof Pernau¹, Leonhard Reindl², Jürgen Wöllenstein^{1,2}

¹ *Fraunhofer Institute for Physical Measurement Techniques IPM, Heidenhofstrasse 8, 79110 Freiburg, Germany*

² *Department of Microsystems Engineering - IMTEK, University of Freiburg, Georges-Koehler-Allee 102-106, 79110 Freiburg, Germany
benedikt.bierer@ipm.fraunhofer.de*

Summary:

The detection of flammable gases is necessary to avoid explosive atmospheres. For this reason, low-cost pellistors are frequently used sensors, although they suffer from high operation temperatures and high power consumption. Within the scope of our work, we present a novel wireless low-power catalytic gas sensor system for flammable gases. The combination of a MEMS-based sensor and low power radio system provide the opportunity to monitor complex infrastructures without using the grid for power supply.

Keywords: flammable gas sensor, catalytic combustion, sensor node, low-power wireless

Background and Motivation

The early detection of flammable gases or explosive gas mixtures is extremely important in order to avoid endangerment of people and the damage of plants and facilities. Flammable gas sensors are sold in millions and are used for energy supply by gas, at filling stations, but also in the private sector for gas heaters and pipes. Due to their high-energy consumption, these sensors can only be operated by grid, whereby the installation of a sensor network becomes complex and expensive. Low energy consumption of the gas sensors offers the possibility to operate sensor nodes for the detection of flammable gases or explosive gas mixtures independently of the power grid. Here, we present a newly developed wireless sensor node for the detection of flammable gases. The node connects the intelligence of a low power wireless transceiver with a MEMS-based low-power, low-temperature catalytic combustion gas sensor.

The wireless gas sensing system

The main challenge is the connection of the gas sensor system to the energy management and the radio system (Figure 1), which should be as efficiently as possible in order to achieve all of the goals set, such as service life, real-time capability, maintenance, range, robustness and mesh network capability. For this purpose, a radio system was developed and evaluated, which uses a unique wake-up strategy to ensure that

all sensors can be reached by radio permanently and in real time and yet have very low energy consumption. In contrast to current wireless communication systems (WLAN, Bluetooth, Zigbee), which minimize their energy consumption through periodic de- and activation [1], this system allows continuous real-time accessibility with low latencies. Since the individual sensor nodes also communicate with each other, measurement data can be recorded in star or multi-hop topology if required. This offers the opportunity of an almost unlimited distance coverage in networks and opens the way for a drastically reduction of costs. The radio system maintained is robust, simple, efficient, maintenance-free and energy self-sufficient. Even the radio protocol has been designed to be particularly robust and immune to interference for use in a safety-critical environment, where each measurement value is confirmed bidirectional at the receiver. These features make it possible to place the measuring system in inaccessible places as well as to use it in a battery-powered mobile environment. The second elementary component is the gas sensor itself. Due to the development of new catalytic materials, the working temperature, which is currently at 450°C-500°C for commercial available sensors, could be decreased to 350°C. By using a MEMS-based hotplate [2] with a very low thermal mass, the power consumption of the sensor module decreases to approximately 100mW. This enables the usage of the sensor for mobile applications as well.

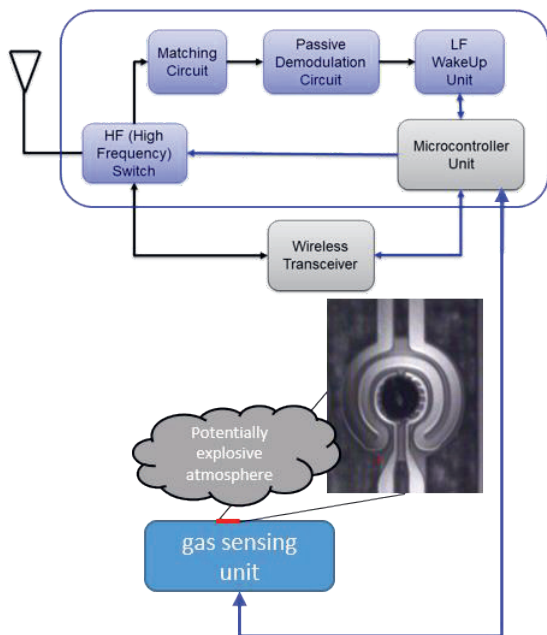


Fig. 1: Overview of the measurement system. The radio module receives the data from the sensor module and could send it to different application depended destinations. The diameter of the sensor is about 300 μm .

Results

For the monitoring of flammable gases, a reliable detection of the lower explosion limit (LEL) is necessary. To report leakages or to evacuate people in harmful areas, 10% of the LEL should be detected. Here we present a gas-sensing device optimized for the methane detection. Figure 2 presents the measured data for three different gas concentrations below the LEL of methane of 4.6% [3]. At a low working temperature of 350°C, the sensor signal shows, after a burn-in step, a very stable baseline and due to the high signal to noise ratio (SNR) concentrations far below the LEL could be safely detected.

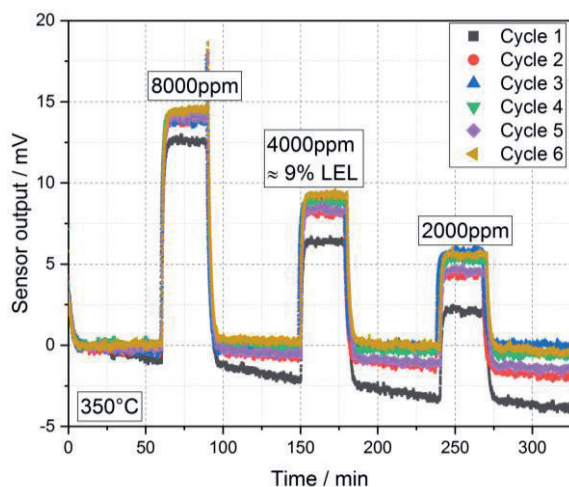


Fig. 2: Sensor output to three different methane concentrations below the LEL. The sensor reliability is shown within six cycles. Due to the high signal to noise

ratio, methane concentrations down to 2000 ppm (4.5% LEL) in dry air could be measured at a sensor temperature of 350°C.

The sensor data could be transmitted to a gateway, which process the data and activates further steps, if necessary. A possible node to node range of over 250 m covers the majority of all industrial and consumer applications.

Conclusion

The use and the development of new materials as well as the optimization of the sensor design enable the reduction of the power consumption, whereby the lifetime of an autonomous sensor system increases significantly. Our investigations illustrate, for the first time, the possibility to develop a remote-query able and networkable low-power sensor system for the detection of flammable gases.

References

- [1] N. Kajikawa, Y. Minami, E. Kohno and Y. Kakuda, "On Availability and Energy Consumption of the Fast Connection Establishment Method by Using Bluetooth Classic and Bluetooth Low Energy," 2016 Fourth International Symposium on Computing and Networking (CANDAR), Hiroshima, 2016, pp. 286-290, doi: 10.1109/CANDAR.2016.0058
- [2] P. Walden, J. Kneer, S. Knobelspies, W. Kronast, U. Mescheder and S. Palzer, Micromachined Hotplate Platform for the Investigation of Ink-Jet Printed, Functionalized Metal Oxide Nanoparticles, *Journal of Microelectromechanical Systems*, 24, 5, 1384-1390 (2015), doi: 10.1109/JMEMS.2015.2399696
- [3] G. De Smedt, F. de Corte, R. Notel , J. Berghmans, Comparison of two standard test methods for determining explosion limits of gases at atmospheric conditions, *Journal of Hazardous Materials*, 70, 3, 105-113 (1999), doi: 10.1016/S0304-3894(99)00163-6.

Ultra-fast gas spectroscopy with a dual-comb spectrometer

Leonard Nitzsche¹, Jens Kießling¹, Sebastian Wolf¹, Frank Kühnemann¹, Jürgen Wöllenstein^{1,2}

¹ Fraunhofer Institute for Physical Measurement Techniques IPM, Heidenhofstraße 8, D-79110 Freiburg, Germany

² University of Freiburg, Department of Microsystems Engineering IMTEK, Laboratory for Gas Sensors, Georges-Köhler-Allee 102, D-79110 Freiburg, Germany
juergen.woellenstein@imtek.uni-freiburg.de

Summary:

Dual-comb spectroscopy has the potential to measure broadband transmission spectra fast and precisely. To employ these features for gas analysis we present a fiber-based dual-comb-spectrometer and compare the spectrum of an HCN filled cell with a simulation using the HITRAN database. Although point-to-point fluctuations across the spectrum show a rms of 4 % fit results indicate that absorptions features with $(\alpha \cdot L) = 0.01$ can be detected within measurement time of 0.5 ms.

Keywords: dual-comb-spectroscopy, gas analysis, fast acquisition, hydrogen cyanide, absorption spectroscopy

Motivation

The study of dynamics in chemical reactions or the tracking of gas concentrations is a field that profits from optical measurement techniques. With the ability to record absorption spectra with a high rate one could investigate reactions as they occur during the removal of methane - an important greenhouse gas - from the atmosphere [1]. Alternatively, the development of combustion engines or monitoring plasma compositions in industrial processes could profit from fast spectra acquisition as well.

Dual-Comb spectroscopy

A frequency comb can be described as a pulsed laser with its optical spectrum composed of multiple discrete modes with identical spacing f_r . Their use as a ruler in the optical domain allows for extraordinary precision in frequency metrology [2]. As the comb spectrum usually covers a broad spectral range, the attenuation caused by a probe, here gaseous samples, can be determined. By superimposing the probing comb with a reference comb - often referred to as dual-comb-spectroscopy [3] - beatings between pairs of comb modes are generated. This effectively realizes a multi-heterodyne detection scheme resulting in a frequency-comb in the radio frequency regime. Here the spacing of the rf-combs Δf_r equals the difference in the comb mode spacing of the respective combs. Interestingly the acquisition rate is also Δf_r . Knowing f_r and Δf_r one can directly map the RF-comb to the optical domain and retrieve the transmission spectra of the

probe with an optical resolution f_r , - here in the order of hundreds of MHz. However, using two combs generated separately as with Titan Sapphire- or fiber-lasers requires a significant effort to ensure phase-synchronization.

Experimental setup

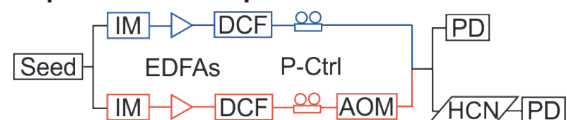


Fig. 1. Sketch of experimental setup for a fiber-based dual-comb-generator. The cw-laser (Seed) is split into two branches (red/blue). Using intensity modulation (IM), amplification (EDFAs) and spectral broadening in a dispersion compensating fiber (DCF) two combs are generated. They are polarization-controlled (P-Ctrl). One comb is shifted in frequency by an acousto-optic modulator (AOM). After superposition a part the dual-comb signal is fed to a photodetector (PD) as reference while the other part passes a sealed cell filled with hydrogen cyanide (HCN) before being detected. Following a different approach [4] we generate two frequency combs using a common continuous wave (cw) fiber-laser (emitting at 1550 nm, frequency drift below 10 MHz/min) leading to mutual-coherence of the combs (see Fig. 1). For each comb the cw-laser is intensity modulated by electro-optic modulators resulting in a pulse train with $f_r = 275$ MHz repetition rate ($f_r + 10$ kHz for the second comb). The spectrum now consists of few 100 modes. After amplification the pulse trains are launched into a dispersion compensating fiber for spectral broadening [5] resulting in 1800 comb modes spanning an optical

bandwidth of 490 GHz. Before superimposing both combs their polarizations are aligned and one comb is shifted by 25 MHz in frequency with an acousto-optic modulator to allow for mapping of the radio-frequency comb to the optical domain without ambiguity. We use two detection channels where one serves as reference. In the probe channel the dual-comb signal passes a multi-pass cell with 78 cm length filled with hydrogen cyanide at 100 Torr. For both channels the multi-heterodyne signal is recorded by a fast photodetector connected to a digitizer. The power spectrum reveals the radio-frequency combs. To remove the comb envelope structure, the probe channel data is divided by the reference channel data. In addition, a constant scaling factor is applied to account for different optical powers reaching the detectors (see Fig. 2).

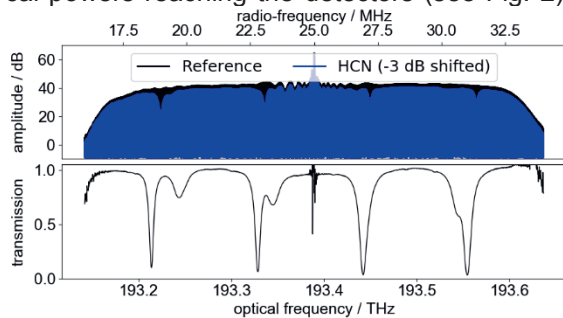


Fig. 2. (top) Dual-comb spectra in the radio-frequency domain showing absorptions due to hydrogen cyanide (blue) compared to a reference channel (black). (bottom) Transmission spectrum mapped to the optical regime.

Results

With this configuration we typically observe 1800 comb modes with amplitudes 42 dB above the noise floor in average for 1 s measurement time. This corresponds to a figure of merit [3] of $2.7 \times 10^7 \text{ Hz}^{1/2}$. A transmission spectrum measured within 0.5 ms is compared with a simulation based on the HITRAN database [6] (see Fig. 3). While the 0.5-ms-data shows a noise rms of 4% the fit allows one to detect absorption features with $(\alpha \cdot L) = 0.01$ at this short time scale.

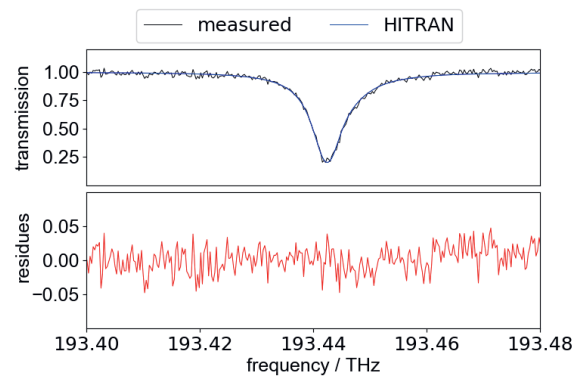


Fig. 3. (top) Zoom-in on HCN absorption feature at 193.44 THz (measurement and HITRAN data). (absorption path 78 cm, prefilled with hydrogen cyanide at 100 Torr. (bottom) Residues show the impact of point-to-point fluctuations across the spectrum.

References

- [1] I. S. A. Isaksen, T. K. Berntsen, S. B. Dalsøren, K. E. Eleftheratos, Y. Orsolini, B. Rognerud, F. Strodal, O. A. Søvde, C. Zerefos, C. H. Holmes, *Atmosphere* 5, 518-535 (2014); doi: 10.3390/atmos5030518
- [2] T. W. Hänsch, Nobel Lecture: Passions for precision, *Reviews of Modern Physics* 78, 1297-1309 (2006); doi: 10.1103/RevModPhys.78.1297
- [3] I. Coddington, N. Newbury, W. Swann, Dual-comb spectroscopy, *Optica* 3, 414-426 (2016); doi: 10.1364/OPTICA.3.000414
- [4] G. Millot, S. Pitois, M. Yan, T. Hovhannisyan, A. Bendahmane, T. W. Hänsch, N. Picqué, Frequency-agile dual-comb spectroscopy, *Nature Photonics* 10, 27-30 (2016); doi:10.1038/NPHOTON.2015.250
- [5] A. Parriaux, M. Conforti, A. Bendahmane, J. Fatome, C. Finot, S. Trillo, N. Picqué, G. Millot, Spectral broadening of picosecond pulses forming dispersive shock waves in optical fibers, *Opt. Lett.* 42, 3044-3047 (2017); doi: 10.1364/OL.42.003044
- [6] R.V. Kochanov, I.E. Gordon, L.S. Rothman, P. Wcislo, C. Hill, J.S. Wilzewski, HITRAN Application Programming Interface (HAPI): A comprehensive approach to working with spectroscopic data, *J. Quant. Spectrosc. Radiat. Transfer* 177, 15-30 (2016); doi: 10.1016/j.jqsrt.2016.03.005

Sensory Options for Earthquake Victim Recovery

Ruchi Jha¹, Vishvachi¹, Walter Lang¹, Reiner Jedermann¹

¹University of Bremen, Institute for Microsensors, actuators and systems (IMSAS), Germany
 rjha612@gmail.com, vishvachisinha@gmail.com, wlang@imsas.uni-bremen.de,
 rjedermann@imsas.uni-bremen.de

Summary:

This paper examines the feasibility of assembling a low-cost sensor device that could be used in case of an earthquake, building collapse or any structural damage to find humans stuck inside the debris. Several experiments in various scenarios were performed to evaluate different sensors individually and three sensors were selected to build a device capable to detecting humans behind an obstacle. After obtaining a result from the sensory elements used for the device, the probability of finding a human is estimated. The results have been tabulated for different detection ranges of the individual sensors and for the preferred sensor in each collapsed building scenario. The device was tested against two laboratory scenarios with a success rate of 93 percent.

Keywords: Body detection, Victim Recovery, Thermal Vision Camera, Gas sensor.

Background, Motivation and Objective

In case of an earthquake or a structural damage a high-risk challenge is generated in searching and saving lives stuck in the debris. According to medical science an injured casualty has a time of 72 hours to survive, given that they get help on time [1], and time becomes a very crucial factor in discovering the victims inside the rubble.

Conventional devices and methods used in such disasters are mobile video camera, sniffing dogs, and audio devices, but could be time consuming in potentially dangerous situations. Also a prototype from NASA called FINDER has also been very useful in finding people stuck in rubble, but is not available commercially [2]. The objective of this paper is to design a cost-effective system to measure the feasibility of different sensory options that can be implemented to search for human body stuck inside debris of a collapsed building. For this purpose, standard sensors were selected and evaluated to detect typical attributes of a living human body such as odor, heartbeat, sound, motion, breathing and heat signature [3].

New Method

The new device combines the readings of three low-cost sensors for an increased probability of finding human body stuck in debris.

Description of the System

Three candidate attributes were selected for victim detection by cost-efficient market-available sensor: a) motion (*RCWL-0516*,

Doppler Effect based digital motion sensor), b) heat signature (*AMG8833, 8x8 pixel infrared thermal camera*), and c) breathing (*T6-713, non-dispersive infrared CO₂ sensor*). The three selected sensors were integrated into a system consisting of an Arduino MEGA processor, a Raspberry Pi, 800x480 HDMI color display and a Bluetooth module HC05.

Experimental Setup

The Experimental setup was broadly divided into the following parts:

(SN1) Individual testing of sensors:

The CO₂ sensor efficiency tests were conducted by placing a human at 30 cm, 60 cm and 1m distance from the sensor. The average and standard deviation of a series of 10 repeated tests were calculated.

The motion sensor tests were performed for two different scenarios to measure the success rate of the sensor as a function of distance. The tests were kept running for 10 minutes and the results were calculated on the basis of correct recognition of motion.

The infrared thermal camera was tested for the quality of thermal image over distance and exposure to human, provided line of sight was available.

(SN2) We used materials like wood, metal, plastic and cardboard to create a closed setup imitating a collapsed building scenario in an indoor environment.

(SN3) Outdoor setup was created with the same set of obstacles to create an earthquake like scenario.

In all the scenarios it was made sure that only one human is present in the test setup. The efficiency of device with all three sensors integrated together was tested in SN2 and SN3.

Results

(a) *Individual testing of sensors:* A significant change of by presence of a human was only observed (50 ppm), when the CO₂ sensor was placed inside an enclosure (Fig1). During indoor measurements, a slight increase of the average CO₂ concentration was observed by moving towards the human, although the standard deviation was higher than the average change. Outdoor measurements were distorted by changing wind conditions.

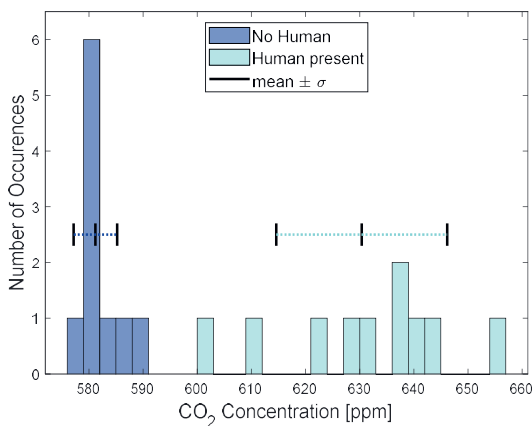


Fig.1. Measured CO₂ concentration inside enclosure

The success rate of motion detection for two commonly made human motions is shown in Fig 2. For up to a range of 4 meters the sensor was able to track both the motion efficiently, but the success rate further declined as the distance between the human and the sensor increased.

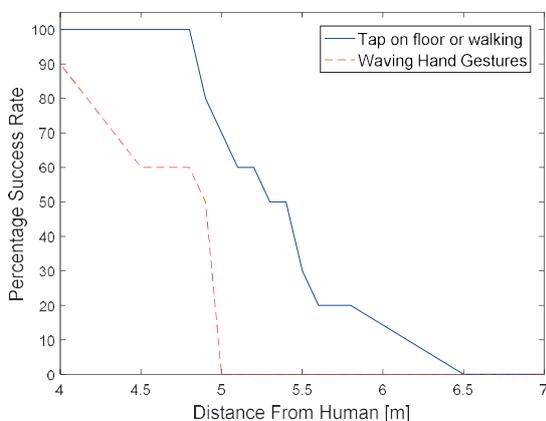


Fig.2. Measured success rate of motion sensor

For AMG8833 camera, it was found that it could detect a human at a range of about 1.5 feet.

(b) Testing of device as whole in collapsed building scenario(s): The device exhibited different behavior. The results from the two multi-sensor scenarios are given in Tab. 1.

Tab. 1: Preferred sensor for Scenario 2 and 3

SN	Preferred sensor and their behavior
2	<p><i>Thermal Camera</i>- Good Images up-to 1.5 feet.</p> <p><i>Motion sensor</i> - Efficient in tracking all movements.</p> <p><i>CO₂ sensor</i> – Able to differentiate the CO₂ values in absence/presence of test victim.</p>
3	<p><i>Thermal camera</i>– worked efficiently, in case of line of sight available.</p>

Discussion

We have evaluated the sensor technologies which could be used for detection of humans. Sensor selection was made on the criteria that there may or may not be line of sight available between the system and the victim in a real earthquake debris. During individual testing of sensors we found that the CO₂ sensor must be placed inside enclosures in the debris or laboratory setup. The motion sensor gave us few false results due to diverse disturbances in open environment. In any case with a line of sight, thermal camera worked efficiently in providing thermal images of trapped human. By integration of the sensors together and testing them as a device in whole, a success rate of 93% for our laboratory test scenarios was obtained. However, in a real world situation, system performance should be improved by using a better motion sensor giving a probability output and thus enabling better algorithms for sensors data fusion.

References

- [1] Huo R, Agapiou A, Brown LJ, The Trapped Human Experiment, NCBI 2011; doi: 10.1088/1752-7155/5/4/046006
- [2] <https://www.jpl.nasa.gov/news/news.php?release=2013-281>
- [3] Di Zhang, Salvatore Sessa, Ritaro Kasai, Evaluation of a sensor system for detecting humans trapped under rubble, doi: 10.3390/s18030852

Evaluation of commercial metal oxide gas sensors for indoor aeration control

J. Zosel¹, M. Mertig¹, D. Deininger², R. Schreiber³, C. Meyer³

¹ Kurt-Schwabe-Institut für Mess- und Sensortechnik Meinsberg e.V., Kurt-Schwabe-Straße 4, 04736 Waldheim, Germany

²Renesas Electronics America Inc., Longmont, CO 8050, USA

³Renesas Germany GmbH, 01069 Dresden, Germany

Summary:

This work reports on measurements with commercially available metal oxide gas sensors (MOX-GS) in different indoor environments together with infrared CO₂ gas sensors (IR-CO₂-GS). From the temporal courses of the MOX-GS a time-dependent CO₂ concentration is estimated ($e(\text{CO}_2)$) by sensor-specific algorithms, which is compared subsequently with the CO₂ concentration, measured with the IR-CO₂-GS. That calculation is based on the hypothesis that humans exhale volatile organic compounds (VOC) parallel to CO₂, which stimulate the MOX-GS. Therefore, a correlation between VOC and CO₂ concentrations can be derived in populated meeting rooms and offices. Measurements in rooms of different sizes and different numbers of attendees confirmed this hypothesis and indicate the possibility to control air condition (HVAC) systems with $e(\text{CO}_2)$ -values as input signals.

Keywords: metal oxide gas sensor, estimated CO₂ concentration, HVAC control

Background, Motivation and Objective

Indoor air quality (IAQ) is of increasing importance for safety and health issues in buildings [1]. Furthermore, an efficient ventilation control in offices, meeting rooms and other indoor environments is fundamental for ideal working conditions and energy saving [2].

Since the air quality is influenced not only by the concentrations of carbon dioxide (CO₂) and humidity (r.H.) but also by the kinds and concentrations of VOC, it is self-evident to investigate beside IR-CO₂-GS also VOC sensitive gas sensors like MOX-GS as signal providers for HVAC control [3]. This approach is also supported by the fact that humans exhale a variety of VOC into indoor air with significant impact to its quality [4].

Description of the Investigation

MOX-GS of the type ZMOD4410 (Renesas Electronic Cooperation) and from two competitors (MX-A/MX-B) were characterized in different indoor air environments of KSI. The monitoring of these sensors was escorted by parallel measurements with four different Infrared (IR)-CO₂-sensors: SCD3x (Senseair AG), K30 (Senseair) and CM1106 (Cubic Sensor and Instrument Co., Ltd.) and MX1102 (Onset Computer Corporation). Four multi-sensor systems (MSS1-4) equally equipped with the sensors mentioned above were operated simultaneously in different indoor environments (offices, meeting rooms and laboratory) over two months and calibrated at start, middle and end of the measurement campaign. The signals of the investigated MOX-

GS were used by algorithms developed by the sensor manufacturer to calculate real-time $e(\text{CO}_2)$ -values, which were correlated for every investigated sensor with the mean value of the IR-CO₂-GS signals $c(\text{CO}_2)_m$. That correlation was quantified by a ratio factor f_c :

$$f_c = \frac{e(\text{CO}_2)}{c(\text{CO}_2)_m} \quad (1)$$

During a measurement the mean value of f_c ($f_{c,m}$) and its percental standard deviation $SD[\%f_{c,m}]$ were determined in the regions $c(\text{CO}_2)_m > 1000$ vol.-ppm and $c(\text{CO}_2)_m < 1000$ vol.-ppm. This limit is known as a threshold for appropriate indoor air quality [5].

For the calibration of the IR-CO₂-GS dry mixtures of CO₂ in synthetic air were used at room temperature, which were monitored also by an Nicolet 8700 FTIR-spectrometer. The MOX-GS were characterized in humidified mixtures of ethanol in synthetic air at room temperature. Both, for calibration and measurements the sensors were positioned in boxes with closed and open lid, respectively, as shown in Fig. 1.

Results

In Fig. 2 the resistance signals of one MOX-GS are provided for the three characterizations at start, middle and end of the measurement campaign. They show a rapid response to the changes of the ethanol concentration, a nearly horizontal plateau and comparably low deviations between the levels at the higher concentrations, indicating a high reproducibility at the adjusted conditions.

The signal rise during the starting period of 3 h in every characterization is caused by the usage of ultra clean air, flushing out the trace concentrations of VOC in the calibration box.

In Fig. 3 the maximum, minimum and mean values of $f_{c,m}$ and $SD[\%f_{c,m}]$ are provided for the complete measurement campaign of MSS1-3, which were operated in offices and meeting rooms without HVAC. The nearer the factor $f_{c,m}$ ranges to 1 and the smaller its relative standard deviation $SD[\%f_{c,m}]$ results, the smaller is the difference between the $e(\text{CO}_2)$ - and the $c(\text{CO}_2)_m$ -values. Since all sensors delivered very similar response curves during characterization, the large differences of $f_{c,m}$ and $SD[\%f_{c,m}]$ between the individual MSS come with the response of the algorithms to the measurement conditions in the different rooms. If the $e(\text{CO}_2)$ -value is intended to be utilized for the regulation of heating, ventilation, and air conditioning systems (HVAC) regulation, its correlation with the $c(\text{CO}_2)_m$ -value above 1000 vol.-ppm (shown in Fig. 3) is much more important than below 1000 vol.-ppm. The finding that in that region all three MOX-GS of the MSS 1-3 deliver $f_{c,m}$ values (white lines in Fig. 1) distributed around the value of $f_{c,m} = 1$ and acceptably low SD values is very encouraging for this application. A comparison of signal courses between measurements with different numbers of attendees in the monitored rooms indicates that the difference between $e(\text{CO}_2)$ - and $c(\text{CO}_2)_m$ values becomes smaller with increasing number of monitored persons. This expectable result was found during all measurements.

References

- [1] A. Cincinelli, T. Martellini, Indoor Air Quality and Health, *Int J Environ Res Public Health* 14(11), 1286 (2017); doi: 10.3390/ijerph14111286.
- [2] T. Leephakpreeda, R. Thitipatanapong, T. Grittiyachot, V. Yungchareon, Occupancy-Based Control of Indoor Air Ventilation: A Theoretical and Experimental Study, *Science Asia* 27, 279-284 (2001); doi: 10.2306/scienceasia1513-1874.2001.27.279.
- [3] D. Ruffer, F. Hoehne, J. Bühler, New Digital Metal-Oxide (MOx) Sensor Platform, *Sensors (Basel)* 18(4), (2018); doi: 10.3390/s18041052.
- [4] J.G. Allen, P. MacNaughton, U. Satish, S. Santanam, J. Vallarino, J.D. Spengler, Associations of Cognitive Function Scores with Carbon Dioxide, Ventilation, and Volatile Organic Compound Exposures in Office Workers: A Controlled Exposure Study of Green and Conventional Office Environments. *Environ. Health Perspect.* 124, 8005–8012 (2015); doi: 10.1289/ehp.1510037.
- [5] Umweltbundesamt, Gesundheitliche Bewertung von Kohlendioxid in der Innenraumlufte, (Bundesgesundheitsblatt - Gesundheitsforschung - Gesundheitsschutz, 2008).

Illustrations, Graphs, and Photographs

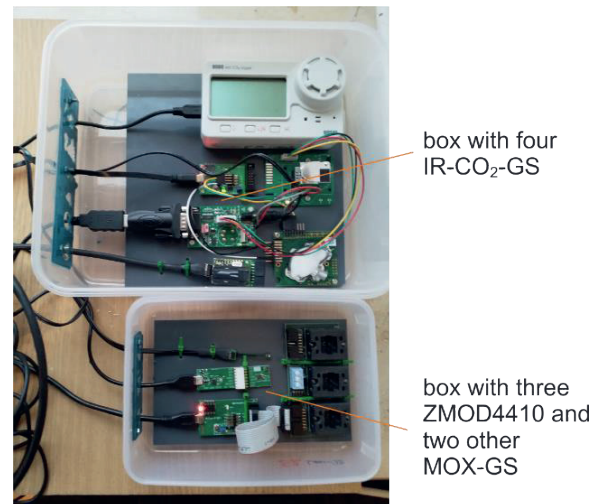


Fig. 1: Image of one of the multi-sensor systems.

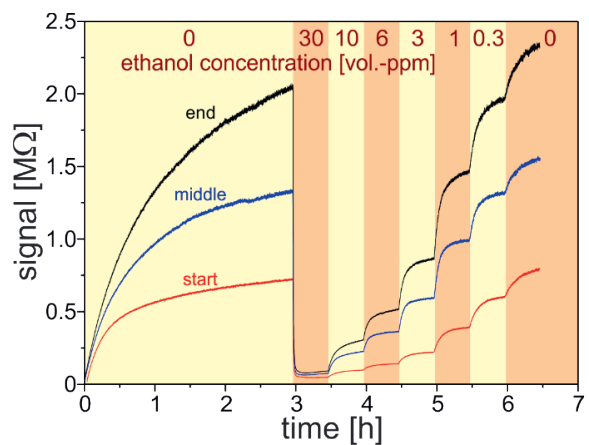


Fig. 2 Response of one ZMOD4410 MOX-GS during characterization in humidified ethanol/air mixtures; r.H. = 30 % at 25 °C.

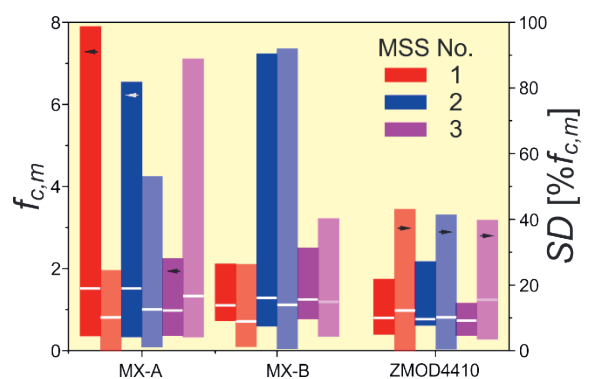


Fig. 3: Ranges of $f_{c,m}$ and $SD(\%f_{c,m})$ for each MOX-GS during the complete measurement campaign, $c(\text{CO}_2)_m > 1000$ vol.-ppm, the mean values of both parameters are indicated with white horizontal lines, the pasty columns indicate the standard deviation SD as labelled by the arrows.

Metal Oxide Nanolayer Decorated Epitaxial Graphene Gas Sensors for Air Quality Monitoring

Marius Rodner¹, Adam Icardi¹, Margus Kodu², Raivo Jaaniso², and Jens Eriksson¹

¹ *Department of Physics, Chemistry and Biology, Linköping University, Linköping, 58183, Sweden*

² *Institute of Physics, University of Tartu, Estonia*

marius.rodner@liu.se

Summary:

Metal or metal oxide decorated two-dimensional material hybrids have been shown to exhibit excellent sensitivity performances if used as chemical gas sensors. We investigated the influence of operating temperature, relative humidity and UV irradiation of various metal oxide nanolayer decorated epitaxial graphene hybrid sensors during exposure to several gases of interest for air quality monitoring. Furthermore, a data treatment method is introduced to further enhance sensor properties.

Keywords: metal oxide, nanolayer, epitaxial graphene, chemical gas sensor, air quality monitoring

Background

Two-dimensional materials like graphene exhibit several excellent properties, which allow the fabrication of gas sensors that can be used for detection of very small gas concentrations. Epitaxially grown graphene on SiC was found to be more sensitive when used as a transducer in a gas sensor than commercially available graphene produced through chemical vapor deposition (CVD) [1]. One method to increase the sensitivity and/or selectivity to specific gases, is the combination of various sensing materials or the decoration of a transducer with a metal oxide nanostructure on top [1,2]. Here, we show that combining epitaxial graphene on SiC with nanolayers (NLs) of well-studied sensing materials leads to enhanced sensitivity towards several gases of interest for air quality monitoring.

Method and materials

Metal oxide decorated epitaxial graphene hybrids have been produced. Nanolayers (few atoms thick) of copper oxide (CuO), iron oxide (Fe₃O₄), vanadium pentoxide (V₂O₅) and zirconium dioxide (ZrO₂) have been used as decoration materials, deposited with pulsed laser deposition [1]. The sensor resistance is measured over time and the response is defined as the difference in % between the saturated/last resistance signal compared to the baseline resistance before gas exposure. The response of the different hybrid sensors towards gases of interest for air quality monitoring with changing operating temperature, relative humidity and irradiation with UV light during the gas measurements was studied. To speed up the sensor response,

the first-order time-derivative of the sensor signal is used as an additional response signal.

Results

Normally, chemical gas sensors need a certain operating temperature before they react with the target gas and an increase in temperature (up to a limit) means an increase in response. An exposure at 50, 100, and 150 °C at zero relative humidity (RH) towards 200 ppb benzene (C₆H₆) and formaldehyde (CH₂O) shows that only at 150 °C, all four sensors were able to sense both gases. While CuO was able to detect gas pulses even down to 50 °C, Fe₃O₄ and V₂O₅ needed at least 100 °C. In contrast, for an exposure towards 25 ppm ammonia (NH₃) at 50 %RH, at 50, 75, 100 and 125 °C, only ZrO₂ has its highest response at 125 °C, while all other sensors exhibit the highest response as 50 °C. While a higher sensor response is normally desired, this can be offset by disadvantages like slower time constants or increased signal noise. For example, only exposures at 125 °C lead to a steady-state response during the 30 min gas exposure. τ_{63} , extrapolated using an exponential fit, gradually increases from approximately 150 s at 125 °C up to 550 s at 50 °C on average.

Besides the operating temperature, relative humidity in the ambient can be another critical parameter for the sensor response of some material/gas combinations. It is known that many metal oxides exhibit a cross-sensitivity towards RH and a higher level of RH in the ambient usually results in a lower gas sensitivity, as the target gas molecules compete with water molecules for available adsorption sites. An exposure towards 200 ppb of C₆H₆ and CH₂O with

50 %RH leads to a decrease in response of on average about one order of magnitude compared to dry conditions. V_2O_5 does not react at all when humidity is introduced. For the case of NH_3 , all sensors except the one functionalized with V_2O_5 exhibit a decrease in sensitivity when changing from a dry to a humid environment, e.g. 20 %RH. A further increase in humidity increases the response again for some samples, even exceeding the response at 0 %RH (ZrO_2). This increase in response with increasing RH and the increase with lower temperatures could be due to a reaction with OH groups or of products of reactions from OH groups and NH_3 , leading to a higher overall response, which is not necessarily only related to the NH_3 exposure itself. This phenomenon was shown to occur for metal oxide gas sensors when operating them at relatively low temperatures in a humid environment [3,4].

The sensitivity and speed of response of a chemical gas sensor was shown to be enhanced through UV irradiation for many different material/gas combinations [5]. Moreover, it was shown that UV irradiation can be used to clean graphene surfaces, thus freeing active sites for target gas interaction [6]. Figure 1 summarizes the responses towards a 30 min exposure of 25 ppm NH_3 at 50 %RH without and with the influence of 355 nm UV irradiation. A clear trend can be observed as the relative sensor response is highest with UV irradiation and decreases with no irradiation for all sensors except ZrO_2 for which the response stays approximately constant. Changing the UV irradiation wavelength from 355 to 265 nm has no significant effect on the sensor response magnitude for the tested materials. However, the shorter wavelength, with its higher energy level, has a stronger impact on the speed of response.

A method to additionally achieve faster time constants is the use of the sensor signal's first-order time-derivative [7]. This is exemplarily shown as the red (lower) curve in Fig. 2, where a Fe_3O_4 NL decorated epitaxial graphene sensor was exposed to 25 and 100 ppm of NH_3 at 75 °C at 50 %RH. The peaks arrive much faster and are also concentration dependent, making it useful as a feature in multivariate analysis [7,8]. Moreover, this signal is more robust against varying exposure and relaxation times with a very stable baseline.

Chemical gas sensors are highly tailorable systems. Exploiting the excellent sensitivity of epitaxial graphene, combining it with a nanostructured metal oxide and adjusting the measurement conditions accordingly to the desired application can lead to high performance gas sensor devices.

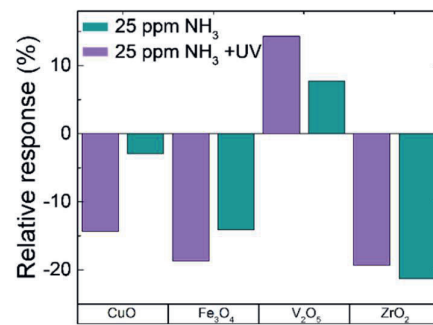


Fig. 1. Relative response towards 25 ppm NH_3 with and without 355 nm UV irradiation.

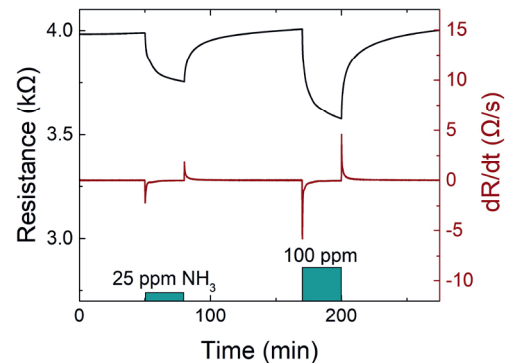


Fig. 2. Resistance over time (upper black) of Fe_3O_4 NL decorated epitaxial graphene sensor with corresponding first-order time-derivative signal (lower red) towards 25 and 100 ppm NH_3 at 75 °C and 50 %RH.

References

- [1] M. Kodu, A. Berholts, T. Kahro, J. Eriksson, R. Yakimova, T. Avarmaa, I. Renge, H. Alles, R. Jaaniso, *Sensors*. 19 (2019) 1–17. doi:10.3390/s19040951.
- [2] M. Rodner, D. Puglisi, S. Ekeroth, U. Helmersson, I. Shteplyuk, R. Yakimova, A. Skallberg, K. Uvdal, A. Schütze, J. Eriksson, *Sensors (Switzerland)*. 19 (2019). doi:10.3390/s19040918.
- [3] N. Barsan, U. Weimar, *J. Electroceramics*. 7 (2001) 143–167. doi:10.1023/A:1014405811371.
- [4] E.C. Dickey, O.K. Varghese, K.G. Ong, D. Gong, M. Paulose, C. a Grimes, *Sensors*. 2 (2002) 91–110. doi:10.3390/s20300091.
- [5] E. Espid, F. Taghipour, *Crit. Rev. Solid State Mater. Sci.* 42 (2017) 416–432. doi:10.1080/10408436.2016.1226161.
- [6] A. Berholts, T. Kahro, A. Floren, H. Alles, R. Jaaniso, *Appl. Phys. Lett.* 105 (2014). doi:10.1063/1.4899276.
- [7] C.H. Wu, G.J. Jiang, C.C. Chiu, P. Chong, C.C. Jeng, R.J. Wu, J.H. Chen, *Sensors Actuators, B Chem.* 209 (2015) 906–910. doi:10.1016/j.snb.2014.12.066.
- [8] S. Marco, A. Gutierrez-Galvez, *IEEE Sens. J.* 12 (2012) 3189–3214. doi:10.1109/JSEN.2012.2192920.

Evaluation of Indoor Air Quality by High School Students

Sebastian Höfner¹, Michael Hirth², Jochen Kuhn², Benjamin Brück³, Andreas Schütze¹

¹Laboratory for Measurement Technology, Saarland University, Germany

²WG Didactics of Physics, Technical University Kaiserslautern, Germany

³Student Research Center Saarlouis, Germany

s.hoefner@lmt.uni-saarland.de

Summary:

To increase environmental awareness of high school students, age 12 to 18, four experiments were developed to investigate indoor air quality (IAQ) and demonstrate influencing factors. Students learn about the functionality of different gas and PM sensors and carry out measurements of different pollutants or materials used in everyday life. They also experience the influence of human breath on IAQ.

Keywords: air quality, environmental awareness, volatile organic compounds, particulate matter, CO₂

Introduction

Air pollution is the single largest environmental health risk in Europe with over 400.000 deaths per year in 2018 [1]. According to the World Health Organization (WHO) air pollution is a major cause for heart diseases and strokes, as well as lung diseases and Alzheimer's [2]. Air quality (AQ) monitoring is important to avoid health risks, especially in the interior, because people spend up to 90% of their time indoors [3]. Despite increasing environmental awareness in recent years, the concept of AQ and especially Indoor Air Quality (IAQ) is often rather diffuse and abstract, especially for teenagers. Indoor air pollutants are usually invisible and odourless, and therefore not detectable with human senses, hence deterioration of IAQ is often not noticed. To create awareness about IAQ, the outreach project "SUSmobil" wants to teach students, age 12 to 18, about air quality and how (I)AQ is determined with low-cost sensors [4]. For this purpose several experiments ("stations") were developed, each of which focuses on different AQ parameters, e.g. particulate matter (PM), volatile organic compounds (VOCs) as well as CO₂ and the sum parameter total VOC (tVOC) as indicators for IAQ.

Experimental Setup

Students work with a circuit board containing three different sensor types to evaluate IAQ, fig. 1. The board is equipped with (1) an infrared absorption sensor to detect CO₂, which also measures temperature and relative humidity, (2) a laser scattering sensor for PM, and (3) a metal oxide semiconductor (MOS) gas sensor to detect VOCs. All sensors are controlled by a microcontroller and the data is displayed with a specially developed software. Students perform

four experiments, so called "stations", during which they learn about different aspects of IAQ.

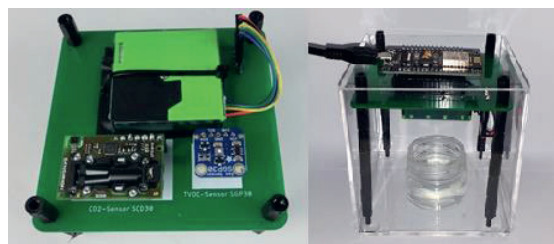


Fig. 1. Left: Circuit Board with three sensors to evaluate IAQ. Right: Investigation of diluted ethanol.

Station 1 – Sensor Test

In the first station, the students familiarize themselves with the software by checking the functionality of the sensors. The students have to think about their own test methods for testing the sensors and write down their procedure. For example, a sudden increase of CO₂ and VOC concentrations is observed when blowing on the board. The PM sensor can be tested by simply rubbing a paper napkin near the sensor.

Station 2 – VOC

The second station is divided into two parts both addressing VOCs. First, the students' nose competes against the gas sensor. The students are tasked to order five different dilutions of ethanol according to their concentration. Three of the five concentrations are below the human odour threshold, whereas the VOC sensor can discriminate all of them, fig. 1 (right). This experiment creates awareness for the need for objective measurements of air pollution.

The second part deals with VOC emissions of everyday products like paints, markers, glues and floors. For every category two examples

with high and low emissions, respectively, were chosen. The students classify the samples on a scale from 0 (“undetectable”) to 6 (“extremely strong”) according to the odour intensity. Then the VOC sensor measures the VOC emission of the samples. Typical results are shown in fig. 2.

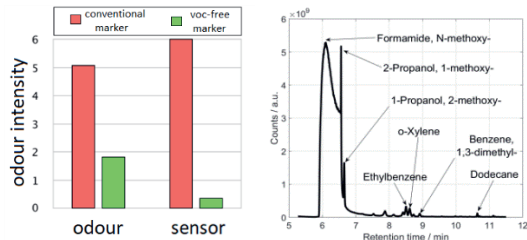


Fig. 2. Left: Odour intensity of two different markers according to the human nose and a VOC sensor from 0 (“undetectable”) to 6 (“extremely strong”). Right: GC-MS reference measurement of the headspace composition of conventional markers.

Both assessments are compared with the actual headspace composition of each material, determined by the reference method GC-MS (gas chromatography–mass spectrometry). The hugely different VOC emissions from objects with the same purpose demonstrate that consumers should consider health aspects, i.e. by taking notice of ecolabels like the “Blue Angel”.

Station 3 – Simulated Interior

The third station deals with IAQ in general. In a first experiment, students learn the function principle of infrared absorption sensors for CO₂.

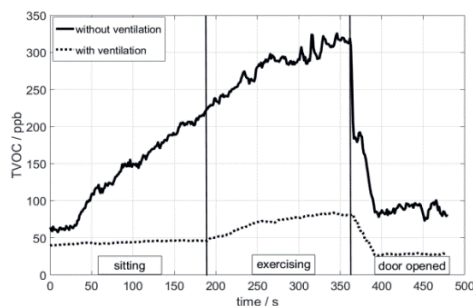


Fig. 3. VOC concentrations over time in the walk-in chamber with (dotted) and without (solid) ventilation.

To simulate an indoor environment, a walk-in chamber was constructed, which can be ventilated by fans. The students track the course of AQ parameters like temperature, humidity, CO₂ and VOCs in the chamber while sitting and doing physical exercises, with and without ventilation. Typical results are shown in fig. 3. Within a few minutes, VOC and CO₂ concentrations reach high values without ventilation, whereas both stay low with ventilation. Students compare sensor results with their senses and, based on their measurements, extrapolate these results to a normal sized room. This experiment shows the importance of regular ventilation to ensure good IAQ.

Station 4 – Particulate Matter

Again, the function principle of a PM sensor is demonstrated in a first experiment. Then, the students investigate PM emissions during cleaning of blackboards with dry and wet sponges, cf. fig. 4.

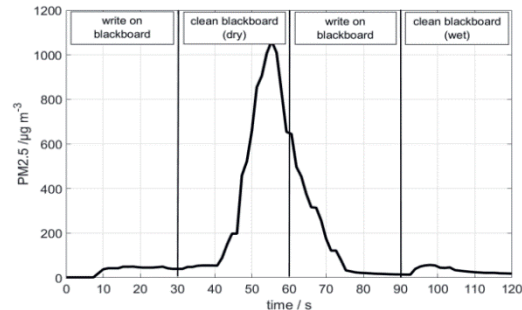


Fig. 4. PM emissions during writing on blackboards (0 – 30 s, 60 – 90 s) and during cleaning with dry (30 – 60 s) and wet (90 – 120 s) sponges, respectively.

Students spend considerable time in classrooms where chalk and blackboards are used. Each dry wiping of the blackboard generates large amounts of PM, whereas the emission of PM remains low when wiping wet. This experiment sensitizes to everyday sources of PM.

Conclusion

In order to convey a multifaceted picture of the subject of environmental metrology, the students perform various experiments addressing different AQ aspects. Students receive information about harmful and environmentally relevant gases and pollutants as well as sources and limit values according to the WHO. Experiments with gas and particle sensors raise environmental awareness and show simple ways to maintain or improve indoor air quality.

Acknowledgment

SUSmobil is sponsored by DBU – Deutsche Bundesstiftung Umwelt.

References

- [1] European Environment Agency, Air quality in Europe — 2018 report, *EEA Report No 12 (2018)*, ISBN: 1977-8449
- [2] WHO, Burden of disease from ambient air pollution for 2012 — summary of results (2014), http://www.who.int/phe/health_topics/outdoorair/databases/AAP_BoD_results_March2014.pdf accessed 21 January 2020.
- [3] European Environment Agency, The European environment — state and outlook (2018), doi: 10.2800/777411
- [4] Höfner, S., Schütze, A., Brück, B., Hirth, M., Kuhn, J. (2019). Citizen Science für Schüler*innen: Durchführung von Umweltstudien mit Smartphone und mobiler Messtechnik, 20. *GMA/ITG Fachtagung Sensoren und Messsysteme*, S. 476 – 481, doi: 10.5162/sensoren2019/6.1.5

Semi-automatic Measurement Device for Long-Term Monitoring of Ammonia in Gas Phase

Kornelia Gawlitza¹, Sergej Johann², Maria Mansurova¹, Harald Kohlhoff², Carlo Tiebe², Jérémy Bell¹, Matthias Bartholmai², Knut Rurack¹

¹ Div. 1.9 Chemical and Optical Sensing, Federal Institute for Materials Research and Testing (BAM), Richard-Willstätter-Str. 11, 12489 Berlin, Germany,

² Div. 8.1 Sensors, Measurement and Testing Methods, Federal Institute for Materials Research and Testing (BAM), Unter den Eichen 87, 12205 Berlin
kornelia.gawlitza@bam.de

Summary (max. 6 lines):

The present paper describes the development of a sensor material that changes its fluorescence in the presence of gaseous ammonia in a relevant concentration range. The implementation into a semi-automatic gas measurement device enables low-cost, precise, simple and fast monitoring of low concentrations of harmful gases, like ammonia, and hence can help to improve the climate monitoring in livestock housing, barns or stables.

Keywords (max. 5): spectroscopy, embedded sensor, environment, air quality

Introduction

Extensive emission of ammonia into the air is known to be a crucial problem since years. Most of the emitted ammonia is generated in the agriculture sector (up to approx. 95 %). Even in the low concentration range does ammonia not only smell intensively but it also has a huge ecological and climatic relevance. In addition, the EU regulation on national emission maxima (NEC-Directive 2016/2284) involves a reduction of ammonia emissions by 29 % in 2030 compared to 2005, mainly to improve animal husbandry. The German Federal Ministry for the Environment, Nature Conservation and Nuclear Safety specifies a limit concentration value in an exhaust gas of 30 mg m⁻³ equal to 41 μmol mol⁻¹ for ammonia [1].

The present work contributes to improve the determination of ammonia in air, for instance through monitoring barn climate, to become more precise, less expensive, simpler and faster. The production of a chemical sensor matrix changing its optical properties in the presence of gaseous ammonia and its implementation into an in-house-developed electronic device usable in the field is described.

Chemical Sensor Matrix

The basic component of the chemical sensor matrix is the fluorescent signaling unit, 1,3,5,7-tetramethyl-2,6-diethyl-boron-dipyrrromethene

(BODIPY) or dye **1**, used in the presented study (Fig. 1). This dye was already described in previous publications in which it has been used for the development of ammonia and pH sensors [2-4], especially due to its unique properties like high photostability, high fluorescence quantum yields and excitation and emission maxima at reasonably long wavelengths in the visible spectral range (529 nm and 545 nm respectively).

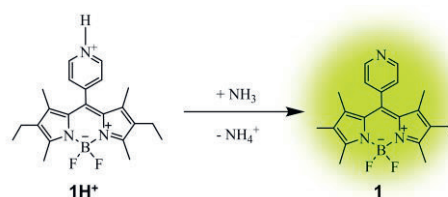


Fig. 1. Scheme of the sensor dye **1**.

The preparation of the sensor material is described in detail elsewhere [2]. Briefly, the wells of a black 96-well microtiter plate with a transparent bottom were filled with 20 μL of a hydrogel-ethanol-water-mixture and 50 μL of **1H⁺** in ethanol (1 mM) with a 12 h drying period in between and in the end. Finally, the plate was sealed with an aluminum foil to avoid contamination before the actual measurement.

Electronic, Mechanical and Optical System

The Fluorescence Spectrum Gas Injection Microtiter Plate Measuring Device (FS-GIMMD) (Fig. 2) was to hold 6 times 96-well microtiter

plates with a transparent bottom which are hermetically sealed with an aluminum foil cover. In total, 567 measurements can be performed with one fully equipped device. Since the prepared plates can be easily replaced by untrained personnel, the setup is suitable for long term tracking of the analyte, for instance to monitor the concentration of ammonia in barns. Each well contains the sensor material, embedded in a hydrogel matrix, being illuminated by an excitation light (LED 500 nm) to produce a fluorescence signal which changes when reacting to ammonia. An automated mechanical-electrical device initiates a given gas mixture and thus simulates different concentrations of gaseous ammonia and allows varying the defined relative humidity. A detailed description of the device and the gas mixing system can be found elsewhere [2]. The measurements were performed by piercing the aluminum cover foil with two needles and passing a defined ammonia concentration over the sensor material for a defined time before moving to the next position where the identical procedure was carried out.

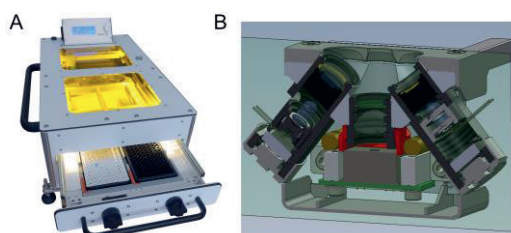


Fig. 2. FS-GIMMD prototype design (A) and a scheme of the optical head (B).

Results and Discussion

As already reported previously, dye **1** is highly fluorescent in the neutral state while protonation induces a quenching of the emission (Fig. 1) [2]. The protonated dye $1H^+$ was embedded in a suitable hydrogel matrix being polar and humid enough to accumulate gaseous ammonia. With a pKa of 2.15 ammonia deprotonates $1H^+$ leading to a fluorescence increase at 570 nm ($\lambda_{ex} = 500$ nm). First attempts with the FS-GIMMD and the optimized sensor material have been done with increasing concentrations of ammonia from 0 to 20 $\mu\text{mol mol}^{-1}$ and at relative humidity of 0 %, 10 % and 25 %. The entire emission range (525 nm to 800 nm) is registered for 10 minutes which was determined to be the optimum response time after performing several runs up to 60 minutes. Fig. 3A shows the course of the spectra measured with the FS-GIMMD for one sensor material purged with 20 $\mu\text{mol mol}^{-1}$ ammonia over 10 minutes. It is clearly visible that the fluorescence maximum at 570 nm increases when the gaseous ammonia is present. Performing the same experiment with increasing concentrations of ammonia (0,

1, 5, 10, 20 $\mu\text{mol mol}^{-1}$) followed by analyzing the change in fluorescence at 570 nm as a function of the concentration nicely demonstrates a linear increase (Fig. 3B). It is also shown that adjusting different relative humidity results in different calibration curves, indicating that the humidity needs to be tracked in parallel to determine real ammonia concentrations.

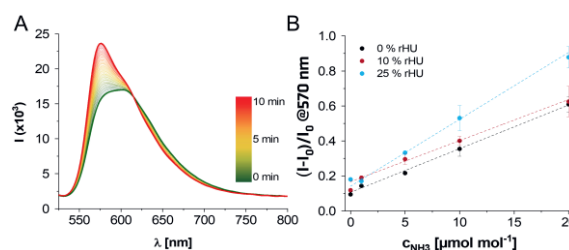


Fig. 3. Time dependent response of sensor material in presence of 20 $\mu\text{mol mol}^{-1}$ ammonia (A) and change in fluorescence at different ammonia molar fractions and relative humidity after 10 min (B) measured with the developed FS-GIMMD ($\lambda_{ex} = 500$ nm).

In addition, the microtiter plates have been stored for 6 months and showed unchanged performance to freshly prepared once, verifying the long-term stability in the applied format.

Conclusion

In conclusion, the foundation was laid for a semi-automated approach to long-term monitor and hence to regulate low concentrations of gaseous ammonia in livestock housing, barns or stables, in an economic, simple, precise and fast manner. After the planned implementation of the humidity dependent calibration curves, the sensor device can be adapted to other relevant harmful gases which enables the use in a broad range of applications.

References

- [1] https://www.umweltbundesamt.de/sites/default/files/medien/1/dokumente/taluft_stand_200207241.pdf, 23.01.2020
- [2] S. Johann, H. Kohlhoff, K. Gawlitza, J. Bell, M. Mansurova, C. Tiebe, M. Bartholmai, Semi-automatic Gas Measurement Device based on Fluorescent Multi-gas Sensors, *IEEE Sensors*, 1-4, (2019); doi: 10.1109/SENSORS43011.2019.8956664
- [3] K. Gawlitza, C. Tiebe, U. Banach, R. Noske, M. Bartholmai, K. Rurack, Novel sensor for long-term monitoring of ammonia in gas phase, *13. Dresdner Sensor-Symposium Proceedings*, 272–276 (2017); doi: 10.5162/13dss2017/P4.02
- [4] R. Gotor, P. Ashokkumar, M. Hecht, K. Keil, K. Rurack, Optical pH Sensor Covering the Range from pH 0–14 Compatible with Mobile-Device Readout and Based on a Set of Rationally Designed Indicator Dyes, *Analytical Chemistry* 89, 8437–8444 (2017); doi: 10.1021/acs.analchem.7b01903

Glass Electrode Half-cells for Measuring Unified pH in Water-organic Solvent Mixtures

Agnes Heering, Frank Bastkowski, Steffen Seitz
 Physikalisch-Technische Bundesanstalt, Bundesallee 100, 38116 Braunschweig, Germany
 agnes.heering@ptb.de

Summary:

Unified pH enables to compare acidities between any given solvent or mixtures thereof. So far only metal solid contact glass electrode half-cells have been used. Three commercial, conventional glass electrode half-cells with inner liquid filling were used to investigate the dependence of the unified pH scale on the different electrodes.

Keywords: unified pH, absolute acidity, glass electrodes, half-cells, organic solvents

Introduction

pH is an important factor in many processes. pH measurement in non-aqueous solvents has several problems and interpretation of obtained pH values is complicated. Because of the significant dependence of the proton activity on the solvent, every medium has its own pH scale. Thus, pH values measured in different solvents cannot be compared. Therefore, it is impossible to differentiate acidities of solutions made with different solvents. Unified pH [1] allows direct comparison of acidities in all media and is measured potentiometrically [2] by measuring directly the potential between two glass electrode half-cells.

The unified acidity scale uses an ideal proton gas as a theoretical, but universal reference point and its absolute chemical standard potential is set to zero. In solutions, the chemical potential of the proton is reduced by interaction with its environment which defines the pH scale of a specific solution [1]. However, the scales of different solutions can be related to each other through their common reference to the proton gas. Thus, their respective acidities can be compared if the pH values are transferred to this common, unified pH scale.

Until now all the unified acidities have been measured with metal solid contact glass electrode half-cells [3]. These electrodes give stable and reproducible signals in non-aqueous solvents and their mixtures with water. From a metrological perspective it is desirable that a measurand does not depend on the instrument used to measure it. Therefore, we investigated the dependence of unified pH measurement results on various kinds of electrodes that are

designed for non-aqueous solutions and that are commonly available.

Method

The unified pH was measured in aqueous mixtures of ethanol. Aqueous standard buffers with pH 4.01, 7.00 and 9.00 were used for validation. The cell used (1) was like the one used in [2], however, a slightly different, because an almost ideal ionic liquid (triethylpentylammonium bis(trifluoromethylsulfonyl)imide, [N₂₂₂₅][NTf₂]) [4-5] was used to eliminate the liquid junction potential.



The potential ΔE measured between two glass electrodes (GE) was converted into ΔpH with eq (2):

$$\Delta\text{pH} = \frac{\Delta E + \text{Int}_{\text{RE}} - \text{Int}_{\text{WE}}}{\text{slope}_{\text{average}}} \quad (2)$$

Where Int_{RE} and Int_{WE} are the intercepts of the reference (GE₁) and working electrode (GE₂), respectively, and $\text{slope}_{\text{average}}$ is the average slope of the two electrodes. Slopes and intercepts are obtained when the potential of an electrode is measured against a reference electrode in aqueous standard buffers.

A so-called ladder approach [2] is used to assign absolute pH values (pH_{abs}) to the measured solutions based on measured ΔpH values ($\Delta\text{pH}_{\text{abs}}$) between different combinations of the solutions in the cell. The pH_{abs} values are calculated by applying a least-squares minimization technique to the measured $\Delta\text{pH}_{\text{abs}}$ values. The consistency standard deviation of the pH ladder is used to evaluate the mismatch between the

measured $\Delta\text{pH}_{\text{abs}}$ and assigned pH_{abs} values. An example of such a ladder is shown in Fig. 1, which shows the measured $\Delta\text{pH}_{\text{abs}}$ values of typical aqueous standard buffers (borate, phosphate and phthalate), the assigned pH_{abs} values and, for comparison, the pH values known from primary pH measurements.

Metal solid contact glass electrodes from Izmeritelnaya tekhnika and glass electrode half-cells with inner liquid filling from Horiba, Metrohm and Mettler-Toledo were investigated. Two cells of each manufacturer were used. All measurements were done at 25 °C.

Buffer pH	pH_{abs}	$\Delta\text{pH}_{\text{abs}}$
9.00	9.00	
7.00	7.00	2.01
4.01	3.92	3.09
		5.07

Fig. 1. pH ladder with aqueous standard buffers. Electrodes from Horiba. Buffer pH 7 was fixed.

Results

The consistency standard deviation, s , is the main characteristic to evaluate the suitability of electrodes. It is affected both by the reproducibility and the stability of the signal. All electrodes give acceptable results in standard aqueous buffers. However, the results from water-organic solvent mixtures are not as good. Differences in the assigned pH_{abs} values can be up to one pH unit.

Tab. 1: pH_{abs} results with water-ethanol mixtures. Percentages given in mass. Buffers pH 7.00 and 4.01 were fixed.

Electrode	50% EtOH	80% EtOH	s
Metrohm 6.0150.100	7.78	8.87	0.10
Horiba Scientific/Laqua Model 1076A-10C	7.38	9.01	0.16
Mettler-Toledo DG300-SC	6.95	8.16	0.13
Izmeritelnaya tekhnika EST-0601	7.44	9.18	0.07

Although the electrodes are meant for non-aqueous solvents, they give quite unstable reading, when used in the investigated cell (1). The drift can be more than 30 mV/h depending on the pair of solvents measured. The higher the content of organic solvent, the less stable is the reading. An example of the stability of the potential is shown in Fig. 2.

The metal contact glass electrodes perform better compared to the electrodes with inner

filling. Work is still in progress to evaluate the cause of inconsistency between the different electrodes and to improve the measurement procedure.

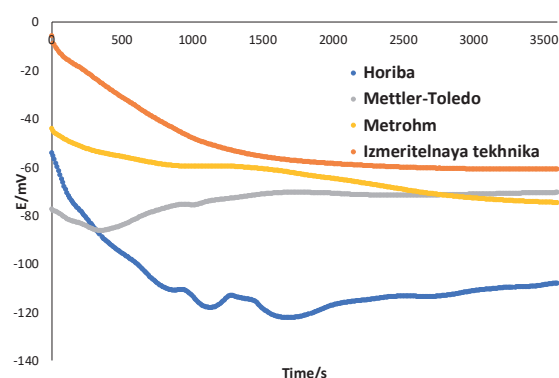


Fig. 2. Stability of potential measured between 80 m% ethanol and 50 m% ethanol during 1 h.

References

- [1] D. Himmel, S. K. Goll, I. Leito, I. Krossing, A Unified pH Scale for All Phases, *Angewandte Chemie International Edition* 49, 6885–6888 (2010); doi: 10.1002/anie.201000252
- [2] A. Suu, L. Jalukse, J. Liigand, A. Kruve, D. Himmel, I. Krossing, M. Rosés, I. Leito, Unified pH Values of Liquid Chromatography Mobile Phases, *Analytical Chemistry* 87, 2623–2630 (2015); doi: 10.1021/ac504692m
- [3] A. A. Beliustin, A. M. Pisarevsky, G. P. Lepnev, A. S. Sergeyev, and M. M. Shultz, Glass Electrodes: A New Generation, *Sensors and Actuators B* 10, 61–66 (1992); doi: 10.1016/0925-4005(92)80012-M
- [4] V. Radtke, A. Ermantraut, D. Himmel, T. Koslowski, I. Leito, I. Krossing, The Ideal Ionic Liquid Salt Bridge for the Direct Determination of Gibbs Energies of Transfer of Single Ions, Part I: The Concept, *Angewandte Chemie International Edition*. 57, 2344–2347 (2018); doi: 10.1002/anie.201707333
- [5] A. Ermantraut, V. Radtke, N. Gebel, D. Himmel, T. Koslowski, I. Leito, I. Krossing, The Ideal Ionic Liquid Salt Bridge for Direct Determination of Gibbs Energies of Transfer of Single Ions, Part II: Evaluation of the Role of Ion Solvation and Ion Mobilities, *Angewandte Chemie International Edition*. 57, 2348–2352 (2018); doi: 10.1002/anie.201707334

Development of an Universal Measuring Instrument for Quality Monitoring of Ultrapure Water

S. Schäfer¹, K. van Dyk², J. Warmer¹, D. Schulze², T. C. Schmidt³, P. Kaul¹

¹ *Bonn-Rhine-Sieg University, Von-Liebig-Str. 20, 53359 Rheinbach/Germany*

² *Innovatec Gerätetechnik GmbH, Von-Liebig-Str. 6, 53359 Rheinbach/Germany*

³ *University of Duisburg-Essen, Universitätsstr. 5, 45141 Essen*

sara.schafer@h-brs.de

Summary:

This work presents the development of a measuring system for the quality control of ultrapure water. The new systems combines ozonation and UV radiation for the oxidation of organic substances. The change in conductivity caused by the oxidation is furthermore correlated with the TOC of the solution.

Keywords: TOC, ultrapure water, ozone, ozonation, AOP

Introduction

The quality of ultrapure water is of particular importance in the pharmaceutical and semiconductor industry. Due to its unique properties it serves as a solvent or starting product for pharmaceuticals and is also used to clean surfaces in the production of high-precision components in semiconductor manufacturing [1]. For this reason, water quality monitoring is of utmost importance and a universal measuring instrument is required.

One method for monitoring the quality of ultrapure water is the measurement of the total organic carbon (TOC) in the water as organic substances are the most common contaminants in water. TOC comprises all organic compounds present in water. For water used in the pharmaceutical industry not only the TOC content but also the temporal development of the TOC due to bacterial growth is a parameter of interest concerning the quality control [2]. Boundary limits and standards for the analysis of TOC are defined by the European Pharmacopeia or the German Institute for Standardization [3] [4].

Conventional methods of TOC determination are based either on thermal oxidation of carbonaceous substances or on wet chemical oxidation. In the latter case oxidation is carried out either by persulfate or UV radiation [5]. All these systems are based on the oxidation of the present organic carbon (OC) and the subsequent detection of the resulting CO₂.

The presented new developed system (**Fehler! Verweisquelle konnte nicht gefunden werden.**) combines two standard methods of oxidation. The oxidation is performed by ozonation in

combination with UV radiation. In contrast to conventional devices in which Hg-vapor lamps are used for UV irradiation, SMD LEDs are used. This enables to reduce the size of the construction considerably. The combination of ozonation and UV-radiation leads to an advanced oxidation process and a significant increase in the oxidation power of the entire system. The system offers three main advantages: it does not require the addition of chemicals - ozone is generated in situ and decomposes without leaving residues and the new system is of significantly smaller footprint and can therefore be easily used at various locations. In addition, it enables online monitoring of the TOC as conductivity is permanently measured.

Experimental

The core of the setup is a 200 mm long quartz glass tube with an inner diameter of 4 mm. This tube serves as reaction chamber. It is wedged between two PTFE blocks. Ozone is generated in situ in water with a so-called "ozone microcell (OMC)", developed by the company Innovatec Gerätetechnik GmbH [5].

Water from an ultrapure water system passes the ozone generator into the quartz glass tube. For irradiation, five SMD LEDs from Neumüller [6] with a wavelength of 275 nm are used. The first conductivity measuring point (C₁) is placed in front of the entrance of the glass tube. After the irradiation section, the gas bubbles are separated from the water by a PTFE membrane. Thereafter, the conductivity is measured a second time (C₂). Furthermore, the water temperature is measured with a Pt1000 sensor.

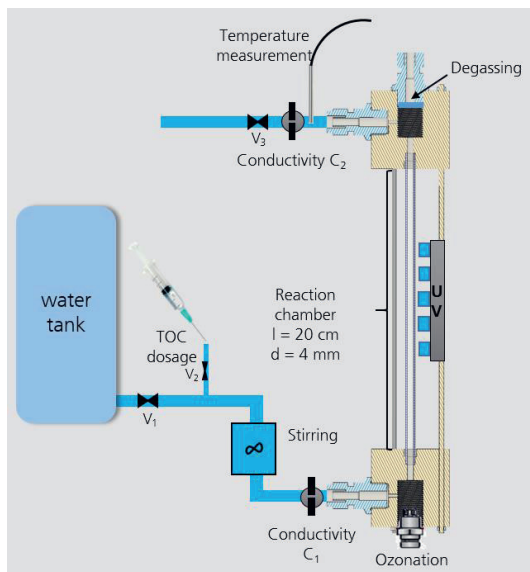


Figure 1: Schematic illustration of the sensor design

The measuring principle is a conductance measurement while the TOC of the solution is oxidized. For this purpose, a defined quantity of OC is permanently added with a syringe pump to the ultrapure water flow. Variation in volume flow of the syringe pump leads to a variation in TOC concentration.

In all experiments 2-propanol serves as source of organic carbon and a constant ozone cell current is applied.

In a five-time repetition, the solution is oxidized with an optical power of 32 mW. In each repetition, LEDs are switched on for two minutes followed by three minutes without UV irradiation. The conductivity and temperature of the water are permanently recorded.

Results

The change in conductivity caused by the oxidation of the TOC solution gives information about the TOC concentration in water. Concentration-dependent measurements are used to correlate the TOC with the change in conductivity as shown in the following figure.

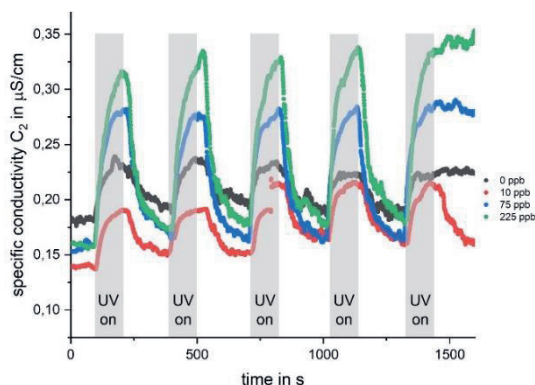


Figure 2: Overlay of four measurements of differently concentrated TOC-solutions, five repetitions

The figure shows an overlay of the results of the measurement of four differently concentrated solutions (0 ppb, 10 ppb, 75 ppb and 225 ppb). The irradiation periods are marked by grey bars (see Figure 2 "UV on").

It is clearly apparent from that figure that conductivity increases with increasing initial OC concentration. This becomes even clearer by comparing the first 100 seconds of the increase in conductivity, which is illustrated in Figure 3.

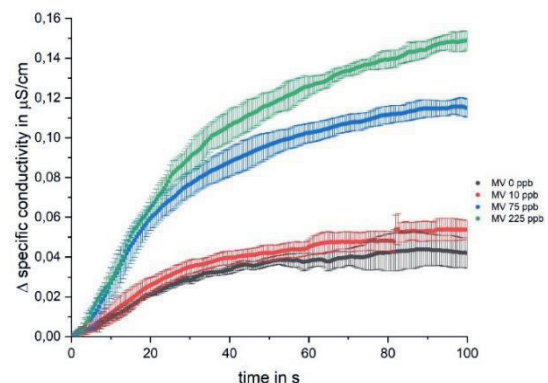


Figure 3: Mean values and standard deviations of normalized TOC measurements while radiation

The mean increase in conductivity is plotted as a function of time for the four different measurements. The irradiation of the ozonated water leads to the formation of highly reactive hydroxyl radicals which furthermore react to form acidic oxidation products. The more OC is added, the higher the increase in conductivity. Even the solution without OC addition shows an increase during oxidation, which is attributed to a residual amount of impurities in the water.

References

- [1] T. Menzel, *Verfahrenskonzepte zur Herstellung von Reinstwasser in der pharmazeutischen und Halbleiter-Industrie*, Wiley-VCH Verlag GmbH & Co. KGaA (2006); doi: 10.1002/3527609008.
- [2] G. Visco, L. Campanella, V. Nobili, *Organic carbons and TOC in waters: an overview of the international norm for its measurement*, *Microchemical Journal* 79, 185 (2005); doi:10.1016/j.microc.2004.10.018.
- [3] European Pharmacopeia 2.2.44 (2014).
- [4] German Institute for Standardization. DIN EN 1484 (1997); doi:10.31030/3042067.
- [5] I. Bisutti, I. Hilke, M. Raessler, *Determination of total organic carbon – an overview of current methods*, *TrAC Trends in Analytical Chemistry* (2004); doi:10.1016/j.trac.2004.09.003.
- [6] Innovatec Gerätetechnik GmbH. Datasheet Ozonemicrocell, (2018).
- [7] Neumüller. Datasheet UV-LED CUD8AF4D, (2018).

HTCC multilayer based on sensitive sensors for water analysis

Claudia Feller, Uwe Partsch, Stefan Körner
Fraunhofer Institute for Ceramic Technologies and Systems IKTS,
Winterbergstraße 28, 01277 Dresden, Deutschland
claudia.feller@ikts.fraunhofer.de

Summary:

Based on a microsystem technology approach, electrochemical sensors for analysis of H^+ , NH_4^+ , K^+ , Ca^{2+} and Cu^{2+} ion concentrations were developed. Starting from a suitable material and process development ion-sensitive thick-film membranes were deposited on a ceramic HTCC multilayer sensor platform. All ion-sensitive electrodes ISEs have a very good response behavior and high sensitivity in the examined measuring range. Thus the ceramic multilayer technology provides as a suitable method to prepare robust and miniaturized multi-sensor for water analysis.

Keywords: Ion-sensitive electrodes, ceramic multilayer technology, thick-film technology

Motivation

Monitoring water quality is essential to protect the environment and health. In the areas of drinking water and wastewater monitoring, intelligent agriculture, food industry, etc., the determination of different ion concentrations is necessary. Users place increasing demands on the sensors with regard to their measuring properties, robustness, miniaturization, geometry variability and manufacturing costs. The sensor requirements are particularly aimed at functional integration and smart, cheap, miniaturized multisensors for mass applications. According to the state of the art usually potentiometric sensors for ion concentration measurements, so-called ion-selective electrodes (ISEs) are used. These ISEs are based on various, mostly precision mechanical manufacturing technologies. Their manufacture is quite expensive and the miniaturization potential is limited. The aim was therefore to overcome these restrictions and to use technologies of ceramic multilayer technology in order to produce cost-effective and miniaturized multi-sensors for water analysis.

Approach

Components made of ceramic multilayer technology have conquered broad areas of application in various areas of electronics and microsystem technology. A ceramic multilayer is an intelligent ceramic packaging, which is produced by 3D structuring and material integration. By the excellent three-dimensional structuring and functionalization of ceramic, robust sensor solutions for the 3D packaging technol-

ogy of sensory microsystems are realized. With sensor miniaturization, the ceramic multilayer technology also offers an economical aspect of sensor production. The aim of the development work was therefore to use the **High Temperature Cofired Ceramics (HTCC)** multilayer technology to implement a ceramic-based integration platform for various ion-sensitive sensors, which can be used in numerous analytical and industrial processes for water analysis.

Results

Using the ceramic HTCC film and multilayer technology, a platform for the integration of electrochemical sensors for water analysis has been developed. The green foils are structured using micromachining processes such as punching, lasering or embossing. Depending on the version (see Fig. 1), sensor arrays of different layouts can be manufactured on top. The individual sensitive layers are obtained by depositing special functional layers on the ceramic using screen printing. The sensitive layers are interchangeable on the sensor array depending on the application. In the presented example, the functional proof for the determination of the measured values pH, Cu^{2+} heavy metal ion as well as the cations Ca^{2+} , NH_4^+ and K^+ in aqueous solutions was provided. The main challenge was the material and process development for the deposition of ion-sensitive thick-film membranes on the ceramic sensor platform. For that the functional materials are processed into powders of small grain size, which are dispersed in an organic binder. The paste is subsequently processed on a three-roll mill in

order to obtain a homogeneous, screen-printable suspension. The firing or curing of the functional layers is carried out according to their sintering properties. A thick film reference electrode is integrated on bottom.

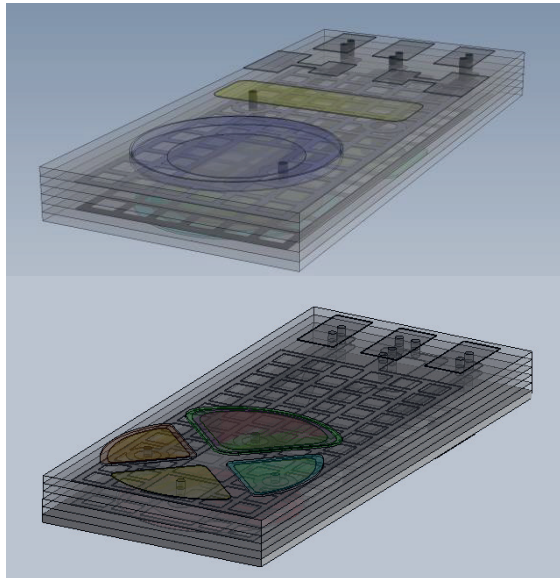


Fig. 1. HTCC sensor platform with two different layouts

The ISEs are potentiometric indicator electrodes that respond to the activity of the type of ion to be determined. Here, potentiometry, as an electro-analytical method of quantitative analysis, uses the concentration dependence of the electrochemical potential. The potentials were measured with a Keithley electrometer at 25 °C.

Mini pH sensor

For the pH-sensitive glass layer, a $\text{SiO}_2\text{-Na}_2\text{O-MgO-MnO}_2$ glass is used that sintered at 640 °C. In order to obtain dense, crack-free glass layers, the coefficient of the thermal expansion of the glass must be matched to that of the HTCC ceramic. The sensor is manufactured on a tile in 55-fold use (see Fig. 2).

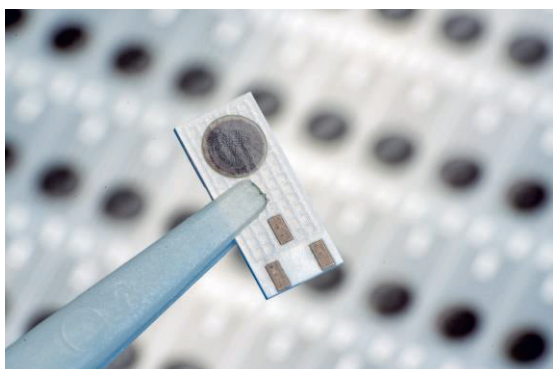


Fig. 2. Mini pH sensor

The slope of the measuring chain in the measurement range from 1.68 pH to 9.18 pH is in good agreement with the Nernst equation for monovalent ions.

Cu^{2+} ISE

In accordance with the thermochemical, crystallization and sintering behavior of the copper chalcogenide glasses, the thick-film pastes made from the glasses were processed in such a way that thin glass membranes were deposited on the HTCC multilayer, which are copper ion sensitive. The sensitivity of a CuAgAsSe thick film electrode is in the measuring range from 10^{-2} M to 10^{-6} M $\text{Cu}(\text{NO}_3)_2$ solution at 27.3 mV / pCu²⁺. This value corresponds to Nernst's behavior for divalent ions and correlates very well with the sensitivity of the bulk material (see Fig. 3).

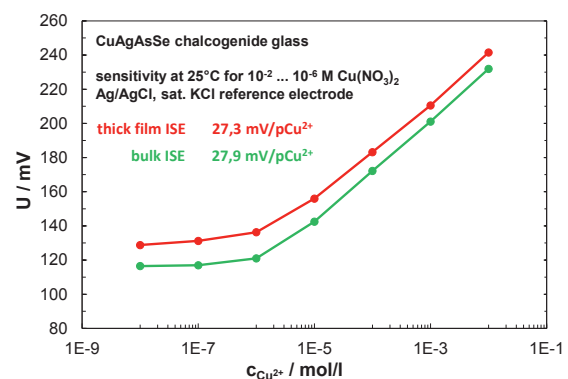


Fig. 3. Characteristic curve of Cu^{2+} ISE in measurement range $10^{-2} \dots 10^{-8}$ M $\text{Cu}(\text{NO}_3)_2$

K^+ , NH_4^+ , Ca^{2+}

The polymer-based, ion-sensitive membranes of the K^+ , NH_4^+ and Ca^{2+} ISEs are screen-printed and cured at room temperature. All ISEs have a very good response and high sensitivity in the studied measuring range in good agreement with the Nernst equation (see Fig. 4).

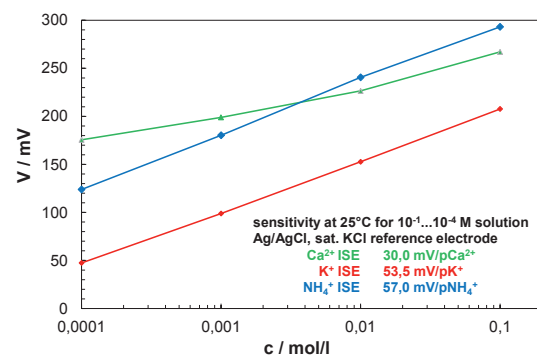


Fig. 4. Characteristic curves of ISEs (K^+ , NH_4^+ , Ca^{2+}) in measurement range $10^{-1} \dots 10^{-4}$ M solution

Development of a glass-fiber-based spectrometer for the determination of drug residues in groundwater

E. Melekhov, V. Abb, T. Weidauer, A. Lechner, M. Kammler
 Regensburg University of Applied Sciences, Centre of Excellence NanoChem
 evgeny.melekhov@oth-regensburg.de

Summary:

Within the scope of this project, a portable measuring device has been developed which enables a cost-effective analysis of organic substances from ppm to the sub-ppm range, such as drug residues in groundwater. The measurement is carried out by means of an exchangeable sensor head. The sensor head used is a nanostructured optical glass fiber glued into a fiber cannula. At the tip of the fiber is a surface-enhanced Raman scattering cell (SERS cell).

Keywords: Surface-enhanced Raman scattering (SERS); Nanostructuring; Analytical spectroscopy; Plasmonics; optical quartz glass fiber

Background, Motivation and Objective

SERS based Raman spectroscopy is a powerful detection technique, which detects organic molecules by vibrational spectroscopy at very low concentrations, e.g. in groundwater or drinking water to the extent necessary for a risk assessment. The SERS effect is mainly due to the high local electric fields generated by the irradiation of suitable nanostructured highly electrically conductive materials such as silver or gold with a laser. Due to the resonances of the surface plasmons in the metallized nanostructures, there are local field increases (hot spots).

Design of measuring device

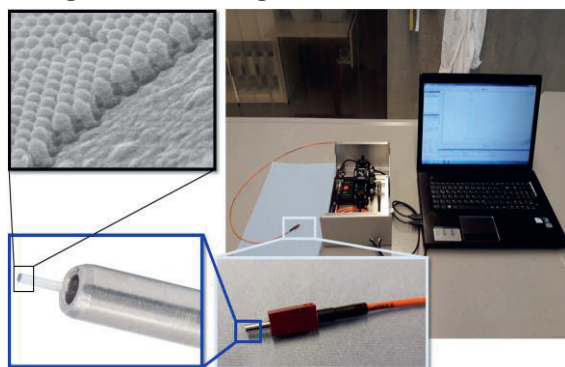


Fig. 1. Construction of a portable SERS-analyzer

Light source of the device is a laser with 785nm wavelength with maximum power of 75mW. The laser is connected to the measurement system via excitation fiber and fiber coupler. The laser beam get to sensor fiber via excitation collimator, line filter, dichroic mirror and objective. Nanopatterned optical fiber, glued

into a fiber ferrule, is connected to the patch cable, sensor fiber respectively via an adapter (see Fig. 1). From the SERS-surface scattered light goes back via sensor fiber to the objective and get then to the spectrometer via dichroic mirror, line filter, eyepiece and detection fiber. The entire system is powered by a laptop via a USB cable. The spectrometer and laser are controlled also by the laptop.

Methods for structuring SERS-active areas

The following chapter describes methods for nanostructuring of SERS active areas on quartz substrates (see Fig. 2). All these methods can be used for structuring of optical quartz glass fiber.

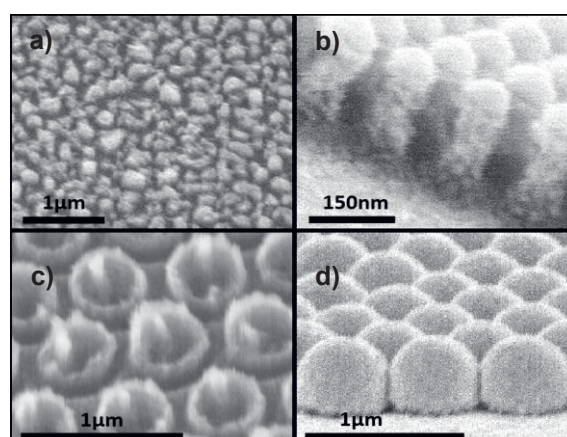


Fig. 2. SEM pictures: a) Metallized nano pillars on a quartz substrate produced by annealing a thin gold layer and dry etching in RIE; b) Metallized nano pillars on a quartz substrate produced by dry etching in RIE using of polystyrene spheres as an etch mask; c) Nano ring cavities on a quartz substrate produced by dry etching in RIE using of polystyrene spheres as an etch mask; d) Metallized polystyrene nano spheres

The first method is based on self-assembly structuring by annealing of a thin metal layer [1]. Other methods are based on Nano Sphere Lithography (NSL) [2]. Here, the spheres can be applied by means of a water technique [3] on the sample surface like a wafer or optical fiber.

First a quartz substrate is coated with 9nm gold via e-beam evaporator and then annealed. This layer breaks up during annealing to very small structures similar islands. This self-assembled structure serves as a mask against CHF_3/Ar plasma [4] for dry chemical etching. Etching process creates small pillars among the Ag nano Islands. For SERS measurement, this structure is evaporated again with Au (see Fig. 2 a)).

Another SERS-active structure can be prepared by nano sphere lithography. This method allows creation of hexagonal grafted nano pillars. In this case, the nano spheres serve as an etching mask in the Reactive Ion Etching (RIE) process. After applying the polystyrene spheres (PS) on a substrate, the size of the spheres is reduced in RIE by oxygen plasma. In the next step, the substrate is dry chemical etched by CHF_3/Ar -Plasma. After the pillars have been etched, PS are removed by O_2 -plasma. The quartz pillars are metallized with Au (see Fig. 2 b)).

For fabrication of Nano Ring Cavities with a pillar in the middle of ring (see Fig. 2 c)) as a SERS-active area, the nano sphere lithography is also used. After reducing the diameter of spheres by O_2 -plasma, a thin layer of Cr is evaporated on spheres as a mask against CHF_3/Ar plasma. After etching process PS are removed by O_2 -plasma. Lastly, the cavities are covered via e-beam evaporator with gold.

In the following method, the polystyrene spheres serves as a nanostructure directly. This technique calls Metal Film over Nanospheres (M FoN) or Ag FoN if Ag is used. After applying the spheres on a quartz-substrate (see Fig. 2 d)) or an optical fiber, they can be covered with gold or silver without further treatments [5], for this experiment the PS are covered with Ag.

Results

For Raman measurements the samples are immersed in 10^{-4} mol/L solution of p-thiocresol in ethanol. After the sample solution is evaporated, the SERS spectrum is recorded.

The difference of Raman spectra obtained by different structuring methods of a quartz glass substrate is shown in Fig. 3.

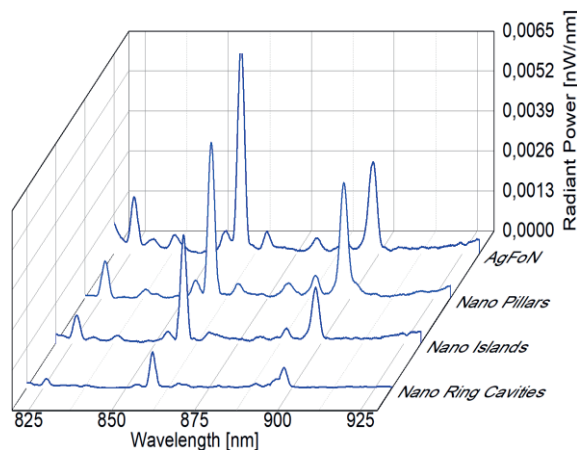


Fig. 3. SERS-spectra of p-thiocresol (10^{-4} mol/L) from quartz glass substrates with different nano structures: Silver Film over Nanospheres (AgFoN); Nano Pillars; Nano Islands; Nano Ring Cavities

Conclusion

With the measuring device and the SERS-active substrates, p-thiocresol with a concentration of 10^{-6} mol/L dissolved in ethanol could be determined. The measurement results show that the organic substances can be measured in the sub-ppm range.

References

- [1] T.-W. Chang, M. R. Gartia, S. Seo, A. Hsiao und G. L. Liu, „A wafer-scale backplane-assisted resonating nanoantenna array SERS device created by tunable thermal dewetting nanofabrication,“ *Nanotechnology* 25, 2014; doi:10.1088/0957-4484/25/14/145304
- [2] C. Haynes und R. P. V. Duyne, „Nanosphere Lithography: A Versatile Nanofabrication Tool for Studies of Size-Dependent Nanoparticle Optics,“ *The Journal of Physical Chemistry B*, pp. 5599-5611, 2001; doi: 10.1021/jp010657m
- [3] M. Pisco, F. Galeotti, G. Quero, G. Grisci, A. Micco, L. V. Mercaldo, P. D. Veneri, A. Cutolo und A. Cusano, „Nanosphere lithography for optical fiber tip nanoprobos,“ *Light: Science & Applications*, 2017; doi:10.1038/lsa.2016.2
- [4] M. A. Rad, K. Ibrahim und K. Mohamed, „Atomic force microscopy investigation of surface roughness generated between SiO_2 micro-pits in CHF_3/Ar plasma,“ *Superlattices and Microstructures*, pp. 597-605, 2012; doi: 10.1016/j.spmi.2012.03.002
- [5] R. P. V. Duyne, J. C. Hulthen und D. A. Treichel, „Atomic force microscopy and surface-enhanced Raman spectroscopy. I. Ag island films and Ag film over polymer nanosphere surfaces supported on glass,“ *The Journal of Chemical Physics* 99, pp. 2101-2115, 1993; doi: 10.1063/1.465276

Thermal-electrical Design Improvements of a New CMOS Compatible Pyroelectric Infrared Sensor Based on HfO₂

Robin Lehmkau¹, Martin Ebemann¹, Doris Mutschall¹, Norbert Neumann¹, Jens Lienig²

¹ InfraTec GmbH, Gostritzer Str. 61, 01217 Dresden (Germany),

² TU Dresden, Institute of Electromechanical and Electronic Design, 01062 Dresden (Germany)
r.lehmkau@infrotec.de

Summary:

The pyroelectric properties of doped hafnium dioxide (HfO₂) are utilized to create a new CMOS compatible infrared sensor element suitable for mass production. In this paper, we propose a new sensor design with the goal of maximizing the temperature sensitivity and optimizing the thermal time constant. Furthermore, a thermal-electrical model of a complete pyroelectric detector is developed to estimate the signal and noise behavior.

Keywords: HfO₂, pyroelectric sensor, CMOS, thermal-electrical model, temperature sensitivity

Introduction

The demand for low cost and high-performance infrared detectors is constantly growing, for example in the area of gas sensing and flame detection. Especially pyroelectric detectors offer a high detectivity for measuring infrared radiation [1]. For a few years, the pyroelectric behavior of HfO₂, deposited on a silicon membrane, has been profoundly studied [2]. The potential advantages, compared to the widely used lithium tantalite (LT), are low cost, because of the CMOS compatibility and a high performance considering a low thermal capacitance and high thermal isolation. The generated pyroelectric current corresponds to the following Eq. (1). Trenches, which are shown in Fig. 1, enable a 3D-structuring of HfO₂ for a larger effective electrical surface A and a higher resulting current.

$$I_{pyro} = p \cdot A \cdot \frac{dT}{dt} \quad (1)$$

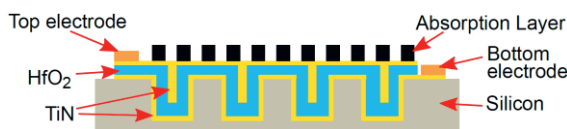


Fig. 1: Cross-section of the structured membrane.

Additionally, a plasmonic absorber replaces a conventional black layer like a metal or polymer coating. This ensures CMOS compatibility of the whole pyroelectric sensor.

The contributions of this paper are the optimization of a new sensor design with respect to a high sensitivity and an appropriate time constant. Besides, the overall pyroelectric performance is evaluated with a new extended SPICE model.

Optimization of the New Sensor Design

According to Eq. (1), the pyroelectric coefficient p is a material specific parameter and is independent of the sensor design. But both the effective surface area A and the temperature change dT/dt depending on the incident radiation power can be optimized. A suitable design of the new sensor element, plotted in Fig. 2, is a thin membrane with beams to an outer frame.

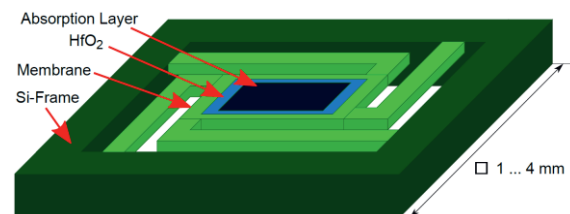


Fig. 2: Proposed design of the sensor element.

The stack including HfO₂ and silicon is structured with etching processes limiting the minimum physical dimensions of gaps, widths and heights. Moreover, the mechanical stability must be guaranteed.

In Fig. 3, COMSOL Multiphysics™ is used to simulate the temperature distribution (left) and the average temperature behavior in the membrane in the time domain (right). The sensor geometry can be optimized for several parameters. For instance, the relative impact of varying the membrane thickness is shown in Fig. 4 for a radiation intensity of 5 W/m². In summary, there is a tradeoff between the temperature sensitivity, time constant and further constraints, like the mechanical stability and maximum layout dimensions.

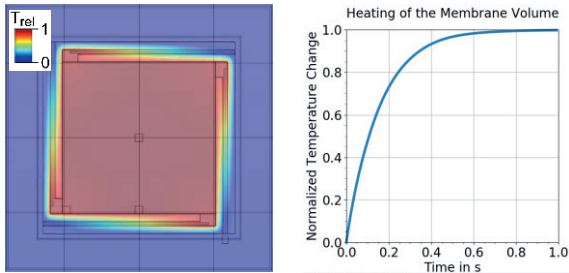


Fig. 3: Steady state of the FEM heat simulation of the sensor element (left) and average temperature settling curve of the membrane (right).

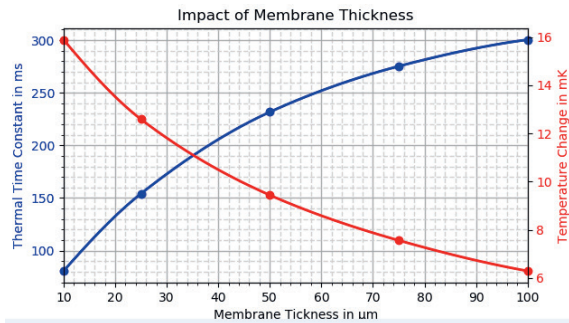


Fig. 4: Dependency of the thermal time constant and temperature change on the membrane thickness.

Thermal Electrical Model for Pyroelectric System

An alternative approach to examine the thermal behavior is to use the thermal electrical analogy and develop a *SPICE* model, proposed in [3]. Spatially concentrated elements, in the form of resistances, connect the heat source with the ambience. The finite element method (FEM) simulation is used to identify the dominating conducting paths, like beams and air gaps, and validate the implemented *SPICE* model. Figure 5 illustrates some of the important thermal resistances for the heat conduction in the simplified sensor. Thermal convection and radiation can be neglected because of a small membrane area and tiny temperature differences.

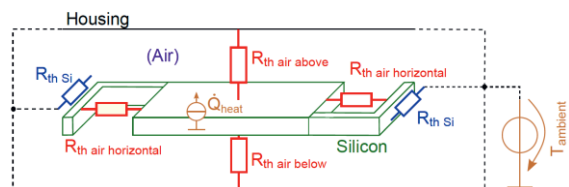


Fig. 5: Spatially distributed thermal resistances.

A new parametrized *SPICE* model has been developed, which can map thermal 3D structures. It requires only a short calculation time and can perform frequency and parameter sweeps, but still differs only few percent from the FEM analysis. In addition, the model can be extended by an electrical circuit to investigate the overall behavior of the pyroelectric detector. The improved model, which is shown in Fig. 6 (top), combines

a thermal 3D-system and a readout circuit including substantial noise sources, like $\tan(\delta)$ -noise of the pyroelectric material.

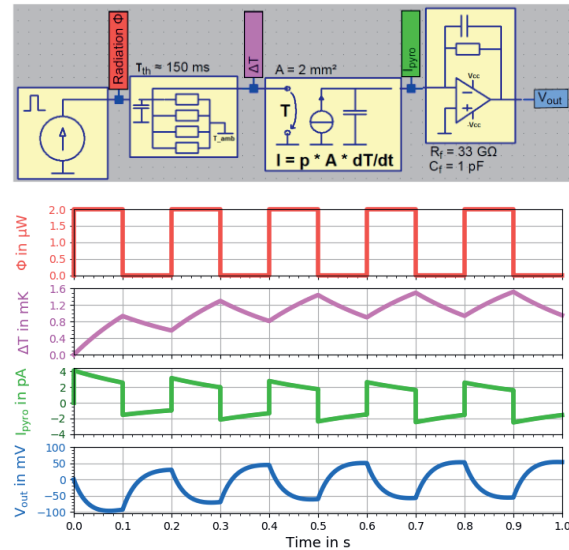


Fig. 6: *SPICE* model of a LT current mode detector (top) and the simulated pyroelectric signals in the time domain during thermal settling (bottom).

For model validation, a typical LT current mode detector is studied. Figure 6 (bottom) demonstrates the rectangular incident radiation as excitation of the model and the output voltage.

Conclusion

A new sensor design based on HfO_2 has been proposed. Different layouts and parameter combinations have been examined to optimize the temperature sensitivity and achieve a suitable thermal time constant in the order of 100 ms. The pyroelectric coefficient of HfO_2 is lower than that of LT, but due to a higher temperature sensitivity and effective area extension by 3D-structuring, a higher pyroelectric current can be obtained. Furthermore, a new *SPICE* model has been realized to estimate the overall performance of a pyroelectric detector combining both a 3D thermal system and an electrical readout circuit.

Acknowledgment

This work was supported by the German Federal Ministry of Education and Research, funding program Photonics Research Germany (No. 13N15141).

References

- [1] H. Budzier, G. Gerlach: "Thermische Infrarotsensoren: Grundlagen für Anwender" *Wiley-VCH* (2010), ISBN: 978-3-527-40960-0
- [2] C. Mart et al.: "CMOS Compatible Pyroelectric Applications Enabled by Doped HfO_2 Film on Deep-Trench Structures", *ESSDERC* (2018), DOI: 10.1109/ESSDERC.2018.8486864
- [3] P. Ramos, F. J. Meca, J. Mendiola, E. Martin.: "A Simple Thermal and Electrical Model of an Infrared Pyroelectric Detector Using Spice", *Ferroelectrics* (2002), DOI: 10.1080/00150190211482

A Radiation Thermometer based on an InGaAs-Photodiode at 1.6 μm for Temperatures down to 80 $^{\circ}\text{C}$

Jonas Bories¹, Ingmar Mueller¹, Berndt Gutschwager¹ and Jörg Hollandt¹

¹Physikalisch-Technische Bundesanstalt, Berlin

Corresponding Author's e-mail address: jonas.bories@ptb.de

Summary:

In the last decade the specific detectivity of InGaAs-photodiodes has improved significantly. Hence, the lower detection limit of InGaAs-photodiode based radiation thermometers at 1.6 μm can be extended. Here, an existing radiation thermometer was equipped with a state-of-the-art InGaAs-photodiode. The radiation thermometer was characterized and calibrated and a reference function has been compiled. The lower temperature limit could be extended from 150 $^{\circ}\text{C}$ down to 80 $^{\circ}\text{C}$.

Keywords: Radiation Thermometer, InGaAs-Photodiode, Characterization, Reference Function

Introduction

The working group “Infrared Radiation Thermometry” of the Physikalisch-Technische Bundesanstalt (PTB) provides non-contact temperature measurements in the range from -170 $^{\circ}\text{C}$ to 962 $^{\circ}\text{C}$ at the highest metrological level. High-quality infrared radiation thermometers are used as transfer instruments as well as for comparison measurements. InGaAs-photodiode instruments are superior to instruments based on thermal detectors in terms of temporal stability and achievable measurement uncertainties in the short wavelength range. However, the operating wavelength around 1.6 μm limits the minimal detectable temperature of InGaAs-radiation thermometers to typically 150 $^{\circ}\text{C}$ to 200 $^{\circ}\text{C}$. In the last decade, the performance of InGaAs-photodiodes increased by several orders in magnitude in terms of specific detectivity. By using a commercial two-stage cooled InGaAs-photodiode, the minimal detectable temperature of a 15 years old lens-free radiation thermometer (LF-IRRT2) was improved from 150 $^{\circ}\text{C}$ to 80 $^{\circ}\text{C}$.

Design of the Radiation Thermometer

The InGaAs-photodiode has an active area of 5 mm in diameter and is operated at a temperature of approximately $-20\text{ }^{\circ}\text{C} \pm 0.005\text{ }^{\circ}\text{C}$ to reduce the wear and tear of the TE-cooler. The temperature is controlled by a custom-built temperature controller. The controller housing also includes a custom-built transimpedance amplifier, tailored for the photodiode. Gains can be set from 10^5 to 10^{10} . An additional voltage gain factor of 10 can be set at every gain to increase the signal level. By means of a so-called reference

function [1] the output signal is converted into a temperature reading. The reference function is given by:

$$i = \frac{A_1 \cdot A_2}{D^2} \int_{\lambda_1}^{\lambda_2} L_{\lambda}(\lambda, t_{90}) \cdot s(\lambda) \cdot \tau(\lambda) \cdot d\lambda \quad (1)$$

with the photocurrent i , $A_{1,2}$ the active areas of a aperture stop and field stop, $\lambda_{1,2}$ the limiting wavelengths, $L_{\lambda}(\lambda, t_{90})$ the spectral radiance of the blackbody at the temperature t_{90} , $s(\lambda)$ the spectral responsivity of the photodiode and $\tau(\lambda)$ the transmission of the interference filter. Assuming a linear responsivity, the input values of Eq. (1) can be determined by measuring the photocurrent i at several known temperatures $t_{s,90}$ and applying a least square fit. In order to obtain a radiation temperature $t_{s,90}$ from the photocurrent i , the temperature is inversely calculated by comparing the measured photocurrent with the photocurrent according to Eq. (1). Figure 1 shows a cut presentation of the LF-IRRT3.

Tab. 1: Specifications of the LF-IRRT3

Component	Nominal value
Aperture stop \varnothing	6.00 mm
Field stop \varnothing	3.71 mm
Distance aperture stop to field stop	243.8 mm
Detectivity (data sheet)	$6.7 \times 10^{13} \text{ cmHz}^{1/2}/\text{W}$
Bandpass of filter	1.55 μm - 1.65 μm
Maximum transmission of filter	81% at 1.6 μm

The main parts are a water-cooled detector housing (1) including an interference filter and the field stop, a set of stray light baffles (2) in a water-cooled housing, a motorized optical shutter (3) and a (4) water-cooled front aperture (aperture stop) with additional heatshield.

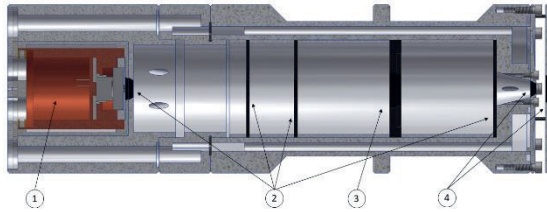


Fig. 1 Cut presentation of the InGaAs-radiation thermometer LF-IRRT3. The parts are listed in the text.

Calibration of the LF-IRRT3

The LF-IRRT3 has been calibrated at the Thermal Imager Calibration Facility (ThermICF) [2] (see Figure 2) of PTB. The ThermICF covers the temperature range from $-60\text{ }^{\circ}\text{C}$ to $962\text{ }^{\circ}\text{C}$ by means of heatpipe blackbodies. Additional large area surface radiators are available in the temperature range from $-15\text{ }^{\circ}\text{C}$ to $500\text{ }^{\circ}\text{C}$ for the full field of view characterization of thermal imagers. The photocurrent of the LF-IRRT3 was measured at several temperatures in the range from $80\text{ }^{\circ}\text{C}$ to $960\text{ }^{\circ}\text{C}$ and the input parameters of Eq. (1) were determined. The LF-IRRT3 together with the read-out electronics (transimpedance amplifier and digital multimeter) was treated as a “blackbox”, i.e. only the radiation temperature $t_{s,90}$ and the photocurrent i were used for the calibration. In the observed temperature range the photocurrent increases from $\approx 10^{-14}\text{ A}$ to $\approx 10^{-6}\text{ A}$. Hence, the full gain range of the transimpedance amplifier has to be used. The gain ratios were determined at four different temperatures to allow an overlap of different gain settings. To simplify the evaluation of the radiation temperature, an approximation of Eq. (1):

$$i = c \cdot \int_{\lambda_1}^{\lambda_2} L_{\lambda}(\lambda, t_{90}) d\lambda \quad (2)$$

with $c = A_1 \cdot A_2 \cdot \tau_0 \cdot s_0 / D^2$ is used. The resulting parameters are given in Table 2. The resulting temperature difference $t_{\text{Instrument}} - t_{s,90}$ according to Eq. (2) is given in Figure 3.

Tab. 2: Input parameters of Eq. (2) obtained by the calibration of LF-IRRT3 against high-quality heatpipe blackbodies of PTB

Parameter (see text)	Value
Instrument const. c	$4.040989 \cdot 10^{-9}\text{ Am}^2\text{srW}^{-1}$
wavelength limit λ_1	$1.542945 \cdot 10^{-6}\text{ m}$
wavelength limit λ_2	$1.645718 \cdot 10^{-6}\text{ m}$

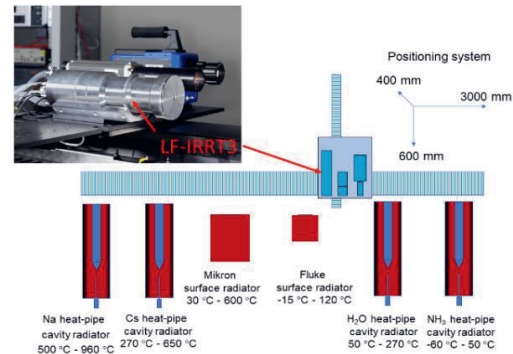


Fig. 2 Schematic of the Thermal Imager Calibration Facility (ThermICF) of PTB. The facility uses four heatpipe blackbodies to provide radiation temperatures traceable to the ITS-90. The LF-IRRT3 is shown mounted on a long-range x-y-z-translation system in front of the heatpipe blackbodies and the surface radiator. The inserted photograph shows the LF-IRRT3 together with a transfer radiation thermometer and a thermal imager

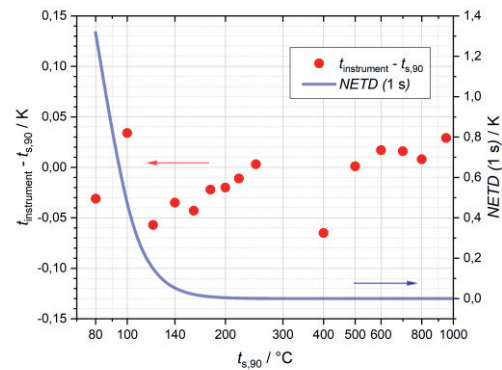


Fig. 3 Difference of the measured radiation temperature $t_{\text{Instrument}}$ of the LF-IRRT3 and the radiation temperature $t_{s,90}$ of the blackbodies (red dots) and the noise equivalent temperature difference (NETD) of the LF-IRRT3 (blue curve) for 1 s integration time

Conclusion

The LF-IRRT3 was developed on the bases of a state-of-the-art InGaAs-photodiode and calibrated against the high-quality heatpipe blackbodies of PTB. The difference $t_{\text{Instrument}} - t_{s,90}$ is below 65 mK and within the expanded uncertainties of the blackbodies for all observed temperatures. However, the necessary integration time increases from 1 s for temperatures above $120\text{ }^{\circ}\text{C}$ to approximately 5 minutes at $80\text{ }^{\circ}\text{C}$.

References

- [1] B. Gutschwager and J. Fischer, “An InGaAs radiation thermometer with an accurate reference function as transfer standard from $150\text{ }^{\circ}\text{C}$ to $960\text{ }^{\circ}\text{C}$ ”, in “Proceedings TEMPMEKO ’99”, edited by J. F. Dubbeldam and M. J. de Groot, 567-572, IMEKO/NMi Delft, 1999
- [2] I. Müller, et al., “Non-contact Temperature Measurement at the Physikalisch-Technische Bundesanstalt (PTB)” submitted to QIRT Journal

Absolute Calibration of the Spectral Responsivity of Detectors in the MIR at the PTB

Tobias Pohl¹, Peter Meindl¹, Uwe Johannsen¹, Lutz Werner¹, Joerg Hollandt¹

¹ Physikalisch-Technische Bundesanstalt (PTB), Abbestraße 2-12, 10587 Berlin, Germany

Corresponding Author: peter.meindl@ptb.de

Summary:

The Physikalisch-Technische Bundesanstalt (PTB) expanded its capabilities of absolute calibration of the spectral responsivity in the mid-infrared (MIR) by equipping a cryogenic electrical substitution radiometer facility with MIR laser radiation sources to enable absolute measurement of radiant power traceable to the International System of Units (SI). Furthermore, the PTB is installing a new MIR detector comparator facility to disseminate the spectral responsivity from the absolutely calibrated transfer standards to other detectors.

Keywords: detector calibration, spectral responsivity, mid-infrared, SI traceable, uncertainty

Introduction

The PTB operates cryogenic electrical substitution radiometers as national primary detector standards to measure radiant power and to calibrate detectors in view of their spectral responsivity. The spectral responsivity $s(\lambda)$ is the ratio between the output signal of the detector and the received radiant power Φ .

Furthermore, the PTB uses different types of transfer detectors, which have been calibrated absolutely against the primary detector standards, for the dissemination of the spectral responsivity.

Currently, the calibration of detectors in the spectral range of the near-infrared (NIR) and mid-infrared (MIR) is of increasing importance, e.g. for remote sensing [1] or radiation thermometry. These applications need, in general, traceability to the International System of Units (SI). Therefore, the PTB is expanding its capabilities of realization and dissemination of the spectral responsivity into the MIR by

- equipping a cryogenic electrical substitution radiometer facility with MIR lasers as radiation sources,
- establishing different types of detectors as MIR transfer standards and
- installing a new MIR detector comparator facility for routine customer calibrations.

Cryogenic electrical substitution radiometer

The measurement principle of cryogenic electrical substitution radiometers is based on the substitution of absorbed radiant power with

electric heating power, which can be measured SI traceable with low uncertainty [2]. Hence, cryogenic electrical substitution radiometers are national primary standards for the measurement of radiant power.

By implementing a CO₂-laser (10.6 μm) and a quantum cascade laser (QCL, 3.96 μm and 9.45 μm) at one of PTB's cryogenic electrical substitution radiometer facilities, absolute detector calibrations of the spectral responsivity in the MIR were enabled. Calibrations are usually performed at power levels between 1 μW and 1 mW.

Calibration of MIR transfer standards

The cryogenic electrical substitution radiometer facility with MIR lasers was used to calibrate the following types of windowless detectors in view of their spectral responsivity:

- thermopile detectors TS-76 (Leibnitz-Institut für Photonische Technologien e.V. Jena)
- pyroelectric detectors (InfraTec)

The properties of these detectors have been improved by an optimized and thermally stabilized detector housing design [3].

The measurement principle of these thermal detectors is based on the heating effect of an absorber. Therefore, the detector responsivity should be spectrally more or less constant assuming that the absorptance of the incident radiant power is independent of the wavelength.

Fig. 1 and 2 show results of spectral responsivity calibrations of a thermopile and a pyroelectric detector, respectively. In fact, only slight

dependencies of the spectral responsivity on the wavelength have been found. Therefore, a linear approach seems to be sufficient for the interpolation of the spectral responsivity $s(\lambda)$ between the results at the laser wavelengths.

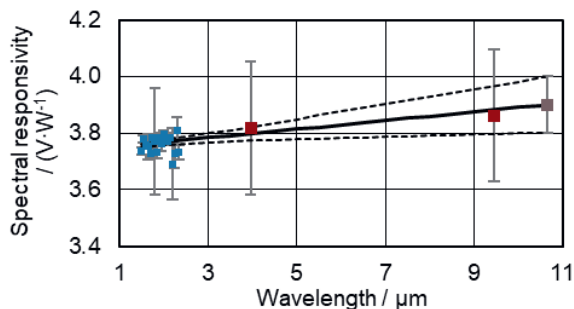


Fig. 1. Spectral responsivity $s(\lambda)$ of a TS-76, measured with a supercontinuum laser (blue), a QCL (red) and a CO₂-laser (brown), including the standard measurement uncertainty.

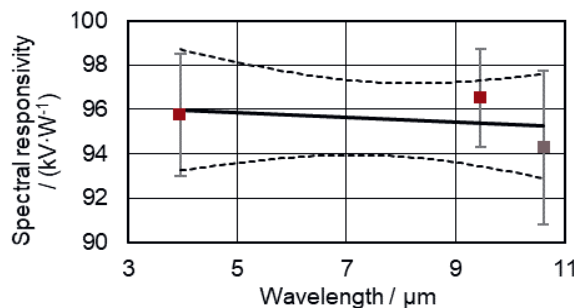


Fig. 2. Spectral responsivity $s(\lambda)$ of a pyroelectric detector at a chopper-frequency of 10 Hz, measured with a QCL (red) and a CO₂-laser (brown), including the standard measurement uncertainty.

The standard measurement uncertainties of the spectral responsivity determined with MIR lasers against the cryogenic electrical substitution radiometer range between 1.3% and 3.6%. The main uncertainty contributions for the calibration at 9.45 μm are given in Tab. 1. Based on these calibrations, the TS-76 and pyroelectric detector were established as MIR transfer standards for the measurement of radiant power.

Tab. 1: Main contributions to the standard measurement uncertainty for the calibration of a pyroelectric detector at 9.45 μm

Noise of detector, source, radiometer	0.85%
Measurement of ZnSe window transmittances at the radiometer	0.30%
Stray radiation	2.1%
Relative standard uncertainty	2.3%

MIR detector comparator facility

The PTB is installing a new measurement facility for detector calibrations in the MIR to disseminate the spectral responsivity from the primary detector standard by using the established transfer standards.

This facility uses laser radiation sources to calibrate various detectors at specific wavelengths and a thermal, broad-band radiation source in combination with a monochromator setup to calibrate detectors at any wavelength by using the interpolated spectral responsivity $s(\lambda)$ of the transfer standards.

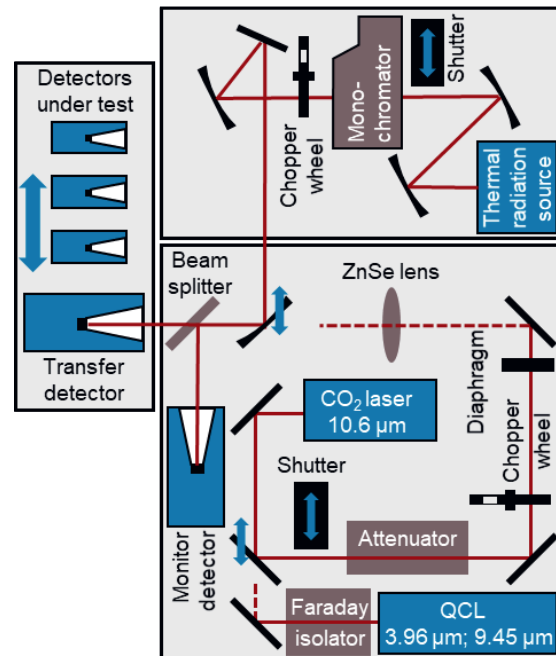


Fig. 3. MIR detector comparator facility

Outlook

Currently, the PTB is developing an additional, independent approach for MIR spectral responsivity calibrations of detectors by using a high-temperature blackbody operating at about 1200 K with a precision aperture. The blackbody radiation is described by Planck's law and is spectrally selected by optical filters with accurately characterized bandpass transmissions.

By this means the detector under calibration is irradiated by a calculable spectral irradiance within the bandpass of the applied transmission filters. First results on the thermopile transfer detectors agree with their calibrations at the cryogenic electrical substitution radiometer.

References

- [1] R. S. Allison et al, Airborne Optical and Thermal Remote Sensing for Wildfire Detection and Monitoring, *Sensors* 16(8): 1310 (2016); doi: 10.3390/s16081310
- [2] J. E. Martin et al, A Cryogenic Radiometer for Absolute Radiometric Measurements, *Metrologia*, 21, 147-155 (1985)
- [3] T. Pohl et al, Measurement of the absolute spectral responsivity in the mid-infrared based on the cryogenic electrical substitution radiometer and an optimized thermopile detector, *Journal of Sensors and Sensor Systems* 8, 195-205 (2019)

Multi-spectral mid-IR Temperature Measurement Using Tuneable Detectors.

Matthew Gillott¹, Fiona Turner¹, Peter Droegmoeller¹

*¹ Ametek Land, Dronfield, UK,
matthew.gillott@ametek.com*

Summary:

Most pyrometers for industrial applications use one or two wavelength bands to measure energy in order to determine the target temperature, but this can lead to errors from incorrect or unknown emissivity or non-greyness. Using a tuneable detector based on a Fabry Perot filter, temperature measurement across a greater number of wavelengths can be performed, and potentially eliminate errors arising from atmospheric gasses and surface emissivity.

Keywords: Infrared, detectors, pyrometers, instrumentation, temperature

Introduction

For many years infrared temperature measurement used a single spectral band to determine target temperature. Picking a suitable spectral band allows the measurement instrument to be selected to suit the application and temperature range: longer wavelength detectors are required to measure lower temperatures. There are several drawbacks to single wavelength pyrometers, the main issue being the need to know the emissivity of the target surface for accurate measurement. Furthermore, since the temperature reading is a simple function of the signal received by the instrument, the reading can be significantly altered by the variable atmospheric conditions as well as obstructions in the signal path from a dirty window or dusty atmosphere.

One solution is to use a ratio pyrometer. Ratio pyrometers use two independent signals from two wavelengths and evaluate the temperature of the target using the ratio of the two signals as shown in Fig. 1. This method can determine the emissivity of the target and is less susceptible to obstructions in the signal path. Accurate temperature measurement using a ratio pyrometer no longer has the same issue with surface emissivity as a single wavelength instrument, however the non-greyness of the surface is now an important factor. The non-greyness of a surface is the ratio of emissivities at the two different wavelengths. A grey target has the same emissivity at both wavelengths.

Increasing the number of measurement wavelengths could provide more information about the target, such as being able to determine the non-greyness and account for

atmospheric issues such as high CO₂ environments. This paper investigates the potential advantages of temperature measurement at multiple wavelengths using a Fabry-Perot interferometer (FPI).

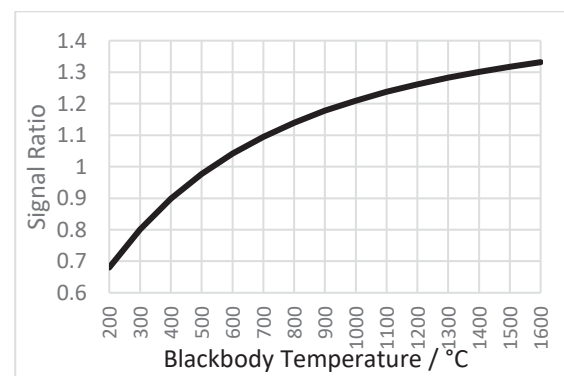


Fig.1 Graph showing the ratio of the infrared radiance from a blackbody at 3.4um to that at 3.8um. The flatness of the curve shows that small errors in non-greyness can lead to large errors in measured temperature.

Experimental Setup

A miniaturised Fabry-Perot interferometer was used to produce a tuneable narrow bandpass filter. The separation of the two reflective surfaces within the interferometer controls the pass band of the filter. In combination with a pyroelectric detector, which provides a relatively even output across multiple wavelengths, a hyper-spectral measurement device was produced. The equipment used in this study utilised an Infratec LFP series detector, which included support electronics for performing closed loop control of the device, ambient temperature compensation and filter stabilisation.

A test instrument was built using the Infratec detector with custom readout electronics. The custom electronics consisted of three main parts, a power supply, an ADC, an MCU and an ethernet interface for access to the data. The ADC used a 16-bit converter to digitise the output signal from the detector and the MCU performed all the required calculations. The detectors and their respective control electronics were interfaced with using a standard UART serial interface. Commands were issued to the detector board for controlling the detector and filter, for example to set the band pass wavelength. The Infratec control electronics provided an adjustable gain for the output signal from the detector which was utilised to improve the dynamic range of the instrument and adjust the working range of the test instrument. Since the instrument used a pyroelectric based sensor, an optical chopper was used to modulate the signal onto the detector. The MCU provided control for the optical chopper motor and synchronised the readings with each chopper cycle.

Measurements were performed using a Land R1500T blackbody calibration source as a target of controllable temperature. The test instrument was focussed on the blackbody from a distance of 1m using focused optics.

Results

The chopped signal output becomes sinusoidal in shape due to the slow response time of the pyroelectric detector, so measurements were made of the peak-to-peak signal intensity variation. For a given detector illumination, the signal intensity could be altered either by adjusting the on-board amplifier gain or speed of the chopper. Graphs were plotted of signal intensity against temperature for each wavelength as shown in Fig. 2. From this data, a function was generated to convert the reading from the detector into a temperature.

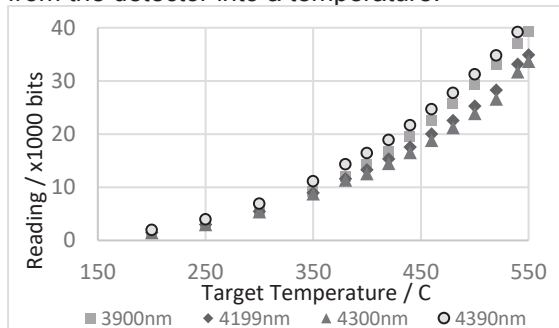


Fig.2 Graph showing the output reading determined by the MCU across several wavelengths and temperatures

The noise was estimated as the standard deviation of 100 readings for each wavelength and temperature combination, as shown in Fig. 3. This chart shows that the noise of the system is viable for taking single wavelength measurements with approximately 1°C accuracy. Further improvements could also be made by performing more signal processing.

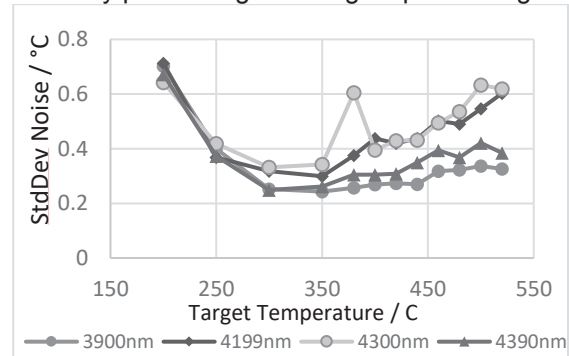


Fig. 3 Graph showing noise of temperature readings across multiple wavelengths and target temperatures

In Fig.4, the signal ratio at the two wavelengths is compared with a theoretical model. The data shows that whilst the shape agrees with that of the theoretical model, the errors in measurement could result in large temperature errors due to the flatness of the curve.

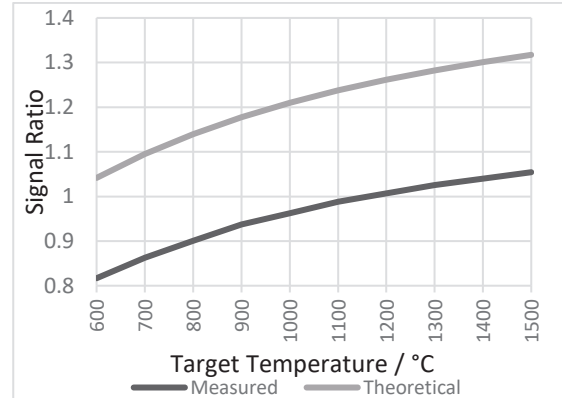


Fig. 4 Graph of ratio of signals at 3.4um to 3.8um for both the test instrument and the model.

Conclusion

The accuracy of the LFP series detector has been measured. Whilst the errors may be too large in the current state for ratio-type measurements, other applications could be possible such as material or surface condition determination. Emissive hot gasses could also be detected and measured independently of the target.

FLAIR Airborne System for Multi-Species Atmospheric Gas Spectroscopy in the mid-IR

L. Balet¹, S. Chin¹, T. Herr¹, F. Lütolf¹, P. Renevey¹, J. Van Zaen¹, S. Dasen¹, J. Gouman¹, G. Buchs¹, G. Vergara², H. Martin³, P. M. Moselund⁴, F. J. M. Harren⁵, C. Hüglin⁶, S. Lecomte¹

1. CSEM SA, Time and Frequency Systems, 2002 Neuchâtel, Switzerland

2. NIT, New Infrared Technologies S.L., Boadilla del Monte, Madrid, 28660 Spain

3. SenseAir AB, 82060 Delsbo, Sweden

4. NKT Photonic A/S, DK-3460 Birkerød, Denmark

5. Trace gas Research Group, IMM, Radboud University, Nijmegen, the Netherlands

6. EMPA, 8600 Dübendorf, Switzerland

laurent.balet@csem.ch

Summary:

We present the realization of the broadband atmospheric gas spectrometer developed in the frame of the H2020 FLAIR project. The system is UAV compatible for deployment in hard to reach location. We also report on its behavior during field testing aboard a zeppelin and a helicopter tracking ship fume.

Keywords: mid-IR spectrometer, atmospheric gas spectroscopy, ship fumes, supercontinuum, MWIR uncooled camera

Background, Motivation and Objective

The World Health Organization statistics shows that approximately 7 million people are killed by air pollution related conditions every year; specifically, in Europe air pollution is presumed to be the cause of 0.3 million premature deaths. The total annual economic cost of air pollution-related health impacts is estimated to exceed USD 1.5 trillion. However, it is often a challenge to measure the level of pollutants in harsh environments and/or remote areas such as volcanic eruption, industrial fires or ship toxic fumes, which are major threat for the respiratory illness, the depletion of the ozone layer and the acid rain. The main goal of the European project FLAIR (Flying ultra-broadband single-shot InfraRed [1]) is to design and build an atmospheric gas sensing spectrometer. Thanks to its lightweight and compact form factor, the whole system including a data processing algorithm can be deployed in an Unmanned Aerial Vehicle (UAV), so that the risk assessment on the multi-species atmospheric gas can be readily performed.

System design

Fig. 1 illustrates the simplified schematic diagram of the FLAIR spectrometer. It consists mainly of 4 parts: a supercontinuum (SC) laser covering a wide wavelength range from 2 to 5 μm , which is broader than the spectrum provided by any commercial Quantum Cascade Lasers (QCLs) and/or optical frequency combs

sources [2-5], a multi-pass cell (MPC) for light-gas interaction, a diffraction grating to disperse the light, and a 2D MWIR array to collect the dispersed spectrum.

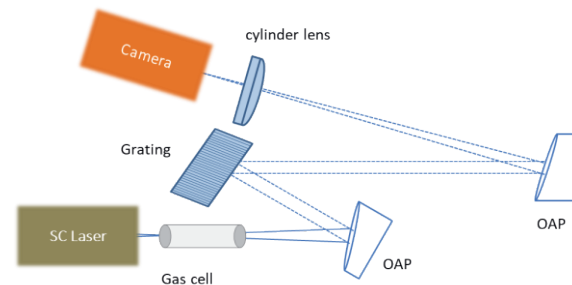


Fig. 1. Simplified schematic diagram of FLAIR spectrometer.

Fig. 2 shows the 3D CAD design of the full system. Its compact size and environmental requirements are compatible with UAVs size, mass, available electrical power and operating environment. A 30 cm long MPC, where the light is reflected back-and-forth to a 10 m interaction length, is implemented inside a thermostatic enclosure where the input air is heated above ambient temperature. The MPC is fitted with sensors for temperature, pressure and humidity measurement since such physical quantities are useful parameters to precisely compute the gas concentration from the measured gas absorption profile. The MWIR camera consists of a Vapor Phase Deposited PbSe

layer on a 128x128 pixels CMOS detector array [6, 7] adapted specifically for this project.

A board computer controls the various subsystems, performs live analysis of the absorption profiles based on HITRAN models, and logs continuously the various parameter, spectra and concentrations.

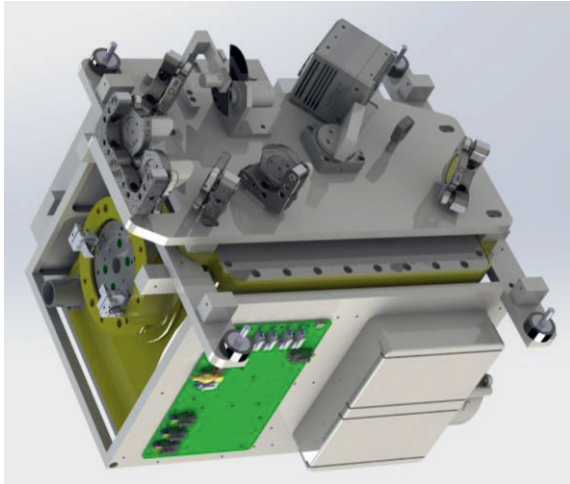


Fig. 2. CAD of the system (35 x 35 x 45 cm³)

In the framework of FLAIR, different spectrometer designs have been investigated [5], and the final choice has been a simple diffraction grating followed by an orthogonally placed cylindrical lens to cover the whole surface of the MWIR camera. This 2-dimensional arrangement allows for the vertical averaging of the multiple horizontal copies of the dispersed spectrum, thus effectively reducing the white noise of the uncooled detector. Moreover, as this type of detectors is subject to from non-uniformity gain [6] this averaging, combined with non-uniformity correction (NUC) provided by NIT, and lock-in detection allow for a substantial SNR enhancement. Fig. 3 shows the good agreement between the measured and HITRAN-simulated methane Q-branch absorption at 500 ppb, which is below the normal atmospheric abundance.

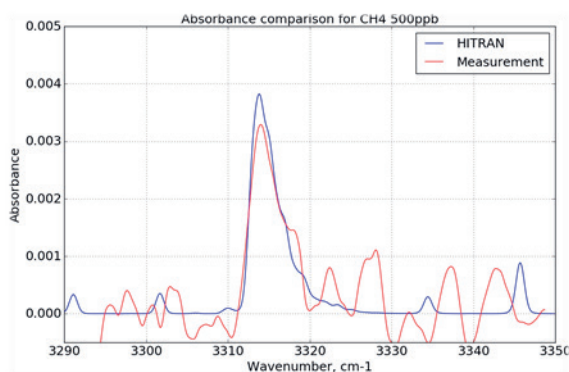


Fig. 3. Measured and HITRAN-simulated Q-branch Methane absorption profile at 500 ppb

System behavior during field testing

Two field campaigns are planned to verify the behavior of the system in real conditions. The first one consists in a flight aboard a zeppelin near Beromünster (CH) in March 2020 where some controlled methane releases will be performed.



Fig. 4. Field testing includes monitoring of ship fumes aboard the coastline of Denmark by the Explicit company (May 2020).

The second is planned for May 2020 and consists in measuring ship fumes from a helicopter (fig. 4) and benchmark the results of the FLAIR system with conventional single-specie gas detectors already available on the helicopter.

Conclusion

A compact, broadband, uncooled MWIR spectrometer for multi-species atmospheric gas analysis with dimensions 35x35x45 cm³ is currently being assembled. Two field-test campaigns will be carried out on flying platforms this spring to validate the performances of the system in real conditions.

- [1] <https://www.h2020flair.eu/> (checked Jan2020)
- [2] M. J. Süess et al, Dual-Section DFB-QCL for Multi-Species Trace Gas Analysis, *Photonics* 2016, 3, 24 (2016); doi: 10.3390/photonics3020024
- [3] M. J. Thorpe et al, Cavity-enhanced optical frequency comb spectroscopy: application to human breath analysis, *Opt. Express* 16, 2387-2397 (2008); doi: 10.1364/OE.16.002387
- [4] S. A. Diddams et al, Molecular fingerprinting with the resolved modes of a femtosecond laser frequency comb", *Nature* 445, 627-630 (2007); doi: 10.1038/nature05524
- [5] J. Gouman et al, Compact UAV compatible broadband 2D Spectrometer for multi-species atmospheric gas analysis, *Laser Congress 2019, OSA Technical Digest*, paper LTu5B.4(2019); doi: 10.1364/LSC.2019.LTu5B.4
- [6] M. Kastek et al. Technology of uncooled fast polycrystalline PbSe focal plane arrays in systems for muzzle flash detection, *Proc. SPIE* 9074, C3I Technologies for Homeland Security and Homeland Defense XIII, 90740A (2014); doi:10.1117/12.2053284
- [7] <https://www.niteurope.com/en/tachyon-16k-fpa/> (checked Jan2020)

New coherent sources for mid infrared spectroscopic applications

F. J. M. Harren

Molecular and Laser Physics, Institute for Molecules and Materials, Radboud University, 6525 AJ Nijmegen, the Netherlands

F.Harren@science.ru.nl

Summary:

An overview will be given on the new coherent sources that became available and can fulfil the needs for analytical spectroscopy in the mid infrared wavelength region. Recent highly-visible applications will be presented.

Keywords: mid-infrared, absorption spectroscopy, trace gas sensing

There is a strong need for new coherent sources in the mid-infrared wavelength region. Mid-infrared spectroscopy is widely used and its application varies from chemical production analysis to calibration of infrared space telescopes. For most of these applications a Fourier Transform Infrared Spectrometers is applied with an infrared lamp. In contrast to a lamp, coherent sources can have long interaction path lengths making them highly sensitive for absorption. Coherent mid-infrared sources were already available directly after the invention of the laser. Consisting of molecular gas discharge lasers, they were able to cover the mid-infrared wavelength region with Watts of laser power. Their disadvantage was their spectroscopic tunability, as they only emit at molecular transitions. Diode lasers were only able to be operated at milliWatts power, at liquid nitrogen temperature. With the invention of the Quantum Cascade laser (QCL) and later the Interband Cascade Laser (ICL). This changed and electrically pumped systems became available in which the wavelength emission was not depending on the band-gap of the material, but on the material design. QCLs and ICLs are covering up the mid-infrared wavelength region, with high frequency emission purity and tens of milli-Watt (up to Watts) of power in a compact design. Such systems are ideal to operate at a specific infrared wavelength a spectroscopic transition in a sensing system, but is not able to operate as an analytic tool. This changed with the external cavity system designs, in which the coverage of QCLs could be extended over hundreds of wavenumbers.

Alternatively, non-linear generation was also able to cover the mid-infrared wavelength region.

To pump non-linear crystals such as Lithium Niobate, near-infrared technologically very well developed telecom lasers are used. Via Optical Parametric Oscillation, Difference Frequency Generation and their varieties can generate high-power, monochromatic, widely tunable infrared light.

To perform analytical spectroscopy, tunability is needed, next to a wide coverage and a reasonable measuring time period to beat a Fourier Transform Spectrometer. This came available with the development of femtosecond lasers and frequency comb systems. Due to this Nobel Prize winning invention a wide spectral coverage became available with excellent frequency control. Due to dual frequency comb spectroscopy a wide wavelength coverage could be investigated at microsecond timescale. These systems are now full in development for both non-linear generation and direct pumped quantum cascade lasers.

Alternatively, an easier variant generation became available. Due to the high intensity of femto-, pico- and nanosecond pulses in fiber cores non-linear spectral broadening takes place, resulting in fiber-based supercontinuum sources with ultra wide spectral coverage, from the near-infrared to 10 micrometers. Examples will be given of supercontinuum sources and frequency combs that are able to replace partially of completely Fourier Transform Spectrometers outperforming them in interaction path length and time resolution.

Spectroscopic systems are moving towards hyperspectral imaging, combining spectral information and spatial coverage. Recent examples

are the use of plasmonics combined with mid-infrared spectroscopy determining molecular nanostructures in biological samples. This has a strong potential to transfer the properties of nanophotonics into medical devices for point-of care disease diagnostic. Another highly visible example is the use of microresonators for chemical analysis, combining high-Q resonators with activated surfaces to analyze extremely sensitive, molecular structures with high selectivity making it an ideal tool for analytical chemistry.

Uncooled high speed MWIR cameras applied to advanced spectrometers

*G. Vergara, R. Linares, R. Gutiérrez, C. Fernández, S. de la Fuente and A. Baldasano
New Infrared Technologies, Vidrieros 30, Boadilla del Monte, 28660-Madrid, Spain*

gvergara@niteurope.com

Summary:

The appearance of new and advanced instrumentation such as supercontinuum laser sources, dual comb spectrometers, virtually imaged phase arrays, powerful processors etc. is bringing the traditional scenario dominated by one channel/multichannel spectroscopy towards a new paradigm where image spectroscopy will play a key role reaching their technological and commercial maturity. Uncooled high speed infrared cameras will be an important actor in the development of affordable and reliable image spectrometers. The paper describes the state of the art in uncooled high speed infrared cameras sensitive in the MWIR. 1-5 microns, spectral range and its application in advanced spectrometers.

Keywords: High speed MWIR, imaging spectroscopy, dual comb hyperspectral imaging

Introduction

The 1-5 microns spectral range is the great interest in gas spectroscopy. Most gases have their strongest features in this region which, in practice, allow to reach good sensitivities even for compact and small spectrometer devices. However, and due to fundamental limitations, sources and sensors working in this region of the spectra have been traditionally burdened by the technological complexity associated to their processing technologies and also to the need, in most of the cases, of using expensive, power starving and bulky coolers.

The development of new materials and devices is changing the panorama in both, MWIR sources and sensors, domains. It is the case of a new family of focal plane arrays developed and processed by NIT. Based on its own technology of polycrystalline PbSe, in 2017 NIT launched the first uncooled high speed MWIR camera of the market.

The appearance of a new family of cameras, sensitive in a wide spectral range, 1 to 5 microns, with good sensitivity in uncooled operation and able to capture images to a high framerate regime will facilitate the development of a new generation of spectrometers based on disruptive concepts such as hyperspectral dual comb imaging.

Uncooled high speed MWIR camera technology

Traditionally all infrared cameras sensitive in the MWIR spectral range have needed to cool

the sensor to temperatures below 100 K. As consequence, their costs and availability have precluded a wider use in industrial and environmental applications. During the last years NIT has launched the first uncooled MWIR camera of the market. The camera heart is a focal plane array of polycrystalline PbSe monolithically integrated with the Si-CMOS ROIC processed according a proprietary method developed by the company.

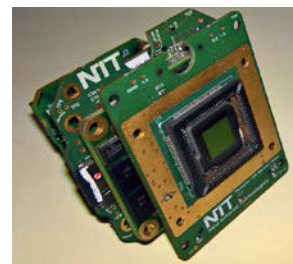


Figure 1 shows the Tachyon 16 K camera core. The picture shows the uncooled MWIR FPA developed and processed by NIT

The camera, which commercial name is Tachyon 16K, is unique. It has outstanding performances in terms of spectral band width, 1 to 4,7 microns, framerate > 2KHz @ full resolution (128x128 pixels), snapshot mode, reliability, compactness and power consumption. All these characteristics makes the camera an excellent candidate for being integrated in advanced spectrometers and active imaging spectroscopy devices.

Tachyon 16K applied to advanced spectrometers

In the frame of the H2020-FLAIR project [1] an European consortium has developed an innovative, versatile and compact spectrometer able to acquire in one shot the concentration of specific gas species. The spectrometer was specifically designed for being integrated airborne platforms. Figure 2 shows a scheme of the FLAIR spectrometer [2].

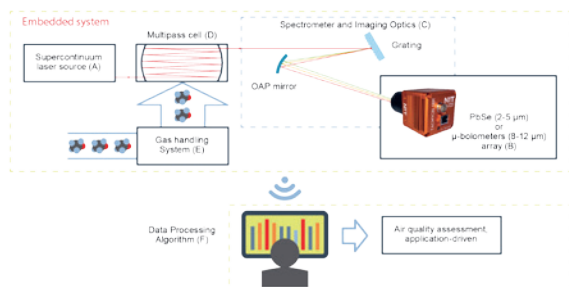


Figure 2.- Sketch shown the spectrometer developed in FLAIR project

The 16.000 pixels of the Tachyon 16K focal plane array combined with a SC laser source, a resonant cavity and different optical elements for dispersing the light allows to capture the gas spectra in one shot. Figure 3 shows the 2D absorption spectra obtained using N_2O reference cell at 1 atm. (Note: The spectra shown corresponds to set up shown in figure 2 but modified with a grating+VIPA (Virtually Imaged Phase Array) configuration.)

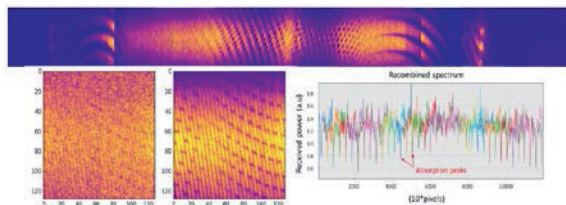


Figure 3.- 2D spectra of N_2O obtained with the first version of the FLAIR spectrometer.

Tachyon 16 K applied to dual comb hyperspectral imaging

Dual Comb Hyperspectral imaging is a novel technique with an extraordinary potential in a wide range of application fields [3]. Recent works [4] have demonstrated the advantages of using the unique performances offered by NIT cameras in terms of framerate, and spectral band sensitivity, for the application. Figure 4 shows the principle of the technique and some experimental results obtained [5] using NIT camera

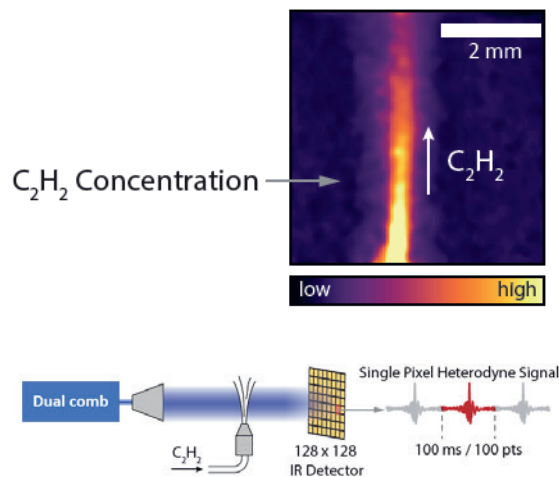


Figure 4.- Image of acetylene concentration obtained using NIT camera (courtesy [5]) and sketch describing dual comb hyperspectral imaging technique.

References

- [1] www.h2020flair.eu
- [2] J. Gourman *et al* Compact UAV compatible broadband 2D spectrometer for multi-species atmospheric gas analysis. *OCIS codes: 010.1120.300.6390*
- [3] P. Martin-Mateos and G. Guarnizo, Towards Hyperspectral dual-comb imaging." *OSA Technical digest 2019*. ISBN: 978-1-943580-61-3
- [4] T. Voumard *et al*. Dual-Comb Hyperspectral Imaging with a high-framerate infrared detector array. Abstract presented at CLEO 2020
- [5] T. Voumard *et al*. Artificial Intelligence for real-time dual-frequency comb hyperspectral imaging. Abstract presented at CLEO 2020

Highly compact laser spectrometers for mobile trace gas sensing applications

*M. Graf, B. Tuzson, P. Scheidegger, H. Looser, A. Kupferschmid, J. Ravelid, and L. Emmenegger
Empa, Laboratory for Air Pollution / Environmental Technology, CH-8600 Dübendorf, Switzerland
Email: manuel.graf@empa.ch*

Summary:

Mid-IR spectroscopy using QCLs allow sensitive, selective, and fast detection of trace gases. Recent developments in multipass cell design and acquisition electronics permit the construction of rugged and lightweight instruments for field application. This is demonstrated by the successful balloon-borne water vapor measurement in the lower stratosphere with an integrated QCL-based spectrometer.

Keywords: mobile instrumentation, tunable laser spectroscopy, mid-IR, trace gas

Introduction

Infrared (IR) spectroscopy is a powerful tool for gas sensing. Especially attractive is the mid-IR spectral region, where molecules have their fundamental absorption bands with cross sections significantly larger than in the near-IR. With the advent of quantum cascade lasers (QCL) as rapidly tunable narrowband light sources, the mid-IR spectral region became accessible for this highly selective and sensitive technique. Today, we experience an increasing demand for compact and lightweight spectrometers to be deployed e.g. on board of cars, drones, or balloons. Such mobile settings enable the monitoring of trace gas concentrations at a high spatio-temporal resolution at urban, rural or industrial sites, or even in the upper atmosphere. Prominent examples are the detection of methane sources aboard of unmanned aerial vehicles or the water vapor measurement in the upper troposphere and lower stratosphere (UTLS). However, the required miniaturization for such applications implies extraordinary constraints in terms of mass, size and robustness, as well as resilience towards the variation of environmental conditions such as temperature and pressure.

Segmented circular multipass cell

In order to enhance the precision and detection limit, absorption spectrometers make use of beam extending multipass cells (MPCs) to increase the interaction path length between the probe laser beam and the sample gas, usually to many tens of meters. These cells are generally a decisive factor with regard to small and lightweight instruments, because conventional designs are often limited in achieving sufficient compactness *and* optical stability. We therefore

developed a versatile concept for compact and well-controlled beam folding which is especially suited for compact and lightweight spectrometers [1]. Thereby, we combine the constructional advantages of toroidal MPCs [2], i.e. compactness, rigidity and low weight, with optimal optical properties: In contrast to the toroidal MPCs, optical noise from interference fringes is inherently reduced by the optically stable design, realized by including spherical segments to the reflective surface. This, furthermore, leads to the acceptance of a wide range of input beam shapes, such that beam pre-shaping can essentially be omitted. Thus, the optical setup is drastically reduced to only the laser, the MPC, and the detector (Fig. 1.). This layout paved the way for highly compact trace-gas spectroscopy under challenging conditions.

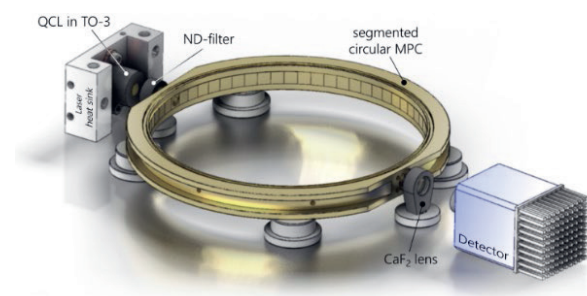


Figure 1: Basic optical layout incorporating the SC-MPC in open-path configuration.

Water vapor in the UTLS

Water vapor is the dominant greenhouse gas, and its abundance in the upper tropospheric and lower stratospheric region (8-25 km altitude) is of great importance to the Earth's radiative balance. Therefore, accurate and frequent

measurement of water vapor concentrations at these altitudes is of utmost importance. We present a compact and rugged laser absorption spectrometer that detects water vapor in the very low ppm range with a precision $<1\%$ [3]. The spectrometer operates at $6\ \mu\text{m}$ requiring an optical path length of 6 m, which is realized by a specifically designed SC-MPC with a mass of only 100 g. The low overall weight of the spectrometer (3.9 kg) enables its flexible and inexpensive deployment to the stratosphere aboard of meteorological balloons. The autonomously operating instrument further benefits from considerable hardware optimization, including FPGA-based data acquisition and economic laser driving electronics [4,5], resulting in an overall power consumption of 15 W. The successful operation at altitudes up to 28 km was recently demonstrated in a flight campaign.



Figure 2: Spectrometer for balloon-borne measurement of water vapor at the UTLS

UAV based methane detection

The assessment of methane leakage from sources such as oil and gas production facilities can be achieved by deploying an unmanned aerial vehicle (UAV) equipped with a methane sensor to map the spatial and temporal variability of emission plumes. We target this application field by an open-path QCL spectrometer that incorporates the presented concepts. The instrument is capable of measuring atmospheric methane at several Hz with a precision below 1 ppb. Its compact and lightweight design (1.6 kg) readily allows its deployment aboard of commercial drones. The instrument was already validated and utilized in numerous field campaigns in Switzerland, Sweden and Romania.



Figure 3: Commercial drone equipped with the methane spectrometer.

References

- [1] M. Graf, L. Emmenegger, and B Tuzson. Compact, circular, and optically stable multipass cell for mobile laser absorption spectroscopy. *Optics Letters*, Vol. 43, Issue 11, 2018, pp. 2434-2437
- [2] B. Tuzson, M. Mangold, H. Looser, A. Manninen, and L. Emmenegger. Compact multipass optical cell for laser spectroscopy. *Optics Letters*, Vol 38, Issue 3, 2013
- [3] C. Liu, B. Tuzson, P. Scheidegger, H. Looser, B. Bereiter, M. Graf, M. Hundt, O. Aseev, D. Maas, L. and L. Emmenegger. Laser driving and data processing concept for mobile trace gas sensing: design and implementation, *Review of Scientific Instruments*, Vol. 89, Issue 6, 2018, pp. 065107-065109.
- [4] M. Graf, P. Scheidegger, H. Looser, B. Stanicki, T. Peter, L. Emmenegger, and B. Tuzson. Mid-IR laser spectrometer for balloon-borne lower stratospheric water vapor measurements, in *Proceedings of the conference on 'Lasers and Electro-optics. CLEO: Applications and Technology' San Jose, California, United States 5-10 May 2019*, p. AM1K.3
- [5] M. Fischer, B. Tuzson, A. Hugi, R. Broennimann, A. Kunz, S. Blaser, M. Rochat, O. Landry, A. Mueller, and L. Emmenegger. Intermittent operation of QC-lasers for mid-IR spectroscopy with low heat dissipation: tuning characteristics and driving electronics. *Optics Express*, Vol. 22, Issue 6, 2014, pp. 7014-7027
- [6] C. Liu, B. Tuzson, P. Scheidegger, H. Looser, B. Bereiter, M. Graf, M. Hundt, O. Aseev, D. Maas, L. and L. Emmenegger. Laser driving and data processing concept for mobile trace gas sensing: design and implementation, *Review of Scientific Instruments*, Vol. 89, Issue 6, 2018, pp. 065107-065109.

Multispecies Trace Gas Sensor for Real-time Quality Control of Stored Fruits

A. Khodabakhsh, K. E. Jahromi, Q. Pan, M. Nematollahi, F. J. M. Harren
Trace Gas Research Group, Department of Molecular and Laser Physics, Institute for Molecules and Materials, Radboud University, 6525 AJ Nijmegen, the Netherlands

a.khodabakhsh@science.ru.nl

Summary:

We present the principles and development of a transportable trace gas sensor based on a broadband mid-infrared spectrometer utilizing a supercontinuum laser source. The sensor is able to simultaneously detect multiple gas species, including various hydrocarbons, aldehydes and alcohols in real-time with sub-ppmv sensitivities. We demonstrate the application of our sensor in real-time measurement of the volatile compounds produced due to the respiration of the fruits in the storage facilities, providing a tool for monitoring the status of the stored fruits and minimizing the fruits wastage.

Keywords: mid-infrared, absorption spectroscopy, trace gas sensing, multi-species, fruit storage.

Introduction

After harvesting, the fruits are usually stored in a cold controlled atmosphere with high carbon dioxide and low oxygen concentrations to maximize the storage time. However, it is estimated that around 10% of fruits are wasted in this storage period, prior to delivering to the market. Various studies have shown that different volatile species released from the fruits are related to fruit wastage via different undesirable processes such as ripening (ethylene), fermentation (ethanol, acetaldehyde and ethyl-acetate), rotting (methanol and acetone) and chilling injury (ethane). Therefore, continuous monitoring of these trace volatile species provides a comprehensive information of the storage status and can be used to fine tune the storage condition, preventing degradation processes at the early stage. Recently, we have developed broadband absorption spectroscopy systems based on mid-infrared supercontinuum sources, capable of multispecies detection with high sensitivity [1,2]. Here we present a fully-operational and transportable prototype sensor, based on one of these systems, which is able to simultaneously measure these volatile species in real-time.

Experimental Setup and Methods

An overview of the fully integrated sensor prototype is depicted in Fig. 1. Three functional parts are integrated, including the optical setup for continuous gas sensing, the gas handling system for automatic gas sampling, and the (opto)electronic compartment containing the

associated power supplies and hardware drivers. The optical setup is based on broadband absorption spectroscopy utilizing a mid-infrared supercontinuum light source [2].

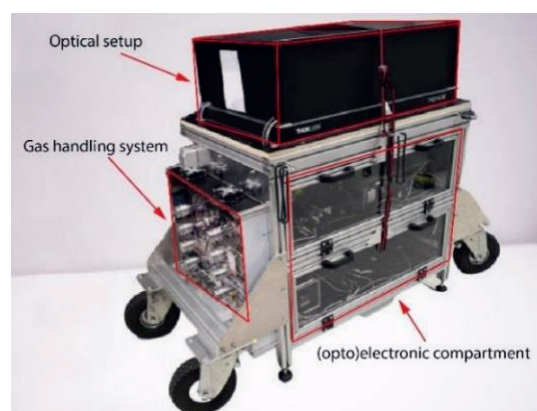


Fig. 1. Graph of variable vs analyte concentration (style "SMSI_Conferences_Caption") for two different temperatures.

To enhance the interaction length between the sample and the laser beam and achieve higher detection sensitivity, the supercontinuum beam was transmitted through a multipass cell (76 m optical path length). The output beam from the cell is diffracted from a grating mounted on a galvo scanner, scanning at 20 Hz. The diffracted beam is recorded by a single photodetector, constructing the absorption spectrum of the gas sample inside the multipass cell. A data acquisition card in combination with a developed LabVIEW program was used to correlate the amplified photodetector signal and the position signal of the galvo scanner, achieving a spectral cov-

erage of 500 cm^{-1} ($2725 - 3225\text{ cm}^{-1}$) and a spectral resolution of 2.5 cm^{-1} . The gas handling system was developed to deliver the gas sample from the storage room to the multipass cell with the possibility of sending the sample back to the storage room to close the loop. Since water vapor is a common interfering species in our sensor, a water trap based on thermoelectric cooling was integrated into the gas handling system. It reduces the humidity level of the gas sample before sending it to the measurement cell. For automated operation as well as signal processing and concentration retrieval, an integrated LabVIEW program was developed for the sensor. A multi-variant curve-fitting algorithm was implemented to the LabVIEW program to perform a global fitting for different species instead of focusing on a specific narrow spectral feature, enhancing the overall precision for multi-species gas sensing. A more detailed description of the setup and signal processing can be found in [2].

Results

A series of laboratory-scale measurements of apples were performed in different atmospheric conditions. First, Off-the-shelf apples (~750 g, royal gala) were stored inside three interconnected glass containers (6 L total volume) filled with nitrogen gas at $21\text{ }^{\circ}\text{C}$. The subsequent fermentation process was monitored by continuously measuring the emitted gas volatiles for 150 minutes. A closed loop configuration was adopted to recycle the gas, mimicking the accumulation process in practical storage rooms. Afterwards, the nitrogen atmosphere was replaced by ambient air, while the measurement of the targeted volatiles continued for 250 minutes. A number of volatile species were detected, including ethanol, methanol, ethane, ethyl acetate, ethylene and acetaldehyde, as shown in Fig. 2A. In particular, a pronounced concentration increase by an order of magnitude was observed for ethanol, confirming the expected fermentation process. The concentration values of other fermentation markers, i.e. ethyl acetate and acetaldehyde, evolved on a similar time scale, reaching a more stable plateau of ca. 8 ppmv after two hours. After changing the storage atmosphere from nitrogen gas to normal air, the concentrations of these volatiles recovered, as the gaseous volatiles were depleted, indicating an ongoing emission from the apples. Note that ethylene production was gradually restored, as ethylene was unlikely to be produced in the previous condition of zero oxygen. Following the fermentation experiment, two rotted apples were added into the containers, leading to a significant concentration increase of methanol, which is a typical volatile marker for rotting. The concentration of eth-

ylene also increased steadily within five hours, whereas the concentrations of other volatiles stabilized after one hour, as shown in Fig. 2B. Each data point corresponds to a measurement time of 5 minutes, and the associated errors are derived from the standard deviation of 10 measurements, each averaged for 30 seconds.

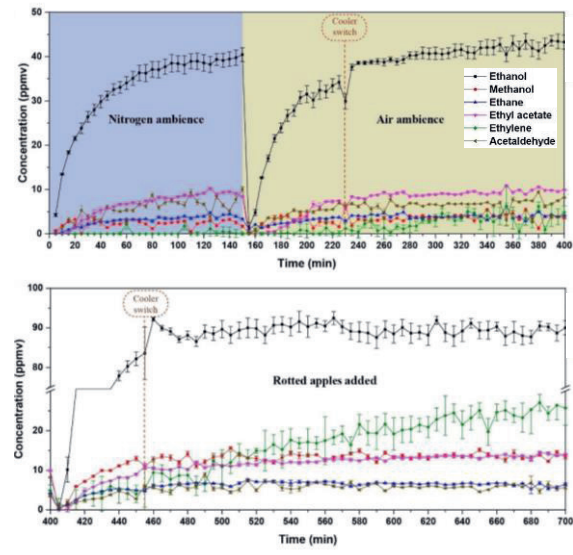


Fig. 2. Concentration evolution of various gas volatiles emitted from apples stored in nitrogen and air atmospheres (A), followed by adding two rotted apples (B).

Conclusions

The developed prototype sensor can automatically and continuously monitor multiple volatiles emitted from fruits, showing application potentials for sampling in commercial fruit storage rooms. In addition, other applications requiring multi-species and real-time trace gas sensing will be targeted, such as environmental monitoring, biomedical research and oil/gas industry. Future work includes a systematic comparison of the developed prototype with standard instrumentation such as GC-MS, while improving the sensitivity to tens of part-per-billion level.

References

- [1] K. E. Jahromi, Q. Pan, L. Hogstedt, S. M. M. Friis, A. Khodabakhsh, P. M. Moselund, F. J. M. Harren, Mid-infrared Supercontinuum-based Up-conversion Detection for Trace Gas Sensing, *Opt. Express*, 27, 24469-24480 (2019); doi: 10.1364/OE.27.024469
- [2] K. E. Jahromi, Q. Pan, A. Khodabakhsh, C. Sikkens, P. Assman, S. M. Cristescu, P. M. Moselund, M. Janssens, B. E. Verlinden, F. J. M. Harren, A Broadband Mid-Infrared Trace Gas Sensor Using Supercontinuum Light Source: Applications for Real-Time Quality Control for Fruit Storage, *Sensors*, 19, 2334 (2019); doi: 10.3390/s19102334

METROLOGICAL CHARACTERIZATION and CALIBRATION of THERMOGRAPHIC CAMERAS in the TEMPERATURE RANGE from 50 °C to 960 °C

Sebastian König¹, Berndt Gutschwager¹, Ingmar Müller¹, Richard D. Taubert¹, Frank Nagel²,
Jörg Hollandt¹

¹ *Physikalisch-Technische Bundesanstalt, Abbestr. 2-12 Berlin, Germany,*

² *DIAS Infrared GmbH, Pforzheimer Str. 21 Dresden, Germany*
sebastian.koenig@ptb.de

Summary:

We present the metrological characterization and calibration of four different types of thermographic cameras for quantitative temperature measurement traceable to the International Temperature Scale of 1990 (ITS-90). All measurements are performed according to the Technical Directives VDI/VDE 5585. Results achieved with different calibration procedures are compared for each type of camera and among the four cameras. An uncertainty budget for the calibration of each camera is set up according to the “Guide to the Expression of Uncertainty in Measurement” and VDI/VDE 5585 Part 2.

Keywords: Thermographic camera, infrared, technical specifications, metrological characterization, calibration

Introduction

New manufacturing methods for uncooled microbometer thermographic detectors have resulted in a rapid development of miniaturized and high-resolution, inexpensive sensors hence opening up an ever-increasing number of new application areas [1]. This development makes contactless temperature measurement with thermographic cameras available to a large number of users. Furthermore, thermographic cameras are more and more applied for quantitative measurements, e.g. to control production processes. It is therefore important to define the relevant technical specifications and to set up dedicated calibration schemes traceable to national and international standards. The German standardization committee VDI/VDE FA 8.16 *Temperature Measurement with Thermal Imagers* has published the Technical Directive VDI/VDE 5585 Part 1 *Metrological Characterization of Thermographic Cameras* [2] in March 2018. This is now being extended into an IEC Technical Specification by the international standardization committee IEC SC65B WG5 *Temperature Sensors*. Currently the Technical Directive VDI/VDE 5585 Part 2 *Calibration of Thermographic Cameras* [3] is in the process of completion. Part 2 specifies in detail different calibration methods of thermographic cameras and the related uncertainties. We have carried out a complete quantitative metrological characterization and calibration according to the

Technical Directives VDI/VDE 5585 for different types of thermographic cameras in the temperature range from 50 °C to 960 °C. The thermographic cameras used differ in their wavelengths and detector types.

Metrological characterization

VDI/VDE 5585 Part 1 gives definitions and standardized procedures for the determination of the relevant technical specifications for non-contact temperature measurement with thermographic cameras. In the following we have determined the relevant specifications for absolute temperature measurement: the non-uniformity, i.e. inhomogeneity of detector responsivity, (NU), the noise equivalent temperature difference (NETD), the inhomogeneity equivalent temperature difference (IETD) and the size-of-source effect (SSE). The SSE of two investigated cameras at 100.0 °C is plotted as an example in Figure 1. The size of the radiating source was gradually increased and the averaged displayed temperatures in the center of the images of the cameras was recorded.

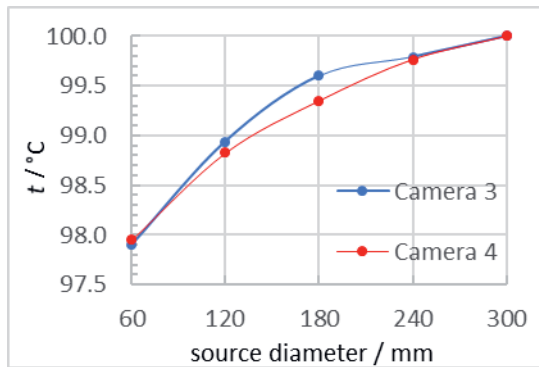


Fig. 1. The SSE of two investigated cameras

Method to improve the NU and IETD

We will present the improvement of the NU and the IETD of thermographic cameras utilizing the Data Reference Method (DRM) [4]. This method was, for example, applied to Camera 3 at a radiator temperature of 100 °C. Figure 2 shows the original image of Camera 3. The observed temperature inhomogeneities partly result from the true temperature inhomogeneity across the plate and, partly, from the imperfect NUC of the camera. In Figure 3 the true radiation temperature distribution of the plate radiator obtained with the DRM is shown.

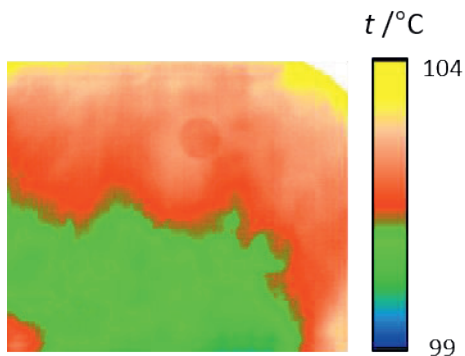


Fig. 2. Radiation temperature image of a plate radiator, setpoint at 100.0 °C taken by Camera 3

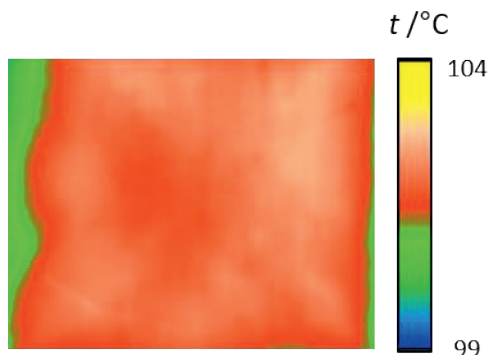


Fig. 3. True radiation temperature distribution of the observed plate radiator after the application of the DRM

Metrological Calibration

The technical directive VDI/VDE 5585 Part 2 distinguishes three calibration procedures: A, B and C. The distinction is drawn by the irradiated detector area. With Procedure C, for example, only the center of the detector array is irradiated and an average temperature is calculated over a defined region of interest (ROI) within the irradiated area (Figure 4). We will introduce all three methods and show exemplary calibration results of the investigated cameras in the temperature range from 50 °C to 960 °C.

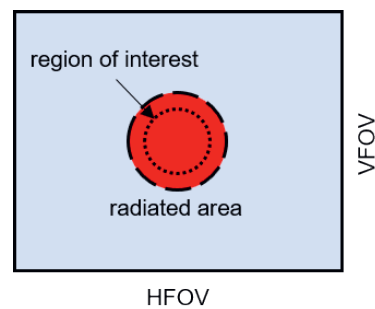


Fig. 4. Calibration Procedure C (VDI/VDE 5585 Part 2): the center of the detector array is irradiated

Uncertainty budget

An estimation of the overall uncertainty budget of the calibration traceable to the International Temperature Scale (ITS-90) was done according to the Guide of the Expression of Uncertainty [5] for the four cameras. The uncertainty budget is essentially dominated by two parts. The SSE has the greatest influence on the camera side and the temperature homogeneity of the calibration radiator used on the source side. Results will be given in the presentation.

References

- [1] Budzier H. and Gerald G. *Thermal infrared sensors: theory, optimisation and practice*. John Wiley & Sons, 2011
- [2] VDI/VDE 5585 Part 1, Technical temperature measurement – Temperature measurement with thermographic cameras - Metrological characterization, Verein Deutscher Ingenieure, Düsseldorf 2018
- [3] VDI/VDE 5585 Part 2, Technical temperature measurement – Temperature measurement with thermographic cameras - Calibration, Verein Deutscher Ingenieure, Düsseldorf 2020
- [4] Gutschwager B. and Hollandt J.: Nonuniformity correction of imaging systems with a spatially nonhomogeneous radiation source, *Applied Optics* 54, Issue 36, 10599-10605, 2015
- [5] ISO, IEC, and BIPM OIML. "Guide to the Expression of Uncertainty in Measurement." *Geneva, Switzerland* 122 (1995)

Evaluation of Cryogenic Preamplifiers for Infrared Focal Plane Array Detectors

Christopher Mandla^{1,2,3}, Max Engelhardt², Naidu Bezawada², Derek Ives², Markus Plattner^{1,3}
¹ MPI for extraterrestrial physics, Gießenbachstraße 1, 85748 Garching, Germany
² European Southern Observatory, Karl-Schwarzschild-Straße 2, 85748 Garching, Germany
³ Technical University of Munich, Arcisstraße 21, 80333 München, Germany

mandla@mpe.mpg.de

Summary:

Infrared focal plane array detectors for instrumentation of ground-based telescopes such as the VLT are operated at cryogenic temperatures to minimize dark current and reduce cosmetics. To achieve high signal integrity, the analogue video outputs of MCT type sensors from Teledyne, Raytheon or Leonardo are typically amplified inside the cryo-environment close to the detector and which requires highly efficient preamplifier designs and devices. Within the scope of this paper, three design concepts built from commercial products are compared and simulated regarding power consumption, bandwidth, and noise.

Keywords: Infrared Detector, Simulation, Preamplifier, Cryogenics, low noise

Motivation

Ground-based infrared telescope instruments translate infrared light of observed objects to digital values (see Fig. 1). The photoelectric effect inside the focal plane array pixels converts photons to electrons and thence to an electrical voltage via a capacitor.

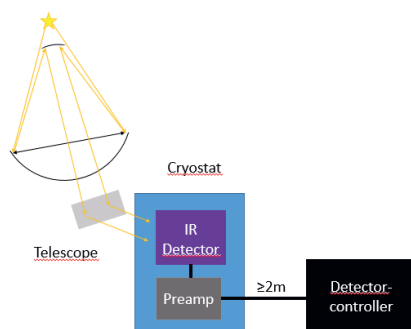


Fig. 1. signal chain of ground-based telescope; from the light of stars to digital units

State of the art infrared focal plane arrays for near- up to mid-infrared astronomy are usually operated at temperatures between 4K to 80K with a readout frequency varying from 100 kHz up to 5 MHz per video channel [1], dependent on the wavelength range. However newly developed detectors are specified to operate at pixel speeds in excess of 10MHz. Preamplifiers allow the detectors to drive longer cables of 2m or

more at high speeds, by applying electronic gain they can increase the signal above external noise sources and by converting single-ended video signals to differential signaling they greatly improve the common mode rejection. Due to these benefits but also to minimize the external capacitive load, the preamplifiers are operated in the cryo-environment close to the detectors.

The requirements of cryogenic preamplifiers for scientific infrared detectors are typically a noise of less than $72\mu\text{V}_{\text{rms}}$, a bandwidth of greater than two times the signal frequency and static power of less than 100mW per channel.

Not all technologies can be used in cryo-environment, for example, ordinary silicon bipolar transistors suffer from low-emitter-base efficiency, making them unusable at temperatures below 100K [2]. GaAs or SiGe compound semiconductor devices, JFETs and MOSFETs are compatible with the cryo-environment and some can even work down to very low-temperature levels [2].

Cryogenic Preamplifier

Cryogenic preamplifiers for infrared detectors have been utilized and developed at ESO for many years [3]. Besides the standard ESO preamplifier design [1] two additional designs are analyzed: a J-FET Source Follower Preamplifier and a 2 Stage Preamplifier.

In the J-FET Source Follower design, a J-FET in a Source Follower configuration is utilized to buffer the high impedance of the detector video output with unity gain. In this design, a single-ended video signal is amplified and routed in parallel with a corresponding reference voltage which is buffered by a second J-FET to form a pseudo-differential signal.

The 2 Stage Preamp design combines a non-inverting cryogenic operational amplifier that buffers the video signal with a differential amplifier which can be realized by the standard ESO Preamp. This configuration only needs one operational amplifier with unity gain in the cryo-environment.

Results

To compare all three designs a simulation with SIMetrix was conducted. For this simulation, a total cable length of 2m is assumed. The spacing between the first and second stage of the 2 Stage Preamp Design is set to 1m.

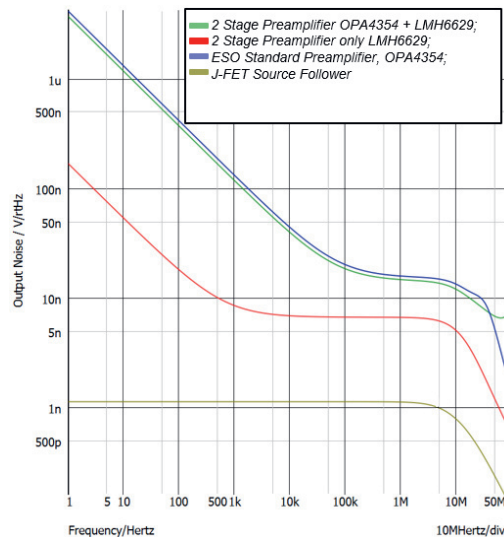


Fig. 5. Output Noise

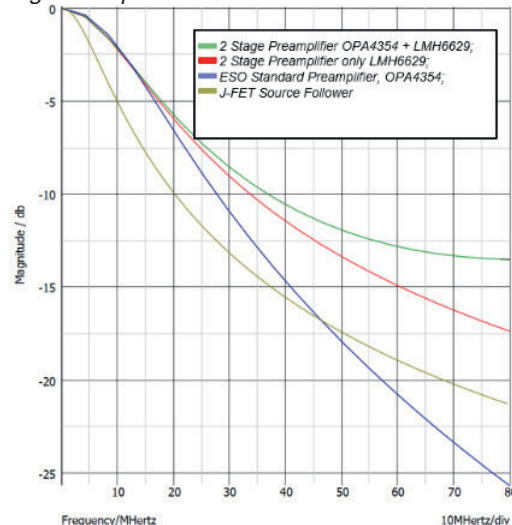


Fig. 6. Bandwidth

An overview of all designs and their simulation results are listed in Tab. 1.

Tab. 1: Overview of Designs and Results

	ESO Pre-amp	J-FET design	2 Stage Pre-amp
Amplifier	OPA4354	J309	1 st stage: LMH6629 or OPA4354 2 nd stage: OPA4354
Static power (mW)	47mW	50mW	Only 1 st stage: 77.5 or 23.5
Gain	3	1	3
noise (μVrms)	~61.9	~3.9	~23 or ~56
BW (MHz)	11.3	6.476	11.3

Conclusion

All designs are less than 100mW static power per channel and are also less than a total noise $72\mu\text{Vrms}$. For slow read-out frequencies, a J-FET Source Follower Amplifier Design is favorable up to frequencies of 2 to 3 MHz due to the small number of required components, low power consumption, and noise. For higher frequencies, the 2 stage Preamp Design seems more favorable as only one operational amplifier with unity gain is required in a cryo-environment. The flexibility to utilize any conventional differential amplifier including bipolar technology as a second stage is an additional advantage that could increase the current Bandwidth to support faster detectors and longer instrument cables. The next step is a dedicated cryogenic test of the two new designs to analyze the actual performance when operated cold.

References

- [1] Ackermann, Jörg & Azman, Suleyman & Gheorghie, Codin & Meier, Dirk & Maehlum, Gunnar. (2018). Multi-Channel Preamp IC for IR-Sensor and FPA Readout. 10.13140/RG.2.2.27382.65607.
- [2] Device and Circuit Cryogenic Operation for Low Temperature Electronics, eds. F. Balestra and G. Ghibaudo, Kluwer Academic Publishers, 2001, ISBN 0-7923-7377-4
- [3] D.Ives et al., Performance evaluation of 5 μm cut-off Hawaii-2RG detectors using the fast readout amplifiers, *High Energy, Optical, and Infrared Detectors for Astronomy IV (2010)*, Proc. of SPIE Vol. 7742 77421S-3; · doi: 10.1117/12.8

Development of a scalable nanotube-microbolometer technology

M. Michel¹, S. Weyers¹, D. Weiler¹, T. Geruschke¹, S. Blaeser¹, E. Zakizade¹, F. Hochschulz¹, H. Vogt^{1,2}

¹ Fraunhofer Institute for Microelectronic Circuits and Systems IMS, Duisburg (Germany),

² Department of Electronic Components and Circuits, University of Duisburg-Essen, Duisburg (Germany)

marvin.daniel.michel@ims.fraunhofer.de

Summary:

Fraunhofer IMS provides a manufacturing process for microbolometer based FIR-imagers (IRFPAs). Beside classical approaches with membranes of microbolometers thermally isolated by lateral legs, Fraunhofer IMS developed a manufacturing process for a thermal isolation realized by nanotubes. This approach benefits the scalability of pixel pitch, because of a pitch-independent thermal isolation. Latest progress in mechanical stability as well as a qualitative characterization of a demonstrator device with 17 μm nanotube-microbolometers on a 17 μm ROIC in QVGA-resolution will be presented.

Keywords: FIR-imager, uncooled imager, microbolometer, nanotubes, scalability, QVGA.

Introduction

Due to recent progress in pixel design of uncooled infrared imagers, pixel size decreased continuously from the latest state-of-the-art pixel size of 17 μm [1, 2]. To achieve the necessary thermal isolation of microbolometer membranes, Fraunhofer IMS developed a nanotube based electrical contact, which also acts as thermal isolation and advantageously, is independent from pixel size [3].

The use of a vertical thermal isolation by nanotubes allows to reduce the pixel size without redesigning the contact area. This opens up the path to a microbolometer technology which is scalable i.e. independent from pixel pitch. One key requirement for a scalable technology is stress management. The effects caused by stress become more prominent with increasing pixel size. Therefore, the technology will be discussed by microbolometers with 17 μm pixel pitch in this paper.

Mechanical Stability of Microbolometer Membranes

For nanotube-microbolometers the filling factor and therefore the absorption area can be increased to nearly 100 %. The microbolometer membrane has to incorporate several functionalities like temperature sensing, absorption, and electrical connection. Since all these functions cannot be covered by one material the membrane is realized as multilayer stack made of

metallic, insulating and sensing material with different mechanical properties. Especially for large membranes compared to small nanotube contacts this can cause highly bent membranes, which can result in membranes touching the substrate causing a thermal bypass and therefore insensitive pixels (Fig. 1).

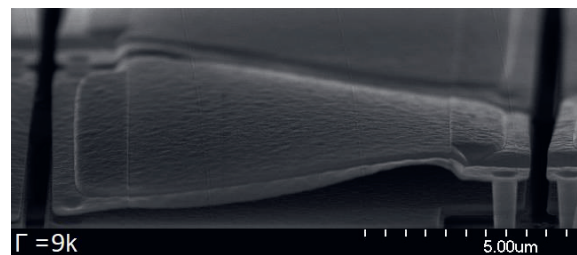


Fig. 1. Highly bent microbolometer membrane.

A set of mechanical test structures was used to evaluate the intrinsic membrane stress of the multilayer material systems (compare Fig. 2).

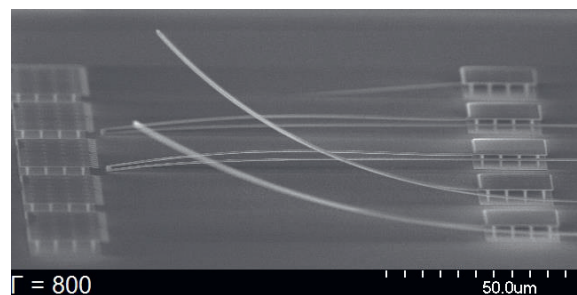


Fig. 2. Long-Short test beams for intrinsic stress measurement.

The lateral deflection of the Long-Short test beams displays the intrinsic mechanical stress of the multilayer stack, whereas the stress gradient is indicated by the vertical curvature of the beams [4, 5].

Intrinsic material stress can be influenced only in a limited way due to process limitations by deposition and patterning techniques. Therefore, the ratio between single layer thicknesses was adapted based on the results of the mechanical test structures. Optimized layer thicknesses avoid large stress gradients over the material stack and result in a smaller out-of-plane deflection.

Nanotube-Microbolometer

A SEM picture of a microbolometer array with improved material stack resulting in a negligible deflection is shown in Fig. 3.

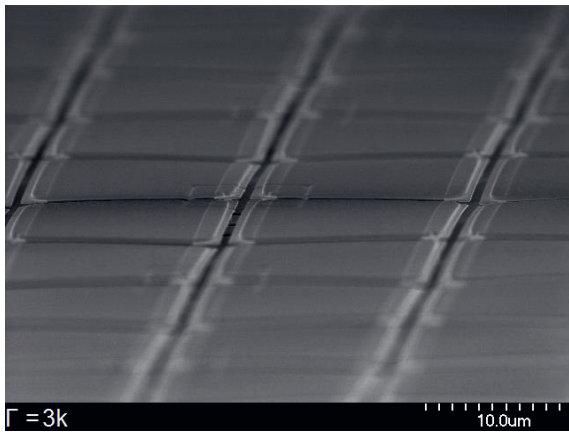


Fig. 3. QVGA-IRFPA of 17 μm nanotube microbolometers.

For qualitatively analyzing the technology a QVGA-IRFPA with 17 μm microbolometers, a digital readout integrated circuit and a chip-scale vacuum package was fabricated. Its performance is given by a test scene in Fig. 4.

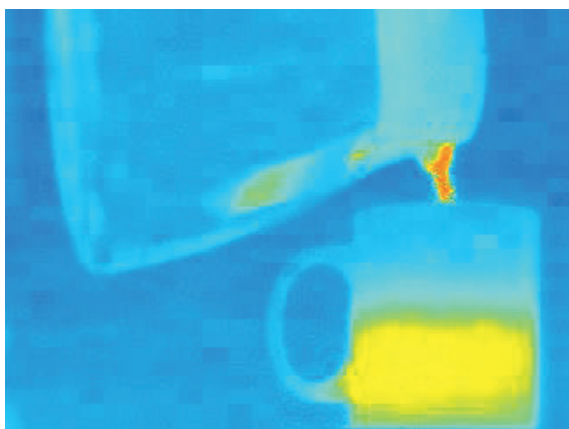


Fig. 4. FIR test picture of hot water flowing in a coffee mug. Image is shown uncompensated and without pixel correction. NETD of the IRFPA is estimated to 230.1 mK with only 2 electrical defect pixels in the QVGA-array.

The filling level of a coffee mug and also the reflection of the mug at the metallic surface of the thermal jug can be demonstrated.

Conclusion

The mechanical stability of the membrane, which was presented at the upper scaling limit of 17 μm pixel size, constitutes a necessary condition for a further enhancement of the nanotube-microbolometer technology.

Minimizing the mechanical stress of the membrane also reduces the mechanical load on the nanotubes. This allows to decrease the wall thickness of the nanotube to improve the thermal isolation and thereby reducing the NETD.

The presented nanotube-microbolometer technology features a simple scalability towards smaller pixel sizes without changing the elemental fabrication process. Therefore, microbolometers with a nanotube contact could be pushed towards the optical resolution limit [6] in the FIR-regime at 5 μm pixel size.

References

- [1] A. Rogalski, Next decade in infrared detectors, *Proc. SPIE 10433, Electro-Optical and Infrared Systems: Technology and Applications XIV*, 104330L (2017); doi: 10.1117/12.2300779.
- [2] D. Weiler, et al., High-performance uncooled digital 17 μm QVGA-IRFPA-using microbolometer based on amorphous silicon with massively parallel Sigma-Delta-ADC readout, *Proc. SPIE 10624, Infrared Technology and Applications XLIV*, 1062419 (2018); doi: 10.1117/12.2304866.
- [3] K.-M. Muckensturm, et al., Measurement results of a 12 μm pixel size microbolometer array based on a novel thermally isolating structure using a 17 μm ROIC, *SPIE Defense+ Security. International Society for Optics and Photonics* (2016); doi: 10.1117/12.2223608.
- [4] Chi S. Pan, Wensyang Hsu, A Microstructure for in situ Determination of Residual Strain, *Journal of Micromechanical Systems* 8, p. 200-207 (1999); doi: 10.1109/84.767116.
- [5] W. Fang, J. A. Wickert, Determining mean and gradient residual stresses in thin films using micromachined cantilevers, *Journal of Micromechanics and Microengineering* 6, p. 301-309 (1996); doi: 10.1088/0960-1317/6/3/002.
- [6] Gerald C. Holst, Ronald G. Driggers, Small detectors in infrared systems, *Optical Engineering* 51, p. 096401-1 –096401-10 (2012); doi: 10.1117/1.OE.51.9.096401.

New high resolution 120x84 Thermopile Arrays for IR Imaging applications

*J. Schieferdecker, M. Schnorr, B. Forg, F. Herrmann, C. Schmidt, W. Leneke, M. Simon,
Heimann Sensor GmbH, Maria-Reiche-Str. 1, D-01109 Dresden
info@heimannsensor.com*

Abstract:

Infrared arrays found their way into wide spread applications in various industries. Due to increasing resolutions and decreasing costs the growth rates for Infrared (IR) imaging sensors and cameras are assumed to continue having double digit annual growth rates also for the coming decade of the 20th. While photon IR detectors have been the drivers for thermal imaging in last century, the innovations in Si microelectronics and MEMS paved the way of success for uncooled thermal detector arrays. Pyroelectric arrays, which lead to the very first automotive night vision camera with 80000 pixels in year 2000 /1/, fell back due to their need of continuous mechanical modulation and the difficulty to integrate pyroelectric sensitive materials into monolithic CMOS structures. After that, micro-bolometers dominated the high resolution imaging markets /2/; while fully monolithic Poly-Si type IR thermopiles were the trendsetters for lower resolution consumer applications.

Unlike the other array technologies the thermopile arrays allow to build true shutterless radiometric IR cameras. The reason is, that thermopile arrays are DC sensitive devices and do not need to be biased. Thermopile arrays with pixel numbers from 8x8, 16x16, 32x32 resp. 32x24 were introduced to mass production for various consumer applications. In addition, the pixel size of 90 μm allowed a first thermopile array with 80x64 pixels /3/. Array formats above 80x64 pixel were so far clearly the domain of micro bolometers or other technologies.

In this paper, Heimann Sensor introduces first thermopile arrays with 60 μm pixel size allowing to extend the application range into thermal Imaging and surveillance. All necessary signal conditioning and readout electronics including SPI interface are monolithically integrated on the sensor chip and allow thermopile arrays up to 120x84 pixels to fit in a standard TO-8 housing.

The digital output via SPI interface reduces the number of necessary connections to 6-pin only. Thanks to integrated 16 Bit AD converters on-chip the sensor arrays can be operated with Frame Rates up to 12 Hz (full resolution) and allow a very wide dynamic range with object temperatures up to 1000 °C. Higher frame rates are possible with setting the ADC resolution to 15 or 14 Bit.

All thermopile arrays and array modules are equipped with an infrared optics. These infrared optics are designated for the required field of view in the application; e.g. from 9-12 deg FOV for far distances up to 120x90 deg FOV for ultra wide field of view.

Since the new 120x84 array chip has 60 μm pixels vs the 90 μm pixels of the 80x64, both chips come with similar focal plane and chip sizes. Due to their identical SPI interface both chips can be mounted in same housing with same optics, giving rise to a “drop in” solution.

Thermal images obtained from the 120x84 demonstrate its abilities for thermal imaging (see Fig. 1 and 2):

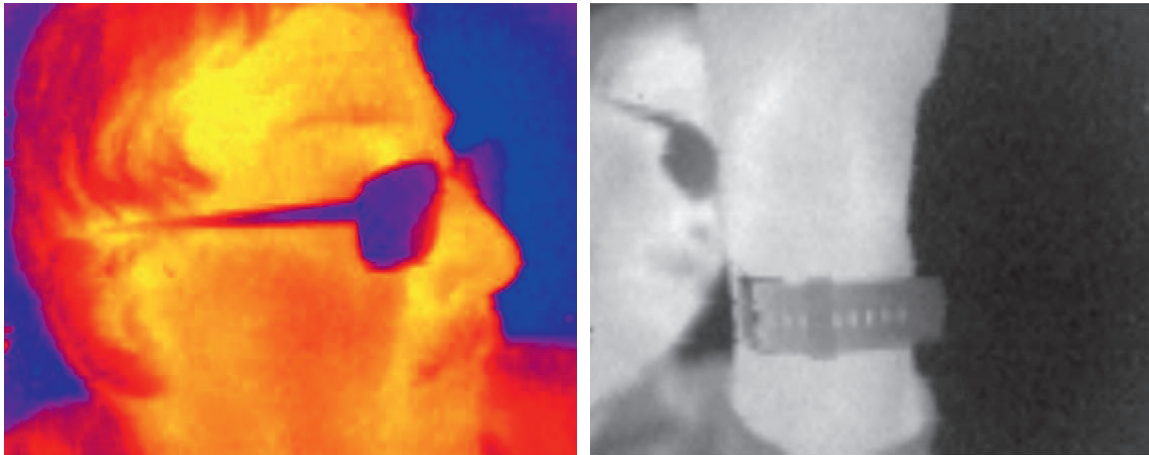


Fig. 1 shows examples for thermal images created by the 120x84 array module.



Fig. 2 Can the IR array 120x84 really detect the “pig in the poke” (Katze im Sack)?

References:

/1/ Martinelli, N., Boulanger S.: “Cadillac de Ville Thermal Imaging Night vision system”, SAE Technical Paper 2000-01-0323, 2000

/2/ T. Hoelter, A. Kathman, A. Richards, M. Walters; “Key Technology Trends and Emerging Applications for Compact Thermal Imagers”, Proceedings, Conference Sensor & Test, Nuremberg, 2015, p. 938.

/3/ Schieferdecker, J.; Schnorr, M., Forg. B.; Herrmann, F., Schmidt, C.; Leneke, W.; Simon, M.: A new family of digital Thermopile Arrays for high volume applications; Proceedings Conference Sensor & Test 2019, Nuremberg, Germany

New techniques in super resolution photothermal imaging for nondestructive testing

S. Ahmadi¹, P. Hirsch¹, J. Lecompaon¹, C. Hassenstein¹, P. Jung², G. Caire², M. Ziegler¹

¹*Bundesanstalt für Materialforschung und -prüfung, 12200 Berlin, Germany,*

²*Technical University of Berlin, Einsteinufer 25. 10587 Berlin, samim.ahmadi@bam.de*

Summary:

In this work we focus on our most recent studies to super resolution (SR) laser thermography. The goal of SR nondestructive testing methods is to facilitate the separation of closely spaced defects. We explain how to combine laser scanning with SR techniques. It can be shown that stepwise as well as continuous scanning techniques are applicable. Finally, we discuss the effect of several experimental parameters and image processing techniques to find the optimal SR technique which leads to the highest reconstruction quality within laser thermography.

Keywords: super resolution, laser thermography, nondestructive testing, laser scanning, photothermal imaging

Introduction

The diffuse nature of heat is mainly responsible for not being able to resolve two closely spaced defects with an infrared (IR) camera. The IR camera measures a Gaussian shaped temperature rise over both defects.

SR techniques have already been used in other scientific areas and are well-known such as in optics [1]. Even in nondestructive testing, SR techniques have been applied, for example in photoacoustics [2]. SR can be realized differently, but all these SR techniques have the same goal which is to enhance (artificially) the spatial resolution to improve the details in the image.

In the recent past, photothermal super resolution techniques have shown that it is possible to overcome the conventional resolution limits in thermography. We could obtain more information in our thermal images by performing appropriated experiments as well as applying image processing algorithms to the measured data.[3].

Since laser scanning is easy to combine with thermography and therefore of high interest for industry in terms of nondestructive and contactless testing [4], we made studies on the applicability of SR techniques. We investigated the influence of experimental parameters such as the laser line width or laser pulse length on the reconstruction quality. We also analyzed the effect of image processing techniques such as superimposing different measurements or choosing suitable regularization parameters for optimizing

our reconstruction results e.g. using compressed sensing based algorithms like the iterative joint sparsity (IJOSS) approach [5].

Methods

To understand how super resolution techniques can be applied in laser line scanning thermography, it is advisable to describe the measured temperature data from the IR camera mathematically. For reflection configuration (we are measuring with the IR camera from the same side where we illuminate at) our temperature field can be described as follows [6]:

$$T(x, z = 0, t) = T_0 + \frac{2}{\rho c_p \pi 4 \alpha} \int_0^t \int_{-\infty}^{\infty} q(x - \tilde{x}, t - \tilde{t}) e^{-\frac{(x-\tilde{x})^2}{4\alpha(t-\tilde{t})}} \frac{d\tilde{t}}{\tilde{t}} d\tilde{x}, \quad (1)$$

where T_0 stands for the initial temperature, ρ for the mass density, c_p for the specific heat, α for the thermal diffusivity, q for the heat flux density. The variation of the laser pulse length is considered by the convolution in time with the variable \tilde{t} and the variation of the laser line width is considered by the convolution in space with the variable \tilde{x} .

Within our SR studies [3, 7] we rewrite equation (1) by using the following equation which describes temperature differences:

$$\Delta T(x, z = 0, t) = T(x, z = L, t) - T_0 = A \cdot x, \quad (2)$$

whereby A represents the thermal point spread function (PSF) which can be described as a Green's Function as a solution of the underlying heat diffusion equation considering the laser line width and laser pulse length. x simply stands for the defect structure in our investigated material, hence x represents absorption coefficients in space.

Since x is - as it describes our defects in space - the variable of interest, we can determine x by calculating the inverse of A according to equation (2). Unfortunately, it is an ill-posed problem so that optimizers have to be used which are looking for a solution for x which leads to $\Delta T - A \cdot x \rightarrow 0$. In our post-processing algorithms we made use of the knowledge of A .

Results

Figure 1 (b) shows an exemplary result after applying the so-called Block-Elastic-Net optimization to the measured data shown in Figure 1 (a).

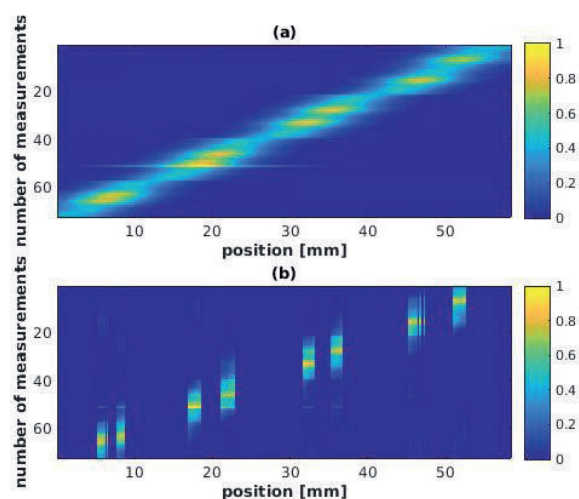


Fig. 1. (a) Measured temperature difference data normalized by the maximum temperature value is shown. We measured films with the infrared camera for each position with a position shift of 0.2 mm. To create this diagram we took the maximum thermogram and calculated the mean over the vertically arranged pixels of the maximum thermogram. One measurement number refers to a measurement at one position. (b) Making use of the Green's function that describes the heat propagation and considering the pulse length of the laser within our used optimization routine Block-Elastic-Net, we found a solution for x which is illustrated in this diagram. The resulting amplitude values are again normalized by the maximum amplitude.

In our studies we have investigated different scenarios by varying experimental parameters such

as the laser pulse length and the laser line width. It turned out that it is beneficial to use narrow laser lines as well as short pulses due to the fact that the thermal PSF does not get wider which makes sense from a super resolution point of view.

Furthermore, we discovered post-processing algorithms which enable us to increase the reconstruction quality of our defects (see the comparison of Figure 1 (a) and (b) by applying Block-Elastic-Net). However, the effectiveness of these algorithms relies on priors such as the joint sparsity of all measurements [3, 5, 7].

References

- [1] Thomas A. Klar and Stefan W. Hell, Subdiffraction resolution in far-field fluorescence microscopy, *Optics Letters* 24 (14), 954-956 (1999); doi: 10.1364/OL.24.000954
- [2] M. Haltmeier et al., Compressed sensing and sparsity in photoacoustic thermography, *Journal of Optics* 18 (11).
- [3] S. Ahmadi et al., Photothermal super resolution imaging: A comparison of different thermographic reconstruction techniques, *NDT & E International Journal* (2019), submitted
- [4] Schlichting et al., Flying Laser Spot Thermography for the Fast Detection of Surface Breaking Cracks, 18th World Conference on Nondestructive Testing (2012)
- [5] P. Burgholzer et al., Super-resolution thermographic imaging using blind structured illumination, *Applied Physics Letters* 111 (3)
- [6] K. D. Cole et al., Heat Conduction Using Green's Functions, 2nd Edition, CRC Press (2010)
- [7] P. Burgholzer et al., Blind structured illumination as excitation for super-resolution photothermal radiometry, *Quantitative InfraRed Thermography Journal* (2019) 1–11.

Detection of initial subsurface defects on coated glass-fiber reinforced composite components by means of active micro-thermography

Friederike Jensen¹, Michael Sorg¹, Andreas Fischer¹

¹ *University of Bremen, Bremen Institute for Metrology, Automation and Quality Science
Linzer Str. 13, 28359, Bremen, Germany
Correspondence: f.jensen@bimaq.de*

Summary:

The surface condition of the leading edge of rotor blades has a significant influence on the lifetime and performance of a wind turbine. The delayed detection of erosion damage results in high maintenance and repair costs. Therefore, a non-destructive in situ measuring method is required for the early detection of erosion damage and initial subsurface. Active thermography fulfills these requirements. First measurement results show that it is possible to visualize damage patterns on rotor blades and to make initial subsurface defects, which often lead to premature erosion, visible.

Keywords: active thermography, edge zone analysis, leading edge erosion, subsurface defects, composite materials

1. Introduction

The impact of rotor blade damages on the lifetime and performance of a wind turbine is significant and the repair of such damage is complex and expensive. The leading edge of a rotor blade is particularly exposed to mechanical and environmental stresses such as during rain, where the drops hit the blade with an impact speed of over 300 km/h. The impact of rain drops gradually removes the coated surface as well as parts of the underlying glass-fiber composite material [1,2]. Figure 1 shows a schematic representation of the structure of the leading edge of rotor blades.

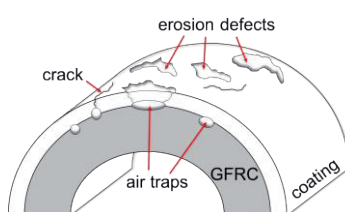


Fig. 1. Schematic sketch of a coated glass-fiber reinforced composite sample with initial defects (air traps) and surface defects

Studies suggest that initial subsurface defects such as pores in the border area between coating and GFRC lead to premature erosion [3]. Current failure analysis is carried out with destructive methods, without taking into account the progress of damage over time and initial subsurface defects in the component [4]. Since maintenance intervals are carried out after visual inspections, defects beneath the surface remain unnoticed. Early detection and evaluation of erosion damage and subsurface defects

before major damage occurs up to total failure of the rotor blade leads to a reduction in maintenance and repair costs. For this reason, the possibility of using active thermography to detect initial subsurface defects in the micrometer range on the leading edge of rotor blades is explored.

2. Measurement approach

Active thermography is selected as the measuring method for the contactless, non-destructive examination of erosion damage and subsurface defects [5], since, in opposite to computer tomography (CT), it can also be used in situ. In active thermography, the test sample is first heated by an energy source and in the subsequent cooling phase the different temperature distribution of the test sample is recorded by an IR camera [6]. The thermograms are then compared with optical images to match their information content. In order to select the optimal parameters regarding camera setup, illumination type and duration for later test series, a test rig is also being developed.

3. Experimental setup

For the thermographic investigations, a first version of a test rig was set up as shown in Figure 2. The test sample, which resembles the leading edge of a rotor blade, is fixed in a rotatable clamping device. An InfraTec 8300 series IR camera with 100 mm lens and 2 distance rings (zoom in completely) is directed at the sample so that it is in focus on the image. Fur-

thermore, a kinematic system is already installed, which is ready for the later integration of a heat source as well as additional sensors. For the first test measurements, heating of the test sample was done off the test rig using a radiant heater. The position of the future heat source integrated in the test rig as well as the position of the future sensors (distance and height) can be controlled by a computer. The IR-camera is also connected to this system to evaluate the acquired image data with the software Irbis3 from InfraTec.

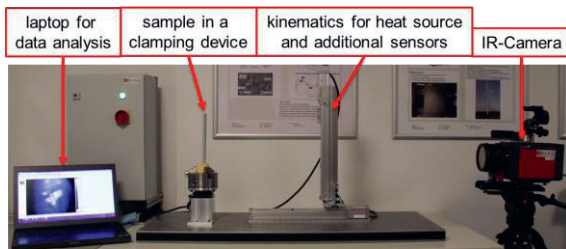


Fig. 2. Current experimental setup for the thermographic examination of test samples

4. Results

The first test measurements were carried out on a sample loaded in the rain erosion system. Figure 3 shows an image of a test sample, an enlarged image section taken with an optical camera and a thermographic image associated with the image section.

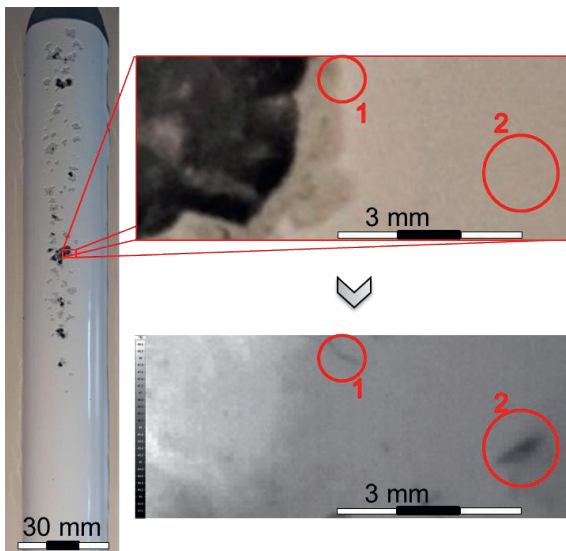


Fig. 3. Left: optical image of the damaged test sample; top right: enlarged optical image of a damaged area; bottom right: thermographic image of the same area; circle 1 and 2: hidden inhomogeneities

Due to the prevailing temperature difference, which is caused during the cooling process by material-dependent heat storage capacities and the resulting different heat transfers, extensive damage to the surface can be detected. Additionally, for example the circles 1 and 2 in the thermogram show areas in the micrometer

range with different thermal properties relative to the coating, which are not visible in the optical image and would therefore remain unnoticed. As a result of the high spatial resolution of the camera with a distance between camera lens and test sample of 440 mm, material inhomogeneities with a size of 60 μm were detected. These material inhomogeneities contribute to the initiation of premature damage at the leading edge of the rotor blade due to rain erosion.

5. Conclusion and Outlook

The experiment shows that active microthermography can be used as a non-invasive, non-destructive measuring method to visualize material inhomogeneities in the micrometer range, that remain hidden during a visual inspection of the leading edge of wind turbine rotor blades. Further investigations including CT reference measurements are necessary to determine the influence of these detected inhomogeneities on premature rain erosion. Finally, in-situ measurements and damage analyses will be conducted on the rotor blade leading edge of a real-scale wind turbine.

6. References

- [1] C. Dollinger, N. Balaesque, N. Gaudern, M. Sorg, A. Fischer, Calculation of the power output loss based on thermographic measurement of the leading edge condition, *Journal of Physics Conference Series* 1037 (2018); doi: 10.1088/1742-6596/1037/5/052011
- [2] A. Sareen, C. A. SAP re, M. S. Selig, Effects of leading edge erosion on wind turbine blade performance, *Wind Energy* 17, 1531-1542 (2014); doi: 10.1002/we.1649
- [3] E. Cortés, F. Sánchez, A. O'Carroll, B. Madramany, M. Hardiman, T.M. Young, On the Material Characterisation of Wind Turbine Blade Coatings: The Effect of Interphase Coating-Laminate Adhesion on Rain Erosion Performance, *Materials* 10, 1146 (2017); doi: 10.3390/ma10101146
- [4] DIN-Arbeitsausschuss NA 002-00-16 AA "Beschichtungen an Rotorblättern für Windenergieanlagen" des DIN-Normausschusses Beschichtungsstoffe und Beschichtungen (NAB)
- [5] R. Montanini, F. Freni, Non-destructive evaluation of thick glass fiber-reinforced composites by means of optically excited lock-in thermography, *Composites: Part A* 43, 2075-2082 (2012); doi:10.1016/j.compositesa.2012.06.004
- [6] P. Meinelschmidt, J. Aderhold, Thermographic Inspection of Rotor Blades, *European Conference on Non-Destructive Testing, Berlin* (2006)

Emissivity Measurement of Semitransparent Samples

Julian Gieseler¹, Albert Adibekyan¹, Christian Monte¹, Jörg Hollandt¹
¹Physikalisch-Technische Bundesanstalt, Abbestrasse 2-12, Germany,
 julian.gieseler@ptb.de

Summary:

The characterization of infrared optical properties of semitransparent samples between 6 μm and 25 μm and between 20 $^{\circ}\text{C}$ and 90 $^{\circ}\text{C}$ is hampered by the fact, that the apparent emittance, reflectance and transmittance are intertwined in the optical signals. We report on an approach for the simultaneous measurement of transmittance and reflectance of semitransparent samples, expanding PTB's established emissivity measurement facilities under air and under vacuum. Measurements of silicon were performed under air, evaluated, and, additionally, validated by independent measurements.

Keywords: Emissivity measurement, semitransparent materials, radiative transport, silicon, infrared optical properties

Introduction

The increasing interest in industrial and scientific applications of semitransparent materials demands the precise and comprehensive measurement of their infrared optical properties. For instance, the non-destructive testing of fiber-reinforced polymers (FRP) by passive or active thermography requires precise knowledge of the emittance of the material to quantitatively identify defects [1]. Semitransparent semiconductors are also widely used as transmitting and reflecting components in infrared optics. For high precision measurements in the infrared wavelength region, the emission of the semitransparent components must be accounted for.

However, infrared optical properties of semitransparent materials at temperatures between 20 $^{\circ}\text{C}$ and 90 $^{\circ}\text{C}$ are difficult to measure because the detected optical signal is a superposition of reflected, transmitted and emitted radiation. Furthermore, the apparent emittance, reflectance and transmittance depend on the sample thickness. Therefore, in a second step, the absorption coefficient and refractive index must be identified. To solve these problems, a new sample holder, a model of radiative transport, and an identification scheme were developed.

Measurement principle

The measurement principle is based on PTB's emissivity measurement of opaque samples [2]. It is a direct radiometric comparison of the observed sample radiance and the radiance of two reference black bodies, operated at different temperatures. Radiance is measured using

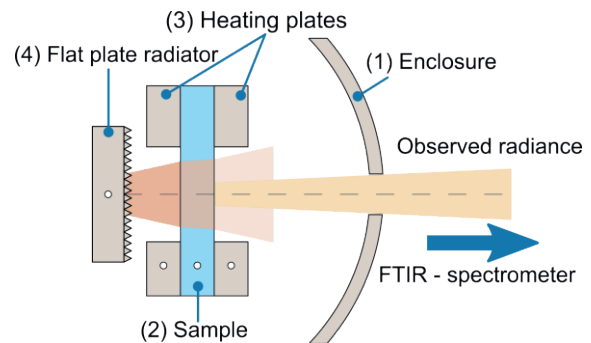


Fig. 1. Schematic view of the measurement setup. The enclosure (1), the sample (2), the heating plates (3), and the flat plate radiator (4) are visible in this sectioned side-on view.

a Fourier-Transform-Infrared (FTIR) spectrometer. The sample is placed in a separate sample holder [3], where it is thermally stabilized (see Fig. 1).

In contrast to opaque samples, where emittance is a surface property, emittance of semitransparent samples is a volume property. To achieve low uncertainties, the temperature not only on the surface, but throughout the entire observed volume must be known. For this purpose, the sample is placed between two annular heating plates which compensate radial temperature gradients, realizing a one-dimensional temperature distribution within the sample. Behind the sample, a temperature controlled flat plate radiator is positioned. The enclosure of the sample holder features a highly emitting coating. Like the radiator, its temperature is controlled as well. All components typically operate between 20 $^{\circ}\text{C}$ and 90 $^{\circ}\text{C}$. Together, the enclosure and the radiator irradiate the sample with precisely known radiation.

For the simultaneous measurement of reflectance and transmittance, at least two independent measurements are required, which are realized by varying the temperature of the flat plate radiator and the enclosure. Because all sources of radiation are well defined, it is possible to explicitly consider reflection, transmission and emission of the sample.

Evaluation scheme

After correcting the background radiation and the spectral responsivity of the FTIR-Spectrometer, reflectance and transmittance are calculated from the observed spectra by a least squares approach. In a second step, the radiative transport equation [4,5] for isothermal samples is solved using the two-flux approach to derive expressions relating emittance, reflectance, and transmittance to the absorption coefficient and refractive index.

Results

Emissivity measurements of an optically polished sample of silicon were performed. The sample is 90 mm in diameter and 5 mm in thickness. The temperatures of the various components are summarized in Tab. 1.

Tab. 1: The nominal temperatures used for the emissivity measurement of silicon. The flat plate radiator was varied over three temperatures, while the temperatures of the sample and enclosure were kept constant.

Component	Temperatures
Enclosure	20 °C
Sample	60 °C
Flat plate radiator	40 °C, 70 °C, 90 °C

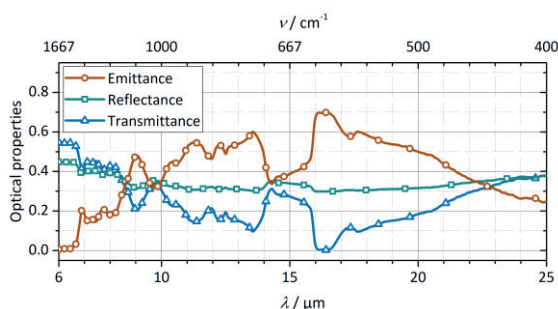


Fig. 2. Results for the apparent emittance (red), reflectance (green), and transmittance (blue) for an optically polished sample of silicon of 5 mm thickness at 60 °C.

Three measurements were performed from which the transmittance, reflectance, and emittance of the silicon sample were identified, the results of which are shown in Fig. 2. The unusually high emittance is due to the large thickness of the sample.

Finally, the setup was successfully validated by independent directional-directional reflectance measurements using a VW-setup and an FTIR spectrometer. The results of both, the direct radiometric comparison and the VW-setup, as well as the confidence interval of the VW-setup are shown in Fig. 3. The measured reflectance agrees within one sigma down to 7 μm, where after the offset is slightly above one sigma.

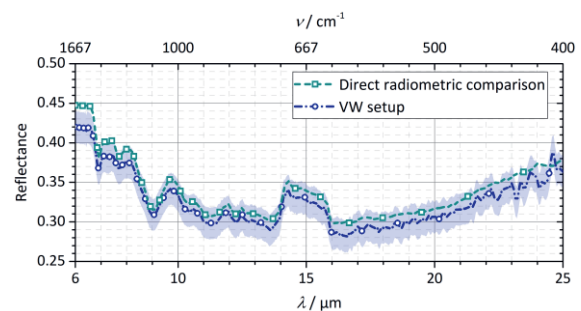


Fig. 3. Validation of the emissivity measurement of semitransparent samples by independent reflectance measurements.

References

- [1] S. J. Altenburg, R. Bernegger, and R. Krankenhagen, Absorption coefficient dispersion in flash thermography of semitransparent solids, *International Journal of Thermophysics* 40.1, 13 (2019); doi:10.1007/s10765-018-2474-0
- [2] A. Adibekyan, et al., Emissivity Measurement Under Vacuum from 4 μm to 100 μm and from -40 °C to 450 °C at PTB, *International Journal of Thermophysics* 36.2-3, 283-289 (2015); doi: 10.1007/s10765-014-1745-7
- [3] J. Gieseler, et al., Entwicklung und Aufbau eines Probenhalters für die Emissionsgradmessung an semitransparenten Materialien, *tm-Technisches Messen* 85.1, 40-48 (2018); doi: 10.1515/teme-2017-0089
- [4] M. F. Modest, Radiative heat transfer, 3rd ed., Academic press, 2013; doi: 10.1016/c2010-0-65874-3
- [5] J. R. Howell, M. P. Mengüç, and R. Siegel, Thermal radiation heat transfer, 5th ed., CRC press, 2015; doi: 10.1201/b18835

Measurement of ^{13}C and ^{18}O Ratio in CO_2 using Quantum Cascade Laser based Tunable Absorption Spectroscopy

Ponkanok Nitzsche¹, Cem Dinc¹, Jürgen Wöllenstein^{1,2}, Katrin Schmitt^{1,2}

¹ Department of Microsystems Engineering (IMTEK), University of Freiburg, Georges-Köhler-Allee 102, 79110 Freiburg, Germany

² Fraunhofer Institute for Physical Measurement Techniques (IPM), 79110 Freiburg, Germany
Tel.-Nr.: +49 761 203-96808, E-Mail: ponkanok.nitzsche@imtek.uni-freiburg.de

Summary:

We present a spectroscopic approach for measurements of ^{13}C and ^{18}O isotopic ratio in carbon dioxide (CO_2) gas using a quantum cascade laser (QCL). A narrow linewidth mid-infrared QCL is continuously scanned across three absorption lines of CO_2 near 2310 cm^{-1} including $^{12}\text{C}^{16}\text{O}_2$, $^{13}\text{C}^{16}\text{O}_2$ and $^{16}\text{O}^{12}\text{C}^{18}\text{O}$ isotopes. The simultaneous detection of three spectral lines permits the determination of simple concentration ratios (R^{13} and R^{18}) in atmospheric CO_2 . With an averaging time of about 10 s both R^{13} and R^{18} reach a precision of 0.2 ‰ and 0.1 ‰, respectively.

Keywords: Gas Sensors, Isotopic Composition Analysis, Optical Measuring System, Absorption Spectroscopy, Quantum Cascade Laser

Motivation

Since atmospheric CO_2 is an important indicator for many climate change researches, an attention focusing on fluxes of CO_2 between the different sources and sinks have been growing. The studies of stable CO_2 isotope ratios offer the possibilities to identify such CO_2 pools via isotopic fingerprint [1]. Traditionally, the stable isotopes are measured by means of sample preparation and isotope ratio mass spectrometry (IRMS). An alternative method for this measurement is tunable laser absorption spectroscopy (TLAS). In contrast to IRMS, TLAS permits a real-time measurement of the isotopic ratio with sufficient precision down to $<0.3\text{ ‰}$ at 1 s averaging time for both $\delta^{13}\text{C}$ and $\delta^{18}\text{O}$ [2].

Spectral Absorption Lines

A mid-infrared, tunable QCL near 2310 cm^{-1} is continuously tuned across three spectral absorption lines of CO_2 isotopes. These spectral lines are chosen in such a way that there is a sufficiently high absorption line strength and low interference with other atmospheric gases. Moreover, there must be at least one absorption line of each isotopes of interest within the laser tuning range and all measuring isotopes should possess a similar absorption line intensity to avoid any detector saturation.

The spectroscopic information, including the vacuum wavenumber ($\tilde{\nu}_0$), Low-state energy (E_L), spectral line intensity ($S(T_0)$), of the selected $^{12}\text{C}^{16}\text{O}_2$, $^{13}\text{C}^{16}\text{O}_2$ and $^{16}\text{O}^{12}\text{C}^{18}\text{O}$ isotopes

are shown in Table 1. The simulated absorption spectrum of these lines using the HITRAN database [3] shows that the measurement must be performed in a negative pressure chamber to minimize line overlapping caused by pressure broadening. In addition, the low state energies of these spectral lines are considerably different, which implies that the isotope ratio measurement is sensitive to temperature variation [4].

Tab. 1: Spectroscopic data of the selected lines

Isotopes	$\tilde{\nu}_0$ in cm^{-1}	E_L in cm^{-1}	$S(T_0)$ in $\text{cm}^{-1}/\text{mol}\cdot\text{cm}^{-2}$
$^{12}\text{C}^{16}\text{O}_2$	2310.002	1454.97	$4.86\cdot 10^{-21}$
$^{13}\text{C}^{16}\text{O}_2$	2310.347	639.63	$6.72\cdot 10^{-21}$
$^{16}\text{O}^{12}\text{C}^{18}\text{O}$	2310.206	278.28	$4.52\cdot 10^{-21}$

Experimental Setup

Figure 1 depicts a schematic of an optical configuration of the system. A temperature controller and current driver (PTC5K-CH and QCL1000 Lab, Wavelength-Electronic) are used with a function generator to control the QCL (HHL680, AlpesLaser) and tune the laser with a frequency of $f_{\text{mod}} = 1\text{ Hz}$. An optical isolator is employed to protect the QCL from back-reflected light. The first split beam is steered into a 10 cm-long hermetically sealed spectroscopic cell filled with a known concentration of CO_2 , which is applied for the calibration of QCL-wavelength. The second beam propagates into

the measurement chamber with an optical path length of $L_{\text{cham}} = 109 \pm 1$ cm. Two photodetectors (PVI-3TE-5, *Vigo System*) are used to detect the optical signal, simultaneously.

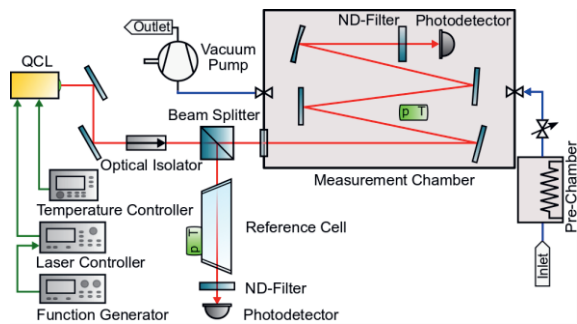


Fig. 1: Schematic sketch of the experimental set-up.

With a diaphragm vacuum pump and a fine-metering valve, the pressure inside the chamber can be reduced and regulated to $p_{\text{cham}} = 100$ mbar. A pre-chamber and measurement chamber are temperature-regulated and heat isolated. A temperature and pressure sensor are integrated inside the measurement chamber.

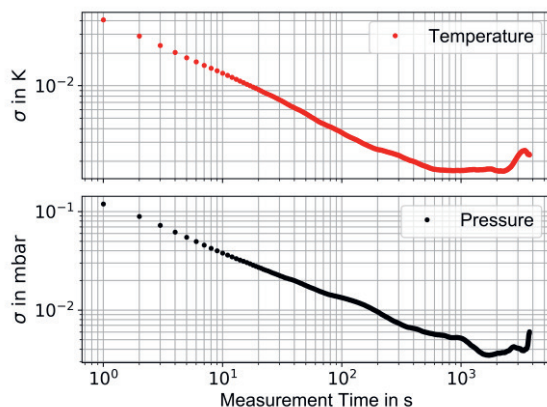


Fig. 2: Allan plots for temperature and pressure measured inside the measurement chamber.

The Allan plot of the time series of the recorded temperature and pressure inside the chamber are shown in Figure 2. The chamber conditions can be controlled with a precision of $\Delta T \sim 13$ mK and $\Delta p \sim 0.04$ mbar after an integration time of 10 s.

Measurement Results

To verify the feasibility and stability of the system, measurement with a constant 396 ppm CO_2 concentration in synthetic air was performed over 1000 s. With a piecewise baseline-correction and curve fitting of Voigt profile, the transmitted spectrum was defined thus, each isotope ratio as $R^{13} = [^{13}\text{C}^{16}\text{O}_2]/[^{12}\text{C}^{16}\text{O}_2]$ and $R^{18} = [^{16}\text{O}^{12}\text{C}^{18}\text{O}]/[^{12}\text{C}^{16}\text{O}_2]$. Employing the Allan Deviation method, the minimum deviation was reached after ~ 10 s, which is illustrated in Figure 3. With this averaging time, the system can achieve a precision of 0.2 ‰ and 0.1 ‰ for R^{13}

and R^{18} , respectively. In order to determine the accurate concentrations and isotopic ratios of CO_2 , the system must be calibrated.

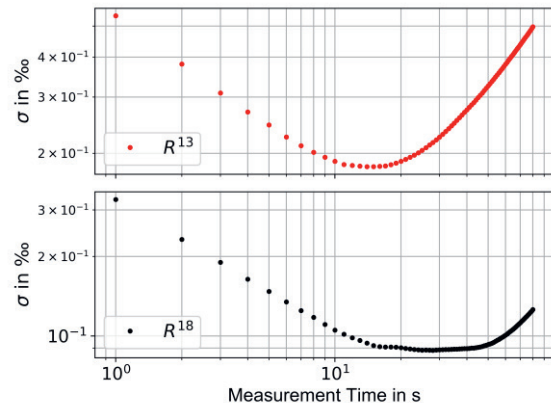


Fig. 3: Allan plot for both concentration ratios R^{13} (above) and R^{18} (below).

Conclusion

In this letter, we present the design and construction of QCL-based tunable absorption spectroscopy for an analysis of CO_2 isotopic compositions. A precise control of temperature and pressure is achieved to 13 mK and 0.04 mbar, respectively. At an integration time of about 10 s the detection limits for R^{13} and R^{18} were estimated by the Allan method as 0.2 ‰ and 0.1 ‰, respectively.

Acknowledgements

This work is funded by Georg H. Endress foundation.

References

- [1] D. E. Pataki, D. R. Bowling, and J. R. Ehleringer, "Seasonal cycle of carbon dioxide and its isotopic composition in an urban atmosphere: Anthropogenic and biogenic effects," *J. Geophys. Res. D Atmos.*, vol. 108, no. 23, pp. 1–8, 2003, doi: 10.1029/2003jd003865.
- [2] B. Tuzson *et al.*, "High precision and continuous field measurements of $\delta^{13}\text{C}$ and $\delta^{18}\text{O}$ in carbon dioxide with a cryogen-free QCLAS," *Appl. Phys. B Lasers Opt.*, vol. 92, no. 3 SPECIAL ISSUE, pp. 451–458, 2008, doi: 10.1007/s00340-008-3085-4.
- [3] R. V. Kochanov, I. E. Gordon, L. S. Rothman, P. Wcisło, C. Hill, and J. S. Wilzewski, "HITRAN Application Programming Interface (HAPI): A comprehensive approach to working with spectroscopic data," *J. Quant. Spectrosc. Radiat. Transf.*, vol. 177, pp. 15–30, 2016, doi: 10.1016/j.jqsrt.2016.03.005.
- [4] P. Bergamaschi, M. Schupp, and G. W. Harris, "High-precision direct measurements of $^{13}\text{CH}_4/^{12}\text{CH}_4$ and $^{12}\text{CH}_3\text{D}/^{12}\text{CH}_4$ ratios in atmospheric methane sources by means of a long-path tunable diode laser absorption spectrometer," *Appl. Opt.*, vol. 33, no. 33, p. 7704, 1994, doi: 10.1364/ao.33.007704.

FT-IR Coupled Goniometer Setup for Characterization of the Spatial and Spectral Emission of IR-Sources

A. Eberhardt¹, C. Weber^{1,2}, M.-L. Bauersfeld¹, J. Wöllenstein^{1,2}

¹ Fraunhofer Institute for Physical Measurement Techniques IPM, Heidenhofstr. 8, 79110, Freiburg, Germany,

² Department of Microsystems Engineering–IMTEK, Laboratory for Gas Sensors, University of Freiburg, Georges-Köhler-Allee 102, 79110, Freiburg, Germany
Andre.eberhardt@ipm.fraunhofer.de

Summary:

We present a FT-IR coupled goniometer setup, which allows the simultaneous spatial and spectral characterization of optical components used in non-dispersive infrared gas sensor systems. The performance of the laboratory setup is demonstrated by comparing reflector and Fresnel lens equipped thermal infrared radiation sources. We show that even the simplest binary Fresnel lenses, when optimally designed, can achieve a thinner emission angle than parabolic mirrors at comparable radiation intensities.

Keywords: Infrared, FTIR, Goniometer, Spatial Emission, Spectral Emission

Motivation

Non-dispersive infrared sensors are widely used in the field of low-cost optical gas sensors. Most of these sensors contain modulated thermal emitters as infrared radiation source [1, 2]. In order to improve the radiation output and therefore the performance of these sources, parabolic mirrors are commonly used. However, these mirrors are complex and expensive to manufacture. Using planar diffractive Fresnel lenses as an alternative may reduce the costs at comparable performance, as they can be produced on a large scale at wafer level using silicon microsystems technology. Diffractive lenses, however, show a pronounced wavelength dependency of the focal length and consequently the emission characteristics of thermal sources depend on the wavelength and angle to the optical axis.

Measurement setup

For the spatially resolved measurements a goniometer setup was developed that can be coupled to a FT-IR-spectrometer. The setup was optimized using raytracing simulations in order to conserve as much radiation as possible without losing radiation inside the spectrometer due to outshining of optical elements while minimizing the captured cone angle. Figure 1 shows the presented measurement setup. The emission source was attached to a rotation stage (a) in a way that its center of front surface was located directly above the rotation axis of the stage. The emitted radiation was collimated using a spherical silver plated mirror (a) with a

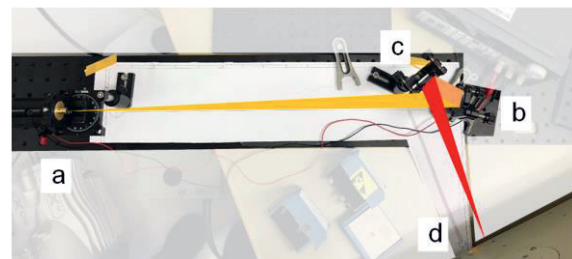


Fig. 1. Photograph of the measurement setup: (a) thermal IR-source, attached to a rotation stage, (b) spherical mirror ($f = 1000$ mm), (c) spherical mirror ($f = 500$ mm), (d) external coupling port of FT-IR-spectrometer and schematic of the optical path (orange to red).

diameter of 1 " and a radius of curvature of 1.000 mm and guided to a second silver plated spherical mirror (b) with a diameter of 1 " and a radius of curvature of 500 mm. This mirror focused the collected radiation into the coupling port (d) of a Fourier-transform infrared spectrometer (FT-IR, Bruker Vertex 80v). The setup captured the radiation of a cone angle of $\pm 1.5^\circ$. For a thermal IR-emitter with a Lambertian emission distribution this means about 0.07 % of the emitted radiation is collected. For this reason a liquid nitrogen cooled MCT-detector incorporated in the spectrometer was used.

Wavelength and angle-resolved emission spectra

The goniometer setup has been used to evaluate the performance of Fresnel lens equipped radiation sources in comparison to classical reflector based ones.

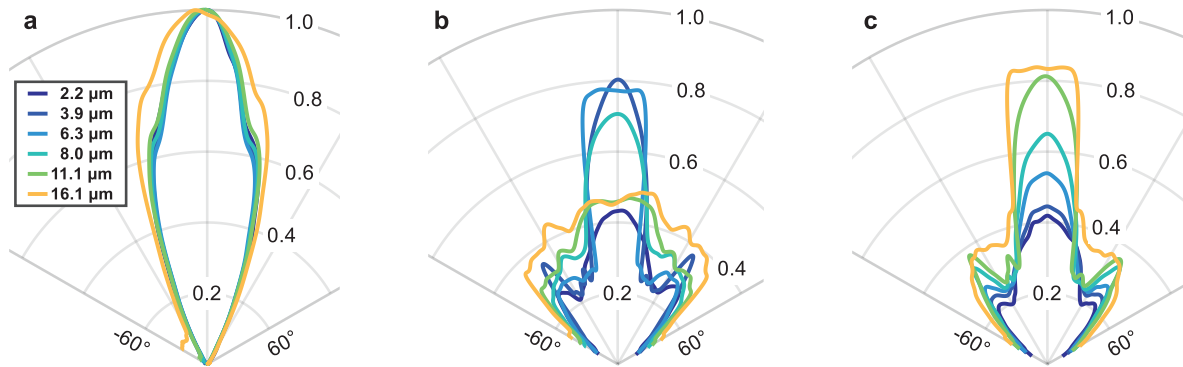


Fig. 3. Results of spectral resolved goniometer measurements for thermal emitters with an parabolic reflector (a), lens F1 (b) and lens F2 (c) in the angular range between -70° and $+70^\circ$

For the measurements, broadband antireflective (AR) coated binary Fresnel lenses made of silicon with a focal length of $f = 10$ mm and design wavelengths of $4.3 \mu\text{m}$ (L1) and $10.5 \mu\text{m}$ (L2) were used. The lenses were placed on conventional cylindrical caps instead of commonly used windows. With this setup, the distance between the emitting and lens surface was about 6.9 mm. These emitters were compared to a source equipped with an externally identical parabolic reflector and a broadband AR-coated germanium window (figure 2). The emitters were operated with a power of 850 mW, resulting in a temperature of about 800°C .

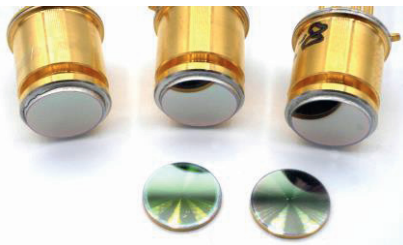


Fig. 2. Photograph of the used sources. From left to right: emitter with parabolic reflector, emitter with Fresnel lens for $4.3 \mu\text{m}$ (F1) and with Fresnel lens for $10.5 \mu\text{m}$ (F2).

We measured FT-IR spectra in the angular range between -70° and $+70^\circ$ in 2° steps. Figure 3 shows the resulting angular spectra of the investigated sources with parabolic reflector (a) and Fresnel lenses F1 (b) and F2 (c) from $2.2 \mu\text{m}$ to $16.1 \mu\text{m}$. All spectra were normalized to the maximum value of the corresponding wavelength of source (a) at an angle of 0° .

As expected, the source with reflector shows no significant wavelength dependence. The two sources with Fresnel lenses show the expected wavelength dependence of the angular spectrum. Above and below the design wavelength, the focal length decreases resp. increases with increasing distance according to the diffractive nature of the lenses.

The geometric layout of sources (b) and (c) results in the best possible focusing performance of the lenses above their design wavelengths at $6.3 \mu\text{m}$ for L1 ($f=6.8$ mm) and $16.1 \mu\text{m}$ ($f=6.5$ mm) for L2, when the emission surface is imaged to infinity. Some spectra show intermediate maxima around $\pm 40^\circ$. These maxima are caused by multiple reflections within the caps.

The full width half maximum angle of both Fresnel-lens equipped sources is 9.4° (L1) and 10.4° (L2) and therefore smaller than the classical reflector based solution with at least 15.1° .

Conclusion

We presented a laboratory setup that allows the simultaneous spatial and spectral characterization of IR-radiation sources with high resolution in the angular range of at least $\pm 70^\circ$. The setup has been used to compare classical mirror-based sources with novel Fresnel-lens-enhanced ones. It turned out that sources with binary Fresnel lenses achieve a performance comparable to parabolic mirror based sources despite their inherently low diffraction efficiency of around 40 %.

The presented setup allows the efficient evaluation of the performance and a subsequent optimization of diffractive element enhanced radiation sources.

Acknowledgements

This work was funded within the “Nanostructured Fresnel optics for MEMS-based IR-emitter” project with the grant number 13XP5019E.

References

- [1] J. Hildenbrand et al., “Micromachined Mid-Infrared Emitter for Fast Transient Temperature Operation for Optical Gas Sensing Systems”, *IEEE Sens. J.* 10.2 (2009): 353-362
- [2] J. Hodgkinson, R. P. Tantam, “Optical gas sensing: a review”, *Meas. Sci. Technol.* 24.1 (2012):012004

Using spatial and temporal shaping of laser-induced diffuse thermal wave fields in thermography

M. Ziegler¹, S. Ahmadi¹, P. Hirsch¹, J. Lecom-pagnon, C. Hassenstein¹, E. Thiel¹, N. W. Pech-May¹

¹Bundesanstalt für Materialforschung und -prüfung, 12200 Berlin, Germany, samim.ahmadi@bam.de

Summary:

The diffuse nature of thermal waves is a fundamental limitation in thermographic non-destructive testing. In our studies we investigated different approaches by shaping the thermal wave fields which result from heating. We have used high-power laser sources to heat metallic samples. Using these spatial and temporal shaping techniques leads to a higher detection sensitivity in our measurements with the infrared camera. In this contribution we show our implementation of shaping laser-induced diffuse thermal wave fields and the effect on the defect reconstruction quality.

Keywords: thermal wave, diffusion, high-power laser, thermography, spatiotemporal shaping

Introduction

In infrared thermography, the interaction of the heat flow with the internal geometry or inhomogeneities in a sample and their effect on the transient temperature distribution is used, e.g. to detect defects non-destructively. An equivalent way of describing this is the propagation of thermal waves inside the sample. Although thermography is suitable for a wide range of inhomogeneities and materials, the fundamental limitation is the diffuse nature of thermal waves and the need to measure their effect radiometrically at the sample surface only [1]. The crucial difference between diffuse thermal waves and propagating waves, as they occur e.g. in ultrasound, is the rapid degradation of spatial resolution with increasing defect depth. A promising approach to improve the spatial resolution and thus the detection sensitivity and reconstruction quality of the thermographic technique lies in the shaping of these diffuse thermal wave fields [2, 3]. For example, narrow

crack-like defects below the surface can be detected with high sensitivity by superimposing several interfering thermal wave fields, closely adjacent defects can be separated by multiple measurements with varying heating structures and defects at different depths can be distinguished by an optimized temporal shaping of the thermal excitation function. We present the latest results of this technology obtained with lasers, i.e. spatially and temporally structureable heating sources and modern numerical methods.

Techniques for shaping thermal wave fields

The spatiotemporal shaping of thermal wave fields can be realized by using different techniques. Thus, we investigated the effect of spatial shaping by using different illumination techniques. These illumination techniques are strongly depending on the material since the absorption spectra differ a lot.

We decided to compare homogeneous illumination (flash over the whole surface of the specimen) with structured illumination (laser lines with a certain width).

To realize structured illumination, we first have used a diode laser in combination with a digital mirror device (DMD) which enabled us to create diverse illumination pattern [4].

Another technique to ensure structured illumination was to use a vertical cavity surface emitting laser (VCSEL) array. The VCSEL array consists of 12 laser lines, the image size could be controlled by using lenses. Hence, the user was able to control the laser line width for our studies.

Instead of using the VCSEL array, we could use a fiber-coupled high-power laser, too. For this laser we have used different optics to create rectangular laser illumination or laser lines with different sizes.

Temporal shaping has also been investigated within our studies. Therefore, we set up a real-time FPGA based control system which was controlled via LabView.

We applied different laser pulse lengths in our experimental studies. In addition, we implemented lock-in thermography where we make use of an amplitude modulation of our laser sources.

Apart from these state-of-the-art techniques we also applied thermal wave interference methods to investigate the improvement of defect detection. In this technique we made use of destruc-

tive interference of two anti-phased amplitude modulated heat source [3].

Further, we investigated the possibility of using pulse compression with our laser sources. Similar to radar applications [5], we try to extract our original pulse compressed signal in our noisy measured data by using the cross-correlation with our original sequence. Therefore, we use different coding techniques by making use of e.g. Barker-codes [6].

Our newest studies refer also to photothermal super resolution inspection techniques [7,8] where we scan the whole surface of a specimen using different illumination techniques which all rely on the same principle: performing a lot of measurements by illuminating different positions using position shifts which are smaller than the laser line width. Consequently, we create a measurement set where some of the measurements are overlapping.

Results using thermal wave field shaping

Our studies have shown that the use of spatial and temporal shaping has a high potential since we could beat the conventional thermographic resolution limits given by simple homogeneous illuminations using flash lamps.

Laser arrays such as our used VCSEL array provide a maximum output power of 2.4 kW which is much higher than the output power of the combination of a laser diode and a DMD since the DMD is not designed for high-power applications.

We discovered that our destructive interference method enables to better resolve narrow sub-surface defects than flash lamps.

Furthermore, it turned out that Barker-Codes could be very helpful to increase the quality of the measured signal which is of high interest if the signal-to-noise ratio is very small.

Finally, our studies have shown that we can also make use of super resolution scanning strategies for better separating closely spaced defects. We could enhance the spatial resolution artificially by deconvolving the measured data with the thermal point spread function.

References

- [1] Burgholzer et al., Thermodynamic Limits of Spatial Resolution in Active Thermography
- [2] M. Ziegler et al., Thermografie mit einem 1D Laser-array – von der flächigen zur strukturierten Erwärmung, Thermografie-Kolloquium 60 (7–8).
- [3] E. Thiel et al., Subsurface defect localization by structured heating using laser projected photothermal thermography, Journal of Visualized Experiments (123).
- [4] E. Thiel et al., Spatial and temporal control of thermal waves by using DMDs for interference based crack detection, Proceedings of the SPIE (2016).
- [5] Cohen, Pulse compression in radar systems, Principles of Modern Radar (1987).
- [6] Ghali et al., Barker coded thermal wave imaging for defect detection in carbon fibre-reinforced plastics (2011).
- [7] S. Ahmadi et al., Photothermal super resolution imaging: A comparison of different thermographic reconstruction techniques, NDT & E International Journal (2019), submitted
- [8] P. Burgholzer et al., Blind structured illumination as excitation for super-resolution photothermal radiometry, Quantitative InfraRed Thermography Journal (2019) 1–11.

Application of Microwave based Electrical Read-Out of Fiber Bragg Gratings in Thermometry

Ulrich Nordmeyer¹, Niels Neumann¹, Xiaozhou Wang¹, Torsten Thiel², Konstantin Kojucharow³, Dirk Plettemeier¹

¹ Chair for RF and Photonics Engineering, TU Dresden, 01062 Dresden, Germany

² AOS GmbH, Overbeckstr. 39a, 01139 Dresden, Germany

³ KMDC, Zur Bleiche 15, 01279 Dresden, Germany
ulrich.nordmeyer@tu-dresden.de

Summary:

The evaluation of optical fiber sensors is conventionally carried out optically by analyzing the amplitude of the transmitted or the reflected light. A novel approach in the form of an electrical read-out was proposed in a former contribution [1]. The underlying concept is to interrogate the optical sensor with an RF modulated laser and carry out a full electrical analysis of the resulting RF signal. The applicability of this electrical read-out method for temperature measurements is investigated in this paper.

Keywords: optical fiber sensors, RF modulated laser, electrical analysis, temperature, radio-over-fiber

Introduction

Optical fiber sensors are available for many purposes. Especially in applications with restricted accessibility, difficulties to integrate the read-out equipment can be overcome by using Radio-over-Fiber (RoF) technology. While the evaluation of optical fiber sensors is conventionally carried out optically by analyzing the amplitude or spectrum of either the transmitted or the reflected light, a novel approach in the form of an electrical read-out was discussed in a former contribution [1]. The underlying concept is to interrogate the optical sensor with an RF modulated laser and carry out a full electrical analysis (amplitude *and* phase) of the resulting RF signal, which is changed by the sensor's characteristics. Due to the inherent presence of an RF signal in this scheme, it is particularly suitable for RoF measurement setups. As up to now, only the theoretical concept of measurements based on the electrical read-out method has been considered, a first approach of quantitative measurements is pursued in this work.

Thermometry based on optical fiber sensors

One of the most frequently measured quantities is temperature. Different types of sensors are suitable to accomplish this task, among these are optical sensors. In comparison to resistance thermometers, their main advantages are the resilience against electromagnetic interference and mechanical shock [2]. On the downside, the measurement uncertainty of optical temperature sensors is around 500 mK whereas resistance temperature sensors achieve 10 mK or

better [2]. Nonetheless, the demand for resilient sensors led to the development of a variety of optical temperature sensing principles. Well investigated ones rely on Fiber Bragg Gratings (FBG). Such sensors are still subject to new studies [3] while being already commercially available [4]. For that reason, this paper focuses on FBG based temperature sensing.

Setup and measurements

The experimental setup (Fig. 1) links closely to the first study in the field of el. read-out [1]. The sensor is a cos-shape apodized FBG (length: 25 mm, stop-band: 1537,67 nm \pm 75 pm). It is thermally attached to a thermoelectric cooler (TEC). A forward calibration of the entire setup is performed at the center wavelength (CWL) of the FBG. The sensor characteristic is then recorded at a controlled temperature of 22.0 °C by a scan with the tunable laser source (TLS) (span: CWL \pm 200 pm, step width: 1 pm). The sweeps on the VNA (2.4 to 2.5 GHz) cover the ISM band ensuring compatibility with RoF setups (power: -20 dBm, RBW: 500 Hz, 1001 pts). Further reference curves are acquired at [21, 23, 24, 25] °C with otherwise identical settings.

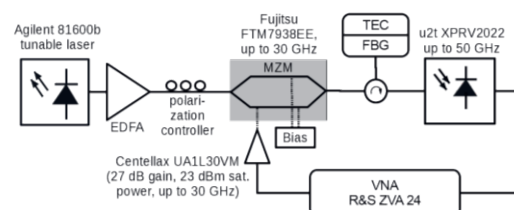


Fig. 1. Block diagram of the experimental setup.

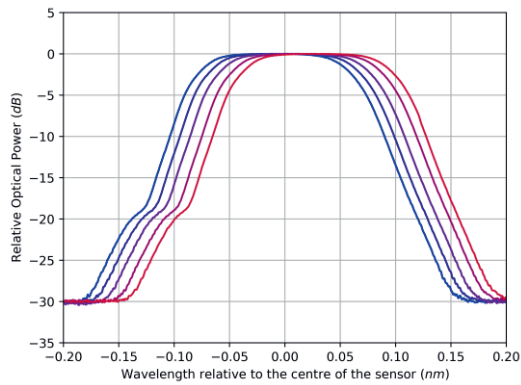


Fig. 2. Electrically derived FBG filter characteristic from 21 °C (blue) to 25 °C (red).

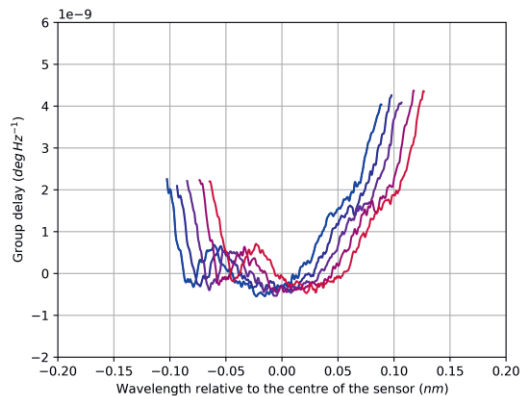


Fig. 3. Group delay characteristic of FBG derived from el. phase from 21 °C (blue) to 25 °C (red).

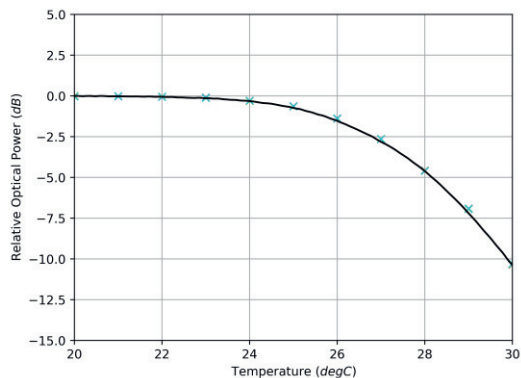


Fig. 4. Relative optical power at different temperatures vs. reference derived from 22 °C curve (black).

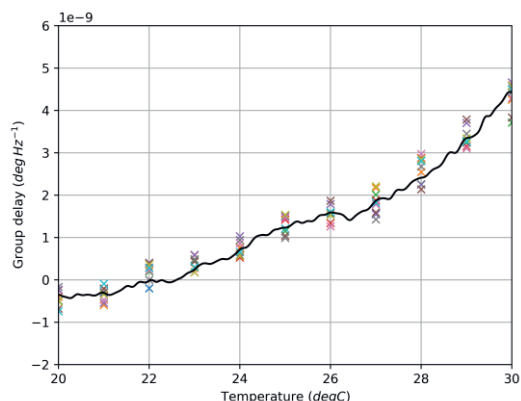


Fig. 5. Group delay at different temperatures vs. reference derived from 22 °C curve (black).

Afterwards, the sensor is heated to various temperatures and the actual measurements are performed by single sweeps on the VNA at each temperature while the TLS remains fixed at 1537.75 nm. Each measurement consists of ten sub-measurements at an interval of 5 s.

Evaluation and Results

For each complex S21 curve of the reference sweeps, the arithmetic mean of the magnitude and the slope of the phase (1st deg. polynomial fit) are calculated across the complete el. BW. The results for the absorption characteristic are shown in Fig. 2. From the visible temperature induced wavelength shift, a temperature coefficient of 9.7 pm/K is resulting, which agrees with other studies pointing out a value of ~ 10 pm/K [5]. In Fig. 3, the group delay characteristics (calculated from the phase slopes) are shown; they lead to the same coefficient value. The single temperature measurements are evaluated likewise. Figs. 4 and 5 show these results and compare them to the related reference characteristics. Both curves are fitted well while the group delay measurements are showing a significantly larger uncertainty of up to 2 K.

Conclusions

Essentially, the temperature reading from the optical power equals the conventional read-out method. In line with this, the results are accurate. Compared to this benchmark, the group delay based measurements possess greater uncertainty but are independent from power fluctuations. Anyway, this study could successfully demonstrate the fundamental suitability of the electrical read-out method for metrology.

Acknowledgement

This work has been funded by the EU and the Free State of Saxony in the project "OSMAT" within ESF-InnoTeam (SAB-Nr. 100329864).

References

- [1] U. Nordmeyer et. al., Microwave based Electrical Read-Out of Optical Sensors, *Sensoren und Messsysteme*, 119-124 (2019); doi: 10.5162/sensoren2019/2.1.2
- [2] Z. Ahmed et. al., Fiber Bragg Grating Based Thermometry, *NCSLI Measure* 10:4, 28-31 (2015); doi: 10.1080/19315775.2015.11721744
- [3] M. Llera et. al., Fiber Bragg grating-based thermometer for drill bit temperature monitoring, *Appl. Opt.* 58, 5924-5930 (2019); doi: 10.1234/s10000
- [4] D. Krohn et. al., Fiber optic sensors: fundamentals and applications. *Bellingham, Washington, USA: Spie Press*, (2014); doi: 10.1117/3.100291
- [5] S. Mihailov, Fiber Bragg Grating Sensors for Harsh Environments, *Sensors (Basel, Switzerland)* 12, 1898-918 (2012); doi: 10.3390/s120201898

Thermographic monitoring of electrical assets by enhanced thermal images for feature extraction

Aydin Boyaci, Stephan Wildermuth

*ABB AG, Corporate Research, Wallstadter Str. 59, 68526 Ladenburg, Germany
aydin.boyaci@de.abb.com*

Summary:

Low-resolution infrared (IR) cameras offer a superior alternative technically and economically for a permanent thermal monitoring of critical components in electrical assets. Therefore, a mapping procedure is developed for the combination of an IR and a visual USB camera which delivers a detail-accurate overlay of the thermal on the visible light image representing the so-called enhanced thermal image. The enhanced thermal images support the component recognition as well as the component recognition in electrical assets showing the temperatures of regions of interest. Finally, combined with the developed correction algorithm for low-resolution IR cameras, temperature features of those regions of interest can be easily extracted for the condition monitoring of electrical assets, such as maximal/minimal, average and environment temperature.

Keywords: Thermal monitoring, medium voltage switchgear, thermal/IR camera, enhanced thermal image, image mapping.

Introduction

Condition monitoring and diagnostics become crucially important for preventing critical overheating failures of electrical assets such as medium voltage (MV) switchgears. Compared to contacting methods like RFID- or SAW- sensors [1], infrared (IR) thermography provides contactless temperature measurement and is suitable for a permanent installation of online temperature monitoring of MV switchgears. Especially in unknown electrical assets for retrofit, the proper installation of stand-alone IR cameras is quite cumbersome during commissioning since, especially in the cold state, it is uncertain if all components of interest are captured by the thermal IR image. A visual USB camera and the subsequent development of a mapping procedure deliver a detail-accurate overlay of the thermal image on a visible light image showing additionally the physical components of the switchgear. The developed image mapping methods for the combination of a visual USB and a thermal IR camera enable the accurate temperature sensing for extracting the temperature features of regions of interest predefined by the user in the visual image.

Temperature monitoring in MV switchgears

Fig. 1 shows the different compartments and components that have to be supervised for a reliable temperature condition monitoring in MV switchgear applications [2,3].

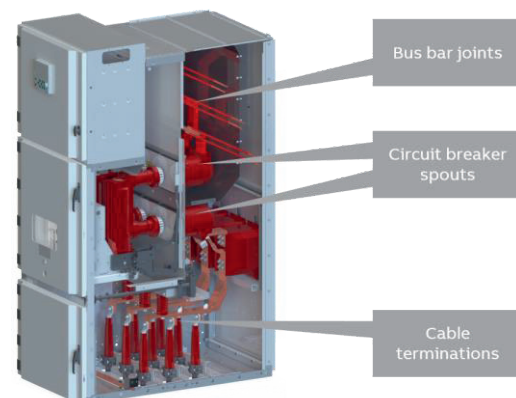


Fig. 1. Schematic view of a medium voltage switchgear panel. Temperature monitoring at the following locations: bus bar compartment (top), upper and lower contacts of the circuit breaker (middle), and cable compartment (bottom).

Enhanced thermal images for temperature feature extraction

The main idea is to provide a detail-accurate overlay of the thermal image on a visible light image which is referred to as enhanced thermal image. Therefore, it is convenient to use a combination of an IR and an USB camera where both lenses possess similar optical characteristics, as for instance similar field of view and fish-eye effect. The image mapping methods are developed by conducting basic tests with both cameras and an uniformly-heated rectangular object with the homogeneous temperature T_{Obj} .

As illustrated in Fig. 2, the mapping method consists of two main steps resulting in an enhanced thermal image as a detail-accurate overlay of the thermal on the visible light image. First, two local coordinate systems are defined in the geometrical center of each image. Then, by considering the fields of view and camera offset, the local coordinate systems of both images are transformed to a common global coordinate system. Finally, both images can be mapped together with respect to the global coordinate system ending up in the enhanced thermal image.

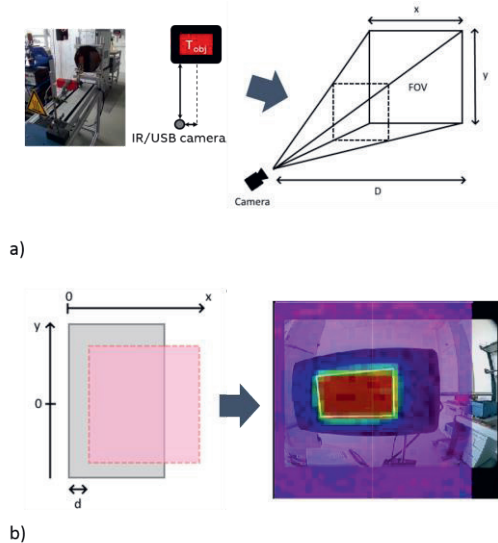


Fig. 2. Overview of the image mapping procedure: a) Schematic measurement setup and determination of field of view for thermal IR image and visual USB image. b) Transformation to a common coordinate system resulting in an enhanced thermal image that is a detail-accurate overlay of both images.

The image mapping method is calibrated with the basic tests performed for the heated block. The calibrated image mapping method is then applied on the use-case of a MV switchgear panel considering the compartment of the breaker spouts.

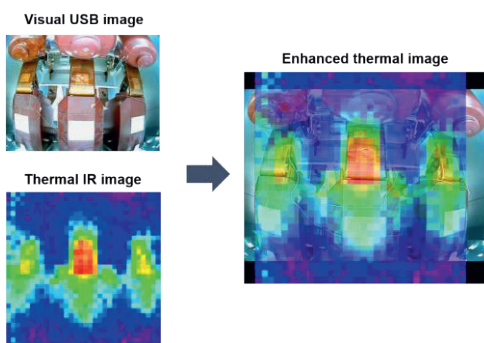


Fig. 3. Demonstration of the image mapping procedure along the section of the breaker spouts of a MV switchgear: Separate thermal IR image, separate visual USB image and enhanced thermal image as overlay of thermal IR and visual USB image.

The enhanced thermal image from Fig. 3 reveals a good agreement between the measured temperature hot spots from the IR image and the individual three phases given in the visual image. The commissioning of electrical assets is now easy to handle since the enhanced thermal image provides the information if all relevant components are fully captured even in the cold state before heating up. Furthermore, the type, topology and compartment of MV switchgears can be identified.

By deriving further mapping methods, we can define the regions of interest to be monitored in the switchgear. As outlined in Fig. 4, the region of interest is manually marked in the visual image with a red rectangle representing the middle phase in the compartment of the breaker spouts. Here, the maximal temperature of the middle phase is automatically extracted as feature. Thus, the developed image mapping methods enable to evaluate semi-automatically the temperature features of the user-defined regions of interest in the switchgear.



Fig. 4. Temperature feature extraction for the middle phase along the section of the breaker spouts of a MV switchgear.

Conclusion

This contribution introduces algorithmic methods to enhance the overall performance of low-resolution, stand-alone IR camera sensors in failure identification of the thermally monitored electrical asset. By using an additional visual USB camera, the presented image mapping methods allow for a temperature feature extraction from regions of interest and thus support the failure identification during online thermal monitoring of switchgears.

References

- [1] J.C. Andle et al., Temperature Monitoring System Using Passive Wireless Sensors for Switchgear and Power Grid Asset Management, CIGRE / CIREC Malaysia, T&D Workshop (2010).
- [2] S. Wildermuth, et al., IR Temperature Measurement System for Condition Monitoring of High Voltage Generator CBs, Sensors and Measuring Systems, Nuremberg, Germany, pp. 1-4 (2014).
- [3] S. Wildermuth et al., Infrared temperature sensing in electrical equipment by low-cost IR cameras, VDE-Hochspannungstechnik, Berlin (2018).

Thermowells with Improved Response Time

Marc Schalles¹, Pavo Vrdoljak², Christian Peuker²

¹ Technische Universität Ilmenau, Ilmenau, Germany,

² Endress+Hauser Temperature and System Products, Nesselwang, Germany

pavo.vrdoljak@endress.com

Summary:

Thermowells are used in various processes as in the Oil & Gas Industry, Life Science Industry or Food & Beverage production to provide a mechanical robust test point for temperature measurement. They enable high immersion length and easier replacement of thermometers. Due to their design, state of the art thermowells decrease the thermal response time of the thermometers. This can be improved significantly by using thermowells with a thermally optimised design. They provide a quicker indication of the process temperature and a more reproducible measurement.

Keywords: industrial thermometer, thermowell, response time, thermal contact, air gap

Background, Motivation and Objective

Thermowells are used in processes, where the thermometer insert may not get in contact with the process medium or when high process temperatures or pressures require a robust design of the test point.

The geometry and dimensions of thermowells can be very different resulting from the requirements of the individual temperature measuring point in the application (see Fig. 1). Hence, length, inner and outer diameter as well as the design of the process connection vary. The thermowells are mostly manufactured of different grades of stainless steel.



Fig. 1. Examples of thermowell designs.

Since a thermowell adds an additional thermal mass and thermal capacity to the system, the

response time of the sensor signal is reduced significantly. The magnitude depends on the dimensions and the material of the thermowell.

To quantify this effect, an investigation of the dynamic properties of thermometer inserts and combinations of inserts and thermowells was performed. The tests were done according to the standard IEC 60751 [1]. It confirmed that the response time of a thermometer strongly depends on the inner design of the thermometer inserts [2]. For well-designed inserts (thermometer) of 6 mm outer diameter one can reach response times $t_{0.9}$ of about 2 s. This is about 80% below the response time of standard inserts (see Fig. 2).

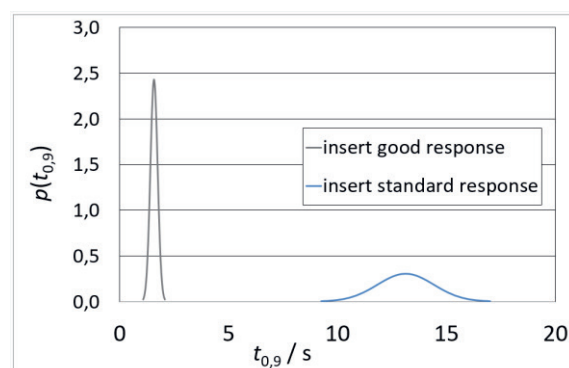


Fig. 2. Graph of distribution of thermal response time $t_{0.9}$ of two different thermometer inserts. $t_{0.9}$ is the time at which the indicated value of a thermometer reaches 90 % of its final value after a step like thermal excitation in water bath with $v=0,2$ m/s. Both thermometer inserts have an outer diameter of 6mm.

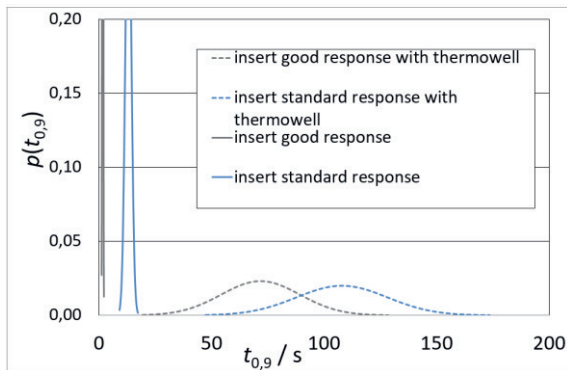


Fig. 3. Graph of distribution of thermal response time $t_{0.9}$. The two thermometer inserts shown in Fig. 1. are additionally measured with standard thermowell with an outer diameter of 11mm.

But, the investigation further revealed that response times of combinations of thermometer and thermowell are much slower than they are for bare inserts (see Fig. 3). They roughly increase by an order of magnitude. Furthermore, the propagation of the response time broadens. This shows that the response is stochastically influenced by dimensional tolerances of the specimen.

Optimisation and Results

The gap between the outer surface of the thermometer insert and the inner surface of the cylindrical thermowell has the biggest influence on the dynamic behavior. This is regardless of the process specific influences or individual application specific thermowell designs.

That is why a thermowell with a new inner design was developed. Here, a solid but flexible gap filler material is used to minimise the air gap. The material equalises dimensional tolerances and improves the thermal contact (see Fig. 4).

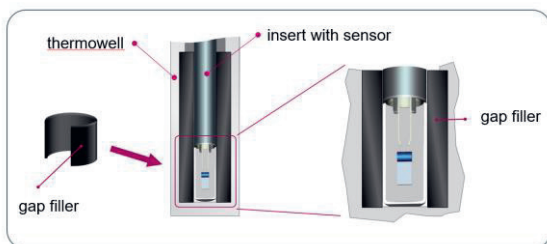


Fig. 4. Improvement of thermal contact by introduction of a gap filler

With this, the response time of thermowell and insert can be reduced drastically (see Fig. 5). Furthermore, the reproducibility of the dynamical behavior is improved, since the distribution of the response time becomes more narrow.

The remaining difference to the response time distribution of the bare inserts is due to the thermal mass and thermal conductive properties of the thermowell.

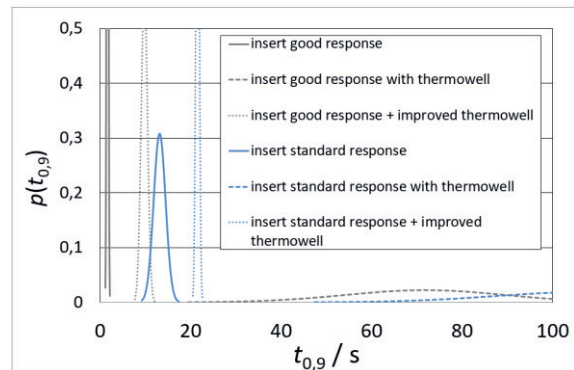


Fig. 5. Graph of distribution of thermal response time $t_{0.9}$. Here, Fig. 3 is expanded by the measured distribution of the thermometer response time with improved thermowells.

A further reduction of the response time could only be theoretically achieved by reduction of the wall thickness of the thermowell or by using of different material. Due to safety reasons this is not practically for the most applications.

References

- [1] DIN EN 60751:2008 Industrial platinum resistance thermometers and platinum temperature sensors, *International Electrotechnical Commission*, 2008
- [2] S. Augustin et. al., Bilateral comparison for determining the dynamic characteristic values of contact thermometers in fluids, *Journal of Sensors and Sensor Systems* 7, 331-337 (2018); doi: 10.5194/jsss-7-331-2018

Computational Laser Metrology using In Situ Calibration for Lensless Fiber Endoscopy

Jürgen Czarske¹, Elias Scharf¹, Robert Kuschmierz¹
¹ Laboratory of Measurement and Sensor System Technique
 TU Dresden, 01062 Dresden, Germany
 juergen.czarske@tu-dresden.de

Summary:

For biomedical applications, lensless holographic fiber endoscopes in needle size based on in-situ calibration have been realized. 4D imaging with cellular resolution and video rate capability is demonstrated.

Keywords: remote phased array, computational optics, calibration, brain imaging, optical tweezing

Introduction

Endoscopes with minimal invasiveness are important for translating various biophotonic techniques, such as 3D imaging, optogenetic cell stimulation, flexible optical tweezers, and to deep tissue in vivo applications. Lensless holographic fiber endoscopes, which do not require any electro-mechanical elements on the distal fiber end, allow a drastic miniaturization of the probe dimensions to only a few hundred microns. Fig.1 show schematically the comparison of the conventional and the novel lensless endoscope.

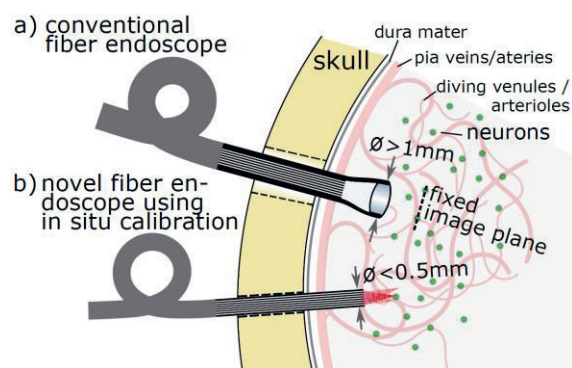


Fig. 1 Schematic comparison of the conventional (a) and the novel endoscope (b), which enables 3D imaging without using lenses.

The lensless endoscope deliver three-dimensional information by exploiting wavefront shaping. Using coherent fiber bundles (CFB) complex light fields can be defined based on remote phased arrays. The transmitted phase pattern is scrambled due to inter-core coupling and random core-to-core phase delays as well as dynamic processes such as bending of the CFB.

The resulting phase distortion Φ_{CFB} has to be measured non-invasively without access to the distal fiber end.

Method: Exploiting scattering in the coherent fiber bundle (CFB) for exploring 3D objects

In order to realize an in-situ calibration, we apply a 150 μm thick glass plate onto the tip of the CFB, see Fig. 2. A guide star is generated through the CFB by illuminating only a single CFB core, which emits a Gaussian laser beam. The light is reflected back into the CFB from the glass plate surface with a predefined wavefront. The phase distortion Φ_{CFB} is recorded holographically after backpropagation through the CFB. Using a spatial light modulator (SLM) and employing digital optical phase conjugation we can now focus directly to the virtual guide star position. In previous work, we employed additional Fresnel lenses on the SLM for 3D focus scanning. In order to speed up the scanning process, phase ramps and lens functions are here added by a 2D galvo scanner for lateral scanning (1 kHz on fast axis) and a tunable lens for axial scanning (up to 50 Hz). 3D scanning with high speed is enabled. The whole diameter of the probe tip is below 500 μm .

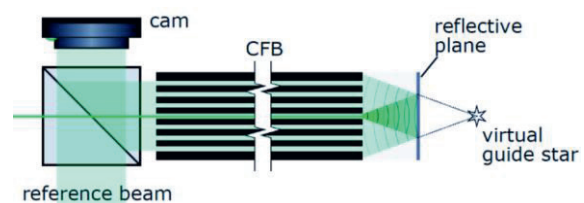


Fig. 2 Scheme of the patented novel in situ calibration method [1,2].

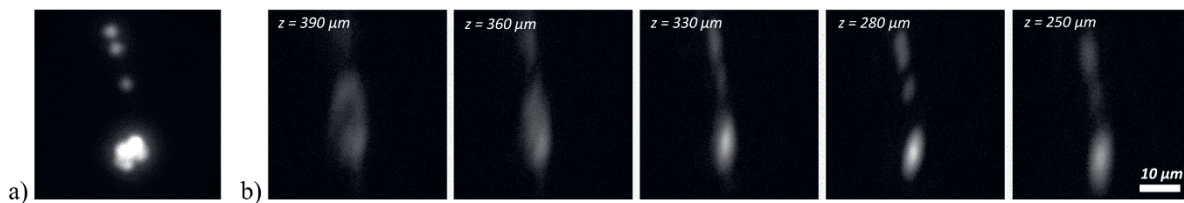


Fig 3. (a) Microscope image of fluorescent beads with 3 μm diameter (b) 3D backwards scan through the CFB

Application

To test the 3D scanning capability, fluorescent beads were applied to a cover glass (see Fig. 3a), positioned at a distance of 280 μm in front of the CFB. The arrangement of the beads in comparison to the reference image can clearly be seen. The maximum scanning speed is currently limited to about 1,000,000 voxels/s by the fluorescence light power, speed of the scanning and detector noise. A diffraction limited focus with a minimum value of 1 μm (FWHM) was determined within the volume of 150 μm x 150 μm x 1000 μm .

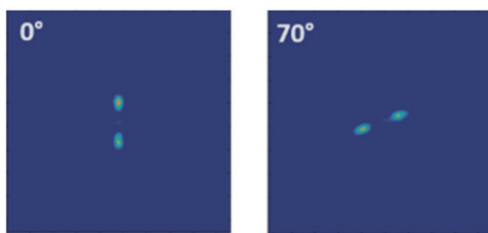


Fig. 4 Examples for rotation of a double focus

Besides optical brain imaging and optogenetic activation of neurons, versatile applications in biomedicine are being pursued. Tomographic refractive index reconstruction for instance in cancer diagnostics relies on a precise cell-rotation. This can be realized by an asymmetric double focus intensity distribution, where the rotation axis is defined by the relative focus position. To test our setup for lab-on-a-chip techniques in vivo cell-rotation we assigned the individual fiber cores randomly to two separate foci. Displaying a Fresnel lens and adequate tilts on each part of the SLM allows the two fiber parts to contribute to the related focal spot. The two main adaptively adjustable parameters of this configuration are the distance of the beam crossing (in this example at 350 μm) and the focal length ($f = 500 \mu\text{m}$), both measured from the fiber facet. Rotating the phase mask on the SLM allows rotating the two spots. Fig. 3b shows the intensity distribution at 500 μm from the fiber facet. The maximum angle deviation amounts to about 1° while the mean deviation is about 0.45°, making this a promising

technique for 3D cell rotation. Fig. 4 shows examples of a double focus.

Conclusion and Outlook

Due to their small diameter, 3D capability and flexibility, holographic fiber endoscopes result in a paradigm shift for biomedicine. Minimal invasively imaging and optogenetic stimulation can be enabled in deep tissue regions. We presented a novel computational technique for in situ calibrating to correct the phase distortions within the coherent fiber bundle with only single sided access. A significant increase in imaging speed was achieved by adaptive optics. 3D fluorescent imaging and complex pattern projection for cell rotation were demonstrated.

Acknowledgement

We thank the Deutsche Forschungsgemeinschaft (DFG) for support with project CZ 55/40-1.

References

- [1] Kuschmierz, Robert; Scharf, Elias; Koukourakis, Nektarios; Czarske, Jürgen W.; "Self-calibration of lensless holographic endoscope using programmable guide stars"; *Optics letters*, 43, 12, 2997-3000, 2018, Optical Society of America
- [2] Scharf, Elias; Kuschmierz, Robert; Czarske, Jürgen W.; "Holographic lensless fiber endoscope with needle size using self-calibration"; *tm-Technisches Messen*, 86, 3, 144-150, 2019, De Gruyter Oldenbourg

Microsecond Optical Frequency Tuning of DFB Laser Diodes for Coherent Optical Frequency Domain Reflectometry

Gregor Saur, Roman Kruglov, Sebastian Schroll, Rainer Engelbrecht
 Polymer Optical Fiber Application Center (POF-AC), Technische Hochschule Nürnberg
 Georg Simon Ohm, Wassertorstr. 10, 90489 Nuremberg, Germany
 rainer.engelbrecht@th-nuernberg.de

Summary:

Optical frequency tuning ranges up to 600 GHz or 4.8 nm have been achieved within microseconds and a standard telecom DFB laser diode operating at 1550 nm. The dynamic optical frequency tuning is induced by electrical current pulse injection and measured using an interferometric setup. Potentially, low-cost sensor systems based on optical coherence tomography (OCT) or coherent optical frequency domain reflectometry (c-OFDR) could be realized, achieving sub-mm two-point range resolution or even better single-point range precision within a few microseconds for a single measurement.

Keywords: tunable lasers, semiconductor lasers, fiber optics, wavelength shift, fiber sensing

Tuning of laser diodes

Fiber bragg grating interrogators, c-OFDR and OCT exploit optical frequency tuning. Strain, temperature and distance can be measured using these techniques.

A larger optical frequency tuning range (FTR) enables better two-point range resolution in reflectometry, which is inversely proportional to the FTR. By driving a laser diode (LD) with a current pulse, the temperature and carrier density in the active zone dynamically changes which in turn produces a fast tuning of the optical frequency.

The FTR for sensor applications had first been investigated for current pulses in the millisecond-range [2]. The strong initial FTR led to the investigation of current pulses in the nanosecond-range with amplitudes exceeding the specified operating current by a factor of 30. Thereby, an FTR of 1.5 THz or 12 nm has been achieved with DFB-LD [1].

This work examines the relevant parameters for optical frequency tuning in the microsecond regime. Compared to nanosecond-pulses it might be possible to provide more energy within the optical pulse and therefore improve the signal-to-noise ratio.

Measurement setup

The optical tuning rate $dv(t)/dt$ of the LD is encoded in the optical power $P(t)$ (interferogram) at the Output of the Mach-Zehnder interferometer (MZI). The interferogram oscillates with the instantaneous beat frequency

$f_{\text{beat}}(t)$, which is calculated using the Hilbert Transformation Compensation Method. The instantaneous optical frequency

$$v(t) = \tau \cdot \int_{t_0}^{t_0+T} f_{\text{beat}}(t) dt \quad (1)$$

during a time interval of duration T can then be calculated using the MZI delay τ . The FTR corresponds to the difference of the optical frequency at the beginning and end of the optical pulse.

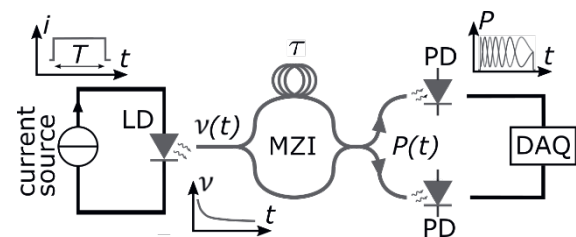


Fig. 1. A fiber-coupled LD is pulsed in the μs -range with an injection current. The thermal increase of the junction leads to optical frequency tuning which creates an interferogram at the MZI output.

Tab. 1 shows the specifications of the used DFB-LD LDM5S515-005.

Tab. 1. Specifications of the used DFB-LD.

LDM5S515-005			
Coax-package, optically isolated, fiber-coupled			
I_{th}	12 mA	λ_0	1549 nm
P_{cw}	12 mW (optical)	I_{cw}	150 mA

Results

Fig. 2 shows the dynamic tuning behavior for a 2 μs current pulse at 200 mA in 100 ns intervals.

During the injection, the LD incorporates a constant heating power. The transition of the junction temperature is exponentially dampened. Hence, the optical tuning rate $dv(t)/dt$ decreases with increasing time of current injection. During the first 100 ns, the FTR is 18 GHz and then drops to 2 GHz after 1 μ s within equal observation length. Hence, 25% of the total 71 GHz FTR occur during the initial 5% of the optical pulse (and thus the optical energy).

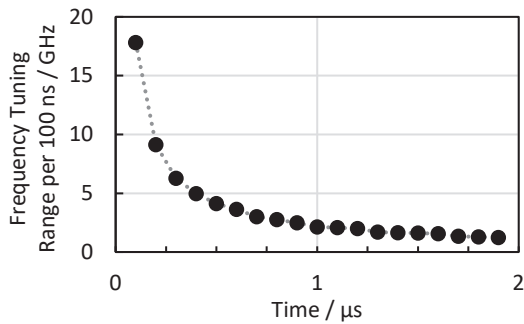


Fig. 2. FTR per 100 ns at 200 mA.

Fig. 3 shows the logarithmical dependence of the FTR on the current pulse width in the μ s-range. Increasing the current pulse width from 1 μ s to 10 μ s doubles the FTR from 54 GHz to 106 GHz (196%), whereas a further increase to 20 μ s yields an FTR of 121 GHz (114%). The optical tuning rate decreases for long pulses because the junction temperature reaches an equilibrium.

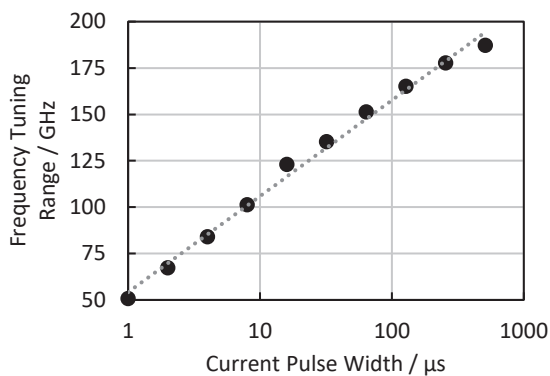


Fig. 3. FTR versus current pulse width at 200 mA.

At first, the optical tuning rate enhances when increasing the current pulse amplitude, followed by a section of linear dependency before the FTR seems to saturate (shown in Fig. 4 for a current pulse width of 10 μ s). The maximum measured FTR for 1200 mA is 600 GHz (about 4.8 nm at 1550 nm). For higher current pulse amplitudes, light emission eventually drops to zero after some microseconds. This is likely due to the temperature dependent optical power and is yet to be examined. Therefore, measurements with current amplitudes above 1200 mA were not taken into account.

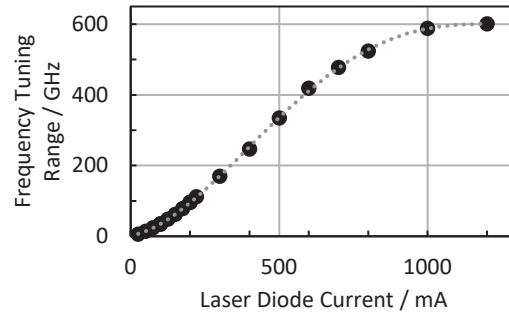


Fig. 4. FTR of a 10 μ s pulse versus LD current.

Conclusion

The dynamic optical frequency tuning of a current pulsed standard 1550 nm telecom DFB laser diode in the microsecond regime has been measured with an interferometric setup. By using short current pulses with amplitudes up to eight times the specified cw-current, optical frequency tuning ranges of 600 GHz or 4.8 nm have been achieved.

While the optical frequency tuning range over current pulse width shows the expected behavior dominated by thermal transients in the laser chip, the maximum tuning range starts to saturate at high currents. This will be part of further examinations, together with reliability considerations and methods to linearize the strongly non-linear temporal frequency sweep.

With the presented results, low-cost sensor systems based on OCT or c-OFDR using standard telecom DFB lasers could be realized potentially, achieving sub-mm two-point range resolution or even better single-point range precision within microseconds. Beyond that, precision is largely dominated by the signal-to-noise ratio and thus, the object reflectivity, not discussed here.

Acknowledgment

This project is funded by "Bayerisches Staatsministerium für Wissenschaft und Kunst" within the "Programm zur Förderung der angewandten Forschung und Entwicklung an Hochschulen für angewandte Wissenschaften" under contract no. H.2-F1116.NÜ/56/3 (FasoDynE).

References

- [1] M. Njegovec, D. Donlagic, Rapid and broad wavelength sweeping of standard telecommunication distributed feedback laser diode, *Optics Letters*, Vol. 38, 11, 1999-2001 (2013); doi: 10.1364/OL.38.001999
- [2] R. Passy et al., Experimental and theoretical investigations of coherent OFDR with semiconductor laser sources, *Journal of Lightwave Technology*, Vol. 12, No. 9, 1622-1630 (1994); doi:10.1109/50.320946

Investigation of a metrological atomic force microscope system with a combined cantilever position, bending and torsion detection system

Yiting Wu, Elisa Wirthmann, Ute Klöpzig, Tino Hausotte

*Institute of Manufacturing Metrology (FMT), Friedrich-Alexander-Universität Erlangen-Nürnberg,
Nägelsbachstr.25, 91052 Erlangen, Germany
yiting.wu@fmt.fau.de*

Summary:

This article presents a new metrological atomic force microscope (MAFM) with adjustable beam position and direction of the cantilever measuring system. An interferometric measurement system measures the position of the cantilever and a quadrant photodiode detects the bending and torsion of the cantilever. To improve the signal quality and reduce disturbing interferences, the optical design was changed in comparison to the system of [3, 4]. The integration of the MAFM in the nanomeasuring machine (NMM-1) offers the possibility of large-scale measurements over a range of 25 mm × 25 mm × 5 mm with subnanometre resolution. A large number of measurements have been performed by this MAFM in combination with the NMM-1. In this short paper, examples of these measurements for determination of step height and pitch and the measurement of an area are demonstrated.

Keywords: metrological atomic force microscope, nanomeasuring machine,

Introduction

Today's progress in areas like nanotechnology and electronics requires metrological accurate object positioning and measurement with a high resolution and high accuracy. Decreasing structural sizes and at the same time feature miniaturization with increasing component dimensions characterize the measurement tasks for micro- and nanomeasuring systems. Since its invention in 1986 [1], the atomic force microscope (AFM) has been widely used in the precision engineering as well as in the micro- and nanotechnology. Currently, optical beam deflection (OBD) systems are mainly used to detect the bending and torsion of cantilevers [2]. Instead, focus sensor detection systems and interferometric detection systems measure the position of the cantilever. Measurements using laser interferometer can be over the laser wavelength directly traceable to the metre definition.

A new version of a metrological laser interferometer-based AFM head has been developed at the Institute of Manufacturing Metrology (FMT). The measuring head was first developed to enable exact interferometric position measurement, performed directly on the reflecting backside of the probe and simultaneous measurement of the position, bending and torsion of the backside of the probe [3]. During the measurement with the AFM, the cantilever is usually slightly tilted (in our system 8°) in order

to avoid contact of the clamping chip with the surface of the measured object. Two tiltable plane mirrors are used as an adjustment unit to adjust both the direction and the position of the focused laser beam. Consequently, the optical axis of the focusing lens in the measuring arm can be perpendicular to the reflecting backside of the cantilever. This adjustment unit is also very useful for adapting the system after exchanging the cantilever or the complete cantilever unit even in case of different tilt angles or lengths of the cantilever. The MAFM has been integrated in the NMM-1 as a probe system and therefore a large area measurement of a range over 25 mm × 25 mm × 5 mm and a resolution of 0.1 nm is realizable.

This short paper reports the design and implementation of the MAFM. Results of step height and pitch determination and areal measurements on different samples are given.

System setup

The measuring head combines a homodyne interferometer and a tilt measuring system, which allows the simultaneous detection of position, bending and torsion of the reflecting surface with one focused beam [4]. A single laser beam is utilized in this measuring head. This results in an advantage of a compact, small measuring head with total dimension of about 110 mm × 130 mm × 40 mm (including

reference arm). Two wedge plates are integrated to minimize disturbing interferences on the position sensitive device (PSD) caused by multiple reflections on the quarter wave plate [4]. While one tiltable plane mirror is fixed, the other tiltable plane mirror can realize an adjustable angle of $\pm 3^\circ$. Accordingly, the adjustable displacement is approximately $250\ \mu\text{m} - 290\ \mu\text{m}$. The new system design is shown in Fig. 1

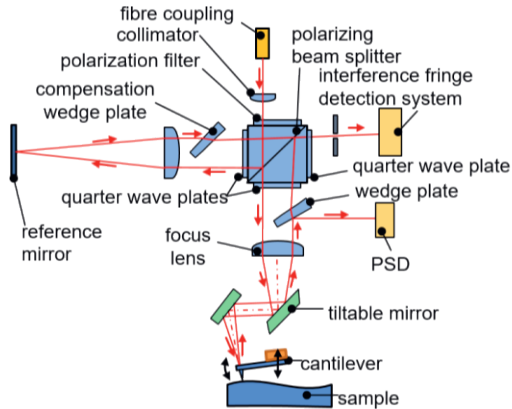


Fig. 1 Functional principle of the metrological AFM system

Measurement Results

In order to carry out measurements correctly, the MAFM was calibrated by the NMM-1. Different measurement tasks were carried out. In the following, exemplary measurements in contact mode with the cantilever PPP-CONTSCR from the company Nanosensors are illustrated. The profile height (z-direction) is the difference between the calibrated AFM bending signal and the z-axis position data of the NMM-1. Fig. 2 shows the measurement on a step height TGZ1 from company NT-MDT with a step height of $(21.4 \pm 1.5)\ \text{nm}$. With a scan speed of $1.5\ \mu\text{m/s}$ and a point distance of $1\ \text{nm}$ the lateral mean mismatch between forward and backward scan is about $15\ \text{nm}$. The step height was calculated according to DIN EN ISO 5436-1. The measured step height is $20.66\ \text{nm}$ with a standard deviation of $1.8\ \text{nm}$. This result agrees with the nominal value.

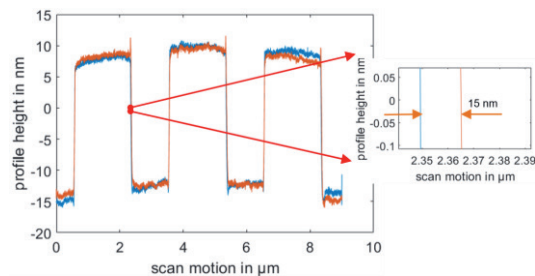


Fig. 2 Step height measured forwards and backward

In order to determine the pitch, the measurements are conducted perpendicular to the gratings TGZ2 with a step height of $(108 \pm 2)\ \text{nm}$

and a period of $(3 \pm 0.01)\ \mu\text{m}$. A scan length of $600\ \mu\text{m}$ was repeated 10 times. Fig. 3 illustrates a section from one repeated measured profile. The mean pitch was calculated using the Fourier transform method [5]. The determined mean pitch is $3.007254\ \mu\text{m}$ with a standard deviation of $61\ \text{pm}$.

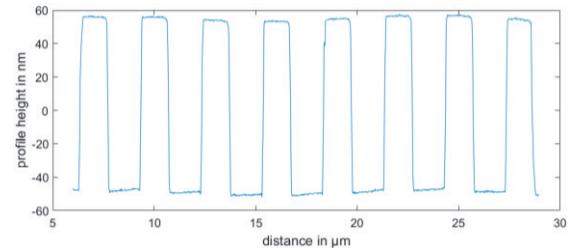


Fig. 3 Measurement on calibration grating (one scanned line)

Finally, an exemplary areal topography scan in macroscopic range is shown in Fig. 4. A $1\ \text{mm} \times 70\ \mu\text{m}$ area of TGZ2 was measured with 10000×14 pixels. Commercial AFMs have a limited scanning range of less than $200\ \mu\text{m}$. Due to the integration of the MAFM in NMM-1 a scan area of $25\ \text{mm} \times 25\ \text{mm}$ can be achieved.

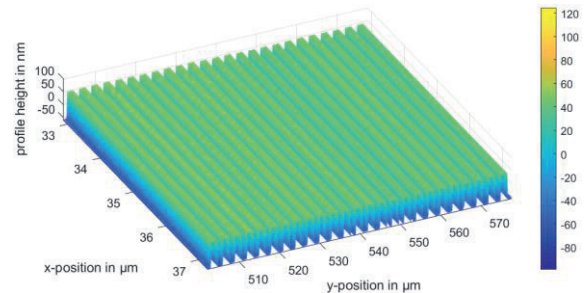


Fig. 4 Section from the scanned area of TGZ2

References

- [1] G. Binnig, C.F. Quate, Ch. Gerber, Atomic Force Microscope, Physical Review Letters 56, 930-933 (1986); doi:10.1103/PhysRevLett.56.930.
- [2] A. Yacoot, L. Koenders, Recent developments in dimensional nanometrology using AFMs, Measurement Science and Technology, 122001 (2011); doi:10.1088/0957-0233/22/12/122001.
- [3] N. Dorozhovets, T. Hausotte, N. Hofmann, E. Manske, G. Jäger, Development of the interferometrical scanning probe microscope, Proc. SPIE 6293, Interferometry XIII. (2006) s. 629311; doi:10.1117/12.680692.
- [4] F.G. Balzer, T. Hausotte, N. Dorozhovets, E. Manske, G. Jäger, Tactile 3D microprobe system with exchangeable styli, Measurement Science and Technology, 094018 (2011); doi:10.1088/0957-0233/22/9/094018.
- [5] G. Dai, L. Koenders, F. Pohlenz, T. Dziomba und H. U. Danzebrink, Accurate and traceable calibration of one-dimensional gratings, Measurement Science and Technology, (2005); doi:10.1088/0957-0233/16/6/001

Optical multi-distance measurements of spur gears

Marc Pillarz¹, Axel von Freyberg¹, Andreas Fischer¹

¹ *University of Bremen, Bremen Institute for Metrology, Automation and Quality Science (BIMAQ),
Linzer Str. 13, 28359 Bremen, Germany
m.pillarz@bimaq.de*

Summary:

Standard gear measuring systems (e. g. coordinate measuring machines) are conditionally suitable for extensive large gear measurements due to individually limited measuring volumes. Therefore, an optical scalable multi-distance sensor system consisting of a confocal chromatic sensor in combination with a rotary table is presented and referenced with a tactile measurement. The determined standard deviation of the profile slope deviation of a small spur gear amounts 1.23 μm . Further, with a suitable calibration strategy, simulations show that uncertainties of less than 1 μm can be achieved.

Keywords: large gear, optical measurement, confocal chromatic sensor, multi-distance measurement, model-based evaluation

Introduction

In dimensional metrology, measurements of large gears are challenging due to high claims on tolerances of single-digit μm [1]. With regard to the manufacturing process of large gears, the standard gear inspection with a random test scope of four teeth is not sufficient. Compared to small gears, asymmetrical heat input and tool wear occur due to the larger chip volume and the longer machining time [2]. Standard gear measuring methods, such as coordinate and gear measuring machines, are only conditionally suitable for extensive large gear measurements due to the fixed measuring volume [3]. Scalable gear measuring approaches are desirable to detect deviation parameters of large gears with 1 μm uncertainty. Recently, optical sensor systems have been investigated for extensive gear measurements. Optical gear measurement approaches based on the triangulation principle are presented in [4, 5]. Guo et al. achieved measurement uncertainties of the profile deviation of the teeth of 1 μm . They used a laser line triangulation sensor in combination with a rotary table. In 2019, Chen et al. investigated an optical gear measurement approach by using moiré projection [6]. The estimated mean measurement uncertainty for the profile deviation is 2.67 μm . In summary, the current state of research shows the potential for optical gear measurement concepts. However, no measurement approach mentions the applicability for large gears. As solution, an optical scalable multi-distance measurement approach for large gear measurements consisting of a confocal chromatic sensor in combination with a

rotary table is presented. Initially, the applicability of the measurement concept is investigated on a small spur gear due to a simpler handling. As fundamental shape parameter the profile slope deviation is to be determined with a desired uncertainty of 1 μm .

Measurement principle

In this article, the profile slope deviation is evaluated for a small spur gear. The profile slope deviation $f_{H\alpha}$ is defined as the deviation of the actual slope from the nominal slope of an involute. The profile slope deviation is determined by a linear regression into the plumb line distances d_{plu} between actual and nominal geometry of the tooth in a defined evaluation range. According to [7], the points P_a of the actual geometry of a tooth flank can be described as function of the points P of the nominal geometry of an involute spur gear and the plumb line distance d_{plu} . To quantify the plumb line distances and thus the profile slope deviation, the inverse problem $d_{\text{plu}}(P, P_a)$ must be solved. Therefore, the actual profile geometry of the tooth flank must be measured. Fig. 1 illustrates the optical multi-distance measurement concept. A confocal chromatic distance sensor is aligned vertically to the teeth in the transverse section of the spur gear and continuously measures the distance to the teeth surface while rotating the gear. By calibrating the sensor system in position and alignment, the distance information is transformed into coordinates in a measurement coordinate system (x, y) . With a model-based evaluation according to [7], the plumb line distances and thus the

profile slope deviation of individual teeth can be calculated.

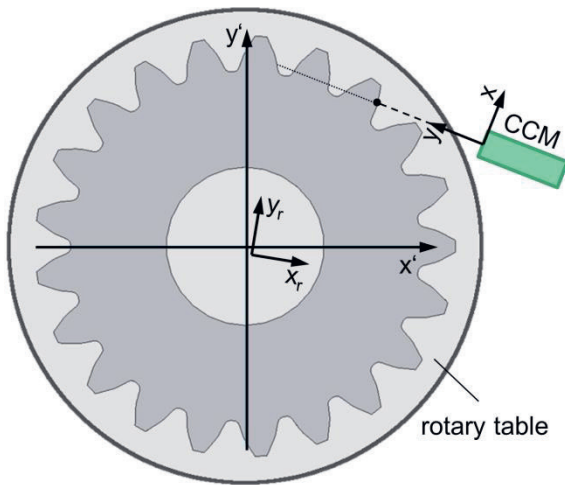


Fig. 1. Measurement principle consisting of a confocal chromatic (CCM) sensor (x, y) in combination with a rotary table (x_r, y_r) measuring the distance to the teeth flanks (x', y') depending on the rotation angle.

Results

In order to proof the applicability of the optical gear measurement system, measurements on a small involute gear with a normal module $m_n = 3.75$ mm and 26 teeth are performed. With a subsequent model-based evaluation, the profile slope deviations of the teeth are determined. The results are referenced with a coordinate measuring machine. Fig. 2 shows the optically detected profile slope deviations and reference values for four random teeth with the single standard deviation for an accessible evaluation range of one third of the tooth height at the tip.

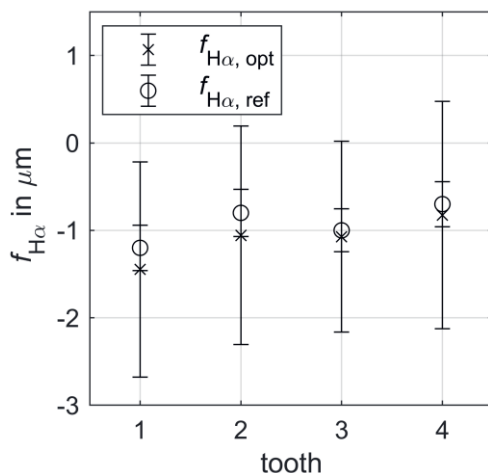


Fig. 2. Profile slope deviation of four random teeth with the single standard deviation. Measured with the optical sensor system $f_{H\alpha, opt}$ and referenced with a coordinate measuring machine $f_{H\alpha, ref}$.

As a result, the optically determined and the reference values of the profile slope deviation are in agreement within the calculated random errors for $k = 1$. While the random error of the reference measurement amounts $0.26 \mu\text{m}$ on average, the random errors of the optical values are 6 times higher and amount $1.23 \mu\text{m}$ on average for $k = 1$. The aimed uncertainty of $1 \mu\text{m}$ is therefore narrowly missed by $0.23 \mu\text{m}$. A general applicability of the sensor concept is nevertheless shown. Main contributions to the random errors are the position and alignment uncertainties due to the sensor calibration. In the future, a suitable sensor calibration strategy must be implemented, in order to reduce the total measurement uncertainty. With a suitable calibration strategy, simulation results show that uncertainties of less than $1 \mu\text{m}$ can be achieved. Hence, a proof of principle of the optical multi-distance gear measurement approach was obtained.

References

- [1] ISO1328-1: Cylindrical gears - ISO system of flank tolerance classification - Part 1: Definitions and allowable values of deviations relevant to flanks of gear teeth, (2013); doi: 10.31030/2773568
- [2] F. Balzer, M. Schäfer, I. Lindner, A. Günther, D. Stöbener, J. Westerkamp, Recent advances in optical gear measurements - A new approach for fast measurements of large gears, VDI-Berichte, vol. 2255, 655–666 (2015)
- [3] F. Balzer, N. Steffens, M. Stein, K. Kniel, Traceable measurement of large gears with micron accuracy: a mandatory basis for reliable wind energy systems, Engineering for a Changing World: Proceedings; 59th IWK, Ilmenau Scientific Colloquium, vol. 59, Technische Universität Ilmenau, september 11-15 (2017)
- [4] M. M. Auerswald, A. von Freyberg, A. Fischer, Laser line triangulation for fast 3D measurements on large gears, The International Journal of Advanced Manufacturing Technology, 100, 2423–2433 (2019); doi: 10.1007/s00170-018-2636-z
- [5] X. Guo, Z. Shi, B. Yu, B. Zhao, K. Li, Y. Sun, 3D measurement of gears based on a line structured light sensor, Precision Engineering, 61, 160-169 (2020); doi: 10.1016/j.precisioneng.2019.10.013
- [6] Y. Chen, J. Chen, Optical Inspection System for Gear Tooth Surfaces Using a Projection Moiré Method, Sensors (Basel), 19 (6), 1450, (2019); doi: 10.3390/s19061450
- [7] D. Stöbener, A. von Freyberg, M. Fuhrmann, G. Goch, Areal parameters for the characterisation of gear distortions, Materialwissenschaft und Werkstofftechnik, 43, 120–124 (2012); doi: 10.1002/mawe.201100898

Multi-sensor system for selective methane measurements in harsh environments

Henrik Lensch¹, Tilman Sauerwald^{1}, Michael Müller², Frank Braunecker², Tomasz Dudziak², Horst Brünnet³, Andreas Schütze¹*

¹Saarland University, Lab for Measurement Technology, 66123 Saarbrücken, Germany

²3S GmbH – Sensors, Signal Processing, Systems, 66115 Saarbrücken, Germany

³Schaller Automation Industrielle Automationstechnik GmbH&Co. KG, 66440 Blieskastel, Germany
h.lensch@lmt.uni-saarland.de

Summary:

We present a multi-sensor system for the detection of methane in crankcases of large dual fuel or gas engines to prevent exceedance of the lower explosion limit (LEL). It contains a total of four sensors each based on a different detection principle. To test the approach two systems were installed at a stationary power plant with a large dual fuel engine for long-term test with an online GC as reference system.

Keywords: sensor array, methane detection, LEL, crankcase, harsh environment

Motivation

Continuously increasing emission regulations in shipping [1] also increase the need for a more environmentally friendly fuel source than marine diesel oil (MDO) or heavy fuel oil (HFO). One solution is to use liquefied natural gas (LNG) as alternative fuel [2]. This is possible in dual fuel engines enabled for methane usage in emission control areas (ECAs) and MDO usage otherwise or in a purely gas driven engine as used in power plant applications. During the operation of these large 4-stroke engines a significant amount of unburned methane can be pushed alongside the piston into the crankcase as so-called blow-by. Continuous operation therefore might lead to an accumulation of unburned methane in the crankcase up to the lower explosive level (LEL) at its worst [3]. Therefore, a device is needed to monitor the methane concentration in the crankcase during the operation of these engines.

Hardware

The system consists of three different parts which can be described as follows.

(1) The sensor block contains the various gas sensors placed sequentially inside a sensor chamber. This sensor array consists of a metal oxide semiconductor (MOS) sensor (Figaro TGS8410), a pellistor (SGX VQ546M), a digital humidity and temperature sensor (Sensirion SHT35) and an electrochemical cell (Alpha-Sense O2-A2). The EC cell is operated at constant voltage, while both the MOS sensor and

pellistor are operated dynamically (temperature-cycled operation, TCO).

(2) The filter and pump systems are placed at the inlet and outlet of the sensor chamber, respectively. The filter is used to prevent particles and lubrication oil from entering the sensor chamber whereas the pump is used to continuously extract atmosphere from the crankcase.

(3) The controller handles the dynamic sensor operation and online methane concentration calculation.

Experimental Setup

The field test systems were installed on a modified 18-cylinder V-engine Pielstick PC 2-5V DFC with 8 MW power. The dual fuel engine is capable of running on MDO or HFO as well as on natural gas. In natural gas operation, the methane concentration in the fuel supply is approx. 98%. Analytical probing revealed a crankcase atmospheric composition as presented in Table 1.

Tab. 1: Crankcase atmosphere composition

Carbon monoxide	< 10 ppm
Carbon dioxide	< 0.1 %
Ethane	< 1 ppm
Propane	< 1 ppm
Butane	< 1 ppm
Formaldehyde	< 1 ppm
Total VOC	< 1 ppm

In the crankcase, a relative humidity of 55 – 60 %r.H. was measured during the test

* currently at: Fraunhofer Institute for Process Engineering and Packaging IVV, Freising, Germany

campaign in combination with a permanent oil mist atmosphere. Two test devices (001, 002) were connected to the crankcase, where one of the systems was installed in line with an online gas chromatograph (GC, type I-GRAPHX S) via PTFE hoses. A flame arrester was used as safety device between test system and crankcase. The test system and the GC were permanently installed to monitor the methane concentration over time and to compare the signals. In order to check the system status and to account for possible signal offsets, fresh air balancing was used every 24 h and a test gas mixture with 3.8 Vol.% methane in synthetic air was applied every 7 days.

Results & Discussion

Fig. 1 shows the methane concentrations as determined by the two independent GasMOS systems plus the GC reference measurement.

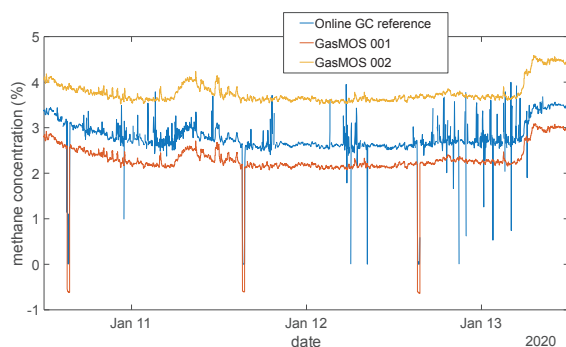


Fig 1: 3-day section of a long-term test at the 8 MW test engine. Both sensor systems follow the reference concentration closely, except an offset, which can easily be compensated.

Both sensor systems follow the shape of the GC reference with a constant offset. One shows a constant higher concentration (1% methane) whereas the other always shows a slightly lower concentration (0,5% methane). Both offsets can be corrected by subtracting a constant offset, as shown in Fig. 2.

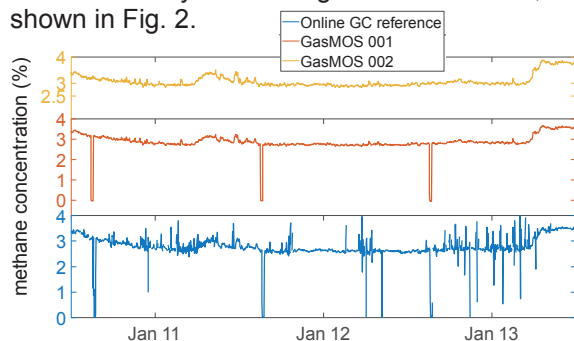


Fig 2: offset compensated long-term test.

The 001 system (red line) as well as the reference from the GC (blue line) show a methane concentration of 0 % every 24 hours, whereas the 002 system (yellow line) shows a methane concentration of 3.8 %. This is caused by the

self-fresh air balancing where the intake is periodically switched to fresh air without any methane. Since the 001 system and the GC are connected in series, the reference air is applied to both, whereas the 002 system is connected in parallel to the others and therefore air is never applied to this system. Nevertheless, both systems show the same trend as the reference. Even small concentration changes (0.05% change in methane concentration) can be detected with all three systems. Therefore, the multi gas sensor system shows a high precision comparable to a commercially available GC but a low accuracy between the systems still exists, due to the offset from the reference. To increase the accuracy, it is possible to subtract the offset with a base line correction where the system intake is periodically switched to an atmosphere without methane [4]. To increase the accuracy even further, it is possible to perform a two-point online recalibration where the system is also periodically exposed to a defined methane concentration.

Conclusion

We have shown that this multi sensor approach yields a promising selective methane determination in harsh environments such as a gas engine. It is possible to determine the methane concentration with a resolution and precision comparable to a commercial reference GC, even with an unknown amount of interfering gases produced by the combustion process of the engine. To eliminate the still existing offset between system and reference, an automated recalibration procedure must be developed and implemented.

Acknowledgements

Part of this research was performed within the project "GasMOS" funded by the European Regional Development Fund (ERDF).

References

- [1] International Maritime Organization, MARPOL ANNEX VI and NTC 2008 with guidelines for implementation, vol. 258, pp. 1–24, 2013.
- [2] F. Burel, R. Tacconi, N. Zuliani, Improving sustainability of maritime transport through utilization of Liquefied Natural Gas (LNG) for propulsion, *Energy*, 57, 412–420 (2013). doi: 10.1016/j.energy.2013.05.002
- [3] H. Brünnet, D. Reppekus, M. Theobald, G. Kornatz, Formation and avoidance of crankcase explosions in large oil, dual-fuel and gas engines, 5th Rostock Large Engine Symposium, Rostock, Germany, September 2018, pp. 280–297.
- [4] S. Di, M. Falasconi, Drift Correction Methods for Gas Chemical Sensors in Artificial Olfaction Systems: Techniques and Challenges, in: *Advances in Chemical Sensors*, Wen Wang, IntechOpen (2012), doi: 10.5772/33411

Compensation of siloxane poisoning of metal oxide semiconductor gas sensors in temperature cycled operation

Caroline Schultealbert, Tobias Baur, Tilman Sauerwald¹, Andreas Schütze
Lab for Measurement Technology, Saarland University, Saarbrücken, Germany
c.schultealbert@lmt.uni-saarland.de

Summary:

We present a method for quantifying the degradation state due to siloxane poisoning of a metal oxide semiconductor gas sensor using temperature cycled operation. The time constant for the generation of surface charge at high temperature increases through poisoning and is only slightly dependent on the gas atmosphere. In addition to indicating a necessary sensor replacement, this signal can also be used for drift compensation based on the exponential relation between sensor signal and this time constant.

Keywords: metal oxide semiconductor, gas sensor, siloxanes, poisoning, stability

Motivation

Metal oxide semiconductor (MOS) gas sensors are promising candidates for several applications due to their excellent sensitivity towards many reducing gases. This of course brings along some drawbacks like poor selectivity but also stability issues. Well-known poisons for MOS sensors are siloxanes [1]. Due to their broad occurrence in personal care and household products problems arise in several applications [2]. The impact of siloxanes on sensors operated at constant temperature have been studied extensively, but investigations on temperature cycled sensors are rarely found. We recently presented first results [3]. However, these measurements involved only very high siloxane dosages, the relatively uncommon siloxane HMDS (hexamethyldisiloxane) and only a small set of gases. Here we present a systematic study on the effect of the more prevalent OMCTS (octamethylcyclotetrasiloxane, [4]) on MOS sensors in temperature cycled operation (TCO) and an approach for self-compensation.

Experimental setup

Measurements were conducted with our gas mixing apparatus (GMA). The sensors were exposed to a concentration of 2 ppm OMCTS for 1-3 hours several times followed by complex characterization measurements. The following gases and concentration ranges were selected: humidity (30-70 %RH), H₂ (500-2300 ppb), CO (40-1750 ppb), acetone (0-800 ppb), ethanol (0-700 ppb), acetaldehyde (0-900 ppb) and toluene (0-1200 ppb). Gas exposures were generated as described in [5], offering all mentioned gases

simultaneously at a randomly chosen concentration within the associated range. 50 mixtures were measured, each held for 20 min. 16 sensors in total were studied (6 different types, 2 working modes, 4 using different types of diffusion barriers). The results presented here focus on the AS-MLV-P2 sensor (ams Sensors Germany GmbH) in TCO with a cycle length of 120 s. The cycle itself is derived from the differential surface reduction (DSR, described in [6]). This means that the sensor is oxidized at high temperature (here 400 °C, 10 s) followed by fast cool down to a lower temperature (100, 150, 200, 250, 300 °C, 14 s each) where the surface reduction (DSR signal, $k_{reduction}$), which is proportional to the concentration of reducing gases, is measured directly via differentiation of the logarithmic conductance:

$$\frac{d}{dt} \ln(G) \propto k_{reduction} \quad (1)$$

Turning the DSR method around gives the opportunity to evaluate the time constant τ for generation of surface charge (differential surface oxidation, DSO) via an exponential fit of $\ln(G)$ during the high temperature phase.

Results

One cycle with the same, constant gas atmosphere is shown in Fig. 1 after different siloxane dosages. Dosages 6.84 & 18.63 ppm·h are excluded here for better overview but agree with other results. The mean value of the cycle is shifted due to the siloxane exposure and the dynamic response at high and low temperatures is slowed down. This indicates that all processes

¹ currently at: Fraunhofer Institute for Process Engineering and Packaging IVV, Freising, Germany.

on the sensor surface become slower due to siloxane poisoning, which corresponds to the deactivation of catalyst and other active surface sites. Fig. 2 shows the DSR signal at 200 °C during several characterizations, yielding a concentration proportional signal that is highly affected by siloxane exposure. The total concentration of reducing gases is indicated by the background color intensity. For this temperature at 9.8 and 12.7 ppm·h the signal is completely deteriorated. For quantification of the degradation state the time constant τ for oxidation at high temperature was evaluated, which is – according to the underlying gas sensor model [6] – independent from the ambient gas atmosphere. Fig. 3 shows histograms of τ for the characterization measurements evaluated during the first high temperature phase in each cycle. The width of the distribution mainly originates from the fact that τ still depends slightly on the atmosphere, but the effect is sufficiently small to allow quantification of the sensor state, e.g., to indicate the need for sensor replacement. Before replacing the sensor, the signal should be corrected to allow correct gas quantification. The correction can be carried out using the same method: Fig. 4 shows the relative decrease of the DSR signal vs. the relative increase in τ for every seventh exposure from the total of 50 gas mixtures. The dashed line represents an exponential fit of the form

$$\Delta_{DSR} = 1.06 \cdot \exp(-0.060 \cdot \Delta\tau) \quad (2)$$

which can be directly used to adjust the poisoned sensor signals in Fig. 2.

Outlook

The presented results include only a small part of the collected data from the corresponding study. More results including other sensors and operating modes, selectivity of MOS sensors and classification as well as other concepts to deal with siloxane poisoning are in preparation.

References

- [1] G. Korotcenkov, B. K. Cho, *Sensors Actuators, B Chem.*, 156 (2011); doi: 10.1016/j.snb.2011.02.024
- [2] D. Ruffer, F. Hoehne, J. Bühler, *Sensors (Switzerland)*, 18 (2018) doi: 10.3390/s18041052
- [3] C. Schultealbert, I. Uzun, T. Baur, A. Schütze, T. Sauerwald, *Dresdner Sensor-Symposium*, P2.04 (2019); doi: 10.5162/14dss2019/P2.04
- [4] C. Rücker, K. Kümmerer, *Chem. Rev.*, 115 (2015); doi:10.1021/cr500319v
- [5] T. Baur, M. Bastuck, C. Schultealbert, A. Schütze, T. Sauerwald, *Dresdner Sensor-Symposium*, 6.3 (2019); doi: 10.5162/14dss2019/6.3
- [6] T. Baur, C. Schultealbert, A. Schütze, T. Sauerwald, *J. Sens. Sens. Syst.* 7, 411-419 (2018); doi: 10.5194/jsss-7-411-2018

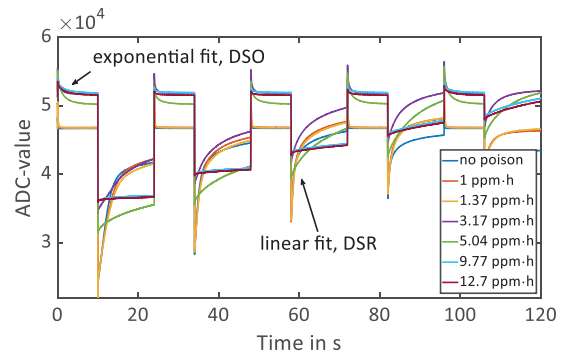


Fig. 1. Signal of one cycle under constant gas atmosphere for different siloxane dosages.

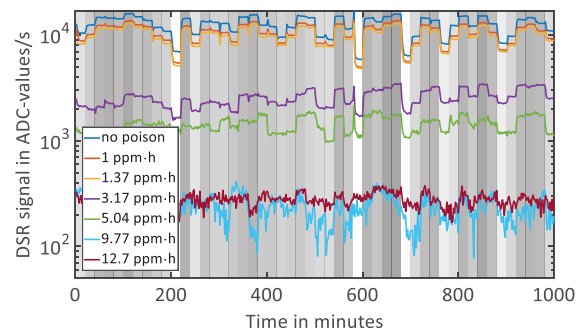


Fig. 2. The DSR signal at 200 °C over time after different siloxane dosages, showing the 50 randomized gas offerings (total concentration indicated by color intensity) held for 20 minutes each.

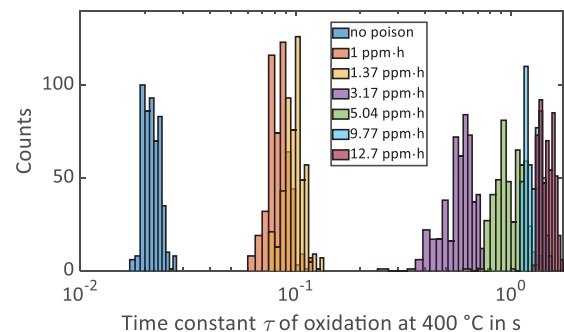


Fig. 3. Histograms of the time constant for oxidation for different siloxane dosages.

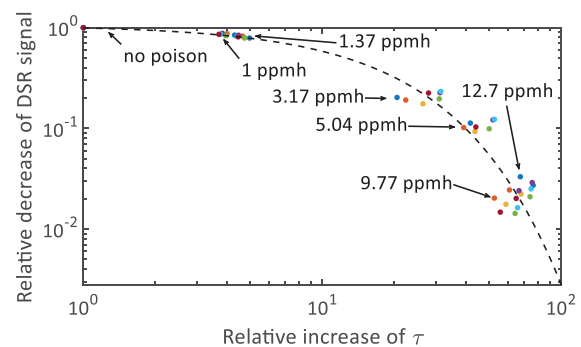


Fig. 4. Relative decrease of the DSR signal used for gas quantification vs. relative increase of the DSO time constant τ indicates that a compensation of siloxane poisoning is possible (every 7th gas offer shown).

Smart gas sensor systems can help to reduce food waste

My Sa Marschibois¹, Tilman Sauerwald^{1}, Martin Leidinger², Thorsten Conrad², Andreas Schütze¹*

¹ Saarland University, Lab for Measurement Technology Saarbrücken, Germany

*² 3S GmbH – Sensors · Signal processing · Systems, Saarbrücken, Germany
m.marschibois@lmt.uni-saarland.de*

Summary:

Food waste in developed countries is an enormous ecological burden, while millions suffer from hunger around the globe. We are targeting novel smart gas sensor systems to reduce food waste mainly from end consumers. Preliminary GC/MS studies during aging of different foods show that typical emissions, e.g. hydrogen sulfide and methanethiol from minced meat, show characteristic compositions reflecting the aging process. This change in gas composition could be detected by low-cost sensor systems. We are planning a methodic study of different foods to identify and detect these patterns.

Keywords: food waste, gas chromatography/mass spectrometry (GC/MS), smart gas sensor, hydrogen sulfide, methanethiol.

Background, Motivation

Approximately a third of the global food production is wasted while approx. one billion people worldwide are suffering hunger. In Europe, mostly fruit and vegetables go to waste or are discarded during production. Around 50% of overall food waste is due to consumer behavior. Since food waste accounts for 3.5 billion tons of CO₂ emissions, it is also a huge burden for the environment. Against the backdrop of today's climate crisis, this is another reason to minimize food waste [1].

Low-cost gas sensor systems could help consumers reduce food waste. Different solutions seem possible, i.e. handheld devices for immediate analysis of dairy products after opening instead of relying on the "best before" date or continuous monitoring of the inside of a refrigerator (cf. FreshMeter technology by Grundig). Specific gas emissions could, e.g., help determine when specific foods should be consumed. These sensor solutions could therefore prevent disposing of edible food or spoilage of food during storage.

Materials and Method

During a preliminary study, food-specific gas patterns indicating aging or deterioration were detected using gas chromatography/mass spectrometry (GC/MS, Thermo Fischer scientific, Trace 13000 Gas Chromatograph, ISQ 7000 Single Quadrupole Mass Spectrometer). As a first example, minced meat was specifically

chosen as it deteriorates quickly and thus allows fast experiments.

Minced meat was first stored in the refrigerator for one week at a temperature of 7°C. Subsequently, it was stored for three days at room temperature while gas samples were taken every 24 hours from the headspace of the vial containing a defined amount of meat. A Restek Rt-q-plot column (30 m length, Ø 0.32 mm, 10 µm film thickness) serves as a separating column. The GC oven's temperature profile was set as follows: Starting temperature at 40°C with a temperature increase of 10°C/min to 230°C final temperature, which is held for 10 min. The GC-oven's temperature cycle thus lasts 30 min.

Results

The GC/MS measurements indicate that hydrogen sulfide and methanethiol could be suitable target gases for indicating the deterioration of minced meat.

Hydrogen sulfide (H₂S) is detected from minced meat stored in a refrigerator without protective gas atmosphere at 7°C for one week, Fig. 1. The observed H₂S concentrations increases further for samples stored at room temperature and reaches its peak after 48 hours. Subsequently, a rapid drop of the H₂S concentrations is observed accompanied by an increase of the methanethiol concentration. After 72 hours at room temperature, the methanethiol concentration exceeds the maximum level for hydrogen sulfide reached after 48 hours, Fig. 2.

* currently at: Fraunhofer Institute for Process Engineering and Packaging IVV, Freising, Germany

This example shows that not only absolute gas concentrations but also changing ratios of various gases can be used to determine the level of aging or degradation of food. This is highly important as the concentration of a single target gas would also depend on the amount of food tested, ambient conditions and the specific measurement set-up, while gas mixture ratios might be more stable under real-life test conditions. Similarly, other target gases could be identified to determine fruit ripening.

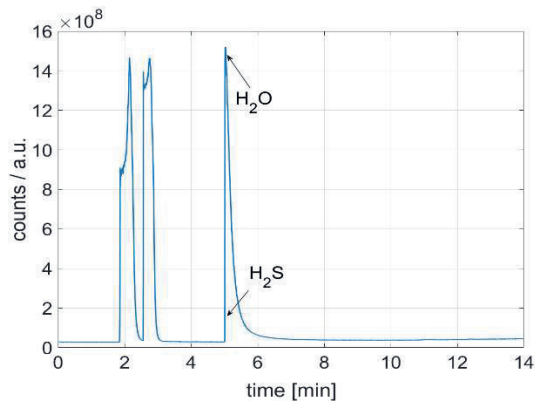


Fig. 1: Hydrogen sulfide emissions from minced meat stored in a refrigerator at 7°C for 1 week.

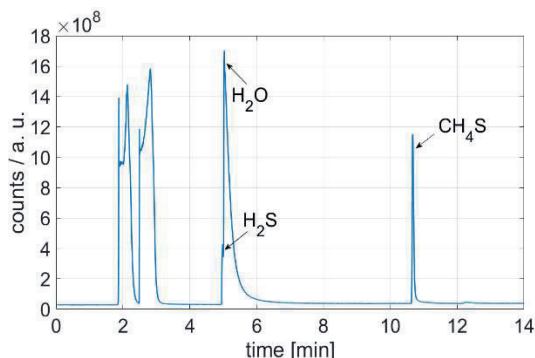


Fig. 2: Hydrogen sulfide concentrations emitted from minced meat decrease after storage at room temperature for 72 hours, while the amount of methanethiol increases rapidly.

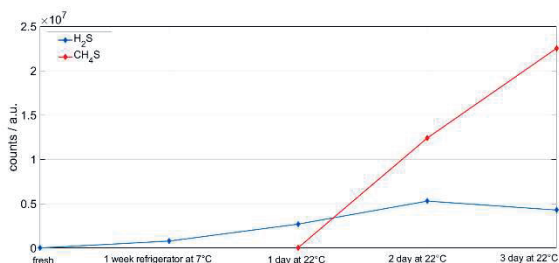


Fig. 3: Levels of hydrogen sulfide and methanethiol during the aging and deterioration of minced meat.

Outlook

Based on these observations, we are currently establishing a test set-up for multiple foods with

multiple samples of each food to determine characteristic patterns during storage and aging. A large refrigerator is equipped with closed storage boxes containing different food samples. The storage boxes are connected to a valve block which allows sampling each headspace of the boxes individually. At defined intervals gas samples from the boxes are automatically analyzed by the GC/MS and in parallel by a multi gas sensor system supplied by the company 3S [2]. The gas sensor system contains two semiconductor gas sensors (UST series 1000 and 2000) which are operated using TCO (temperature cycled operation) [3].

Food to be tested include different fruits (banana, citrus fruits,...) and vegetables (tomatoes, potatoes,...).

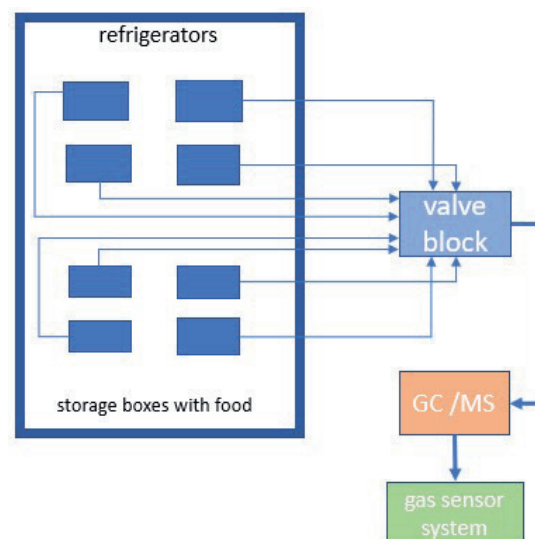


Fig. 4: Sketch of the test set-up with refrigerator with measuring unit, GC/MS and gas sensor system.

Acknowledgment

This work is sponsored by the DBU – Deutsche Bundesstiftung Umwelt in the frame of the project SiVERiS.

References

- [1] „UN beklagen Umweltschäden durch verschwendete Lebensmittel“, <https://www.zeit.de/wissen/umwelt/2013-09/un-lebensmittel-verschwendung-umwelt>
- [2] 3S GmbH - Sensors, Signal Processing, Systems, www.3s-ing.de
- [3] A. Kreiter, T. Sauerwald, A. Schütze, T. Conrad, Selective detection of (E)-hexenal in the sub-ppm range and of ethanol in the low-ppm range using semiconducting gas sensors with temperature cycled operation (TCO), SENSOR 2013 - 16th International Conference on Sensors and Measurement Technology, Nuremberg, Germany, May 14 - 16, 2013.

Systematic Investigations on the Reaction Potential of Catalytic Sensor Materials

Olena Yurchenko^{1,2}, Hans-Fridtjof Pernau¹, Laura Engel¹, Benedikt Bierer¹, Martin Jäggle¹, Jürgen Wöllenstein^{1,2}

¹*Fraunhofer Institute for Physical Measurement Techniques IPM, Heidenhofstr. 8, 79110 Freiburg, Germany,*

²*Department of Microsystems Engineering—IMTEK, University of Freiburg, Georges-Koehler-Allee 102, 79110 Freiburg, Germany
olena.yurchenko@ipm.fraunhofer.de*

Summary:

We present Simultaneous Thermal Analysis (STA) as a systematic approach for investigation of catalytic activity at ideal conditions and for thermal stability. The investigations were performed on different cobalt oxide samples differing in particle size, which is a promising catalyst for methane oxidation. The obtained results demonstrate the reliability of the method for preselection of catalysts for their application in catalytic gas sensors.

Keywords: metal oxide catalysts, catalytic activity, catalytic gas sensor, Simultaneous Thermal Analysis (STA), catalyst preselection.

Background, Motivation and Objective

In the field of safety technology, catalytic sensors, so-called »pellistors«, are commonly used for detection of flammable gases such as hydrocarbons. The heat produced during catalytic oxidation of the combustible gas on the catalytic layer corresponds to its concentration in environment. The nowadays pellistors usually operates at high temperatures (>450°C) to ensure the proper detection of methane which is the most inert combustible gas.

However, the high operation temperatures entail some disadvantages such as high power consumption and lowered catalyst stability. Reducing the operating temperature will contribute to decrease the power consumption and increases of sensor operating life due to improving of catalyst aging. To reduce the operation temperature, catalysts of high activity and stability are required, especially for detection of methane.

However, the choice of suitable catalysts for the targeted gas sensor applications is not easy from different points of view. Firstly, catalysts used in sensors are complex systems consisting of catalysts and various additives allowing their integration into the sensor and generates the mechanical stability of the layer. Additives can affect the catalyst activity as well as stabil-

ity and their effect is difficult to identify by gas sensor characterization. Secondly, the response detected by a sensor is the complex reaction as well, determined by the whole sensor system. Thirdly, the preparation process of individual sensors is quite extensive. That additionally limits the amount of tested catalyst samples and the variation of parameters.

To overcome these limitations, existing by investigations of pellistor gas sensors, different calorimetric methods can be used to perform the preselection of the catalysts [1, 2]. The usage of additional gas analyzing systems makes the calorimetric investigations more reliable. We used Simultaneous Thermogravimetry-Differential Thermal Analysis System coupled with Quadrupole Mass Spectrometer (STA-QMS) to investigate systematically the effect of particle size distribution and morphology of Co₃O₄ on its catalytic activity for methane oxidation and its thermal stability. The focus of investigation was on lower operation temperatures (<400°C). Spinel Co₃O₄ was reported as a promising catalyst for methane combustion [3]. The investigations aim at the ascertainment of Co₃O₄ applicability as catalyst or as support of metallic catalyst in pellistors achieving low operation temperatures.

Description of the New Method

The commercially available STA (NETZSCH, STA 409 CD-QMS 403/5 SKIMMER) was adapted for the investigation of catalytic activity at dry conditions. The temperature difference between reference and sample crucible (contained ≈ 20 mg sample) was converted by software in DTA signal ($\mu\text{V}/\text{mg}$) corresponding to catalytic activity. Due to the heat release during catalytic oxidation, the DTA signal shows a negative output. The signal normalization to sample weight allows systematic investigations and direct comparison between different samples.

Results

To investigate the effect of particle size distribution on catalytic activity, commercial Co_3O_4 (400 mesh, $37 \mu\text{m}$) was wet grinded in a zircon jar by means of a planetary ball mill for different durations (between 0.5h and 16h). Additionally, Co_3O_4 was synthesized by precipitating procedure obtaining nanosized particles.

Fig. 1 illustrates the dependence of DTA response of commercial Co_3O_4 on the grinding time at different temperatures. The increasing the grinding time leads to successive improving the catalytic activity, especially for the first four hours of grinding. Further increasing the grinding time has no significant effect on improving the catalytic activity.

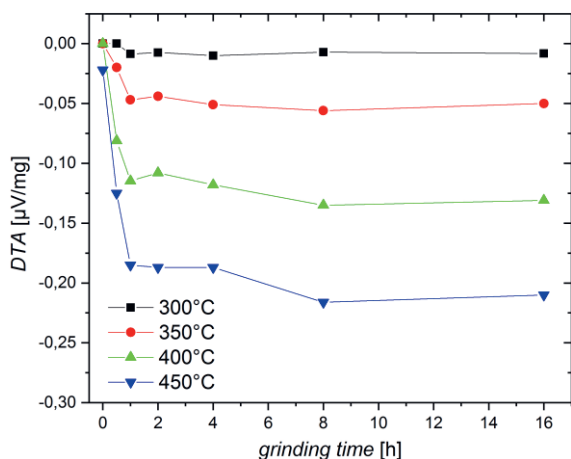


Fig. 1. DTA response as a measure of catalytic activity obtained at CH_4 oxidation (1 vol.% in dry air) on commercial Co_3O_4 catalysts as a function of grinding time and operation temperature.

Fig. 2 shows that for this catalyst, a pronounced activity is observed at 450°C . In contrast, the synthesized Co_3O_4 with initially nanosized particles shows already at 350°C a considerably higher activity. For both kinds of catalyst, the thermic stability test (synthetic air/methane alternation at 350°C and 450°C) were undertaken (Fig. 3). As expected, synthesized nanosized Co_3O_4 exhibits slightly

lower thermal stability than commercial one originated from operation at high temperatures (450°C).

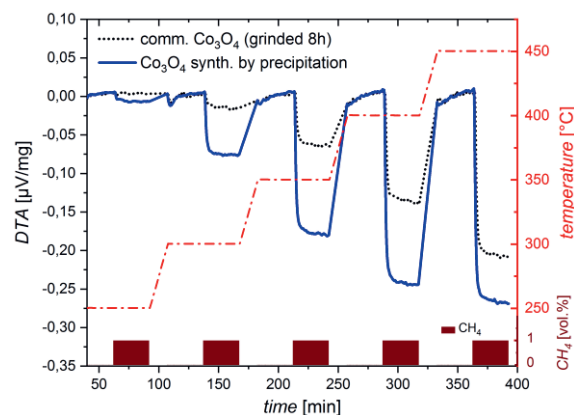


Fig. 2. DTA response to the exposure of 1 vol.% CH_4 in dry air for 30 min at temperatures between 250 – 450°C for two different Co_3O_4 catalysts; a rinsing with synthetic dry air for 30 min was used to achieve a base line.

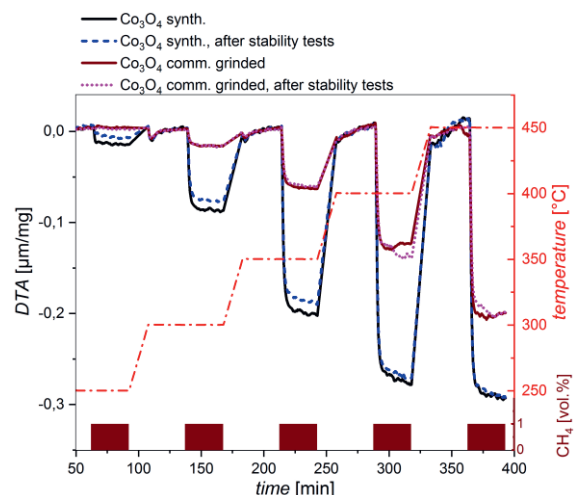


Fig. 3. DTA response to the exposure of 1 vol.% CH_4 in dry air for 30 min at temperatures between 250 – 450°C for two different Co_3O_4 catalysts before and after thermal stability investigations.

References

- [1] J.Loskyl, W.F.Maier, K.Stoewe, Application of a Simultaneous TGA-DSC Thermal Analysis System for High-Throughput Screening of Catalytic Activity. *ACS Comb. Sci.* 14, 600–604 (2012); doi:10.1021/co3000659.
- [2] G. Hakvoort, X. Xiaoding, Decomposition of methanol vapour over solid catalyst, measured by DSC. *J. Thermal Anal.* 37, 1269–1279 (1991); doi:10.1007/BF01913860
- [3] Z. Pu, H. Zhou, Y. Zheng, W. Huang, X. Li, Enhanced methane combustion over Co_3O_4 catalysts prepared by a facile precipitation method: Effect of aging time. *Appl. Surf. Sci.* 410, 14–21 (2017); doi:10.1016/j.apsusc.2017.02.186.

The Optimization of a Photoacoustic Refrigerant Sensor System Using a Three-Chamber Concept

Mahmoud El-Safoury¹, Christian Weber^{1,2}, Olaf Kiesewetter³, Jürgen Wöllenstein^{1,2}

¹ *Fraunhofer Institute for Physical Measurement Techniques IPM, Heidenhofstrasse 8, 79110 Freiburg, Germany*

² *Department of Microsystems Engineering - IMTEK, Georges-Köhler-Allee 102, 79110 Freiburg, Germany*

³ *UST Umweltsensortechnik GmbH, Dieselstrasse 2 und 4, 99331 Geratal OT Geschwenda, Germany
mahmoud.el-safoury@ipm.fraunhofer.de*

Summary:

Ever since the ban of the refrigerant R134a in 2017 for all newly manufactured vehicles, due to its high global warming potential, the necessity of low-cost, reliable and precise refrigerant measuring devices has arisen. We present a photoacoustic gas detector for the refrigerants R134a and the environmentally-friendly alternative R1234yf. The sensor consists of a detection, an absorption and a filter chamber. The influence of the filter chamber length on the sensor signal was evaluated and a signal drift, originating from filter chamber leakage, was successfully eliminated and validated by FTIR measurements.

Keywords: Photoacoustic detector, photometer, refrigerants, R1234yf, R134a

Background, Motivation and Objective

Carbon-fluorine based refrigerants are classified as greenhouse gases due to the high global warming potentials (GWP) [1]. The refrigerant R134a has a GWP value of 1300 (according to the fifth assessment of the IPCC from 2013) when compared to carbon dioxide. This led to a, since 2017 effective, European ban on R134a air conditionings for all newly manufactured vehicles [2]. The hydrofluoroolefin R1234yf is considered an environmentally less harmful alternative (GWP of 4) and shows similarities in the thermodynamic properties [1]. R1234yf is far more expensive than R134a. To prevent illegal refillings of cheaper gas mixtures containing both refrigerants, low-cost refrigerant gas analyzers are required. We present a newly developed photoacoustic (PA) R134a and R1234yf detection method, with special focus on the optimization of the filter chamber geometry and the reduction of sensor signal drifts.

The Three-Chamber Photoacoustic Detector

An IR broadband light source and a commercially available MEMS microphone were used. The large main absorption bands of R134a and R1234yf coincide, which makes it difficult to identify a quantitative gas mixture, that consists of both refrigerants [3]. A separated detection of the individual gases in a gas mixture was achieved with the three-chamber concept. The PA cell (Fig. 1) consists of a detection (DC), an absorption (AC) and a filter chamber (FC).

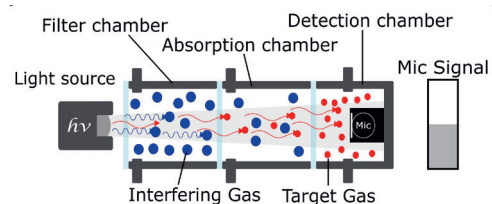


Fig. 1: The three chamber based PA detector. The filter chamber is filled with the intruding gas, while the detection chamber consists of the microphone and the target gas. The examined gas mixture is introduced into the absorption chamber.

The MEMS microphone and the target gas are hermetically sealed into the DC. The AC is filled with the analyzed gas sample. Additionally, the FC is filled with the known intruding gas, to manipulate the spectrum of the IR light source, removing the spectra of non-target gases. An ideal FC would absorb all photons of the intruding gas before reaching the AC and by that, reducing the cross sensitivity of the detector towards the interfering gas. The leftover photons are absorbed afterwards by the introduced target gas in the AC, reducing the light intensity reaching the DC. The detected microphone signal in the DC drops, depending only on the target gas concentration in the AC and independent of the interfering gas.

Influences of the Filter Chamber Length

Three filter chambers with varying lengths (20, 50 and 80 mm) were manufactured (by SIMEK GmbH) for an experimental determination of the

FC geometry influences on the detected signal. The following experiments were carried out with a R1234yf detector. Therefore, the DC is filled with R1234yf and gets hermetically sealed. The filter chambers were filled through silicone tubes with the interfering gas R134a. The silicone tube were mechanically shut with a clamp during the following experiments. To test the efficiency of the FC, the two refrigerants were separately introduced into the AC, while varying the concentrations of the respective gases (Fig. 2). The respective refrigerant concentrations were set to 40, 60 and 80 vol.-% at a flow velocity of 50 ml/min.

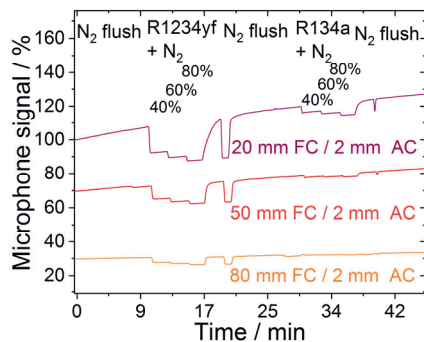


Fig. 2: R1234yf detector: Influence of the filter chamber length on the cross sensitivity and absolute signal strength.

The measurement results show a reduction of the cross sensitivity with increasing FC lengths, while the absolute signal strength and therefore the signal-to-noise ratio is reduced with increasing length (Fig. 2). The functionality and importance of the FC were verified by these measurements. The drift in the plots is resulted by the escaping R134a out of the not gas-tight filter chambers.

Optimizing the Filter Chamber

To assure a complete hermetic closure of the FC, metallized silicon windows were soldered to the respective window openings of the 50 mm long FC. In a second step, the tested FC was filled with R134a. Subsequently, the filling tubes of the chamber were mechanically crimped and soldered afterwards, resulting in a gas tight sealing (Fig. 3).

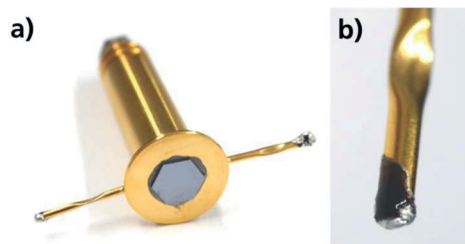


Fig. 3: a) The gas filled filter chamber after a hermetic sealing with soldered silicon windows. b) The crimped and solder sealed filling tubes.

The experimental results in Fig. 4 include measurements before (red) and after (black) the solder sealing of the gas filled filter chamber. The respective measurements were executed for about 18 hours to check the long-term stability of the detected R1234yf sensor signal. The AC was filled with N₂ during the measurements. It can be observed in Fig. 4, that the black curve of the gas filled FC with an additional solder sealing is a perfect straight line with no observable drift effect occurring, while the red curve shows an exponential increase of the sensor signal and reaches a plateau after 13 hours. The signal of the mechanically sealed FC (red curve) increased by 75% from its original value due to the loss of R134a from the not gas tight FC.

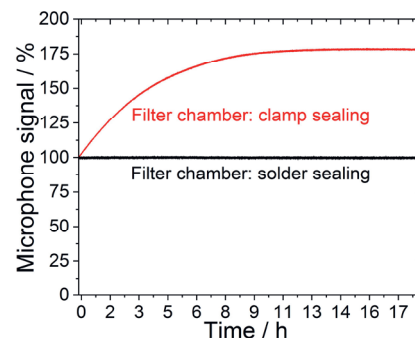


Fig. 4: Comparison of the R1234yf sensor signal long-term stability before and after a soldered sealing of a 50 mm long filter chamber (filled with R134a).

Conclusion

The experiments with the different gas filled filter chamber lengths showed, that an increase in the FC length reduces the cross sensitivity and the signal strength of the sensor system simultaneously. The measurements showed strong drifting of the sensor signal, which was eliminated after hermetically sealing the FC. A solder sealing of the gas filled measurement system chambers showed long term sensor signal stability.

References

- [1] B. Minor and M. Spatz, "HFO-1234yf low GWP refrigerant update," *International Refrigeration and Air Conditioning, Conference, paper 937*, 2008.
- [2] European Union, "Directive 2006/40/EC of the European Parliament and of the Council of 17 May 2006 relating to emissions from air-conditioning systems in motor vehicles and Amending Council Directive 70/156/EEC," *Off J Eur Union*, vol. 1, 2006.
- [3] C. Weber, M. El-Safoury, A. Eberhardt, K. Schmitt, J. Wöllenstein, "Miniaturisierte photoakustische Detektoren für den Nachweis fluorhaltiger Kältemittel," *VDI/VDE-Gesellschaft Meß- und Automatisierungstechnik -GMA-, Düsseldorf; Informationstechnische Gesellschaft -ITG-*, pp. 322–327, 2019.

Multispectral Readout System for Detecting Tiny Color Changes of Gas Sensitive Colorimetric Dyes

C. Weber^{1,2}, M. El-Safoury¹, C. Pannek¹, L. Engel¹, A. Eberhardt¹, M.-L. Bauersfeld¹, J. Wöllenstein^{1,2}

¹ Fraunhofer Institute for Physical Measurement Techniques IPM, Heidenhofstr. 8, 79110, Freiburg, Germany

² Department of Microsystems Engineering—IMTEK, Laboratory for Gas Sensors, University of Freiburg, Georges-Köhler-Allee 102, 79110, Freiburg, Germany

Christian.weber@ipm.fraunhofer.de

Summary:

We present a simple sensor setup for detecting very small color changes of gasochromic materials. The sensor includes up to ten LEDs for capturing different spectral channels, ranging from ultraviolet to the near infrared. In order to detect diminutive color changes of dyes at gas concentrations in the sub ppm range, the system includes a differential photodiode circuit, as well as two additional photodiodes to determine the absolute reflectance of the dyes.

Keywords: optical readout, color, gas sensor, colorimetric, carbon monoxide

Motivation

Current smoke detectors for residential use are predominantly based on the stray light principle. Detecting the light scattered by smoke particles, they feature two main disadvantages: The detection method can hardly differentiate between particles emitted from fires and harmless dust or fog particles. In addition, the detectors can only identify fires, which emit larger amounts of smoke particles. Especially for smoldering fires, this is not always the case.

In order to overcome these disadvantages, the combination with sensors for the detection of gases, emitted by fires, is advantageous [1]. The emission of carbon monoxide (CO) is a very specific indicator for burning processes and therefore, the detection of CO is ideally suited for this application. Measuring CO at an early fire stage requires a highly sensitive and selective detection method. The colorimetric gas sensing principle (also known as gasochromic principle) meets these requirements. It relies on a color changing chemical reaction of the target gas with a specifically tailored dye. In this work, we present a setup that is able to read out even very tiny color changes of gasochromic dyes in the presence carbon monoxide for fire detection purposes.

Readout System for Gas Dependent Color Change

In the presented measurement system, the color detection is accomplished by illuminating the dye with ten LEDs of different wavelengths and measuring the reflected light intensities in their respective spectral ranges.

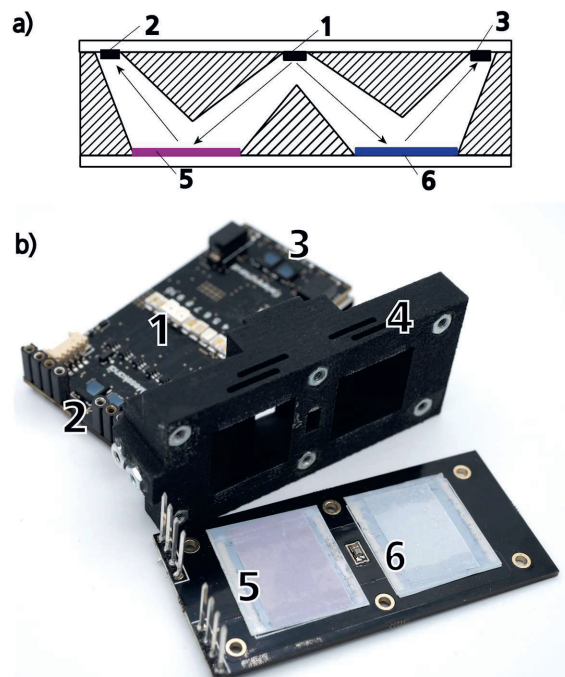


Fig. 1. (a) Cross section and (b) photograph of the sensor system with LEDs (1), measurement detectors (2), reference detectors (3), enclosure (4), gas sensitive dye (5) and reference dye (6).

For a concentration variation in the sub ppm range, the reflection change can be as small as 10^{-3} %. The reflection or scattering of light that does not interact with the dye reduces the apparent color change in addition. In order to resolve the small color change, we use a differential detection principle consisting of two antiparallel photodiodes with a symmetrical arrange-

ment (see Fig. 1). One of the photodiodes receives the reflected light from the gasochromic dye, while the other one receives it from a reference dye that does not react to the target gas. The antiparallel interconnection of the photodiodes enables a differential measurement where only the reflection difference, which primarily depends on the gasochromic dye, remains. For an absolute reflection measurement, there are two single channel photodiodes placed beside the differential detectors.

As shown in Fig. 1, the system comprises a 3D printed enclosure with a W-shaped beam path. This ensures a defined symmetrical light distribution, while absorbing stray light that does not interact with the colorimetric dye.

The ten LEDs with wavelengths ranging from 395 to 940 nm are driven successively. The photo current of the single channel diodes is amplified with $2.7 \cdot 10^6$ V/A, while the photodiode signal of the differential channel is amplified with $2.7 \cdot 10^8$ V/A. An average LED current of 400 μ A is modulated sinusoidal at 20 kHz, while the detector signals are captured and filtered by a digital lock-in algorithm having 1 s averaging time and running on an onboard PSoC6 microcontroller. Fig. 2 shows the upper part of the system with activated LEDs.



Fig. 2. Picture of the system's upper part, containing LEDs, photodiodes, analog and digital electronics, and an USB interface. The reference photodiodes are on the left while the measurement photodiodes are placed on the right. Deviant from the normal operation, all LEDs are activated simultaneously.

Measurement Setup for CO

In order to detect CO with the developed sensor system, it is equipped with a gasochromic dye based on a binuclear rhodium complex, which was synthesized as described in [1]. The complex reacts with CO, showing a color change from purple to yellow. It is adsorbed on nanostructured silica particles, which were glued to PET foil and applied to the sensor system using double-sided tape. As reference dye, uncoated silica particles were used (shown also in Fig. 1). The measurements with the developed setup

were performed at the Fraunhofer IPM gas laboratory. The sensor system was placed in a gastight box with a volume of 500 cm³. A flow of synthetic air through the box with 50% r.h. at 2 l/min was established. By adding CO to the gas mixture, concentrations of 1, 10 and 100 ppm CO were realized.

Gas Measurement Results with the Rhodium Complex Based Dye

The experimental results of the sensor system (three spectral channels with the highest color change) are shown in Fig. 1. A signal drift, originating from the step of ambient CO and humidity to synthetic air, can be observed. The three spectral channels at 430, 490 and 630 nm resolve all CO steps. The blue channel (430 nm) shows a reaction of 0.4 a.u. to 1 ppm CO during the first 30 s. With the single channel data, this reaction can be estimated to correspond to an absolute reflection change of $3 \cdot 10^{-4}$. The blue channel shows a 6σ noise of 0.03 a.u. Therefore, less than 100 ppb of CO might be resolvable with the system.

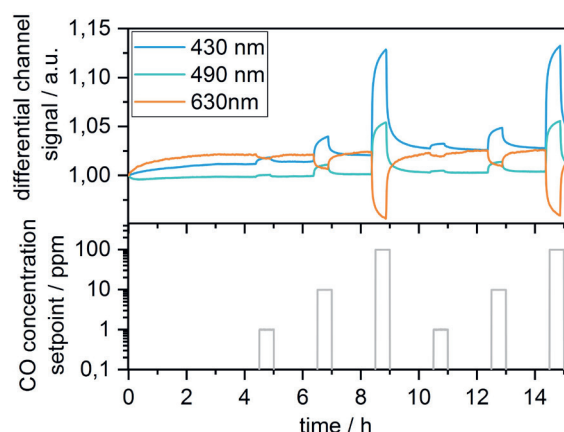


Fig. 3. Normalized signal of the differential detector for the spectral channels with the highest color change together with the CO concentration set point plotted over the measurement time.

Conclusion

Within the scope of this work, we developed a multispectral readout circuit, which enables the detection of diminutive color changes of gasochromic dyes. Our measurement results, with a rhodium complex based dye, show the possibility to detect 1 ppm CO with an SNR >10.

References

- [1] A. Duric, H. Ebner, M. Forster, I. Vinage: "Development of a multi-sensor detector for fire detection and life safety applications", 14th International Conference on Automatic Fire Detection AUBE09, Duisburg Germany 2009.
- [2] F. Cotton, A. Chakravarty, D. Tocher, J. Tocher, Structural and Electrochemical Characterization of the Novel Ortho-Metalated Dirhodium(II) Compounds $Rh_2(O_2CCH_3)_2[(C_6H_5)_2P(C_6H_4)_2]^*2L$, *Organometallics* 4 (1985) 8–13

NO detection by pulsed polarization with Pt interdigital electrodes on yttria stabilized zirconia

Nils Donker¹, Moritz Müller¹, Anastasiya Ruchets², Daniela Schönauer-Kamin¹, Jens Zosel², Ulrich Guth³, Ralf Moos¹

¹ Department of Functional Materials, University of Bayreuth, 95440 Bayreuth, Germany

² Kurt-Schwabe-Institut für Mess- und Sensortechnik e.V. Meinsberg, 04736 Waldheim, Germany

³ Dresden University of Technology, Department of Chemistry and Food Chemistry, Dresden, Germany
funktionsmaterialien@uni-bayreuth.de

Summary:

Pulsed polarization measurements were performed on Pt | YSZ sensors. These consist of four interdigital electrodes (IDEs), two on the upper and two on the lower side of the YSZ-substrate. IDEs with an electrode gap and width of 150 and 300 μm were tested. The sensors were operated one-sided and double-sided. It was found that the sensors operated on one side showed a significantly better symmetry in the signal path. This symmetry, in turn, makes it possible to halve the measuring time. In general, the sensitivities were very similar in all operating modes and show no dependency on the investigated gap.

Keywords: pulsed polarization, Pt | YSZ, NO detection, interdigital electrodes, exhaust gas sensor

Motivation

Pulsed polarization is a new method to measure nitrogen oxides without a reference. In contrast to common measuring principles such as potentiometry or amperometry, this method uses a signal that depends not only on the concentration of the analyte gas but also on time. This method is therefore comparable to cyclic voltammetry [1] or the thermo-cyclic operation of sensors [2], meaning it is a dynamic method.

The pulsed polarization technique has mainly been tested for operation with planar Pt|YSZ|Pt sensors and lambda probes so far [3–5]. A less considered field is the use on sensors with interdigital electrodes [6]. On the one hand, the effect of the spatial proximity of both electrodes is interesting, since the polarization creates a strongly oxidizing as well as a strongly reducing local surrounding at the electrodes. On the other hand, interdigital electrodes have the advantage that both electrodes can be produced in one step, resulting in more symmetrical with the same morphology.

Experimental

A pulsed polarization cycle is schematically shown in Fig. 1. The sensor is periodically and alternately polarized with a constant voltage U_{pol} for a fixed duration t_{pol} . Since this voltage does not correspond to the thermodynamic behavior, the sensor subsequently discharges to its state of equilibrium. This self-discharge of the sensor is significantly accelerated in the presence of

NO. This is utilized in pulsed polarization by measuring the self-discharge $U_{\text{discharge}}$ of the sensor between alternating polarization pulses. If this self-discharge is accelerated, lower voltages are reached earlier. By evaluating these voltages at fixed times, a sensor signal can be generated (U_{signal}).

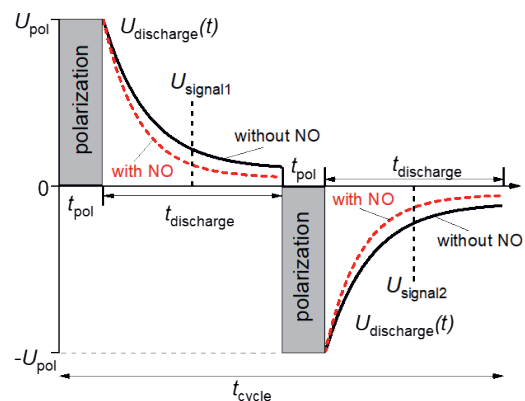


Fig. 1 Overview of a pulsed polarization cycle

For the pulsed polarization measurements, the sample is polarized for $t_{\text{pol}} = 0.5$ s with a voltage of $U_{\text{pol}} = 1$ V. The sensor discharges for $t_{\text{discharge}} = 10$ s between the alternating polarizations.

Sensor elements have been fabricated using 300 μm thick yttria stabilized zirconia substrates and screen printed platinum interdigital electrodes on both sides as depicted in Fig. 2. The distance between the finger electrodes as well as the line width was 150 and 300 μm .

The sensor elements were placed in a tube furnace and heated up to 400 °C in base gas consisting of 10 % O₂ and 2 % H₂O in N₂ at a gas flow of 200 ml/min. NO concentrations in the range from 5 ppm up to 50 ppm were admixed stepwise with base gas.

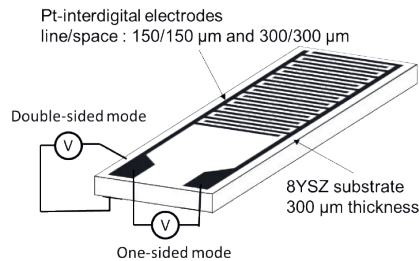


Fig. 2 Sensor layout with IDEs on both sides

Results and discussion

Fig. 3 shows the accelerated discharge 0.5 seconds after positive (solid) and negative (dashed) polarization. The voltage values in the base gas at this time serve as a reference. In the one-sided mode, the sensors show a very symmetrical signal for both electrode distances. Thus the voltage differences for the positive and the negative polarization are almost identical. Also among each other, both measurements show only very small differences (a)(b). In contrast, the sensors operated on both sides show differences in the discharge after positive and negative polarization (c)(d). However, the sensitivity of the double-sided operated sensor after negative polarization is higher than that of the one-sided operated sensors.

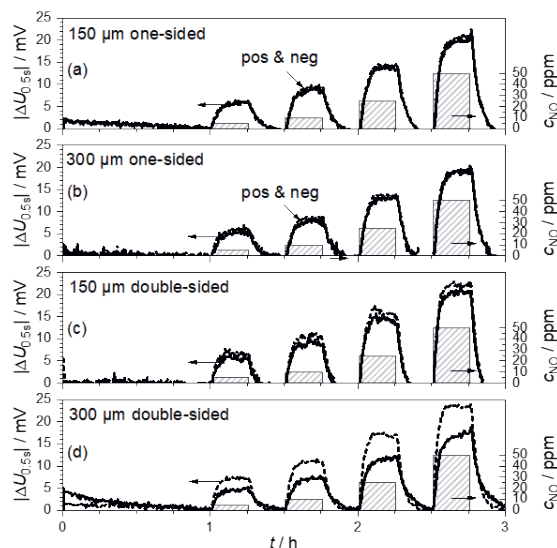


Fig. 3 Voltage differences $|\Delta U_{0.5s}|$ between a discharge in the base gas and in 5, 10, 25 and 50 ppm NO, measured 0.5 s after positive (solid) and negative (dashed) polarization. $U_{pol}=1$ V, $t_{pol}=0.5$ s, $t_{discharge}=10$ s

Impedance spectroscopy measurements before and after pulsed polarization operation (not

shown here) show electrolyte resistances of 600 to 1000 Ω for the double-sided 150 μm sensor and the single-sided 300 μm sensor, respectively. The almost doubling of the electrolyte resistance and the small influence on the sensitivity show that the electrolyte resistance seems to have only a small influence on the sensor effect. The electrodes seem to have the greater effect. This can be concluded in particular from the very symmetrical signals of the IDE electrodes with positive and negative polarization. No difference can be seen between the 150 μm and the 300 μm interdigital electrodes. Possibly, the electrode distances are still too large to influence each other.

However, the symmetrical signals allow to use both polarization directions ($U_{signal1}$ and $U_{signal2}$ in Fig. 1) for the concentration evaluations by using the absolute values. This allows for halving the measuring time.

Outlook

It could be shown that the interdigital electrodes do not influence each other at the minimal distance of 150 μm. The next step would therefore be a further reduction of the electrode distance. On the one hand, this would allow a miniaturization of the sensor, on the other hand it would possibly provide a better insight into the sensing mechanism.

References

- [1] A. Ruchets, et al., Selectivity improvement towards hydrogen and oxygen of solid electrolyte sensors by dynamic electrochemical methods, *Sens. Actuators B*, 53–58 (2019); doi: 10.1016/j.snb.2019.03.063.
- [2] X. Zhang, et al., Mixed-potential gas sensor with PtAu-8YSZ sensing electrode: Electric potential difference measurements at isothermal and thermo-cyclic operation, *Sens. Actuators B*, 107–112 (2015); doi: 10.1016/j.snb.2014.10.106.
- [3] N. Donker, et al., Influence of polarization time and polarization current of Pt|YSZ-based NO sensors utilizing the pulsed polarization when applying constant charge, *Sens. Actuators B*, 28–33 (2019); doi: 10.1016/j.snb.2019.03.060.
- [4] S. Fischer, et al., Detection of NO by pulsed polarization of Pt|YSZ, *Solid State Ionics*, 288–291 (2014); doi: 10.1016/j.ssi.2014.01.022.
- [5] S. Fischer, et al., Method for detection of NO_x in exhaust gases by pulsed discharge measurements using standard zirconia-based lambda sensors, *Sens. Actuators B*, 780–785 (2010); doi: 10.1016/j.snb.2010.03.092.
- [6] S. Fischer, et al., Detection of NO by pulsed polarization technique using Pt interdigital electrodes on yttria-stabilized zirconia, *Procedia Eng.*, 620–623 (2014); doi: 10.1016/j.pro-eng.2014.11.565.

Selective and Reliable Amperometric H_2O_2 Sensor based on Au-ZnO Heterostructure Electrode

Mohammad Karbalaei Akbari¹, [Serge Zhuiykov¹](mailto:serge.zhuiykov@ugent.be),
¹ Gent University Global Campus, 119 Songdomunhwa-ro, Yeonsu-gu,
 Incheon 21985, South Korea
serge.zhuiykov@ugent.be

Summary:

Au-ZnO heterostructures were fabricated on the 4-inch SiO_2/Si substrates by the atomic layer deposition (ALD) technique for their subsequent use as sensing electrodes in amperometric H_2O_2 sensor. The results showed that the sensors based on Au-ZnO heterostructures possess high sensitivity of $0.53 \mu\text{A}\mu\text{M}^{-1}\text{cm}^{-2}$, excellent long-term stability, wide linear H_2O_2 detection range of $1.0 \mu\text{M}$ to 120mM , low limit of detection (LOD) of $0.78 \mu\text{M}$ and excellent selectivity at the normal operation conditions.

Keywords: Heterostructures, Au-ZnO, H_2O_2 , amperometric chemical sensor, atomic layer deposition

Introduction

Development of 2D heterostructures for the usage in electrochemical sensors has been an established trend during last decade of the 21st century. Several technologies have been dominated in this trend including RF sputtering, chemical vapor deposition, hydrothermal method, solvothermal method, thermal evaporation, sol-gel, mechanical exfoliation etc. However, ALD, as an emerging technology, has not yet been fully exploited its features towards the development of reliable electrodes for the measuring devices. There are several reasons for that including relatively high costs, availability of precursors, specific ALD temperature window for deposition, lack of reliable recipes etc. Nevertheless, the advantages of ALD are far superior to the existing capabilities of other techniques. ALD is the only one technology, which enables fabrication of conformal, defects-free semiconductor 2D films and their heterostructures on the wafer scale with precise control of the thickness of sensing electrode during fabrication at the Ångström scale.

2D Au-ZnO heterostructures for H_2O_2 sensors were ALD-fabricated on the Si/SiO_2 wafer with Au electrodes. After deposition, all wafers were diced into the sensor segments of $\sim 1.0 \times 1.0 \text{ cm}$ for further annealing and characterization (Fig. 1). Experimental data for variable angle spectroscopic ellipsometric measurements of ALD developed ZnO with the thickness of 1.3 nm is presented in Fig. 1(right). All fabricated Au-ZnO samples were annealed in air for 3 h at 250°C with the heating rate of $0.5^\circ\text{C}/\text{min}$ for improvement of their crystallinity.

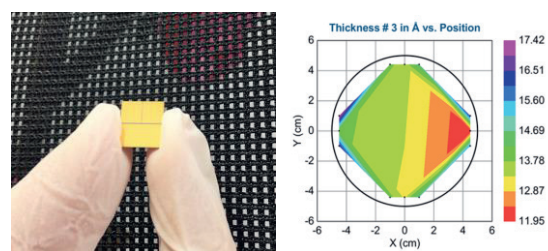


Fig. 1. Optical image of the 1.0 cm^2 sensor structure (left) and the spectroscopic ellipsometric mapping of thickness of ZnO nanofilms in Å on 4-inch Si/SiO_2 wafer (right).

Results

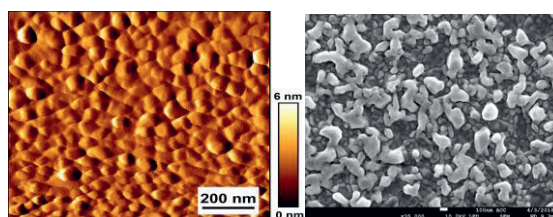


Fig. 2. AFM image of bare Au electrode (left) and SEM image of Au-ZnO heterostructure after annealing at 250°C .

Fig. 2 depicts AFM measurement of the flat Au electrode prior to annealing and SEM image of Au-ZnO heterostructure in which the initial thickness of ZnO films was 1.3 nm . SEM shows a rough ZnO surface compared to similar thickness 2D WO_3 and TiO_2 nanofilms after annealing. It is clearly visible that ZnO nanofilms owing to their extreme thin thickness (1.3 nm) were aggregated and agglomerated into island-like Au-ZnO

heterostructures with the average size of the particles of approximately ~50-100 nm.

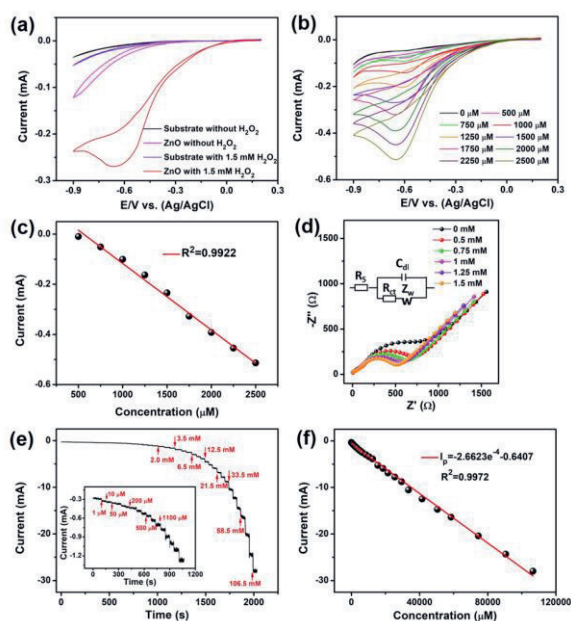


Fig. 3. (a) Measured CVs for the blank sensor substrate and Au-ZnO electrode at the absence and presence of 1.5 mM H_2O_2 ; (b) CV curves of ZnO with the different concentrations of H_2O_2 . (c) Corresponding linear plot of the current peak versus H_2O_2 concentration, (d) Nyquist plots of 1.3 nm thick ZnO with various H_2O_2 concentrations of in 5 mM $\text{K}_4\text{Fe}(\text{CN})_6$, (e) Chronoamperometric current response of Au-ZnO-based sensor to the changes of H_2O_2 concentration, (f) Corresponding linear plot of the current versus H_2O_2 concentration.

Improvement in H_2O_2 detection was clearly observed between the blank substrate and the sensor based on Au-ZnO heterostructure, as depicted in Fig. 3a. In order to understand it further, experiments continued with CV measurements at the different H_2O_2 concentrations (Fig. 3b) until the upper detection limit of 120 mM was established. The peak current was found to be linearly proportional to the increase of H_2O_2 concentration (Fig. 3c), which indicated the efficient electro-catalytic activity of Au-ZnO heterostructures without any fouling effect and indirectly reflected fast electron transfer reactions on the Au-ZnO heterostructures. Noteworthy, EIS measurements, presented in Fig. 3d, shown that the Nyquist semicircle becomes smaller and the R_{ct} value gradually decreased as the measuring H_2O_2 concentration increased, indicating improved electron transfer rate. Moreover, in order to evaluate the linear response range, sensitivity and the LOD of H_2O_2 , chronoamperometric measurements at various H_2O_2 concentrations were carried out for the Au-ZnO heterostructures. Fig. 3e shows typical current time dynamic response at changes of concentration from 2.0 μM to 106.5 mM. H_2O_2 was added approximately every 50 s.

The inset image displays the lower concentrations range from ~1.0 μM to 1100 μM . From *i-t* curves, the response time to the different H_2O_2 concentrations for all measurements was found. In fact, 2D Au-ZnO heterostructures showed fast response time and all steady-states were achieved within ~2.0 seconds. The corresponding calibration curve for H_2O_2 detection by 2D Au-ZnO heterostructures is presented in Fig. 3f. Heterostructures demonstrated remarkable linearity in chronoamperometric responses to the changes of H_2O_2 concentration from ~1.0 μM to 120 mM with the correlation coefficient higher than 0.99.

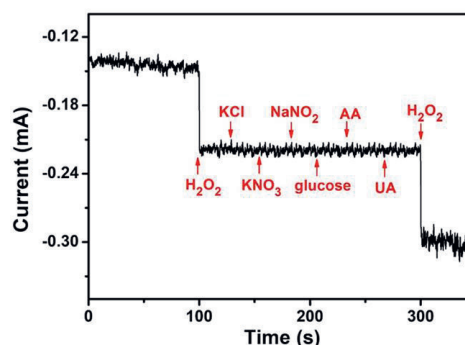


Fig. 4. Interference study of the H_2O_2 sensor based on Au-ZnO heterostructure at the presence of 10 μM H_2O_2 and 1.0 mM of different interfering chemicals at 25°C.

Responses of 2D Au-ZnO-heterostructures to the different interfering agents including glucose, KCl, NaNO_2 , AA, UA, KNO_3 are clearly displayed in Fig. 4. It should be stressed that the concentration of the additional chemicals was about 100 times higher (1000 μM) and about 50 times higher for glucose (500 μM) than the existing H_2O_2 concentration (10 μM). It is evident from this figure that the sensor based on 2D Au-ZnO heterostructures is almost insensitive to all added chemicals.

Conclusions

ALD-developed Au-ZnO heterostructures have clearly demonstrated high performance towards H_2O_2 sensing, especially at the low concentrations levels. Specifically, our amperometric sensor exhibited not only high sensitivity of 0.53 $\mu\text{A}\mu\text{M}^{-1}\text{cm}^{-2}$ within a wide H_2O_2 concentrations range from 1.0 μM to 120 mM, but also rapid response/recovery time (~2.0 s), low LOD of 0.78 μM and excellent selectivity and long-term stability compared with the sensors based on micro-structured ZnO and other semiconductor oxides. Au-ZnO interface enabled considerable *surface-to-volume* ratio in electrode, which allowed the measuring chemical agent to reach the inside of the heterostructure more easily.

Resonant Sensor for In-Situ Gas Detection in Heat Treatment Processes

*Sebastian Schroeder*¹, *Alexander Strauß*², *Peter Quadbeck*² and *Holger Fritze*¹,
¹*Clausthal University of Technology, Am Stollen 19 B in 38640 Goslar, Germany,*
²*Fraunhofer Institute for Manufacturing Technology and Advanced Materials, Winterbergstraße 28 in 01277 Dresden, Germany,*
Sebastian.schroeder@tu-clausthal.de

Summary:

A gas sensor for monitoring of the furnace atmosphere in the production of titanium and carbon based components is tested. The gas sensor is based on γ -cut $\text{Ca}_3\text{TaGaSi}_2\text{O}_{14}$ (CTGS) piezoelectric single crystal substrates and thin metal oxide sensor films. TiO_2 and $\text{Pr}_{0.2}\text{Ce}_{0.8}\text{O}_2$ sensor films are used for the detection of hydrocarbons, which are formed during the heat treatment of the components mentioned above. The concentration of hydrocarbons provides feedback on the progress of the processes. The successful operation of the gas sensor at temperatures up to 800 °C and in reducing atmospheres is shown.

Keywords: Gas sensor, high-temperature, bulk acoustic wave, thin-films, metal oxides

Background, Motivation and Objective

Manufacturing of high performance materials like titanium or carbon often requires the use of organic additives during shape forming process. Afterwards, these organic additives must be removed (debinding), which requires high temperatures and is, therefore, energy consuming. Monitoring of decomposition products during heat treatment enables an energy-saving production due to tailored temperature adjustment. For example, the start temperature of decomposition and complete debinding can be identified. Furthermore, the product quality will improve due to more careful heat treatment [1].

The debinding is performed in inert gas atmospheres or in vacuum. Therefore, a high-temperature stable gas sensor withstanding reducing atmospheres is needed. At laboratory-scale, IR spectrometers can be used for selective detection of debinding products. Nevertheless, optical measurement techniques shall not be used routinely in industrial environments due to the required optical path and high costs.

Description of the New System

The gas sensor evaluates changes in sensor film properties, e.g. mass and conductivity, for different metal oxides. It is based on γ -cut CTGS single crystals which are operated in thickness shear mode by applying an ac voltage via screen printed keyhole shaped platinum electrodes. The metal oxide thin films are deposited on top of the electrodes via pulsed laser

deposition. The presence of reducing gas atmospheres affects the conductivity and density of these metal oxides by adsorption/desorption of gas molecules or stoichiometry changes due to e.g. formation of oxygen vacancies. The density change is determined by operating 5 MHz CTGS single crystals as gravimetric sensors, having a mass sensitivity of about $35 \text{ cm}^2 \text{ Hz } \mu\text{g}^{-1}$ even at 800 °C [2]. In addition, a modified electrode layout of such resonators enables to monitor the sensor film conductivity, thereby improving gas selectivity. The related electrode and sensor film layout are shown in Fig. 1.

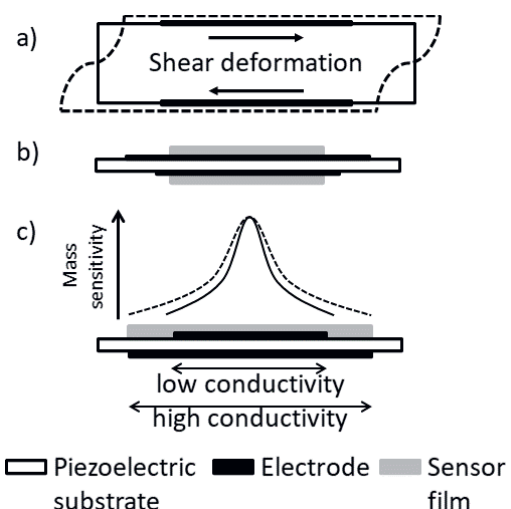


Fig. 1. Piezoelectrically excited resonator with sensor film. (a) Shear deformation, (b) microbalance mode and (c) conductivity mode.

In conductivity mode, a change in sensor film conductivity increases/lowers the excited resonator area, e.g. an increased film conductivity, increases the excited resonator area and, consequently, decreases the resonance frequency. As a consequence, the mass sensitivity and, thereby, the resonance frequency f_R change due to modification of the Gaussian like mass sensitivity distribution and of the piezoelectric stiffened shear modulus [3]. Resonance frequency shifts Δf_R of resonators operated in microbalance mode are a result of mass uptake or loss [4] due to surface adsorption/desorption processes or release/ incorporation of oxygen in the metal oxide.

Results

TiO₂ and Pr_{0.2}Ce_{0.8}O₂ sensor films operated in conductivity and microbalance mode are used to investigate the debinding of carbon and titanium based materials (see Fig. 2 and Fig. 3.). The response of the sensor films is measured

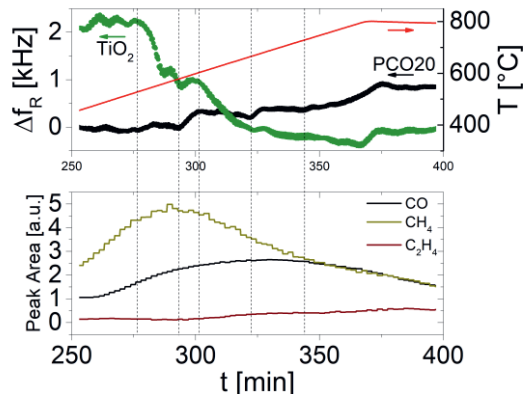


Fig. 2. Shift of resonance frequency Δf_R of resonator coated with TiO₂ and Pr_{0.2}Ce_{0.8}O₂ sensor films operated in conductivity and microbalance mode, respectively, for debinding of a carbon based material. In addition, changes in gas concentration are observed using an IR spectrometer.

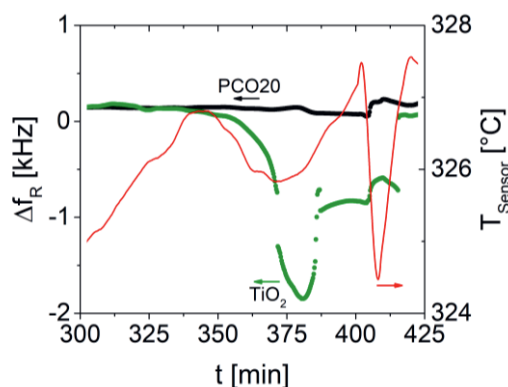


Fig. 3. Shift of resonance frequency Δf_R of resonator coated with TiO₂ and Pr_{0.2}Ce_{0.8}O₂ sensor films operated in conductivity and microbalance mode, respectively. The debinding of a titanium based material is observed in an industrial furnace.

throughout the heat treatment, but for clarity only debinding periods are shown.

In laboratory experiments, changes in gas concentration are additionally acquired using an IR spectrometer to evaluate the response of the sensor films. Fig. 2 shows the debinding of a carbon based material at a constant heating rate of 3 K min⁻¹ in nitrogen atmosphere. Decrease and increase of f_R are observed for resonators operated in conductivity and microbalance mode, respectively. These responses are expected due to the increase of conductivity for TiO₂ sensor films and mass loss (oxygen) for Pr_{0.2}Ce_{0.8}O₂ sensor film. Shifts in resonance frequency Δf_R are a result of increasing methane, ethane and carbon monoxide concentration, because they decrease the oxygen partial pressure of the furnace atmosphere. Fig. 3 shows the debinding of a titanium based material in argon atmosphere and in vacuum of ca. 50 mbar. The sensor films are located in exhaust line of the furnace, which is heated to 200 °C. Here, the response of the TiO₂ sensor film is of special interest. At ca. 335 min, when the furnace reaches 382 °C, the resonance frequency starts shifting as a result of increasing formation of reaction products which affect the conductivity of TiO₂. A maximum frequency shift Δf_R is observed at about 380 min. After about 415 min, when the furnace reaches 485 °C, Δf_R approaches the base level again. The frequency shift indicates the gas formation and marks presumably the start and completion of the debinding.

In order to improve sensitivity and selectivity of the gas sensor, resonator parameters like thickness and electrode/film diameter as well as sensor film parameters like film thickness and mass can be tuned.

References

- [1] P. Quadbeck, A. Strauß, S. Müller, B. Kieback, "Atmosphere monitoring in a continuous sintering belt furnace", *Journal of Material Processing Technology* 231 (2016), 406-411, doi: 10.1016/j.jmatprotec.2016.01.015
- [2] Y. Suhak, M. Schulz, H. Wlfmeier, W. L. Johnson, A. Sotnikov, H. Schmidt, S. Ganschow, D. Klimm, H. Fritze, "Langasite-Type Resonant Sensors for Harsh Environments", *MRS Advances* 1 (2016), 1513-1518, doi: 10.1557/adv.2016.109
- [3] H. Fritze, D. Richter, H. L. Tuller, "Simultaneous detection of atmosphere induced mass and conductivity variations using high temperature resonant sensors", *Sensors and Actuators B* 111-112, 200-206 (2005); doi: 10.1016/j.snb.2005.06.036
- [4] G. Sauerbrey, "Verwendung von Schwingquarzen zur Wägung dünner Schichten und Mikrowägung", *Zeitschrift für Physik* 155, 206-222 (1959), doi: 10.1007/BF01337937

Errors in Relative Humidity Measurements Due to Slow Temperature Response

Hannu Sairanen

Vaisala Oyj, Vanha Nurmijärventie 21, 01670 Vantaa, Finland
hannu.sairanen@vaisala.com

Summary

Relative humidity calibrations are usually completed at static conditions i.e. both temperature and dew-point temperature is stabilized prior to reading values of the device under test and references. This kind of static calibration is justified by reduced uncertainty and more simple calibration stations. Following this, humidity transmitters are usually specified in stable and static conditions, which is problematic in terms of real world non-static environments. In this work effect of humidity transmitters thermal response times are studied and two different probe types are compared. Due to change of temperature a humidity transmitter which is specified to have accuracy of 1%rh might cause measurement error of about 5 %rh depending on stabilization time, level of temperature change and other environmental conditions.

Keywords: Hygrometer, humidity, humidity sensor, temperature, temperature measurement, response time, accuracy

Introduction

Specifications for humidity transmitters are usually defined in stable and static conditions. Also, calibrations of the transmitters are usually performed at static conditions. However, in real world - unlike in calibration stations - the conditions hardly ever are static. Thus, it is important to understand error sources in changing environments.

Lately within the EMPIR HIT project emphasis was put on development of dynamic relative humidity calibration set-ups [1]. As part of the project VTT-MIKES developed such a set-up and successfully characterized it [2]. However, the VTT-MIKES calibration apparatus does not respond – at least not at yet - to demand of calibrations at changing temperature.

In this study measurement results from Vaisala's HMP9 [3] were compared to other typical humidity probe at changing environments. The results indicate that the lower thermal mass HMP9 is significantly faster in terms of thermal response than the other probe type. At the same time the HMP9 is significantly faster in terms of humidity. Additionally, measurement errors are compared to the probes specifications.

Background

Externally humidity probes are typically tubular structures with external diameter of about 10 mm as described in Fig. 1. Depending on me-

chanical solutions every kind of probe have unique thermal mass and thus thermal response time. However, the common thing is that every probe requires some time to measure targeted temperature. Moreover, prior to stabilized temperature is achieved, inside the filter of the probe temperature is typically different than at the target measurement environment. Following this, as relative humidity is temperature dependent, also measured relative humidity is influenced. This kind of error is nearly impossible to correct by calibrations as the thermal response time depends not only on the probe type but also on measurement environment. Factors such as flow speed around the probe, speed of temperature change, gas concentrations, and pressure have significant effect on thermal response time.



Fig. 1. An example of a typical humidity probe. Sensor of the probe (illustrated on the probe on red) is located inside the probe filter.

Measurements

Measurement error caused by slow temperature response was studied by measurements with two different humidity probe types from different manufacturers. Another probe was a typical about 10 mm diameter humidity probe and the other one was Vaisala's about 5 mm

diameter HMP9. Another external difference along with the size is the material of the probe. Vaisala is using stainless steel while the other manufacturer is using plastic. Both of the probe types have accuracy specification of about 1 %rh.

The measurements were completed with 3 Vaisala's HMP9 and also 3 typical humidity probes. All six probes were placed inside a heat chamber in such way that they all were equally in front of the fan of the chamber. In addition, none of the probes touched walls of the chamber. The tests were performed by carrying out a temperature ramp presented in Fig. 2. The ramp was repeated three times. A more detailed example of the performed measurements along with measured humidity values is shown in Fig. 3.

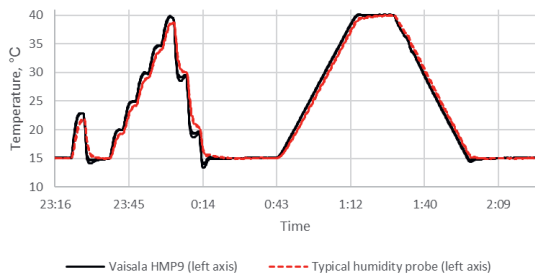


Fig. 2. During the test temperature of the chamber was varied in the range from 15 °C to 40 °C.

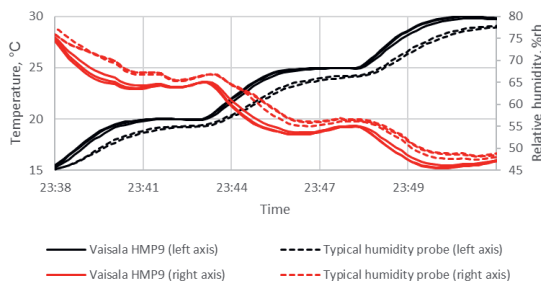


Fig. 3. As part of the test, temperature was increased 5 °C at a time in 5 min interval. Here is an example data indicating differences in response times and thus measurement errors.

Results

According to Fig. 2 and Fig. 3 typical humidity probes have slower response time in terms of temperature that can be seen also in humidity readings in Fig. 3. In the beginning of the measurement (see Fig. 3.) all temperature readings were consistent, but after the temperature increases the bigger probes indicated lower temperature readings due to slower thermal response (see Fig. 4). However, according to a separate calibration all of the probes indicated within 0.1 °C the same temperature also at elevated temperatures.

In terms of humidity the thermal response time causes also error as can see from Fig. 3. Differences between the two probe types from 15 °C to 20 °C and from about 75 %rh to 65 %rh are shown in Fig. 4. as a function of delayed time from temperature change.

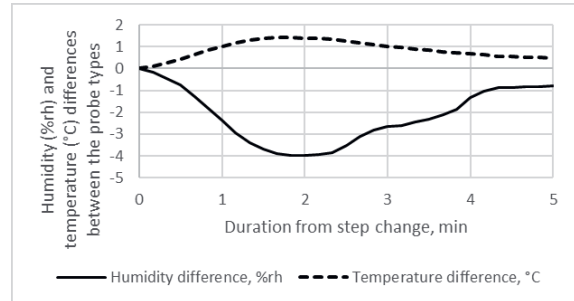


Fig. 4. Humidity and temperature differences between typical humidity probe and Vaisala's HMP9 when temperature of a heat chamber is increased from 15 °C to 20 °C.

The differences between the probe types were even greater at cooling steps. In fact, the typical humidity probes were unable to record overshoot of the heat chamber temperature (See Fig. 2 at 0:14). Maximum difference that were measured during the tests was 5.1 %rh, which is far more than what is specified in datasheets of the probes.

Conclusions

Thermal mass of a humidity probe is a key parameter when choosing the best probe type. According to this work, too large probe can cause significant error in terms of measurement accuracy. As shown in this work, in changing non-static environments measurement error can be five times greater than measurement accuracy specified in product datasheets.

References

- [1] M. Heinonen, F. Arpino, R. Bosma, L. Cavallarin, G. Cortellessa, M. Dell'Isola, V. Ebert, V. Fernicola, E. Georgan, A. Giannattasio, R. Högström, D. Hudoklin, A. Kentved, J. Nielsen, P. F. Ostergaard, A. Peruzzi, T. Pietari, R.-J. Pouw, S. Tabandeh, W. van Schaik und S. Wagner, „Towards improved humidity measurements at high temperatures and transient conditions,“ in 17th International Congress of Metrology, CIM 2015, Paris, 2015.
- [2] R. Högström, J. Salminen und M. Heinonen, „Calibration of hygrometers at non-static conditions,“ Measurement Science and Technology, Bd. 31, Nr. 3, 2019.
- [3] Vaisala Oyj, 2019, online: <https://www.vaisala.com/en/products/instruments-sensors-and-other-measurement-devices/instruments-industrial-measurements/hmp9>.

PVDF-SPEEK Blend based resistive humidity sensors

Zubair Ahmad¹, Shoaib Alam Mallick², Farid Touati³

¹ Centre for Advanced Materials (CAM), Qatar University, P.O. Box 2713 Doha, Qatar

² Department of Electrical Engineerin Qatar University, P.O. Box 2713 Doha, Qatar
zubairtarar@qu.edu.qa

Summary:

We have investigated the effect of sulfonated poly Ether Ether Ketone (SPEEK) on the thermal stability, sensitivity, and hydrophilicity of polyvinylidene fluoride (PVDF) films based resistive humidity sensors. The spin coating technique has been used to deposit PVDF-SPEEK thin film on the ITO interdigitated electrode. The surface morphology of the PVDF-SPEEK blend film was studied by Field Emission electron microscopy (FESEM) analysis. The impedance response of the PVDF-SPEEK blend film showed that the addition of SPEEK enhances the sensitivity of the sensing film at a lower humidity levels.

Keywords: Sensitivity, impedance, sensors, poly (Ether Ether Ketone), hydrophilicity

Background, Motivation an Objective

Monitoring and controlling the humidity level is an essential element in various industrial applications. For instance, in electronic and optical device fabrication monitoring of humidity levels are essential [1, 2]. To develop the polymeric humidity sensor which has shorter response and recovery time and exhibits small hysteresis. For this purpose, we investigated polyvinylidene fluoride (PVDF) piezoelectric polymer. PVDF is a polymer that has high thermal stability, excellent electrical properties and highly resistive to the chemicals. Owing to these unique properties of PVDF, many researchers are investigating the PVDF based sensing film for humidity sensing applications [3, 4]. Blending of polymers is a well-known method to enhance the hydrophilicity of the sensing film is to introduce the hydrophilic polar group (SO₃H) within the polymer chain [5]. The sulfonation of PEEK occurs by introducing the hydrophilic sulfonic groups (SO₃H) within the PEEK. This sulfonation of polymer significantly improves the absorptions of water molecules and proton conductivity which will increase the sensitivity of the humidity sensors [6].

we have investigated the effect of sulfonated poly (Ether Ether Ketone (SPEEK) on the humidity sensing properties of polyvinylidene fluoride (PVDF). The surface morphology of the sensing film was studied by FESEM analysis.

The hydrophilicity of the sensing film was studied by the contact angle method.

Description of the New Method or System

The spin coating technique has been used to deposit the PVDF-SPEEK composite blend solution on the ITO/glass electrode (from Osilla). An optimization process for the rotation speed and the rotation time to form an even equilateral spread of the solution were done. The rotation speed and rotation time were optimized to 6000 rpm and 50 seconds. To analyze the effect of different concentration of SPEEK on PVDF-SPEEK blend morphology, hydrophilicity, and humidity sensing characteristics, we prepared 1 wt %, 3wt% and 5 wt% 7.5 wt%, 10 wt% and 15 wt% of SPEEK separately and kept the PVDF concentration constant at 2.5 wt%. The hydrophilicity of the new nanocomposite film was measured by the optical contact angle machine through the SCA software. The morphological analysis to determine the homogenous and surface defect of the blend film is done by the Field Emission Scanning Electron Microscope (FESEM). Whereas the to determine the thermal stability of the composite was done by the TGA analysis. The electrical characterization of humidity sensors was carried out by our previously reported method [7]. Figure1 shows the schematic diagram of preparation of the PVDF-SPEEK blend solution, its deposition via spin coating and the characterization of the sensing film.

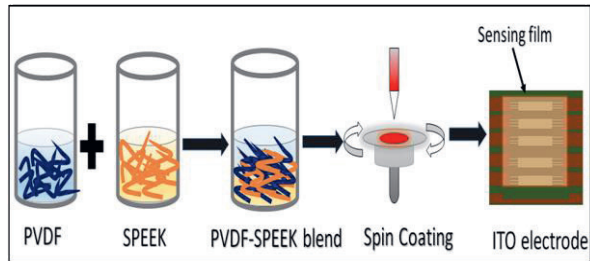


Fig.1. Schematic diagram of the spin coated PVDF-SPEEK resistive humidity sensors.

The electrical response of the fabricated PVDF-SPEEK humidity sensors was conducted in a sealed chamber with a humidifier connected with the chamber. The reference humidity meter was placed inside the sealed chamber. The capacitance was measured by the MS5308 LCR meter with it being clipped to the electrode with the sensing film. Figure 2 shows the set up used in in the electrical response with the inclusive components such as the humidity sensor, LCR meter, humidifier, and the nitrogen Derrite.

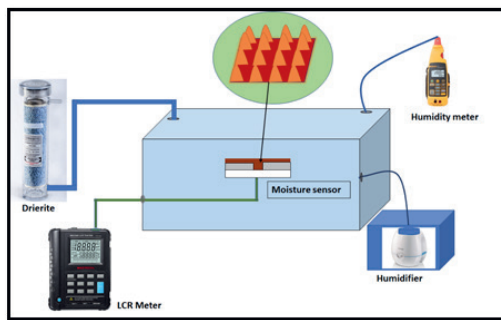


Fig.2. The electrical characterization setup for capacitive based humidity sensor.

Results

Morphological Analysis:

Morphology of the PVDF-SPEEK blend film determines the distribution of SPEEK within the blend film matrix. Morphological study of the PVDF-SPEEK blend film performed by FESEM analysis. Figures 2a and 2b show the FESEM analysis of PVDF-SPEEK blend film with a concentration of SPEEK is 5wt% and 10 wt%. The FESEM analysis reveals that PVDF-SPEEK (5 wt%) blend film has a uniform distribution of SPEEK with film surface is defect free. However As the concentration of SPEEK increases (10 wt%) within the blend membrane the spherical structures appear on the surface of the film. Due to the higher concentration of SPEEK higher amount of sulfonic group (SO_3H) presents on the blend membrane which may form the spherical formation [8].

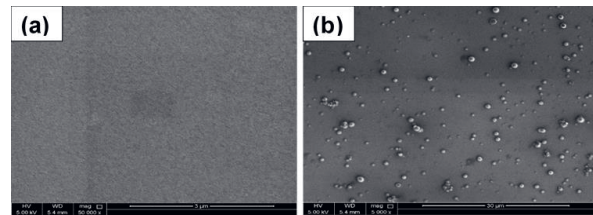


Figure 1. FESEM micro graph of (a) PVDF- SPEEK blend (5 wt%) (b) PVDF-SPEEK (10 wt%) blend film

Thermal Stability Analysis:

The thermal stability of the PVDF-SPEEK blended film was investigated by Thermal gravimetric analysis (TGA).Figure 3 plots the thermal behavior of PVDF-SPEEK blend with different concentration of SPEEK (1 wt%, 3wt%, 5 wt%, 7.5 wt%, 10 wt% and 15 wt%). TGA analysis reveals that the PVDF-SPEEK blend with lower concentrations of SPEEK is more stable.

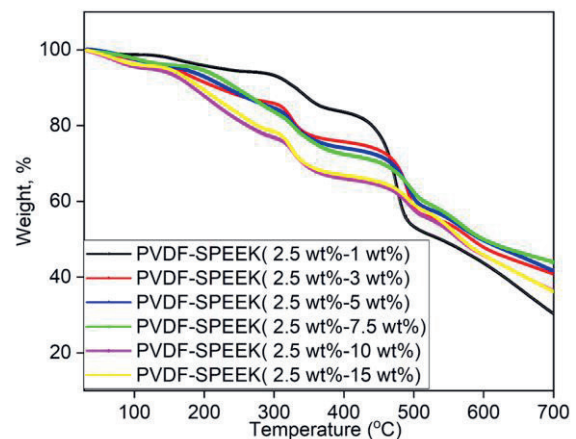


Fig3.Shows the TGA analysis of PVDF-SPEEK composites with the concentration of SPEEK varied from 1wt% to 15wt%.

Hydrophilicity of PVDF-SPEEK blend

The hydrophilicity of the sensing film measured by the contact angle method. As the concentration of SPEEK increases in the PVDF-SPEEK blended film the contact angle decreases which is mainly due to the sulfonic acid group present in SPEEK. This increase in hydrophilicity of blended film enhances the sensitivity of the film. Table. 1: Contact angle measurements of PVDF, PVDF-SPEEK (2.5 wt%-1 wt%) composite, and PVDF-SPEEK (2.5 wt%-5 wt%) composite films.

Sample Type	PVDF Film	PVDF- SPEEK (2.5 wt%-1wt%) composite film	PVDF-SPEEK (2.5 wt% - 5 wt%)
Contact angle image			
Contact angle	92.25°	85°	75.8°

Electrical Response:

The PVDF-SPEEK (2.5 wt%-5 wt%) blended film based resistive sensors show high sensitivity, stable response and low hysteresis as compared to pure PVDF film. The developed PVDF-SPEEK (2.5 wt%- 5 wt%) resistive sensors are excellent for sensing low humidity levels. The inset in figure 4 shows the stable and repeatable response and recovery cycle of the PVDF-SPEEK (2.5 wt%- 5 wt%) resistive sensor. The calculated response and recovery time are found to be 25s and 40s respectively.

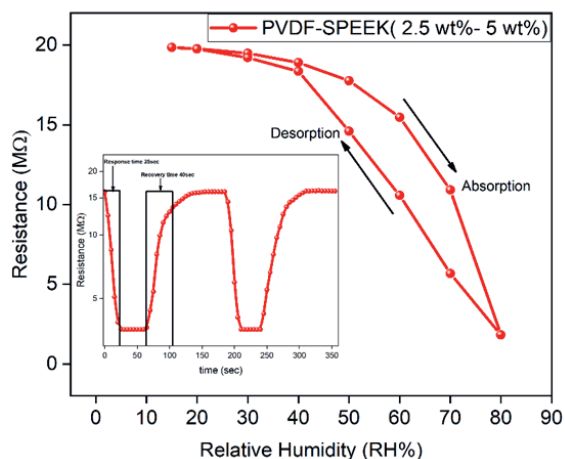


Fig4. Represent the absorption and desorption response of the PVDF-SPEEK (2.5 wt%- 5 wt%) based resistive humidity sensor. Inset shows the response and recovery cycle (40–85% RH) of PVDF-SPEEK (2.5 wt%-5 wt%) based sensor.

Conclusion:

The effect of different concentration of SPEEK on the morphology, thermal stability and electrical response of the PVDF-SPEEK blend was studied. The morphological analysis was achieved by FESEM analysis which established that higher concentration of SPEEK not uniformly blend within the PVDF polymer chain. It can be also observed that as the concentration of SPEEK increases the hydrophilicity of the PVDF-SPEEK blend increase as well. This increase in hydrophilicity of blended film enhances the sensitivity of the film. The PVDF-SPEEK (2.5 wt%-5 wt%) blended film based resistive sensors show high sensitivity, stable response and low hysteresis as compared to pure PVDF film. The response and recovery times of the PVDF-SPEEK (2.5 wt%- 5 wt%) resistive sensor are found to be 25s and 40s respectively. The developed PVDF-SPEEK (2.5 wt%- 5 wt%) resistive sensors are excellent for sensing low humidity levels.

Acknowledgment

This study was made possible by GSRA3-1-1116-14016 from the Qatar National Research Fund (a member of Qatar Foundation). The findings made herein are solely the responsibility of the authors. The authors are also very grateful to the Centre for Advanced Materials (CAM), Qatar University for the inclusive support.

References

- [1] X. Zhuang, Y. Mai, D. Wu, F. Zhang, and X. Feng, "Two-dimensional soft nanomaterials: a fascinating world of materials," *Advanced Materials*, vol. 27, no. 3, pp. 403-427, 2015; doi.org/10.1002/adma.201401857
- [2] P. Wang, Y. Wang, and L. Tong, "Functionalized polymer nanofibers: a versatile platform for manipulating light at the nanoscale," *Light: Science & Applications*, vol. 2, no. 10, p. e102, 2013; doi:10.1038/lsa.2013.58
- [3] D. Hernández-Rivera, G. Rodríguez-Roldán, R. Mora-Martínez, and E. J. S. Suaste-Gómez, "A capacitive humidity sensor based on an electrospun PVDF/graphene membrane," vol. 17, no. 5, p. 1009, 2017; doi.org/10.3390/s17051009
- [4] M. Batumalay, S. W. Harun, N. Irawati, H. Ahmad, and H. J. I. S. J. Arof, "A study of relative humidity fiber-optic sensors," vol. 15, no. 3, pp. 1945-1950, 2014; doi:10.1109/JSEN.2014.2368979
- [5] T. Kavc, W. Kern, M. F. Ebel, R. Svagera, and P. J. C. o. m. Pölt, "Surface modification of polyethylene by photochemical introduction of sulfonic acid groups," vol. 12, no. 4, pp. 1053-1059, 2000; doi.org/10.1021/cm991158p
- [6] B. Smitha, S. Sridhar, and A. J. J. o. M. S. Khan, "Synthesis and characterization of proton conducting polymer membranes for fuel cells," vol. 225, no. 1-2, pp. 63-76, 2003; doi.org/10.1016/S03767388(03)00343-0
- [7] S. Mallick, Z. Ahmad, F. Touati, R. J. S. Shakoar, and A. B. Chemical, "Improvement of humidity sensing properties of PVDF-TiO₂ nanocomposite films using acetone etching," vol. 288, pp. 408-413, 2019; doi.org/10.1016/j.snb.2019.03.034
- [8] G. Dönmez and H. J. I. J. Deligöz, "A comparative study on sulfonated PEEK and PVDF blend membranes for direct methanol fuel cells," vol. 2, no. 2, p. 11, 2015; doi.org/10.15379/2410-1869.2015.02.02.02

Cure Monitoring using Single-Sided NMR

*Norbert Halmen¹, Linda Mittelberg¹, Eduard Kraus¹,
Benjamin Baudrit¹, Thomas Hochrein¹, Martin Bastian¹*

*¹ SKZ – German Plastics Center, Friedrich-Bergius-Ring 22, 97076 Würzburg, Germany,
n.halmen@skz.de*

Summary:

In industrial production, adhesives are often the preferred joining agent of choice. However, there is currently no standard method for non-destructive monitoring of the adhesive bond quality. In order to solve this issue, the use of single-sided NMR is suitable. This work demonstrates exemplarily for an adhesive that the NMR signal correlates very well with the curing. Thus, it is possible to create process models, which allow the monitoring of adhesive curing.

Keywords: Adhesives, curing, monitoring, NMR, prediction

Motivation

Driven by e-mobility and lightweight construction, adhesives have become increasingly important in recent years. In industrial production, they are often the preferred material of choice for joints due to their wide range of material types and properties. With the increasing use of adhesives, their quality assurance during the manufacturing process is also gaining in importance [1]. However, only destructive methods exist currently for testing adhesive joints. For this reason, there are various research approaches to enable non-destructive process control. Air-coupled ultrasound [2], terahertz [3] or single-sided nuclear magnetic resonance (NMR) [4] are suitable for this purpose. A recent research project focuses on the near-process monitoring of adhesive joints. First results are presented in the following.

Single-sided NMR for process monitoring

NMR measures nuclear spin relaxation times. These correlate very well with the molecular mobility of adhesive molecules. The decrease in relaxation times over time allows the non-destructive evaluation of the curing state of an adhesive. Beyond that, single-sided NMR offers a further advantage due to its special design. It enables cure monitoring of adhesive at different depth levels – even through the non-metallic joined components.

The single-sided NMR signal, which is evaluated e.g. by echo sums, can be used for the formation of process models due to its good correlation with various reference methods [4] and high reproducibility. This allows the definition of a process window for characteristic values such as viscosity or ion conductivity. In addition to

process control, post-production testing is possible. Since single-sided NMR devices use rare earth permanent magnets, a constant magnet temperature is necessary due to their temperature sensitivity. In the case of hot samples, this is achieved by thermal decoupling or, in the case of adhesives, by small – and at the same time practice-related – layer thicknesses. When using thin adhesive films, only minimal temperature changes < 1 K are measured, which do not noticeably influence the magnet temperature.

NMR vs. rheological testing

As an example for the good correlation of single-sided NMR and rheological testing results of the two component epoxy adhesive DELO-DUOPOX AD840 are shown. The rheological reference tests in the plate/plate rheometer (Haake Mars, Thermo Fisher Scientific Inc.) were performed as double determination with a measuring frequency of 1 Hz, a gap distance of 1 mm and a temperature of 25 °C. For the measurements with the single-sided NMR (NMR-Mouse PM5, Magritek GmbH) a classical CPMG pulse sequence with 128 echoes and a measurement volume of 13 mm x 13 mm x 100 µm (L x W x H) was used as in previous work [4]. The samples consisted of two 1 mm thick cover glasses with an adhesive layer of (90 ± 10) µm thickness in between. The room temperature during the double determination of the adhesives was between 23 and 26 °C.

The signal curves of the echo sums as well as the viscosity during the adhesive curing together with the times of initial and functional strength according to the manufacturer's information are shown in Fig. 1.

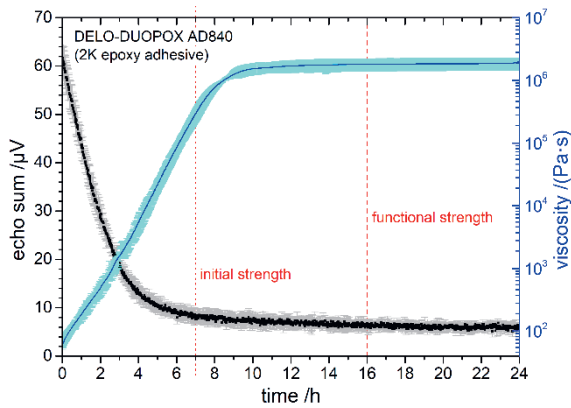


Fig. 1. Comparison of measurement curves of single-sided NMR and plate/plate rheometer.

The signal curves of the measurements in the rheometer show a relatively constant uncertainty range. For NMR measurements, the average relative error is about 11 %. The time uncertainty results mainly from the different starting times of curing after mixing and measurement. The variance of the echo sums results both from the different adhesive layer thicknesses and from potential inhomogeneities during mixing or network formation – the latter also applies to sample preparation in the plate/plate rheometer.

Process model for 2K epoxy adhesive

In the NMR experiments, the echo sums – as amplitude-weighted mean value of the relaxation times T_2 [5] – showed a bi-exponential course and can thus be fitted by equation (1):

$$A_{es} = A_{short} \cdot e^{-\frac{t}{T_{2m,short}}} + A_{long} \cdot e^{-\frac{t}{T_{2m,long}}} \quad (1)$$

Together with the rheometer measurement values, a process model can be generated which assigns a corresponding viscosity value to each echo sum at a certain point in time (see Fig. 2). This allows to monitor whether the viscosity values are still within the desired process window during the curing process.

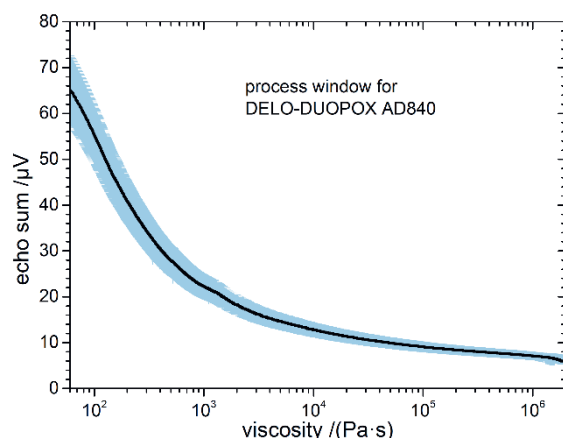


Fig. 2. Process model for DELO-DUOPOX AD840 linking echo sums with viscosity values.

The presented process model works well for characteristic times of curing. It can be assumed that a reduction of the uncertainty range of NMR measurements is possible by a more precise scheduling of the measurement start and by a more precise adjustment of comparable adhesive layer thicknesses.

The evaluation method demonstrated here can be applied in a similar way to other reference methods such as differential scanning calorimetry (DSC) and dielectric analysis (DEA). Furthermore, a transfer to characterize resins curing in composites is also possible.

Summary and Outlook

Single-sided NMR is well suited for non-destructive monitoring of adhesive curing in adhesive bonds. Thus, it is possible to create process models. In the further course of the project besides glass, also plastic substrates will be bonded. Furthermore, the research will be extended to one-component light-curable adhesives. In addition, the investigation of a possible correlation of the NMR values with the later bond strength – at the same pretreatment and adhesive layer thickness – is planned.

Acknowledgement

The project 20564 N of the research association "Foerderungsgemeinschaft fuer das SKZ" is funded by the German Federal Ministry of Economics and Energy (BMWi) through the German Federation of Industrial Research Associations (AiF) as part of the program to promote joint industrial research (IGF) based on a resolution of the German Parliament. We would like to thank for the financial support.

References

- [1] Gemeinschaftsausschuss Klebtechnik (GAK), Roadmap Klebtechnik, Frankfurt a. M. (2016)
- [2] G. Schober; L. Orf, B. Baudrit, M. Bastian, T. Hochrein, Inline monitoring of the adhesive curing with contactless ultrasound, *Joining Plastics* 13, 90-95 (2019)
- [3] S. Sommer, T. Probst, E. Kraus, B. Baudrit, G.E. Town, M. Koch, Cure monitoring of two-component epoxy adhesives by terahertz time-domain spectroscopy. *Polym. Sci. Ser. B* 58, 769-776 (2016); doi: 10.1134/S1560090416060154
- [4] N. Halmen, C. Kugler, E. Kraus, B. Baudrit, T. Hochrein und M. Bastian, Single-sided NMR for the measurement of the degree of cross-linking and curing, *J. Sensors Sens. Syst.* 7, 21-30 (2018); doi: 10.5194/jsss-7-21-2018
- [5] B. Blümich, J. Perlo, und F. Casanova, Mobile single-sided NMR, *Prog. Nucl. Magn. Reson. Spectrosc.* 52,197-269 (2008); doi: 10.1016/j.pnmrs.2007.10.002

Development of disposable antibiotic drug sensor based on screen-printed electrode modified with magnetic nanocomposites

Yingyot Poo-arporn¹, Saithip Pakapongpan², Rungtiva P. Poo-arporn³,

¹ Synchrotron Light Research Institute, 111 University Avenue, Nakhon Ratchasima, 30000, Thailand,

² Thailand Organic and Printed Electronics Innovation Center, National Electronics and Computer Technology Center, NSTDA, Pathum Thani 12120, Thailand,

³ Biological Engineering Program, Faculty of Engineering, King Mongkut's University of Technology Thonburi, Bangkok 10140, Thailand
 rungtiva.pal@kmutt.ac.th

Summary:

This research work reported the development of a new disposable electrochemical chloramphenicol (CAP) sensor based on the use of a screen-printed electrode (SPE) modified with an iron oxide magnetic nanoparticles doping on graphene. The electrochemical and electrocatalytic characteristics of the modified SPE were recorded using cyclic voltammetry (CV) and differential pulse voltammetry (DPV). The proposed sensor showed fast response to CAP and good sensitivity. The sensor had a detection range over the concentration ranges of 0.5 to 700 μM , with a detection limit of 95.4 nM (S/N=3).

Keywords: antibiotic drug, electrochemical sensor, differential pulse voltammetry, screen-printed electrode, magnetic nanocomposite

Introduction

Chloramphenicol (CAP) is an effective antibiotic drug against a wide variety of gram-positive and gram-negative bacteria. However, CAP have an extremely bad effect on human health, which can even lead to diseases [1]. The Food and Drug Administration in many countries have set a strict residue limit for CAP [2]. Based on this fact, there is an urgent need for a sensitive and accurate method for the determination of CAP in milk samples. Up-to-now most of the analytical methods towards this determination require a well-equipped laboratory, trained personnel, high capital expenditure and involve time-consuming sample preparation steps [3-4]. These added to the cost and complexity of assay. Among the variety of sensors reported, electrochemical methods that have shown potential applications in the detection of CAP rely on low instrumental cost, high simplicity, sensitivity, accuracy, reliability, and fast analysis [5-7]. Interestingly, so far an iron oxide magnetic nanoparticles doping on graphene nanocomposite ($\text{Fe}_3\text{O}_4/\text{Gr}$) has not been developed for the electrocatalytic detection of CAP. Herein, we developed a new type of disposable electrochemical sensor for rapid determination of CAP by the use of the $\text{Fe}_3\text{O}_4/\text{Gr}$ nanocomposite.

Method

The fabrication of $\text{Fe}_3\text{O}_4/\text{Gr}$ nanocomposites was described elsewhere [8]. Briefly, GO 20 mg was dispersed into EG 60 ml by ultrasonic treatment. $\text{FeCl}_3 \cdot 6\text{H}_2\text{O}$ 1.6 g, NaOH 1 g and urea 6 g were added into the above solution following magnetic stirring. The resultant homogenous mixture was transferred to a Teflon-lined stainless-steel autoclave, sealed and heated at 200 °C for 12 h. Then, the solution was cooled down and washed by deionized water and ethanol for several times.

The synthesized $\text{Fe}_3\text{O}_4/\text{Gr}$ was modified on SPE by drop casting and dried in a desiccator.

Results and Discussion

The pH value and the accumulation time were determined in order to find an optimal operational condition for CAP sensing. Thus, the pH value was optimized by measuring the CV responses of modified electrodes in 0.5 mM CAP. As given in Fig. 1A, it was seen that the oxidation peak current change increased (from pH 4.0 to 7.0) and then slightly decreased for higher pH values. Then, pH 7.0 was chosen for used as the supporting electrolyte in all subsequent analytical experiments.

The effect of accumulation time on the differential pulse voltammetry (DPV) response current at modified electrode was studied in the range of 5 to 120 second. As shown in Fig. 1B, the peak current of 50 μM CAP at modified electrode increases as the accumulation time increases from 5 to 10 seconds. The result might attribute to the increased amount of CAP molecules on the nanocomposite at electrode surface. After 10 second, the current response was then decreased gradually. Thus, the accumulation time of 10 s was chosen as optimal accumulation time for CAP. The possibility of this phenomenon was due to the rapid adsorption and blocking of excess CAP at modified electrode surface which could be limited the amount of molecules on electrode surface lead to surface saturation.

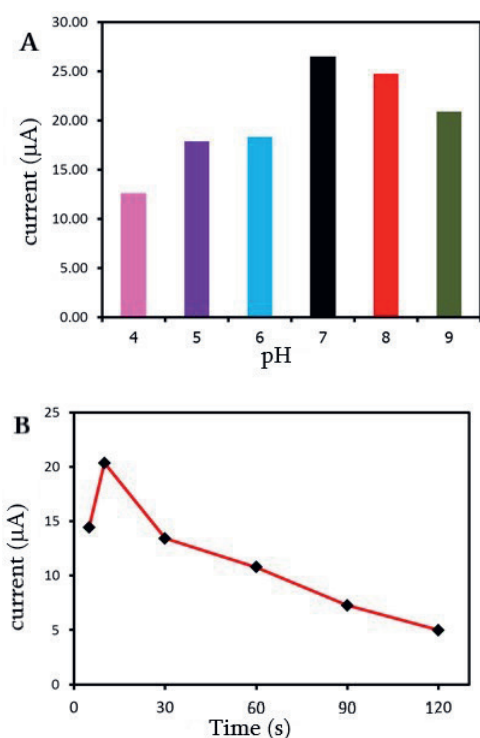


Fig. 1. The effect of the pH (A) and accumulation (B) on the peak current of 50 μM CAP at $\text{Fe}_3\text{O}_4/\text{Gr}/\text{SPE}$.

In order to study the electrochemical performance of $\text{Fe}_3\text{O}_4/\text{Gr}/\text{SPE}$ to CAP, the experiments were carried out by DPV under the optimum conditions. Fig. 2 displayed the DPV signal response for different concentrations of CAP from 0.5 μM to 700 μM . As expected, the oxidation peaks current increased with the increased of analytes concentration. The resulting calibration plots (inset in Fig. 2) are a good linear over the range from 0.5 μM to 600 μM with the corresponding linear regression equation of $y = 0.0238x + 2.6909$ ($R^2 = 0.984$) and a sensitivity of 238 $\mu\text{A}/\mu\text{M}$. The detection limit was calculated to be 95.4 nM at a signal-to-

noise ratio of 3 ($S/N=3$). The developed sensor is a promising sensor for simple, inexpensive and sensitive detection of CAP.

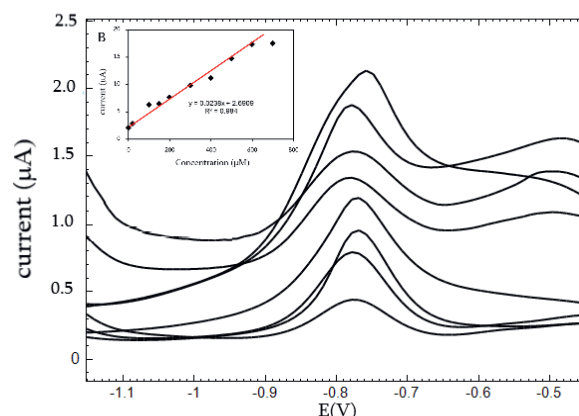


Fig. 2. DPVs of the $\text{Fe}_3\text{O}_4/\text{Gr}/\text{MSPE}$ at the CAP concentration from 0.5 μM to 700 μM . Inset: Calibration curve between the peak current and CAP concentration.

Conclusion

We have successfully developed the disposable electrochemical sensor for the rapid determination of CAP using iron oxide magnetic nanoparticles doping on graphene. The results indicated that the sensor show an excellent electrocatalytic activity, high selectivity, sensitivity, wide range and low detection limit.

References

- [1] A. F. Forti, G. Campana, A. Simonella, M. Multari, G. Scortichini, *Analytica Chimica Acta*, vol. 529, pp. 257–263, 2005.
- [2] M. J. Bogusz, H. Hassan, E. Al-Enzai, Z. Ibrahim, M. Al-Tufail, *Journal of Chromatography B*, vol. 807, pp. 343–356, 2004.
- [3] Y. Yang, J. Chen, Y.-P. Shi, *Talanta*, vol. 97, pp. 222–228, 2012.
- [4] C.-I. Ke, Z.-h. Wang, J.-I. Gan, Y.-g. Gu, K. Huang, L.-d. Li, Q. Lin, *RSC advances*, vol. 4, pp. 2355–2359, 2014.
- [5] J. Borowiec, R. Wang, L. Zhu, J. Zhang, *Electrochimica Acta*, vol. 99, pp. 138–144, 2013
- [6] M. Govindasamy, S.-M. Chen, V. Mani, R. Devasenathipathy, R. Umamaheswari, K.J. Santhanaraj, A. Sathiyam, *Journal of colloid and interface science*, vol. 485, pp. 129–136, 2017
- [7] A. Gevaerd, C.E. Banks, M.F. Bergamini, L.H. Marcolino-Junior, *Electroanalysis*, vol. 31, pp. 838–843, 2019.
- [8] Y. Poo-arporn, S. Pakapongpan, P. Pholpabu, R. P. Roo-arporn, in *The 12th Biomedical Engineering International Conference (BMEiCON2019)*, pp.1–4, Ubon Ratchathani (Thailand) and Pakse (Laos), November 19–22, 2019.

Fiber Optical Sensing System for Simultaneous Manometry, pH-metry and Bilimetry in Oesophagus

K. Schroeder¹, T. Habisreuther¹, M. Zeisberger¹, M. Becker¹, M. Rothhardt¹, F. Chiavaioli², M. Hahn³, O.-M. Rados³, F. Mönkediek³, S. Goerlich⁴, J. Gäbler⁴, A. Taddei⁵, M. N. Ringressi⁵, I. Bartolini⁵, P. Cecchi⁶ and F. Baldini²

¹Leibniz IPHT, Albert-Einstein-Straße 9, 07745 Jena, Germany,

²CNR, Institute of Applied Physics, Via Madonna del Piano 10, 50019 Sesto Fiorentino, Italy,

³OSCOMED GmbH, Am Lindenbach 3, 96515 Sonneberg, Germany,

⁴JETI Technische Instrumente GmbH, Tatzendpromenade 2, 07745 Jena, Germany,

⁵Careggi University Hospital, Largo Brambilla 3, 50134 Firenze, Italy,

⁶Cecchi S.R.L., Viadotto del Ponte all'Indiano 20, 50142 Firenze, Italy

kerstin.schroeder@leibniz-ipht.de

Summary:

We present first development results of a portable fiber optic sensing device capable to perform simultaneously esophageal manometry, pH-metry and bilimetry. It will provide physicians a compact and reliable tool to perform exhaustive diagnosis in gastroesophageal reflux pathologies. Pressure measurement along the esophagus is performed with an array of optical fiber Bragg grating (FBG) sensors. The sensors for the measurement of pH and bile are based on the change of absorption caused by the parameter under investigation.

Keywords: fiber optic sensor, multi-parameter sensing system, fiber Bragg grating, compact interrogation unit, esophagus manometry, pH-metry and bilimetry

Background, Motivation and Objective

The esophagus transports food from the mouth to the stomach. Anatomically, it is an elastic tube of tissue with sphincters at both ends. The sphincters function to keep the tube empty from external (food) and internal (acid) intrusions. Swallowing and transport of food to the stomach is a highly coordinated neuromuscular event. Dysfunction of the peristaltic transport mechanism causes a variety of diseases like GERD, esophageal adenocarcinoma, heartburn or pyrosis, achalasia and nutcracker esophagus. When the clinical picture remains unclear, the functionality of the esophagus has to be examined with sensors ([1], [2], [3]). A clearly defined goal is to enhance the spatial resolution, the sensitivity, and the speed of these examinations as well as the comfort to the patient.

In order to have a correct clinical picture and to be able to perform a correct diagnosis, the measurement of more than one parameter in the gastroesophageal apparatus is necessary, mainly esophageal pressure, pH and bile. Within our project (started in Jan 2019) a device is under development, which will measure all three parameters with a portable device over 24h.

Description of the New Method and System

A principle of the sensing catheter with the location of the different sensors is given in figure 1. In table 1 the projects targets are compared to the state of the art.

Besides the innovation of the sensor combination an improvement of the single sensors in comparison to former results and an optimization of the interrogation units is under development. Within this article we present new results on manometer sensor modelling and the improvement of the catheter functionality. An improvement of the pH-sensors is actually presented in [5].

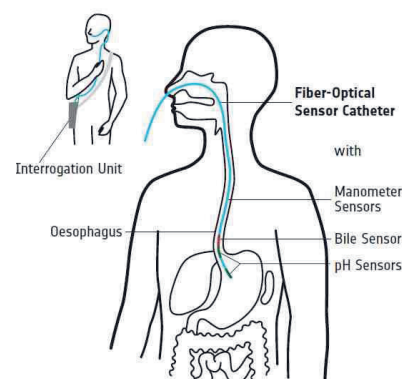


Fig. 1: Principle of the multi-parameter sensing system with positions of manometer- pH- and bile sensors within the measurement catheter.

Table 1: Comparison of different sensor characteristics, research targets and states of the art in gastroesophageal clinics application.

	Parameter	Project target	State of the art
Manometer	Pressure range	0-375 mmHg	0-200 mmHg
	Pressure resolution	1 mmHg	1 mmHg
	Spatial resolution	2.5 cm	10 cm - 1 cm
pH sensor	Measurement Range	1-8 pH units	1-8 pH units
	Accuracy	0.05 pH units	0.1 pH units
	Response time	≤ 20 s	10-30 s
Overall parameters	Diameter	< 4.8 mm	no combined catheter exist

Results

First feasibility tests have shown that optical fiber sensors are suitable for pressure measurements meeting the required stability of the compound material (Fig. 2) as well as the required response of the sensor head to pressure changes (Fig. 3).

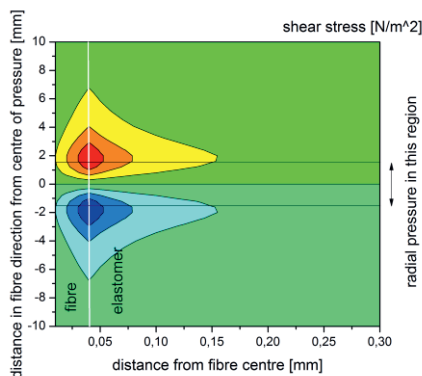


Fig. 2: Simulation of the shear stress at the fiber - elastomer interface with bare fiber with a soft elastomer as a pressure transducer.

A first transducer concept uses the conversion of radial forces into fiber elongation via transverse deformation (see e.g. [4]). Here the interface between fiber and polymer has to transfer high forces and needs a careful optimization. A calculation of shear stress under a pressure of 1 mbar over 3 mm length and 3 mm catheter diameter is given in fig. 2. To avoid sensor deconstruction, the design was chosen to get the

shear stress significant smaller tensile strength of the elastomer and the interface allow.

An alternative transducer concept (based on a membran in direct contact to the FBG) is also under investigation. The sensor response to pressure is shown in figure 3. The test was carried out in a typical pressure range like in an oesophagus. Pressure changes within the region of some seconds. Sensor2 (red) shows the influence of an improved design in comparison to sensor1 (black). Sensor2 shows a sensitivity of ~0.58 pm/mbar.

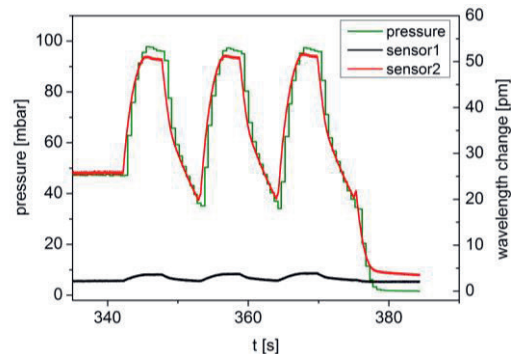


Fig. 3: Response to pressure change of different sensor designs.

Outlook

First measurement systems with combined sensors are planned to be tested at the end of 2020.

Acknowledgements

We thank the Federal Ministry of Education and Research for funding the research project as part of the EU's "PhotonicSensing" with FKZ 13N14753.

References

- [1] Bhatia, S. J. Oesophageal Manometry: An Overview, *J. Postgrad. Med.*, 39(1), 33–35 (1993); doi: 10.1117/12.921830
- [2] J. W. Arkwright, et.al., In-vivo demonstration of a high resolution optical fiber manometry catheter for diagnosis of gastrointestinal motility disorders, *Opt. Express*, 17(6), 4500– (2009); doi: 10.1364/OE.17.004500
- [3] F. Baldini, et.al., Miniaturised optical fiber pH sensor for gastro-esophageal applications, *Proc. of SPIE Vol. 8794* 87941Q-1 (2013); doi: 10.1117/12.2026074
- [4] M. Becker, et.al.: Characterization of Fiber Bragg Grating based Sensor Array for High Resolution Manometry, *Proc. of SPIE Vol. 8439* 843902-1 (2012); doi: 10.1117/12.921830
- [5] F. Chiavaioli, et.al.: Optical fiber device for simultaneous manometry, pH-metry and bilimetry in esophagus (OPTIMO), SPIE Photonics Europe, doi: av. In April 2020

Mimicking Biological Sensorimotor Systems by Opto-electronic Artificial Neurobotics

Serge Zhuiykov¹, Mohammad Karbalaee Akbari¹

¹ *Gent University Global Campus, 119 Songdomunhwa-ro, Yeonsu-gu, Incheon 21985, South Korea*
serge.zhuiykov@ugent.be

Summary:

Principally new artificial bioinspired optoelectronic sensorimotor system based on inorganic optical synapse (In-doped TiO₂) assembled into a liquid metal (galinstan) actuator for the controllable imitation of opto-genetically engineered neurons in the biological motor system is reported. The innovatively fabricated sensorimotor system is characterized by the low-energy consumption and precise modulation of electrical and mechanical outputs.

Keywords: Sensorimotor device, liquid metal actuator, galinstan, optical synapse,

Introduction

Principally new approach consisting of artificial synapse innovatively incorporated into the liquid metal actuator device to imitate sensorimotor functions is proposed and executed in the present research. To imitate the biological motoneurons behavior, a visible light sensitive TiO₂ optical synaptic device is integrated into a liquid metal actuator, which acts as artificial muscular component. Schematically this approach is presented below in Fig. 1. In the developed device, the indium (In)-doped TiO₂ optical synapse plays the role of visible light sensor, which receives optical signals and then generates informative postsynaptic current and potential pulses. The employed doping technique has broadened the optical sensitivity of ultra-thin high bandgap TiO₂ film to visible light region. The transfer of controlled potential pulses to the liquid metal actuator induces the mechanical motion, which in turn, mimics the muscular contraction/relaxation in the artificial neuro-robotic device. The following investigation of mechanisms behind the mechanical motion provides valuable insights towards the motor function of fabricated sensorimotor system. This achievement is fulfilled by precise design and optimization of sensorimotor components.

There are just a few cases which make a substantial step forward to confront the fundamental challenges of the development of biological sensorimotor systems [1]. In bioscience, an integration of the visible light-driven artificial synaptic device with a motor system can trigger several fundamental applications in cutting-edge technologies including optical wireless

devices, light-driven robotics, neurological optoelectronic sensorimotors, microfluidic chips and nano-pumps in drug delivery systems.

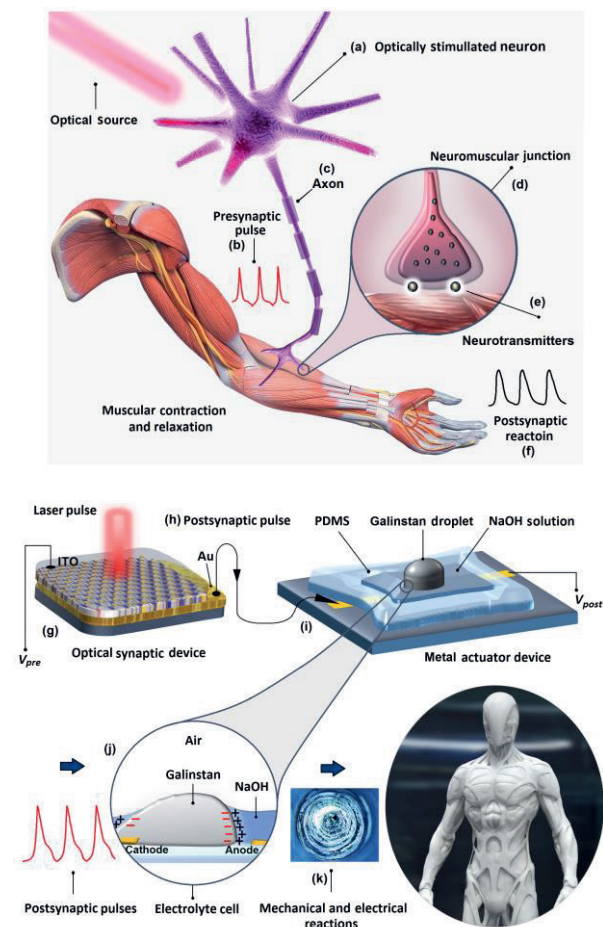


Fig. 1. The scheme of opto-genetically engineered neuron system (top) and artificial optoelectronic sensorimotor device (bottom).

Results

Artificial sensorimotor system (memristor) was made using In-doped 7.0 nm thick TiO₂ film on Au electrodes. The optical synapse was stimulated by successive laser pulses with the same amplitude at the different frequencies to imitate the short-term plasticity (STP) to long-term plasticity (LTP) transition in a biological system. The results demonstrate that the optical stimuli with lower pulse intervals are beneficial for facilitation the LTP capabilities. Observations confirmed that the shorter pulse intervals resulted in the higher gain values, which is consistent with the effect of residual generated carries on the following pulses.

The actuator device was made by using liquid metal (galinstan) (Fig. 2a). The liquid metal droplet in the bath of NaOH solution technically constitutes an electrochemical cell, which receives the postsynaptic pulses (Fig. 2b) from the optical device. The imposition of conductance vibration (Fig. 2c) and postsynaptic pulses (Fig. 2d) leads to the reconfiguration of the charge distribution on the surface of galinstan droplet in NaOH. It facilitates the mechanical oscillation of liquid metal in NaOH bath resembling a neuromuscular electronic system in robotic devices. By applying patterned optical pulses, the weight and rhythm of the potential signals can be designed, and consequently, the motion of galinstan actuator can be accurately controlled.

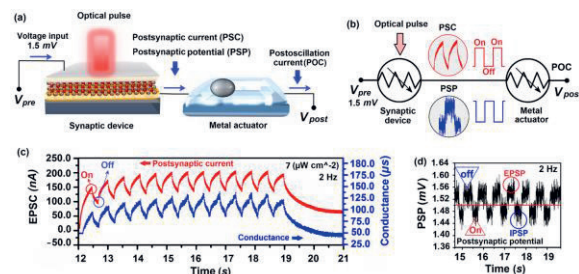


Fig. 2. Sensorimotor system (a) and its corresponding circuit (b), excitatory postsynaptic potentials (EOSC) and conductance variation on the device illuminated by $7 \mu\text{W cm}^{-2}$ pulsed light $\lambda=530 \text{ nm}$ and (d) corresponding variation of patterned postsynaptic potential (PSP) pulses of the same device.

Figure 3 shows the scheme of galinstan droplet, its actual top view and the light contrast developed image. By applying a singular external potential, the galinstan/NaOH system acts as an electrolyte cell. The power consumption for a singular heartbeat oscillation caused by 0.1 sec optical pulse was calculated. The difference between EPSC and voltage variation ($V_{\text{Max}} - V_{\text{Bias}}$) were used to calculate the required power consumption for oscillation of galinstan droplet. Regarding the voltage

variation, it was found that a singular oscillation, activated by 0.1 sec pulse duration, by average needs 1.2 - 0.3 μW power and approximately consumes 30 nJ energy.

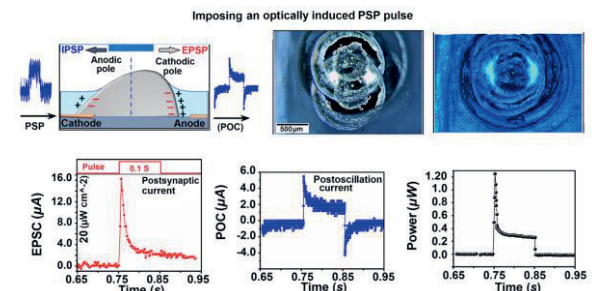


Fig. 3. The observation and characterization of oscillation behavior of galinstan droplet.

Figure 4 illustrates typical mechanical oscillation with different frequencies and measurement of mechanical oscillation. It was discovered that at the shorter pulse intervals and higher light frequencies, the galinstan droplet acts as another synaptic component in the system where the charge transfer through the galinstan/liquid electrolyte interface controls the output current of sensorimotor system.

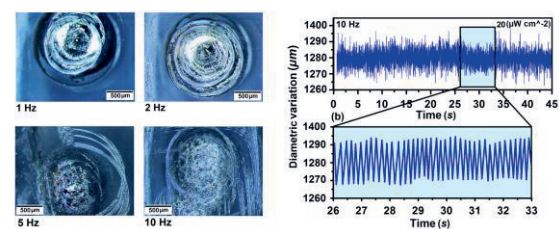


Fig. 4. The modulation of oscillation of galinstan droplet. Typical transitional motion of a $1280 \mu\text{m}$ diameter galinstan droplet by applying sequential PSP pulses originated from the optical synapse.

Conclusions

The present study demonstrated outstanding capabilities of the artificially developed bio-inspired opto-electronically sensorimotor device with optical synaptic and actuating components to modulate the functionalities of optogenetically engineered biological motor systems. In fact, developed optically stimulated synapse is a memristor with visible light-sensitive component, which has facilitated various synaptic dynamics. The characterization studies revealed that the potentially activated electrochemical mechanisms are behind the oscillation of liquid galinstan droplet.

References

- [1] M.K. Akbari, S. Zhuiykov, A bioinspired optoelectronically engineered artificial neurobotics device with sensorimotor functionalities, Nature Communications 10 (2019) 3873; doi.org/10.1038/s41467-019-11823-4

Explosion Pressure Measurement and Thermal Shock

Tim Krause¹, Detlev Markus¹, Mirko Meier²

¹ *Physikalisch-Technische Bundesanstalt, Bundesallee 100, 38116 Braunschweig, Germany*

² *Kistler Instrumente AG, Eulachstrasse 22, 8408 Winterthur, Switzerland*

Tim.Krause@ptb.de

Summary:

Transient thermal loads on piezoelectric pressure sensors as a result of an explosion lead to a heat flux which results in a reduction of the measured pressure amplitude as well as an increase of the scatter of the measurement results. The effects of this so-called thermal shock depend on the type of sensor and can be reduced by suitable measures, e.g. thermal protection layers of RTV (Room-Temperature-Vulcanizing) silicone.

Keywords: flameproof enclosures, explosion pressure, piezoelectric pressure sensor, thermal shock, thermal protection

Introduction

Information on the maximum pressure rise time and the maximum pressure of explosions is needed to assess the effects of explosions and to evaluate safety measures to prevent explosion accidents [1]. The analysis of a recent international proficiency testing program has shown that all the participants involved use piezoelectric pressure sensors to measure pressure signals over time. Furthermore, it turned out that one of the main reasons for the scattering of the results was the missing or insufficient protection of the sensor membrane against temperature influences [2].

The influence of thermal effects on piezoelectric pressure sensors during cylinder pressure measurement in combustion engines is a subject of frequent investigations and publications [3, 4]. This involves many explosions per minute leading to a nearly static thermal load on the pressure sensor which results in a thermal zero shift and thermal sensitivity change [5]. In the case of individual explosions, such as those occurring during type testing of flameproof enclosures [6], the explosions occur with rapid temperature changes. Here, the temperature gradient error, the so-called thermal shock, causes the greatest thermal load. For this application there are only very few studies and publications carried out so far [7]. This led to the motivation of this work to conduct further investigations regarding the influence of the thermal shock and measures to prevent it in this specific field of work.

Experimental set-up

In this work a spherical enclosure made of stainless steel with a volume of 10 l is used. The fuel-air mixture consists of 31 Vol-% H₂ in air in accordance with IEC 60079-1 [6]. The mixture is ignited by two electrodes in the center of the sphere. Thirteen piezoelectric pressure sensors of different types and sensor designs to be tested are mounted flush in brass adapters in the housing wall. To increase the statistical significance, at least two sensors of the same type were used. Furthermore, a heat flux measuring sensor in the design of a pressure sensor is installed to determine the heat flux. The explosion pressure measurements and heat flux determination are each performed with and without preparation to prevent thermal shock. The preparation material used consists of a 1 mm RTV silicone layer which is applied to the sensor membrane.

Results

The results in Fig.1 compare different piezoelectric pressure sensors with and without preparation against thermal shock. The explosion pressures are normalized to the highest mean explosion pressure $p_{\max} = 7.59$ bar by sensor S7. This work focuses on the Kistler 6031 and Kistler 601CAA sensors, as these are used very frequently by testing laboratories. The other ones are only shown for overview to demonstrate the variety of the possible sensors to be used and to show the differences in thermal shock behavior. It can be observed that for eight of the thirteen pressure sensors (S4, S5, S7, S8, S9, S10, S11 and 6031) the measured

explosion pressure without applied RTV silicone drops significantly compared to the measured values with 1 mm RTV silicone. For the remaining five pressure sensors (S1, S2, S3, S6 and 601CAA), the measurements with and without RTV silicone are consistent within the measurement accuracy.

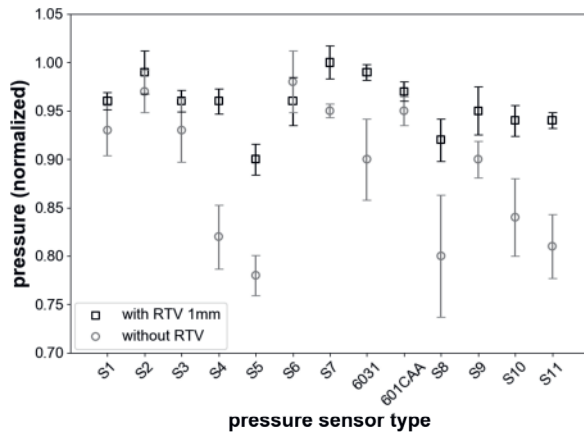


Fig.1. Comparison of different pressure sensor types with and without thermal protection (RTV silicone).

Furthermore, it can be observed that the scatter of measured values for eleven pressure sensors without RTV silicone is higher than with applied RTV silicone.

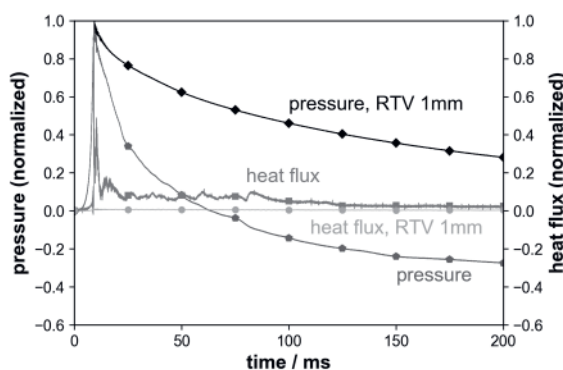


Fig.2. Pressure curves and heat flux graphs for 601CAA sensor with and without RTV silicone.

Fig. 2 shows the pressure curves over time for the 601CAA sensor and the associated heat flux for both cases, with and without RTV silicone. No effect of thermal load is visible in the range of pressure rise. But as soon as the flame front reaches the sensor, clear differences can be observed. The deformation of the membrane as a result of the heat flux results in a force that opposes the pressure force. In the case without thermal protection, the heat flux increases rapidly leading to a slight reduction of the pressure amplitude as can be seen in Fig. 2. Afterwards the pressure signal drops significantly. In contrast, no significant heat flux can be measured when using thermal protection.

Conclusions

Due to the rapid temperature rise caused by an exothermic explosion, a pressure measurement is influenced for this application by dynamic temperature loads. Each type of pressure sensor is affected differently by the thermal shock. The intensity of the reaction depends mainly on the design of the sensor, especially that of the membrane. If the membrane is designed so that it neither stretches nor compresses the piezoelectric crystal of the pressure sensor when deformed due to thermal load, the effects of the thermal shock can also be reduced (see 601CAA in Fig.1). Nevertheless, it can be stated that almost all piezoelectric pressure sensors react to thermal shock, which has a negative effect on the actual explosion pressure measurement. When determining explosion pressures, it is therefore recommended that the pressure sensors used be protected against the influence of the thermal shock. The use of 1 mm RTV silicone has proven to be an appropriate measure to reduce the heat flux into the sensor which prevents an interference with the measured pressure signal and additionally reduces the scatter of the measured values.

References

- [1] M. Hattwig, H. Steen (Eds.), Handbook of explosion prevention and protection, Wiley-VCH, Weinheim, (2004)
- [2] T.Krause, D.Markus, Herausforderungen bei der dynamischen Messung von Explosionsdrücken, *tm - Technisches Messen* 84, 101-110 (2017); doi: 10.1515/teme-2016-0051
- [3] S. Lee, C. Bae, R. Prucka, G. Fernandes, Z. Filipi, D.N. Assanis, Quantification of Thermal Shock in a Piezoelectric Pressure Transducer, *SAE Brasil Fuels & Lubricants Meeting*, SAE International, (2005); doi: 10.4271/2005-01-2092
- [4] R. A. Stein, D. Z. Mencik and C. C. Warren, Effect of Thermal Strain on Measurement of Cylinder Pressure, *SAE Transactions* 96, 442-449 (1987)
- [5] J.Tichý, G.Gautschi, Piezoelektrische Meßtechnik, *Springer-Verlag*, (1980)
- [6] International Electrotechnical Commission, IEC 60079-1, Explosive Atmospheres - Part 1: Equipment Protection by Flameproof Enclosures "d", Edition 7.0, (2014)
- [7] R. A. Kach, A. A. Adamczyk, Effects of thermal loading on pressure measurement in a combustion bomb, *Review of Scientific Instruments* 56, 1274 (1985); doi: 10.1063/1.1137991

Redundant Pressure Sensor Based on Steel and Ultra-Thin Glass Strain Gauges

Dennis Wachter, M.Sc.¹, Günter Schultes, Prof. Dr.²
¹ ZeMA gGmbH, Eschberger Weg 46, D-66121 Saarbrücken,
² htw Saar, Goebenstraße 40, D-66117 Saarbrücken
 dennis.wachter@zema.de

Summary:

A pressure sensor with the goal of enhanced reliability and built-in redundancy is developed using the possibilities offered by highly sensitive and high temperature stable thin films. The sensors show promising results with potential application for high temperature applications and incorporate a modular approach using an ultra-thin glass based strain gauge with redundant Wheatstone bridges joined to a monolithic stainless steel membrane by glass soldering.

Keywords: pressure sensor, reliability, glass, thin film, strain gauge

Background, Motivation and Objective

In many applications, pressure sensors are important devices to control the pressure in fluids and gases. This is often done to realize closed-loop controls or for safety reasons. In case the pressure is relevant to security, two separate sensors are installed to allow a conformity check of the redundant pressure signals. This entails not only higher costs, but also increases complexity, overall size and requires multiple pressure connectors. To counteract this, we developed a sensor with built-in redundancy and high flexibility utilizing some advantages our highly sensitive thin-films provide, with the primary goal of enhanced reliability and long-term stability. The concept is based on a monolithic sensor design; i.e. the steel body is one-piece without any welding connection. We chose a modular approach for more flexibility regarding different pressure ranges and various mechanical connectors.

Description

The modular approach resulted in the development of a universal strain gauge design, which can be joined to various mechanical variants of a monolithic steel pressure membrane. The sensor body is designed with an internal screw thread, allowing it to be paired with male stud couplings common in industry. This allows the use of widely available, mass produced parts and therefore a cost-efficient possibility to offer a variety of pressure connectors without the need for welding while still keeping the overall design compact.

The strain gauge carrier consists of highly temperature resistant ultra-thin glass, cut in circular geometry by means of a laser. The glass carrier greatly reduces cross-sensitivity from moisture, which especially can be a challenge with foil strain gauges. A glass soldering process is adapted for joining the strain gauge to the steel pressure membrane. As a further advantage, the membrane's surface need not to be sanded and polished as would be necessary if an insulating layer like SiO₂ is to be sputtered. The ultra-thin glass already has a smooth surface with less than 1 nm RMS.

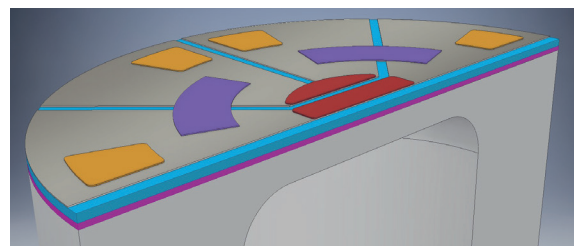


Fig. 1. Half-section of a sensor showing one of two Wheatstone bridges that are laser-structured into a thin film (grey color) on ultra-thin glass substrate (blue). The glass is joined to the steel membrane by means of a glass solder (magenta). Yellow markings indicate the zones for electrical contacts.

In addition to a strong bond, the glass soldering process results in a compressive stress state of the glass carrying strain gauge, if the different thermal expansion coefficients are chosen in a way that the steel membrane has the highest and the glass has the lowest coefficient. This helps to avoid tensile stress states in the glass substrate, susceptible for crack formation [1].

Thus, even under applied pressure the glass circumference ideally remains free of tensile stress, allowing for a non-perfect glass cutting quality.

The thin film material allows the sensor to not only endure the necessary soldering temperature of over 450 °C but also enable the appropriate, simultaneous thermal conditioning of the thin film strain gauge [2][3]. By adjusting the heating and cooling ramps, the thin film may be modified in order to reduce the sensors overall temperature sensitivity.

The design comprises two electrically independent Wheatstone bridges on the midway divided pressure membrane. After the joining process, a contact PCB is glued to the sensor and the bridges can be contacted electrically by a bonding process as shown in Fig. 1. This concludes the manufacturing process and the sensor bridges are then calibrated simultaneously.

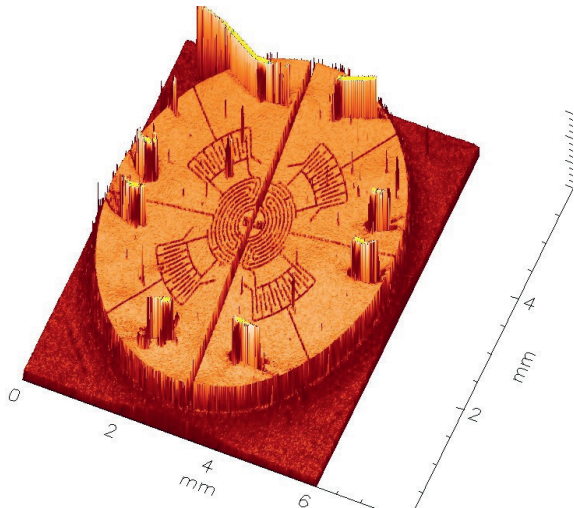


Fig. 1. 3D optical scan of a glass strain gauge surface showing the structure of the dual bridge design with resistors and the foot marks of eight bonds.

Results

The sensors show promising results despite the novel usage of the pressure membrane area. As hoped for, the individual bridges display similar, but not identical behavior. For instance, identical bridge signal drifts would cancel the advantage of multiple signals in detecting long-term run-away. Because of this, mechanical asymmetries due to tolerances, positioning offsets and even inhomogeneity in the thin film can actually be a benefit. Non-identical bridge behavior can also be induced on purpose by using different strain gauge layouts for bridge A versus bridge B. Table 1 shows a prototype with identical layouts for both bridges, but different sensitivities likely due to a strain gauge misalignment of around 0.2 mm.

Tab. 1: Exemplary characteristics of one prototype with a nominal pressure of 200 bar

	Temp. °C	Sensitivity mV/V	Hysteresis % full scale
Bridge A	30	7.404	0.053
	80	7.512	0.054
	125	7.611	0.046
Bridge B	30	6.433	0.055
	80	6.524	0.063
	125	6.607	0.046

The split-membrane approach has shown potential and has the advantage of allowing a simpler mechanical design compared to available redundant pressure sensors with dual membranes, as only one pressure channel and membrane are required. Thus, lathe turning the sensor body without additional reworking is an option.

An operating temperature of up to 125 °C was the original goal of development, but measurements indicate potential for higher temperature applications, as rising temperatures do not seem to have negative effects on measurements within the temperature range. Fig. 2 shows a creep measurement at 125 °C for 180 min. Similar errors have also been measured for much longer exposure times of several days.

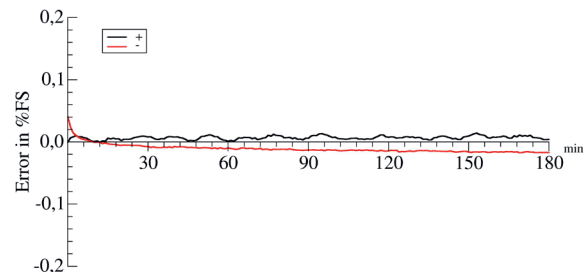


Fig. 2. Typical creep measurement of a 200 bar sensor at 125 °C for 180 min. The ripples in the pressurized state (black) result from closed-loop pressure regulation and do not appear when the pressure is relieved (red).

References

- [1] A. Siber, K. Koger, Messzellenanordnung für einen Drucksensor mit Kraftmesselement aus Glas; Patent DE102006023724B4
- [2] M. Cerino, D. Göttel, A.C. Probst, G. Schultes, Schichtwiderstand mit einem kohlenstoffhaltigen Widerstandsmaterial und Verfahren zu dessen Herstellung; Patent DE102015006057A1
- [3] G. Schultes, H. Schmid-Engel, S. Schwebke, U. Werner, Granular metal-carbon nanocomposites as piezoresistive sensor films – Part 1: Experimental results and morphology, JSSS 7, 1–11 (2018); doi: 10.5194/jsss-7-1-2018

Miniaturized System for Vapor Pressure Measurement using a Combination of Knudsen Cell and Nanobalance

Michal Schulz¹, Holger Fritze¹

¹ *Institute of Energy Research and Physical Technologies,
Clausthal University of Technology, Am Stollen 19 B, 38640 Goslar, Germany
michal.schulz@tu-clausthal.de*

Summary:

A miniaturized system for measurement of vapor pressure is presented. It consists of a Knudsen cell and a langasite based resonant nanobalance. The molecular beam from the cell hits the surface of the nanobalance and forms a thin film which results in an increase of the mass and thus in a shift of the resonance frequency. The mass sensitivity of the high-temperature stable nanobalance enables even detection of single monolayers of deposited material. The resonance data is analyzed using impedance spectroscopy as well as frequency counting techniques.

Keywords: piezoelectricity, Knudsen effusion, impedance spectroscopy, microgravity

Introduction and Objectives

Precision data for the free enthalpy of pure substances and alloys, which is essential for development of new materials, improvements in process control as well as determination of application limits of new material systems, can be obtained through vapor pressure measurements [1]. It is commonly determined by means of mass spectrometry on a molecular beam produced by a resistively heated Knudsen cell [2,3]. Conventional systems exhibit however several drawbacks. The sample stays in contact with the crucible and thus a risk of contamination is given. Furthermore the investigated material cannot evaporate equally in all directions. Finally, the size of the experimental setup is not suited to be applied in systems like e.g. microgravity levitation systems in which the above-mentioned disadvantages do not exist.

The miniaturized system presented here overcomes the aforementioned limitations as the conventional mass spectrometer is replaced by a nanobalance, resulting in significant reduction of size. It allows the measurement of the Knudsen effusion during e.g. electromagnetic levitation experiments. The capabilities of the system are validated during German Aerospace Center (Deutsches Luft- und Raumfahrt, DLR) and European Space Agency (ESA) parabolic flight campaigns (PF) in 2018, 2019 and 2020.

Description of the System

The nanobalance system for Knudsen effusion measurements is shown schematically in Fig. 1.

It consists of a regular Knudsen cell and a high-temperature stable nanobalance based on piezoelectric langasite resonators ($\text{La}_3\text{Ga}_5\text{SiO}_{14}$, LGS). The molecular beam from the cell hits the surface of the nanobalance and forms a thin film which results in an increase of the mass and thus in a shift of the resonance frequency. An additional shutter placed between Knudsen cell and resonator (not shown in the schema) allows to interrupt the deposition process during the experiment.

Due to the proximity of the resonator, heating by infrared radiation from the sample has to be taken into account. Therefore, the system uses

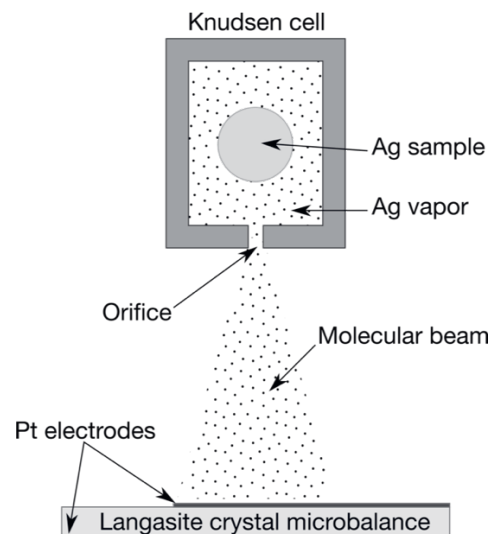


Fig. 1. Function principle of a nanobalance-based set-up for the measurement of a Knudsen effusion.

a Pt-100 resistive temperature sensor placed in the vicinity of the resonator. In combination with temperature compensation techniques, such as application of the 3rd overtone [4], shifts of the resonance frequency due to increasing mass load are decoupled from disturbing temperature effects.

Experimental

The system is tested in combination with the TEMPUS electromagnetic levitation facility from the DLR. There, the material systems Ag and Ag₆₀Cu₄₀ are annealed in the temperature range from 850 to 950 °C. The shutter between Knudsen cell and nanobalance is opened as soon as the sample is levitating and its temperature stabilizes. The temperature of the LGS resonator is recorded using a Keithley DVM-2000 digital voltmeter. The duration of the experiment is limited to approximately 20 seconds, which is determined by the length of the microgravity condition during parabolas.

The frequency shift is measured using two different approaches. The first is the impedance measurement of LGS in the vicinity of its resonance frequency (both fundamental mode and the overtones). The data acquired using a network analyzer (Agilent E5100A) is calibrated in order to exclude the stray capacitances caused by the resonator support and the wiring. Subsequently, a Lorentz curve is fitted to the conductance peak, giving information about the resonance frequency and Q-factor of the resonator. This method is however limited to a sampling rate of about 1 Hz.

Another measurement method incorporates an oscillator circuit driven by the LGS resonator. The oscillator circuit operates at the series resonance frequency. The latter is recorded using a calibrated and temperature compensated 10 ns time base. Finally, the data is analyzed and stored in form of a resonance frequency as a function of time. This system allows recording of resonance frequency at a rate of up to 100 Hz.

Results and Discussion

The Ag samples are analyzed in microgravity conditions during PF in 2018 and 2019. Thereby, the data is acquired at a temperature ranging from 1173 to 1373 K (see Fig. 2). The lowest measured mass flow rate of Ag is 1.5 ng/s at 1193 K. The results are compared with numerical simulations of the system made using Comsol Multiphysics 5.3a [5] and found to be in good agreement.

The Ag₆₀Cu₄₀ sample is analyzed during PF of ESA in 2020.

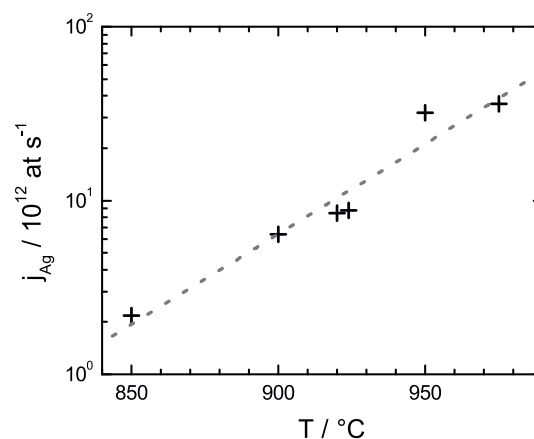


Fig. 2. Ag molecular flux as a function of temperature.

Conclusions

The miniaturized system presented here enables vapor pressure measurement in microgravity conditions. The vapor pressure of pure Ag and Ag₆₀Cu₄₀ are determined and confirm the usability of the system. The measurements using an oscillator circuit allow determination of the resonance frequency at high sampling rates.

Acknowledgment

The authors thank the Federal Ministry for Economic Affairs and Energy (Bundesministerium für Wirtschaft und Energie, BMWi) for financial under the grants 50RP1511 and 50WM1855.

References

- [1] K. Hilpert, Potential of mass spectrometry for the analysis of inorganic high-temperature vapors, *Fresenius' Journal of Analytical Chemistry* 370, 471-478 (2001); doi: 10.1007/s002160100835
- [2] A.M. Booth, T. Markus, G. McFiggans, C.J. Percival, M.R. McGillen, D.O. Topping, Design and construction of a simple Knudsen Effusion Mass Spectrometer (KEMS) system for vapour pressure measurements of low volatility organics, *Atmospheric Measurement Techniques* 2, 355-361 (2009)
- [3] D. Henriques, V. Motalov, L. Bencze, S. Fürtauer, H. Flandorfer, T. Markus, Experimental thermodynamic study of the Cu-Li-Sn system by Knudsen Effusion Mass Spectrometry, *Journal of Alloys and Compounds* 687, 306-311 (2016); doi: 10.1016/j.jallcom.2016.06.091
- [4] H. Fritze, High-temperature bulk acoustic wave sensors, *Measurement Science and Technology* 22, 012002 (2011); doi: 10.1088/0957-0233/22/1/012002
- [5] COMSOL Multiphysics® v. 5.3a. www.comsol.com. COMSOL AB, Stockholm, Sweden.

Multifunctional Stick-Slip Sensor

Klemens Gintner¹, Michael Weber¹, Bernhard Beck¹

¹ *University of Applied Sciences Karlsruhe, Faculty MMT, Moltkestr. 30, 76133 Karlsruhe, Germany, klemens.gintner@hs-karlsruhe.de*

Summary:

A new type of stick-slip sensor is presented. The signals of a pressure sensor and an acceleration sensor are advantageously used to evaluate the quality of a gripping process. The motion profile of the gripper and also the minimum mass of the gripped object can be determined at the same time. Such a sensor can be used, for example, in robotics or in prosthetics (hand prostheses).

Keywords: Stick-slip sensor, additional information, grip quality assessment

Motivation: Evaluation of gripping process

The evaluation of a gripping process is important in many applications, e.g. in robotics, because the handling of objects must be evaluated or carried out correctly. This is also the case with hand prostheses, which should allow a secure grip.

Description of the New Sensor System

It is a sensor system on a gripper - e.g. thumb on a hand prosthesis or a gripper on a robot arm. An acceleration sensor with at least one axis (better two or even three axes) is required to detect the relative movement (= slipping due to the tangential force $\underline{F}_{T,X}$ in x-direction) between the sensor and the object to be gripped. The acceleration sensor is located in a conical base body, which can oscillate tangentially in x-direction to the holding force $\underline{F}_{N,Z}$ parallel to the z-axis when an object slips through ("elastically" mounted) - see Figures 1, 2 and 3.

The corresponding (oscillation) frequency depends, among other things, on the geometry of the base body and the frequency is typically above 120 Hz (see Fig. 5). By suitable frequency-selective evaluation using low-pass and high-pass filters, slipping of an object to be gripped can be detected at the resonant frequency of the base body.

An example of the evaluation algorithm of the acceleration signals to detect slipping is shown in Figure 4. The given values are to be understood as an example.

The evaluation also allows the movement of the gripper to be detected, as the corresponding frequency range is significantly lower than the resonance frequency of the base body (usually higher than 120 Hz). Thus, for example, the

movement of the gripper can be detected and, if necessary, better controlled.

With the help of a pressure sensor at the point of contact of the base body, the holding force in z-direction can be determined, which also allows conclusions to be drawn about the minimum mass of the object to be gripped. All this enables further plausibility checks to be carried out so that slippage can be detected even better. Further details can be found in [1].

The three-dimensional acceleration can also be used to determine the orientation of the object to be gripped (e.g. the direction of the acceleration due to gravity). If an additional rotation rate sensor (yaw rate sensor) is used, the trajectory of the gripper can be followed even better.

The following sensors were used for the first measurements:

Force or pressure sensor: QTC (Quantum Tunneling Composite) single-point sensor QTC SP200-05 from Peratech [2] and three-axis acceleration sensor: LIS344ALH from ST [3].

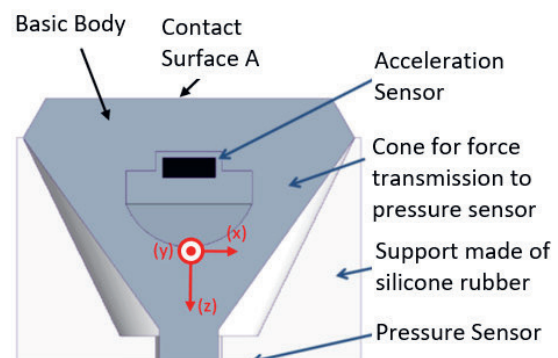


Fig. 1: Sectional view of the sensor

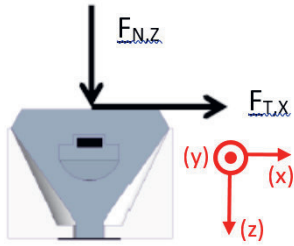


Fig. 2: Forces on basic body: Here: Normal force $F_{N,z}$ and tangential force $F_{T,x}$

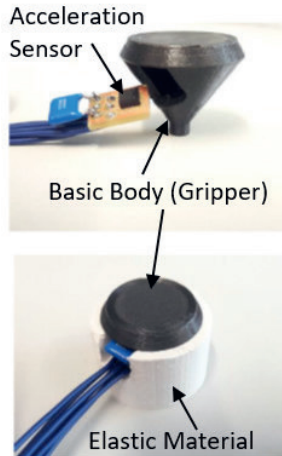


Fig. 3: Images of the sensor above: circuit board and acceleration sensor below: with silicone rubber (elastic material)

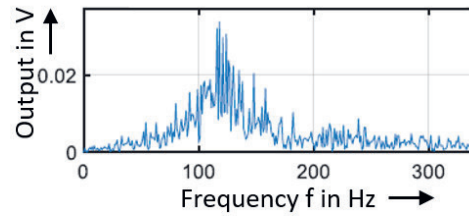


Fig. 5: Output of acceleration sensor a_x in Volt as a function of frequency f in Hertz

Conclusion

By data fusion of different sensors (force and acceleration sensors), both the force for gripping and a relative movement between gripper and object (slipping) can be detected and evaluated. Additionally, it is possible to detect the movement of the gripper and to estimate the minimum mass of the object to be gripped. A patent application has already been filed.

References

- [1] M. Weber, „Untersuchung zur Kraftanalyse bei Handprothesen“, *Master Thesis, Mechatronics, University of Applied Sciences Karlsruhe, 2018*
- [2] Peratech Holdco Limited: Peratech - <https://www.peratech.com/sp200-05/> Version: 15. August 2018
- [3] STMicroelectronics: LIS344ALH. https://www.st.com/content/st_com/en/products/mems-and-sensors/accelerometers/lis344alh.html. Version: 15. September 2018

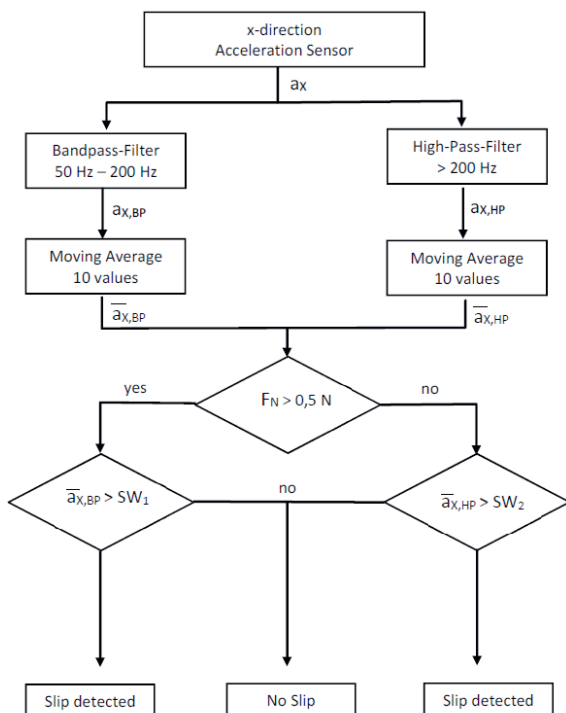


Fig. 4: Example of an evaluation algorithm for the detection of slippage

Investigations to Determine the Clamping Force of Screw Connections

*Th. Frank, A. Grün, H. Jayaprakash, M. Kermann, S. Jagomast, A. Cyriax, C. Maier, Th. Ortlepp
Forschungsinstitut für Mikrosensorik GmbH, Konrad-Zuse-Straße 14, 99099 Erfurt, Deutschland,
tfrank@cismst.de*

Summary:

A screw is a machine element for frictional connection of two or more components. Particularly security-relevant connections require regular checks. Subsequent checking of the assembly preload is not possible without various additional measures. It is advantageous to monitor the assembly preload. The article describes two methods for determining the clamping force using silicon strain gauges. The clamping force stretches the screw shaft, compresses the elements to be joined and deforms both the screw head and the nut or washer. The deformation of the screw head or the washer contains all information about the clamping force. The described use of the silicon strain gauges enables the deformation to be precisely recorded. The clamping force can be determined via the deformation.

Keywords: silicon, piezoresistive, stress, force tensions, screw shaft, assembly preload, strain gauges, washer, clamping force

Investigations to determine the clamping force of screw connections

A screw is a machine element for the frictional connection of two or more components. The tightening torque creates the clamping force between the screw head and the nut thread. The maximum permissible preload is defined by the screw diameter and the strength class of the screw. For a permanently secure and functional connection, it must be ensured that the preload is within a defined tolerance range over the entire service life. Particularly security-relevant connections require regular checks. A subsequent check of the assembly preload is not possible without various additional measures. By default, the tightening torque is checked manually. It is advantageous to monitor the assembly preload. The article describes two methods for determining the clamping force with strain gauges made of silicon. The clamping force tensions the screw shaft, compresses the elements to be connected and deforms both the screw head and the nut or washer. The deformation of the screw head or the washer contains all information about the clamping force. The deformation can be recorded precisely by using the silicon strain gauges described. The clamping force can be determined via the deformation.

strain gauges. A mechanical load in the doped areas leads to a change in the conduction mechanism, which changes the resistance. Here, the piezoresistive resistors are monolithically integrated into the silicon component by diffusion or implantation. Compared to standard metal strain gauges, the integrated semiconductor resistors have a higher coupling factor and significantly higher long-term stability.

Due to the piezoresistive properties of the silicon orientation $\langle 100 \rangle$ used, the measuring resistances are differentiated transversally and longitudinally. The change in resistance is similar in amount but with the opposite sign. A measuring bridge is built from two pairs of these measuring resistors, see Fig. 1.

To analyze the mechanical stress, the silicon strain gauge (according to Fig. 1.) is attached to the spring body. At the optimal position there is a large difference between mechanical tension in the X and Y direction. If there is no such optimal position, another construction is necessary. This is necessary because the silicon strain gauge has a symmetrical structure and does not have its own anisotropy. No other structure is possible in the silicon material used.

Force measurement in microsystem technology is usually based on strain-sensitive resistors,

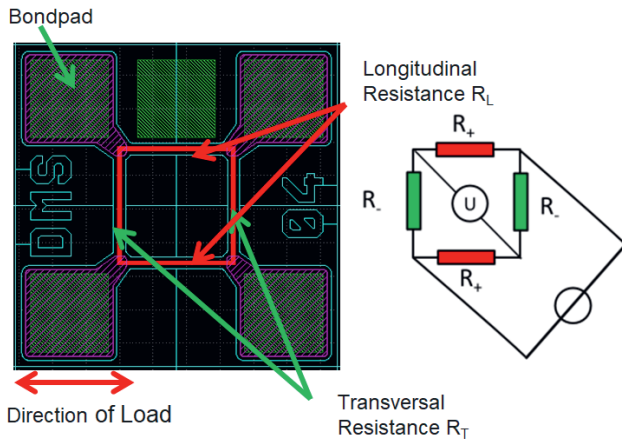


Fig. 1. Silicon strain gage with complete measuring bridge with two resistors for the longitudinal and the transverse effect.

Joining the strain gauge

The silicon strain gauges are joined using glass frit. Fig. 2 shows the joined silicon strain gauges. The electrical contact for signal processing is ensured by wire bonding.

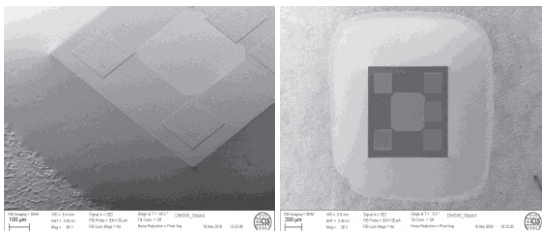


Fig. 2. Silicon strain gauge, fitted with glass frit on a steel spring body.

Placement on the screw head

The screw head is deformed by the clamping force. To determine this, strain gauges are placed on the head. The sensors can be attached directly to the screw head or via a mounting bracket. The mounting bracket enables easy mounting on larger screws. To enlarge the measuring span, the mounting bracket is provided with a bar, see Fig. 3. The measured values for an M33 are shown in Fig. 4.

Placement on the washer

Like the screw head, a washer also deforms. The use of the washer is more complex. The position of the bolt and washer depends on the tolerance. To compensate for this, at least three sensors are required. The measured values for a washer are shown in Fig. 5.

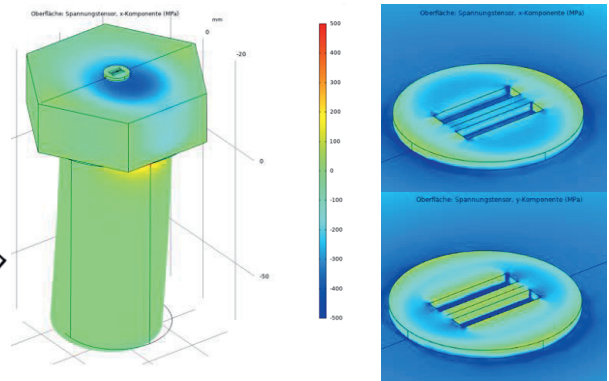


Fig. 3. Silicon strain gauge, mounting bracket.

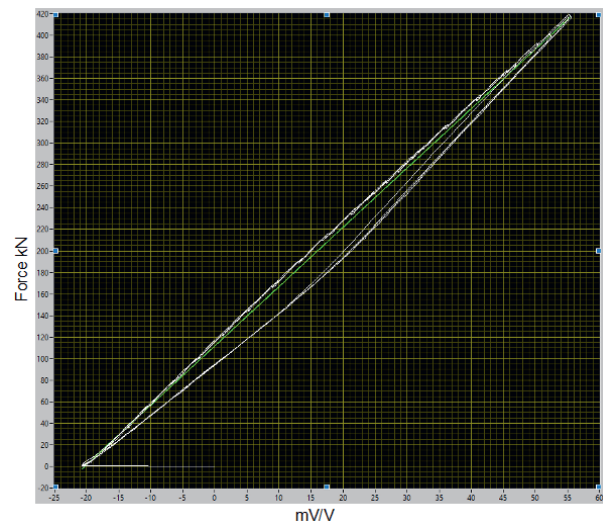


Fig. 4. Measured values for an M33, measurement signal vs. clamping force.

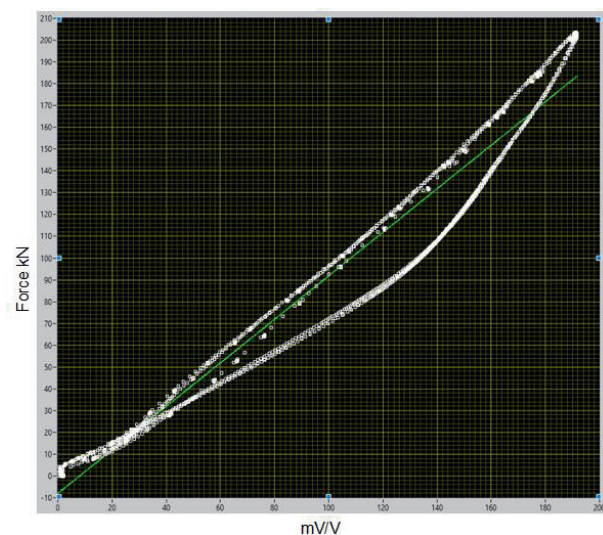


Fig. 5. Measured values for an M27 washer, measurement signal vs. clamping force.

Simulation of the Temperature Influence of an Inductive Sensor for the Geometry Detection of Rotating Components

C. Lehmann¹, M. Rogowski¹, S. Fisahn¹, H. Garbe¹

¹ *Leibniz Universität Hannover – Institute of Electrical Engineering and Measurement Technology, Appelstr. 9a, 30165 Hannover Germany, Email: lehmann@geml.uni-hannover.de*

Summary:

In this work, the influence of temperature on the output signal of an inductive sensor for the detection of geometric changes in rotating magnetically conductive components was investigated. For the study, the measurement system is modeled and simulated in a numerical field computation software. A radial displacement of the sensor and changes in the magnetic properties of the permanent magnet used are examined. A signal change of up to 14.9% could be proved over the required temperature range. The results show the need to suppress radial displacement and to record the temperatures at the magnets.

Keywords: inductive sensor, simulation study, temperature compensation, permanent magnets, geometry detection

I. Motivation

There are many areas of application for monitoring of the air gap in rotating components in industry like turbines or engines. It is often very important that geometric changes can be detected early during operation. An inductive sensor consisting of a permanent magnet and a coil can be used for local geometry detection of rotating magnetic conductive components. The rotating component is magnetized via the permanent magnet and the resulting change in the magnetic flux is detected in the coil via an induced voltage. In field measurements geometric changes could be determined due to the induced voltage signals during operation. After the machine had come to a standstill overnight, the signals showed strong deviations, which indicates a temperature influence of the measuring system. For this reason, the influence of temperature on the sensor signal is analyzed using a simulation study. The aim of this work is to be able to compensate the influence via signal processing.

II. Simulation study

The magnetic field simulation program used for the simulation study is based on the finite element method. Firstly, the model of the rotating system is created on the basis of CAD data. Then the magnetization characteristics are inserted for the used materials. The simulated induced voltage signal of the sensor for a known geometry at a temperature of 20 °C is shown in

Fig. 1 and serves as a reference state for further investigations.

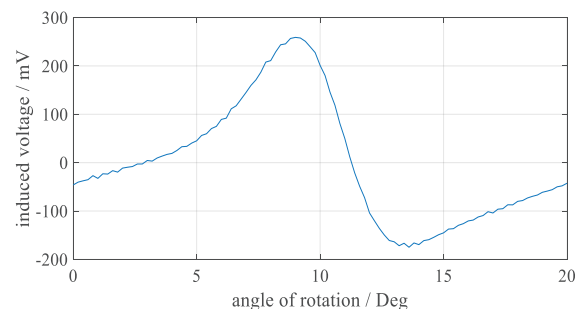


Fig. 1. Simulated induced voltage signal of the sensor via the angle of rotation.

A change in temperature has different overlapping effects on the sensor system. The two most significant changes for the sensor signal are the expansion of the drum cover on which the sensor is mounted, which leads to a radial displacement of the sensor, and the change in the magnetic properties of the permanent magnet. These two approaches are examined and evaluated in the study.

a. Radial displacement

The sensor system is attached to the drum casing. Since the attachment points of the curved cladding are clearly spaced from the sensor, a radial displacement can be assumed. The increased distance between the sensor and the rotating component leads to an increased air gap and thus to a smaller change in the magnetic flux

density through the coil. This results in a lower induced voltage in the sensor. Static heating tests on the real component result in a shift of up to one millimeter between the axis of rotation and the sensor due to the temperature expansion of the drum casing. Fig. 2 shows the differential voltage between the induced voltage of the shifted state and that of the initial state.

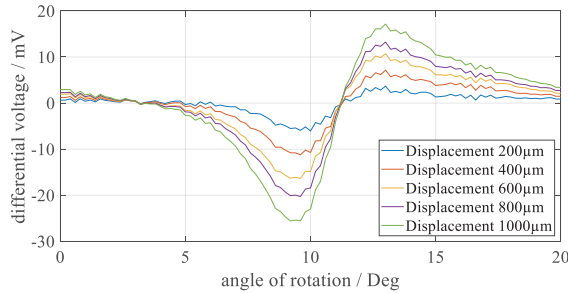


Fig. 2. Differential voltage of the induced voltage between the initial system and the shifted state.

The differential voltages have an almost proportional relationship with the displacement. Furthermore, a slight spread of the extreme points of the induced voltage signals can be seen, which results from the extreme point position of the differential voltage. The changes due to the considered radial shift in the examined value range amount up to 9.2% for the maximum induced voltage. Therefore, it can be concluded from the simulation results that the radial displacement has a significant influence on the sensor signal. If the displacement is known, the influence in signal processing can be compensated on the basis of the deterministic behavior. Since the measurement of the radial displacement of the sensor is problematic in terms of accuracy, the displacement should be structurally restricted in order to be able to optimize the accuracy of the geometry detection.

b. Properties of the permanent magnet

The remanence of permanent magnets is temperature-dependent and can be described in good approximation in the work area using equation (1) [1]. The temperature coefficient α is material-specific and is specified by the manufacturer of the permanent magnet.

$$B_{R, \vartheta} = B_{R, 20^\circ\text{C}} (1 + \alpha(\vartheta - 20^\circ\text{C})) \quad (1)$$

The remanence of the permanent magnet decreases with increasing temperature ϑ . The lower magnetic field leads to less flooding in the rotating magnetically well-conducting component and thus to a smaller change in the magnetic flux density through the coil. As a maximum temperature, 70 °C can be expected from the heating of the bearings. A magnet made of neodymium-iron-boron is installed in the sensor under investigation. The temperature-dependent

remanence is implemented in the simulation model. Fig. 3 shows the differential voltage between the induced voltage of the specified temperature and that of the initial state.

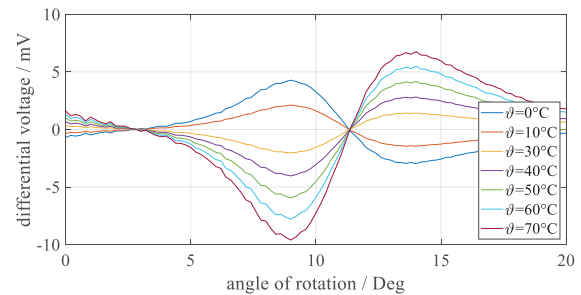


Fig. 3. Differential voltage of the induced voltage between the initial system and the temperature-varied state.

The signal of the differential voltage for the investigated temperatures shows a linear amplification of the induced voltage signal. An almost constant gain factor of -5.7% between 0 °C and 70 °C could be proved in the simulation. This shows that the magnetic properties of the material of the permanent magnet have a significant influence on the sensor signal. Since the relationship can be regarded as almost linear, a temperature change can be compensated in the signal processing. This requires a temperature measurement on the permanent magnet, which must be taken into account when designing the sensor.

III. Results

The results of the simulation study show the significant influence of temperature on the signal induced by the sensor. A maximum change of 14.9% of the maximum induced voltage upon superposition of the radial displacement and the change in the magnetic properties can be determined in the examined value ranges to the initial state. These results show the need for constructive countermeasures to prevent radial displacement of the sensor and to detect the temperature on the permanent magnet. Due to the almost linear relationship between the temperature and the remanence of the permanent magnet, this influence can be compensated in signal processing if the change is measured.

References

- [1] K. Schüller, K. Brinkmann, Dauer magnete: Werkstoffe und Anwendungen, Springer-Verlag, (1970); doi: 10.1007/978-3-642-93002-7

Mode analysis for long, undamped cantilevers with added diamond tips of varying length for fast roughness measurements

Heinrich Behle¹, Uwe Brand¹

¹ Physikalisch-Technische Bundesanstalt, Bundesallee 100, 38116 Braunschweig, Germany
heinrich.behle@ptb.de

Summary:

In this article we present an FEM analysis of the change in resonance behaviour of 5 mm long piezoresistive cantilevers when they are modified with pencil shaped diamond tips of varying length. In a setup with glued cantilever base the length of the fixed bearing was examined as well. Simulations show that for a free cantilever base length of one fifth of the base no base oscillations occur. Base oscillations only occur for higher order modes of resonance with free base lengths greater one fifth.

Keywords: FEM, Mode analysis, diamond tips, piezoresistive Si-cantilever, roughness measurements

Introduction

For traceable roughness measurements in high aspect ratio microstructures the national metrology institute Physikalisch-Technische Bundesanstalt developed a profilometer [1] that makes use of cantilevers with integrated Si-tips and piezoresistive strain gauge [2]. This *Profilscanner* is a promising candidate for miniaturization of roughness measurements on-the-machine. In industrial applications measurement speed is to be minimized, therefore an analysis of the sensor behaviour for high traverse speeds is in order.

Probe system with CAN50-2-5

The probe attachment is shown in figure 1. A CAN50-2-5 cantilever (CiS Forschungsinstitut für Mikrosensorik, Germany) is glued to a holder and wire bonded on the same side, leaving a free length of the cantilever base L_1 and a fixed bearing length L_2 (see fig. 2).

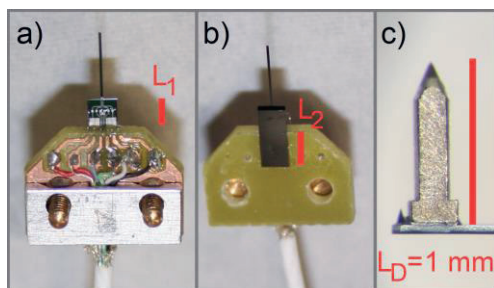


Fig. 1. holding plate for cantilever a) top view with bond wires, length of free cantilever L_1 Si base b) bottom view, glued length L_2 of Si base c) added pencil shaped diamond tip of length L_D

This holder is then applied to the Profilscanner setup and brought into contact with a sample surface. The cantilevers have a piezoresistive Wheatstone bridge at the connection point between cantilever and its Si base. A pencil shaped diamond tip is attached to the end of the cantilever, substituting the function of the wear prone Si tip (see fig. 2).

Surface Induced Excitation of Cantilevers

Independent of the nature of surface-probe interaction and neglecting other sources of excitation, the frequency of excitation f for a cantilever scanning over a sample is directly proportional to the traverse speed v of the probe over the sample

$$f = \frac{v}{\lambda_s}$$

where λ_s denotes the geometric wavelength of the sample surface [3]. Measuring with higher traverse speeds thus leads to a shift of excitation frequencies. To estimate if this may shift the excitations near resonance and induce distortions in our probe system, we computed the eigenfrequencies of the system.

FEM Modeling

The FEM simulation program *COMSOL Multiphysics* (version 5.3) was utilized to vary the parameters of the added diamond tip and the fixed bearing of the glued Si base. An eigenfrequency study for a geometry as shown in figure 2 was performed, using the *COMSOL solids*

module. It searches for complex analytical solutions λ of the eigenvalue problem

$$-\rho \omega^2 u = \nabla S$$

$$-i \omega = \lambda$$

with ρ the material density, $\omega = 2\pi f$ the real eigenfrequencies of the system and u the displacement field. The first 10 eigenfrequencies for all combinations of the following parameters were computed:

L_D in mm: 0.4 / 0.6 / 0.8 / 1.0 / 1.2 / 1.4 / 1.8 / 2.0

L_2 in mm: 2.5 / 3.0 / 3.5 / 4.0

Where L_2 was a fixed bearing. Additionally, all L_2 were computed for the cantilever without added pencil shaped diamond tip, denoted as $L_D = 0$. Higher values or smaller steps for L_2 were not of interest, since the bonding pads on the cantilever must be visible to be bonded, and since the gluing of the base to the holder is done manually.

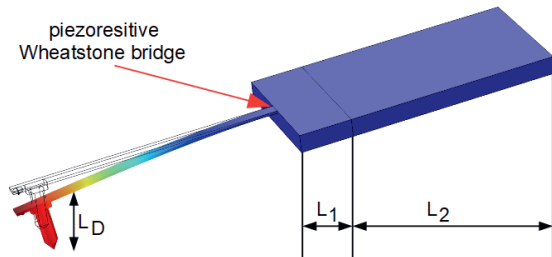


Fig. 2. geometric model of CAN50-2-5 type silicon cantilever with added pencil shaped diamond tip of length L_D . Silicon base with free length L_1 and fixed bearing length L_2 . Position of piezoresistive measuring bridge marked with red arrow. Shape of cantilever's first mode shown in pseudo colors.

Results

All simulations show a shift of eigenfrequencies to lower values for longer diamond tips, as expected for an oscillating beam with one-sided added mass. Two modes are shown exemplary in figures 3 and 4.

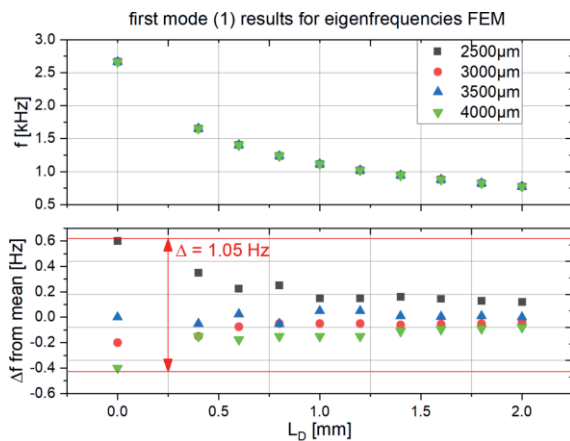


Fig. 3. FEM simulation results for first modes of probing system. Insignificant influence of fixed bearing length.

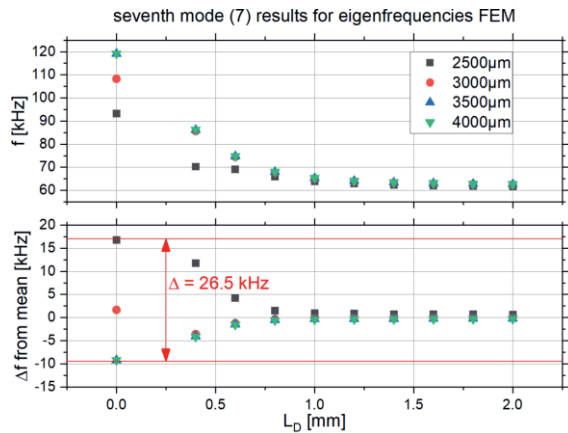


Fig. 4. FEM simulation results for seventh modes of probing system. First mode of 10 with significant influence of fixed bearing length.

Only higher order modes showed base oscillations after point examinations at the piezoresistive Wheatstone bridge. For all fixed bearing lengths $L_2 > 3.0$ mm the base oscillation was non-existent for all 10 simulated modes.

In conclusion only a combination of a cantilever base glued with a free length of the base greater than 1 mm and surface induced excitations in higher modes $n > 6$ can lead to a distortion of the bridge signal.

Acknowledgements

The author wants to thank Dr. Zhi Li for proof-reading the initial manuscript and gratefully acknowledges technical support from Mutaib Zackaria and Lars Daul as well as financial support through the European Union's European Metrology Programme for Innovation and Research (EMPIR), Grant no. 17IND05 *Micro-Probes*.

References

- [1] M Xu, *et al.*, Surf. Topogr.: Metrol. Prop. 2 (2014)
- [2] E Peiner, *et al.*, Meas. Sci. Technol. 19 (2008)
- [3] DJ Whitehouse, Handbook of Surface Metrology, IOP (1994)

Smart Ratchet Tie-Down Straps for Monitoring Cargo Safety

Ing. Yuqian WU¹, Dr. Zhichun YAN¹

¹ BCM SENSOR TECHNOLOGIES bvba, Industrie park, Brechtsebaan 2, 2900 Schoten, BELGIUM;
yuqian.wu@bcmsensor.com

Summary:

Newly designed wireless load pins (WLP) have been introduced here, by which traditional ratchet tie-down straps (RTS) have been developed into a smart ratchet tie-down straps (SRTS) in order to monitor the tension of the straps. Multiple SRTS can work with one monitor to form a Wireless Tension-Detect-and-Alert System (WTDAS) for cargo safety application. In case any SRTS becomes loosened or overloaded during transportation, the SRTS will wirelessly communicate with the monitor for its status change, and the monitor fixed on the dashboard in the driver cabin will alert the driver.

Keywords: cargo safety, wireless, smart ratchet tie-down strap, force sensor, tension monitoring

Background, Motivation and Objective

For safety reasons, it is advantageous to be able to monitor the tensile force of tie-down straps for cargo safety during transportation. For example, this would allow a truck driver to be alerted whenever one of RTS's on the truck becomes loosened or overloaded while driving.

In patent US8847758, the deformable element within the force sensor is a thin walled sleeve concentrically surrounding an axle bolt of a strap ratchet. This solution has a few problems as listed below:

- 1) If the thin sleeve would rotate slightly, the strain measured by the measuring element for the same force would be slightly different.
- 2) By being attached to the thin sleeve, the measuring element and its wiring are quite unprotected and can be damaged or corroded in use.
- 3) This design is an additional component.

In patent application CN101486329A, there is no communication with a remote sensor monitoring device.

Description of New Sensor and System

The WLP as shown in Fig. 1 can function as a bolt of a traditional RTS by fixing WLP in the frame of the RTS where the strap is attached on. In this way, the WLP turns a traditional RTS into a smart RTS (SRTS), as shown in Fig. 2,

which can monitor the tension of the strap. Multiple SRTS's can work with one monitor to form a WTDAS. On the monitor, e.g., as shown in Fig. 3, there are several LED's. Each LED uses 3 colors to indicate three statuses of the corresponding SRTS – green refers to fastened straps, red to loosened or overloaded straps, and orange to an error status (e.g., low battery, disconnection, etc.). In case a SRTS becomes loosened during transportation, this SRTS will wirelessly communicate with the monitor for its status change, and the monitor which is fixed on the dashboard in the driver cabin will alert the driver by turning the corresponding LED from green to red color and having its alarm triggered. Once the loosened SRTS is tightened again, the corresponding LED goes back to green color and the alarm stops.

In such the WTDAS, the monitor has been pre-set to wirelessly communicate with number of specific SRTS (i.e., specific WLP). Therefore, the user can set up the WTDAS without need for any computer, and each of the systems works independently, i.e., different systems do not interfere each other.

Results

Taking a ready-made WTDAS as example, the WTDAS has features as follows:

- 1) One monitor as shown in Fig. 3 has 16 LED's and can communicate with up to 16 smart RTS (i.e., with 16 WLP);

- 2) Communication signal: license-free 2.4GHz radio frequency;
- 3) Communication distance: 20 meters for truck use;
- 4) Independent system without interference of another system;
- 5) Capacity of WLP: 5kN;
- 6) WLP powered by: 2x 1/2AA batteries;
- 7) Batter life: depending on use conditions (i.e., operating temperature, communication distance and communication rate), if the WLP works at room temperature and communicates with the monitor in distance of 20 meters without any obstacles by rate of 1 time per minute, the battery life is estimated to about 1 year;
- 8) IP rating of WLP: IP66.

Illustrations, Graphs, and Photographs



Fig. 1. Photo of two WLP's



Fig. 2. Photo of a smart RTS



Fig. 3. Photo of a smart RTS

Packaging concepts and development progress of ceramic thermocouples for up to > 1800 °C

*Paul Gierth, Lars Rebenklau, Bing Feng, Hans-Peter Martin
Fraunhofer IKTS, Winterbergstrasse 28, 01277 Dresden, Germany
paul.gierth@ikts.fraunhofer.de*

Summary:

Measurement of temperatures is critical for many technical applications in the modern industries. Common used temperature sensors are based on metallic and not many alternatives are given until today. Therefore, semiconductive ceramic materials based on boron carbide were developed to generate miniaturized thermocouples for temperatures up to > 1800 °C. An overview of the ongoing development process of the system embedding of this kind of thermocouples is given. Risks and chances of ceramic thermocouples were discussed.

Keywords: high temperature, thermocouple, ceramic, packaging

Motivation

The measurement of temperatures is critical for many technical applications in the modern industries. Different measurement concepts can be used depending on process temperatures. Most common are thermocouples (TC) consisting of two different metallic. Many of the common metallic combination [1] show acceptable long time stability at high temperatures up to 1400 °C. For temperatures measurement above 1800 °C are only thermocouples type A and C (combinations of Wolfram and Rhenium) possible combinations, which have insufficient long time stability. Infrared thermography could also be used but has many disadvantages according sensitivity and system price. Therefore, a clear demand on long time stability thermocouples for temperature ranges above 1800 °C is given. First ceramic thermocouples were already described in the 1980s [2]. Fundamental working principles were demonstrated in this publication, but many technology problems could not be solved until today. Especially, a not very high diffusion stability between the used ceramic components was not acceptable. Therefore, novel ceramic composites were developed [3], which show very promising electrical and thermoelectrically characteristics. But now, this materials needs to be transferred into a system concept to generate workable thermocouples.

Semiconductive ceramic thermocouples

Semiconductive ceramic materials based on boron carbide were developed to generate miniaturized thermocouples for temperatures up to

> 1800 °C. Therefore, extrusion and high temperature interconnection technologies needs to be developed. Additionally, signal analysis algorithms were reviewed to improve the system.

Results

Materials based on boron carbide and different metallic borides were developed as paste-like mass and characterized after sintering. The first results are very promising (see Fig. 1).

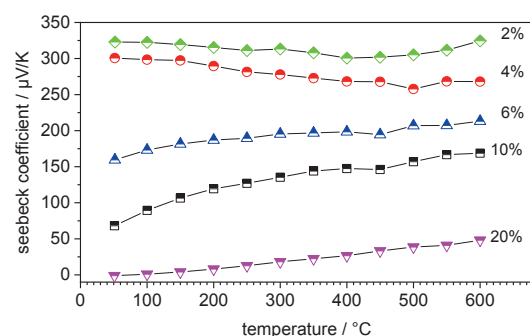


Fig. 1. Seebeck coefficients of sintered boron carbides with different mass-% of metallic borides.

Implementation situation for thermocouples in different oven types with temperatures > 1800 °C were evaluated. Based on these results, first system concepts were developed and realized. The materials can be extruded in different shapes in a nearly endless length, but are limited in the length of available sintering ovens. Therefore, all system designs assuming an interconnection between semiconductive ceramics and metallic compensation cables inside the oven chambers.

Compensation cables with identical characteristics like the developed ceramics are not available. Therefore, the measured temperature T_1 must be referenced to the temperature T_2 at the interconnection joints between ceramic and metallic parts (see fig. 2). Additional electromotive force EMF_b can be negligible if both metallic wires are made of the same material.

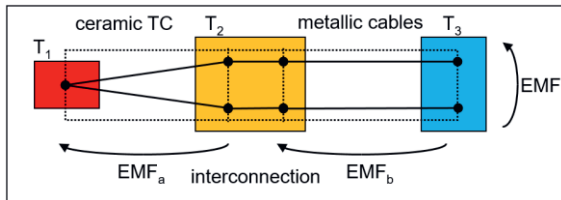


Fig. 2. Forming of the measurement signal of ceramic thermocouples with metallic cables.

Unlike common metallic TC, the reference temperature area can't be implemented in the voltage measurement tool. Therefore, a concept for controlled and measurable reference temperatures was developed (see Fig. 3)

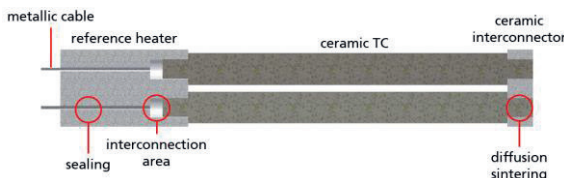


Fig. 3. System concept for ceramic TC with reference heater at interconnection joints.

The interconnection joints between metallic parts and ceramics were integrated in a small insulating ceramic element. This element compensates temperature differences between the interconnection joints, which could influence the measuring signal by generating additional thermo voltages. Interconnection joints itself could be generated by brazing, active soldering or welding. Especially the already in thermocouples industries well established welding technology would be preferable. Boron carbide could be welded i.e. with platinum or nickel wires. This kind of joints can withstand very high temperatures as seen in Fig. 4.

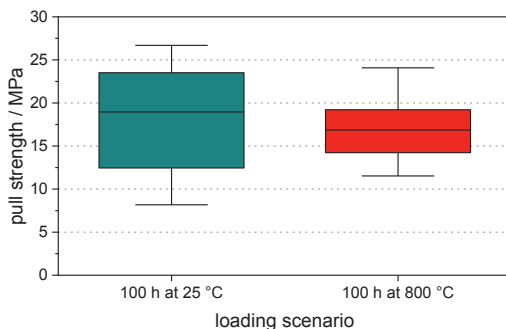


Fig. 4. Pull strength of welded platinum wires on boron carbide after different loading scenarios.

This basic system design is compatible to industrial thermocouple terminal heads and can be mounted in a neck tube. Temperature measurement at this reference area could be realized by implementing an additional metallic thermocouple in a hole inside the insulating ceramic reference area. In that way, measured temperature T_1 is always referenced to a resulting temperature T_2 . This requires complex signal analyzing algorithms, so that a constant reference temperature T_2 would always be preferred. Such constant temperature can be realized by functionalizing the insulating ceramic at the interconnection area into a temperature controlled reference area by screen printing platinum heating areas on its surface. Therefore, needed heating energy to generate an adjustable reference temperature between 300 °C to 800 °C was calculated. Corresponding heating resistances are designed (see Fig. 5).



Fig. 5. Realized adjustable high temperature reference areas. Left: screen-printed layout of orange heater area and blue interconnection pads, right: realized functional samples with blue insulating surface coating.

By using these adjustable reference elements, the heat transfer from the hot end of the ceramic TC to the cold end could be reduced. Therefore, a much better temperature signal stability and an improvement of the sensor long time stability is expected. Additionally, a self-monitoring of the TC is possible by the wide adjustability of the reference temperature.

Conclusions

Ceramic TC are a promising alternative to metallic elements in terms of increasing EMF values and long-time stability. System integration could be more complex compared to common TC, but offers interesting alternative measurement and self-alignment aspects.

References

- [1] DIN Standard 60584-1: Thermocouples – EMF specification and tolerances, Beuth Verlag, 2014.
- [2] Hunold, K. et al. (1982). German Patent No. DE3235838. Kempton, Germany.
- [3] Martin, H-P, Feng, B, Michaelis, A. Pressureless sintering and properties of boron carbide composite materials. Int J Appl Ceram Technol. 2019; 00: 1– 6. <https://doi.org/10.1111/ijac.13423>.

Validation of high temperature stable sensor packaging materials and methods

Paul Gierth, Lars Rebenklau, Henry Barth
 Fraunhofer IKTS, Winterbergstrasse 28, 01277 Dresden, Germany
 paul.gierth@ikts.fraunhofer.de

Summary:

Many modern sensor concepts are only limited in their operating temperature because of insufficient packaging solutions. Therefore, novel-packaging concepts need to be evaluated on all interconnection levels. This work summarizes possible materials, technologies and characterization methods for reaching high temperature stable packages. Especially materials for sensor chips mounting inside ceramic packages and package connector mounting up to 600 °C were focused and discussed.

Keywords: high temperature, packaging, ceramic, interconnection, resistance welding

Motivation

Modern technology trends like big data need reliable data sources. Sensors in all kind of fields are the basic elements of these technologies. Generated sensor signals are needed for process simulation or controlling especially during challenging production processes of materials or electronic components. Challenging for most kind of sensors is, that many of these processes take place at very harsh environments, like high pressures, acid atmospheres or simply high temperatures. Existing packaging technologies are based on integrating a sensor element in a metallic or ceramic package and hermetically sealing it. All therefore needed process steps need to be further developed to fulfill requirements of higher environmental temperatures. The complete sensor packaging process can be splitted into five separate steps according Fig. 1.



Fig. 1. Process flow of sensor element packaging.

Packaging process is divided into package material selection (step 1), package connection if needed (step 2), assembling of the sensor element inside the package (step 3), interconnection between package and sensor element (step 4) and hermetical package enclosing (step 5). Influence of high temperatures on ceramic packages and their electrical characteristics is already discussed in [1]. Long time stability of welded interconnection joints at high temperatures was evaluated in [2].

Present study is focusing on connection and assembling technologies. Main aim is demonstrate methods for brazing pins on ceramic packages and developing mechanical characterization methods for assembling materials up to 600 °C.

Technology development and characterization method up to 600 °C

Technology for generating high temperature stable brazing connections to ceramic packages were developed. Outstanding achievement of the underlying project is the development of a shear test method up to 600 °C, which is compatible to commercially available shear test tools. Degradation mechanisms of different interconnection materials could be inspected in that way insitu during the real conditions.

Characterization of brazed package joints

Kovar pins with ENIG finish were brazed using mainly silver-based brazing solders on different kind of metallization. Materials and process conditions have been widely varied to generate a better understanding of their influence on the mechanical joint characteristics.

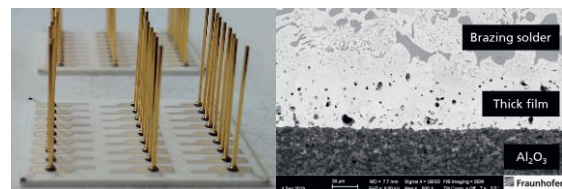


Fig. 2. Brazing of Kovar connectors on ceramic substrates. Left: brazing samples, right: cross section of brazed contact

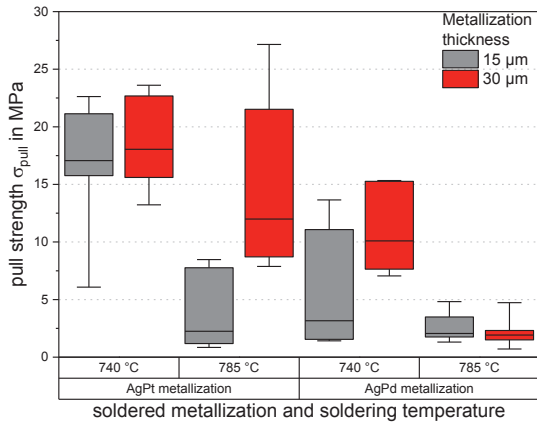


Fig. 3. Mechanical characteristics of brazed high temperature connection joints und various conditions

High temperature stable brazing joints could be generated and correlations between process conditions, material selection and resulting mechanical characteristics could be given.

Characterization of assembling joints up to 600 °C

Active solders, sintering materials or ceramic adhesives, could be used to realize high temperature stable sensor assembling inside a ceramic package. Ceramic adhesives should be preferred because they show nearly comparable thermal expansion to the package itself. Mechanical stability of these kind of joints could in most cases only be inspected before and after a high temperature storage but not under real conditions. Therefore, a high temperature shear-strength measurement setup has been developed (Fig. 4).

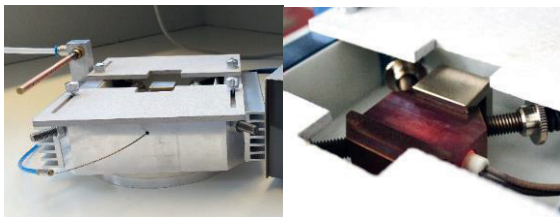


Fig. 4. High temperature shear test rig. left: complete rig with cooling airflow and temperature control, right: core heating table heated up to 600 °C.

The developed test rig was mounted on a Dage Series 4000 shear-force measurement tool and different high temperature adhesives were evaluated. It could be found that all kind of ceramic adhesives show completely different mechanical joint characteristics und different test temperatures (Fig. 5). Even promising materials, which should withstand temperatures up to over 900 °C, could show enormous interface degradations und real conditions (Fig. 5 SiO_2).

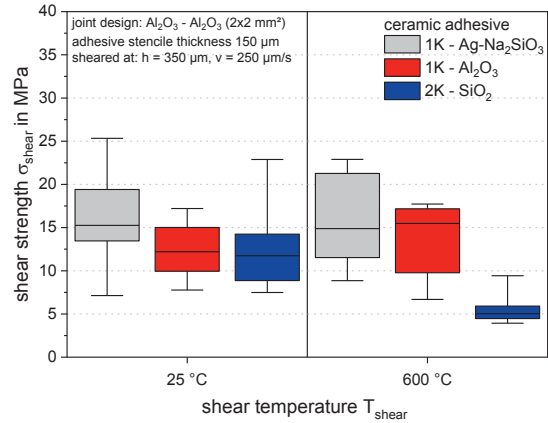


Fig. 5. Comparison of assembling adhesive joint strength at different test temperatures

This method is highly recommended for initial material screening before expansive long time storages at high temperatures takes place. For example, a degradation trend of the SiO_2 adhesive and an increasing cross-linking trend of the Al_2O_3 conductive as shown in Fig 6 could already be postulated by the initial measurement at 600 °C (compare Fig 5).

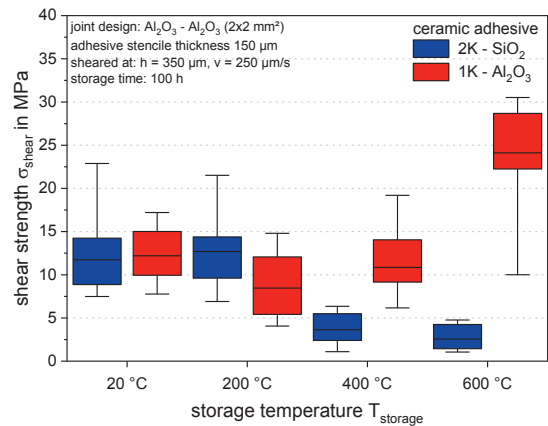


Fig. 6. Changing in assembling adhesive joint strength after high temperature storage for 100 h

References

- [1] L. Rebenklau, P. Gierrth, H. Barth, High-Temperature Packaging for Sensors, PCIM Europe 2019, 1-7 (2019); ISBN: 978-3-8007-4938-6
- [2] P. Gierrth, L. Rebenklau, Development and analysis of high temperature stable interconnections on thick films using micro resistance welding for sensors and MEMS, 7th Electronic System-Integration Technology Conference (ESTC), 1-5 (2018), doi: 10.1109/ESTC.2018.8546509.

Multiphysics Electro-Thermal Simulation of Pt Microheater Structures for Gas Sensing Application

Francis Oliver Vinay Gomes¹, Stephan Linke¹, Paul Wafo², Vincent Leger²

¹ TE Connectivity Sensors Germany GmbH, Hauert 13, 44227 Dortmund, Germany

² TE Sensor Solutions, 4 Rue Gaye-Marie, 31027 Toulouse, France
Oliver.Gomes@te.com

Summary:

Air quality sensing is growing fast in several applications, such as monitoring air quality in automobiles, smart homes or industrial processes. Metal-oxide semiconductor-based sensors require a chemical inert microheater with long lifetime and fast response time. To meet the requirements of the next-gen microheaters, a thorough understanding of the complex interplay between the underlying thermal conduction, convection and radiation processes is needed, which is obtained through FE simulations. The results will help to optimize and miniaturize microheater design arrays for next-gen gas sensors.

Keywords: platinum thin film, microheater, gas sensing, high temperature, multiphysics simulation

Motivation

Today the air quality sensor (AQS) market is dominated by the automotive industry. But in the future additional demand is seen from smart homes and wearables for localized information of the environment. A metal-oxide semiconductor (MOS)-based AQS consist of a μ -heater which provides uniform temperature (>300 °C) crucial for the optimal functioning of the MOS gas sensor (Fig. 1a).

Platinum (Pt) μ -heaters are chemically inert, with long lifetime, fast response and allow handling of higher temperature and current density. The next-gen AQS will have low power miniaturized arrays of μ -heaters for improved detection of multiple gases. Understanding of the Pt μ -heater is essential to meet customer product specification at lower production cost (scaling). Therefore, ANSYS thermo-electric simulations of Pt μ -heaters were performed to establish a model of the current μ -heater design. This model can be further used to develop and optimize the next-gen μ -heaters.

Method – Electro-Thermal Analysis

First, a three-dimensional (3D) model is set up in the finite element (FE) program. During the simulation and the result analysis, parameters such as maximum temperature, temperature uniformity, power consumption and current density are considered essential as they affect the performance of the microheater (Fig. 1b). These parameters are determined by factoring in appropriate material characteristics and boundary conditions. From the prospect of sim-

ulation, the material characteristics: thermal conductivity of Silicon Rich Nitride (SiRN) as membrane material and the IR-emission coefficient from Pt (ϵ_{Pt}) are significant – but not available from literature in the temperature range up to 1000 °C precisely [1-3].

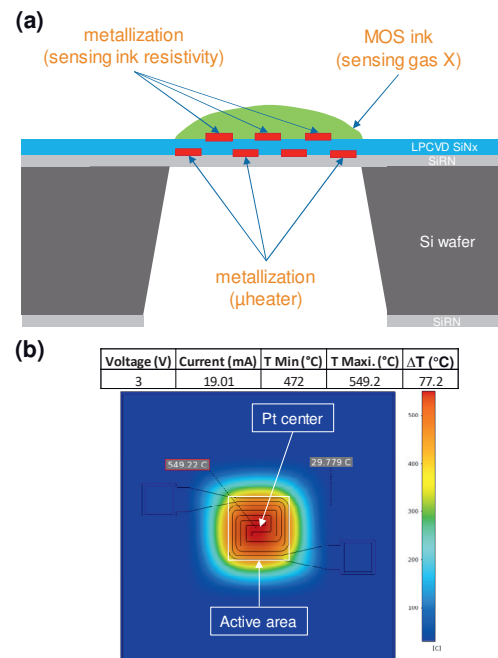


Fig. 1. (a) Cross-section view of the MOS-based air quality sensor. (b) Simulated thermal heat distribution at 3V.

Characteristics of the Pt Microheater

The performance of the Pt μ -heater is given by the maximum temperature vs. applied power curve i.e. for a certain applied power using

pulse-width modulation (PWM) technique the μ -heater reaches a defined temperature at steady state crucial for the working of the MOS gas sensing film. In our simulation we accounted for the different modes of heat transport i.e. conduction, convection and radiation (Fig. 2). The gray curve shows almost a linear behaviour if only conduction and convection are considered. However, non-linear behaviour was observed when radiation mode was accounted. The orange curve demonstrates the expected non-linear curve when all three modes of heat transport are simulated i.e. at an applied power of 36 mW and 55 mW we obtain temperature of 360 °C and 510 °C, respectively. Furthermore, the radiation impact is less visible from 0 – 65 mW but above 65 mW non-linearity in the curve is observed.



Fig. 2. Simulated maximum temperature vs. applied power curve for combinations of different modes of heat transport.

Different Modes of Heat Transport

Fig. 3 shows the contribution rate with increasing temperature for each mode of heat transport where three distinct regions have been observed.

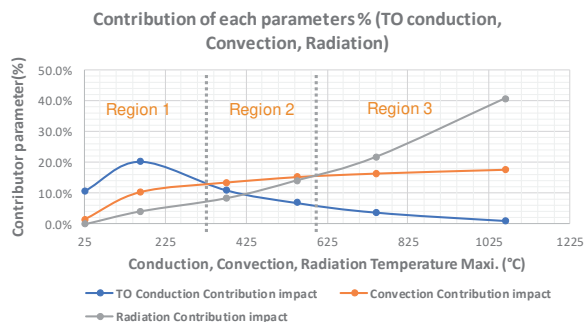


Fig. 3. Contribution rate for different modes of heat transport.

In region 1 (25 °C – 315 °C), conduction dominates i.e. the heat transport takes place via the SiRN membrane (mainly), silicon body and the TO-39 header. In region 2 (315 °C – 585 °C), contribution from convection is more important i.e. heat dissipated to ambient environment. We also observe the radiation and conduction contribution are gradually increasing and decreasing, respectively. In region 3 (> 650 °C), radiation mode dominates as the μ -heater starts to glow red. The convection contribution remains constant through the different regions but the

decrease in conduction contribution with increasing temperature is attributed to boundary conditions which results in a qualitative heat analysis of each dissipation modes.

Comparison of I-V Characteristics

The I-V characteristics generated from the electro-thermal FE model (green curve) were compared with fabricated MEMS Pt μ -heater measurement results (blue curve) as shown in Fig. 4. The simulated I-V curve trails very close to the fabricated Pt μ -heater measurement. This implies the developed FE model can be used to predict the thermo-electric behaviour of Pt μ -heater on suspended membranes with reasonable accuracy. The approach will help to miniaturize the microheater design to meet future requirements and predict its electro-thermal behaviour without the need of fabrication, thereby saving cost.

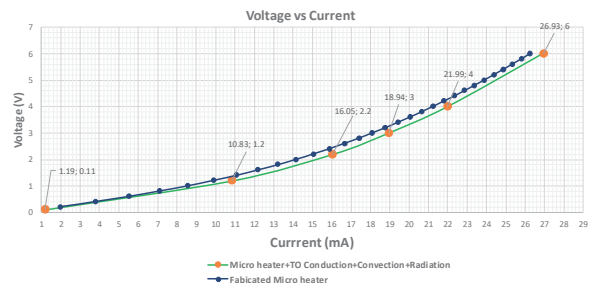


Fig. 4. Comparison of I-V characteristics for fabricated Pt microheater (blue curve) and simulated Pt microheater (green curve).

Outlook

In summary, Pt μ -heater for MEMS-based AQS has been studied in detail. Principle of joule-heating has been discussed to understand the working principle of the μ -heater which satisfies some requirements such as low power consumption and better temperature uniformity with low risk to break and burn through. Crucial parameters such as maximum temperature, temperature uniformity, power consumption and different modes of heat transport have been discussed. In the end, the simulation results from the multiphysics FE model align with real measurements which will help to reduce the development time for next-gen Pt μ -heater arrays.

References

- [1] A. E. Kaloyeros, et al., *ECS Journal of Solid-State Science and Technology*, 6 (10) 691-714 (2017); doi: 10.1149/2.0011710jss
- [2] S. Deemyad, et al., *Review. of Sci. Instruments*, 79, 086105 (2008); doi: 10.1063/1.2966394
- [3] S. Ingvarsson, et al., *Optics Express*, 15 (18), 11249-11254 (2007); doi: 10.1364/OE.15.011249

Equivalent Circuit Model and Evaluation of Inductive Conductivity Sensors

Michael Vogt¹, Malte Mallach², Theresia Lange², Jan Förster²

¹ KROHNE Messtechnik GmbH, Duisburg, Germany,

² KROHNE Innovation GmbH, Duisburg, Germany

m.vogt@krohne.com

Summary:

Inductive sensors allow for contactless measurement of the electrical conductivity of liquids. A first magnetic coil is used for inducing an eddy current into the liquid, and this current is measured with a second coil. In this contribution, an equivalent circuit model is presented, including also a parasitic direct coupling and the liquid's electrical permittivity. It will be shown analytically and with measurement results that the real part of the ratio of the measurement voltages has to be evaluated and that a trans-impedance amplifier with a small input-impedance has to be used for accurate measurements.

Keywords: Measurement sensor, electrical conductivity, liquid, coil, eddy current

Introduction

The measurement of the *electrical conductivity* of liquids is an important task in many industrial processes [1]. In the case of *aggressive* liquids (acids, bases, etc.), preferably *inductive* conductivity sensors are used, because no electrodes are in contact with the liquid [2].

Inductive Conductivity Sensors

Fig. 1 shows the setup of an inductive conductivity sensor, which is *immersed* into the liquid:

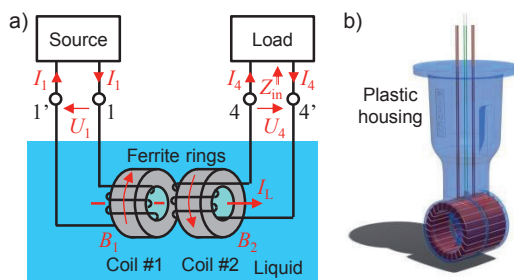


Fig. 1. Inductive conductivity sensor: a) Principle and connection setup, b) sensor design with housing.

The first toroidal coil #1 is driven by a sinusoidal voltage U_1 at an angular frequency $\omega = 2\pi \cdot f$ (frequency f), resulting in a current I_1 and a magnetic inductance B_1 . The latter induces an *eddy current* I_L into the *liquid*, and this current is flowing through the inner hole of the sensor housing and its surrounding. The eddy current I_L causes a magnetic inductance B_2 in the second toroidal coil #2, which induces a voltage U_4 . The coil #2 is loaded with a *trans-impedance*

amplifier (with an input-impedance Z_{in}), resulting in a current $I_4 = U_4 / Z_{in}$.

Equivalent Circuit Network

In Fig. 2, an equivalent circuit network (ECN) of the sensor in Fig. 1 is shown:

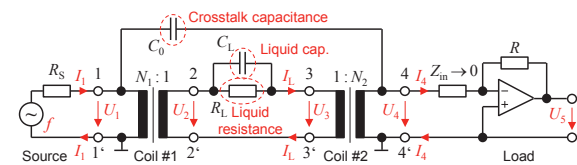


Fig. 2. Inductive conductivity sensor: Equivalent circuit network.

The *electrical conductivity* σ_L of the *liquid*, which is to be measured here, is included in the *conductance* $G_L = 1 / R_L = \sigma_L / k_{cell}$ (*resistance* R_L) of the liquid, with the so-called '*cell constant*' k_{cell} of the sensor (depending on its geometry). The two coils (*numbers of windings* N_1 and N_2 , *inductances* L_{11} and L_{44}) together with the current loop through the conductive liquid are each represented by an ideal, lossless transformer [2]. Furthermore, the ECN in Fig. 2 also includes a *parasitic crosstalk capacitance* C_0 (*direct coupling* between the two coils), and the *capacitance* $C_L = \epsilon_L / k_{cell}$ of the *liquid* (permittivity $\epsilon_L = \epsilon_{r,L} \cdot \epsilon_0$, relative permittivity $\epsilon_{r,L}$, vacuum permittivity ϵ_0). Based on Fig. 2, the following ratio H_m between the *output voltage* $U_5 = -R \cdot I_4$ and the *excitation voltage* U_1 is given:

$$H_m = \frac{U_5}{U_1} = -R \cdot \frac{\frac{N_2}{N_1} + j\omega \cdot R_L \cdot (N_2^2 \cdot C_0 + \frac{N_2}{N_1} \cdot C_L)}{Z_{in} \cdot (1 + j\omega \cdot R_L \cdot C_L) + R_L \cdot N_2^2 \cdot (1 + j\omega \cdot Z_{in} \cdot C_0 + Z_{in} / (j\omega \cdot L_{44}))} \quad (1)$$

The concept of the sensor is to measure the voltages U_5 and U_1 and to assess their ratio H_m in order to estimate the resistance R_L of the liquid (and so the conductivity σ_L) by means of (1). However, the parameters L_{44} , C_0 , and also Z_{in} can significantly *change* over different samples of the same type of sensor, and also over temperature, aging, etc. For this reason, these parameters and also the *unknown* C_L have to be *eliminated* from the measurement (compare [1]). This can be achieved by using a *trans-impedance amplifier* with a sufficiently *small* input-impedance Z_{in} , a sufficiently *large* angular frequency ω , and a *large* inductance L_{44} giving $|Z_{in}| \ll \omega L_{44}$, and $|Z_{in}| \ll 1/(\omega C_0)$, and $|Z_{in}| \ll R_L \cdot N_2^2 / |1 + j\omega R_L C_L|$. Under these conditions, H_m is given as follows, see (1):

$$H_m = \frac{U_5}{U_1} = -R \cdot \left(\frac{1}{N_1 \cdot N_2 \cdot R_L} + j\omega \cdot \left(C_0 + \frac{C_L}{N_1 \cdot N_2} \right) \right) \quad (2)$$

The result in (2) shows that R_L is now directly accessible from the *real part* $\text{Re}(H_m)$ of the voltage ratio H_m , scaled by the *numbers of windings* N_1 and N_2 of the two coils:

$$\text{Re}(H_m) = \text{Re} \left(\frac{U_5}{U_1} \right) = -\frac{1}{N_1 \cdot N_2} \cdot \frac{R}{R_L} \quad (3)$$

Because of this scaling in (3), *inductive* sensors are preferably used for liquids with *large* conductivities σ_L (i.e. with *small* resistances R_L). In contrast, conductivity sensors with *Galvanic coupling* are to be preferred for liquids with *small* conductivities [1].

Experimental Evaluation

Measurements have been performed with a sensor (with $k_{\text{cell}} = 6.25 \text{ cm}^{-1}$, $N_1 = N_2 = 25$, $L_{11} = L_{44} = 12 \text{ mH}$, $f = 2.5 \text{ kHz}$, $R = 1 \text{ k}\Omega$) in order to verify the findings above and to evaluate the achievable measurement accuracy and range. The voltage ratio H_m has been directly measured with a calibrated *vector network analyzer* (model Bode 100; OMICRON electronics GmbH, Klaus, Austria). For measurements under *known* and *well-defined* conditions, the liquid has been replaced by a *metallic wire* (as current loop) through the inner hole of the sensor. The loop has been loaded with a changing *lumped* resistance $R_L = 12 \Omega \dots 220 \text{ k}\Omega$. For each different R_L , an according *nominal given* conductivity $\sigma_L = k_{\text{cell}} / R_L$ has been calculated. In Fig. 3, the *measured nominal* conductivity σ_L over the varying *given* conductivity is shown for both, using the *magnitude* $|H_m|$ of the voltage ratio H_m only and for using the *real part* $\text{Re}(H_m)$ of H_m :

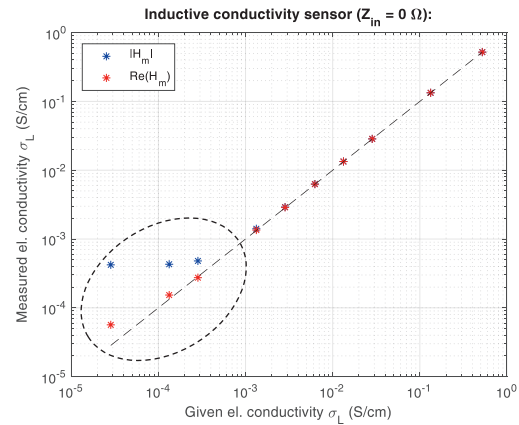


Fig. 3. Measured nominal conductivity: Magnitude and real part of voltage ratio (for $Z_{in} = 0 \Omega$).

The results confirm that the measurement range of the sensor can be largely *extended* towards small conductivities by using the *real part* of the voltage ratio H_m and a *small* input-impedance ($Z_{in} \rightarrow 0$) in order to eliminate the influence of the unknown parasitic elements. In Fig. 4, same plots as in Fig. 3 are shown, but now for a *large* input-impedance $Z_{in} = 330 \Omega$:

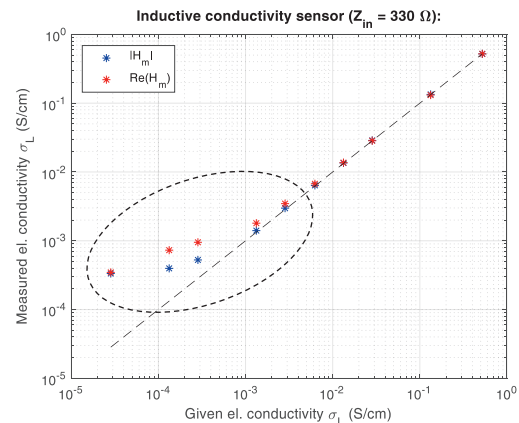


Fig. 4. Same as in Fig. 3 (but for $Z_{in} = 330 \Omega$).

It can be seen that the measurement error is now, as expected, much larger with both, using the real part and the magnitude of H_m . In conclusion, a *trans-impedance amplifier* with a *small input-impedance* has to be used, and the *real part* of the voltage ratio has to be evaluated to guarantee for precise measurements over a large measurement range.

References

- [1] M. Vogt, S. Hidalgo, M. Mallach, T. Lange, J. Förster, T. Musch, Concepts for accurate electrical conductivity measurement of liquids in industrial process analytics, *Sensoren Messsyst.*, 105-112, (2019); doi: 10.5162/sensoren2019/1.4.3
- [2] K. Striggow, R. Dankert, The exact theory of inductive conductivity sensors for oceanographic application, *IEEE J. Oceanic Eng.*, vol. 10, 175-179, (1985); doi: 10.1109/JOE.1985.1145085

Design of Planar Capacitive Transducers for the Detection of Road Surface Wetness

Jakob Döring, Dennis Lepke, Karl-Ludwig Krieger

Institute of Electrodynamics and Microelectronics (ITEM.ae), University of Bremen, Germany
doering@item.uni-bremen.de

Abstract

The increasing level of automation in today's motor vehicles causes road surface wetness detection to steadily gain in importance. One suitable approach is the detection with planar capacitive sensors on a motor vehicle's wheel arch liner. In order to design transducers for the detection of road surface wetness, different figures of merit are analyzed by means of the finite element method (FEM) and set in relation to specific design parameters in this paper. Furthermore, we propose three complementary design domains enabling the distinction of a wide range of wetness levels.

Keywords: Planar capacitive sensors, interdigital transducers, wetness detection, vehicle safety systems, finite element method.

Introduction

Even nowadays, road surface wetness can still be considered a reason for traffic accidents, since it can lead to a significant loss of tire traction. As today's vehicles do not provide direct information about the road's current surface wetness, the driver has to estimate it intuitively and experience-based, which can have fatal consequences in case of misjudgments. Furthermore, knowledge of road surface wetness will gain in importance due to highly or fully automated driving.

In [1], we presented a novel approach for road surface wetness detection with planar capacitive sensors on a vehicle's wheel arch liner. Since a wet road surface causes tires to whirl up water in the form of drops, the sensors can detect the impinging drops and thus indirectly infer road wetness. Due to a correlation of road wetness, wheel speed and the size and quantity of whirled-up water drops, a distinction between wetness levels is basically possible. In order to classify a wide range of wetness levels, one possible approach is to arrange different sensor designs on the wheel arch liner. As the design parameters have a significant impact on its characteristics, the electrode design is essential to meet the application's requirements [2]. Therefore, we present the design of complementary planar capacitive transducers enabling the distinction between wetness levels in this paper.

Preliminaries

In order to design transducers with regard to the classification of a wide range of wetness levels,

we use COMSOL Multiphysics for two-dimensional electrostatic FEM simulations. In this paper, we focus on flexible printed circuit boards as they are ideally suited for the integration on a wheel arch liner [1]. Therefore, design parameters that are generally manufacturable are considered in the simulations, as depicted in Fig. 1. As previous work has shown, increasing the ratio of electrode width w to distance d improves SNR [2]. Thus, in consideration of design limitations, the distance is constantly kept at $150\ \mu\text{m}$ in the simulations. Furthermore, we define a fixed electrode area of $50\ \text{mm} \times 50\ \text{mm}$. The fixed electrode distance and area result in a dependency of width w and the number of digits n :

$$w = \frac{a - d \cdot (2 \cdot n - 1)}{2 \cdot n}. \quad (1)$$

Additionally, the active sensing area's length l_{sa} , which is used to determine the approximated absolute capacitance, is dependent on w :

$$l_{\text{sa}} = a - 2 \cdot (w + d). \quad (2)$$

In order to meet all boundary conditions n can be varied from 2 to 83 in the simulations.

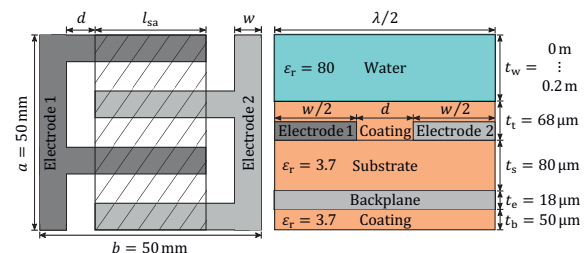


Fig. 1. Schematic top view (left) and cross-section view (right) of an interdigital transducer.

Discussion

For the classification of different wetness levels, two fundamental figures of merit in sensor design are the dynamic range and the penetration depth. Due to a trade-off between these factors, the choice is essential to meet the application's requirements [1, 2]. In Fig. 2, the penetration depth and the dynamic range are shown against the possible number of digits. With an increasing number of electrode fingers, the penetration depth decreases from around 13 mm to 0.01 mm. Furthermore, the dynamic range significantly increases until a point is reached, where the major part of the electric field progressively concentrates on the coating area due to a declining penetration depth. Since there is no benefit of a greater number of digits for the target application, we focus on the range of 2 to 20 digits, as shown in Fig. 2 (right).

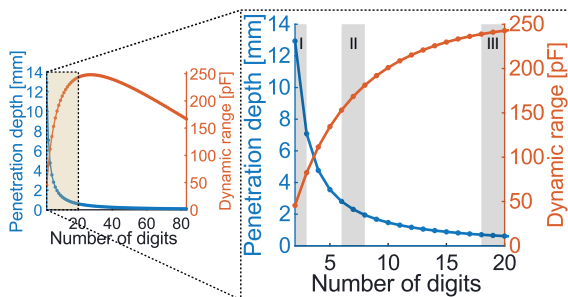


Fig. 2. Penetration depth and dynamic range against the number of digits.

In order to classify between different wetness levels, we exemplarily choose three design domains (I-III, Fig. 2) suitable for the application's requirements. For a more detailed analysis of the three domain's characteristics, Fig. 3 shows the sensitivity $\Delta C/C$ for an increasing water layer thickness t_w from 0.005 mm to 6 mm against the studied number of digits. Furthermore, the difference between the asymptotic capacitance and the capacitance at different water layer thicknesses $\Delta C_\infty = C(t_w \rightarrow \infty) - C(t_w)$ is shown, displaying the remaining part of the dynamic range.

Due to its high penetration depth (> 7 mm), the first design domain enables to distinguish between greater water layer thicknesses. In contrast to the other domains, the dynamic range is more evenly distributed within these thicknesses. Although the domain's dynamic range is small in comparison, for t_w of 2 mm there are still about 25 % of it left, as shown in Fig. 3. However, there are disadvantages regarding the classification of smaller water layer thicknesses.

The second domain covers a wide classification range of water layer thicknesses. Besides the dynamic range, which approximately doubles, the sensitivity significantly increases for all water layer thicknesses. Due to the lower penetration

depth of about 2 mm – 3 mm, the upper distinction limit is decreasing, as depicted in Fig. 3. On the other hand, the difference between smaller water layers widens, enabling even to distinguish in the range of micrometers.

In order to distinguish between very small water layer thicknesses with a good resolution, the third domain is proposed. Here, the maximum in dynamic range and sensitivity for given boundary conditions is approximately reached. Especially the high difference for very small water layers is advantageous. Since there is always a trade-off, the increasing number of digits leads to a penetration depth of about 600 μm to 700 μm in this domain. Therefore, the asymptotic capacitance is reached early, resulting in disadvantages with regard to greater thicknesses.

In summary, the three proposed design domains are complementary regarding the distinction of various wetness levels. Hence, they enable to cover a wide range of wetness levels.

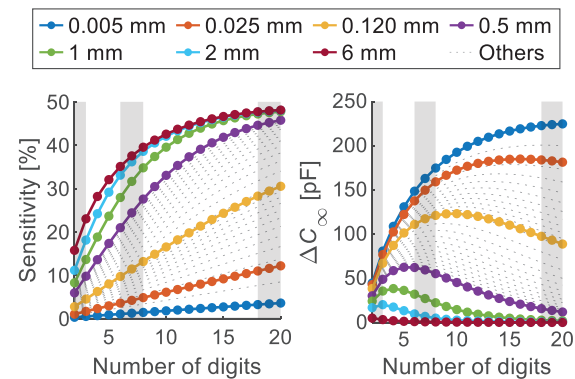


Fig. 3. Sensitivity and difference between the asymptotic capacitance and the capacitance at different water layer thicknesses against the number of digits.

Conclusion

In this paper, we presented the design of complementary planar capacitive transducers for the detection of road surface wetness. By means of FEM simulations different figures of merit were analyzed and set in relation to the specific design parameters. Furthermore, we exemplarily proposed three design domains enabling the distinction of a wide range of wetness levels due to their characteristics.

References

- [1] J. Döring, L. Tharmakularajah, J. Happel and K.-L. Krieger, "A novel approach for road surface wetness detection with planar capacitive sensors," *Journal of Sensors and Sensor Systems*, vol. 8, no. 1, pp. 57–66, 2019, doi: 10.5194/jsss-8-57-2019.
- [2] J. Döring, L. Tharmakularajah, and K.-L. Krieger, "Study of interdigital electrode structures for the detection of water spray," *Tagungsband*, pp. 700–707, 2019, doi: 10.5162/sensoren2019/P2.7.

Resistance Wire Thermometers for Temperature Pulse Measurements on Internal Combustion Engines

*Varun Venkataraman*¹, *Yushi Murai*²,

*Michael Liverts*², *Ramis Örlü*², *Jens H.M. Fransson*², *Ola Stenlås*^{1,3}, *Andreas Cronhjort*¹

¹CCGEx, Dept. Machine Design, KTH Royal Institute of Technology, 100 44 Stockholm, Sweden

²CCGEx, Dept. Engineering Mechanics, KTH Royal Institute of Technology,
100 44 Stockholm, Sweden

³Scania CV AB, 151 87 Södertälje, Sweden

Varun Venkataraman: varunve@kth.se

Summary:

This study revisits the design of resistance wire thermometers (RWTs) for measuring time-resolved temperature pulsations of the exhaust gas on internal combustion engines. RWTs with gold coated tungsten wires were fabricated and tested on a heavy-duty diesel engine. Experimental results indicate their utility in such harsh environments with the addition of a protective ceramic coating over the welded joints. The influence of the coating on sensor geometry and response will be elucidated through shock tube and gas stand experiments.

Keywords: cold-wire anemometry, exhaust system, pulsating flow, time-resolved measurement

Background, Motivation and Objective

Time-resolved temperature measurements of unsteady flows remain a pertinent challenge. For instance, pulsatile flow measurements on internal combustion engines (ICEs) remain to be addressed. The ICE exhaust constitutes a harsh environment for sensors with maximum temperature (over 1000 °C), pressure (over 4 bar absolute), and flow velocity (over 200 m/s) along with the presence of contaminant particles and vibrations. Incorporating time-resolved temperature data of ICE exhausts in the design process would aid in the further development of turbocharging and aftertreatment systems. This is an enabler towards more efficient and clean ICEs which are expected to remain significant in the effort to curb climate change [1].

Temperature measurement techniques such as radiation thermometry, laser diagnostics and ultrasound have been proven to work under engine combustion conditions [2]. However, their use in standard engine testing remains limited owing to their complexity and the need for optical access. Conventional temperature measurement techniques for engine testing such as thermocouples and resistance wire thermometers (RWTs) show potential for application considering the relatively simple and inexpensive construction. The trade-off between sensor strength and frequency response, however, remains to be addressed. Herein, thermocouples exhibit difficulties in fabrication

and unfavourable material properties [3]. While RWTs can be fabricated by welding fine wires in the order of microns, limited studies have been performed under ICE exhaust conditions. Tungsten is a suitable wire material with favourable strength-to-response properties. An anti-oxidative coating is required for high temperature applications, albeit it melts at the weld.

In this study, the design of RWTs is investigated under ICE exhaust conditions with emphasis on the impact of a ceramic coating over the welded joints on sensor life and response.

Sensor Construction

RWTs (or *cold-wires*) are widely used in wind tunnels and turbulence research wherein the flow conditions are significantly different from an ICE's exhaust. Differences include high amplitude temperature pulsations in addition to the aforementioned harsh environment.

Alterations from the conventional design included the use of a high temperature ceramic adhesive and thicker prongs (1 mm steel wire) for reduced deformation and heat loss attenuation. Additionally, the tungsten wires were gold coated. The prongs extended 5 mm from the sensor body to reduce boundary layer interference. The prongs were wedge shaped to maximize the wire aspect ratio and minimize end conduction losses. The wire diameters were 5 and 10 μm . Fig. 1 depicts both uncoated and ceramic coated sensors with a 5 μm wire.

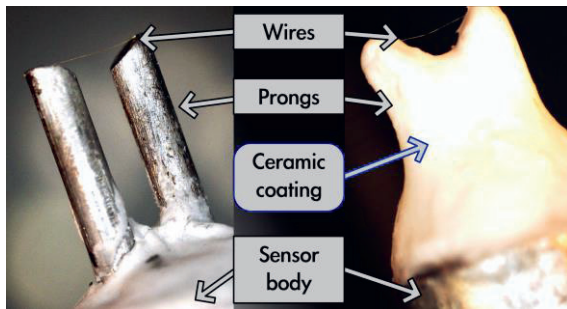


Fig. 1. Uncoated (L) and ceramic coated (R) sensors

Experimental Setup and Methodology

Experiments were performed on a single-pipe exhaust of a Scania D13 heavy-duty diesel engine (see Fig. 2). This setup enables fundamental studies of the exhaust gas flow while protecting the turbocharger from sensor breakdown debris. The test section was equipped with two RWTs, a 3 mm sheathed K-type thermocouple and fast pressure transducers.

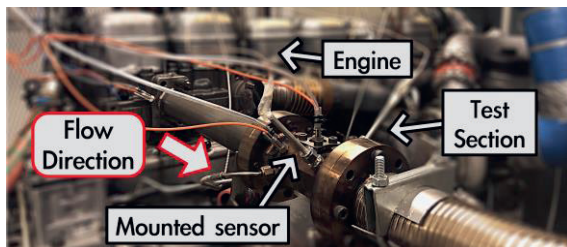


Fig. 2. Single-pipe exhaust with test section

Signal conditioning of the RWTs was performed using Dantec Streamline constant current anemometry (CCA) modules. The signal was sampled at every 0.1 crank angle degrees (CAD). This corresponds to a sampling frequency of 36-72 kHz depending on the engine speed. Fast sampling of 100 engine cycles was performed every 5 minutes until 15 minutes of operation for temperature stabilisation at each operating point. The test sequence is shown in Fig. 3.



Fig. 3. Tested engine operating points

Results and Discussion

The uncoated 5 and 10 μm sensors failed after 7 minutes (at operating point 1) and 85 minutes (at operating point 6) of testing respectively. The wire failed at the welded joint as apparent from Fig. 4. However, the ceramic coated 5 μm

sensor endured engine operation until operating point 6. Thus, an over tenfold increase in sensor life was observed with the addition of a ceramic coating. Fig. 5 shows the cycle averaged temperature pulse measured by the sensors after 5 minutes at operating point 1.

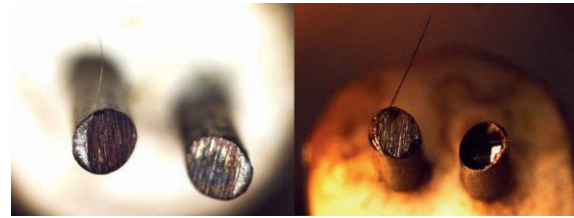


Fig. 4. Wire failure: uncoated 5 μm (L) and 10 μm (R)

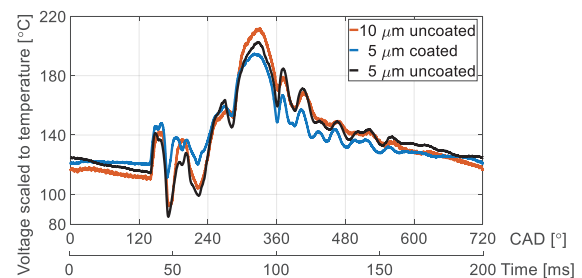


Fig. 5. 100 cycle averaged temperature pulse

Conclusion

Application of a ceramic coating to the welded joints appears to extend sensor life under ICE exhaust conditions. However, its response changed due to the coating. Dynamic response characterisation in a shock tube and sensor design studies in a gas stand will provide insights into the frequency response characteristics of coated sensors. A detailed discussion will be presented at the conference. Testing the developed sensor at higher engine loads will determine the limit of RWTs under ICE exhaust conditions.

Acknowledgements

This study was financed by the Swedish Energy Agency and the Competence Center for Gas Exchange (CCGEx).

References

- [1] J. R. Serrano, R. Novella, and P. Piqueras, "Why the development of internal combustion engines is still necessary to fight against global climate change from the perspective of transportation," *Appl. Sci.*, vol. 9, no. 21, 2019, doi: 10.3390/app9214597.
- [2] H. Zhao and N. Ladommatos, "In-Cylinder Gas Temperature Measurement," in *Engine Combustion Instrumentation and Diagnostics*, Warrendale, PA: SAE, 2001, p. 640.
- [3] A. Olczyk, "Problems of unsteady temperature measurements in a pulsating flow of gas," *Meas. Sci. Technol.*, vol. 19, no. 5, 2008, doi: 10.1088/0957-0233/19/5/055402.

Power over POF – A Short Overview

S. A. Dengler¹, J. Fischer¹, M. Luber¹, H. Lenkowski², C. Schüßler², K. Carruth²,
P. Urbaneck², O. Ziemann¹

¹ Technische Hochschule Nürnberg Georg Simon Ohm – Polymer Optical Fiber Application Center (POF-AC), Wassertorstr. 10, 90489 Nürnberg, Germany,

² Technische Hochschule Nürnberg Georg Simon Ohm, Laboratory for embedded systems, Wassertorstr. 10, 90489 Nürnberg, Germany
simon.dengler@pofac-th-nuernberg.de

Summary:

There are various applications in high voltage, explosive or high electromagnetic interfered environments that require sensors with an electrical isolation from other components of a system. The basics of possible solution, based on optically powered sensor links, were shown previously [1]. Because of different requirements for the applications, a variety of system approaches has been developed (available power for sensor purposes; length between the control node and the sensor; speed of transmitted data etc.). Key requirements and the current approaches will be discussed below.

Keywords: remotely powered sensors, galvanic isolation, sensor networks, polymer optical fiber, power over fiber

Introduction

Due to their application in automotive and consumer market, electronic sensors are versatile, mature, cost-efficient and can measure several parameters. However, many applications make it important to electrical isolate the sensors from other parts of the connected system. This is often necessary in high voltage or in high electromagnetic interfered environments, like for monitoring high-power semiconductors, monitoring systems in magnetic resonance imaging or controlling electric motors.

The needed full electric isolation can be achieved by remote optical powering (Power over Fiber). A simple and cost-effective version of power over fiber is using a Polymer Optical Fiber (POF) as light guide in comparison to the usually used Glass Optical Fiber (GOF). GOF always requires laser diodes as power source. The backward data link is built by specific transmitters and receivers using a second fiber or splitters. POF enables the use of LED as power and data sources. A unique feature of LED is the capability of light-to-electrical current conversion with a reasonable speed and efficiency [1]. Therefore, an extremely simple and economic sensor connection can be set up with two identical LED and one POF.

The two different concepts for a Power over Fiber with POF system including a data transmission from the sensor to the remaining system are shown in Fig. 1.

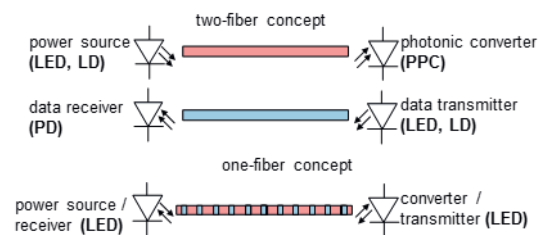


Fig. 1. Different concepts for power over POF systems.

One-fiber system

The one-fiber concept is based on a standard high power LED as power source and an identical LED as photonic power converter (PPC) (and as data transmitter and receiver in the backward direction). If the LED size matches to the fibers diameter, we can achieve efficient coupling into and out of the fiber. LED with different wavelengths can be used. These are red LEDs (usually based on gallium arsenide or gallium phosphide) or blue LEDs, based on gallium nitride.

The benefit using red LEDs is the higher mutual responsivity of around 0.1 A/W. However, due to the lower open circuit voltage (V_{OC}), of around 1.7 V, it is necessary to use some kind of voltage conversion system, like a step-up converter or an energy harvester. This results in an, even if more power efficient, more complex and therefore more expensive system. The wakeup time when powering after some shut down time might be long (seconds, up to minutes) dependent on the charge time for the used capacitors.

On the other hand, using a blue LED enables the possibility to directly start a microcontroller (in a few microseconds), since the open circuit voltage is substantially higher (usually about 2.4 V), which allows an operation without the risk of brownouts. Nevertheless, a capacitance and a step-up converter, at least behind the microcontroller, is still necessary. It stores the energy and rises the voltage high enough to use the converter LED as transmitter for the data transmission. However, the system is still much less complex regarding the components and the microcontroller can start-up directly, enabling the design of an all-in high responsive system.

Demonstration setups for one-fiber system

Our first system was designed for a few mW per sensor to be usable with several standard sensors over medium distances (see Fig. 2). To achieve this a special energy-harvesting component with a large capacitor is used. It uses a red high power LED as power source / Rx and an identical LED as PPC / Tx. The available power on the sensor decreases with the POF length (by about 0.2 dB per meter). Furthermore, it depends on the duration necessary for data back-transmission with power supply offline. If no down time of the power supply for data transmission is considered, the maximal electrical power input is 9.5 mW (up to one meter fiber length). The drawback of this system is a long charge time of the capacitance of a couple of minutes as well as long measurement cycles due to the energy harvesting circuit.

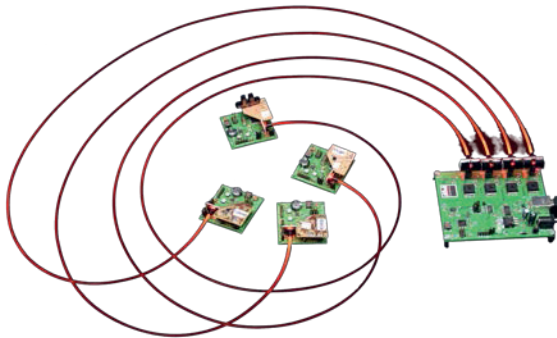


Fig. 2. One-fiber "Power over POF" demonstrator

A second system is optimized for high-speed measurements. It is based on a blue high power LED, which enables a concept with a fast starting microcontroller. It performs temperature measurements with a sampling frequency of 125 Hz. The controller is directly connected to the converter LED and a Step-Up Converter is used to provide the necessary voltage for the LED as transmitter. The drawback of this system is the limited energy available for a connected sensor system and in this very concretely setup, the limitation for an analog sensor.

Two-fiber system

The two-fiber concept consists of a light source and PPC with one fiber for energy transmission and a transmitter and receiver with a second fiber for the data transmission from the sensor to the central node. The benefit of this system is the constant power supply of the sensor board even during the data transmission. In addition, it is possible to use optimized components for data transmission. As power sources, high power LEDs with different wavelength, depending on the photonic converter on the sensor board, can be used. In addition, VCSEL or laser diodes can be used, if the PPC is IR sensitive, like a stacked converter. The benefit in this case is a much higher achievable voltage (up to 5 V).

Demonstration setups for two-fiber system

A realized example for a two-fiber system is a level sensor using a blue LED as power source and an InGaP photo diode (InGaP-PD), which was originally designed for multilayer solar cells, as PPC. For the data transmission, commercial 1 Mbd optical data communication components are used. The high efficiency of the PPC allows the system to function with a LED with only 20 mA current as power source. The drawback however is the high cost of the InGaP-PD.

Another investigated system is using two high red power LEDs as power source and converter. For data communication, due to simplicity, identical red LEDs were used. The system is designed to realize a fast, low cost temperature measurement with a sampling frequency of 1 kHz. The drawback of this system is the use of a special energy-harvesting chip, which results in a complex and expensive design. Other various systems contain e.g. Step-Up converter instead of the energy harvesting chip and bidirectional data communication between the sensor board and the central node, using red LED for power and data communication.

The newest developments are based around two-fiber systems using blue LED for power supply and commercial data communication components with red LEDs. This would allow systems without any voltage conversion. Furthermore, these systems should allow long fibers or sensor networks using only one board with, in this case, up to eight strain gauges.

References

- [1] J. Fischer, et al., Isolated sensor networks for high-voltage environments using a single polymer optical fiber and LEDs for remote powering as well as data transmission, *J. Sens. Syst.* 7, 193-206 (2018); doi: <https://doi.org/10.5194/jsss-7-193-2018>

Pillar

Measurement Science

Minimal Model Selection for Calibrating a Hall-Stress-Temperature Multisensor System Using LASSO Regression

M. Berger¹, S. Huber², C. Schott², O. Paul¹
¹ University of Freiburg, IMTEK, Germany,
² Melexis Technologies SA., Bevaix, Switzerland.
 berger@imtek.de

Summary:

The proposed method takes advantage of LASSO regression to select a reduced-complexity polynomial model for calibrating nonlinear multisensor systems, while addressing the trade-off between higher accuracy and smaller calibration effort. The method is applied to compensate the nonlinear thermal and mechanical cross-sensitivities in a Hall-stress-temperature multisensor system. It enables to (i) reduce the calibration effort, measured by the number of model parameters, by a factor of 1.5 within the space of 4th-order polynomial models without compromising accuracy or to (ii) improve the accuracy by strategically including higher-order polynomial terms without increasing the number of model parameters.

Keywords: Calibration, multisensor system, regularization, LASSO, model selection.

Background

The model selection for nonlinear multisensor systems (MSS) is a crucial task, since the calibration and computational effort grows rapidly with increasing model complexity, e.g. polynomial order P and number of sensors in the system [1]. Regularization methods such as the least absolute shrinkage and selection operator (LASSO) regression have been applied to reduce model complexity of biomarker data [2] and chemical nanosensors [3]. This study demonstrates how to successfully combine LASSO regression and ordinary least square regression (OLSR) in the context of nonlinear MSS calibration.

Description of the New Method

When the LASSO regularization parameter λ is varied from 0 to 1, the number of calibration parameters in the multiple polynomial regression of MSS calibration data is progressively reduced from the full number to zero [4]. At the same time, the achievable accuracy progressively worsens, since contributing parameters are suppressed. However due to statistical variability in sensor data, for a given reduced number of parameters, LASSO may provide several competing reduced models. Evaluating all of them on the calibration data from an ensemble of MSS using OLSR allows then to identify the one best suited for modelling the general response of the MSS. Thereby, the method allows to strategically address the trade-off between model complexity of nonlinear MSS and the achieved accuracy.

Results

Figure 1 illustrates the procedure for selecting the optimal reduced polynomial compensation function f_{comp} allowing to make the sensitivity S_H of a Hall sensor system independent of temperature T and stress σ .

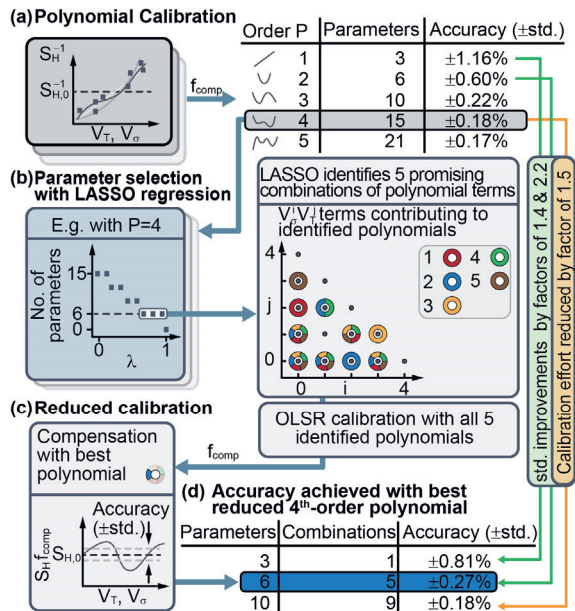


Fig. 1. Schematic diagram of the applied method for selecting minimal nos. of calibration parameters. (a) Conventional polynomial OLSR calibration of inverse Hall sensitivity up to polynomial orders 5 and achieved accuracies. (b) Polynomial term selection using LASSO illustrated for $P = 4$; identification of 5 reduced polynomial candidates, each with 6 terms. (c) OLSR calibration with 6 remaining parameters and (d) Accuracy achieved with best LASSO-reduced 4th-order-models with 3, 6, and 10 remaining parameters.

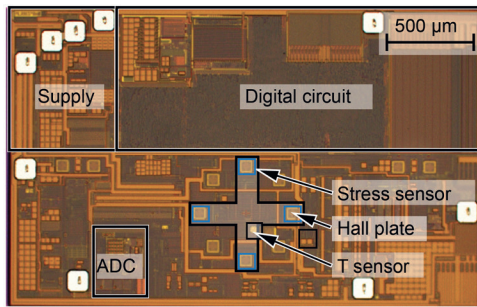


Figure 2: Optical micrograph of the CMOS Hall-stress-temperature sensor system designed to measure magnetic field B values compensated for temperature T and stress σ .

For each of 12 samples of MSS (Fig. 2), 88 calibration load cases and 44 test load cases are used to validate the procedure. An automated measurement setup (Fig. 3) enables the application of a magnetic induction of ± 25 mT, temperature variations in the range of -40 °C to 125 °C, and forces up to 15 N resulting in compressive isotropic mechanical in-plane stress down to about -100 MPa. The calibration data of the samples are shown in Fig. 4. The inverse relative Hall sensitivity S_H^{-1} is taken as the regressand, whereas the T sensor signals V_T and σ sensor signals V_σ serve as regressors. The outcome is $f_{\text{comp}}(T, \sigma)$, which turns the cross-sensitive S_H into the T and σ compensated, constant $S_{H,0} = S_H f_{\text{comp}}$. As an example, starting with a 4th-order polynomial regression with 15 parameters, depending on the MSS sample LASSO produces 5 different polynomial models with only 6 remaining parameters (see Figs. 1(b) and 5). For each of these models, an OLSR calibration is performed on the calibration data of all MSS and the best model is identified (see Fig. 1(c), blue polynomial); it results in a compensated sensitivity

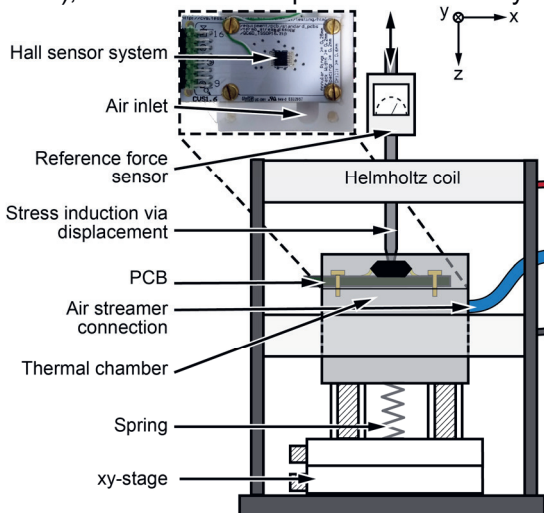


Figure 3: Schematic and photograph of automated measurement setup for calibrating Hall-stress-temperature sensor systems. Induction B , temperature T , and stress σ are applied via Helmholtz coil, air stream into thermal chamber, and mechanical loading mechanism, respectively.

with an uncertainty of $\pm 0.27\%$ (see Fig. 6). This is twice as good as the accuracy achieved with a 2nd-order polynomial with 6 parameters as well, but resulting in an uncertainty of $\pm 0.60\%$. Likewise (see Figs. 1(a, d)), the LASSO reduction to 3 and 10 parameters, implying the same calibration effort as full 1st and 3rd-order models, lead to significant accuracy gains from 1.16% to 0.81% and from 0.22% to 0.18%, respectively.

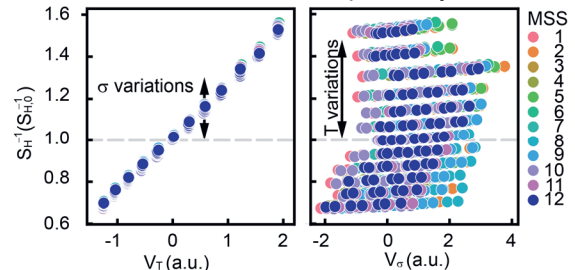


Figure 4: Measured calibration data: T and σ dependent, uncompensated inverse Hall sensitivity of 12 MSS vs. respective output signals V_T (left) and V_σ (right) of T and σ sensors.

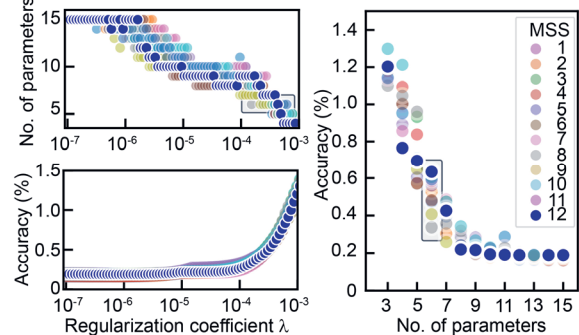


Figure 5: LASSO selection of reduced polynomials (with reduced nos. of model parameters) depending on the wanted accuracy (left). Several polynomials are identified from the individual MSS (right); the best one is chosen by applying OLSR to all MSS.

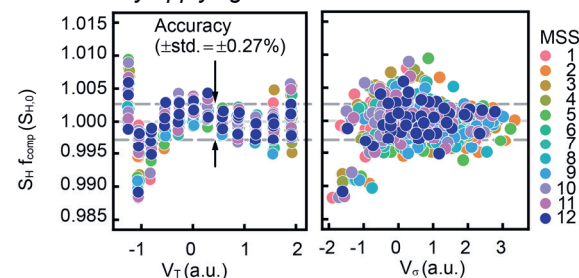


Figure 6: Hall sensitivities of 12 MSS compensated with the best 4th-order polynomial f_{comp} with only 6 parameters.

References

- [1] M. Berger, S. Huber, C. Schott, and O. Paul, *IEEE Sensors J.* 19, no. 16, pp. 7005-7014 (2019); doi: 10.1109/JSEN.2019.2913567.
- [2] J. Lever, M. Krzywinski, and N. Altman, *Nat. Methods* 13, no. 10, pp. 803–804 (2016); doi: 10.1038/nmeth.4014.
- [3] Q. Tao, F. Lan, M. Jiang and G. Li, *Proc. IEEE-NANO 2017*, pp. 113-117 (2017); doi: 10.1109/NANO.2017.8117436.
- [4] Pedregosa et al., *JMLR* 12, pp. 2825-2830 (2011).

Building up precision measuring chains with the DMP41 high precision amplifier

*André Schäfer; Hottinger Baldwin Messtechnik - HBM,
Darmstadt, Germany, andre.schaefer@hbkworld.com*

Summary:

DMP41 is the world most precise instrument for strain gauge-based measurements. The DMP series has been used as a reference device in the mechanical laboratories of the national metrology institutes around the world for decades. Characteristics of the newest member are explained for different application cases.

Keywords: DMP41, DMP40, strain gauge, force, torque, pressure, transducers, sensors, calibration system

Introduction

By its nature requirements to precision measuring chains always have been high. However, with the turn of the millennium the requirements, namely by the automotive industry have grown again. New standards and guidelines, such as DIN EN ISO / IEC 17025 and IATF 16949, ensure that industrial processes are more closely linked to the SI system and industrial development and the resulting higher accuracy requirements were also the reason why metrologists consider SI to be essential.

When highest precision of results counts, sensors and measuring amplifiers based on strain gauge technology are first choice for many different mechanical quantities, such as force, torque or pressure [1], [2].

According to Frost & Sullivan mechanical calibration systems are the second largest group of calibration systems at all and have the best growth expectation. The widest range of equipment is offered by our company group "Hottinger Brüel Kjør" (abbreviation HBK), consisting of Hottinger Baldwin Messtechnik GmbH (abbreviation HBM) in Germany and Brüel & Kjør Sound and Vibration A/S (abbreviation BKSV) in Denmark, who both mechanical calibration systems in their portfolio. As a powerful group of specialists, we develop and market mechanical calibration systems for mechanical engineering in the automotive industry.

We now offer a very wide scope from reference force, torque and pressure transducers of HBM, of course the High Precision instruments of HBM, completed by vibration and acoustic calibration systems solutions as well as sound level meter calibration systems of BKSV and we are offering a very wide scope of calibration services as well.

On the Brüel & Kjør side a major milestone is the standardization of vibration calibration systems, which represent the biggest portion at BKSV.

The four standard systems 3629 (versions 3629-A, 3629-B, 3629-C and 3629-D) are made for different frequency ranges and based on comparison calibration of vibration transducers have been launched lately as a standardized calibration system, so they can be delivered of the shelf.

Traceability, its necessities and needs

Even if you are hardly aware of this, the metrological traceability is of great importance for our everyday life. To take again the example of automobile construction, it is unthinkable without correct mechanical parameters. Traceability ensures that a measurement result can be related to a standard or is related to it. A traceable measurement value is based on this recognized standard due to an uninterrupted chain of comparative measurements with a known measurement uncertainty.



Figure 1: TN Torque transfer normal in its new look

It has been mentioned that transducers, which are based on strain gauges (S.G.), have the smallest measurement uncertainties for tracing back force, torque and pressure. For this reason, they are used as reference transducers and transfer standards for inter-comparisons.

As a manufacturer of measurement technology solutions, HBM has acquired the necessary special know-how in a decades-long development to offer reference measuring chains.

As an example, HBM's TN reference torque transducers shortly have been optimized for international comparison measurements. The challenge here is that a monolithic design in the form of a shaft is required for comparative measurements. Such shaft type sensors can only be "open" and not, as with the large number of transducers based on strain gauges, hermetically encapsulated. This poses the challenge of making the transducer immune to fluctuations in the relative humidity. This is necessary even though the laboratories are air-conditioned, since the transducer must be sent from laboratory to laboratory. The version used for the reference torque transducer TN shows such a low moisture dependency that "climate adaptation" can take place in a very short time. This means that the total time for such an inter-comparison (meaning the time to run through all laboratories including the transfer time) can be shortened. Several NMIs confirm it is an important issue [3], [4].

DMP41- the most Precise Instrument for strain gauge-based measurements

Since the signal coming from the Wheatstone bridge of a strain gauge-based transducer is very small (usually 2mV/V), a measuring chain must be formed with a "bridge amplifier", an amplifier based on a Wheatstone bridge, in order to be able to display or process the result. The requirements for these precision measuring amplifiers are even higher than the requirements for the associated transducers.

This is where precision amplifiers come into play. Today the precision amplifier DMP41 from HBM is the most accurate amplifier for measurements based on strain gauges worldwide and thus ideally suited for international comparison measurements [5]. It is the result of more than four decades of further development of the DMP series. DMP39 high precision instrument started in 1980, DMP40 in 1995 and DMP41 in 2013.



Figure 2: DMP 41 high-precision instrument

Conclusions

It has been shown, that with the turn of the millennium requirements, namely by the automotive industry have grown again. New standards and guidelines ensure that industrial processes are more closely linked to the SI system and industrial development and the resulting higher accuracy requirements were also the reason why the metrologists considered a new SI to be essential.

The basis for this development are strain gauge-based reference sensors and high precision amplifiers with ADC, signal conditioning allow a new performance but still a reduction of complexity of measurement. That includes the possibility of reduction of uncertainty by combining analogue signals with digital compensation [6], [7].

References

- [1] Karl Hoffmann, An Introduction to Stress Analysis and Transducer Design using Strain Gauges, HBM 1978, see hbm.com
- [2] Kobata, T.; Sabuga, W. et al "Final Report on Supplementary Comparison APMP.M.P-S8 in Hydraulic Gauge Pressure from 100 MPa to 1000 MPa", APMP & EURAMET 1000 MPa Hydraulic pressure interlab. comparison" 2012
- [3] Schäfer, A. "TN" torque transfer standard with improved usability for inter-laboratory comparisons, XXII IMEKO World Congress, Belfast, UK, 2018
- [4] Khaled, K. M.; Röske, D.; Abuelezz, A. E.; The influence of temperature and humidity on the sensitivity of torque transducers, Journal Meas. 94: p.186-200, 2016
- [5] Schäfer, A., Kitzing, H. DMP41 – a new chapter of ultra-precision instrument for strain gauge; IMEKO World Congress, Busan, Rep. of Korea
- [6] Schäfer, A. The ultra-precision instrument DMP41 -first experiences & appropriate filter settings, IMEKO 22nd TC3, 12 th TC5 and 3rd TC 22 International Conferences 2014, Cape Town, South Africa
- [7] Schäfer, A. DMP41 – The Most Precise Instrument for strain gauge-based measurements IMEKO TC3, TC5, TC16 TC22 Conference, due to CoVid19 shifted to 15-17 Nov. 2020, Cavtat-Dubrovnik, Croatia

Increasing the sensitivity in the determination of material parameters by using arbitrary loads in ultrasonic transmission measurements

Dmitrij Dreiling¹, Dominik Itner², Nadine Feldmann¹, Hauke Gravenkamp², Bernd Henning¹

¹Measurement Engineering Group, Paderborn University, Paderborn, Germany

²Structural Analysis of Plates and Shells, University of Duisburg-Essen, Essen, Germany
dreiling@emt.uni-paderborn.de

Summary

Due to the increased use of polymers in research and industry, the non-destructive determination of material parameters is gaining importance. In order to determine the material parameters of a polymer, transmission measurements through waveguide specimens can be evaluated. However, sensitivity analyses show a high uncertainty in the determination of the mechanical shear parameters. As a means to increase the sensitivity to these parameters, different excitations are investigated.

Keywords: ultrasound transducer, sensitivity optimisation, material characterisation, polymers, scaled boundary finite element method

Motivation

The development of measurement systems based on ultrasound becomes increasingly reliant on modelling and numerical simulations, which in turn require a good knowledge of the material's mechanical and acoustic properties. There are several waveguide-based approaches of non-destructive material characterisation, which in general differ not only in the measurement principle chosen but also in the specimen's geometry, e.g. plate-like or cylindrical. This contribution is focused on a measurement setup which applies ultrasound transmission through a hollow cylindrical specimen, and has previously shown low sensitivity to the material parameters that describe the shear behaviour [1]. One approach to increase this sensitivity is to replace the currently applied full-surface excitation of the measuring system by a locally segmented excitation.

Figure 1 shows a schematic of the measurement setup, consisting of a transmitting and receiving transducer and the cylindrical specimen. The material parameters are determined in an inverse procedure, i.e. by minimising the deviation between the measured signal and a simulation result [2].

Simulation model

Cylindrical samples are advantageous in that the measurement setup can be kept relatively simple and the forward simulation model for the inverse pro-

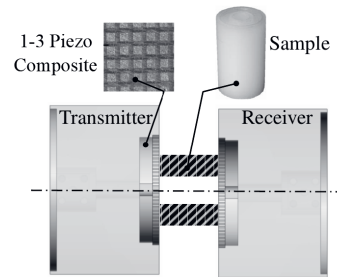


Fig. 1. Measurement system for the characterisation of polymer materials using transmission measurements of a hollow cylindrical waveguide [1].

cedure can be assumed axially symmetrical. The elasticity matrix C describing the material in Voigt's notation, assuming transversely isotropic material behaviour, depends on five independent constants E_L, E_T, ν_L, ν_T and μ_L and is given by

$$C = S^{-1} = \begin{bmatrix} 1/E_T & -\nu_T/E_T & -\nu_L/E_L & 0 & 0 & 0 \\ -\nu_T/E_T & 1/E_T & -\nu_L/E_L & 0 & 0 & 0 \\ -\nu_L/E_L & -\nu_L/E_L & 1/E_L & 0 & 0 & 0 \\ 0 & 0 & 0 & 1/\mu_L & 0 & 0 \\ 0 & 0 & 0 & 0 & 1/\mu_L & 0 \\ 0 & 0 & 0 & 0 & 0 & 1/\mu_T \end{bmatrix}^{-1}.$$

Here, E is Young's modulus, ν Poisson's ratio and μ the shear modulus. As a transversely isotropic material is assumed, a directional dependence of the material parameters is given, indicated by the subscript L for longitudinal and T for transversal direction. The parameter μ_T is given by $\mu_T = \frac{E_T}{2(1+\nu_T)}$.

Since segmented loads, e.g. circumferential segments, have to be considered for increased sensit-

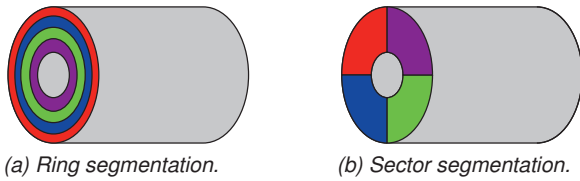


Fig. 2. Schematic of different segmented excitations.

ivity, a three-dimensional simulation model is necessary. As the transmission pulses have a centre frequency of 1 MHz and above, a standard 3D finite element simulation is not feasible especially for an inverse procedure, as it would require a high spatial discretisation made necessary because of the small wavelength of the acoustic waves. Due to the given axially symmetric shape of the test specimens, the application of the Scaled Boundary Finite Element Method (SBFEM) is particularly suitable [3]. The fact that one direction is solved analytically (in this case the axial direction) leads to improved computation efficiency. SBFEM can be extended to make those segmented loads applicable and provide a sufficiently accurate approximation of the output signal in an acceptable time.

Sensitivity analysis

The dimensionless scaled sensitivity $\Upsilon_{p_i}(t)$ is defined as the scaled sensitivity of the cause p_i to an observation $y(t)$ at an operation point p_i^* [4]:

$$\Upsilon_{p_i}(t) = \left(\frac{\delta y(t)}{\delta p_i} \Big|_{p_i^*} \right) p_i^*,$$

In this case, the cause p_i is any of the five independent parameters of the matrix C , and the observation is a result of the simulation, i.e. the mechanical displacement on the back of the hollow cylinder. The sensitivities are determined using the central difference quotient by varying each parameter by $\pm 1\%$. Appropriate material parameters similar to polyamide 6 ($E_L = E_T = 3.76 \text{ GPa}$, $\nu_L = \nu_T = 0.3157$, $\mu_L = 1.36 \text{ GPa}$, $\rho = 1150 \frac{\text{kg}}{\text{m}^3}$) are used as the operating point. As an approximation to the transmission signals used in the measurement setup, a Gaussian modulated sine with a centre frequency of 1 MHz is used as an input signal. In both cases of segmented excitation, see figure 2, the signal is phase-shifted by 90° between neighbouring segments (Indicated by colour).

Due to the different orders of magnitude, normalisation is useful when quantifying the sensitivities of the material parameters. Figure 3 shows Υ with respect to μ_L with comparable results to Bause et al. [1]. A difference between the full surface excitation compared to one with four radial segments (rings) and four circumferential segments (sectors) becomes apparent. Especially excitation with four rings shows a significant increase in sensitivity. In order to compare the dif-

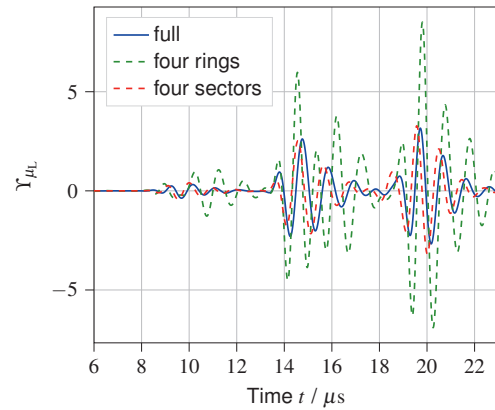


Fig. 3. Dimensionless scaled sensitivity of μ_L with full surface, four rings and four sectors excitation.

ferent types of excitation, the composite scaled sensitivity [4] can be calculated:

$$\bar{\Upsilon}_{p_i} = \sqrt{\frac{1}{T} \int_0^T (\Upsilon_{p_i}(t))^2 dt}$$

For an full surface excitation the composite sensitivity is $\bar{\Upsilon}_{\mu_L, \text{full}} = 0.68$. At four circumferential segments depicted in figure 3 is $\bar{\Upsilon}_{\mu_L, \text{sect}} = 0.73$, thus the sensitivity is increased by 7% with regard to the full surface excitation. Excitation with radial segments (rings) shows $\bar{\Upsilon}_{\mu_L, \text{ring}} = 1.79$, a significant increase by about 150%.

Conclusion

The SBFEM was successfully used to provide accurate results with circumferential loads. It has been demonstrated that an increase in sensitivity to the shear modulus μ_L can be achieved by a locally segmented excitation. Thereby Υ_{μ_L} increases significantly, especially using a ring segmentation.

Literature

- [1] F. Bause, H. Gravenkamp, J. Rautenberg, B. Henning: Model based sensitivity analysis in the determination of viscoelastic material properties using transmission measurements through circular waveguides, *Physics Procedia* 70 (2015)
- [2] F. Bause, H. Gravenkamp, J. Rautenberg, B. Henning: Transient modeling of ultrasonic guided waves in circular viscoelastic waveguides for inverse material characterization, *Measurement Science and Technology* 26 (2015); doi: 10.1088/0957-0233/26/9/095602
- [3] H. Gravenkamp, C. Birk, C. Song: Simulation of elastic guided waves interacting with defects in arbitrarily long structures using the Scaled Boundary Finite Element Method, *Journal of Computational Physics* 295 (2015)
- [4] M. C. Hill: Methods and guidelines for effective model calibration, *Water-resources investigations report* 98-4005, (1998)

Measurements at Laser Materials Processing Machines: Spectrum Deconvolution, Including Uncertainties and Model Selection

Rolf Behrens¹, Björn Pullner¹, Marcel Reginatto¹

¹ Physikalisch-Technische Bundesanstalt (PTB), Bundesallee 100, 38116 Braunschweig
Rolf.Behrens@PTB.de

Summary:

Laser materials processing can lead to the production of unwanted X-rays. Their dose rate and spectral distribution have now been accurately determined for the first time.

Keywords: Spectrometry, Laser materials processing, Bayesian analysis, Model selection, Uncertainty

Background, Motivation and Objective

Materials processing by means of laser radiation is an established method that has been used for many years. More recently, ultrashort pulsed laser radiation is being increasingly used for this purpose. When using high peak intensities of more than 10^{14} W/cm² at the laser focus, unwanted X-rays are generated [1],[2]. These X-rays were measured for the first time in an application environment of industrial laser materials processing.

Measurements and Data Evaluation

For the measurements, a thermoluminescence detector (TLD) based few-channel spectrometer was used (see Fig. 1) [3],[4]. The penetration depth of the X-ray radiation in the spectrometer depends on the energy, so that the energy-resolved and absolute spectrum of the radiation, including the uncertainties of the spectrum can be determined from the dose values in the TLD layers by means of mathematical methods (Bayesian deconvolution).

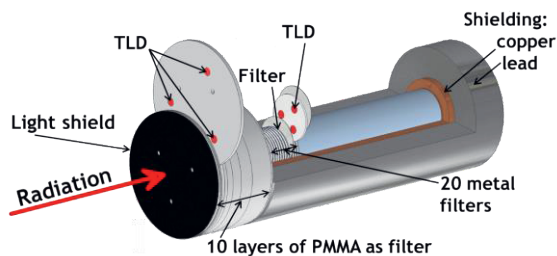


Fig. 1. Sketch of the TLD-based spectrometer. Basic principle: The deeper the radiation penetrates the spectrometer, the higher its energy.

The experimental setup is shown in Fig. 2 and the main laser parameters are listed in Tab. 1. Bayesian data evaluation was performed using the WinBUGS software [5] which, besides the photon spectrum, also supplies the corresponding uncertainties and coverage intervals.

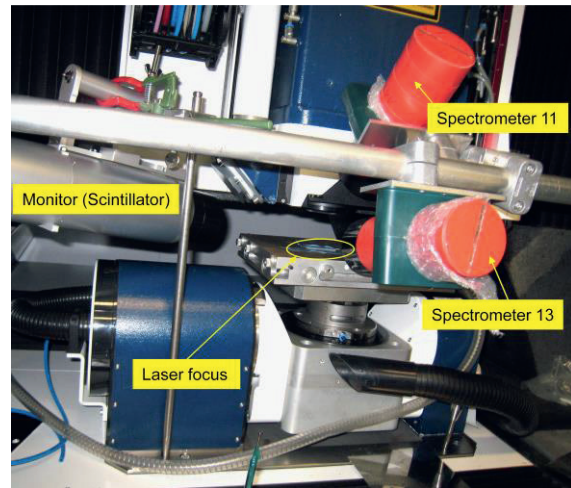


Fig. 2. Picture of the experimental setup.

Tab. 1: Parameters of the laser

Parameter	Value
Wavelength	1030 nm
Average power	78 W
Pulse energy	195 μ J
Pulse length (FWHM)	924 fs
Repetition rate	400 kHz
Focus diameter	16 μ m
Angle between laser beam and workpiece	90° (from top)
Focus intensity	$2.1 \cdot 10^{14}$ W/cm ²
Workpiece materials (at different experiments) and photon emission angles	Tungsten (13° and 46°), an alloy ¹⁾ (31°) and stainless steel (31°)

¹⁾ 92.5 % mass fraction tungsten; 3.75 % mass fraction iron; 3.75 % mass fraction nickel

The following prior information for the photon spectra was included in the data evaluation: i) a smooth rise with increasing energy due to the fact that there was at least about 10 cm of air absorption between the laser focus and the spectrometer front; ii) an exponential decrease at higher energies (due to well-known laser-plasma interaction mechanisms); iii) a peak in the spectrum at the energy of the characteristic fluorescence radiation of the workpiece material. Further details including the validation of the method (irradiation in known photon fields and subsequent data evaluation with the same prior information) are given in the literature [8],[9].

Results

Fig. 3 shows the absolute photon fluence spectra per materials processing time together with their 95 % coverage intervals for the four measurements normalized to a distance of 10 cm from the workpiece.

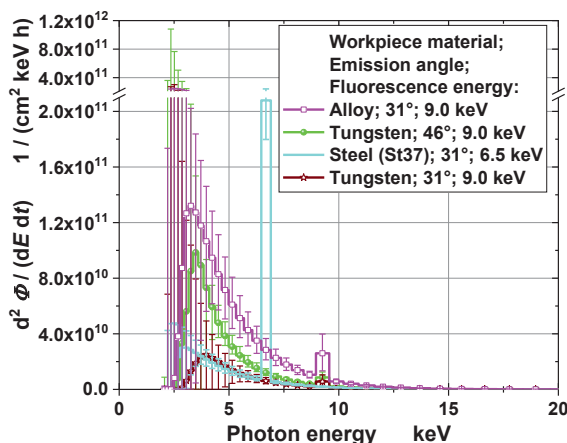


Fig. 3. Photon fluence spectra together with their 95 % coverage intervals. Note the broken ordinate.

The fluence spectra were converted to dose equivalent using the corresponding conversion coefficients [6],[7]. The resulting dose rate depends on the processed material and its nature. The maximum dose rates of the following radiation protection quantities were 7300 mSv/h in $\dot{H}'(0,07)$, 71 mSv/h in $\dot{H}'(3)$ and 4 mSv/h in $\dot{H}^*(10)$. Such high dose rates would exceed legal dose limits within a few minutes to one hour (for the local skin dose estimated by $\dot{H}'(0,07)$ and the eye-lens dose estimated by $\dot{H}'(3)$), or a few hours (for the effective dose of the whole body estimated by $\dot{H}^*(10)$). Fortunately, in the normal case, the laser processing is performed in a laser protection housing which is sufficient to absorb the photons. If, however, the laser intensity in materials processing rises in the future, the laser protection housing may no longer be sufficient to shield the photons.

Conclusions

The measurements performed, traceable to the SI for the first time, not only provide manufacturers and users of ultrashort pulse lasers with important radiation protection information for the design of machines, but have also provided important input for recent legislative procedures in the field of radiation protection in Germany. Meanwhile, machines with even higher laser intensities are already under development. Therefore, the measuring method presented here will become even more relevant in the future.

References

- [1] C. Gerhard, W. Viöl und S. Wieneke, Plasma-Enhanced Laser Materials Processing, *Plasma Science and Technology - Progress in Physical States and Chemical Reactions*, Prof. Tetsu Mieno (Ed.), InTech, (2016) doi: 10.5772/61567
- [2] S. Nolte, F. Schrepel und F. Dausinger (Editors), Ultrashort pulse laser technology – Laser sources and applications, *Springer Series in Optical Sciences* (2016) doi: 10.1007/978-3-319-17659-8
- [3] R. Behrens and P. Ambrosi, A TLD-based Few-channel Spectrometer for Mixed Photon, Electron, and Ion Fields with High Fluence Rates, *Radiat. Prot. Dosim.* 101, 73 (2002) doi: 10.1093/oxfordjournals.rpd.a006062
- [4] R. Behrens, A spectrometer for pulsed and continuous photon radiation, *J. Instrum.* 4, P03027 (2009) doi: 10.1088/1748-0221/4/03/P03027
- [5] D.J. Lunn, A. Thomas, N. Best, D. Spiegelhalter, WinBUGS – a Bayesian modelling framework: Concepts, structure, and extensibility, *Statistics and Computing* 10, 325 (2010) doi: 10.1023/A:1008929526011
- [6] International Commission on Radiation Units and Measurements (ICRU), Conversion Coefficients for use in Radiological Protection against External Radiation. *ICRU Report 57* (1998) doi: 10.1093/jicru/os29.2.Report57
- [7] R. Behrens, Conversion coefficients for $H'(3;\Omega)$ for photons, *J. Radiol. Prot.* 37, 354 (2017) doi: 10.1088/1361-6498/aa51e8
- [8] R. Behrens, B. Pullner, M. Reginatto, X-Ray Emission from Materials Processing Lasers, *Radiat. Prot. Dosim.* 183, 361-374 (2019); doi: 10.1093/rpd/ncy126
- [9] R. Behrens, M. Reginatto, Bayesian Spectrum Deconvolution Including Uncertainties and Model Selection: Application to X-Ray Emission Data Using WinBUGS, *Radiat. Prot. Dosim.* (2019); doi: 10.1093/rpd/ncy286

Artificial Intelligence with Neural Networks in Optical Measurement and Inspection Systems – Opportunities and Challenges

*Michael Heizmann¹, Alexander Braun², Markus Hüttel³, Christina Klüver⁴,
Erik Marquardt⁵, Michael Overdick⁶, Markus Ulrich⁷*

¹*Institute of Industrial Information Technology (IIIT), Karlsruhe Institute of Technology (KIT),
Hertzstr. 16, D-76187 Karlsruhe, Germany, michael.heizmann@kit.edu,*

²*University of Applied Sciences Düsseldorf, Germany*

³*Fraunhofer IPA, Stuttgart, Germany, ⁴University of Duisburg-Essen, Germany*

⁵*VDI e. V., Düsseldorf, Germany, ⁶SICK AG, Waldkirch, Germany*

⁷*Karlsruhe Institute of Technology (KIT), Germany*

Summary:

Optical measuring and inspection systems play an important role in automation as they allow a comprehensive and non-contact quality assessment of products and processes. In this field, too, systems are increasingly used that apply artificial intelligence and machine learning, especially by means of artificial neural networks. Results achieved with this approach are often very promising and require less development effort. However, the supplementation and replacement of classical image processing methods by machine learning methods is not unproblematic, especially in applications with high safety or quality requirements, since the latter have characteristics that differ considerably from classical image processing methods. In this contribution, essential aspects and trends of machine learning and artificial intelligence for the application in optical measurement and inspection systems are presented and discussed.

Keywords: Artificial Intelligence, Machine Learning, Neural Networks, Optical Measurement and Inspection Systems, Machine Vision

Introduction

Machine vision plays nowadays an important role within measurement technology. Since the amount of image data generated by such systems is rapidly increasing there is a growing need for automated evaluation of the image data.

If the inspection task can be formulated as a “rule”, this rule can be implemented in a “classical” image processing algorithm. For many tasks, however, this classical approach cannot be followed. There can be different reasons for this. The limit between “good” and “bad” may be difficult to define. This limit may even not be defined explicitly, but only implicitly given by numerous examples. For these tasks, artificial intelligence (AI) and machine learning (ML) based on artificial neural networks come into play. On the one hand, such systems try to approximate the human ability to recognize patterns, which make them suitable to deal with fuzzy limits. On the other hand, ML based systems are configured by means of training, making them especially adequate when the inspection task is given by examples.

In recent years, artificial neural networks have demonstrated their capability to an ever increasing extent. By now, systems based on

AI and ML made solutions available for a large variety of inspection tasks.

Potential of Machine Learning for Machine Vision, Measurement and Automation

Currently, the main technology drivers for ML in machine vision are the automotive industry, communications and consumer electronics, medical imaging and public safety. In machine vision, ML approaches in general and CNNs (convolutional neural networks) in particular are mainly used for classification, detection, and segmentation. Figure 1 shows an application where pill bags are checked for their correct content by detecting different types of pills.

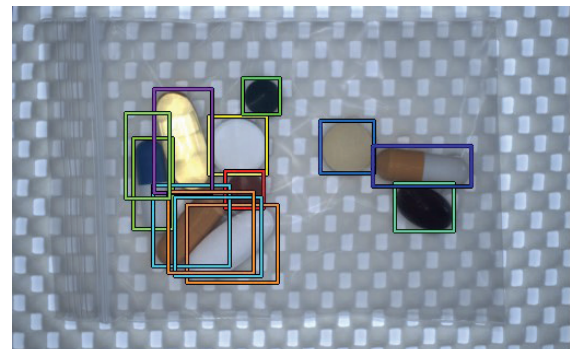


Fig. 1: Example for a detection task: a CNN detects different pills to check the correct content of a pill bag [1].

Machine Learning can be applied in different fields within measurement and automation: First, it can be used within components for measurement and automation with built-in or subsequent data processing based on ML. Second, machine learning can be applied in the production of devices for measuring and automation; and third, it serves in the overall lifecycle of such devices (from installation over operation to decommissioning).

Challenges for Machine Learning in Machine Vision

However, the benefits of machine learning do not come for free. Above all, the application of ML methods and in particular CNNs requires a sufficient amount of representative training data. The effort required to provide this training data can be immense very great in practice. The data must be meaningful and sufficient for the task at hand. Figure 2 shows an example of grapes that are to be sorted. In the annotated training images, all relevant events (perfect berries, rotten berries etc.) must be present and the events must be contained in all relevant characteristics (e. g. light and dark grapes).

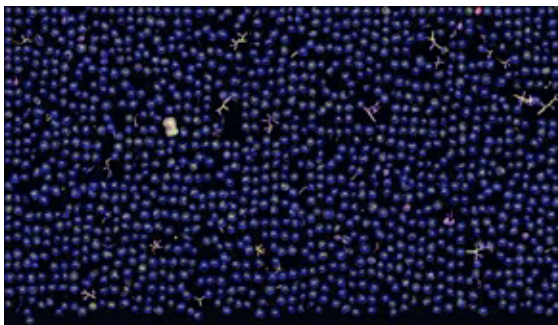


Fig. 2: Data used for learning – here grape berries during sorting – must be representative and robust (image source: Fraunhofer IOSB, Karlsruhe)

Since training data are in principle quality-relevant and therefore sensitive, they are valuable resources that must be treated and protected as such. In case that meaningful data is not available in sufficient quantities for the training of machine learning, concepts must be developed to reduce the need for real, annotated learning data.

In practical use, there are even more challenges. In addition to technical aspects, it is important to take into account the economic aspects. For example, many machine learning processes still require immense computing power. The use of machine learning is often difficult when high demands are made on freedom from defects, since machine learning methods are currently often not able to secure

the required low error rates. While there are recognized methods for determining the measurement uncertainty for classical measurement systems (also in machine vision) [2], such a method is still missing for machine learning based measuring systems. Finally, systems using ML often do not have a continuous behavior, which means that small changes in the input to the systems (the images) might lead to large changes in their output (the classification).

Current fields of action

ML is currently one of the dominant research areas in MV. Active research deals with developing methods to make ML based decisions comprehensible and explainable. Another field of activity in MV is to provide a meaningful measure of reliability or confidence of the results of machine learning approaches. With the standards VDI/VDE/VDMA 2632-3 [3] and VDI/VDE/VDMA 2632-3.1 [4], general guidelines for the evaluation of classifying MV systems already exist and will be extended to ML based approaches.

Anomaly detection, active learning, the avoidance of catastrophic forgetting, the use of simulated data, tools for supporting the compilation of training data, learning with few, but representative examples (few-shot learning) are – amongst others – further research topics that are followed at present.

In addition to these scientific and technical challenges, suitable framework conditions must be created. Among others, important aspects are the protection of data used for learning and the necessity for a legal framework for the use of data.

References

- [1] MVTec Software GmbH. HALCON/HDevelop Reference Manual. HALCON 19.11, 2019.
- [2] Evaluation of measurement data – Guide to the expression of uncertainty in measurement, 2018.
- [3] VDI/VDE/VDMA 2632 Part 3:2017-10 Machine vision/industrial image processing – Acceptance test of classifying machine vision systems. Beuth Verlag, Berlin, 2017.
- [4] VDI/VDE/VDMA 2632 Part 3.1:2019-08 (Draft) Machine vision/industrial image processing – Acceptance test of classifying machine vision systems – Test of classification performance. Beuth Verlag, Berlin, 2019.

Visualizing Neural Network Decisions for Industrial Sound Analysis

Sascha Grollmisch^{1,2}, David Johnson¹, Judith Liebetrau¹

¹ Fraunhofer IDMT, Ilmenau, Germany

² TU Ilmenau, Ilmenau, Germany

jsn@idmt.fraunhofer.de

Summary:

Recent research has shown acoustic quality control using audio signal processing and neural networks to be a viable solution for detecting product faults in noisy factory environments. For industrial partners, it is important to be able to explain the network's decision making, however, there is limited research on this area in the field of industrial sound analysis (ISA). In this work, we visualize learned patterns of an existing network to gain insights about the decision making process. We show that unwanted biases can be discovered, and thus avoided, using this technique when validating acoustic quality control systems.

Keywords: Industrial sound analysis, acoustic quality control, machine learning, neural networks, visualization, layer-wise relevance propagation

Background, Motivation and Objective

Neural networks have improved classification systems in audio research fields such as Acoustic Event Detection and Music Information Retrieval. Similar approaches have also been shown to be useful for acoustic quality control systems [1]. Instead of differentiating between sound events or music genres, the task is to detect machinery and product faults using sounds containing only subtle changes, which are often audible to experienced machine operators. The aim of Industrial Sound Analysis (ISA) is to automatically detect these differences in audio signals within the human auditory range. In [1], the surfaces of metal balls were able to be classified with high accuracy using a deep feed forward neural network (DNN) even with noisy conditions. Even though high classification performance was reported, the decision making process of the DNN was not investigated. Understanding networks' decisions is important for creating explainable classifiers and avoiding potential biases. In this work, we visualize information about a DNN's decision using layer-wise relevance propagation technique (LRP) [2]. Additionally, an artificial bias is added to the dataset to show how such a problem could be discovered and possibly avoided before the quality control system is implemented in real-world production lines.

Visualization Techniques

Several methods have been developed to visualize the decision making process of non-linear classifiers such as neural networks,

attempting to make the so called "black box" more understandable. One approach is to propagate the gradient of the resulting class back through the neural network to the input feature space. The state-of-the-art LRP method modifies the backpropagation rules such that the back-propagated signal is weighted with each layers activations to produce less noisy heatmaps [2]. LRP has been shown to be effective in fields such as image recognition for visualizing information about a network's decisions and uncovering unwanted biases in the dataset as well as in the classifier, e.g. identifying that a neural network makes decisions using visible watermarks present only in some images [3].

Dataset and Experiment

For the use case of metal ball surface detection the IDMT_ISA_METAL_BALLS dataset was published together with results from a DNN baseline system [1]. The dataset contains several metal balls with three different surfaces (*eloxed*, *coated*, and *broken*) which pass by a microphone on a metal slide. This sound is automatically recorded and cut to 400 ms for further analysis. The reported baseline system uses a magnitude spectrogram obtained from a STFT as input, and achieved 98.8% file-wise accuracy on a separate test dataset. To visualize the decision making process of the DNN, we concatenated spectral time frames of the test data and overlaid them with corresponding heatmaps obtained using LRP. The heatmaps were extracted using the iNNvestigate

framework [4] with alpha 1 and beta 0. Furthermore, we use the IDMT_ISA_METAL_BALLS dataset to explore the potential for uncovering biases using visualization techniques. For this experiment, we created a modified dataset in which a 10kHz sine wave is added to the *broken* class samples to determine if a classifier uses this bias to make its decisions.

Results

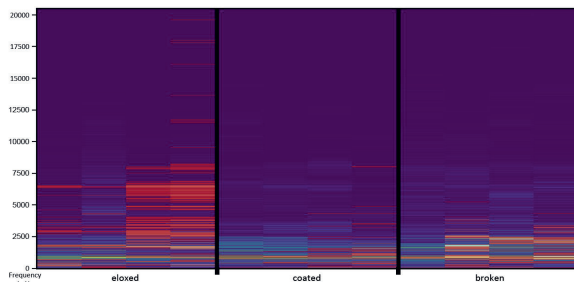


Fig. 1. Decision heatmaps for each class (*eloxed*, *coated*, and *broken*) without bias.

Fig. 1 shows heatmaps for the unchanged dataset, plotted on top of the magnitude spectrograms, indicating the origin of the neural network's decisions in red (slightly important) to yellow (very important). While heatmaps are a valuable tool for image classifiers, they are harder to interpret or validate for spectrograms of industrial sound sources, especially when the correct solution is unknown beforehand. The important frequencies vary slightly for all examples of one class. This makes it hard to identify an easy to understand decision pattern for each class.

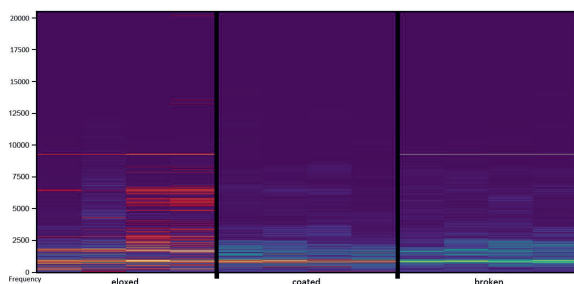


Fig. 2. Decision heatmaps for each class with 10kHz sinusoidal bias in the *broken* class.

While validating the classifier for complex sound scenarios can be difficult, uncovering unwanted behavior may be feasible using visualization methods. We demonstrate this using a sine wave as an unwanted bias. Adding the sine wave to the *broken* class during training and test improved the baseline accuracy from 98.8% to 99.4%, since that class could be classified perfectly with the added bias. The plots in Fig. 2 show that the model is trained to make decisions for the *broken* class using the added sine wave. Additionally, the absence of energy at 10kHz for

decisions regarding the *eloxed* class is also noticeable.

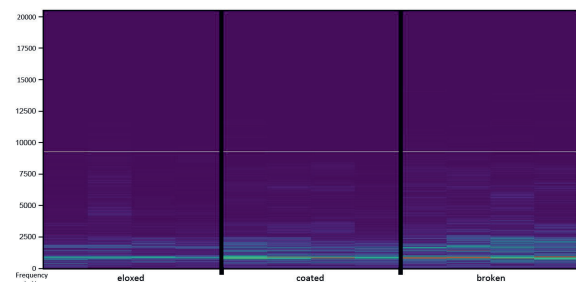


Fig. 3. Decision heatmaps for each class with a 10kHz sinusoidal bias in each class.

By adding the sine wave to all classes in the test set, the accuracy dropped to 33.3%. All files were classified as *broken* showing that our artificial bias worked. Furthermore, it can be seen in Fig. 3 that a bias instead of the actual characteristics of the original audio was picked up by the classifier, providing an explainable reason for the misclassifications.

Conclusion

While neural networks are a promising direction for building acoustic quality control systems, the reason for the classifier's decision are hard to explain due to the non-linearity of the model. State-of-the-art visualization techniques from image recognition research, such as LRP, have the potential to provide insights on the decision making process of the neural network. Compared to natural images it may be difficult to validate the complex frequency patterns which were found. However, our experiments showed that it is a potential method for discovering unwanted biases in datasets. Future work could be to transfer the resulting heatmaps to the audio domain, in addition to the visual domain, to make the decisions audible and possibly easier to interpret.

References

- [1] S. Grollmisch, et al., Sounding Industry: Challenges and Datasets for Industrial Sound Analysis, *EUSIPCO*, A Coruna, Spain, 2019
- [2] S. Bach, et al., On Pixel-Wise Explanations for Non-Linear Classifier Decisions by Layer-Wise Relevance Propagation, *PLoS ONE* 10(7): e0130140 (2015), doi: 10.1371/journal.pone.0130140
- [3] S. Lapschkin, et al., Unmasking Clever Hans Predictors and Assessing What Machines Really Learn, *Nature Communications* (2019), doi: 10.1038/s41467-019-08987-4
- [4] M. Alber, et al., iNNvestigate neural networks!, arxiv: 1808.04260

This work has been partially supported by the German Research Foundation (BR 1333/20-1, CA 2096/1-1).

Adaptive algorithms for linear position measurement applications

Andreas Voss, Axel Bartos
TE Connectivity Sensors Germany GmbH, Hauer 13, 44227 Dortmund
Andreas.Voss@te.com

Summary:

The advancing digitalization of manufacturing (“smart factories”) will create a high demand of position sensors. Besides environmental monitoring, position sensing will play a key role in future production processes. In summary, position measurement needs to become modular and scalable to different sensing dimensions with demanding accuracy requirements. xMR (magneto-resistive) technologies can give answers to achieve adaptive sensor systems under the objective of finding an optimum application solution in terms of performance, size and price.

Keywords: magneto-resistive, linear measurement, adaptive learning, contactless, sensor array

The system point of view

Designed as a miniaturized sensor system, position sensors must be as simple as possible due to customer acceptance and yet cover many requirements in terms of measuring distance, accuracy and performance. Although by definition, magnets are part of the measurement system, the sensor should work with existing magnets. For this purpose, an adaptive learning algorithm at the end of the line test (EOL) or during commissioning at the customer site is required. Miniaturization can be achieved by integration (MR sensor + ASIC) or by a new technological approach, which makes it possible to save measuring points and thus sensors, while achieving the desired measurement accuracy. Tunnel magneto resistive (TMR) technology [1] promises this simplification, since complex signal amplification can be omitted, and the technology is ready for direct chip-integration on ASICs.

Methodology of magnet movement measurement

Moving a permanent magnet on a linear path along an xMR [2][3] sensor establishes a characteristic output curve which can be used for a determination of the magnet position. Fig. 1 shows all three components of the magnetic field created by a magnet moving parallel to the z-axis with a certain distance of the magnet to the sensor in y-direction. It stands out, that the y-component will be a good choice to use for a position determination, as it is continuous and free of singularity from its maximum to minimum.

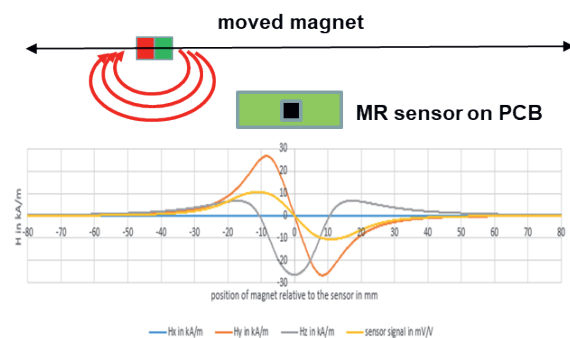


Fig. 1. Characteristic curve of magnet displacement along AMR sensor, y-component with continuous singularity-free function.

Using a simple Look-Up-Table (LUT) approach will solve the position mapping for different magnet-shapes and distances between sensor and magnet. Although this single-sensor magnetic mapping only covers a short distance, it forms the basis of an absolute measurement system for the sensing of longer distances by being scalable and adaptable to customer requirements as part of a linear sensor kit [4].

Absolute algorithm approach

The logical next step is the arrangement of a series of sensors (see Fig. 2), which cover the entire magnetic movement.

When implementing an absolute measurement, only a single screenshot of the magnetic field distribution along the sensor array is possible. Now the whole characteristic sensor curve is populated with measurement points – one or two of them are situated in the linear region of the curve - all others are arranged at the left and right section of the curve.

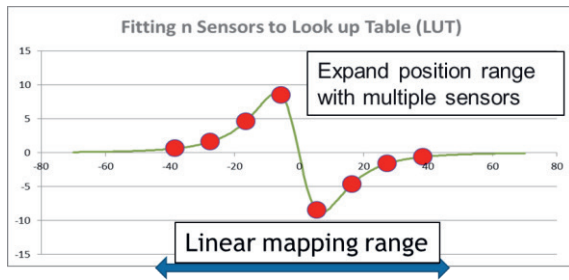


Fig. 2. Expanding range with an array of AMR sensors.

A first approach is to find an algorithm, which determines the sensor(s) in the linear region and apply the LUT approach for one sensor described above. A smarter (and more robust) way is to include the available information from all sensors to determine the position. A closer look to Fig. 2 reveals a perfect match of the characteristic curve (green) with the single sensor signals (red dots) which will be the base of the now described procedure:

One algorithm doing that fitting task is the method of least squares (LS) [5], where the square of distances between all sensor node values $s(n)$ and correspondent look-up-table values $LUT[s(n)]$ are summed up to find a local minimum, just where the LUT curve has its best match with the measured m sensor values as shown in the following formula:

$$Q(\Sigma \rightarrow Min) = Min \left(\sum_{n=1}^m \sqrt{\{s(n) - LUT[s(n)]\}^2} \right) \quad (1)$$

Runtime improvements can be achieved by using adaptive weighted averages [6] and golden ratio methods [7], resulting in up to 5 times faster position calculations than using formula (1) in stand-alone mode.

Adaptive LUT learning

Suppose to have a learning system, that can teach itself the LUT for position determination. This is very useful when a standard sensor system needs to be adapted to a customer's application without HW changes. It requires a learning step with the application magnet, for example during the EOL Test. After the sensor installation, a full-scale movement of the magnet needs to be executed, while the sensor system is in learning mode. A prerequisite for this feature is to ensure that the movement is done with a constant velocity (which results in a constant Δd in Fig. 3). In this case the LUT learning algorithm can calculate the curve shape autonomously and normalizes the measured data as the real distance Δs of the sensor elements on the hardware is known by design.

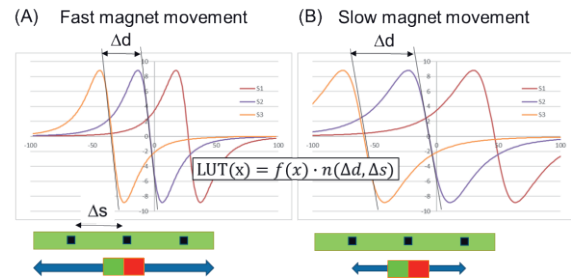


Fig. 3. Fast or slow (constant) magnet movement during learning step lead to real LUT.

A big advantage of this learning step is the possibility to map different magnets and inaccuracies of the magnet system in the LUT, as induced by e.g. slightly magnetic materials in the application housing or piston of hydraulic and pneumatic actuators.

Outlook

Since small sizes often offer an application advantage, sensor technologies are moving into focus which can make their contribution here. TMR will play a key role, as this technology provides an effect amplitude of approx. 1 Vpp at 5 V supply. This allows TMR sensors to be wired directly to the ADC of an MCU or ASIC, opening the door to direct integration of both parts into one component housing. In combination with intelligent bus interfaces [8], the hardware simplification could lead to half of the system space needed today. The future is found in a combination of intelligent adaptive software approaches to cover platform solutions which in best case could be adapted to a wide range of customer applications by simple customizing.

- [1] M. Jullière: Tunneling between ferromagnetic films. In: Physics Letters A. Band 54, 1975, S. 225–226
- [2] Thomson, W., "On the electrodynamic qualities of metal: effects on the electric conductivity of nickel and of iron", Proc. Roy. Soc. London, A8, 1857, S. 546-550
- [3] R.Hunt, A Magnetoresistive Readout Transducer, IEEE Transactions on Magnetics 6(1):150 - 154 · April 1971
- [4] WO 2011160796A3
- [5] W.Press, S. Teukolsky, W. Vetterling, B. Flannery; Numerical Recipes in C: The Art of Scientific Computing, ISBN 0-521-43108-5, p.671
- [6] N. Bronstein, K. A. Semendjajew u. a.: Taschenbuch der Mathematik. 2nd. edition. 1995, ISBN 978-3817120086 p. 629
- [7] Florian Jarre, Josef Stoer: Optimierung. Springer, Berlin 2004, ISBN 3-540-43575-1, S. 130 ff.
- [8] DE102016002420A1

Lean data with edge analytics: Decentralized current profile analysis on embedded systems using neural networks

Thomas Kűfner^{1,2}, Andrė Gerhard Trenz², Stefan Schőnig³

¹University Bayreuth, Universitatsstr. 30, 95447 Bayreuth, Germany,

²Fraunhofer IPA, Universitatsstr. 9, 95447 Bayreuth, Germany

³Maxsyma GmbH & Co. KG, Neustadter Strasse 9, 92685 Floss, Germany
thomas.kuefner@uni-bayreuth.de

Summary:

This short paper introduces a system for the detection of operating states based on current profiles of a production plant with an artificial neural network at the machine's edge in almost real-time. The system called "CogniSense" consists of a sensor for signal acquisition, a microcontroller for data pre-processing and a single-board computer for data main processing. With the system, current profiles of a test engine are acquired and analyzed, so that 26 defined operating states can be reliably detected with a classification accuracy of over 95%.

Keywords: artificial neural networks, condition monitoring, edge analytics, embedded systems, IoT

Introduction

Industry 4.0 is characterized by the digitization and networking of machines and systems in production [1]. With this, the amount of data in production is increasing, providing information about processes and thus enables the autonomous monitoring, control and optimization of value creation processes [2, 3]. Condition monitoring uses this data in production plants to obtain relevant information about the condition of plant components in almost real-time [4]. Consequently, production plants can be monitored autonomously, plant faults can be detected early, maintenance requirements can be recognized in advance and measures can be planned according to needs [5]. For this, the analysis of current profiles with the aid of machine learning methods is a promising approach - not least because current profiles are available in every electrical system, have high information content and can usually be recorded with cost-effective sensors [6, 7]. Artificial neural networks (ANN) are already used in production planning and control as well as in process and quality analysis [8, 9]. In [10] further applications of ANN in production are listed.

Experimental design and methodology

This paper shows that classification of different operating states (OS) by using ANN on embedded systems during operation in almost real-time is possible. For this, the "CogniSense", consisting of current sensor, microcontroller (MCU) and single-board computer (SBC) is

presented. Current profiles of 26 different OS of a test engine are acquired with 12 kHz and pre-processed at the MCU. A frequency analysis is carried out at the SBC and the training of the ANN is done. After this, the 26 OS can be classified during operation in near real-time.

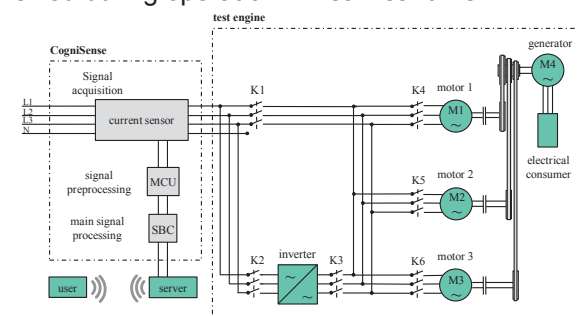


Fig. 1. Schematic of test engine and "CogniSense"

The test engine, as shown in fig. 1 comprises three different electrical motors, operating with or without an inverter. A generator driven by these can be equipped with different electrical loads. This results in the 26 reproducible OS. Fig. 2 shows selected rms-current-profiles of five OS. The individual measurements are not synchronized. The resulting time offset is up to one second and can impair the learning success of the ANN. This is solved by a discrete Fourier transformation. In [10], a system is presented that uses a multilayer perceptron (MLP), a feedforward ANN, to detect six different OS in current profiles of the main supply of the test engine with a classification accuracy (CA) of 99.82%. This ANN is optimized in this paper

with respect to memory requirements and CA (>95%), to make it suitable for execution on embedded systems in near real-time.

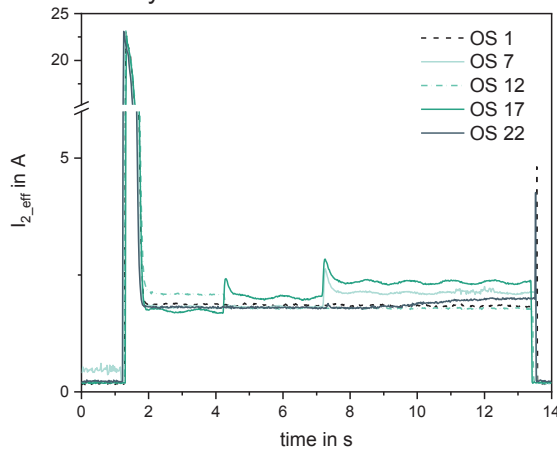


Fig. 2. Comparison between five different OS.

In addition, the limits of the MLP regarding the minimum amount of training data are examined. The basic concept is first mentioned in [11].

Results

Table 1 shows the results. MLP 1 and MLP 2 are close to the optimum, confirming the reliable recognition of the developed system.

Tab. 1: Training parameters and test results

MLP / number of OS	training samples		parameters			test samples		CA [%]
	total	per OS	epochs	batch- size	iter- ations	total	per OS	
1 / 6 OS	420	70	100	60	700	750	25	99,33
2 / 11 OS	770	70	100	55	1400	275	25	98,04
3 / 6 OS	78	13	225	39	450	150	25	95,33
4 / 11 OS	198	18	225	33	1350	275	25	95,85
5 / 16 OS	880	55	225	80	2475	400	25	95,45
6 / 21 OS	1344	64	225	84	3600	525	25	95,31
7 / 26 OS	1950	75	225	78	5625	650	25	95,23
8 / 26 OS	1924	74	225	78	5625	650	25	94,83

The results of MLP 2 show that detection becomes increasingly complex with rising OS. For MLP 3 to MLP 7 there is a requirement for the lowest possible amount of training data while maintaining the CA. Like MLP 1, MLP 3 classifies six OS, whereby the training data is reduced from 70 to 13 samples per OS. Despite this, the CA is 95.33%, but the number of epochs must be increased. The same applies to MLP 4 with eleven OS where the training data per OS is minimized to 18. This shows that the ANN requires only a small number of training samples per OS for a low number of OS. MLP 5, 6 and 7 show that a further increase of the OS to a rise of the total number of training

samples required for reliable classification leads. In addition, the learning process in MLP 7 is significantly slower than in MLP 3, since the number of iterations and the batch size rises. MLP 8 cannot maintain the lower limit of the CA with 94.38% by only removing one training sample. For the classification of the 26 OS of the test engine, at least 75 training samples per OS are necessary. In practice, “CogniSense” can be used for condition monitoring of plants and the automated detection of defects and signs of wear during operation. Further research questions include whether new conditions during operation can be recorded, adapted and continuously monitored.

References

- [1] C. Manzei, L. Schleupner, R. Heinze, Industrie 4.0 im internationalen Kontext – Kernkonzepte, Ergebnisse, Trends. Berlin (2016)
- [2] D. Hecker, I. Döbel, S. Rüping, V. Schmitz, A. Voss, Künstliche Intelligenz und die Potenziale des maschinellen Lernens für die Industrie. *Wirtschaftsinformatik & Management*, 9, Nr. 5, (2017); doi: 10.1007/s35764-017-0110-6
- [3] M. Steven, Industrie 4.0: Grundlagen – Teilbereiche – Perspektiven. Stuttgart (2019)
- [4] E. Abele, R. Anderl, J. Metternich, A. Wank, O. Anokhin, A. Arndt, T. Meudt, M. Sauer, Effiziente Fabrik 4.0: Einzug von Industrie 4.0 in bestehende Produktionssysteme. *ZWF – Zeitschrift für wirtschaftlichen Fabrikbetrieb*, 110, Nr. 3, (2015); doi: 10.3139/104.111293
- [5] G. Reinhart, Handbuch Industrie 4.0: Geschäftsmodelle, Prozesse, Technik. München (2017)
- [6] R. Corne, C. Nath, M. El Mansori, T. Kurfess, Enhancing Spindle Power Data Application with Neural Network for Real-Time Tool Wear/Breakage Prediction during Inconcel Drilling. *Procedia Manufacturing*, Nr 5, (2016); doi: 10.1016/j.promfg.2016.08.004
- [7] P. Bhattacharyya, D. Sengupta, S. Mukhopadhyay, A. B. Chattopadhyay, On-line tool condition monitoring in face milling using current and power signals. *International Journal of Production Research*, 4, Nr. 46, S. 1187 – 1201. (2008); doi: 10.1080/00207540600940288
- [8] M. Freitag, M. Kück, A. Ait Alla, M. Lütjen, Potenziale von Data Science in Produktion und Logistik: Teil 1 – Eine Einführung in aktuelle Ansätze der Data Science. *Industrie 4.0 Management*, 31, Nr. 5, S. 22 – 26, (2015); www.researchgate.net/publication/284158759
- [9] C. May, PPS mit Neuronalen Netzen: Analyse unter Berücksichtigung der Besonderheiten der Verfahrensindustrie. Wiesbaden, (1996)
- [10] T. Küfner, H.-J. Uhlemann, B. Ziegler, Lean Data in Manufacturing Systems: Using Artificial Intelligence for Decentralized Data Reduction and Information Extraction. *Procedia CIRP*, 72, (2018) doi: 10.1016/j.procir.2018.03.125
- [11] T. Küfner, A. Reger, S. Schöning, A PLC-Based Measuring System for Machine Crosslinking and Monitoring. *24th International Conference on Production Research: ICPR*, Polen, (2017) doi: 10.12783/dtetr/icpr2017/17638

Application of Machine Learning Algorithms for the Analysis of an Optical Fiber Sensor for Use in Endovascular Coiling of Intracranial Aneurysms

S. Shojaei Khatouni¹, J. C. E. Ewald¹, H. K. Trieu¹

¹Institute of Microsystems Technology, Hamburg University of Technology, Hamburg, Germany.
Sohrab.shjoaei@tuhh.de

Summary:

Using a test rig, two different fiber bragg grating sensors were exposed to temperature changes, compressive loads and bendings. The light spectrum reflected by them was analyzed with respect to these three effects, utilizing machine learning algorithms. The results show that the models of the sensors are suitable for detecting and differentiating the effects of bending and temperature changes with sufficient accuracy.

Keywords: fiber Bragg grating, pressure measurement, temperature measurement, curvature measurement, machine learning

Background

Compared to other diseases like coronary heart disease, intracranial aneurysms (IA) have a fairly low incidence of 2-6% in adult population [1]. Regardless, this pathological condition of intracranial arterial blood vessels has a very high 30-day mortality of approximately 50% after rupture, and therefore subarachnoidal haemorrhage [2]. A commonly used approach to prevent intact IA from rupturing, or stabilize already ruptured IA is endovascular coiling. During this procedure IAs are filled with coils, to stop blood circulation, initiate coagulation and therefore stabilize the bulge. The coils are administrated by pushing them through a catheter into the IA. Currently, there is no method to perform any in situ measurement of the pressure applied on the wall of the aneurysm during this procedure, even though studies indicate, that high pressure can lead to intraoperative ruptures, which appear in 2,6–4,4% of coiled intracranial aneurysms [3]. This work presents machine learning (ML) algorithms for data evaluation of a fiber optic, fiber bragg grating (FBG) based sensor, which was developed to be integrated into the coiling procedure.

Machine Learning for FBG Sensors

The most commonly used parameter for evaluation of FBG based sensors is the Bragg wavelength λ_B . Light with this wavelength is reflected by otherwise almost unreflective FBG. The Bragg wavelength is a function of the grating period Λ as well as the refractive index n :

$$\lambda_B = 2n\Lambda \quad (1)$$

Unfortunately, the refractive index and the grating period of a fiber Bragg grating are influenced by its temperature, axial strain, and curvature. These dependencies are given by:

$$\Lambda = \Lambda_0 \left(1 + \frac{1}{E} \sigma_z + \alpha_T \Delta T \right) \quad (2)$$

$$n(x) = n_0 - \frac{n_0^3 x}{2R} [-(p_{11} + p_{12})\nu + p_{12}] \quad (3)$$

Therefore, mere axial pressure measurements are possible, only if measures are taken in order eliminate the cross-sensitivity of FBG sensors, or to extract the feature of interest. The sensor described in this work is designed to measure axial strain while being bent and under changing thermal conditions. There, these disturbances have to be taken into consideration while measuring the pressure. The simultaneous exposition of FBG sensors to these three influences is uncommon. Therefore, no appropriate analysis models can be found in literature. Hence, analysis carried out in this work is focused on the fundamental decoupling of the different parameters. For this purpose a fiber-optical sensor with three FBGs was analyzed, using multi-layer perceptrons (MLP) and Gaussian process regression (GPR). This approach is based on congeneric analyses performed in [4] and [5]. The fiber-optic sensor was put into a thermo-regulated (± 0.1 °C) hydrostatic pressure (± 0.1 bar) chamber. In addition, the sensor was put into a variable radius fixture. Measurements were performed with following parameters:

Tab. 1: Measurement parameters

Series	A	B
Number FBGs	1	2
Bending radius	15–105 mm	–
Pressure	0–10 bar	0–10 bar
Temperatur	35–37 °C	34–39 °C
Number of Measurements	359	400

Results

To choose proper input signal features for the ML algorithms a manual feature extraction was performed on the raw sensor data. A combination of signal energy, 3dB bandwidth and the Bragg wavelength showed the best performance, allowing sufficient distinguishability of bending curvature, temperature and pressure acting on the FBG sensor. Cross validation (CV) and root-mean-square-error (RMSE) values were used for evaluation of estimation accuracy.

Tab. 2: Performance of GPR vs. MLP

Variable	Measurement series	Method	Error
Curvature	A	GPR	4,1 mm (CV)
		MLP	7,7 mm (RMSE)
Temperature	A	GPR	0,12 °C (CV)
		MLP	0,12 °C (RMSE)
	B	GPR	0,11 °C (CV)
		MLP	0,13 °C (RMSE)
Pressure	A	GPR	2,8 bar (CV)
		MLP	2,9 bar (RMSE)
	B	GPR	2,1 bar (CV)
		MLP	2,1 bar (RMSE)

The CV and RMSE of curvature and temperature estimations being within the accuracy of the devices used for reference measurements indicate a sufficiently high number of measurements. The GPR model performed better or equally well as the MLP model with regard to all three parameters. The axial pressure estimations of both of the two models were insufficient in accuracy, with a coefficient of determination of $R^2 = 0,05$ and a CV error of 2.1 bar.

The bending curvature predicted by the GPR model is shown in Figure 1, with its coefficients of determination being $R^2 = 0,98$.

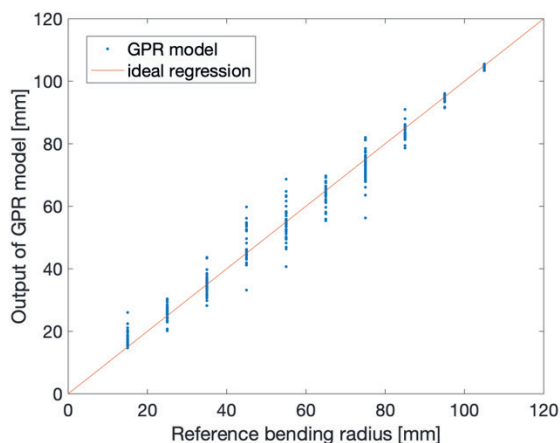


Fig. 1. Estimations of sensor bending by the GPR model for given, actual reference bending of the sensor.

Figure 2 shows the GPR models predictions of the temperature having a lower but similarly sufficient coefficient of determination ($R^2 = 0,96$).

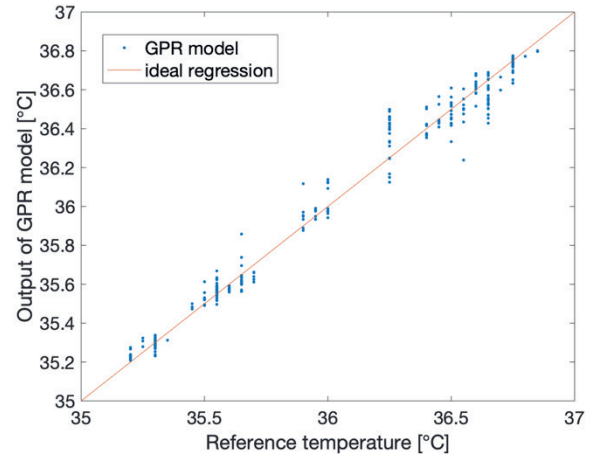


Fig. 1. Temperature estimation by the GPR model,

Conclusion

We have shown that both Gaussian process regression and multilayer perceptron modelling are suitable for differentiating and quantifying the effects of temperature and curvature on FBG sensors. In order to enable a sufficient prediction of pressure, we suggest that temperature sensitivity of the sensor is decreased by adding a liquid crystal polymer cladding to the sensor. This could partially compensate the thermal strain and therefore reduce cross-sensitivity.

Literature

- [1] W. Hacke, Neurologie, Berlin, Heidelberg: Springer, 2010.
- [2] M. e. a. Mehra, „Intracranial Aneurysm: Clinical Assessment and Treatment Options,“ *Biomechanics and Mechanobiology of Aneurysms*, pp. 331-372, 2011.
- [3] I. J. Abecassis *et al.*, „Complication Avoidance and Management of Endovascular Treatments,“ in *Intracranial Aneurysms*, Amsterdam: Elsevier Inc., 2018, pp. 431–460.
- [4] M. G. Xu *et al.*, „Simultaneous measurement of strain and temperature using fibre grating sensors,“ in *Tenth International Conference on Optical Fibre Sensors*, 2004, vol. 2360, no. September 1994, pp. 191–194.
- [5] J. Sun *et al.*, „Application of an artificial neural network for simultaneous measurement of temperature and strain by using a photonic crystal fiber long-period grating,“ *Meas. Sci. Technol.*, vol. 18, pp. 2943–2948, 2007.

Operational Measurement Uncertainty and Bayesian Probability Distribution

Raghu N. Kacker¹, Rüdiger Kessel², Klaus-Dieter Somme³

¹ National Institute of Standards and Technology, Gaithersburg, MD 20899, US

² Metrodata, Braunschweig D-38100, Germany

³ Technical University of Ilmenau, Ilmenau, Germany

Email of corresponding author: raghu.kacker@nist.gov

Summary:

The JCGM documents have undermined the operational concept of uncertainty in measurement established by the GUM and restored the pre-GUM practice of stating possible error relative to the true value, supposedly to align with Bayesian interpretation. It is possible to revise the JCGM documents to agree with the operational view of uncertainty in measurement as well as align them with Bayesian thinking.

Keywords: Bayesian inference, Metrology, Probability, True value, Uncertainty in measurement

Introduction

The signal contribution of the 1993 Guide to the Expression of Uncertainty in Measurement (GUM) is the operational concept of measurement uncertainty [1]. It departs from the earlier views which were about stating possible error relative to the true value. The Joint Committee for Guides in Metrology (JCGM) documents have restored the pre-GUM view by introducing a coverage interval as the dominant expression of uncertainty, where a coverage interval is an interval containing the true value with a stated probability [2]. So, we reiterate the operational concept of uncertainty in measurement. The JCGM-101 states that a coverage interval corresponds to Bayesian interpretation [2]. The JCGM is developing a new GUM aligned with Bayesian interpretation [3]. We offer an alternative interpretation of a Bayesian probability distribution that corresponds to the operational measurement uncertainty. This short paper is based on references [4-7].

True value

The earliest attempts to quantify uncertainty in measurement were based on statistical estimation. A large part of statistical estimation is about predicting an outcome which could become known later. The object of prediction is called the true value. In metrology, it is difficult to define the idea of true value [8]. The JCGM-200 defines true value as a *quantity value consistent with the definition of a quantity* [9]. A quantity value is a known value which is

assigned by definition or by measurement. Thus, a true value cannot be a quantity value. The JCGM-200 definition of true value is indefensible. In metrology, true value and error, however defined, are unknowable; therefore, they cannot be a basis for any decision or action.

Operational uncertainty in measurement

A measurand is a magnitude of a property of something (a phenomenon, body, or substance) that is intended to be measured. A result of measurement consists of the measured value (best assigned value) and its associated uncertainty. The essential GUM is the GUM excluding Annex G and its links with the rest. The essential GUM guides us to think of measurement not as estimating (determining) a true value but as assigning a result of measurement to describe (characterize) the measurand. Uncertainty in measurement is a *parameter, associated with a result of a measurement (measured value), that characterizes the dispersion of the values that could reasonably be attributed to the measurand* [1]. Here, the word 'reasonably' refers to the bases for the assigned result of measurement being reasonable. Uncertainty in measurement is an operational concept that does not refer to the idea of true value. The GUM states the following. *The focus of this Guide is on the measurement result and its evaluated uncertainty rather than on the unknowable quantities "true" value and error (see Annex D). By taking the operational views that the result of a measurement (best assigned*

value) is simply the value attributed to the measurand and that the uncertainty of that result is a measure of the dispersion of the values that could reasonably be attributed to the measurand, this Guide in effect uncouples the often-confusing connection between uncertainty and the unknowable quantities “true” value and error [1]. Uncertainty in measurement is an evaluated expression. It does not include uncertainty from unrecognized components of uncertainty and from those components which are believed to have negligible contribution.

A measuring system is required for measurement of an unknown quantity. It compares the unknown quantity with an appropriate reference value provided by a measurement standard (etalon). The reference values are intended to remain constant over time and space and form a coherent system. In metrology, only an observed deviation of a measured value from a reference value is relevant. Measuring instruments and material measures that form the measuring system are maintained through a hierarchy of calibrations using measurement standards of progressively increasing metrological qualities such as reference standards, secondary standards, and primary standards. The higher-level measurement standards are calibrated with national and international measurement standards. National and international measurement standards and measuring techniques of highest metrological qualities are assessed by inter-comparison for metrological compatibility. Measured values that are traceable to the same reference values (through hierarchical chains of calibrations) are metrologically comparable in time and space. The worth of a result of measurement for a quantity is determined by metrological compatibility (lack of significant difference) with independent results for the same quantity without invoking true values. Every result of measurement should be supported with the measurement function and complete uncertainty budget, so incompatible results can be investigated [4].

Operational Bayesian probability distribution

Suppose Θ is a random variable with a probability distribution $\pi(\Theta)$ which expresses the state of knowledge about a quantity. The domain of $\pi(\Theta)$ is the range of possible values for that quantity. Suppose (θ_l, θ_h) is a result of measurement expressed as an interval for that quantity where θ_l and θ_h are any two possible values of Θ and $\theta_l < \theta_h$. Now suppose $\tau[\Theta]$ is a conceptual true value of that quantity. The theoretical Bayesian interpretation of $\pi(\Theta)$ is that it describes the probability that the true value $\tau[\Theta]$ lies within the interval (θ_l, θ_h) . This interpretation agrees with the JCGM-101 idea of a coverage interval, but it disagrees with the operational concept of measurement uncertainty established by the GUM. An operational interpretation of $\pi(\Theta)$ is that it is a probability (degree of belief) distribution for the values that could be attributed to the quantity in view of the presently available information. Thus, $\pi(\Theta)$ describes the probability associated with a result of measurement expressed as the interval (θ_l, θ_h) . The operational interpretation agrees with the essential GUM and aligns with Bayesian thinking.

References

- [1] GUM (1993)
https://www.bipm.org/utils/common/documents/jcgm/JCGM_100_2008_E.pdf
- [2] JCGM-101 (2008)
https://www.bipm.org/utils/common/documents/jcgm/JCGM_101_2008_E.pdf the DOI of the articles
- [3] Metrologia 49 (2012) 702-705
- [4] Metrologia 44 (2007) 513-529
- [5] Measurement 65 (2015) 61-70
- [6] Measurement 88 (2016) 194-201
- [7] Measurement 127 (2018) 525-532
- [8] Journal of Research of NIST 67C (1963) 161-195
- [9] JCGM-200 (2012)
https://www.bipm.org/utils/common/documents/jcgm/JCGM_200_2012.pdf

Light Stimulation of Gas Sensors with an LED Array in a Compact Setup

Robert Falkowski, Julian Joppich, Tobias Baur, Tilman Sauerwald¹, Andreas Schütze
Lab for Measurement Technology, Saarland University, Saarbrücken,
r.falkowski@lmt.uni-saarland.de

Summary:

The development and test of a multi-wavelength setup for optical stimulation of gas sensors consisting of an LED driver board and a gas measurement chamber is presented. The aim of this work was to facilitate dynamic sensor measurements under variable light wavelength and intensity to investigate the potential of light stimulation for improved sensor performance, i.e. sensitivity and selectivity. The setup was tested on two different sensors in varying gas atmosphere to evaluate its performance.

Keywords: light stimulation, LED array, gas sensor, tungsten oxide, tin dioxide

Motivation

Recent investigations on metal oxide gas sensors under light illumination show promising approaches for increasing sensitivity [1] and selectivity [2] at room temperature. Light activated gas sensors are expected to show a wavelength dependent reaction to various components of a gas mixture. The ideal wavelength is dependent on the sensor material and preparation as well as the target gas or gas mixture to be detected. As the response of semiconductor gas sensor under light stimulation is difficult to predict from first principles or modeling, empirical measurements at varying wavelengths have the potential of revealing characteristic sensor responses for specific gases even in mixtures. The measurement setup presented here enables easy switching between wavelengths and even simultaneous use of several wavelengths with static and dynamic stimulation.

Setup

A circuit board consisting of an LED driver (TLC59116-Q1, Texas Instruments) and twelve SMD LEDs with fifteen wavelengths in the range from 278 nm to 1300 nm, each with individual series resistors, was designed. The LEDs are grouped together on a 1.1 by 1.1 cm area and can be controlled individually. The intensity is adjustable via pulse width modulation (PWM).

The measurement chamber (see Fig. 1) enables a sensor (TO-5 package) to be mounted centered opposite to the LED array with a 1 cm gap. A thin fused quartz plate (GE124) placed between two PTFE parts below the LED array

separates the gas channel with sensor from the LED chamber. The setup enables continuous measurements with any of the fifteen wavelengths without the need for installing a different light source. Both the LED driver and the gas sensor are connected to a microcontroller and are controlled and read out similar to [3]. Illumination control and sensor response are therefore synchronous.

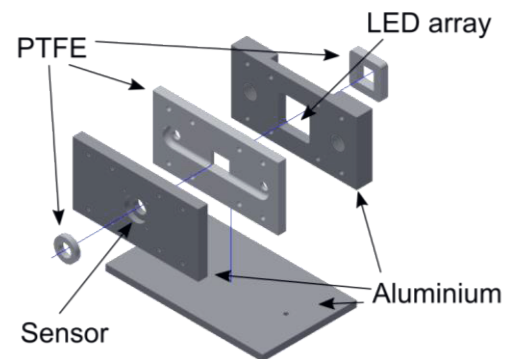


Fig. 1. Measurement chamber for dynamic light stimulation of gas sensors during gas exposure.

Measurement

The optical intensity of every LED was determined as a function of the duty cycle using photodiodes (FDS100 and FDS010, Thorlabs), thus allowing stimulation at different wavelengths with comparable intensity. Two commercial MOS gas sensors (SnO₂-based: AS-MLV-P2, ams Sensor Solutions Germany; WO₃-based: GGS 5530, UST Umweltsensortechnik) were exposed to varying concentrations of nitrogen dioxide (NO₂) and nitric oxide (NO) with and without background atmosphere (550 ppb H₂, 250 ppb CO

¹ Currently at Fraunhofer Institute for Process Engineering and Packaging IVV, Freising, Germany.

and 50 % relative humidity) in zero air generated with a gas mixing apparatus [4]. The different LEDs were switched on successively with breaks in between. The response to light stimulation at room temperature (RT) was calculated by subtracting the sensor conductance before light exposure from the end value and normalizing to the start value.

Results

In the first measurement, the AS-MLV-P2 was exposed to zero air and 200 ppb NO₂. Here, the three longest wavelengths were excluded as previous tests had shown no response under infrared excitation. Fig. 2 shows the calculated response for each wavelength. The LED intensities have not been normalized and the data are presented in logarithmic scale. Sensor response in 200 ppb NO₂ atmosphere is significantly smaller compared to zero air by a factor of about 10. The increase in conductivity can be attributed to additional electrons transferred into the conduction band. The results imply a preferred adsorption of NO₂ under light activation. This effect can be observed even below the band gap of SnO₂ of 3.7 eV, corresponding to 335 nm [5].

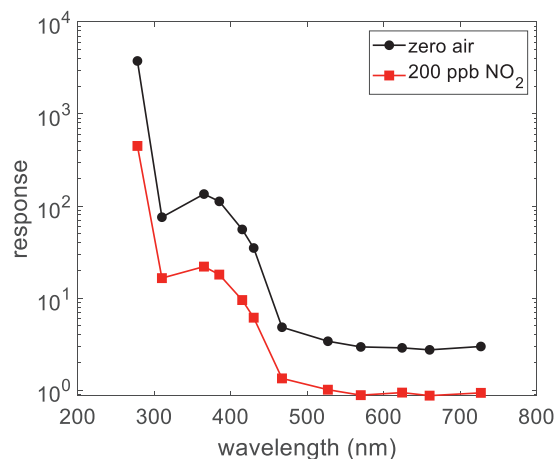


Fig. 2. Response for an AS-MLV-P2 operated at RT to twelve wavelengths from UV to red in zero air (black) and with 200 ppb NO₂ (red), logarithmic scale.

A more detailed experiment was performed with the WO₃ based GGS 5530 sensor. For better comparability of the response at different wavelengths the LED intensities were adjusted to the peak intensity of the weakest LED. The resulting response patterns for four different gas mixtures are shown in Fig. 3.

Compared to the previous measurement, the response of the GGS 5530 is considerably smaller, which might in part be due to the thicker sensor layer. Furthermore, the response in zero air is lowest while it was highest for the AS-MLV-P2. The response increases with addition of background gases and then decreases again with addition of NO or NO₂. Although WO₃ has a

nominal band gap of 3.5 eV [6], a significant response at the corresponding wavelengths (278 and 310 nm) is only observed with background gas (CO, H₂), but not in zero air. This indicates a direct influence of the light stimulation on the chemical interaction on the sensor surface.

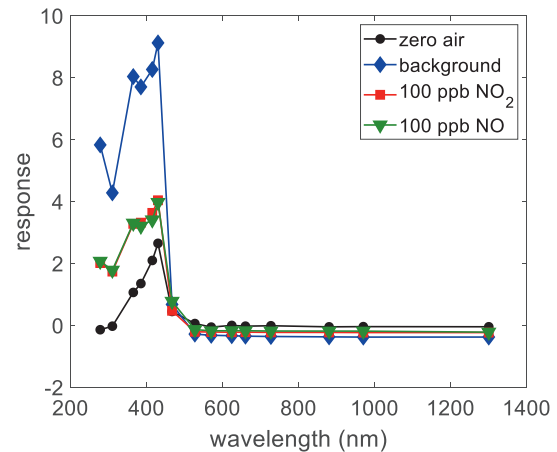


Fig. 3. Linear response of a GGS 5530 gas sensor operated at RT to stimulation with all the wavelengths in four gas mixtures. Measurements for NO₂ and NO were performed in background atmosphere.

Outlook

The setup presented allows simple successive light stimulation of gas sensors mounted on TO-5 headers. First measurements provide an insight into the complex chemistry of gas sensors which can be influenced by light activation, potentially achieving more selective behavior. The influence of intensity and the simultaneous use of several wavelengths needs further investigation.

References

- [1] C. Zhang, A. Boudiba, P. De Marco, R. Snyders, M.-G. Olivier, M. Debliquy, *Sens. Act. B*, 181, 395-401 (2013), doi: 10.1016/j.snb.2013.01.082
- [2] O. Casals, N. Markiewicz, C. Fabrega, I. Gràcia, C. Cané, H. S. Wasisto, A. Waag, J. D. Prades, *ACS Sensors* 4 (4), 822-826 (2019), doi: 10.1021/acssensors.9b00150
- [3] T. Baur, C. Schultealbert, A. Schütze, T. Sauerwald, *tm - Technisches Messen*, 85 (7-8), 496-503 (2017), doi: 10.1515/teme-2017-0137
- [4] N. Helwig, M. Schüler, C. Bur, A. Schütze, T. Sauerwald, *Meas. Sci. Technol.* 25, 055903 (2014), doi: 10.1088/0957-0233/25/5/055903
- [5] S. Baco, A. Chik, F. Md. Yassin, Study on Optical Properties of Tin Oxide Thin Film at Different Annealing Temperature. *Journal of Science and Technology*, 4(1) (2012)
- [6] L. G. Teoh, J. Shieh, W. H. Lai, I. M. Hung, M. H. Hon, *Journal of Alloys and Compounds*, 396 (1-2), 251-254 (2005), doi: 10.1016/j.jallcom.2004.12.005

Analysis of accuracy requirements to the meteorological sensors used to compensate for the influence of the Earth's atmosphere in high precision length measurement

P. Nevezhnikov, V. Kupko, T. Panasenko, A. Prokopov, V. Skliarov, A. Shloma
National Scientific Centre "Institute of Metrology",
Myronosytska 42, 61002 Kharkiv, Ukraine
 Corresponding Author's e-mail address: pavel.nevezhnikov@metrology.kharkov.ua

Summary:

The influence of the Earth's atmosphere on the results of high precision distance measurement on the baselines of up to 5 km can be taken into account due to the information on the mean integral refractive index of air along the baseline being measured, obtained with temperature, air humidity and pressure sensors. The ways on improving the accuracy of such an account, as well as the requirements to the characteristics of the respective sensors for various approximations by quadrature formulas of the mean integral refractive index are discussed.

Keywords: length measurement, meteorological sensors, refractive index, gradient method, GeoMetre

Background, Motivation and Objective

Meteorological sensors (temperature, air humidity, pressure) are widely used to obtain the measurement information necessary to determine corrections that compensate for the effect of the Earth's atmosphere on the results of distance measurement on near-Earth baselines. Instrumental (dispersion) methods for accounting the influence of the atmosphere [1] for baselines of up to 5 km still have not found practical application. For this reason, the correction of the atmosphere's influence on the results of length measurement on such baselines is currently grounded on the use of traditional methods for determining corrections using data on the mean integral refractive index of air (\bar{n}). Measurement of meteorological parameters for calculating \bar{n} are carried out using temperature, humidity, pressure sensors located at discrete points of the path being measured.

Increasing the accuracy requirements for length measurement leads to the need to improve the accuracy of methods and instruments of determining \bar{n} including the meteorological sensors. In this paper, the results of research carried out within the GeoMetre project (under EMPIR), in terms of the development of methods and means of taking into account the influence of the Earth's atmosphere to achieve the distance measurement uncertainty of not more than 1 mm on the baselines of up to 5 km, are discussed.

The research has been performed using the gradient method for determining the mean integral refractive index of air. The gradient method for determining the mean integral refractive index of air is the common name of methods based on the use of quadrature formulas with summands depending on the values of the gradient of the refractive index of air at discrete points on the integration interval along the baseline being measured by the range finder.

Description of the New Method

The analysis of the measurement equation shows that the fulfillment of the above requirements is possible using modern high precision laser rangefinders, if the measurement uncertainty of the mean integral value of the refractive index of air on the trace being measured is not more than $5 \cdot 10^{-7} \cdot L^{-1}$ (L in km).

The exact value of the mean integral refractive index of air \bar{n} is determined by the relation

$$\bar{n} = \frac{1}{L} \int_0^L n(\sigma) d\sigma, \quad (1)$$

where σ is the ray coordinate, measuring along the electromagnetic radiation propagation path; L is the path length; $n(\sigma)$ is a function describing the change in the refractive index along the baseline (trajectory of the radiation).

In the process of research, possible options for

representing the integral (1) by quadrature formulas satisfying the accuracy requirements formulated above are considered. With this, the main attention is paid to the analysis of the relations for \bar{n} obtained using the trapezoidal method (valid for a uniform distribution along the path of measuring points of local values of the refractive index of air, determining \bar{n} through the quadrature formula), Euler-Maclaurin method (for a uniform distribution of the above points) and Hermite polynomials (for a non-uniform one) [2-4].

It is shown that the potential accuracy of the widely used in practice relation for \bar{n} obtained by representing the integral (1) by the quadrature formula using the trapezoidal method is significantly lower than the potential accuracy of the corresponding quadratures obtained using the Euler-Maclaurin representation and Hermite polynomials. This result is due to the appearance of additional summands in the Euler-Maclaurin and Hermite quadratures, taking into account the contribution of the gradients of the refractive index of air and the angles of arrival of the signal at the end points of the baseline. Therefore, the method using the \bar{n} representation by quadrature formulas according to Euler-Maclaurin or Hermite was called gradient method of \bar{n} determination [2-4].

Results

The accuracy requirements for the meteorological sensors necessary for the practical implementation of the above methods for determining the mean integral refractive index of air are formulated taking into account the number of points, their location on the baseline being measured and weather conditions.

In the calculations, the most accurate relation was used, connecting the local values of the refractive index of air with the meteorological parameters of the atmosphere – Ciddor's formula [5].

As a result of the research, it was shown that the instrumentation capabilities available at the linear geodetic polygon of the National Scientific Centre "Institute of Metrology" for measuring pressure, temperature, air humidity at the points of determining local values of the refractive index, as well as the visible zenith angles and

gradients of the refractive index at the end points of the baseline (that is, all the input quantities necessary for the implementation of the analyzed methods) allow to obtain the mean integral refractive index of air with the uncertainty of not more than $5 \cdot 10^{-7} \cdot L^{-1}$ (L in km).

References

- [1] M.T. Prilepin, A.N. Golubev, Instrumentalnyye metody geodezicheskoy refraktometrii [Instrumental methods of geodetic refractometry]: *Itogi nauki i tekhniki, Ser. Geodeziya i aerofototsyemka [Findings of Science and Technology. Series Geodesy and Aerophotography]*, M.: VINITI, Vol. 15, 91 (1979) (In Russian).
- [2] P. Neyezhmakov, A. Prokopov, V. Skliarov, On the accounting for the influence of the Earth's atmosphere on the results of distance measurement realized by lasers, *Journal of Physics: Conf. Series* 1065 (2018) 142008; doi:10.1088/1742-6596/1065/14/142008
- [3] P. Neyezhmakov, A. Prokopov, I. Trevogo, K teorii gradiyentnogo metoda opredeleniya sredneintegral'nogo pokazatelya prelomleniya vozdukh pri dal'nomernykh izmereniyakh na prizemnykh trassakh [On the theory of the gradient method for determining the mean integral refractive index of air in distance measurement on near-Earth traces], *Suchasni dosyagnennya geodezychnoi nauky ta vyrobnytstva – Modern achievements of geodesic science and industry*, II (36), 28–31 (2018) (in Russian).
- [4] P. Neyezhmakov, A. Prokopov, Analiz tochnosti hradiyentnogo metodu vyznachennya serednointegralnogo pokaznyka zalomlennya povitrya [Accuracy analysis of the gradient method for determining the mean integral refractive index of air], *Ukrainian Metrological Journal*, 4, 43-48 (2018) (In Ukrainian); doi:10.24027/2306-7039.4.2018.155754
- [5] P.E. Ciddor, Refractive index of air: new equations for the visible and near infrared, *Applied Optics*, 35(9), 1566-1573 (1996); doi:10.1364/AO.35.001566

Acknowledgement

This study was performed under the European joint research project named EMPIR 18SIB01 GeoMetre Large-scale dimensional measurements for geodesy. This project has received funding from the EMPIR programme cofinanced by the Participating States and from the European Union's Horizon 2020 research and innovation programme.

Difficulties in Understanding and Teaching the Definition of the Kilogram in the Revised SI

Joaquín Valdés¹

¹ Universidad Nacional de San Martín, 25 de Mayo y Francia, 1650 San Martín, Prov. Buenos Aires, Argentina
jvaldes@inti.gob.ar

Summary:

Different options were discussed before reaching the final agreement on the new definitions of the SI units, especially with regard to the kilogram. A definition of the kg based on a mass, such as an atom or the electron, would have been preferable for ease of understanding, among other reasons. In this paper we will discuss some educational experiences on ways to teach what is now a kilogram to different audiences, including people that is rather unaware of the Planck constant.

Keywords: metrology, SI, definitions, kilogram, education.

Addressing questions on the new definition of the kilogram

Now we have to explain to a wide audience, including technicians and university graduates from the most diverse disciplines, who do not necessarily know what the Planck constant h is, that the kilogram is no longer the mass of “the weight that was in Paris”, but it is defined by taking the fixed numerical value of h to be $6.62607015 \times 10^{-34}$ when expressed in the unit Js. It was already known from the very beginning of discussions around the redefinition of the SI units how difficult it would be to explain what a kilogram is based on a fixed value of h . The question of understandability was present in several important publications, at least since 2007, until shortly before the final approval of the redefinition [1,2]. One of the two prevailing arguments to support the finally adopted definition of the kilogram was the need of electrical metrology to bring into the SI the realizations of the volt and the ohm, providing exact numerical values for the Josephson constant $K_J=2e/h$ and the von Klitzing constant $R_K=h/e^2$. The second was that h is a constant more fundamental than the mass of an elementary particle.

An evasive way to explain what a kg is would be not to answer exactly what the new definition says, telling instead that one of the possible ways of “realizing” the new kilogram is by counting atoms. Most of that people may have some idea of what an atom is, so they can imagine that by putting together a huge amount of atoms one obtains a mass similar to the one of “the weight that was in Paris”. So far the explanation could become understandable even by

elementary school pupils. The following immediate question will be of course how is it done to gather so many atoms. This paves the way for explaining the efforts made with the silicon sphere. The answer is not incorrect, since both realizations, the so called silicon route or atomic kilogram and the electric kilogram using the Kibble balance, provide a link between the Planck constant and a macroscopic mass [3].

A friendly way we use to address the very definition of the kilogram for those requiring a prior introduction to the Planck constant is to motivate them with the question of why does a fluorescent tube emits light. Next we introduce Bohr's atom model, the difference in energy ΔE between two levels, and the emission of a photon with frequency ν , presenting the Planck equation $\Delta E=h\nu$. Primary school students will have to wait to be more advanced.

Once introduced h , the unavoidable next question will be what the relationship of h with a mass m is. A possible answer is bringing to light Einstein's equation $E=mc^2$. In this way the connection between m and h was even presented for a time on the BIPM website, linking Einstein's equation with that of Planck. Nevertheless, care should be taken when combining both equations. The mass m in Einstein's equation refers to the rest mass of an object. The frequency ν in Planck's equation usually refers to photons emitted with that frequency. Because photons are massless particles, equating both energies to show the relationship between h and m requires a particular consideration with respect to the mass to which m refers. This mass m could be, for example, the change in

mass Δm of the particle when it emits a photon of frequency ν . The students we appeal so far may be already thinking about the university education that they will choose.

A second answer to the question of the relationship of h with a mass m may be explaining the realization of the electric kilogram via Kibble balance. Using any version of didactic watt balances one may explain the operation principle of the same, but not the relationship of the mass that is being weighed with h . To do this, it is inevitable addressing the equations of Josephson effect and quantum Hall effect to determine h from the measured product of K_J^2 and R_K . According to the experience gathered in our chair of metrology during more than 20 years teaching the SI, it is not required that the audience necessarily have completed a course in quantum physics. The essence of both quantum effects can be explained to those with basic knowledge in natural sciences, without developing the results starting from the Schrödinger equation. Our students are already in the university, but not following law, accounting, humanities, or architecture.

Hands-on Learning

In 2015 two experimental educational solutions for the realization of the kilogram were published; one for the electric kilogram [4] and a second for the atomic kilogram [5], both to 1% relative uncertainty or less.

The first is a watt balance of LEGO blocks constructed at the National Institute of Standards and Technology. It allows explaining how the value of a mechanical force is precisely given by electrical measurements. In the words of its authors: "Unfortunately, it still requires some abstraction to explain how electrical power is related to the Planck constant via the Josephson effect and the quantum Hall effect". That is the bridge to be crossed in order to understand the relationship between mass and h . Learning by doing is not only a matter of children.

The second is a rather simple experiment conceived by R. Davis [4]. After measuring the dimensions and mass m of a high purity aluminium cube, he estimated the number N of aluminium atoms inside the cube, taking the edge dimension a of the aluminium unit cell as determined in 1955 by X-ray diffraction. Next the atomic mass of aluminium $m_a(\text{Al})$ is estimated, also $m_a(^{12}\text{C})$, the atomic mass of carbon-12 and the atomic mass constant m_u . As the molar mass constant was exactly 1g/mol before the revision of the SI, a value for the Avogadro constant N_A is calculated from the measurement of m_u . Using the equation for the ionization of a hydrogen-like atom, N_A and h appear linked themselves and with other constants

known to very small uncertainty. From the measured value of m_u results also a value for h . We found it more interesting and less expensive to implement this latest experiment, coming this way with various metrological applications to engineering students and also to a pre-university technical education level. With a homogenized aluminium cube (not free of imperfections and impurities) specially prepared by an Argentine manufacturer of electrolytic aluminium, the difference between the mass calculated counting atoms and the mass measured by weighing turned out to be 0.1%, or less.

A long term task

Educating for the new kilogram can be a task for decades. Meanwhile, the atomic masses community will continue using the non SI unit dalton instead of the kilogram. This scenario of living with two different units of mass may change with the irruption of a third technology quite different from the watt balance and the silicon experiments [6]. After retiring "the weight that was in Paris" we will no longer have another 140 years without changing the way we teach what a kilogram is.

Acknowledgement

The author thanks Jorge Sánchez for his commitment with the hands-on teaching concept regarding the new definition of the kilogram.

References

- [1] P. Becker, P. De Bièvre, K. Fujii, M. Glaeser, B. Inglis, H. Luebbig & G. Mana, Considerations on future redefinitions of the kilogram, the mole and of other units. *Metrologia*, 44, 1–14 (2007); doi:10.1088/0026-1394/44/1/001
- [2] N. Fletcher, R. S. Davis, M. Stock & M. J. T. Milton, Modernizing the SI – implications of recent progress with the fundamental constants. (2015). <https://arxiv.org/ftp/arxiv/papers/1510/1510.08324.pdf>
- [3] J. Stenger & E. O. Göbel. The silicon route to a primary realization of the new kilogram (Letter to the Editor), *Metrologia*, 49, L25–L27 (2012). doi:10.1088/0026-1394/49/6/L25.
- [4] L. S. Chao, S. Schlamminger, D. B. Newell, J. R. Pratt, F. Seifert, X. Zhang, G. Sineriz, M. Liu, and D. Haddad. A LEGO Watt balance: An apparatus to determine a mass based on the new SI, *Am. J. Phys.* 83 (11), 913-922, (2015). <http://dx.doi.org/10.1119/1.4929898>
- [5] R. S. Davis, What Is a Kilogram in the Revised International System of Units (SI)?, *J. Chem. Educ.* 92, 1604–1609, (2015). doi:10.1021/acs.jchemed.5b00285
- [6] J. Valdés. Reviewing the Revised International System of Units (SI). *Advances in Imaging and Electron Physics*, 211, 121-186 (2019). ISSN 1076-5670 <https://doi.org/10.1016/bs.aiep.2019.05.001>

Optical microphone-based acoustic response analysis for non-contact non-destructive testing

Georg Kaniak¹, Fabian Lücking¹, Wolfgang Rohringer¹, Nils Panzer¹, Balthasar Fischer¹

¹ XARION Laser Acoustics GmbH, Ghegastraße 3, 1030 Vienna, Austria
w.rohringer@xarion.com

Summary:

In this paper, we present a compact, non-contact non-destructive testing setup based on laser excitation and air-coupled detection of ultrasound within a 2 MHz acoustic bandwidth. The setup is comprised of a miniaturized Optical Microphone as air-coupled ultrasound detector, and a compact excitation laser head, both of which are fibre-coupled. We show results from applying this setup to differentiate between production batches of small ceramic components with varying quality in terms of their acoustic response. We demonstrate that the acoustic data is well suited for AI-based data analysis.

Keyword: optical microphone, sensor, coda wave, laser excitation, ultrasound testing, air-coupled ultrasound, contact-free NDT, in-line

Introduction

The steadily increasing complexity of production processes in combination with ever decreasing tolerances for manufacturing errors drives a strong need for fast, in-line capable non-destructive testing (NDT) methods for quality control.

Here, we present a compact, contact-free NDT setup making use of laser-excited ultrasound for identifying defective parts within a production line. The approach is based on a highly optimized, air-coupled optical ultrasound sensor, with a unique bandwidth of 10 Hz to 2 MHz in air. Combined with a laser to excite ultrasound in a part under test, the 'acoustic fingerprint' of the component under test is analysed. These fingerprints allow to distinguish between defective and good parts with high selectivity. The setup is compact and easy to (retro-)fit into production lines. Due to the contact-free nature of the method, it allows fast in-line testing in various production settings, offering significant advantages to state-of-art contacted ultrasound testing methods.

Optical Microphone

The core technology behind the presented method is an innovative approach to measure soundwaves with an all-optical effect. A soundwave locally modulates the density and therefore the optical refractive index of air. These small variations ($\sim 10^{-9}$ per Pa) are detected by making use of a laser-probed Fabry-Pérot inter-

ferometer (see Fig. 1). It converts the refractive index change into an optical signal suitable for photo-detection [1].

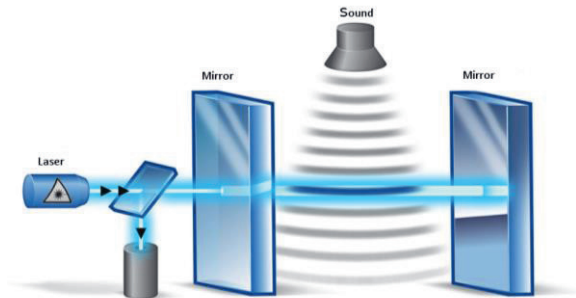


Fig. 1: Function principle of the Optical Microphone.

This all-optical approach is not influenced by any mechanical resonances, therefore it offers an uncommonly broad bandwidth as well as a flat frequency response. The sensor head has a small footprint (5 mm diameter) and is optically fiber-coupled.

Laser excitation

By exposing the surface of a sample to a short, high energy laser impulse, the photo-thermal mechanism [2] will excite a thermo-elastic shockwave. This shockwave propagates as a broadband ultrasound transient through the sample.

Acoustic response analysis

The ultrasound propagation is strongly influenced by the mechanical properties and struc-

ture of the sample. Defects, such as cracks or delaminations, lead to scattering, diffraction and interference, and consequently alter the ultrasound response emitted to the surrounding air, causing distinct 'acoustic fingerprints'. The Optical Microphone is able to detect these signals in a broad frequency range enabling spectral analysis. In the following, we show the application of the presented setup to the characterization of quality variations between different production runs for small ceramic components.

NDT of small ceramic elements

The presented setup was used to differentiate between production batches of cylindrical ceramic elements with ~15 mm length. The production batches vary in quality, with one batch previously identified as prone for failure. The samples were illuminated by the excitation laser on one end. The acoustic response formed by waves propagating along the cylinder axis was recorded on the other cylinder end with an optical microphone (Eta450 Ultra).

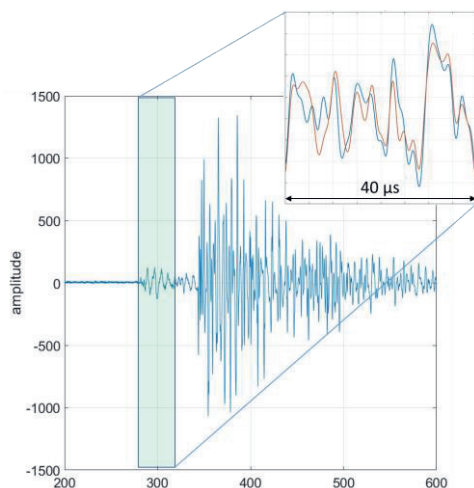


Fig. 2: Exemplary acoustic signal. The signal consists of a sound wave propagating through the ceramic part, relevant for analysis (highlighted), and a high-amplitude delayed component travelling through air from the excitation zone to the microphone.

Results

Segments of the recorded signals (Fig. 2) from 175 different samples were subjected to a correlation analysis, revealing clustering according to the different production batches. Figure 3 displays the Pearson correlation coefficients for each pair of signals, where brighter areas indicate higher correlation. While certain batches feature significant cross-correlation, notably the nOK-labelled batch (cluster 5 in Figure 3) deviates from the remaining samples in terms of its acoustic response.

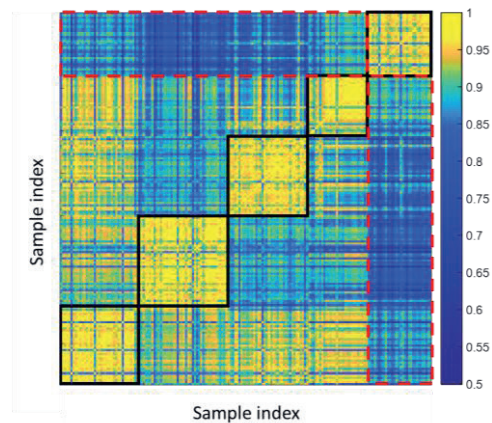


Fig. 3: Pearson correlation between acoustic signals as shown in figure 1 from 175 samples. Black boxes indicate production batches, the red-dashed box highlights the low-correlation between faulty batch 5 and the rest of the samples.

The recorded signals are well-suited for classification by different machine learning algorithms. The preliminary result of classification by a support vector machine (SVM), trained on 50% of the available data, is shown in figure 4.

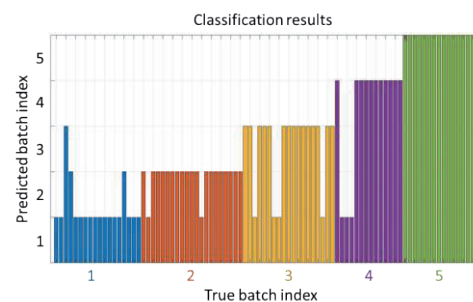


Fig. 4: Classification by machine learning. Different colors indicate production batches, the y-axis indicates the batch classification by the algorithm.

86% of the test data has been classified correctly according to the batch labelling provided for the samples. The influence of quality variations within each batch on the classification results is a question under current investigation.

Conclusions

We presented an innovative non-contact ultrasound NDT setup and its application towards quality control for small ceramic components. The setup has interesting prospects for in-line integration in various industries, such as testing of precision welds or quality control in semiconductor industry.

References

- [1] Fischer, B. 'Optical microphone hears ultrasound.' *Nature Photon* **10**, 356–358 (2016).
- [2] Davies, S.J. et al. 'Laser-generated ultrasound: its properties, mechanisms and multifarious applications. *J. Phys. D* **26**, 3, 329-348 (1993)

Condition Monitoring of Machine Elements using Magneto-resistive Sensors

Dr. Rolf Slatter
Sensitec GmbH, Lahnuau, Germany
rolf.slatter@sensitec.com

Summary:

Intelligent sensors are a key enabling technology for availability-oriented business models (e. g. “pay-per-use” models) in the manufacturing and power generation industries [1]. Intelligent sensors also provide data as a basis for “data as a service” business models [2]. Both these trends make use of sensors to provide information concerning the health or condition of machinery, which is used, in turn, to enable preventive maintenance and so ensure the high availability of the machines concerned.

Keywords: Condition Monitoring, Machine Elements, Sensors, Magnetic Sensors, Magneto-resistive effect

Many different methods are applied to gather information about the condition of machines. A classic approach is to measure vibration and acoustic emission is an associated technique. Furthermore temperature can be measured and wear monitored by analyzing debris in lubricants. However, most of these approaches are limited to applications in specific fields and are rarely used in broad industrial applications. Recently, two new approaches have gained in acceptance, namely the measurement of “Instantaneous Angular Speed” (IAS) [3] and “Motor Current Signature Analysis” (MCSA) [4]. Both techniques can use existing sensors, provided they are small, precise and robust, as well as featuring a high bandwidth and low power consumption [4, 5]. Machine and plant builders often have the additional requirement that they wish to use existing sensors or measurement points, rather than increase system complexity by adding additional sensors.

Magneto-resistive (MR) sensors are capable of fulfilling this complex set of requirements. The results of two recently completed BMBF-funded R&D projects demonstrate the potential of MR sensors for the condition monitoring of electro-mechanical actuators including gearboxes and other mechanical transmission elements, such as ballscrews [6, 7]. In both projects tooth sensor modules (see Fig. 1), based on the giant magneto-resistive (GMR) effect are used to monitor both the instantaneous angular speed of gears (see Fig. 2) as well as the wear of transmission components (see Fig. 3). Use is also made of current sensors based on the anisotropic magneto-resistive (AMR) effect for

motor current signature analysis, by measuring the stator current of the electric motor (see Fig. 4). Even though the current sensors are mounted in the inverter of the electro-mechanical drive, it has been shown that the sensors are sensitive enough to measure the feedback from mechanical vibrations in the gearbox or ballscrew with high resolution.

These techniques are opening up completely new cost-effective and reliable opportunities for condition monitoring of machine elements as a basis for predictive maintenance models.

This paper will describe the basic functions of MR sensors and their specific advantages compared to other sensor principles. The results of the a.m. state-funded projects will be described alongside a number of industrial applications. The paper will conclude with an outlook concerning new methods of signal processing, such as machine learning, which are leading to even better predictions concerning machine condition [8].

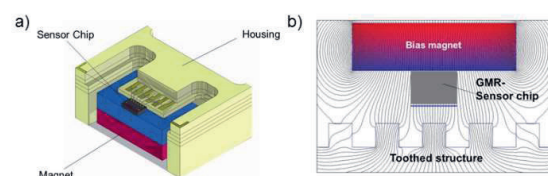


Fig. 1: GMR Tooth Sensor Module (Source: Sensitec GmbH)

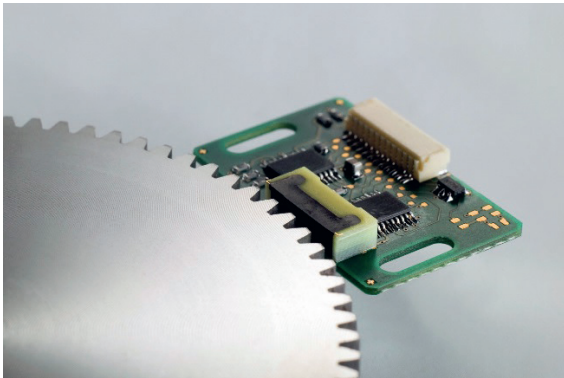


Fig. 2: Application Example (Source: Sensitec GmbH)

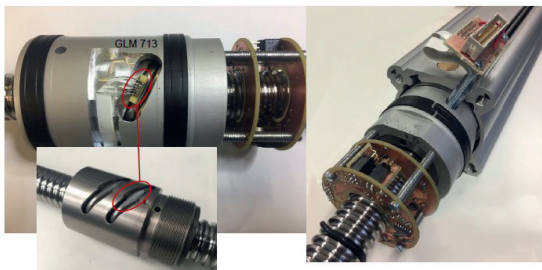


Fig. 3: Monitoring of ball and race wear in a ballscrew using a GMR sensor (Source: Sensitec GmbH)

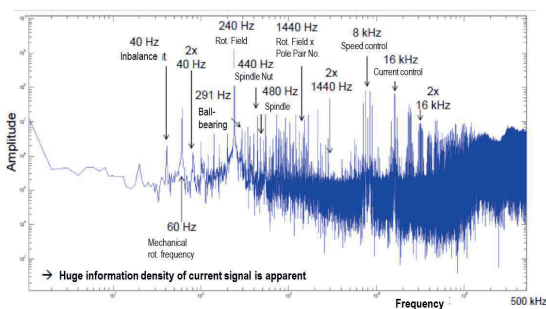


Fig. 4: Frequency spectrum for electro-mechanical linear actuator measured using an AMR current sensor in the inverter (Source: ZEMA gGmbH)

References

- [1] Kölsch, P. et al: "A novel concept for the development of availability-oriented business models", *Procedia CIRP* 64 (2017) pp. 340 – 344
- [2] Schmitt, R. & Voigtmann, C.; "Sensor information as a service – component of networked production", *J. Sens. Sens. Syst.*, 7, 389–402, 2018
- [3] Zeng, Q. et al: "Planetary Gear Fault Diagnosis Based on Instantaneous Angular Speed Analysis", *Proc. of 23rd International Conference on Automation and Computing*, University of Huddersfield, September 2017
- [4] Slatter, R.: "Emerging magnetic sensor technologies for condition monitoring and non-destructive testing", *Proc. of Smart Systems Integration Conference*, Copenhagen, March 2015
- [5] Slatter, R.: "Intelligente Sensoren als Enabler smarterer Produktsysteme", *Proc. of SysLM Tagung 2017*, Kaiserslautern, October 2017
- [6] Wiegel, T. & Seewig, J.: "Robust wear-detecting sensor concepts to realize innovative services and availability-oriented business models in capital goods industry", *Proc. of 14th MR-Symposium*, Wetzlar, March 2017
- [7] Helwig, N.: "Modular Sensor Systems for real time Process Control and Smart Condition Monitoring using XMR sensor technology", *Proc. of 14th MR-Symposium*, Wetzlar, March 2017
- [8] Slatter, R.: "Condition Monitoring of Gearboxes using Magnetoresistive Sensors", *Proc. of 8th International Conference on Gears*, Munich, September 2019

Inline Inspection of Ceramic Tape Casting Processes by Means of Optical and Eddy Current Methods

Manuela Heymann¹, Stefan Münch¹, Martin Schulze¹, Beate Capraro², Dirk Schabbel², Andy Vogel²,
Thomas Härtling^{1,3}

¹ Fraunhofer Institute for Ceramic Technologies and Systems IKTS, Maria-Reiche-Strasse 2, 01109
Dresden, Germany,

² Fraunhofer Institute for Ceramic Technologies and Systems IKTS, Michael-Faraday-Strasse 1,
07629 Hermsdorf, Germany

³ Technische Universität Dresden, Institute of Solid State Electronics, Mommsenstraße 15, 01069
Dresden, Germany

thomas.haertling@ikts.fraunhofer.de

Summary:

Tape casting is a ceramic forming technology used to produce planar ceramic components by means of a doctor-blade process. However, industrial casting plants are currently not equipped with inline measurement tools which allow detecting of defects and determine quality parameters of the ceramic tape. Here we use laser triangulation, camera-based monitoring and eddy current measurement tools to acquire different tape quality parameters. Initial results of the implementation of these tools and the insights gained by sensor data fusion will be presented.

Keywords: tape casting, process monitoring, ceramics, optical inspection, eddy current

1 Introduction

Tape casting is a highly productive method for producing large, flexible tapes of functional materials very efficiently and cost-effectively in roll-to-roll processes. Applications for the tapes range from classic ceramic microsystem technologies (LTCC and HTCC) and the current strategic field of battery research to filtration, gas separation, and a variety of special functional tapes. Finely ground ceramic powders are dispersed under addition of suitable dispersants, organic binders and plasticizers. The resulting viscous casting slurry undergoes a doctor-blade process and subsequent drying done in a drying channel of several meters of length. The result is a very thin ceramic tape with flat surface.

The tapes produced can show several defects such as air pockets, bubble formation, large particle inclusions, density fluctuations of the slurry and fluctuations of the tape thickness. At present, industrial casting plants are not equipped with process monitoring tools which allow detecting of defects and determine quality parameters inline. As a result, defects and parameters outside specification margins are only detected after the manufacturing process and the operators face high costs due to rejects.

The authors intend to evaluate measuring methods for defect detection, to develop an inline application and in future adapt the information of the different methods to an overall description of the tape quality.

Measuring method used here are laser triangulation for thickness determination at the beginning and end of the drying channel (measurement of wet and dry film thickness), optical inspection, and the eddy current technology at the end of the drying line (detection of inclusions, material defects, holes, deviation in dielectric constant). The methods have been evaluated and optimized with regard to hardware, location and method of implementation, data generation and evaluation, and were integrated at a demonstration casting plant.

In this contribution we show results of the different monitoring systems and the effects on operating tape casting machines.

2 Measurement System

For thickness measurement four laser triangulation sensors (Keyence, LK-H087) were installed (a static reference and a dynamic sensor each at the beginning and the end of the drying line). Hence, they were applied in differential mode to determine the film height. Furthermore, optical

inspection is carried out with a single line camera (Teledyne Dalsa Linea) and alternating illumination in reflecting and transmission mode. Images were acquired exploiting the movement of the ceramic foil under the line sensor of the camera. This system was intended to detect defects in the ceramic foil. As a third component, an inline eddy current array probe set up by Fraunhofer IKTS [1] was installed at the backend of the drying line. This system allows to evaluate especially the (di)electric properties of the cast foil. It was operated in reflection mode.

3 Results

After the implementation of the described measurement tools initial results were obtained which allow a first inline characterization of the ceramic tape. For demonstration, a sample casting with an Al_2O_3 -slurry was carried out. The tape width was 150 mm, the doctor-blade gap $150\ \mu\text{m}$ (tape wet thickness) and casting velocity $0.8\ \text{m/min}$.

Thickness measurement results (backend of drying line) are displayed exemplarily in Fig. 1.

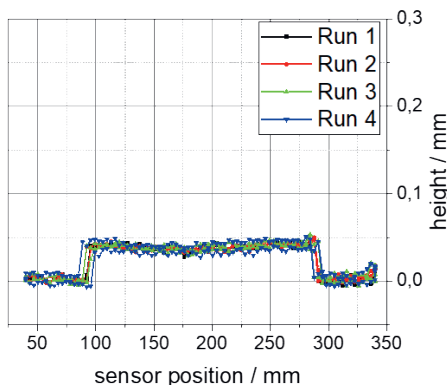


Fig. 1 Inline thickness measurement of the dry ceramic green tape.

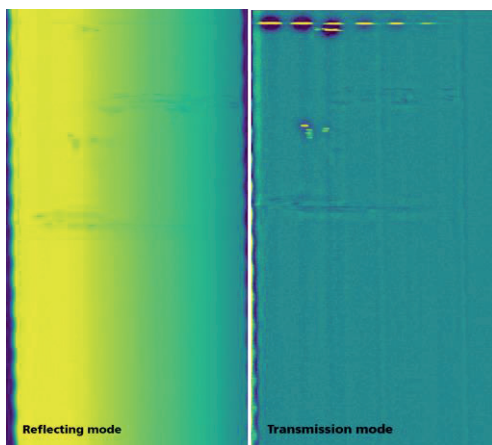


Fig. 2 Optical inspection with alternating illumination: left reflecting mode; right transmission mode. On the top right, a series of holes is detected which leads to exclusion of this foil are for further processing.

The optical inspection tool allows to detect specific defects (holes), favorably in transmission mode (see Fig. 2, top). Finally, a first test of the eddy current setup allows to detect NdFeB particles in the foil. They are marked as blue spots in the image in Fig. 3.

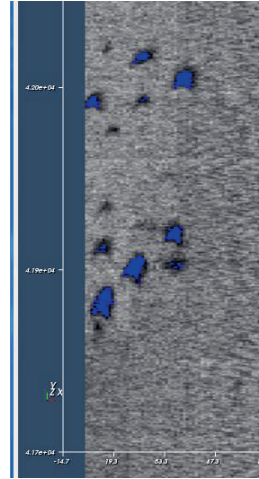


Fig. 3 Detection of NdFeB particles (blue spots) by means of the eddy current system.

Based on these first results and the ongoing work, our contribution will provide a detailed description of the measurement system in use, a classification of detectable defects and the benefits achieved by fusing the data of all three measurement tools.

References

- [1] M. Wild, A. du Barét, S. Reuber, M. Schulze, H. Heuer, M. Wolter, A. Michaelis, Analysis and monitoring of the percolating network of battery electrode films during the drying process using eddy current technology, Lecture, *International Battery Production Conference IBPC 2019*, 5.11.2019

Characterization of Sand and Sand-Binder Systems from the Foundry Industry with Impedance Spectroscopy

*Luca Bifano*¹, *Alice Fischerauer*¹, *Alfred Liedtke*², *Gerhard Fischerauer*¹

¹ *Chair of Measurement and Control Systems, Universität Bayreuth, 95440 Bayreuth, Germany,*

² *Michenfelder Elektrotechnik, An der Fahrt 4, 55124 Mainz, Germany, mrt@uni-bayreuth.de*

Summary:

It would be very advantageous if the condition of molding materials (sand-binder systems) in regenerator units used in foundries could be monitored in real-time. This work presents the results of investigations in this direction. It is shown that the condition monitoring can possibly be based on impedance spectroscopy because the resulting curves are characteristic of the material used. New and used sands as well as two-component mixtures of sands and binders showed a systematic behavior, which allows the sand or the composition of the mixture to be identified (classified) in the future.

Keywords: Foundry, sand, bentonite, condition monitoring, impedance spectroscopy

Background

The raw material sand is mined more than the natural regeneration of the sand deposits can compensate [1, 2]. One reason for this is that the foundry industry needs the sand to produce so-called lost forms and cores with binders like bentonite. As a consequence, used sand is now routinely recycled to save on raw material and to avoid the expensive disposal of used sand in landfills.

As the type and quality of sand play an important role in foundry applications, the qualification of the raw and regenerated materials is defined by industry regulations. In Germany, e. g., the guidelines are drafted by the Bundesverband der Deutschen Gießerei-Industrie (Federal Association of the German Foundry Industry, BDG). As yet, laboratory tests are the standard method [3].

To achieve optimum results at the lowest possible cost, the sand condition needs to be monitored during the recycling process. Our goal is to base such a condition monitoring on impedance spectroscopy. Known results from the literature indicate that the characteristics of different raw materials such as grain size distribution, crystal structure, and moisture may be distinguishable with this method. For example, [4] shows how the permittivity of bentonite depends on its water content. Ref. [5] describes the complex permittivity of sand-bentonite-water mixtures by a plausible model. We have now extended this approach and have investigated whether the various moulding materials can be characterized by impedance measurements.

Measurement Setup

Our measurement setup comprised a circular cylindrical cell, which could be filled with the material under test (MUT). The cell was equipped with two opposing copper electrodes (diameter 13 cm, plate spacing 4 cm), which were soldered to two coaxial cables. The bottom and top electrodes were respectively glued to a wooden plate and a Makrolon cylinder. The casing of the cell was made of a polymer. The impedance of the MUT-filled cell was measured by an LCR meter E4890A from Agilent in the frequency range from 20 Hz to 1 MHz.

The results presented in this work pertain to the materials listed in Table 1. MUT 1 was a quartz sand suitable for foundries. MUT 2 was a chromite sand that used for molded parts subject to high thermal loads. The average grain diameter was 0.2 mm MUT 1 and 0.3 mm for MUT 2.

Tab. 1: Chemical composition (percentage mass fractions) of the examined materials. B. = Bentonite.

MUT	Mass fraction in %					
	SiO ₂	Al ₂ O ₃	Cr ₂ O ₃	Fe ₂ O ₃	MgO	B.
1	99.53	0.01		0.01	0.01	0
1a	(As MUT 1 with heating to 800 °C.)					
2	0.7	14.8	46.4	28.2	9.5	0
3a	98.53	0.01		0.01	0.01	1
3b	96.54	0.01		0.01	0.01	3
3c	94.55	0.01		0.01	0.01	5
3d	91.57	0.01		0.01	0.01	8
3e	89.58	0.01		0.01	0.01	10

A sample of MUT 1 ("MUT 1a" in Table 1) was exposed to 800 °C for more than 88 hours, then cooled and measured again. This simulated the

casting process and the associated thermal load on the sand. The two differently processed samples of the quartz sand are referred to as “new sand” (MUT 1) and “old sand” (MUT 1a) in the following. The materials termed MUT 3a through 3e in Table 1 were samples of MUT 1 mixed with various amounts of bentonite.

Results

Figure 1 shows the Nyquist plots of measured test-cell impedances for various materials. The results of eleven independent measurements of MUT 2 were plotted to convey an idea of the reproducibility of the measurement. For the quartz sand (MUT 1 and MUT 1a), the reproducibility was even better so that it was justifiable to plot the mean values only (result of nine and five independent measurements in the case of MUT 1 and MUT 1a, respectively). The relative standard deviations in the resistance $\text{Re}\{Z(f)\}$ and the reactance $\text{Im}\{Z(f)\}$ were below 1.21 % and 0.07 %, respectively, at all frequencies for MUT 1. The corresponding numbers for MUT 1a were 0.77 % and 0.02 % for MUT 1a.

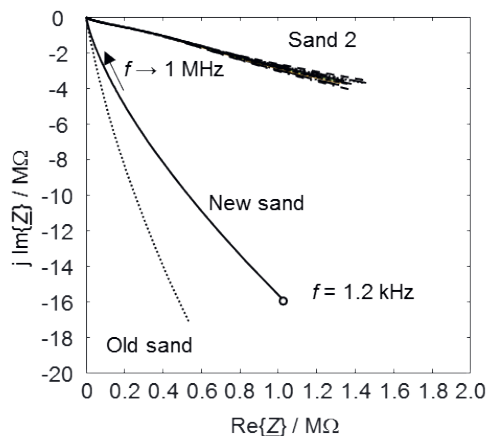


Fig. 1. Measured test-cell impedance with MUT 1, MUT 1a, and MUT 2, respectively.

The measured impedances may be approximately interpreted in terms of parallel RC circuits. The slope of the curve in the Nyquist plot is then equal to $-\tan(\omega RC)$. At equal frequencies, thermally processed sands (MUT 1a) lead to steeper slopes than the other sands, corresponding to higher values of R , i. e., lower electrical conductivities. This is attributed to the fact that the sand grain surface partly bursts when heated. This leads to an increased porosity and more air in and between the sand grains. SEM images of the grain surface and a decrease in the bulk density corroborate the explanation.

By a similar line of reasoning, MUT 2 is more conductive than the quartz sands. The reason is the higher packing density (more conduction paths) and the different composition (Fe^{2+} ions in the crystal lattice) [3, 6].

The measurement results for sand-bentonite mixtures (MUT 3a through 3e in Table 1) are visualized in Fig. 2. The electrical conductivity obviously increases with the bentonite content. This is plausible as bentonite contains cations and water molecules in its lattice [3].

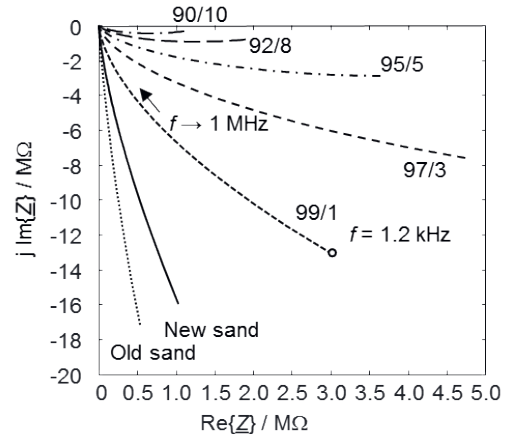


Fig. 2. Measured test-cell impedance with MUT 3a through 3e. The curves for MUT 1 and MUT 1a are given for comparison's sake.

Conclusion

Our study of sand and sand-binder mixtures clearly demonstrates that it is possible to classify the materials based on impedance measurements. The transfer of these results to a measurement system usable for the in-process condition monitoring within sand regenerators in foundries appears highly desirable. This is the subject of ongoing work.

Acknowledgment

This work was supported by the German Federal Ministry for Economic Affairs and Energy, grants number ZF4152305DB8 and ZF4556201DB8.

References

- [1] J. Götze, M. Göbbels, *Einführung in die Angewandte Mineralogie* (Introduction to Applied Mineralogy; in German). Berlin: Springer, 2017.
- [2] N. N., *Sand and sustainability. UN Environmental Programme*, Geneva, Switzerland, 2019.
- [3] W. Tilch, H. Polzin, and M. Franke, *Praxishandbuch bentonitgebundener Formstoff* (Practical manual for bentonite-bound molding material; in German). Berlin: Schiele & Schön, 2019.
- [4] H. Kaden et al., “Low-frequency dielectric properties of three bentonites at different absorbed water states,” *J. Colloid Interface Sci.*, Vol. 411, pp. 16–26, Dec. 2013.
- [5] T. A. Belyaeva et al., “The effect of very low water content on the complex dielectric permittivity of clays, sand-clay and sand rocks,” *Meas. Sci. Technol.*, Vol. 28, No. 1, (8pp), Jan. 2017.
- [6] M. Okrusch, S. Matthes, *Mineralogie* (Mineralogy; in German). Heidelberg: Springer, 2005.

Non-destructive validation method for understanding water uptake processes of moldings in electronic packaging

Paul Gierth, Lars Rebenklau, Uta Gierth, Ulrike Langklotz, Michael Schneider
 Fraunhofer IKTS, Winterbergstrasse 28, 01277 Dresden, Germany
 paul.gierth@ikts.fraunhofer.de

Summary:

The long time stability of molding compounds in electronic packages is critical for many applications. Modern characterization methods focusing on pass / fail criteria, so that a deeper understanding of degradation mechanisms could not be achieved in that way. EIS and FTIR, commonly used in corrosion research, were transferred and demonstrated as validation method for the water uptake and chemical changing during loading scenarios. The usability of these non-destructive methods will be demonstrated and the results were used to generate degradation models for such molding materials.

Keywords: Electrochemical impedance spectroscopy, Fourier transform infrared spectroscopy, molding compound, degradation mechanism

Motivation

All electronic devices consist of metallic conductors and insulating materials as substrates or moldings. Interfaces between these materials groups are unavoidable. Main purpose of mainly organic molding materials are corrosion protection of conductors and electronic components. Therefore, the longtime stability of these materials against different loading scenarios is critical for many applications. Usually, modern test scenarios only focus on pass or fail results, e.g. mechanical characterization methods like shear strength measurement following MIL Std. 883 [1]. Such tests are regularly performed before and after defined loading scenarios like damp heat, temperature cycling or pressure cooker treatment. Unfortunately, the results only summarize the accumulated alteration at the time of test. An deep understanding of the fundamental reaction processes or kinetics can't be achieved in that way, but is necessary for further improvement of materials and technologies. Therefore, transferring these methods from the corrosion research on electronic materials can overcome this not acceptable state of knowledge.

EIS and FTIR for electronic industry

Electrochemical impedance spectroscopy (EIS) and Fourier-transform infrared spectroscopy (FTIR) are standard methods in the corrosion research. Using these methods to characterize electrical and chemical conditions of a molding or encapsulation in-situ during loading scenarios can help to generate degradation models of these inspected materials.

Results

Epoxy based molds with typical applications like encapsulation or dam and fill were selected and cured on printed circuit boards (PCB) with electroless nickel immersion gold (ENIG) finishes. These samples were aged for up to 96 h in a pressure cooker test according [2] and further inspected regarding their shear strength stability on the substrate surface (see Fig. 1)

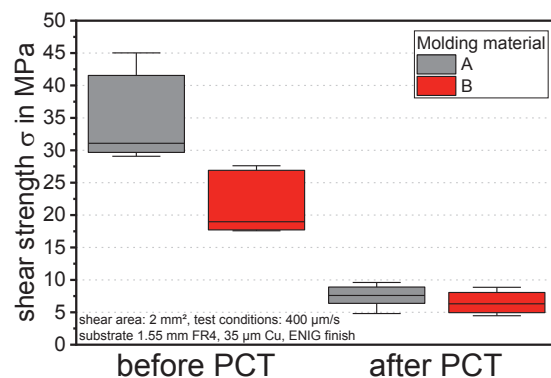


Fig. 1. Shear strengths of epoxy based molds from ENIG surfaces before and after pressure cooker treatment (PCT)

The optical inspection of all fracture zones shows adhesive as well as cohesive failure mechanisms. Consequently, no clear degradation mechanism could be observed. Optical inspection of the molding surface shows, that mold A shows in some regions defects like blisters, pinholes or inclusions. Mold B seems to be nearly free of defects.

Further samples were inspected with EIS and FTIR before and after PCT to generate a better understanding of the degradation mechanism.

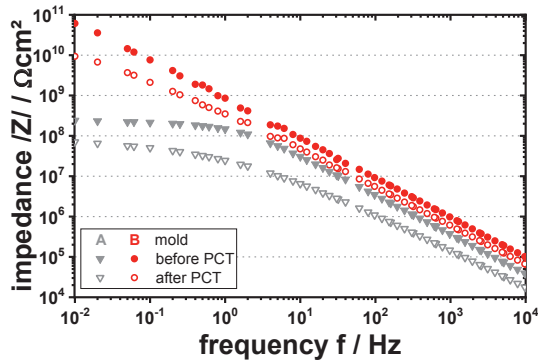


Fig. 2. EIS: Impedance of mold A (left) and B (right) before and after pressure cooker treatment (PCT).

EIS helps to get more into detail and focusing on electrical parameters of the molding compound itself. Especially the change in capacity during different loading scenarios is used to calculate water uptake WU of the material by using eq. (1) according [3].

$$WU = \frac{\lg\left(\frac{C_t}{C_o}\right)}{\lg 80} \cdot 100 \text{ (Vol. \%)} \quad (1)$$

The water uptake was calculated to approximately 21 Vol.% for mold A and 11 Vol.% for mold B. The different results indicate different water penetration scenarios. For the nearly perfectly cured mold B, liquids could only penetrate the material by a more or less homogeneous diffusion across the mold. A mold with several surface defects (mold A) offers the possibility for inhomogeneous penetration of any kind of liquids into deeper material regions along preferred paths and accelerates the degradation in this way. Selective penetration could be found in phase shift of the impedance during EIS measurement and was used to generate following equivalent circuits according [4, 5].

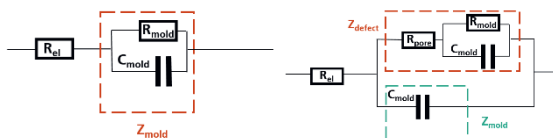


Fig. 3. Equivalent circuits of molds on metallic surfaces without surface defects (left) and with liquid penetrated pores (right).

Therefore, pre-existent defects previously detected by optical microscopy of mold A could clearly be seen in the initial EIS measurement (lower impedances) and their influence on environment stability could be described using the shown methods. In that way, a better understanding of different degradation mechanisms

could be found without destruction of the molding samples, which demonstrates the usability of this measurement method as material and application controlling method. For a complete understanding of the ongoing degradation mechanisms during the applied loading scenarios FTIR inspections must be applied. This method focus on the actual material state instead on the electrical characteristics of the material. In that way, alteration of material due to environmental impact or degradation can be inspected more in detail (see Fig. 4).

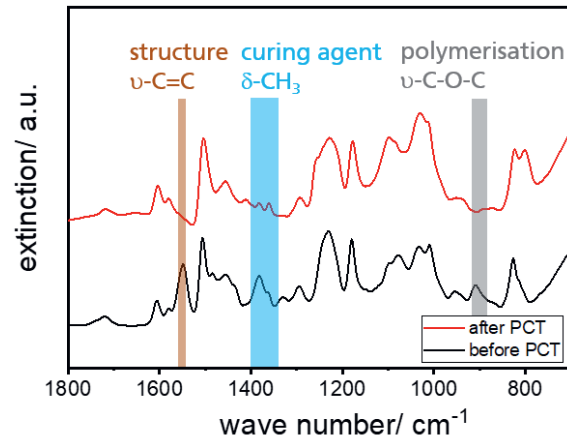


Fig. 4. FTIR band spectrum of mold A before and after pressure cooker treatment with highlighted changes in characteristic wavelengths.

The obviously change in intensity of characteristic bands of aromatics, solvents or epoxy indicates a significant change of the material during the load scenario. Results like this are appropriate to generate better understanding in material degradation mechanism and material state monitoring over product lifetime cycles. Therefore, methods like EIS and FTIR are highly recommended to be transferred from the corrosion research to the electronic industries.

References

- [1] Military Specification (MIL)-883, Method 2019.9 Die shear strength, revision E, Department of Defense, 1991.
- [2] DIN Standard 60749: Part 33 accelerated moisture resistance, Beuth Verlag, 2004.
- [3] D. M. Brasher, A. H. Kingsbury, electrical measurement in the study of immersed paint coatings in metal, Journal of Applied Chemistry, 1954.
- [4] U. Rammelt, habilitation thesis, TU Dresden 1991.
- [5] G. Grundmeier et al.: Electrochim. Acta 45 (2000) 2515

An Approach for Feature Interpolation Between Classes to Simplify Calibration of Sensor Systems for Odour Monitoring

Julian Joppich, Manuel Bastuck¹, Andreas Schütze, Tilman Sauerwald²
Lab for Measurement Technology, Saarland University, Saarbrücken, Germany,
j.joppich@lmt.uni-saarland.de

Summary:

An approach for the augmentation of n-dimensional data was implemented and tested using artificial and real gas sensor data. With this method, a new (super)class is generated from two or more smaller classes by interpolating between these initial classes. It can be useful, for example, to assign a larger part of the feature space to a specific group of substances when performing classification tasks. Interpolation between two normally distributed classes generates very good results. For the interpolation between more than two classes or between inhomogeneous classes, several approaches were tested.

Keywords: class interpolation, features, classification, temperature cycled operation, MOS gas sensor

Background and Motivation

Model training is an important task for any sensor application. Prior to training, a sufficient data set has to be created, including reference data such as class assignments. Typically, a larger dataset can only be generated by conducting more measurements, which is time consuming and expensive, especially for gas sensors for odour classification. Moreover, for classification tasks of gas mixtures, the data set might still contain distinct gaps as only a limited number of gas concentration combinations can be tested efficiently. Especially if a group of gases is to be classified as one class and not identified individually, an approach to close these gaps and form a (super)class from two or more smaller classes might be desirable, which is the idea of the class interpolation presented here. We tested gases with similar odour, i.e. Sulphur compounds.

Interpolation Method

The interpolation is implemented as a MATLAB function based on a description of every class by its centroid and covariance matrix to represent the n-dimensional feature "cloud". This implies that the classes are assumed to follow an n-dimensional normal distribution. Based on the centroids, the relation between two classes can be determined (distance and connection vector). The interpolated class is then built by successively generating normally distributed random clouds with a given centroid, covariance matrix and number of data points, with each of these variables being linearly interpolated between the

two initial classes. An important parameter is the step length between the two classes. It is calculated from the extension of the individual class in the direction of interpolation weighed by the square root of the norm of the covariance matrices of the classes. For every sequentially generated cloud, the covariance matrix is reduced by a factor of two preventing the algorithm from generating too widespread clouds and extrapolating too far beyond the original margins. The size of the combined (super)class is reduced to max 10 times the size of the initial classes by transferring only every k-th artificial data point to the final array. This step reduces the computational expense if the algorithm is applied repeatedly and the risk of an unintended higher weight of the new class in relation to the initial classes.

Example Data

The experimental data used for testing the interpolation method were obtained from a gas measurement similar to [1]. A temperature cycled AS-MLV-P2 (ams Sensor Solutions Germany) was exposed to different mixtures of hydrogen sulphide (H₂S), dimethyl sulphide (DMS) and ammonia (NH₃) in varying hydrogen concentrations. The slopes of the logarithmic sensor conductance at low temperature plateaus were calculated according to the DSR model [2] with the toolbox DAV³E [3] and extracted as features. The cycle contains six low temperature plateaus, resulting in a six-dimensional feature space. As one gas class contains several concentrations, the classes are very inhomogeneous.

¹ Currently at WIPOTEC GmbH, Kaiserslautern, Germany.

² Currently at Fraunhofer Institute for Process Engineering and Packaging IVV, Freising, Germany.

Results

The interpolation between two normally distributed classes is always successful. However, if a class contains several sub-clusters, e.g. different concentrations of a gas, or if at least one of the input classes is of a more elongated shape, the resulting new class might have unexpected and not predictable shapes, sizes and densities. The same is true for the successive interpolation between three classes (interpolation between classes 1 and 2, followed by interpolation between the new class and class 3). In the case of three classes, it is more successful to first combine two classes to a temporary new class and then perform the interpolation with the third class. Fig. 1 depicts such an interpolation for three artificial random classes in 3D. The two classes at the bottom were combined first in one temporary class, interpolation of the temporary class with the class at the top resulted in the final class (cyan).

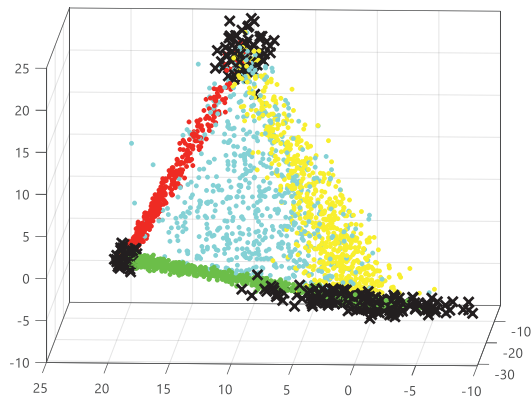


Fig. 1. Interpolation (cyan) between three artificial data clouds (black). The red, yellow and green data points represent the results of every possible two-class interpolation between the three initial classes.

The classes (features) of the two Sulphur compounds (H_2S and DMS) of the gas measurements were interpolated similarly. Instead of interpolating all H_2S and DMS concentrations directly, two temporary mixed classes were built by combining lower and higher concentrations of both gas classes, followed by an interpolation between the resulting two temporary classes, which lead to satisfactory results (Fig. 2).

Summary and Outlook

The implemented interpolation method leads to good results for all normally distributed classes tested and with some adjustments of the interpolation approach also for non-normally distributed classes. However, the robustness of the algorithm could be improved further and it needs to be tested on more datasets. Moreover, the performance of the interpolated (super)class for classification, e.g. when performing a linear discriminant analysis, will be tested.

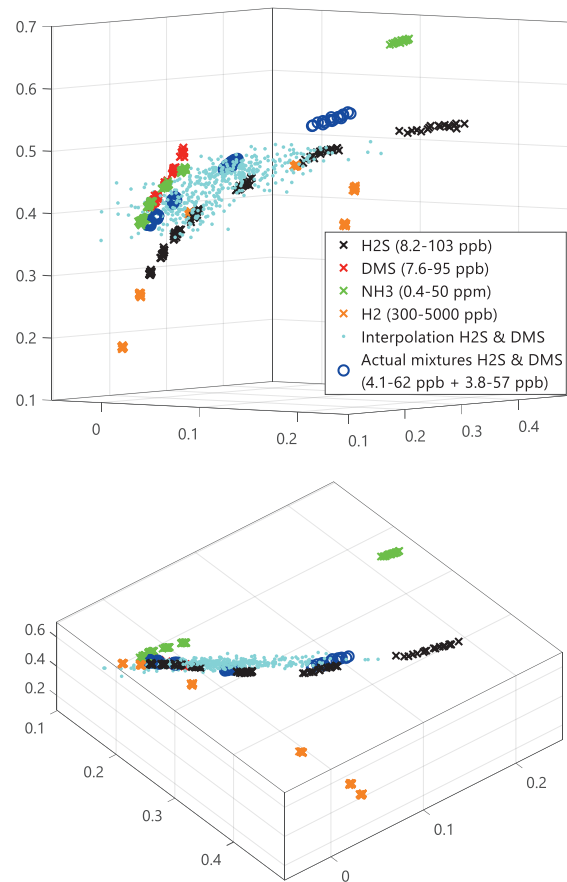


Fig. 2. 3-dimensional representation of the (6-dimensional) interpolation (cyan) between two classes (H_2S and DMS) from two perspectives. Individual gases and their interpolation form one plane, on which the actual mixtures of both gases (blue) lie also. Only a mixture with higher concentrations (highest blue data points) lies outside the interpolated class.

Acknowledgements

This work was carried out within the SEPEG project, funded by the Federal Ministry for Education and Research (BMBF) under project number 01IS17087. We thank our partners 3S – Sensors, Signal Processing, Systems GmbH, Saarbrücken, and Olfasense GmbH, Kiel, for the important contributions and the good cooperation.

References

- [1] J. Joppich, A. Schütze, T. Sauerwald, Unterscheidung und Quantifizierung von Geruchsstoffen im ppb-Bereich mit temperaturzyklisch betriebenen MOS-Sensoren, 20. GMA/ITG-Fachtagung Sensoren und Messsysteme 2019, 482-487 (2019); doi: 10.5162/sensoren2019/6.2.1
- [2] T. Baur, C. Schultealbert, A. Schütze, T. Sauerwald, Novel method for the detection of short trace gas pulses with metal oxide semiconductor gas sensors, *J. Sens. Syst.* 7, 411-419 (2018); doi: 10.5194/jsss-7-411-2018
- [3] M. Bastuck, T. Baur, A. Schütze, DAV3E – a MATLAB toolbox for multivariate sensor data evaluation, *J. Sens. Syst.* 7, 489-506 (2018); doi: 10.5194/jsss-7-489-2018

Robust Optimization of Self-x Sensory Electronics in Presences of Environmental Variations for Industry 4.0

Qummar Zaman¹, Senan Alraho¹, Andreas König¹

¹Lehrstuhl Integrierte Sensorsysteme (ISE), TU Kaiserslautern Deutschland, qummar@eit.uni-kl.de

Summary:

This paper introduces a new methodology to robustly optimize the re-configurable self-x ICs for industry 4.0 in the presence of environmental uncertainty (EU). For handling the EU, variance measure methodology has been selected due to its simplicity. The traditional particle swarm optimizer has been amended by adaptively adjusting its acceleration coefficients and expanding its selection procedure. The performance of the proposed modifications has been tested on two bench-marking functions. The extrinsic evaluation of the proposed algorithm has also been done on an instrumentation amplifier.

Keywords: Instrumentational amplifier, Sensory electronics, Self-x properties, Robust optimization, adaptive weight robust particle swarm optimizer.

Background, Motivation and Objective

The reliability, performance and accuracy of sensory electronics (SEs) are significantly improving with the introduction of self-x (self-calibration, self-healing, etc.) properties for industry 4.0. To introduce self-x properties in reconfigurable SEs, evolutionary and meta-heuristic algorithms have shown superiority and powerful capabilities in addressing the multi-objective optimization problems. A considerable amount of literature is available for the introduction of self-x properties in integrated electronics (ICs) [1]. However, the optimization of ICs in the presence of uncertainties is very rare [2]. In general, there are three different types of uncertainties in ICs, i.e., drift due to fabrication process (input uncertainty), uncertainty due to imperfect observer: (output uncertainty) and environmental uncertainty (EU). While in [2] authors have recently proposed the noise immune meta-heuristic algorithms for handling the input and output uncertainty of sensory electronics for industry 4.0, the primary objective of this paper is the robust optimization of reconfigurable ICs in the presence of EU.

Traditional particle swarm optimizer (PSO) is being elected as an optimizer for this research. Wide swing reconfigurable indirect current feedback instrumentational amplifier (CFIA) [3] which is an integral part of SEs is being chosen as a test vehicle for extrinsic evolution of the suggested optimizer. Transistors widths of CFIA are serving as a tuning knobs and system output is being analyzed by the robust optimizer for its online trimming as shown in Fig. 1. For tack-

ling EU, variance measure has been adopted due to its simplicity [4]. The details of the output and input uncertainties can be found in [5].

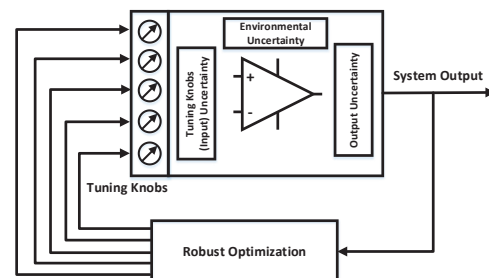


Fig. 1. Types of uncertainties in ICs.

Description of the Proposed Methodology

As already mentioned, PSO has been selected as an optimizer for this research. Due to objective space complexity of fully differential CFIA [6], a sigmoid-function-based weighting strategy [7] is being used to adaptively control the cognitive and social scaling factors, which indirectly optimize the exploitation and exploration while enhancing the convergence rate simultaneously. The basic structure of the proposed adaptive weight robust particle swarm optimizer (AWRPSO) is analogous to confidence-based robust optimization presented in [4], however, AWRPSO adaptively adjusts the acceleration coefficients along with taking EU into account.

AWRPSO begins with random initialization followed by the evolution of cost function. Then the variance measure will be evaluated to confirm the robustness of the solution. The particle's personal or global best is being amended in case of better fitness value. The cogni-

tive c_1 and social c_2 scaling factors are being updated according to the following equations

$$c_1 = c_2 = F(D) = \frac{a}{1 + e^{-c(D-d)}} + b$$

where $a = 0.5$, $b = 1.5$, $c = 0.000035 \times \text{search range}$ (distance between upper & lower bound of particle), $d = 0$ and $D = P_{p \text{ or } g}(k) - x_i(k)$ which represent the distances of the particle i to its p_{best} or g_{best} at k_{th} iteration. After that, the particle's velocity and position are being updated, this procedure continues until maximum iterations. The details of the remaining AWRPSO parameters can be found in [2].

Results

For performance visualization of AWRPSO, further two different bench-marking functions (Schwefel & Griewank) from [2] are being opted [7]. To compare the exploitation and exploration capabilities of AWRPSO, three modifications of PSO are selected from the literature [8], i.e., linearly decreased inertia weight (PSO-LDIW), PSO with constriction factor (PSO-CK) and PSO with time-varying acceleration coefficients (PSO-TVAC). This experiment is performed using 30 particles and 750 iterations, while the convergence curve is computed by taking the mean of 100 runs which is depicted in Fig. 2. It is apparent that the convergence performance of the proposed AWRPSO is better than other.

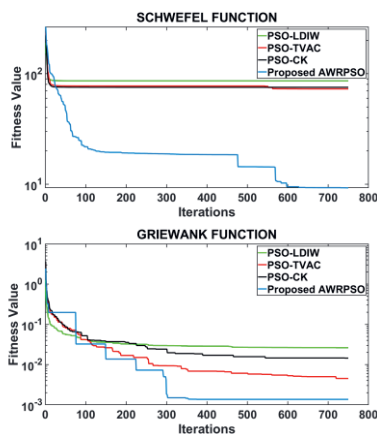


Fig. 2. Mean convergence curve comparison of AWRPSO and other state-of-art PSO.

AWRPSO is also employed on CFIA for its extrinsic evaluation. CFIA circuit is implemented by using AMS CMOS 0.35 μm technology. There are twenty-one tuning knobs (degree of freedom) and six objectives for this design test: bandwidth ≥ 40 MHz, gain ≥ 90 dB, phase margin $\geq 60^\circ$, power dissipation ≤ 2 mW, slew rate (SR) ≥ 50 V/ μs and input common mode range (ICMR) [-1 V, 1 V]. Moreover, all transistors' length is kept constant to 1 μm and AWRPSO

only alters the widths with step size of 1 μm . The detailed schematic diagram of CFIA can be found in [3]. For multi-objective optimization, an agglomerative approach is applied [2]. EU is modelled by varying the temperature from -40°C to $+85^\circ\text{C}$ and the performance deviation of CFIA is illustrated in Fig. 3. It can be seen that without considering EU, the performance of CFIA deviates significantly, while for the robust solution the performance deviation is only 1/8 in case of gain. Hence the proposed extrinsic optimization promises more efficient intrinsic optimization or dynamic reconfiguration. For the intrinsic evolution of AWRPSO, we are actively working on designing of the reconfigurable SE with self-x properties for industry 4.0.

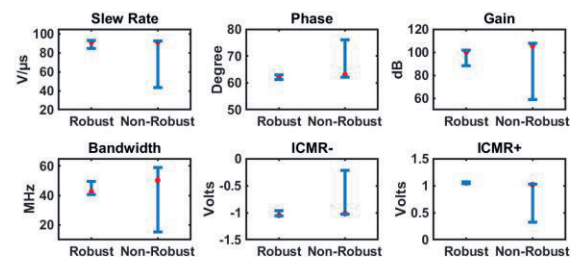


Fig. 3. Comparison of robust and non-robust solution.

References

- [1] Andraud, M., Stratigopoulos, H. G., & Simeu, E. "One-shot non-intrusive calibration against process variations for analog/RF circuits." IEEE TC&S I: R.P. 2016 Sep 23;63(11):2022-35.
- [2] Zaman, Q., & König, A. "Self-x integrated sensor circuits immune to measurement noise in the presence of input perturbation by using robust optimization." *tm-Technisches Messen* 86.s1 (2019): 107-111.
- [3] Alraho, S., & König, A. "Wide input range, fully-differential indirect current feedback instrumentation amplifier for self-x sensory systems." *tm-Technisches Messen* 86.s1 (2019): 62-66.
- [4] Mirjalili, S., Lewis, A., & Mostaghim, S. "Confidence measure: a novel metric for robust meta-heuristic optimisation algorithms." *Information Sciences* 317 (2015):114-142.
- [5] Beyer, H. G., & Sendhoff, B. "Robust optimization—a comprehensive survey." *Computer methods in applied mechanics and engineering* 196.33-34 (2007): 3190-3218.
- [6] De Oliveira, Arthur Campos, et al. "An optimization-based methodology for efficient design of fully differential amplifiers." *Analog Integrated Circuits & Signal Processing* 90.1 (2017): 149-163.
- [7] Liu, Weibo, et al. "A Novel Sigmoid-Function-Based Adaptive Weighted Particle Swarm Optimizer." *IEEE transactions on cybernetics* (2019).
- [8] Liu, Weibo, et al. "A novel particle swarm optimization approach for patient clustering from emergency departments." *IEEE Transactions on Evolutionary Computation* 23.4 (2018): 632-644.

Three-directional Drift Correction Method Based on Iterative Closest Point (ICP) Algorithm

Johannes Degenhardt¹, Rainer Tutsch², Gaoliang Dai^{1}*

¹ *Physikalisch-Technische Bundesanstalt, Bundesallee 100, 38116 Braunschweig, Germany*

² *Technische Universität Braunschweig, IPROM, Schleinitzstraße 20, 38106 Braunschweig, Germany*

**) corresponding author: Gaoliang.Dai@ptb.de*

Summary:

A new method for evaluating and correcting full three-dimensional drift in AFM measurements has been proposed. The method applies two measurement sets: (A) Multiple measurements with reduced resolution and thus reduced measurement time and drift; and (B) One detailed measurement with higher spatial resolution at costs of longer measurement time and larger drift. The data sets are aligned using the iterative closest point (ICP) algorithm to quantitatively evaluate the drift in full 3D. The obtained drifts are then applied to correct the measured data sets to significantly reduce drifts.

Keywords: drift correction, AFM, data fusion, iterative closest point (ICP) algorithm, nanometrology

Background and motivation

Accurate and traceable three dimensional (3D) measurements of complex nanostructures are a crucial and challenging task for e.g. the state-of-the-art nanoelectronic industry. Atomic force microscopy is a widely applied technique for 3D metrology of complex nanostructures with high spatial resolution. To obtain true 3D measurements of complex nanostructures, two kinds of AFM techniques such as flared AFM tip and tilting AFM technique have been widely used.

At the Physikalisch-Technische Bundesanstalt (PTB), a 3D-AFM based on the flared AFM tip has been successfully developed and applied for calibration services [1]. It has the benefit of full 3D measurements of nanostructures with a single AFM measurement. However, due to the complex tip shape of the flared AFM tip, it is difficult to measure dense nanopatterns. To solve this problem, currently a new 3D-AFM based on the tilting tip technique is being built up. Using this technique, a nanostructure is measured by an AFM tip tilting in different angles, where the obtained AFM images will be then fused to derive the real 3D topography of the nanostructure. Owing to the sharp AFM tip applicable in the tilting AFM, it has the advantage of measuring high dense patterns. To accurately realize data fusion in the tilting-AFM, the drift compensation is becoming a critical issue [2].

Concept

Drift in AFM is a time dependent shift in the relative position of the AFM tip and the sample. When occurring during measurements drift causes distortions in the recorded data and thus significantly impacts the measurement accuracy.

Better temperature stabilization via active or passive temperature control is a widely applied measure for reducing drift. In high-precision nanometrology, however, even such measure is insufficient. Thus, drift correction becomes essential.

The basic concept of the drift correction is based on the fact that the drift is time dependent. A reduced measurement time usually suffers less from drift. Reduction of measurement time either requires an increase in measurement speed, or a reduction of measured data. As higher measurement speed degrades measurement performance due to e.g. tip wear and/or measurement noise, the reduction of recorded data in a single measurement is a better approach to follow. Therefore, our drift correction method applies two measurement sets which are taken at the same area of the sample: (A) Multiple consecutive measurements with reduced resolution and thus reduced measurement time and drift; (B) One detailed measurement with higher spatial resolution at costs of longer measurement time and larger drift. By correlating the two data sets, the drift correction can be performed without de-

grading the measurement quality, as detailed below.

Each of the measurements in A provides a set of data points, containing information of the sample topography, slightly distorted by drift. A simple method to correct the 3D drift, is to merely correct the measurement sets A. By aligning the point sets with each other using the Iterative Closest Point (ICP) algorithm, the positional offsets between measurements in A can be evaluated, which reveals the 3D drift of each measurement. By fitting the curve of the evaluated 3D drift v.s. time to a polynomial function for each axis, respectively, the 3D drift functions of the tool can be approximated. The drift function can then be applied to correct the drift of individual measurement points based on their acquisition time. After the correction, the multiple point sets in A can be merged and aligned to a single point set with dramatically reduced drift. However, because of slightly different residual drift in the merged data set and small inaccuracies during the alignment process, a remaining problem is that the merged set of surface points shows an increased noise level.

To overcome this problem, the drift correction method can be extended. In this case, the measurement set B is measured additionally. Then, the merged data set A, which has corrected drift as mentioned above, is applied as a reference data set to correct the data set B. In such a way, the resulting data set has both advantages of the merged data set A (i.e. reduced drift) and B (i.e. high measurement resolution and low noise level).

In the detailed correction algorithm, the data set B is divided into several segments, usually with a certain overlap. Then they are individually aligned to the reference data set A using ICP algorithm, and the offsets of the segments are determined. Such offsets reveal the 3D drift of the data set B using A as the reference. Finally, the drift of each point in data set B can be corrected.

Results

Both simulations and experiments have been carried out, showing good performance of the proposed method. In the simulation, AFM measurement data sets A (with a point density of 30 nm) and B (with a point density of 10 nm) are simulated with several given drift curves. The corrected 3D drifts are compared to the given data to evaluate the performance of the method. The result indicates that the drift can be reduced from more than tens of nanometers to a few nm or even below.

The applicability of the correction method has been demonstrated with real experimental data

shown in Fig. 1. Fig 1(a) and (b) show a data set B before and after applying the drift correction, respectively. It can be clearly seen that the distortion of the line structure due to the drift is significantly improved.

Conclusion & Outlook

Drift is a general problem in high precision measurements and metrology applications. The method proposed in this paper shows a promising performance for correcting drift distortions in AFM measurements. The idea is applicable for other measurement applications as well.

The performance of the proposed drift correction method depends on several factors, for instance, the measurement time of the data sets in A, as well as the accuracy of the ICP algorithm. Quantitative investigation of these issues will be performed in the near future.

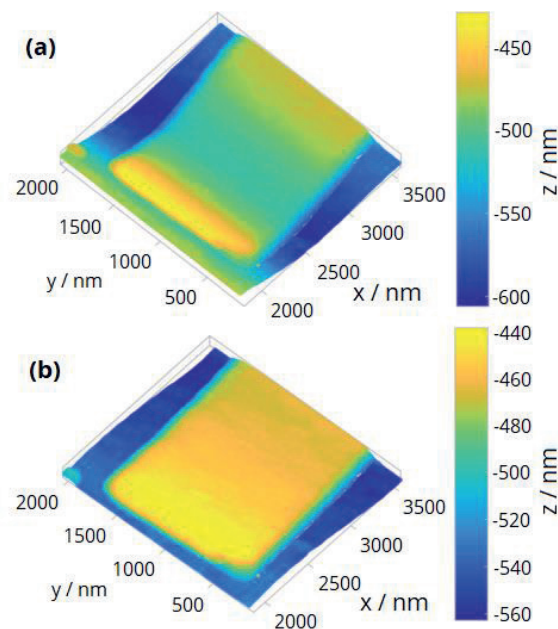


Fig. 1. Measured data set B shown as (a) before, and (b) after the application of the proposed drift correction method, respectively.

References

- [1] G. Dai, K. Hahm, F. Scholze, M.-A. Henn, H. Gross, J. Fluegge, H. Bosse, Measurements of CD and sidewall profile of EUV photomask structures using CD-AFM and tilting-AFM, *Meas. Sci. Technol.* 25, 13-26 (2014); doi:10.1088/0957-0233/25/4/044002
- [2] R. Kizu, I. Misumi, A. Hirai, K. Kinoshita, S. Gonda, Linewidth calibration using a metrological atomic force microscope with a tip-tilting mechanism, *Meas. Sci. Technol.* 30, 7-13 (2019); DOI: 10.1088/1361-6501/aaf02a

Compensation of Strong Aberrations with a Time Reversal Virtual Array for Ultrasound Imaging

Lars Grüter¹, Richard Nauber¹, Christian Kupsch¹, Jürgen Czarske¹
¹ Chair of Measurement and Sensor System Techniques
 TU Dresden, 01062 Dresden, Germany
 lars.grueter@tu-dresden.de

Summary:

Ultrasound-based imaging represents an inexpensive and mobile alternative to x-ray-based techniques for medical diagnosis of stroke. However, skull-induced acoustical aberrations need to be compensated to maintain image quality. We propose a non-invasive calibration method that utilizes two independent acoustical accesses and a time reversal virtual array (TRVA). The proposed method is characterized in a model experiment and results in an improvement of the lateral resolution and the peak to background ratio by 35% and 10% respectively.

Keywords: ultrasound, time reversal, imaging, system identification

Introduction

Strokes are one of the most frequent causes of death [1]. The prompt diagnosis and distinction between the ischemic and hemorrhagic subtype is extremely critical to a successful therapy and avoidance of long-term disabilities in patients. Mobile transcranial ultrasound imaging, available in the ambulance, could drastically reduce the time to diagnosis compared to x-ray-based imaging techniques, which are only available at a hospital. However non-invasive imaging of the brain with ultrasound is obstructed by the skull bone which induces significant aberrations that degrade the image quality [2].

It has been shown that strong aberrations induced in linear heterogenous media, for example a multi-mode wave guide [3], can be corrected by a time reversal virtual array (TRVA). This requires system identification by an acoustical point source [3] or reflector behind the aberrator and is therefore invasive. Here we propose a non-invasive method to calibrate a remote time reversal virtual array (RTRVA) utilizing a second acoustical access. An application of this method could reduce the effects of skull-induced aberrations degrading the image quality in context of transcranial imaging.

Method

A TRVA is calibrated by identifying the system's impulse response between the virtual transducer elements of a TRVA and an ultrasound array. This is achieved by exciting a sound wave, ideally corresponding to a Dirac delta function, at the position of each virtual element

which propagates through an aberrator, is then received with the ultrasound array (A1) and time reversed [3]. The proposed method excites the required calibration signal in a non-invasive manner by transmit focusing successively with a second ultrasound array (A2) on the element positions of the RTRVA as illustrated in Fig. 1. Based on the time invariant nature of sound propagation in linear media [4], convolving this received pattern with signals received at A1 during B-mode imaging estimates the signal at each element of the RTRVA free of aberrations.

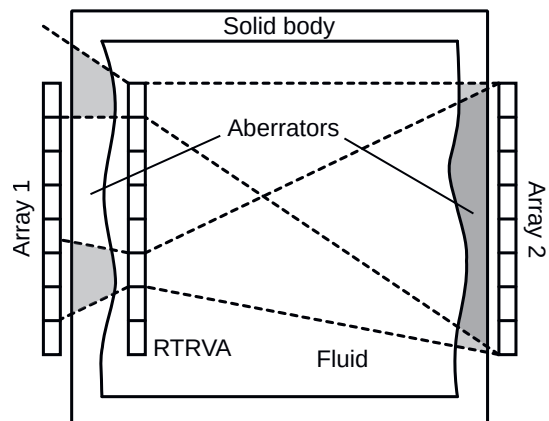


Fig. 1 Focusing on virtual elements during RTRVA calibration. The shaded areas highlight the traversed parts of the solid body for two different focus points.

Both arrays, A1 and A2, can access the region of interest only through aberrators. However due to the geometry of the arrays, different aberration-inducing parts of the solid body are traversed for different focus points during the calibration phase. Aberrations induced between A2 and the RTRVA do not contribute to the

compensation when operating the calibrated RTRVA and represent an undesired calibration error inherent to the method. However, due to the relatively large distance between A2 and the RTRVA compared to the aperture of the latter, this calibration error is almost constant for all virtual elements. This mainly leads to an unknown positional offset of the RTRVA.

Experimental Characterization

The proposed calibration method was evaluated inside a water-filled 3D printed resin model. The experimental setup was chosen similarly to Fig. 1 with two phased ultrasound arrays as described in Tab. 1. After calibration of the TRVA a copper wire with a diameter of 0.5 mm was placed as a point source between both real arrays.

Tab. 1: Parameters of the experimental setup.

Sound frequency	2 MHz
Sound speed in resin	2700 m/s
Sound speed in water	1497 m/s
Imasonic 1,5D Phased Array (A1)	
Element count (used)	128 (64)
Element width	0.26 mm
Pitch	0.3 mm
Sonaxis SNX140623 ME128-LMP10 (A2)	
Element count (used)	128 (64)
Element width	0.4 mm
Pitch	0.5 mm
RTRVA	
Element count	64
Element width	2 mm
Pitch	0.3 mm

Utilizing the modular phased array ultrasound system described by Mäder et al. [5] conventional delay-and-sum beamforming with A1 and the RTRVA yielded the results shown in Fig. 2. The RTRVA can compensate the aberrations induced by the uneven wall thickness and significantly reduces the intensity of artifacts in the lateral direction. For the utilized resin model, the RTRVA can reduce the lateral half-width of the point-spread function by up to 35% while increasing the axial half-width by 133%. The latter is likely caused by the calibration signal transmitted by A2 which is only an approximation of a Dirac delta function and therefore leads to a temporal widening of the estimated impulse response. This propagates to the axial beam width during focusing and the axial resolution.

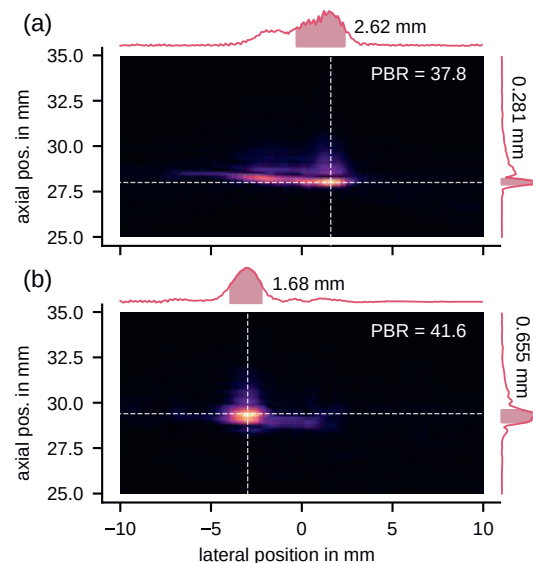


Fig 2. Resolution and half-widths of a sub-wavelength point source (a) without correction and (b) with a RTRVA.

Conclusion and Outlook

The experimental characterization has shown that the proposed novel calibration method clearly improves the signal quality. In the future, the method can be applied to a skull phantom to examine the effects on image quality in detail.

Acknowledgement

This research was funded by Deutsche Forschungsgemeinschaft, grant number Cz 55/43-1.

References

- [1] H. Wang et al. "Global, regional, and national life expectancy, all-cause mortality, and cause-specific mortality for 249 causes of death, 1980–2015" *The Lancet* 388.10053, 1459-1544 (2016); doi: 10.1016/S0140-6736(16)31012-1
- [2] F. Fry, and J. Barger. "Acoustical properties of the human skull." *The Journal of the Acoustical Society of America* 63.5, 1576-1590, (1978); doi: 10.1121/1.381852
- [3] M. Kalibatas, R. Nauber, C. Kupsch, J. Czarske, "Flow Field Imaging With Ultrasonic Guided Waves for Exploring Metallic Melts", *IEEE Trans. Ultrason., Ferroelect., Freq. Control*, 65.1, 112-119 (Jan. 2018); doi: 10.1109/TUFFC.2017.2771525
- [4] M. Fink, "Time reversal of ultrasonic fields. I. Basic principles," *IEEE Trans. Ultrason., Ferroelect., Freq. Control*, 39.5, 555–566 (Sep. 1992); doi: 10.1109/58.156174
- [5] K. Mäder et al., "Phased array ultrasound system for planar flow mapping in liquid metals." *IEEE Trans. Ultrason., Ferroelect., Freq. Control*, 64.9, 1327-133 (2017); doi: 10.1109/TUFFC.2017.2693920

Determination of Murnaghan constants of plate-shaped polymers under uniaxial tensile load

Sarah Johannesmann¹, Sebastian Becker¹, Manuel Webersen¹, Bernd Henning¹

¹ Measurement Engineering Group, Paderborn University, Warburger Straße 100, 33098 Paderborn, Germany
johannesmann@emt.uni-paderborn.de

Summary

For finite element simulations of mechanic devices the material parameters of each constituent material must be known. Depending on the applied loads to the component, high stresses changing the materials' mechanical behaviour might have to be considered. Therefore measurements are performed under a constant uniaxial tensile stress and the material parameters are identified.

Keywords: ultrasound, acoustoelastic effect, effective elastic constants, Murnaghan constants, polymers

Introduction

Acoustic material parameters are often identified in an inverse measurement procedure, where measurement and simulation results are compared by a cost function while varying the input parameters of the forward model. The forward model can be computed both analytically or numerically assuming Hook's law for small displacements. For greater displacements nonlinearity should usually be considered in the forward model. In this article the material's behaviour under stress is described by the changes in the elasticity matrix, while the forward model itself does not consider the tensile stress. Through these changes the Murnaghan constants [1] are computed.

Measurement setup

During the whole measurement the tensile stress σ_T applied at the specimen (Fig. 1) is kept constant by a programmable logic controller. Then short, high

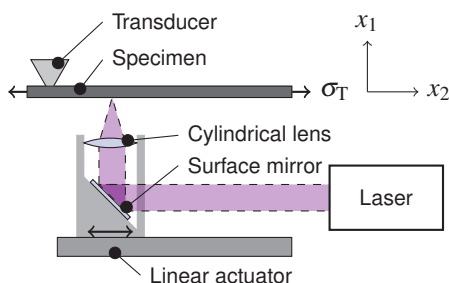


Fig. 1. Measurement system, adapted from [2].

power, laser pulses are focused on the specimens surface to excite acoustic plate waves thermoacoustically, which are received by an ultrasonic transducer. Varying the propagation distance by shifting the op-

tical unit and recording the respective received signals lead to a time and frequency dependent matrix. Application of a two-dimensional Fourier transform results in a matrix depending on frequency and wavenumber, where the propagating modes become visible as ridges.

Material parameter identification

The material identification described in [2] uses a forward model assuming acoustic linearity and plane-strain to compute the plate's eigenfrequencies from given wavenumbers. An optimisation algorithm finds the model's elasticity matrix for which the computed dispersion diagram fits best to the frequency and wavenumber dependent matrix obtained from measurement. Because of the uniaxial load σ_T in x_2 -direction (Fig. 1) during the measurements, the material properties change depending on the spatial direction, so that an orthotropic material is assumed in the identification.

Evaluation under constant load

Using the Effective Elastic Constants (EECs) [3] to describe the changes of the elasticity matrix \mathbf{C} the stress-strain relation results in

$$\boldsymbol{\sigma} = (\mathbf{C}_0 + \delta\mathbf{C}) \boldsymbol{\varepsilon}, \quad (1)$$

where the entire elasticity matrix consists of the elasticity matrix \mathbf{C}_0 measured with a tensile load of $\sigma_T = 0$ and the change $\delta\mathbf{C}$ under stress $\sigma_T \neq 0$ w.r.t. \mathbf{C}_0 . Four elasticity coefficients are identified for each tensile load σ_T :

$$\mathbf{C} = \begin{pmatrix} c_{11} & c_{12} & 0 \\ c_{12} & c_{22} & 0 \\ 0 & 0 & c_{66} \end{pmatrix} \quad (2)$$

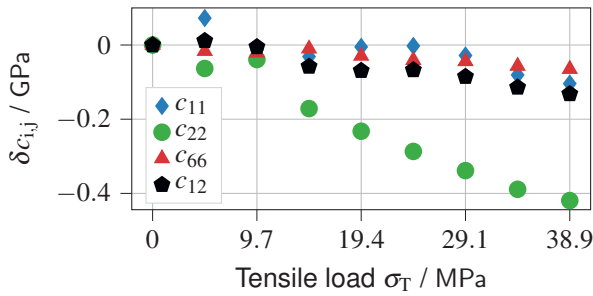


Fig. 2. Absolute change of elasticity coefficients $\delta c_{i,j}$ w.r.t. the elasticity coefficients $c_{0,i,j}$ identified for a tensile load of $\sigma_T = 0$ for specimen 1.

Without any outer stress σ_T the isotropic elasticity matrix is fully described by the Lamé constants $\lambda = c_{12}$ and $\mu = c_{66}$.

Acoustoelastic effect

An initial isotropic material with Lamé parameters λ , μ and density ρ_0 under an uniaxial tensile load is described by

$$\rho_0 v_{11}^2 = \lambda + 2\mu - \frac{\sigma_T}{3\lambda + 2\mu} \left[2l - \frac{2\lambda}{\mu} (m + \lambda + 2\mu) \right] \quad (3)$$

$$\rho_0 v_{22}^2 = \lambda + 2\mu - \frac{\sigma_T}{3\lambda + 2\mu} \left[2l + \lambda + \frac{\lambda + \mu}{\mu} (4m + 4\lambda + 10\mu) \right] \quad (4)$$

$$\rho_0 v_{66}^2 = \mu - \frac{\sigma_T}{3\lambda + 2\mu} \left[m + \frac{\lambda n}{4\mu} + 4\mu \right] \quad (5)$$

with the sound velocities

$$v_{ii} = \sqrt{\frac{c_{ii}}{\rho}}, \quad (6)$$

where v_{11} and v_{22} are the longitudinal sound velocities and v_{66} is the transverse sound velocity [4] of a wave propagating in x_2 , polarised in x_1 -direction. Knowing the material's Lamé constants and sound velocities the equations are solved to determine the Murnaghan constants m , n and l .

Results

Polycarbonate plates of 3 mm thickness are evaluated exemplarily. Measurements during an applied load up to $\sigma_T = 39$ MPa (8 kN) are performed and the orthotropic elasticity matrix is identified. As Fig. 2 shows, the elasticity parameter c_{22} and so the longitudinal wave velocity in the direction of load σ_T are influenced most significantly, while the elasticity coefficient in x_1 -direction (perpendicular to the load) c_{11} changes least. This trend corresponds to the effective elastic moduli determined under constant controlled stress by Brillouin spectroscopy [5]. In general the Murnaghan constants can be determined for each tensile load σ_T . Therefore the mean of the computed Murnaghan constants is shown in Tab. 1. Despite the

Tab. 1. Determined Murnaghan constants m , n and l of polycarbonate.

Specimen	m / GPa	n / GPa	l / GPa
1	-7.8	-21.1	-66.5
2	-7.7	-30.2	-54.3
3	-7.6	-30.9	-52.3
Literature [6]	-12.2	-32	-50

neglection of nonlinearity, the determined Murnaghan constants are quite similar to the ones from [6], where they were computed from the elasticity tensor coefficients shown in [5], measured through Brillouin spectroscopy. Some differences are expected due to material production tolerances and thus different density and Young's modulus for the computation.

Conclusion

Murnaghan constants are determined by a change of the elasticity coefficients assuming a linear relation. Despite the approximations the values are quite similar to results found in literature. However this influence should still be considered in the forward model in future works. Also acoustic absorption phenomena, temperature and uncertainty influence should be regarded.

Literature

- [1] F. D. Murnaghan: Finite Deformations of an elastic solid, *American Journal of Mathematics* 59 pp. 235–260 (1937); doi:10.2307/2371405
- [2] S. Johannesmann, T. Brockschmidt, F. Rump, M. Webersen, L. Claes, B. Henning: Acoustic material characterization of prestressed, plate-shaped specimens, *Sensoren und Messsysteme* pp. 231–234 (2018)
- [3] M. Duquennoy, M. Ouafouh, D. Devos, F. Jenot, M. Ourak: Effective elastic constants in acoustoelasticity, *Applied Physics Letters* 24 (2008); doi: 10.1063/1.2945882
- [4] D. S. Hughes, J. L. Kelly: Second-Order Elastic Deformation of Solids, *Physical Review* 92 pp. 1145–1149 (1953); doi: 10.1103/PhysRev.92.1145
- [5] J. K. Krüger, C. Grammes, K. Stockem, R. Zietz, M. Dettenmaier: Nonlinear elastic properties of solid polymers as revealed by Brillouin spectroscopy, *Colloid and Polymer Science* 269 pp. 764–771 (1991); doi: 10.1007/BF00657442
- [6] G. V. Dreiden, A. M. Samsonov, I. V. Semenova: Bulk elastic strain solitons in polycarbonate, *Technical Physics Letters* 37 pp. 500–502 (2011); doi: 10.1134/S1063785011060046

Model-based acoustic identification of hidden layers

Sebastian Wöckel, Hendrik Arndt

*ifak - Institut für Automation und Kommunikation e.V.,
Werner-Heisenbergstr. 1, 39106 Magdeburg (Germany),
sebastian.woeckel@ifak.eu*

Summary:

This contribution discusses a model-based method to identify hidden layers by non-contact air-coupled ultrasound inspections. The method implies a model fitting of the sound propagation in the multi layered media and a derivation of media properties. The modelling and the estimation technique are evaluated with measurement and simulation data of ideal stacked solid and fluid layers, which are “thin” ($< 1 \dots 10$ mm) in relation to the acoustic wavelength (> 5 mm).

Keywords: air coupled ultrasound, parameter estimation, non-destructive evaluation, material characterization, layer peeling

Motivation

The non-destructive physical evaluation of hidden in-between (mostly adhesive) layers is a sophisticated task. Physical parameters of the thin adhesive layer, including its thickness, material distribution, density and elasticity, determine the stability and durability of the assembly. A common inspection technique bases on ultrasound. Depending on the application a direct contact, immersion or air-coupled techniques are applied. Although the first provides the highest signal-to-noise ratio and resolution, it is limited to point-selective measurements. The second water-coupled technique provides an automatic scanning, keeping the SNR and resolution, whereat the construction component needs to be immersed in a waterbed. The inspection with air-coupled ultrasound provides the highest degree of freedom – concerning the technical realization. Its main drawbacks are the low defect sensitivity caused by the high reflection loss at the air-solid interface (power balance $P_{out}/P_{in} \sim 10^5$) and the low resolution due to the wavelength accordingly frequency ranges (< 1 MHz).

In this context, a signal-oriented method is discussed to overcome the mentioned drawbacks of air-coupled inspections. The idea bases on the fast estimation of the sound propagation in the multi layered media [1] including an automated derivation of acoustic media properties (mainly density, sound velocity, effective damping and elasticity) by using a genetic algorithm. The modelling and the estimation technique are exemplified on simulation and empirical data of multiple stacked solid and elastic (adhesive) layers, which are “thin” (< 1 mm) in relation to the acoustic wavelength (> 5 mm). This contribution

focuses on the estimation of the parameters of a hidden layer, using a simple laboratory measurement setup. This measurement rig provides the ultrasonic air coupled transmission (S_{21}) or reflection (S_{11}) measurement on a planar multi-layer structure. The thicknesses of the plates, the in-between layer as well as the transducers distances can be adjusted in steps of $\Delta h = 100$ μm . For continuous variation of (ρ_1, c_1, h_1) the hidden layer forms an open cavity filled with a viscous liquid.

The main outcome is an algorithmic method, which delivers supplemental information by a complete acoustic characterization of the medium.

Model: linear Mason-Graph

The sound propagation through a system of layers can be modelled as a two port network which is characterized by its transfer (S_{21}) and reflection (S_{11}) functions. In time-domain the relative distances and the amplitudes contain the information on the velocity (c_i) and damping (α_i) within each layer and the reflection and acoustic contrast (ρ_i, c_i) at each interface. To extract that information a Mason-graph is used, which converts the sound propagation to a deterministic two port network. Such graph delivers an analytic expression for the transient wave at each knot of the graph, including all multiple propagation paths, reflections due to acoustic contrasts (ρ, c) and delays (Δt) caused by different sound velocity (c). The analytic form of the transfer function S_{21} of a 3-layer-system (Fig. 1) including

the transmission within the layers (T_i) and the reflection at the interfaces ($R_i = \Gamma_i$) can be expressed by:

$$S_{21} = \frac{1}{\Delta} T_1 T_5 \prod_{i=1}^4 \sqrt{1 - R_i^2} T_{i+1} \quad (1)$$

$$\begin{aligned} \Delta = & 1 + T_2^2 R_1 R_2 + T_3^2 R_2 R_3 + T_4^2 R_3 R_4 + T_2^2 T_3^2 R_1 R_3 \\ & + T_3^2 T_4^2 R_2 R_4 + T_2^2 T_3^2 T_4^2 R_1 R_4 \\ & + T_2^2 T_4^2 R_1 R_2 R_3 R_4 \end{aligned}$$

The main advantage of such an analytic expression is the higher processing speed in an iterative optimization procedure instead of a simulation.

Layer Peeling with Parameter Estimation

For adapting the model parameters p to the measurement y_{meas} a minimization of the cost-function f calculating the residual $r(p)$ is applied. The residuals combine the deviation between the model $y_i(p)$ and the measurement y_{meas} by using the difference of the absolute values (signal envelopes via Hilbert-transform) according to the first order Laplace-formulation:

$$\begin{aligned} \min f_{L1} &= \min \|r(\tilde{p})\|_1 = \\ & \min \sum_{i=1}^m |\tilde{y}_i(\tilde{p}) - y_{\text{Meas},i}| \quad (1) \\ f_{L1}(\rho, c, \alpha) &= \sum \left\| \log \frac{||\text{Hilbert}(y_{\text{Model}})||}{\log \frac{||\text{Hilbert}(y_{\text{Meas}})||} \right\| \end{aligned}$$

The logarithmic version of the first order norm delivers a smooth curve for prediction of the global minima and a steep decent in the region of the minimum itself. The latter supports an effective and fast gradient optimization. The parameter estimation is divided in two consecutive steps using a differential evolution algorithm for predicting the starting values p_0 [2] and a gradient based algorithm calculating the material parameters p .

Results

The model equation exemplified here (1) is adequate for a perpendicular incidence only. The accuracy of the 1D-Model estimation mainly depends on the mechanical setup of the measurement the radial symmetry of the transducers and the angular deviation of the incident acoustic field. According to the idealized transmission function for an angular incident acoustic field [3] the error for the layer thickness, the sound velocity and the density of the hidden (unknown) layer will be in size of 5% for each 1° deviation of the incident angle. In laboratory measurements and according to the method above, the thickness of the unknown hidden layer can be estimated with an absolute deviation of 5%. The corresponding error for the density and damping coefficient are $<10\%$ and $>20\%$ respectively, mainly due to the error propagation [4]. By the help of empiric data as well as 2D-simulations, the performance of

the algorithm was evaluated (Fig. 2). According to the bandwidth of the transducers ($B = 90 \text{ kHz}$) only a reduced region along the theoretical trace of the transmission function S_{21} (white dotted line) can be used for the calculation. However, even in that case, such algorithm delivers quantitative values of the hidden material and the thickness of the layer.

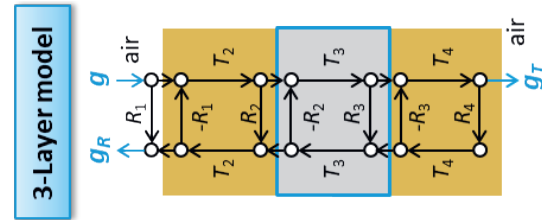


Fig. 1. Mason-Graph of a 3-layer-system; T -Transmission function, R – Refelction function, g - Signal

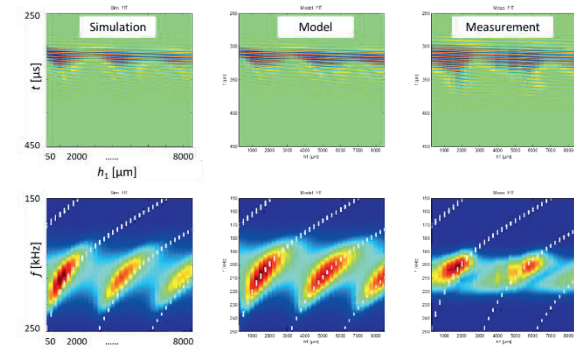


Fig. 2. Comparison of FEM-Simulation, 1D-Model (1) and Measurement for an ultrasonic transmission on a 3-layer-system (Acrylic (6 mm) – Water (variabel) – Acrylic (6 mm)) with burst-excitation of (207.5 kHz +/- 45kHz).

References

- [1] F. Hägglund, et.al 'Model-based estimation of thin multi-layered media using ultrasonic measurements', IEEE Transactions on Ultrasonics, Ferroelectrics and Frequency Control, vol. 56, no. 8, pp. 1689–1702, 2009.
- [2] J. E. Carlson, 'Characterization of thin layers in multi-layered structures: on the problem of finding starting values for numerical solutions to inverse problems', in 2009 IEEE Ultrasonics Symposium : Rome, Italy, 20 - 23 September 2009, 2010, pp. 1537–1540.
- [3] Rose, Ultrasonic waves in solid media, 2008
- [4] Bedürftig, Modellgestützte Ultraschall-Messverfahren zur Bestimmung akustischer Größen, Bachelor thesis, Univ. Magdeburg, 2014

Guided Wave Based Characterization of Mechanical Parameters and Wall Thickness of Metal Tubes

Michael Ponschab, Lisa Petzold, Daniel A. Kiefer, Stefan J. Rupitsch
 Friedrich-Alexander-University Erlangen-Nürnberg (FAU), Sensor Technology, Erlangen, Germany
 michael.ponschab@fau.de

Summary:

Modelling phenomena of structural mechanics requires the knowledge of mechanical parameters of the utilized material. Moulding of the material during the manufacturing process, e.g. drawing pipes, may alter the material properties slightly. In comparison to classical destructive measurement methods, which involve samples of specific shapes, or classical ultrasonic testing, requiring a minimum material thickness, the proposed method based on laser vibrometry and guided ultrasonic enables a simultaneous estimation of the elastic constants and the wall thickness of a pipe.

Keywords: guided waves, ultrasound, material characterization, inverse method, numerical modelling

Introduction

The development of new measurement devices often involves detailed simulations in advance. In order to make more precise predictions of the later behaviour, appropriate material parameters are necessary. Modelling structural mechanical problems, e.g. eigenmode analysis, depends on the linear elastic constants, density and geometry. Classical ultrasound-based methods of measuring the elastic constants rely on time-of-flight measurements. However, the axial resolution limits the minimum material thickness, which may be investigated [1].

Recently, researchers started to utilize guided ultrasonic waves, as they provide a greater sensitivity. Propagating guided waves split into different modes, each possessing a unique frequency-dependent wave speed represented by dispersion curves. These mode properties depend on the material and geometric constants and are therefore well suited for material characterization purposes.

The research on guided wave based material characterization started with analytical calculations on time-domain data [2] and went on to model-based characterization of isotropic [4] and orthotropic [3] plates as well as plates with nonlinear material behaviour [5]. In a recent work [6], we proposed an advancement of characterization of elastic constants of plates by using long-time broadband signals, a laser-scanning measurement system and an optimized modelling method. In this contribution, we want to transfer these ideas to thinwalled pipes with a view to precisely

determine the averaged wall thickness and the pipe's linear elastic constants.

Measurement Setup

The aim of measurements with the setup shown in Fig. 1 is the acquisition of frequency resolved wavenumbers by measuring time-space dependent data of propagating guided waves. The waves are excited by a bonded piezoelectric element of size $35 \times 2.9 \times 0.2 \text{ mm}^3$, driven by an arbitrary function generator and a voltage amplifier. We use coded signals to excite the piezoelectric element [6]. Metallic pipes with diameters around 60 mm and wall thicknesses of 1 mm to 2 mm are mounted on a high precision rotation stage. The pipe is rotated in 630 steps with about 0.01 rad per step. To obtain wavenumbers, we transform the rotation angle to Cartesian coordinates using the nominal outer radius of the pipe. Time-dependent normal surface velocities are measured by a

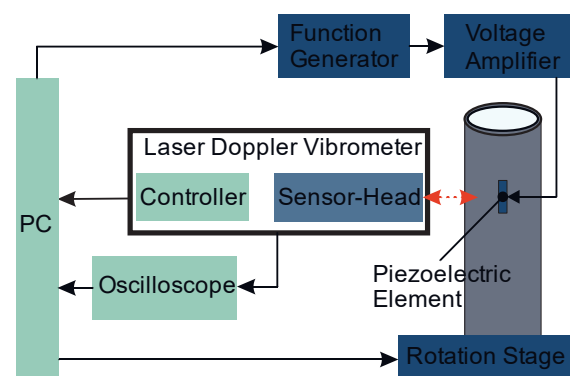


Fig. 1. Measurement setup for the acquisition of time and space dependent normal surface velocities.

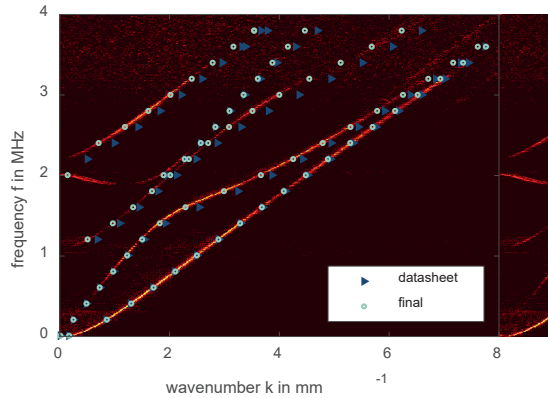


Fig. 2. Comparison of dispersion curves from simulation with start and final parameters plotted over measurement data. Steel 1.4301; $D=60.3$ mm, $h=1.5$ mm.

laser Doppler vibrometer and are recorded by an oscilloscope. The vibrometer's nominal bandwidth is 1.5 MHz, but since absolute velocity amplitudes are not relevant for our examination, we were able to capture dispersion curves up to 3 MHz.

Inverse Characterization Algorithm

Frequency-dependent wavenumbers are obtained from measured normal surface velocities by taking the 2D fast Fourier transform (see Fig. 2). A numerical model, shown in [6], is iteratively optimized in such way that the quadratic deviation between the measured wavenumbers and the calculated ones is minimized. The parameter vector \mathbf{p} , containing the desired constants, namely the longitudinal and transversal wavespeeds c_l , c_t and the wall thickness h , gets adjusted during each iteration step. The starting values are chosen as the nominal values from literature. For convergence analysis, \mathbf{p} has been randomly altered by $\pm 10\%$. In most cases, the algorithm converged in a few steps and returned accurate final parameters (Fig. 2).

Results

Samples of two aluminium, one steel and one brass alloy were investigated. Parameters for all samples could be found such that measurement data and model output match (see Fig. 2). During the repetition of the measurement procedure, uncertainties of parameters with a standard deviation of about 1% were observed. The obtained results show a good agreement with reference values from conventional time-of-flight measurements with longitudinal and shear wave contact transducers, as can be seen in Tab. 1.

Acknowledgement

The Chair of Sensor Technology is grateful for financial support by Diehl Metering.

Tab. 1: Results of characterization method. Reference measurements are shown in columns REF. Results of inverse characterization and percentage deviation follow in columns IC.

material	REF			IC		
	h (mm)	c_l (m/s)	c_t (m/s)	h (mm) dev (%)	c_l (m/s) dev (%)	c_t (m/s) dev (%)
AlCuMg	1.13	-	3280	1.08 (4.4)	6700 (-)	3090 (5.8)
AlMgSi	1.94	6450	3230	1.95 (0.5)	6480 (0.5)	3200 (1.2)
Steel	-	5980	3190	1.44 (-)	5770 (3.5)	3190 (0.1)
Brass	1.05	4730	2260	1.05 (5.00)	4630 (2.1)	2190 (3.1)

References

- [1] J. L. Rose, *Ultrasonic waves in solid media*, Cambridge University Press (2014); ISBN: 0521548896
- [2] W. P. Rogers, *Elastic Property Measurement Using Rayleigh-Lamb Waves*, *Research in Nondestructive Evaluation* 6, 185–208 (1995); doi: 10.1080/09349849508968098
- [3] S. Johannesmann, J. DÜchting, M. Webersen, L. Claes und B. Henning, An acoustic waveguide-based approach to the complete characterisation of linear elastic, orthotropic material behaviour, *tm Technisches Messen* 85, 478–486 (2018); doi: 10.1515/teme-2017-0132
- [4] L. Ambrozinski, P. Packo, L. Pieczonka, T. Stepinski, T. Uhl und W. J. Staszewski, Identification of material properties - efficient modelling approach based on guided wave propagation and spatial multiple signal classification, *Structural Control and Health Monitoring*, 22, 969–983 (2015); doi: 10.1002/stc.1728
- [5] M. Ponschab, D. A. Kiefer und S. J. Rupitsch, Towards an Inverse Characterization of Third Order Elastic Constants Using Guided Waves, *2019 IEEE International Ultrasonics Symposium*, 1264–1268 (2019), doi: 10.1109/ULTSYM.2019.8926294
- [6] M. Ponschab, D. A. Kiefer und S. J. Rupitsch, Simulation-Based Characterization of Mechanical Parameters and Thickness of Homogeneous Plates Using Guided Waves, *IEEE Transactions on Ultrasonics, Ferroelectrics, and Frequency Control*, 1898–1905 (2019); doi: 10.1109/TUFFC.2019.2933699

Fundamentals of Dynamic Sensor Positioning with Nanoscale Accuracy by an Inverse Kinematic Concept

Guido Straube¹, Sebastian J. Fischer Calderón¹, Ingo Ortlepp¹, Eberhard Manske¹

¹ Technische Universität Ilmenau, Ehrenbergstr. 29, 98693 Ilmenau, Germany
guido.straube@tu-ilmenau.de

Summary:

A recent challenge in measurement science is the growing demand for machines allowing nanoscale positioning and measuring in large volumes. The moving stage principle typically used for these applications needs to be altered, considering the mass of the moving stage growing with the measuring volume. This paper proposes an inverted kinematic concept and discusses two approaches to the reconstruction of mirror profiles to compensate for deviations in the mirror topographies.

Keywords: metrology, interferometry, nanoscale, profile reconstruction, simulation

Introduction

Two developments in recent semiconductor production technologies lead to highly challenging requirements on measuring machines: the growing diameter of processed wafers and the diminution of the single structures and their pitches. To address this persistent trend a nano positioning and nano measuring machine (NPMM) with an inverse kinematic concept is proposed.

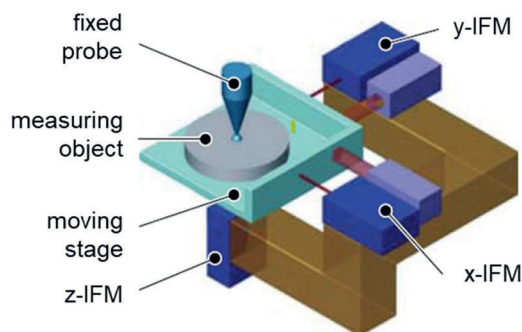


Fig. 1. Operation principle of the NPMM-200. The measuring object is placed upon the moving stage. [4]

State of the Art

The first nano measuring machine developed at the Technische Universität Ilmenau, the NMM-1 [1], has a movement range of $25 \times 25 \times 5 \text{ mm}^3$. Similar to the recent trends, proposed progress formulated in the International Technology Roadmap for Semiconductors (ITRS-Roadmap) [2], had to be addressed. Therefore, the next incarnation, the NPMM-200 [3], has a measuring volume of $200 \times 200 \times 25 \text{ mm}^3$ (see Fig. 1). In these machines the sensor is fixed and the movement is realized by a stage. Three interferometers (IFMs) capture the movement in the three axes x , y and z . The virtual intersection of

the IFM beams is located in the contact point of the sensor on the measuring object. Hence, the Abbe principle is followed consequently which allows the NMM-1 and NPMM-200 to achieve nanoscale precision.

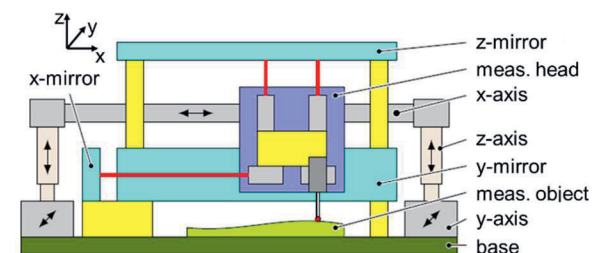


Fig. 2. Illustration of the inverse kinematic concept. The measuring head with the IFMs and the sensor is moved, whereas the mirrors are fixed and the driving system is placed outside the measuring volume. [4]

Limitations and Inverse Concept Proposal

With a proposed motion range of $700 \times 700 \times 100 \text{ mm}^3$ for the next incarnation of the NPMM, the mass of the moving stage and the measuring object is estimated to be approx. 300 kg [4]. Along with the demands on the dynamics to keep measuring times in an acceptable range, the high positioning precision and the increased heat influx of more powerful propulsion systems, this leads to a conflict. In order to allow the expansion of the motion range without drastically increasing the mass to be moved, an inverse concept is proposed (see Fig. 2). Due to the realization of a lightweight measuring head ($< 1 \text{ kg}$), the Abbe principle could no longer be strictly followed. In order to compensate for this imperfection, in every axis an additional IFM is placed, which allows to observe and control tilt errors.

Mirror Reconstruction

The inverse kinematic concept poses a novel challenge. Caused by the dimensions of the mirrors and the scanning movement of the measuring head, deviations from the ideal flat mirror profile lead to positioning errors, which need to be compensated. Since the removal of the mirrors is unfeasible, their deviation has to be examined in the mounted state. Two different approaches are analyzed. The triangulation method utilized the two IFM beams. Simplified to a one-dimensional movement along the x-axis, whereas the two IFM beams sample the z-mirror, equation (1) can be used to reconstruct the profile.

$$R(x_i) = \frac{m(x_i+d/2) - m(x_i-d/2)}{d}k + C \quad (1)$$

With m being the distance measured by the IFMs, R the contour of the mirror, d the distance between the two IFM beams, k the sampling distance and the constant C refers to a non-reconstructable straight line, which can be found via calibration. In order to test the quality of the reconstruction and to establish a tool for comparison of the reconstruction methods, topographies of different mirrors are measured with a Fizeau-IFM and the sampling and reconstruction are simulated. Results are shown in Fig. 3.

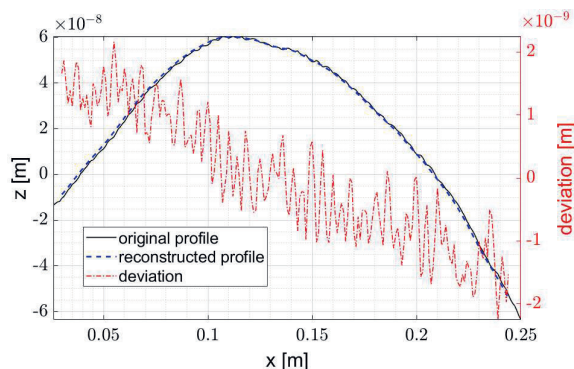


Fig. 3. Reconstruction of a mirror profile with the triangulation method.

The Traceable Multiple Sensor (TMS) method combines a system of at least two coupled distance sensors and an angular measurement system to reconstruct a 2D mirror topography and precisely separate the influences of the mirror deviation, the scanning stage error, the yaw angle and systematic errors of the distance sensors [5]. The linear actuation of the sensor head allows to generate an overestimated linear equation system by evaluating every sensor signal at overlapping positions of the sensor head. This leads to the following equation:

$$\vec{m} = A \vec{\vartheta} \quad (2)$$

where \vec{m} represents the measured distances and angles, A the design matrix according to the

measurement strategy and $\vec{\vartheta}$ the unknown parameters. The solution of $\vec{\vartheta}$ is determined by applying the least square method. It is shown that the TMS-Method is able to measure mirror topographies with standard uncertainty below 0.25 nm and even smaller standard deviations [6].

Conclusion and Outlook

Due to large masses to be moved, the moving stage principle reaches its limits with increasing measuring volume. To overcome this constraint an inverse concept with a moving measuring head is proposed. The two discussed mirror reconstruction methods show potential to compensate for flatness mirror deviation, up to the nanoscale range. In future work a single axis demonstrator will be brought into operation in order to verify the simulation results and subsequently a three axis demonstrator will be set up.

Acknowledgments

This project is funded by the Deutsche Forschungsgemeinschaft (DFG) under contract 279458870.

References

- [1] G. Jäger, E. Manske, T. Hausotte, H.-J. Büchner, Nano Measuring Machine for Zero Abbe Offset Coordinate-measuring, *tm – Technisches Messen Plattform für Methoden, System und Anwendungen der Messtechnik* 67, 7-8 (2000); doi: 10.1524/teme.2000.67.7-8.319
- [2] The International technology Roadmap for Semiconductors (ITRS), *Executive Summary*, (2013); url: <http://www.itrs2.net/itrs-reports.html>
- [3] G. Jäger, E. Manske, T. Hausotte, A. Müller, H.-J. Büchner, Nanopositioning and nanomeasuring machine NPMM-200 – a new powerful tool for large-range micro- and nanotechnology, *Surface Topography: Metrology and Properties* 4.3, 034004 (2016); doi: 10.1088/2051-672x/4/3/034004
- [4] I. Ortlepp, E. Manske, R. Füßl, Dynamic sensor positioning in large measuring volumes by an inverse kinematic concept, *IOP Conf. Series: Journal of Physics: Conf. Series* 1065.14, 142009 (2018); doi: 10.1088/1742-6596/1065/14/142009
- [5] C. Elster, I. Weingärtner, M. Schulz, Coupled distance sensor systems for high-accuracy topography measurement: Accounting for scanning stage and systematic sensor errors, *Precision Engineering* 30.1, 32-38 (2006); <https://doi.org/10.1016/j.precisioneng.2005.04.001>
- [6] C. Weichert, P. Köchert, E. Schötka, J. Flügge, E. Manske, Investigation into the limitations of straightness interferometers using a multisensor-based error separation method, *Measurement Science and Technology* 29.6, 064001 (2018); <https://doi.org/10.1088/1361-6501/aab7e3>

Towards 3D-Motion Tracking of Instrumented Flow Followers in Large Vessels

Lukas Buntkiel¹, Sebastian Reinecke¹, Uwe Hampel^{1,2}

¹ *Helmholtz-Zentrum, Dresden-Rossendorf (HZDR), Bautzner Landstr. 400, 01328 Dresden, Germany,*

² *Chair for Imaging Techniques in Energy and Process Engineering, Technische Universität Dresden, 01062 Dresden, Germany
l.buntkiel@hzdr.de*

Summary:

A concept for 3D-motion tracking of instrumented flow-following sensor particles, equipped with a gyroscope, accelerometer, magnetometer and pressure sensor, has been developed. Consisting of an error state Kalman filter (ESKF) the algorithm can track the attitude of the sensor particle in relation to a reference coordinate system permanently, even under high acceleration, which interferes the attitude estimation because it is based on measuring the gravitational acceleration. Experimental results show, that using the ESKF for attitude estimation is giving accurate results even under high body acceleration.

Keywords: error state kalman filter, motion tracking, fluid dynamics, sensor particle, soft sensor

Motivation

The investigation of the fluid flow in large-scale plants or vessels like biogas fermenters or activated sludge tanks, is limited because currently applied instrumentation only measures locally. To optimize the use of energy and resources in such plants, the flow patterns inside the vessels need to be known. To overcome the limitations of local sensors, the concept of instrumented flow-following sensor particles has been developed at HZDR [1].

The aim is, to recover the acceleration, velocity and position of the sensor particle in the vessel over time, to track the flow pattern. Therefore, sensor particles are equipped with an accelerometer, a gyroscope, a magnetometer and a pressure sensor. Since the measurements are taken in body coordinates, the reconstruction of the attitude of the sensor particle in relation to the vessel is of fundamental importance. An absolute attitude is obtained by combining the measurement of acceleration due to gravitation and earth magnetic field aiding the attitude calculated from the measured angular velocity.

In this short paper, we show that an error state Kalman filter (ESKF) as presented in [2] can be used to estimate the attitude of the sensor particle in the presence of a permanently disturbing high acceleration. High in this context means that the acceleration is about 85% higher than in 90% of the vessel volume. The validation is based on the following experimental method.

Method

To investigate the developed algorithm, the inertial measurement unit BNO055 from Bosch Sensortec and an Arduino Due were strapped as a unit to a rotating table, as shown in fig. 1. The setup measures body acceleration, angular velocity and the earth magnetic field with a sampling rate of 100 Hz. These measurements were fed into the algorithm, which filtered the input data and corrected the initial bias, inherent to all sensors. The noise characteristics of all sensors were identified beforehand and are listed in [2]. All these quantities were then used by the ESKF to estimate attitude and the acceleration in vessel coordinates.

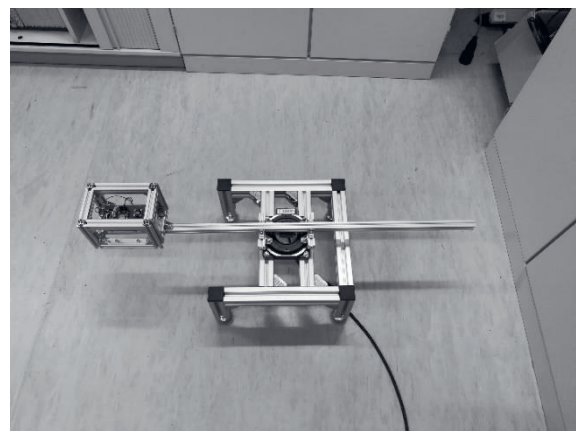


Fig 1: Experimental setup for circular motion of sensor particles on a rotary table.

As an example of a typical motion one can find in round vessels a circular motion was chosen. The radius of the circle was 42.5 cm and the angular velocity of the motor was 180 °/s, which results in a radial acceleration of 4.2 m/s² and a measured body acceleration of $\mathbf{a}_m^B = [4.2, 0, 9.81]$ m/s². The measurement time was 10 minutes. The motion was started after about 70 seconds, to estimate the initial bias of the sensors. The motor was set to make 120 turns and the start and end position were identical, making it easy to identify the correct attitude estimation of the filter. The prefiltered body acceleration is depicted in fig. 2.

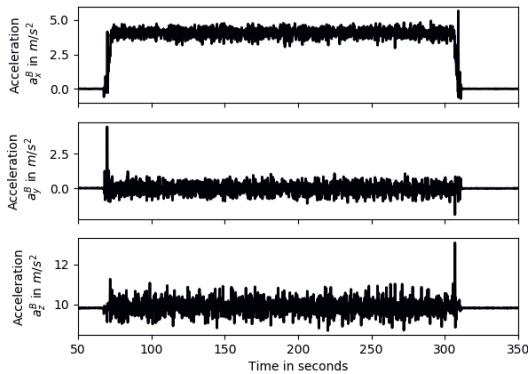


Fig 2: Extract of the filtered body acceleration \mathbf{a}_x^B , \mathbf{a}_y^B and \mathbf{a}_z^B .

Results

The estimated attitude is shown in fig. 3 and represented as unit quaternion, where \mathbf{q}_x , \mathbf{q}_y and \mathbf{q}_z are the axis of rotation, \mathbf{q}_w is the magnitude of this rotation and $|\mathbf{q}| = 1$. For a circular motion around the z-axis \mathbf{q}_x and \mathbf{q}_y are expected to be zero. The estimated attitude fits the expected one with only small deviations. Especially the start and end attitude are equal. Values of \mathbf{q}_x and \mathbf{q}_y are close to zero, meaning that there is only a small error introduced by the difference between $|\mathbf{a}_{ref}| = 9.81$ m/s² and $|\mathbf{a}_m^B|$. The oscillation on \mathbf{q}_x and \mathbf{q}_y seen in fig. 3 occurs due to imperfect alignment of the sensor axes with the

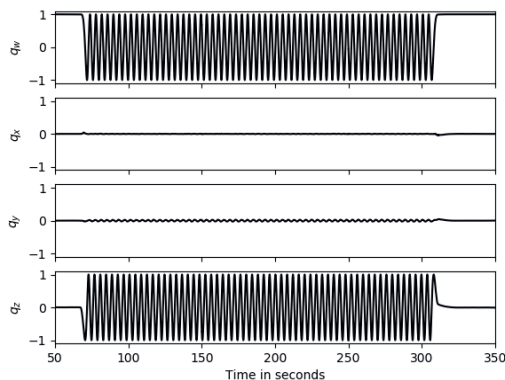


Fig 3: Extract of the estimated attitude in unit quaternion $|\mathbf{q}| = |[\mathbf{q}_w, \mathbf{q}_x, \mathbf{q}_y, \mathbf{q}_z]| = 1$ representation.

arm mounted on the rotation table. Besides the small deviations. Fig. 4 shows an extract of the acceleration transformed into vessel coordinates using the estimated quaternion by removing the acceleration due to gravitation and using

$$\mathbf{a}^{vessel} = \mathbf{q} * \mathbf{a}^B * \mathbf{q}^{-1},$$

where \mathbf{q}^{-1} is the inverse of the quaternion \mathbf{q} .

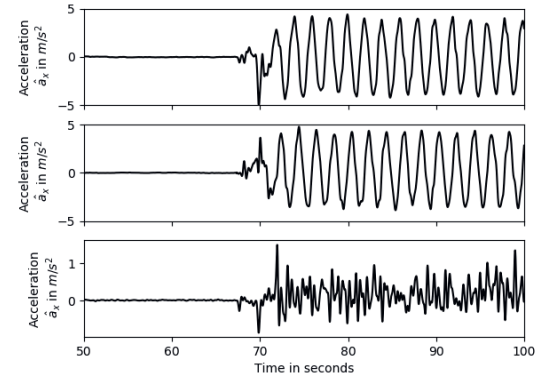


Fig 4: Extract of the estimated acceleration $\hat{\mathbf{a}}_x$, $\hat{\mathbf{a}}_y$ and $\hat{\mathbf{a}}_z$ in vessel coordinates.

As to be expected for a planar circular motion the acceleration in vessel coordinates is sinusoidal after starting the motion. The acceleration on $\hat{\mathbf{a}}_z$ in fig. 4 appears due to improper alignment of the accelerometer with the arm, vibration of the rotating table and measurement noise.

Conclusion

The motion-tracking algorithm introduced in [2] can reconstruct the attitude and acceleration of the sensor particle in relation to the vessel even if a high acceleration is measured which interferes with the attitude estimation. This forms the basis to extract velocity and position and, due to the pressure sensor, allows a statistical analysis of the vertical acceleration profile. Further development will focus on enhanced measurement quality of the ESKF to improve the flow tracking performance.

Acknowledgments

This research is part of the project 'NeoBio' funded by the Federal Ministry of Food and Agriculture under the funding code FKZ 22032618.

References

- [1] Thiele, S., Da Silva, M. J., & Hampel, U. (2010). Autonomous sensor particle for parameter tracking in large vessels. *Measurement Science and Technology*, 21(8), 085201.
- [2] Buntkiel, L., Reinecke, S. F., & Hampel, U. (2019). 3.5-Inertiale Lage- und Bewegungsverfolgung für instrumentierte Strömungsfolger zur Strömungscharakterisierung. *Tagungsband*, 52-58, DOI: 10.5162/14dss2019/3.5.

Unmanned Aircraft Based Gamma Spectrometry System for Radiological Surveillance

Maksym Luchkov^{1,2}, Stefan Neumaier¹, Arturo Vargas²

¹ *Physikalisch-Technische Bundesanstalt (PTB), 38116 Braunschweig, Germany*

² *Institute of Energy Technologies (INTE), Technical University of Catalonia, 08028 Barcelona, Spain*

Corresponding author: maksym.luchkov@ptb.de

Summary:

In the framework of the European "Preparedness" project, PTB is developing a spectrometer based dosimetric system that can be operated while being attached to an unmanned aerial vehicle (UAV). Built around 1.5" CeBr₃ scintillation detector, the radiation monitoring system records spectra alongside with temperature and flight telemetry at 0.5 Hz acquisition rate and transmits these data to a ground station where an algorithm calculates dose rates and activities. The presented aerial test results illustrate system's ability to precisely target a source and provide a good estimation of its activity.

Keywords: Radiation monitoring, spectro-dosemeter, cerium bromide, UAV, "Preparedness"

Introduction

In the aftermath of a nuclear or radiological event, the metrologically sound data on the ground and air contamination is of major importance for decision-makers to manage the emergency response in a timely and adequate manner. As an example, following the Fukushima Daiichi nuclear accident, weeks had gone till the first detailed radiation distribution map was available. A significant problem in tracking radioactive release was that the majority of radiation monitoring stations on the plant site were disabled by the tsunami, and this absence of reliable local data amplified the evacuation burden in the region. This disaster uncovered the lack of tools in the radiation protection field necessary to assess the radiological situation in time-resolved but accurate way.

The airborne radiation monitoring is the key to the fast contamination assessment following a radiological event. The conventional way involves deploying manned helicopters or small airplanes. Whilst being good for the large-scale evaluation of the radiological situation, this approach bears the problems of crew exposure and low spatial resolution due to the high altitude and flight speed, thus over-averaging terrain features (trees, rooftops, etc.) and, therefore, the contamination profile. The use of unmanned airborne monitoring systems offers the benefits of the high-resolution aerial measurements, especially in the areas otherwise inaccessible by big aircraft (e.g. NPP vicinity), and the operating personnel protection, as devices can be controlled from a safe distance.

Equipment

Nowadays, it is hard to catch the booming drone industry which brings regular advances in UAV technology, so we have designed a radiation monitoring system as a standalone device that can be mounted onto any drone with sufficient payload capacity. Thus, being independent of the carrier, the spectrometer is accompanied by a RasPiGNSS positioning module, SF11C laser altimeter, MS5607 barometer (altitude redundancy sensor) and a 2.4 GHz XBee transceiver. The spectrometric module resides in a 3D-printed housing and consist of 1.5" CeBr₃ scintillator with a photomultiplier tube readout, compact 120 MS/s BPI base and PT1000 platinum temperature sensor. The aluminum plate that provides device-mounting points and supports remaining system components is fixed on top of the detector housing. The brain of the system is a Raspberry Pi Model 3B microcontroller. The system is powered with a 5200 mA Li-ion battery which gives about 4 hours of operational time. The device weighs 1.5 kg; its dimensions in cm are H23 x L20 x W17 (see Fig. 1). The ground station, a laptop with another 2.4 GHz XBee transceiver, establishes peer-to-peer communication with the monitoring system and receives data every 2 seconds. The acquisition and control software is written in Python 3.5.

Method

The detector is a spectro-dosemeter, meaning it matches or even surpasses the accuracy of the best modern dosimeters while having the advantage of providing spectral information.



Fig. 1. The radiation monitoring system mounted onto a DJI M600P drone.

In environmental radiation monitoring, the measured dosimetric quantity is the ambient dose equivalent $H^*(10)$. Here, it is derived using the following formula:

$$H^*(10) = \sum v_i N_i \quad (1)$$

where N_i is the number of counts in channel i and v_i is the conversion coefficient for the mean energy of channel i . The conversion coefficients were calculated using PTB reference irradiation fields. For energy bands, where quasi-monoenergetic γ -ray sources were unavailable, coefficients were derived from Monte Carlo simulation in Geant4 radiation transport code. The method of the spectrum to dose conversion without deconvolution is thoroughly described in [1]. Practically, a spectrum is not grouped into energy bands, but the energy dependence of the conversion coefficients is approximated with a function [2]. This way, the uncertainties of fit parameters are propagated into uncertainties of conversion coefficients.

The algorithm of source location and activity restoration from the aerial data goes as follows:

- 1) From the dose rate at a flight altitude $\dot{H}^*(10)$ subtract the background dose rate $\dot{H}^*(10)_{bg}$ which can be measured separately or taken from mission periphery data points;

$$\dot{H}^*(10)_{src} = \dot{H}^*(10) - \dot{H}^*(10)_{bg} \quad (2)$$

- 2) With the source contribution $\dot{H}^*(10)_{src}$ left, define a surface activity mesh and calculate response factors f_{ij} at grid points:

$$\dot{H}^*(10)_{src} = \Gamma A/r^2 \rightarrow f_{ij} = \Gamma/r^2 \quad (3)$$

where Γ is the isotope dose rate constant and r is the source-detector distance;

- 3) With the matrix of response factors F , source dose rate vector \mathbf{H} and surface activity vector \mathbf{A} , the general equation is:

$$\mathbf{FA} = \mathbf{H} \quad (4)$$

To recover the activity vector, the optimization problem with regularization must be solved as detailed in [3].

Results

Within the scope of the ‘‘Preparedness’’ project, an unmanned aircraft systems intercomparison exercise was carried out at the aerial site in Mollerussa, Spain. While the complete results will be published elsewhere, we present here a single scenario with the localization of a ^{137}Cs point source with an activity of 346 MBq. The flight was performed at a 20 m altitude with a speed of 2 m/s and the line spacing of 20 m. Fig. 2 depicts the $\dot{H}^*(10)_{src}$ distribution at a flight altitude. The circular pattern of dose rate values clearly indicates that a point source has been detected, and the responsible isotope can be determined from the spectrum. To find the precise location and activity of the source, the eq. (4) was solved. The restored position is just 3.1 m far from the origin which is incredibly accurate considering that drone traveled 4 m per measurement; the restored activity is (398 ± 27) MBq which encompasses the true value within 2 standard deviations.



Fig. 2. Increase in ambient dose equivalent rate at a flight altitude during 346 MBq ^{137}Cs point source localization mission; source position is cross marked.

Acknowledgements

This work is supported by the European Metrology Programme for Innovation and Research (EMPIR), JRP-contract 16ENV04 ‘‘Preparedness’’. The EMPIR initiative is co-funded by the European Union’s Horizon 2020 research and innovation programme and the EMPIR Participating States.

References

- [1] H. Dombrowski, Area dose rate values derived from NaI or LaBr₃ spectra, *Rad. Prot. Dosim.* 160 (4), 269-276 (2014); doi: 10.1093/rpd/nct349
- [2] A. Röttger, P. Kessler, Uncertainties and characteristic limits of counting and spectrometric dosimetry systems, *J. Env. Rad.* 205-206, 48-54 (2019); doi: 10.1016/j.jenvrad.2019.04.012
- [3] S. Zhang et al., Mapping radiation distribution on ground based on the measurement using an unmanned aerial vehicle, *J. Env. Rad.* 193-194, 44-56 (2018); doi: 10.1016/j.jenvrad.2018.08.016

An Advanced Multi-Parameter Condition Monitoring System for Lubricants and Hydraulic Fluids

*Thomas Voglhuber-Brunnmaier¹, Alexander O. Niedermayer²,
Friederich Feichtinger², Bernhard Jakoby¹*

¹ Johannes Kepler University, Altenbergerstr. 69, 4040 Linz, Austria

² Micro Resonant Technologies, Hafenstr. 47-51, 4020 Linz, Austria
Thomas.voglhuber@jku.at

Summary

A compact measurement unit for fluid monitoring based on simultaneous measurement of viscosity and density is introduced. It will be shown that measuring fluid parameters over varying fluid temperature provides additional monitoring parameters and enhances data consistency. Suitable temperature models are demonstrated. Measurement results are discussed, which show the potential of this approach and the applicability of the measurement system in an industrial environment.

Keywords: viscosity, density, tuning fork, oil sensor

Introduction

In order to reduce maintenance costs as well as the risk of unplanned downtimes, industry gradually adopts online condition monitoring (OCM) methods combined with predictive or proactive maintenance approaches. Enabled by the increasing level of automation, plenty of data can be made available to maintenance personnel and condition monitoring algorithms, and sophisticated evaluation methods can be implemented to assist in planning of maintenance actions. With the implementation of such data based decision methods, the reliability and precision of the collected data obviously has significant impact on the effectiveness of the maintenance actions triggered. Furthermore, the sooner a problem can be identified, the easier and cheaper the appropriate maintenance action will be. So in many cases, the benefit of a sensor increases over proportionately with its accuracy and long term stability.

In this contribution, we present an innovative method to increase data reliability, as implemented in a novel fully automated online condition monitoring system for hydraulic fluids and lubricating oils. The device continuously monitors the viscosity, mass density, and several other relevant parameters of the fluid. With the integrated active temperature control, measurement data can be acquired at any desired reference temperature and thus are independent of the operating conditions of the machine. By cyclic variation of the temperature, additional information is provided and used for validating the consistency of the data.



Fig. 1. Condition monitoring system for industrial use.

Monitoring System

Fig. 1 shows the compact OCM system. The temperature controlled measurement cell within the system, houses the vibrating quartz tuning fork sensor (QTF), a Pt100 temperature sensor and a capacitive relative humidity sensor as shown in Fig. 2. From the fluid induced resonance changes of the QTF, the viscosity and density of the fluid are determined [1,2]. As viscosity shows significant temperature dependence, it needs to be measured at well-defined temperatures. Therefore, a precise thermoelectric temperature controller is implemented which can be used to cycle temperature and to determine additional characteristic fluid parameters. These comprise the temperature coefficient of the density and various viscosity-temperature indices such as the VTC, the VI or the m-value [3]. Although not discussed in this publication, the system also provides the electrical fluid parameters [4] and the relative humidity, which, if measured over temperature, yields a true multi-parameter characterization of the fluid under test.

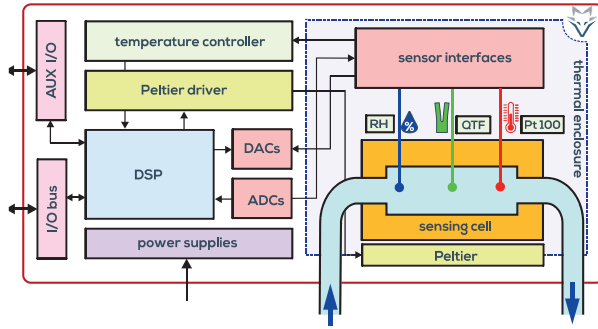


Fig. 2. Components of the OCM system.

Results

A common model for describing temperature dependence, is the Vogel-Cameron model (VCM) [3] which we use in an adapted form (1) such that the model parameter η_{40} represents the viscosity at the usual reference temperature for viscosity of $\vartheta_0=40^\circ\text{C}$. Parameters A and B are the slope of the normalized viscosity curve (see Fig. 3), and the original temperature offset variable of the VCM, respectively.

$$\eta(\vartheta) = \eta_{40} e^{\frac{A(\vartheta-40^\circ\text{C})(40^\circ\text{C}+B)}{B+\vartheta}} \quad (1)$$

$$\Delta\eta/\eta|_{\vartheta=40^\circ\text{C}} = A\Delta\vartheta|_{\vartheta=40^\circ\text{C}} \quad (2)$$

$$\rho(\vartheta) = \rho_{15} \cdot (1 + C \cdot (\vartheta - 15^\circ\text{C})) \quad (3)$$

The viscosity vs. temperature curves for two oils (5W30 and HLP 46) and the heat transfer fluid Marlotherm SH (MT SH) are shown in Fig. 3. The curves differ apparently, but the slope parameter A is very similar for all fluids (see Tab.1). However, the B parameter, characteristically around 110°C for oils, is only 63°C for MT SH. Standardized viscosity-temperature parameters such as VTC or VI-Index [2] are based on kinematic viscosity $\nu=\eta/\rho$, and therefore the density (ρ) measurements provided by the instrument can be used to calculate these values, as well. The density changes in Fig. 3 are linear over temperature and therefore the model in (3) can be applied. The temperature coefficient C is therefore independent of the reference temperature, (usually 15°C for density) and given in Tab. 1. The average fitting errors between model and data are approx. 0.2% for viscosity and 0.01% for density, which underscores the applicability of the models.

Conclusions

A novel measurement system for simultaneous measuring of viscosity and density over temperature was introduced. The suitability of temperature models which require only a minimum of parameters was verified.

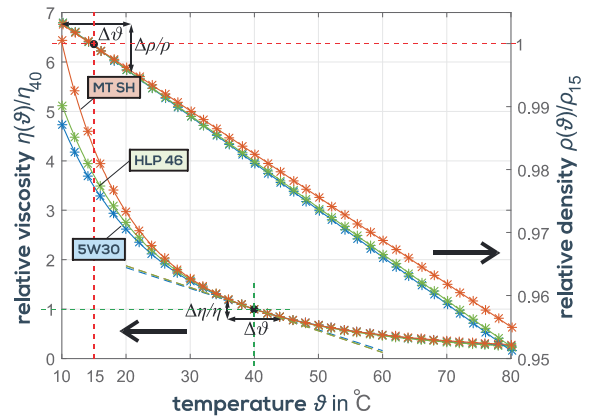


Fig. 3. Measured viscosities and densities (*) and the models in (1) and (3) using the fitting parameters in Tab. 1.

Fluid	η_{40} mPas	ρ_{15} g/cm ³	-A %/K	B K	-C 10 ⁻³ /K
5W30	56.67	0.85	4.20	117.16	0.728
HLP46	36.12	0.86	4.38	112.18	0.718
MT SH	16.98	1.05	4.39	63.15	0.671

Tab.1. Fitting parameters for the three fluids.

The parameters of the model were defined such, that they represent physical quantities and are therefore easier to relate to certain oil alterations. Due to the demonstrated low fitting errors, it can be assumed that abnormal sensor function can be detected, if fitting accuracy is impaired, or sudden changes of the parameters occur.

Acknowledgement

This research was partly supported by Linz Center of Mechatronics (LCM) in the framework of the Austrian COMET-K2 programme.

References

- [1] A.O. Niedermayer, T. Voglhuber-Brunnmaier, M. Heinisch, B. Jakoby, Accurate Determination of Viscosity and Mass Density of Fluids using a Piezoelectric Tuning Fork Resonant Sensor, Proceedings SENSOR 66-71. (2015), doi: 10.5162/sensor2015/A2.4
- [2] T. Voglhuber-Brunnmaier, A.O. Niedermayer, F. Feichtinger, B. Jakoby, (2019). Fluid sensing using quartz tuning forks—Measurement technology and applications. *Sensors*, 19(10), 2336.
- [3] Mang, T., & Dresel, W. (Eds.). (2007). *Lubricants and lubrication*. John Wiley & Sons.
- [4] Voglhuber-Brunnmaier, T., Niedermayer, A. O., Feichtinger, F., Reichel, E. K., & Jakoby, B. A multi-parameter physical fluid sensor system for industrial and automotive applications. *tm-Technisches Messen*.

Electromagnetic Sensors for Online Condition Monitoring of Medium Voltage Cables

Muhammad Shafiq¹, Kimmo Kauhaniemi¹, Amjad Hussain², Lauri Kutt³
¹ University of Vaasa (Finland), ²American University of Kuwait (Kuwait),
³Tallinn University of Technology (Estonia)
Muhammad.Shafiq@uwasa.fi

Summary:

Increased use of medium voltage (MV) cables demands for efficient condition monitoring in order to carry out timely predictive maintenance especially during incipient fault conditions emerging due to insulation degradation. This paper presents a comparison of the design and performance parameters of the Rogowski coil and high frequency current transformer sensors for measurement of partial discharge (PD) signals emitted from the PD defects. This work is performed in the laboratory environment that provides a practical approach for developing electromagnetic sensor for PD measurements.

Keywords: Electromagnetic sensor, condition monitoring, distribution network, medium voltage cable, partial discharge.

Background

Effectiveness of the predictive maintenance depends on the capability of the condition monitoring solution that requires suitable sensors for measurements in power system components. The performance of the sensors plays a vital role in reliability of the diagnostics during condition monitoring. Selection of suitable sensors and their design is determined based on the characteristics of the signals to be measured.

The use of MV cables is increasing around the globe and already installed cables are aging. Operational and environmental stresses deteriorate the dielectric insulation of the cables that causes the emission of the PD signals. PD faults are incipient and provide an early indication of the incoming cable failure [1]. Suitable sensors can be deployed to measure the PD signals for detection and location of the insulation faults. PD signals have high frequency (10s of megahertz-MHz) and low amplitude (few milliamperes- mA) that makes the design of the measurement sensors complex [2]. Specific sensors are used for measurements in specific power components. Because of non-intrusive sensing capability, installation possibility around the cable shielding, and operational behavior, Rogowski coils (RC) and high frequency current transformers (HFCT) are considered as the most suitable sensors for accurate PD monitoring in MV cables [3].

An ample amount of work has been done in order to explore the capabilities of RC and

HFCT sensors for PD measurements [2]. However, the available work mostly describes the operation of these sensors standalone. This paper presents a comparative study to observe the design and operational performance of both the sensors (RC and HFCT) in order to assess their suitability for PD measurements in the MV cables based on experimental analysis.

Description of the Experimental Investigation

Sensitivity and bandwidth are the major performance parameters of these sensors. Sensitivity can be defined as the voltage output/PD input current at a certain frequency while the bandwidth is considered as the range of frequency across which the sensitivity of the sensors remains 0.707 of the peak output.

Tab. 1: Geometrical parameters

Parameter/Sensor	RC	HFCT
Inner diameter	3.4 cm	3.45 cm
Outer diameter	6.1 cm	6 cm
Core height	2 cm	2 cm
Number of turns	48	48
Wire diameter	1.7 mm	1.7 mm
Core shape	Rectangular	Rectangular

The geometrical dimensions of both the sensors has been taken as same (as shown in Table 1). However, the core of RC is air core

while the HFCT has a ferrite core. The PD calibrator and associated circuitry is used to generate the typical PD pulse that is measured by both the sensors simultaneously as shown in the Fig. 1. A high frequency digital storage oscilloscope (DSO) is used for capturing the output signals measured by both sensors.

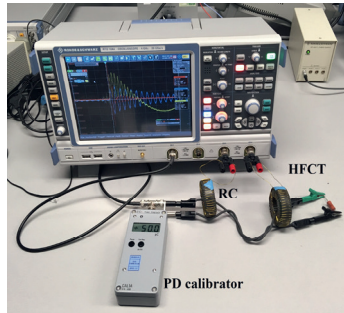


Fig. 1. Experimental setup for measurement of PD signals using RC and HFCT

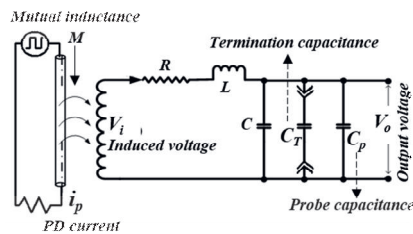


Fig. 2. Electrical model of the PD sensors

Reliability of the measurement and its interpretation depends on the accuracy of the electrical model (Fig. 2) developed during design stages. Inductance and capacitance of the sensors determine the sensitivity and bandwidth of the sensors. It has been found that geometrical parameters based mathematical models pose considerable limitations in obtaining the inductance and capacitance of the sensors accurately. In this work experimental method to determine the electrical parameters is used. The methodology is based on comparing the resonant frequencies (f) of RC and HFCT for different known capacitors (C_T) connected across the output of the sensors. The f is expressed as

$$f = \frac{1}{2 \cdot \sqrt{L \cdot (C_i \cdot C_T \cdot C_p)}}$$

Results and Conclusions

Considering the inductance and capacitance of the sensors, frequency-dependent impedance characteristics determines its resonant frequency that formulates its bandwidth. Experimentally determined resonant frequency of the RC and HFCT sensors is 30.3 MHz and 1.9 MHz respectively. For the same calibrated PD current pulse i_p , the sensitivity of RC is observed as 0.013 V/unit Ampere at 30.3 MHz while the sensitivity of HFCT is measured as 0.05 V/unit

Ampere at 1.9 MHz. For the same geometrical parameters, lower resonant frequency and higher sensitivity of the HFCT (as compared to RC) is because of its magnetic core. The magnetic permeability of the ferrite core in HFCT is considerably higher as compared to that of the air core RC. On one hand, the higher permeability μ_r results in higher magnetic flux density (B) that increases the output voltage V_o . On the other hand, this increase in permeability increases the inductance of the coil that reduces the resonant frequency of HFCT sensor.

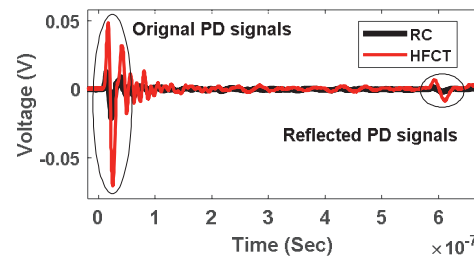


Fig. 3. Experimental PD measurements on MV cable

Comparing the sensors' performance, HFCT presents greater sensitivity while the RC shows greater bandwidth. As shown in Fig. 3, both the sensors are able to measure the PDs on a MV XLPE cable. However, the HFCT's measured signal is significantly stronger than that of RC. MV cables present significant attenuation and dispersion to the PD signals during their propagation that reduces the amplitude and frequency of the PD pulses. In such cases, sensitivity becomes more a concern. Therefore, based on the observed performance, HFCT can be considered as a preferred measurement solution as compared to RC for PD monitoring in cables.

Acknowledgement

This work is supported by Academy of Finland under project grant Grant No. 309412 and FUSE (Future Smart Energy) project funded by Business Finland (Grant No. 7038/31/2017).

References

- [1] Eigner et al. "An overview on the current status of partial discharge measurements on AC high voltage cable accessories." *IEEE Electrical Insulation Magazine* 32.2 (2016): 48-55. doi:10.1109/MEI.2016.7414231
- [2] Fernando, et al. "Application of HFCT and UHF sensors in on-line partial discharge measurements for insulation diagnosis of high voltage equipment." *Sensors* 15.4 (2015): 7360-7387. Dio: 10.3390/s150407360
- [3] Shafiq et al. "Online condition monitoring of MV cable feeders using Rogowski coil sensors for PD measurements." *Electric Power Systems Research* 167 (2019): 150-162. doi:10.1016/j.epsr.2018.10.038

Blockchain platforms as solution for a secure data transfer and a secure payment system

From sensor supplier to service provider

Haid; Markus¹, Boyaci; Ishak¹, Biswas; Jeetr¹, Berezowski; Nick¹

¹ CCASS (Competence Center For Applied Sensor Systems) University Darmstadt, Birkenweg 8, 64295 Darmstadt, Germany
Markus.haid@ieee.org

Summary:

Localization sensors, so-called intelligent UWB tags, can be connected via blockchain platforms on site at the user's premises. These can then independently conclude so-called smart contracts with applications via the blockchain. Applications can then access localization data and pay the price specified in the Smart Contracts with tokens to the tag. The application thus pays for each access to the sensor. This would transform sensor manufacturers from sensor supplier to service provider.

Keywords: sensor, blockchain, IoT, smart contracting, service supplier

INSIGHT-CHAIN

In the main title, please use initial capital letters; do not capitalize articles (like "the"), coordinate conjunctions ("and"), and prepositions ("of", "in") under four letters in length.

Within the research project INSIGHT-CHAIN of the CCASS in Darmstadt a blockchain platform was developed, to which localization sensors, so-called intelligent UWB tags, are connected on the user site.

Smart-contracting

Via the blockchain, these can then independently conclude so-called smart contracts with applications that want to access the localization data of the UWB (ultra-wide-band) localization system and which then pay a price specified in the contract to the tag in the form of tokens. In this context, tokens are cryptocurrencies that is not or not yet listed. The application therefore pays for each access to the sensor. Thus, sensor suppliers could set themselves up within the framework of the digital transformation in order to gradually change the business model from sensor supplier to service supplier as required.

Algorithms and resources

In addition to this, the tag now also has the option of buying intelligent algorithms offered as software applications via the blockchain. These

can be developed and offered for use as AI-algorithms by other suppliers and made available via the blockchain, also via payment.

In the same way, access to computing power is contractable (contractually controllable) if a sensor does not have computer resources available for an algorithm or software.

Services

In addition to the possibility to sell the entire localization system in software and hardware to the customer, another new business for sensor suppliers is the use of the blockchain platform INSIGHT-CHAIN, which allows to be paid per smart contract. This corresponds to the current requirement to pay for services offered instead of investing in a localization or navigation system.

Typical areas of application could be, for example, the flexible use of localization information within production and logistics. These are currently being developed, planned, installed and sold to customers by sensor suppliers as a complete localization system in a combination of tags and so-called nodes (reference points), gateways and an evaluation platform.

With the blockchain platform INSIGHT-CHAIN, the customers of the sensor manufacturers will in future have the opportunity not to purchase the system as a combination of hardware and

software, but rather, comparable to a leasing vehicle, to purchase access to the localization system as a service according to access (on demand). This means that the sensor manufacturer can act as a service supplier in the future and would be ideally positioned to meet the new emerging needs for bookable and subscribable services and information in the field of localization and navigation.

State of the art

A number of blockchain projects already exist in the area of data handling. However, these are essentially pure data marketplaces, mostly in B2C, i.e. business to consumer, solutions.

Furthermore, the state of the art is pure data handling platforms. In the present project it is about an exchange of evaluated data or localization information, which has been prepared by AI algorithms, for use by superimposed or administrative processes and can be used as shared services in the industrial and logistic environment.

The blockchain platform INSIGHT-CHAIN could therefore be used as an information provider.

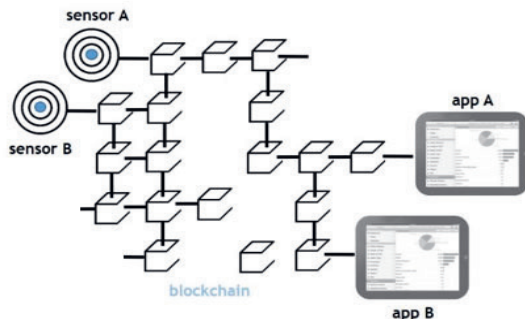


Fig. 1. Blockchain Plattform

Blockchain

Blockchain as a revolutionary technology, known as a decentralized organization system of a crypto currency, offers great potential for solving the project described here. The Blockchain technology was first published in connection with the crypto currency Bitcoin in 2009.

Basically, the blockchain forms a decentralized, distributed, common and unchangeable database, which stores all transactions between the nodes or users via a direct peer-to-peer connection. The blockchain protocol structures information in a chain of blocks, where each

block stores a set of transactions that are executed at a certain time. Blocks are linked together by a reference to the previous block and form a chain.

Before a new transaction, i.e. a new block, is connected to the chain, it must first be uniquely verified by the users of the blockchain according to the consensus principle. This ensures decentralization, the elimination of middlemen and in addition to speeding up the transaction.

The encryption technology of the block chain ensures the integrity and authenticity of the database and the anonymity of the users. Since the block chain is a distributed database, each node has the same information. This redundant storage guarantees data integrity after distribution and protects the data against compromise.

The blockchain contains a list of all past transactions, which in turn provides the verification basis for the new data block. Since every verified transaction is unchangeably chained in the block chain, it is protected against subsequent manipulation. The integration of a time stamp within each block also preserves the chronology.

References

- [1] Haid, Markus; INSIGHT-CHAIN the Blockchain Plattform, Blockchain-Conference, Berlin, 2019
- [2] Haid, Markus; With Sensors and Blockchain in the Internet of Things, Science Square, Hannover Messe 2019

Adaptable System for Diagnosing Sensor Faults for Application on Engine Test Benches

Michael Wohlthan¹, Gerhard Pirker¹, Andreas Wimmer²

¹ LEC GmbH, Inffeldgasse 19, A-8010 Graz, Austria

² Graz University of Technology, Institute of Internal Combustion Engines and Thermodynamics, Inffeldgasse 19, A-8010 Graz, Austria
michael.wohlthan@lec.tugraz.at

Summary: This paper presents a new approach for a diagnostic system that detects and isolates sensor faults at engine test benches. The modular system as well as the combination of physics-based and data-driven modelling concepts allow highly flexible application on various types of engine test benches. The adaptability of the system is validated using measurement data from two different engine test benches.

Keywords: fault diagnosis, engine test bench, model-based diagnosis, sensor faults, adaptable system

Motivation and Objective

Experimental investigations on engine test benches are a significant cost factor in current combustion engine development. To keep the number of required tests and their associated costs low, it is essential that sensor faults and measurement errors are detected in an early stage [1]. Fritz [2] estimates that up to 40% of test bench time is lost due to faults that are detected too late. Because of the increasing number of sensors and actuators in combustion engines, reliable validation of test results by one person alone has become nearly impossible. On the whole, there is a need for an automated diagnostic system that evaluates measurement data quality and identifies faulty measurement sensors. The great challenge in applying a diagnostic system at engine test benches is that they are often subject to frequent changes in the test engine. Therefore, the diagnostic system must be able to be adapted easily to different types of test engines.

System Description

The proposed diagnostic system works according to the procedure shown in Fig. 1. The test bench produces measurement data (x_i stands for the measured value of any sensor) which is then checked by a diagnostic procedure consisting of three steps: modeling, fault detection and fault isolation. In the modeling step, the diagnostic system is adapted to the changeable test engine because modeling is either done online and automatically with data-driven methods [3][5][6] or initially before the test is started using an engine component-specific (cylinder, turbocharger,

throttle valve, etc.) model library containing physics-based models [7]. Each model ultimately delivers a residual r , which serves as a fault indicator based on the deviation between measurements and model equation-based computations [3].

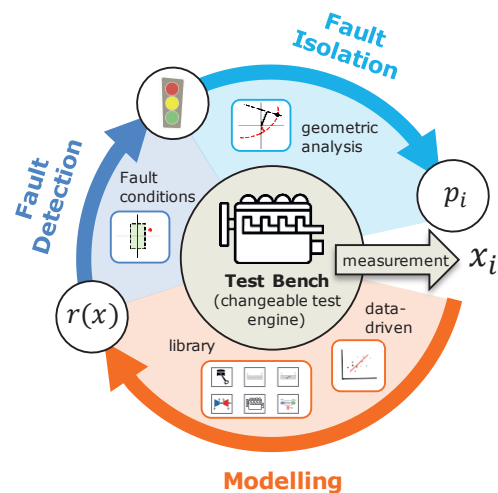


Fig. 1. Scheme of diagnostic procedure

In the second step, fault detection is performed in order to determine whether a fault has occurred in the respective measurement. This is done by checking fault conditions (1).

$$|r| > thr \quad (1)$$

Thus, a fault is detected if the value of the residual exceeds a certain threshold thr . Finally, it is determined which sensor is faulty. In this third and final step, fault probabilities p_i are calculated for all considered sensor values x_i using a

geometrical classification method based on the distance evaluation between error propagation curves and residual state points [8].

Results

The following figure shows the diagnostic results of two different test engines. The first engine is a multicylinder diesel engine (layout in Fig. 2, left) and the second a single-cylinder research engine (layout in Fig. 2, right). The diagnostic system is adapted to these engines using different models. This happens either automatically through the online training of data-driven models or by choosing different component-specific modules from the physics-based model library.

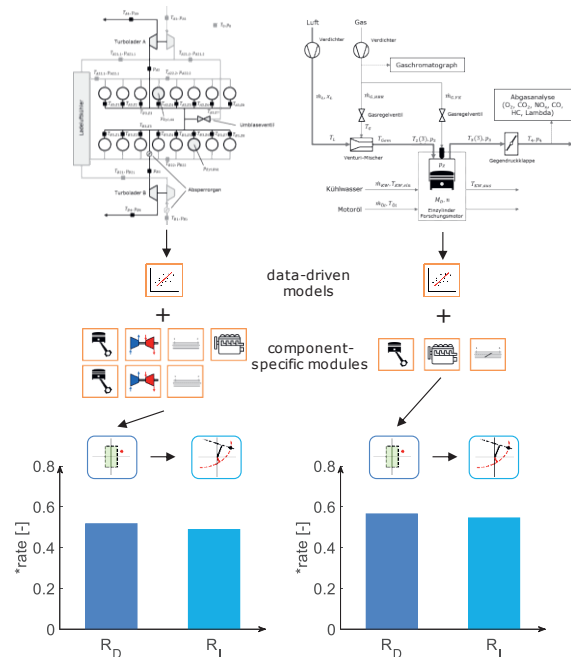


Fig. 2. Comparison of the diagnostic results of a multicylinder diesel engine (left) and a single-cylinder research engine (right)

Evaluation quantities are necessary for an objective validation of the diagnostic system. To evaluate fault detection independently of fault isolation, two quantities are introduced: the detection rate (2) and the isolation rate (3).

$$R_D = \frac{\text{number of correctly detected faults}}{\text{number of actual faults}} \quad (2)$$

$$R_I = \frac{\text{number of correctly isolated faults}}{\text{number of actual faults}} \quad (3)$$

Fault-free measurements from real test bed operation provide the initial basis for the analysis. In order to obtain the large number of faulty measurements necessary for the evaluation of the two quantities, abrupt faults with different timings and different intensities are simulated for all

implemented sensors. Fault diagnosis is then performed with all measurement data obtained in this way. Finally, the overall detection rate and the overall isolation rate are calculated.

Conclusions

Two important conclusions can be derived from the results shown in Fig. 2. Despite the great differences between the test engines, comparable diagnostic results are achieved. This shows that the diagnostic system can be used flexibly with different test engines because of its adaptability. At this point, it should also be mentioned that the scope of application is not limited to combustion engines. The modular approach can generally be applied to other test bed systems as well if the corresponding model library has been developed for it. Furthermore, it can be seen in Fig. 2 that in both cases, the isolation rate R_I is only slightly below the detection rate R_D , which means that nearly every fault that is detected is also correctly isolated.

References

- [1] A. Flohr, Konzept und Umsetzung einer Online-Messdatendiagnose an Motorprüfständen. Dissertation, Technische Universität Darmstadt (2005)
- [2] S.C. Fritz, Entwicklung und Umsetzung einer zentralisierten Messdatendiagnose für Motorprüfstände als integrierter Bestandteil des Prüfsystems. Dissertation, Technische Universität Darmstadt (2008)
- [3] R. Isermann, P. Balle, Trends in the Application of Model Based Fault Detection and Diagnosis of Technical Processes. *Control Engineering Practice*, Vol. 5 (1997); doi: 10.1016/S0967-0661(97)00053-1
- [4] D. Schadler, Model based methods for fault diagnostics at engine test beds, *ISCCRO18: 2nd International Statistical Conference in Croatia* (2018)
- [5] D. Schadler, Modellbasierte Methoden zur Fehlerdiagnose an Motorprüfständen. Masterarbeit, Technische Universität Graz (2016)
- [6] D. Schadler, E. Stadlober, Fault detection using selected data and updated regression models, *Measurement Vol. 140* (2019); doi: 10.1016/j.measurement.2019.04.010
- [7] M. Wohlthán, Methoden zur Fehlerdiagnose an Motorprüfständen, Dissertation, Technische Universität Graz (2019)
- [8] M. Wohlthán, G. Pirker, A. Wimmer, Modular Fault Diagnosis System for Engine Test Bed Measurements. *SAE Int. J. Commer. Veh.* 10 (2017); doi: 10.4271/2017-01-0386

Safety Sensor Applications with Graphical Programming

Nick Berezowski¹, Markus Haid¹, Jeet Biswas¹, Ishak Boyaci¹

¹ *University of Applied Science Darmstadt, Schöfferstraße 3, Darmstadt, Germany
nick.berezowski@h-da.de*

Summary:

This research recommend the use of a a graphical full variability programming language for safety-related sensor system developments, in order to create framework conditions that result in a general approach for graphical sensor applications. A graphical programming language represents a language whose basic elements consist of blocks, symbols and lines between them, not like text-based or superimposed visual languages with ASCII-formatted semantics.

Keywords: Functional Safety, Graphical Programming Language, Graphical Full Variability Programming Language, Recent Developments, LabVIEW

Introduction

Graphical programming languages offer a visual development design that increasingly focuses on natural human thought structures, which frees up thinking resources for content-related problem-solving approaches [1]. They can serve as essential means of communication when using fourth generation programming languages [1]. This suggests that graphical programming languages, with the ability to visually represent abstract control flow and data flow structures, can be considered fourth generation programming languages, and thus serve further development as well as functional security.

From a technical point of view, graphical programming languages are just another depiction of the implementation that is very similar to the models of text-based languages, but represent the implementation of graphical languages. Thus, they can substitute for well-known semi-formal methods, such as UML, provided that appropriate regulations are adhered to.

Since there is no research on this topic so far, the question of feasibility arises.

Theoretical Fundamentals

There are numerous standards for functional safety. Some are described in Fig. 1. These are updated and rewritten irregularly in order to provide descriptions of the current state of technology. Among other things, emphasis is placed on tendentious technology innovations in order to consider them for future projects. [2]

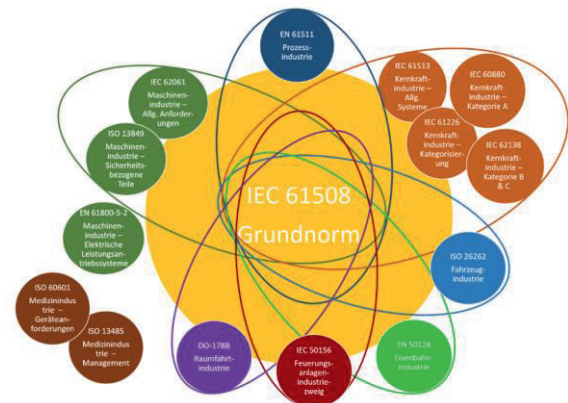


Fig. 1. Overview of functional safety standards.

For an initial process development in sensor systems only the basic standard IEC 61508 is needed.

To create a qualifiable development in a graphical development environment requires specific methods and approaches that can not be dictated solely by the development environment and require a clear definition in terms of functional safety.

General structures

During the specification of requirements for safety-related systems, all relevant informations, such as requirements for the system, subsystems and components, must be recorded. Semiformal and formal methods can provide a detailed specification of the requirements. Due to their graphical structures, semiformal methods are to be understood as similar to graphic code and thus preferable to formal methods. If possible, computer-aided specification tools should be used, which reduce the error potential during execution and lay the

basis for traceability. This is divided into forward and backward traceability. Forward traceability should be possible, especially at higher safety integrity levels between all phases of the software safety lifecycle [3]. A computerized tool could support these relationships.

Programming Languages Structure

To comply with the sensor requirements of the basic standard, a language subset must be defined which excludes the use of unsafe programming code constructs and checks their compliance with static analysis tools. [3]

A graphical programming language to be used must have a strict typing [3]. This means that type conversions must be obvious. Compliance checking can be done through in-program programming tests or, if necessary, additional static testing.

Since no already certified tools exist, tried-and-tested tools and translators should be used. These must be regarded as established and not error-prone in the relevant area of a safety-related system to be used. A test and verification environment that compares executable code with source code can provide additional confidence for individual sensor systems, but not for the complete environment. [3]

Programming Structures

There is a possibility that a graphical programming language may self-comply with some semiformal models, such as state transition diagrams and flowcharts, allowing for requirement determination and modeling close to programmatic implementation, potentially shortening development time and the necessary framework.

The rules of structured programming must be applied. Defensive programming can only be used in necessary places, since it also worsens the understanding of the complete program. [3]

The modular approach offers several sub-methods, all of which must be adhered to in a graphical programming language [3]. Some graphical languages inherently have a modular flow-controlled structure that supports these methods.

In general, a monitoring device should work with separation between monitoring and monitored computer in order to demonstrate a general independence for the introduction of a programming language. [3]

Completed Work

First, various standards and guidelines for functional safety and authoritative literatures for graphical programming languages were ana-

lyzed to make reference to the prior art. Based on the basic IEC 61508 standard, a rough concept with various possible solutions for software development in graphical programming languages was developed. The different methods and procedures let us derive an overall architecture using semiformal methods, which creates a direct relationship between design, development and programmatic implementation of a sensor application. It was possible to create a theoretical concept for an architecture framework, which should consist of project management, configuration management, test management, design and development tools in order to create a comprehensible link with the programming language and physical system.

Further Work

Currently, the previous knowledge for graphical full variability programming language apply. Here, an implementation was created that provides the basis for testing and validation through the use of semiformal methods and model-based analyzes. The basis for this is the establishment of safety functions via finite state machines. Based on the limitations of the language scope by means of language subsets, expert interviews should be conducted, if possible, with responsible persons involved in current established qualified procedures. This gives the basic work for recommendations for developing a policy in a special graphical programming language. Subdivisions into software, hardware and management have already been taken. Nevertheless, software structures can provide the basis for safe hardware and sensoric structures.

After developing the basic safety-related methods and procedures, as well as developing recommendations for a guideline, the findings must be tested and applied to a special graphical programming language and sensor systems. The programming language G in the development environment LabVIEW provides the best framework for this.

References

- [1] Ludwig Coulmann (Hrsg.) (1993): Programmvisualisierung bei Sprachen der 4. Generation - Visualisierung von NATURAL-Programmen. SpringerLink.
- [2] DIN EN 61508-1, Februar 2011: DIN EN 61508-1 (VDE 0803-1):2011-02.
- [3] DIN EN 61508-3, Februar 2011: DIN EN 61508-3 (VDE 0803-3):2011-02.

Fracture Detection of Bearings in Long-Term Measurements Using a Feature-Based CUSUM Algorithm

Andreas Beering¹, Anton Zitnikov², Karl-Ludwig Krieger¹

¹ Chair for Automotive Electronic Systems (ITEM.ae), University of Bremen, Germany

² University of Bremen, Germany

{beering, zitnikov, krieger}@uni-bremen.de

Abstract:

In this paper, a new approach for fracture detection on tapered roller bearings is presented, which is based on a feature-based CUSUM algorithm. For this purpose, experimental investigations are presented in which fractures in bearings are generated by overload. The vibration signals are recorded throughout the entire bearing lifetime in the test, from which features are later extracted and used for fracture detection. More specifically highlighted as features in this paper are the standard deviation and the clearance factor, which are often used in the context of detecting damage to rotating machinery.

Keywords: Damage Detection, Condition Monitoring, Predictive Maintenance, Vibration Analysis, CUSUM Algorithm

Introduction

In the field of condition monitoring, a large number of machine components are already monitored in order to optimize processes or detect damage. However, many areas have not yet been sufficiently investigated, so avoidable machine failures still occur. This includes undetected bearing damage, which often result in further machine damage. One solution to avoid this consequential damage in the future could be the detection of initial damage by analysing vibration data.

Previous approaches of detecting faults in rotating machine elements were largely based on envelope analysis of vibration signals, in which damage is detected on the basis of previously calculated damage frequencies [1]. A further approach of the detection of bearing damage uses feature extraction, followed by a classification [2]. Furthermore, with regard to long-term measurements, wear was generated by loading of deep groove ball bearings and estimates of remaining useful lifetime were investigated [3].

This publication presents a study of long-term measurements on tapered roller bearings, and the detection of fractures in the vibration signal via the application of the CUSUM algorithm to previously extracted features. This calculates and compares the cumulative sum of a measured value if this exceeds a threshold value [4].

Experimental Setup

In order to investigate the vibration behavior of bearings in long-term tests, a laboratory test rig

was set up, shown in Fig. 1. A bearing socket has been manufactured which can hold different bearing sizes. Piezoelectric vibration transducers can be attached by means of screw connections. A defined radial force can be applied to the bearing's outer ring by means of a screw attached to the bearing socket as shown in Fig. 1 (a). The bearing, which is set in the socket, is connected with an electrical motor via a low-vibration coupling.

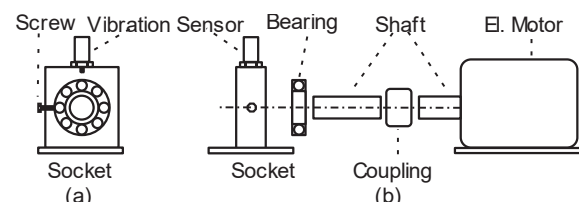


Fig. 1. Experimental setup for the investigation of bearings in frontview (a) and sideview (b).

During the measurement the vibration transducer was sampled with a sampling rate of 20 kHz and a resolution of 24 bits.

Experimental Results

The damage pattern occurring due to the outer ring fractures is shown in Fig. 2.

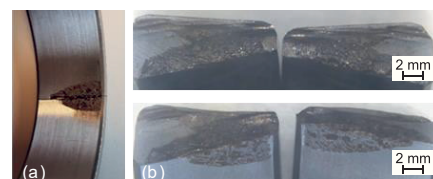


Fig. 2. Occurred fracture on the outer ring with pitting (a). Close-up view of the fracture in the scanning electron microscope (b).

In addition to the actual fracture of the outer ring, significant pitting can be seen at the edge of the fracture. Furthermore, material fatigue effects can be seen inside the material due to the dark discoloration of the material.

For the investigation of the long-term measurements, characteristics from time windows of 2000 samples each were first extracted and standardized. For closer examination the standard deviation σ and the clearance factor CF, calculated as shown in Eq. 1 [5], are considered.

$$CF = \frac{x_{\max}}{\left(\frac{1}{N} \sum_{i=1}^N \sqrt{|x[i]|}\right)^2} \quad (1)$$

The statistically occurring feature values before and after fracture of the bearing's outer ring are compared. Fig. 3 shows the probability density function and the fitted normal distribution for both standardized features \widehat{CF} and $\widehat{\sigma}$ before and after the fracture.

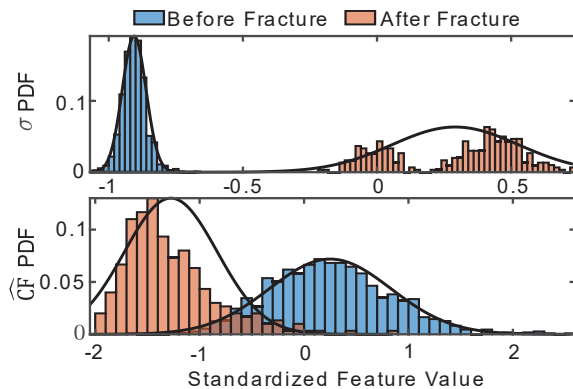


Fig. 3. Probability density function (PDF) of standard deviation and clearance factor with fitted normal distribution before and after fracture of the outer ring.

The PDF shows that both characteristics follow a normal distribution before the fracture. After the fracture there is a deviation of the mean value of both features. The curves of the PDF no longer follow a normal distribution after the fracture. Furthermore, it can be seen that the distribution of $\widehat{\sigma}$ results in a bimodal distribution after the fracture. The standard deviations and mean values of both features over the range before fracture (1100 time windows) and after (300 time windows) are listed in Tab. 1.

Tab. 1: Mean value and standard deviation of the considered features before (BF) and after fracture (AF).

	μ_{BF}	σ_{BF}	μ_{AF}	σ_{AF}
$\widehat{\sigma}$	-0.905	0.045	0.292	0.236
\widehat{CF}	0.250	0.582	-1.275	0.444

The CUSUM algorithm is applied to the extracted features to realise a change detection. Fig. 4 shows the calculated cumulative sum for the two

features previously considered, as well as the standardized feature value itself over time.

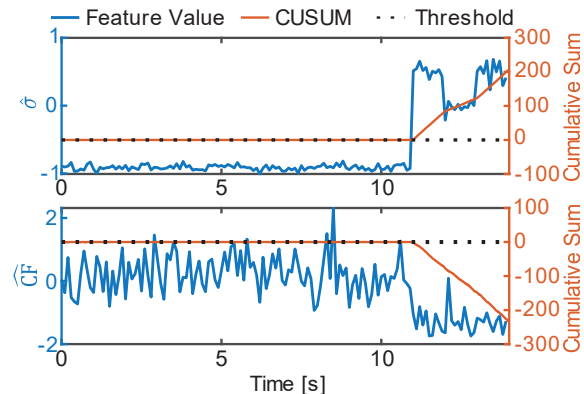


Fig. 4. Standard deviation and clearance factor plotted over time with associated cumulative sum.

At the point where the cumulative total exceeds a threshold value of 3σ of the characteristic value, the fracture is detected. In both features a fracture is detected after 11 hours which corresponds to the real fracture time. Both features can therefore be assumed to be suitable for bearing fracture detection.

Conclusion

In this paper a detection of experimentally generated fractures in tapered roller bearings was presented. For this purpose, bearing fractures due to overload were generated in a laboratory setup and the vibration signal was recorded. Subsequently, the standard deviation and the clearance factor were determined as features to detect fractures based on the CUSUM algorithm. On the results obtained, it can be assumed that both characteristics used are suitable for breakage detection.

References

- [1] G. Brian and K. Starry, „Rolling Element Bearing Analysis“, *Materials Evaluation*, Vol. 70, No. 1 pp. 78-85, 2011.
- [2] A. Beering, J. Döring and K.-L. Krieger, „Feature-based analysis of reproducible bearing damages based on a neural network“, *20. GMA/ITG-Fachtagung Sensoren und Messsysteme Tagungsband*, pp. 451-456, 2019, doi:10.5162/sensoren2019/5.4.2
- [3] K. Medjaher, N. Zerhouni, J. Baklouti et al., „Data-driven prognostics based on health indicator construction: Application to PRONOSTIA's data“, *IEEE ECC*, pp. 1-6, 2013, doi: 10.23919/ECC.2013.6669223.
- [4] M. Basseville, „Detection of Abrupt Changes: Theory and Application“, *Prentice Hall*, pp. 35-43, 1993, doi: 10.1080/00401706.1994.10485821.
- [5] A. K. Nandi, H. Ahmed, „Condition Monitoring with Vibration Signals: Compressive Sampling and Learning Algorithms for Rotating Machines“, *Wiley-IEEE Press*, p. 40, 2020, doi: 10.1002/9781119544678.

Inductive Communication and Localization of Wireless Sensors in Photoreactors

David Demetz¹, Alexander Sutor²

¹ *Institute of Measurement and Sensor Technology, UMIT – Private University, Hall in Tirol, Austria
david.demetz@umit.at*

² *Institute of Measurement and Sensor Technology, UMIT – Private University, Hall in Tirol, Austria
alexander.sutor@umit.at*

Summary:

We propose a method for inductive communication and localization of wireless sensors in photoreactors. In past, methods for internal illumination of photoreactors have been presented. Wireless light emitters (WLE) have been developed to counteract the limited penetration depth of light in photoreactors. Photoreactors are used to cultivate photosynthetic active microorganisms and cells or to perform photocatalytic reactions. The WLE are powered from outside the reactor through a loosely coupled inductive link. The intermediate frequency (178 kHz) electromagnetic field with a magnetic flux density of approx. $B = 1$ mT is produced by multiple coils driven by an Class-E amplifier [1]-[3]. The next step is the inclusion of sensors to measure crucial parameters such as e.g. temperature, pH-value or oxygen and carbon dioxide concentrations in order to control the various processes. Additionally the information about the position of the sensor inside the photoreactor leads to a spatial resolution of the measured parameter.

Keywords: inductive communication, inductive localization, wireless sensors, photoreactor, 3d-coil

Introduction

To control the processes in those photoreactors various parameters have to be measured e.g. temperature, pH-value, UV-illumination or other chemical concentrations. To counteract the drawback of measuring the named parameters only at one point inside the photoreactor, we present methods for the wireless communication and localization of wireless powered, unfixed sensors. Because of the promising propagation properties of magnetic fields in water and in salty water, we chose the inductive layer for the communication and the localization task. The authors of [4] also make use of this advantage for the inductive communication through human tissue for assistive listening devices. For our photoreactor use, we set the modulation frequency at a factor 1.66 above the frequency of the power link in order to prevent interferences by harmonics. We also will take the standard frequencies like 433 MHz in consideration; this frequency band is used as a communication layer in a similar project [5]. The drawback of higher frequencies is their high damping factor in electrically conducting media.

Inductive OOK communication

As modulation technique for the data transmission, we use the on-off-keying (OOK); this is implemented like in [4] with an on-off switched Hartley-oscillator as transmitter. In a first step, in

order to simulate the single sensor data bits we use the integrated circuit LMC555 to generate the on-off signal. As a receiver, we use an LC-tank tuned to the same frequency as the Hartley-oscillator.

Inductive sensor localization

To solve the localization task of the transmitting coil, we make use of the well-defined spatial propagation of the magnetic dipole field. As shown in [6], the magnetic field of an one-loop coil, excited with the current $i = I \cos(\omega t)$, at a position defined by the distance x from the loop center and the off-axis angle φ , is completely described by its radial (1) and tangential (2) components. N is the number of turns and A the area of the coil.

$$H_r = \frac{NIA}{2\pi x^3} \cos \varphi \quad (1)$$

$$H_t = \frac{NIA}{4\pi x^3} \sin \varphi \quad (2)$$

If the transmitter and the receiver have the same orientation (x -axis aligned, y - and z -axis parallel), the transmitter-receiver coupling is described by the Eq. (3). \mathbf{f}_{rx} is the receiver signal vector, \mathbf{f}_{tx} the transmitter signal vector; x is the distance between them and C is a constant factor derived from the coil properties and the sensor gain [6].

$$\mathbf{f}_{rx} = \left(\frac{C}{x^3}\right) \mathbf{S} \mathbf{f}_{tx} \quad (3)$$

$$\mathbf{S} = \text{diag}(1, -0.5, -0.5)$$

We have simplified the localization task by assuming that the transmitting coil is always aligned with the vertical z-coordinate like shown in Fig. (1) (in general, this alignment of the transmitter is important also for the power link). Measuring the magnetic field components in the x- y- and z-direction at one known spatial point allows us to calculate a direction vector \mathbf{r} that points from the measuring point to the position of the transmitter. Making use of the spherical coordinate system, this direction vector is defined by two angles α and β ; α represents the rotation angle around the z-axis, β the rotation around the y-axis. The coupling between transmitter and receiver is defined by Eq. (4). $\mathbf{f}_{tx} = (0 \ 0 \ a)^T$ is the signal vector of the transmitter. It is an unknown value in z-direction since the current in the transmitter coil is unknown (it depends on the position of the transmitter in the photoreactor). \mathbf{T}_α is the rotation matrix around the z-axis and \mathbf{T}_β the rotation matrix around the y-axis and \mathbf{f}_{rx} is the vector with the measured x- y- and z-components of the transmitter magnetic field at receiver side.

$$\mathbf{f}_{rx} = \left(\frac{C}{x^3}\right) \mathbf{T}_\alpha^{-1} \mathbf{T}_\beta^{-1} \mathbf{S} \mathbf{T}_\beta \mathbf{T}_\alpha \mathbf{f}_{tx} \quad (4)$$

The angles α and β of the direction vector \mathbf{r} in spherical coordinates (and the value a) can be calculated by solving the equation system (4).

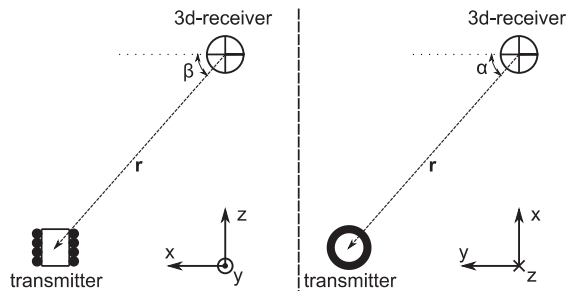


Fig. 1. Alignment of transmitter and receiver

Results

We performed measurements with a 3d-receiver. This receiver consists out of three identical LC-tanks with the coils positioned orthogonally to each other. The measured signals are digitalized using the *National Instruments USB-6366* I/O device. The software *Matlab* is used to control the I/O device and for solving the Eq. (4). The measurements for the angle α were performed with a constant distance of 28 cm between transmitter and receiver; the results are shown in Fig. (2).

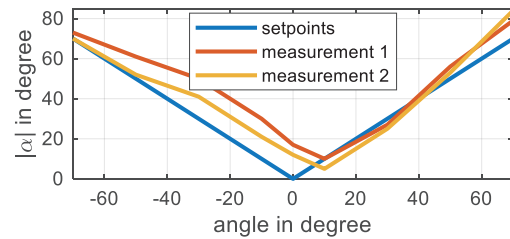


Fig. 2. Setpoints and measured angles for α

Discussion

The feasibility is proofed by the measurements illustrated in Fig. (2), the results on one side of the receiver are more accurate than on the other. This property needs closer investigations. Since we get multiple solutions for the angles α and β by solving the Eq. (4), the next step is to automate the task of finding the correct solution. The exact transmitter position can be found by adding one or more 3d-receivers at different places. This leads to multiple direction vectors from known positions. Finding the point of minimal distance between them should lead us to the exact transmitter position.

References

- [1] M. Heining, A. Sutor, S. Stute, C. Lindenberg and R. Buchholz, „Internal illumination of photobioreactors via wireless light emitters;“ *Journal of Applied Phycology*, vol. 27, pp. 59-66, 2015, doi:10.1007/s10811-014-0290-x.
- [2] A. Sutor, M. Heining und R. Buchholz, „A Class-E Amplifier for a Loosely Coupled Inductive Power,“ *Energies*, Bd. 12, Nr. 6, 2019, doi: 10.3390/en12061165.
- [3] B. O. Burek, A. Sutor, B. W. Bahnemann und J. Z. Bloh, „Completely integrated wirelessly-powered photocatalyst-coated spheres as a novel means to perform heterogeneous photocatalytic reactions,“ *Catal. Sci. Technol.*, Bd. 7, Nr. 21, p. 4977–4983, 2017, doi: 10.1039/c7cy01537b.
- [4] J. Edelmann, R. Stojakovic, C. Bauer und T. Ussmueller, „An Inductive Through-The-Head OOK Communication Platform for Assistive Listening Devices,“ *2018 IEEE Topical Conference on Wireless Sensors and Sensor Networks (WiSNet)*, p. 30–33, 2018, doi: 10.1109/WISNET.2018.8311556.
- [5] T. Lauterbach, F. Lenk, T. Walther, T. Gernandt, R. Moll, F. Seidel, D. Brunner, T. Lücke, C. Hedayat, M. Büker und A. Peters, „Sensospheres - mobile, miniaturisierte sensorplattform für die ortsungebundene prozessmessung in reaktionsgefäßen,“ in *Dresdner Sensor-Symposium 2017*, Hotel Elbflorenz, Dresden, 2017, doi: 10.5162/13dss2017/2.6.
- [6] F. H. Raab, E. B. Blood, T. O. Steiner und H. R. Jones, „Magnetic position and orientation tracking system,“ *IEEE Transactions on Aerospace and Electronic Systems*, p. 709–718, 1979, doi: 10.1109/TAES.1979.308860.

Indirect geometry measurement method for in situ application in laser chemical machining

Merlin Mikulewitsch¹, Dirk Stöbener^{1,2}, Andreas Fischer¹

¹ *University of Bremen, Bremen Institute for Metrology, Automation and Quality Science (BIMAQ), Linzer Str. 13, 28359 Bremen, Germany*

² *University of Bremen, MAPEX Center for Materials and Processes, Germany
m.mikulewitsch@bimaq.de*

Summary:

The optical geometry measurement of submerged micro-surfaces in chaotic fluid environments, e.g. for electric discharge machining (EDM) or laser chemical machining (LCM), is challenging when the specimen feature high aspect ratios and steep surface gradients. To avoid reflection-caused artifacts at steep gradients, fluorescent molecules are added to the fluid, whose fluorescence is detected with a confocal setup. A model-based signal processing enables an indirect measurement in fluid layers > 1 mm and is capable to cope with process-inherent bubbles and surface gradients up to 84°.

Keywords: micro geometry, optical measurement, in situ, fluorescence, signal modeling

Introduction

The laser chemical machining (LCM) process uses an electrolytic fluid and localized heating by a laser to generate a material removal in submerged workpieces. It produces microstructures with high aspect ratios, high surface gradients and small edge radii. In contrast to competing processes such as micro-milling or laser ablation there is no thermal stress induction or tool wear [1]. However, the in situ conditions hinder conventional optical methods of geometry measurement. Interferometric methods such as white light interferometry suffer from measurement deviations caused by thermal gradients and refractive index fluctuations [2]. Confocal microscopy is prone to artifacts caused by the high surface angles and curvatures [3] typically produced with the LCM process. However, an indirect measurement using confocal fluorescence microscopy shows promise for in situ application, since it does not capture the light reflected by the specimen, but the light emitted by a fluorescent liquid covering it. The detected fluorescence signal $S(z)$ can be limited to a small volume around the focal plane of the objective by axial light sectioning produced by confocal microscopy (cf. Fig. 1), where a pinhole, confocal to the objective lens, attenuates light far outside the focal plane. This way, a signal is only detected when the so-called confocal volume intersects the fluorescent fluid. The surface geometry can then be determined by the change of the fluorescence signal produced by pointwise scanning of the confocal

detection volume from fluid surface to specimen surface. The method was successfully used on metallic microspheres with high curvatures by coating their surface with a thin fluorescent film < 100 nm [3]. It was shown that a measurement was possible even at angles > 75° from the surface normal with a lateral resolution comparable to conventional confocal microscopy without generation of artifacts. This paper aims to determine the influence of fluid contaminants (e.g. gas bubbles) and high surface angles on the measurement in thick fluid layers.

Model-based indirect measurement method for thick fluid layers

To determine the specimen surface position z_0 with micrometer precision in the thicker fluid layers > 1 mm present in the LCM process, a model-based evaluation of the fluorescence signal $S(z)$ is necessary [4]. The signal model is based on a simplified confocal volume function in the shape of a 3D-Gaussian function. It represents the spatial distribution of the contributions of all infinitesimal volume elements to the total fluorescence signal. The signal function $S(z)$ at position z is obtained by weighting the confocal volume function with a depth dependent absorption term and integrating it over all spatial dimensions [4]. To cope with small deviations due to inclined surfaces, the model was extended by two additional terms, resulting in

$$S(z) = S_0 e^{\epsilon(z-z_1)} \left[\operatorname{erf}\left(\frac{z-z_0}{2\Xi} + \epsilon\Xi\right) - \operatorname{erf}\left(\frac{z-z_1}{2\Xi} + \epsilon\Xi\right) + K_1 \cdot \left(\operatorname{erf}\left(\frac{z-z_2}{2\xi} + \epsilon\xi\right) - \operatorname{erf}\left(\frac{z-z_1}{2\xi} + \epsilon\xi\right) \right) \right] + K_2 e^{-\frac{(z-z_2)^2}{2\sigma^2}}, \quad (1)$$

with ϵ being the attenuation coefficient, ξ/Ξ confocal volume parameters and S_0 , $K_{1,2}$, σ and z_2 weighting parameters. The desired position z_0 (specimen surface) is obtained by using the model function $S(z)$ for a non-linear least-squares approximation of the measured data.

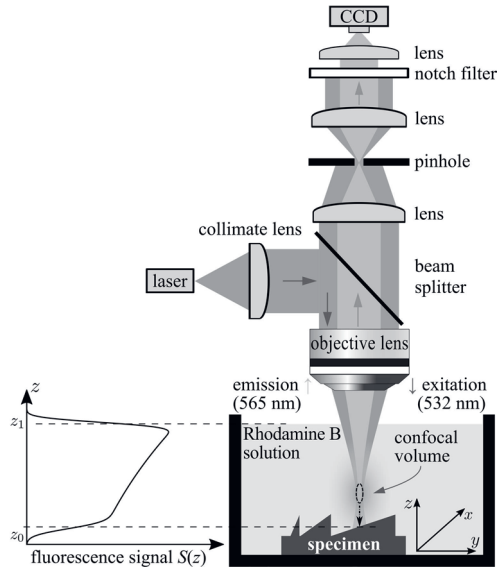


Fig. 1. Principle of confocal microscopy based indirect measurement. The specimen surface position z_0 is obtained from the fluorescence signal $S(z)$.

Results

To determine the influence of the inclination on the indirect measurement, three different inclinations were measured. The fluorescence intensity signals for three points on the 65° inclined surface of the submerged specimen, as well as the model functions approximated with Eq. (1) are shown in Fig. 2a). The resulting surface positions z_0 are marked as black circles. The measurement was performed on three different surface inclinations 35°, 65° and 85°. The surface positions z_0 for one line in y -direction on each surface are shown in Fig. 2b) respectively. The deviations from a linear fit of the measurements were shown to be of equal magnitude as those of the reference measurement with conventional confocal microscopy. In contrast to the reference measurements however, no artifacts were observed with the indirect measurement on the 85° surface. To determine the influence of the LCM process environment on the measurement, bubbles were created by chemical reaction of phosphoric acid and a non-passivating specimen material, see Fig. 2c). The measurements with bubbles in the optical path are shown in Fig. 2d). The fluorescence signal is shown to exhibit increased noise, dependent on bubble density. However, the model-based signal evaluation enables the determination of the surface position z_0 even under the influence of increased signal noise. In conclusion, the indirect geometry measurement

method is suitable for the in situ application in thick and contaminated fluid layers similar to the LCM or EDM process environments and enables measurements even on highly inclined surfaces up to 84.3°.

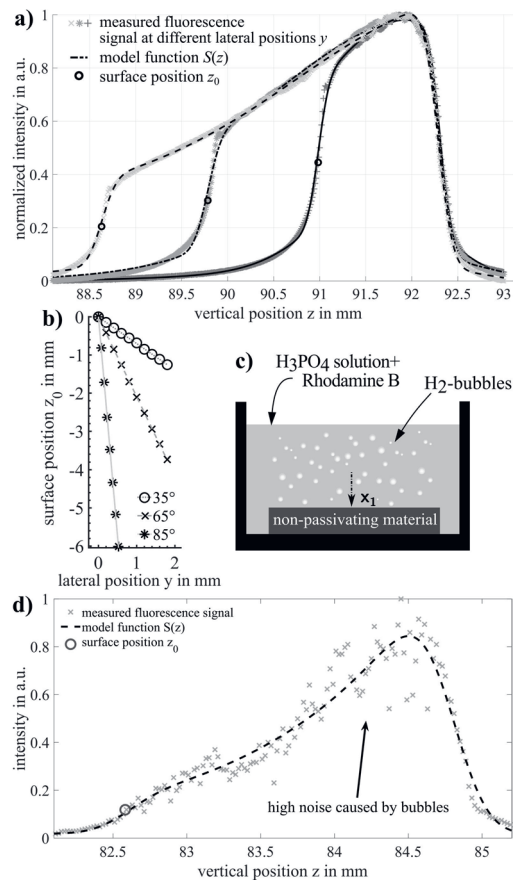


Fig. 2. a) Signal and model fit for three y -positions on a 65° inclined surface. b) Surface position for different inclinations (with linear fit). c) Setup to generate gas bubbles induced by chemical reactions d) Signal at position x_1 with bubbles in optical path.

References

- [1] H. Messaoudi, M. Mikulewitsch, D. Brand, A. von Freyberg, A. Fischer, Removal behavior and output quality for laser chemical machining of tool steels, *Manuf. Rev.* 6, 13 (2019); doi: 10.1051/mfreview/2019015
- [2] C. Gerhard, F. Vollertsen, Limits for interferometric measurements on rough surfaces in streaming inhomogeneous media, *Prod. Eng. Res. Devel.* 4, 141-146 (2010); doi: 10.1007/s11740-010-0224-7
- [3] J. Liu, C. Liu, J. Tan, B. Yang, T. Wilson, Super-aperture metrology: overcoming a fundamental limit in imaging smooth highly curved surfaces, *J. Microsc.* 261, 300-306 (2016); doi: 10.1111/jmi.12334
- [4] M. Mikulewitsch, A. von Freyberg, and A. Fischer, Confocal fluorescence microscopy for geometry parameter measurements of submerged micro-structures. *Opt. Lett.* 44, 1237-1240 (2019); doi: 10.1364/OL.44.001237

Experimental set-up for sensors evaluation in a controlled environment

Alexandre Bescond¹, François Gaie-Levrel¹, Lola Bregonzio-Rozier¹, Tatiana Macé¹

¹ Laboratoire National de Métrologie et des Essais 1 Rue Gaston Boissier, 75724 Paris Cedex 15, FRANCE
alexandre.bescond@lne.fr

Summary:

Sensors appear to be a very promising technology for monitoring air pollution in the world. Main advantages are the improvement of the spatial and temporal resolution. However, accuracy and reliability of these technologies must be assessed. In this work, we will describe an experimental set-up in a controlled environment in terms of temperature and relative humidity. Sensors have been tested with different ranges of aerosol concentrations and their performance has been evaluated.

Keywords: Sensors, environment, monitoring, aerosol, mass concentration, air pollution

Introduction

Regular monitoring of particulate mass concentrations is carried out by regional Air Quality Survey Networks (AQSNs). Many member states rely on instruments having determined their equivalence to the gravimetric reference method (CEN/TS 16450:2013). Filtration-based methods, like oscillating element microbalances (TEOM) and radiometric gauges are commonly used. But many optical instruments can also be implemented such as photometers [1], particle counters [2], [3] and optical spectrometers [4], [5]. The evaluation of mass concentration measurement devices is therefore essential in order to ensure their metrological performance. Concerning sensors, several issues are raised in terms of controlled variability for operating points combining temperature, relative humidity, particle concentration and aerosol chemical composition. In this work, we will present an experimental set-up in a controlled environment dedicated to sensors performance evaluation.

Experimental set-up

Exposure chamber consists of a stainless steel enclosure and is equipped with injection modules for the introduction of aerosols and gases and sampling in order to connect the reference instrumentation. A calibrated thermo-hygrometer is used to measure the temperature and relative humidity in the exposure chamber. (See Fig. 1).

Particle size distribution of the generated aerosols within the exposure chamber was measured using a Scanning Mobility Particles Sizer (SMPS) and an Aerosol Particles Sizer (APS).

The SMPS allows to measure a number size distribution in a range of electric mobility diameters between 10 nm and 1 μm , while APS allows to determine the particle concentration in number as a function of the aerodynamic diameter for a size range from 0.6 to 20 μm .

Particulate mass concentrations are measured using a TEOM 50°C microbalance coupled to a PM₁₀ / PM_{2.5} sampling head with a time resolution of 30s.

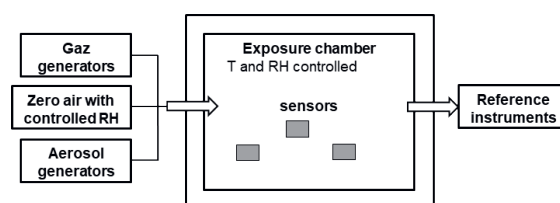


Fig. 1. Schematic diagram of the instrumental set-up for the metrological evaluation of cost sensors performance.

Results

Different types of Arizona dust have been used to achieve target particulate mass concentrations successively generated in the exposure chamber in order to evaluate sensors in PM_{2.5} and PM₁₀ (See Tab. 1). All results presented below have been done at 20°C and 50% RH.

Thus, four reference concentrations were generated for PM_{2.5} and PM₁₀, i.e. $0.9 \pm 2.3 \mu\text{g}/\text{m}^3$; $61.7 \pm 3.8 \mu\text{g}/\text{m}^3$; $116.8 \pm 4.8 \mu\text{g}/\text{m}^3$; $244.3 \pm 4.4 \mu\text{g}/\text{m}^3$ and $0.9 \pm 2.3 \mu\text{g}/\text{m}^3$; $55.1 \pm 3.8 \mu\text{g}/\text{m}^3$; $87.7 \pm 3.5 \mu\text{g}/\text{m}^3$; $217.0 \pm 4.2 \mu\text{g}/\text{m}^3$ respectively.

Tab. 1: PM₁₀ and PM_{2.5} average mass concentrations measured within exposition chamber with reference instrument (TEOM 50°C)

PM _{2.5} (µg/m ³)		PM ₁₀ (µg/m ³)	
Average	Standard Deviation	Average	Standard Deviation
0.9	2.3	0.9	2.3
61.7	3.8	55.1	3.8
116.8	4.8	87.7	3.5
244.3	4.4	217.0	4.2

Determination of accuracy and linearity of three sensors (C1, C2, C3) in PM_{2.5} and PM₁₀, average values and standard deviations of quarter hourly measurements were calculated after stabilization of each mass concentration. Linearity results are shown in Fig. 2 for 3 sensors in comparison with reference method for PM_{2.5}. The tests performed show similar behaviour between the sensors with slopes between 0.172 and 0.194 for PM_{2.5}, and R² regression coefficients between 0.991 and 0.994. For PM₁₀, the slopes obtained are between 0.277 and 0.328 with regression coefficients R² between 0.970 and 0.988.

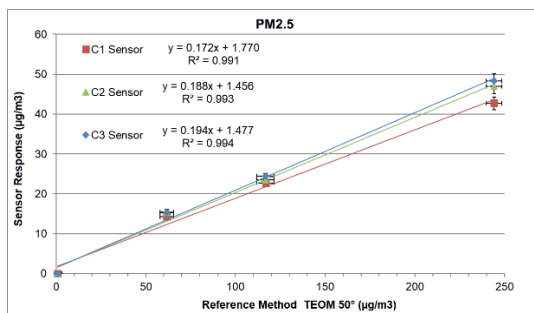


Fig. 2. Graphical representation of the results of the linearity and accuracy tests for PM_{2.5}

Conclusion

This study allowed the development and optimization of sensors evaluation protocol by the implementation of dedicated instrumentation associated with the generation of aerosols and reference measurements around an exposure chamber. The environmental conditions associated with this protocol in terms of temperature and relative humidity were 20.0 °C ± 0.5 °C and 50% ± 2% respectively. In terms of prospects, this evaluation protocol will be optimized by associating controlled temperature and relative humidity conditions in order to test the effect of these parameters on the performance of the sensors.

Bibliography

- [1] J. Gebhart. « Optical direct-reading techniques: light intensity systems ». *Aerosol Measurement: Principles, Techniques, and Applications*. p. 419-454. 2001.

- [2] P. Görner. X. Simon. A. Boivin. et S. Bau. « Sampling efficiency and performance of selected thoracic aerosol samplers ». *Annals of work exposures and health*. vol. 61. n° 7. p. 784-796. 2017.
- [3] J. Binnig. J. Meyer. et G. Kasper. « Calibration of an optical particle counter to provide PM_{2.5} mass for well-defined particle materials ». *Journal of aerosol science*. vol. 38. n° 3. p. 325-332. 2007.
- [4] C. Sioutas. « Evaluation of the measurement performance of the scanning mobility particle sizer and aerodynamic particle sizer ». *Aerosol Science & Technology*. vol. 30. n° 1. p. 84-92. 1999.
- [5] P. P. Hairston. F. D. Dorman. G. J. Sem. et J. K. Agarwal. *Apparatus for measuring particle sizes and velocities*. Google Patents. 1996.
- [6] E. Austin. I. Novosselov. E. Seto. et M. G. Yost. « Laboratory Evaluation of the Shinyei PPD42NS Low-Cost Particulate Matter Sensor ». *PLOS ONE*. vol. 10. n° 9. p. e0137789. sept. 2015.

Form and Mid-Spatial-Frequency Measurement of Unknown Freeform Surfaces

Tobias Binkele¹, David Hilbig¹, Mahmoud Essameldin¹, Thomas Henning¹, Friedrich Fleischmann¹
¹ University of Applied Sciences Bremen, Neustadtswall 30, 28199 Bremen, Germany

Summary:

Components with freeform surface give optical designers more degrees of freedom and can reduce the size and weight of optical systems significantly. However, one cannot manufacture it, if one cannot measure it. Thus, measurement systems have to evolve simultaneously. To meet up with these highly demanded requirements, we have developed a new measurement technique for freeform specular surfaces. This measurement technique is able to detect form and mid-spatial-frequency characteristics for known and even unknown freeform surfaces.

Keywords: metrology, surface characterization, freeform surfaces, experimental ray tracing, specular surfaces

Introduction

With optical components having spherical or aspherical surfaces, designers are limited in the design of optical systems, as occurring aberrations have to be compensated by other optical components. Using components with freeform surfaces can help prevent aberrations to occur or compensate easier. This reduces the number of optical components needed and gives designers the opportunity to create lighter and more compact designs, e.g. folded telescopes with freeform mirrors [1].

However, with the development of a new type of optical components comes the need for measurement systems to verify the manufacturing. This need has not been fulfilled sufficiently yet. We target this need with a measurement technique called Experimental Ray Tracing (ERT) [2]. It has initially been introduced in 1988 and has proven its abilities in several applications like characterization of optical systems and secondary optics for LEDs or refractive index measurement [3-5]. In this paper we present how to use ERT for the reconstruction of known or even unknown freeform surfaces.

Methodology

The original setup has been proposed to measure optical components in transmission. Obviously, this does not work for specular surfaces. Thus, we have altered the setup in a way that an incident ray with the direction \mathbf{i} is pointed onto the surface under test (SUT) under a certain angle. At the point of intersection I with the surface, the ray is reflected into a new direction \mathbf{r} . A schematic sketch of the setup is shown in Fig. 1. This

direction is dependent on the direction of the incident ray and the surface normal \mathbf{g} . By determining the positions C_1 and C_2 of the redirected ray in two parallel planes, the direction

$$\mathbf{r} = C_2 - C_1 \quad (1)$$

of the reflected ray can be detected.

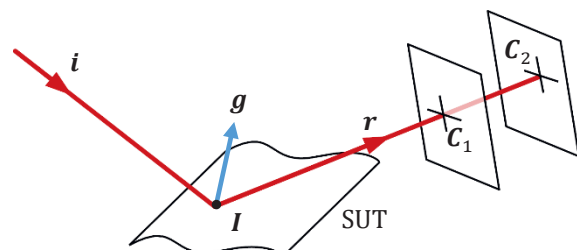


Fig. 1. Schematic sketch of the setup with the incident ray direction \mathbf{i} , the point of reflection I , the normal \mathbf{g} , the reflected ray direction \mathbf{r} and the two detected ray positions C_1 and C_2 .

Having the incident ray direction \mathbf{i} and the reflected ray direction \mathbf{r} and their corresponding unit vectors $\hat{\mathbf{i}}$ and $\hat{\mathbf{r}}$, the unit vector

$$\hat{\mathbf{g}} = \frac{\hat{\mathbf{r}} - \hat{\mathbf{i}}}{\sqrt{2 \cdot (1 - (\hat{\mathbf{i}} \cdot \hat{\mathbf{r}}))}} \quad (2)$$

of the normal can be determined using vector geometry [6]. So far, this shows how one single point is observed. To get information about multiple points on the surface, the SUT is moved in lateral directions. This leads to a field of surface normal vectors. Introducing a coordinate system, the field of normal vectors can be converted into surface slopes. Using appropriate numerical integration methods, the surface can be reconstructed from the slopes [7].

Measurement setup

To perform experiments according to the methodology described above, proper hardware solutions have to be found. The incident ray is represented by a narrow laser beam with a diameter of $100\ \mu\text{m}$. A linear xy -linear table performs the lateral displacement of the SUT. The movement directions of these stages also provide the direction of the coordinate system for the surface reconstruction. The detection of the reflected beams direction is realized by using a camera with a blank chip on a linear stage. Moving the camera realizes the parallel detection planes. Using centroid calculation methods on the detected intensity distribution leads to the beam position. A photo of the setup is shown in Figure 2.

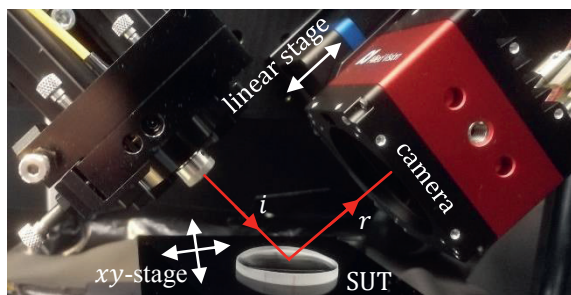


Fig. 2. Photo of the experimental setup with the incident ray direction i , the reflected ray direction r and the hardware components.

As SUT we have chosen a polynomial freeform. The surface follows the function

$$s(x, y) = 3.5 \cdot 10^{-3} \cdot x^2 - 2.5 \cdot 10^{-3} \cdot y^2 - 2.5 \cdot 10^{-5} \cdot x^4 + 3.5 \cdot 10^{-5} \cdot y^4. \quad (3)$$

The surface has a circular clear aperture of $24\ \text{mm}$ within it shows a PV sag of appr. $500\ \mu\text{m}$ and a max. surface angle of appr. 10° . The SUT has been sampled with an even grid with $100\ \mu\text{m}$ sample distance over the clear aperture. This leads to a total number of 45217 sample points. The sample is shown as the SUT in Figure 2.

Results

The results show that the measurement technique was able to reconstruct the surface as one can see regarding the reconstructed surface sag shown in Figure 3. Subtracting the model from the reconstructed surface and subtracting the first 36 Zernike terms from the deviations, one can see the mid-spatial-frequency deviations detected by the measurement. Regarding these mid-spatial-frequency deviations, shown in Figure 4, one can see fabrication marks as well as three fiducials added for better orientation of measurement results.

Conclusion

In this paper, we have proposed a new measurement technique for the measurement of known and unknown freeform surfaces. The results

show that the technique is able to reconstruct the SUT while detecting mid-spatial-frequency deviations simultaneously.

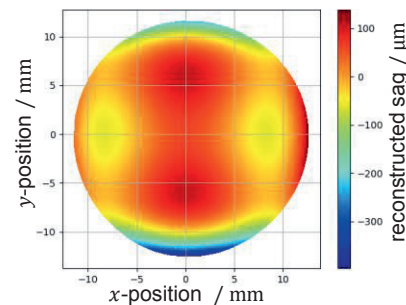


Fig. 3. Diagram of the reconstructed surface.

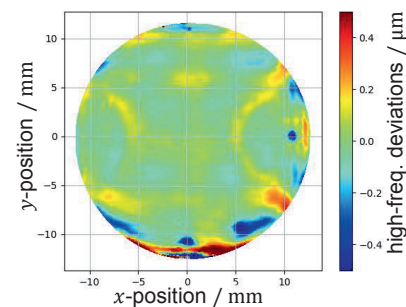


Fig. 4. Diagram of the mid-spatial-frequency deviations of the reconstructed surface from the model.

References

- [1] K. P. Thompson, J. P. Rolland, Freeform Optical Surfaces: A Revolution in Imaging Optical Design, *Optics and Photonics News* 23, 30-35 (2012); doi: 10.1364/OPN.23.6.000030
- [2] G. Häusler, G. Schneider, Testing optics by experimental ray tracing with a lateral effect photodiode, *Applied Optics* 27, 5160-5164 (1988); doi: 10.1364/AO.27.005160
- [3] T. Binkele, D. Hilbig, T. Henning, F. Fleischmann, Determination of the paraxial focal length using Zernike polynomials over different apertures, *SPIE Proceedings Volume* 10110 (2017); doi: 10.1117/12.2251442
- [4] T. Binkele, D. Hilbig, M. Essameldin, T. Henning, F. Fleischmann, Component-Level Test of Complex Beam Shaping Optics for Quasi-point Sources, *Frontiers in Optics + Laser Science* (2019); doi: 10.1364/FIO.2019.JW3A.1
- [5] T. Binkele, R. Dylla-Spears, M. A. Johnson, D. Hilbig, M. Essameldin, T. Henning, F. Fleischmann, Characterization of gradient index optical components using experimental ray tracing, *SPIE Proceedings Volume* 10925 (2019); doi: 10.1117/12.2511072
- [6] A. Mikš, P. Novák, Determination of unit normal vectors of aspherical surfaces given unit directional vectors of incoming and outgoing rays: comment, *JOSA A* 29, 1356-1357 (2012); doi: 10.1364/JOSAA.29.001356
- [7] W. H. Southwell, Wave-front estimation from wave-front slope measurements, *JOSA* 70, 998-1006 (1980); doi: 10.1364/JOSA.70.000

FEM Model of a Tactile Sensor Based on Inductance Measurements and Magnetosensitive Elastomer

Simon Gast¹, Klaus Zimmermann¹

¹ Technische Universität Ilmenau, Technical Mechanics Group Max-Planck-Ring 12
98693 Ilmenau Germany,
simon.gast@tu-ilmenau.de

Summary:

This paper presents a concept of a tactile sensor based on multiple planar coils with overlapping regions and a magnetosensitive elastomer layer. The sensor setup is simplified to a two-dimensional problem. Experimental investigations are compared with an electro-mechanical model. This model is able to simulate inductance changes of less than 0.1% caused by a deformation. The trend of the modeled curves fits the experimental data in a way to draw conclusions about the range and dependency of the inductance change on the depth of indentation.

Keywords: magnetosensitive elastomer, adaptivity, tactile sensor, FEM simulation, electromechanics

Introduction

Magnetosensitive elastomer (MSE) consists of an elastomer matrix with embedded magnetic particles. Several technical applications have been proposed that utilize MSE as a transducer for sensor applications or as actively controlled soft element. Kawasetsu et al. proposed a tactile sensor based on MSE and planar coils and investigated their size dependency [1, 2]. In this paper, a tactile sensor concept based on an electromechanical model is presented. This concept uses the MSE as a tunable compliance and multiple planar coils for sensing its deformation. The behavior of multiple overlapping coils is rather complex to analyze and simulate. Hence, this first approach is limited to model a single coil and the magnetic interaction with a deformed MSE layer. All simulations are based on two-dimensional finite element method (FEM).

Sensor Concept

The setup of the sensor concept is shown in Fig. 1. It consists of multiple layers incorporating an MSE. The base plate is constructed by a circuit board holding multiple planar coils with overlapping regions. Sequenced inductance measurements of these coils provide data on a deformation of the MSE caused by an indenter. Each measurement is done by driving the coil as part of an oscillating circuit at its resonance frequency. Due to the high frequency and low amplitude of this oscillation, the alternating magnetic field can be superposed with an additional external quasi-static magnetic field. This field is used to control the compliance of the

MSE. The effect of the sensor is based on measuring inductance changes of less than 0.1%. Therefore, the simulations need to be accurate enough to reproduce these small changes.

Theory of Operation

An indentation results in an inductance change depending on three variables. The first two are the planar coordinates of the deformation relative to the center of the coil (x - and y -position). The third variable h is given by the indentation depth. At least three inductances have to be measured for every indentation, in order to obtain those variables.

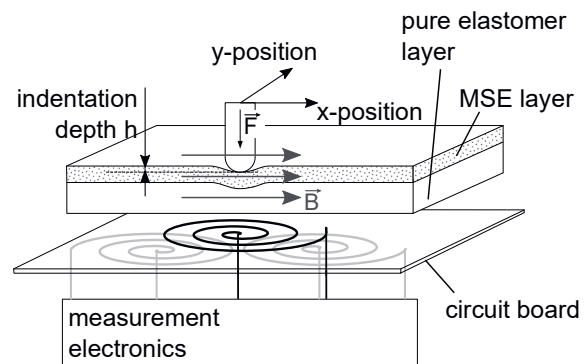


Fig. 1. Concept of the tactile sensor.

Experiments

The measurement electronics consist of three modules: an "Inductance-to-Digital" converter driving the coil as part of an oscillating circuit at its resonance frequency, an analog multiplexer and a microcontroller used for sequencing all coils. In order to compare the experimental

results to the simulations, the setup shown in Fig. 1 is simplified using only one hexagonal planar coil with a two layer winding. The experiment is performed by a linear shifted indentation of constant depth h along the small semi-axis of the coil.

Electromechanical FEM Model

The simulations are done with ANSYS Workbench 19.1. The model is built by two not coupled modules. Firstly, a two-dimensional static mechanical FEM component models the deformation of the cross-section. Secondly, a two-dimensional magnetostatic Maxwell component models the inductance of the cross-section of a single coil. The indentation depth h and the x -position of the experiment define the dimensions of the plane of both models. The indenter is modeled as a rigid body and the two elastomer layers as incompressible linear elastic material. The simulated deformed contour is post-processed with MATLAB R2018b and transferred to the Maxwell 2D simulation. The purpose of this step is to obtain the contour by calculating the displacement for every node of the mesh. Furthermore, the inductance is found by a Maxwell 2D Simulation including the imported area of the deformed MSE layer. The FEM Maxwell model is parametric for the x -position of the deformation and the depth of indentation h . Every cross-section of the coil winding is considered to be extended along a straight infinite line. The parameters for the simulation are listed in Tab. 1.

Tab. 1: Parameters of the simulation

parameter	value
relative magnetic permeability of the MSE	2.7
Poisson's ratio of the elastomer	0.4999
coil turns per layer	40
coil diameter	26.2 mm
MSE thickness	2 mm
pure elastomer thickness	6 mm

Results

In Fig. 2, the experimental results are compared to the simulations. The area of the coil with sufficient sensor signal is present around the peak at the center. Regarding the qualitative trend, both curves are similar. Furthermore, the simulated curves picture the increasing signal with increasing indentation depth occurring also in the experiment. The error for a central deformation ranges between 5.6% and 102.7%.

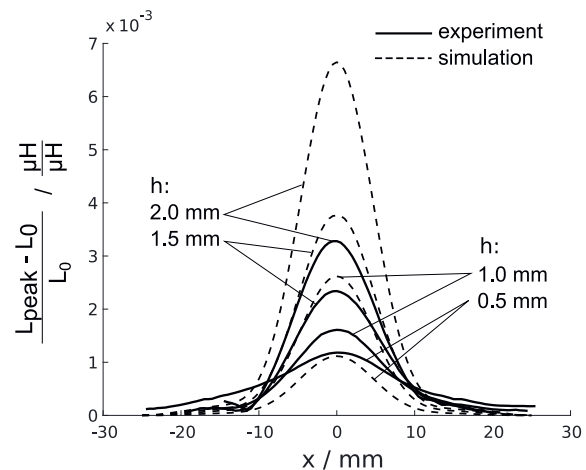


Fig. 2. Simulation and experimental results for a shifted indentation of alternating depth h .

Discussion and Conclusion

The proposed concept is based on the spatial distribution of the magnetic field of a single planar coil. Hence, the setup requires only a small number of parts and is cost-efficient to manufacture. Firstly, the model proves to be capable of reproducing inductance changes of less than 0.1%. Additionally, the magnitude and the qualitative trend of the simulated inductance change correspond to the experiment. This can be used to estimate the width of the area with sufficient sensor signal. Further investigations will focus on error reduction. The deviation of the model is assumed to be caused by simplifications regarding the size of the coil in the third dimension. In a next step the FEM model will be extended by considering dielectric properties of the material influencing the parasitic capacity of the planar coil. Additionally, the geometry of the model will be improved to include the shape and symmetry of the real planar coil.

References

- [1] T. Kawasetsu, T. Horii, H. Ishihara and M. Asada, Flexible Tri-Axis Tactile Sensor Using Spiral Inductor and Magnetorheological Elastomer, in *IEEE Sensors Journal* 18, no. 14, 5834-5841 (2018); doi: 10.1109/JSEN.2018.2844194
- [2] T. Kawasetsu, T. Horii, H. Ishihara and M. Asada, Size dependency in sensor response of a flexible tactile sensor based on inductance measurement, *IEEE Sensors Journal* 2017, 1-3 (2017); doi: 10.1109/ICSENS.2017.8233908

Acknowledgements

This work was supported by the Deutsche Forschungsgemeinschaft (DFG) within the SPP 1681 research program under the projects ZI 540/17-3 and PAK 907.

Photonic Measurement System for Load Detection in a Neuro Interventional Training Model

S. Shojaei Khaotuni¹, L. Rennpferdt¹, H. K. Trieu¹

¹Institute of Microsystems Technology, Hamburg University of Technology, Hamburg, Germany.
Sohrab.shojaei@tuhh.de

Summary:

A measuring system based on flexible silicone waveguides is presented in this work. A proof of principle of the bending-loss sensing unit was performed in a previous work [3]. The subject of this paper is to report different sensor designs, fabrication, as well as the linear response of the sensing unit in a predetermined force range. The linear behavior was achieved by a multimode waveguide design and the associated fabrication method for the waveguides of the sensor unit.

Keywords: PDMS waveguide, flexible pressure sensor, photonic pressure sensor, multimode photonics

Introduction

A common medical practice for the treatment of intracranial aneurysms is coiling [1]. In the procedure, several coils are inserted into the aneurysm in order to fill the void and hence stop blood flow. It is crucial to control the forces coils exert on the walls of the aneurysm. A neuro interventional training model (NTM) with 3D printed phantom aneurysm has been developed in order to eliminate the need of animal testing for the practice of the interventionalists performing the procedure described [2]. This work presents a measuring system that can be integrated into the phantom aneurysm of the NTM to detect and measure exerted loads during the training, making this key performance indicator available to the practitioners.

Description of the System

The pressure sensing system consists of an electronic and a photonic unit. The electronic unit acquires and processes the sensor data while providing an adjustable light source for the exchangeable photonic sensor unit. Detected loads were displayed in real-time. The sensing unit is made out of a flexible multimode waveguide array. In order to maximize the covered sensing area straight, curved, and split waveguide designs are investigated. The interface to the electronic unit is designed as a plug, assuring easy exchangeability and thus adaptability to different settings.

Fabrication of the PDMS waveguide

The sensing unit is a flexible fiber-optic system made of a Polydimethylsiloxane (PDMS) based waveguide array. The waveguide cladding and carrier, made out of silicone from Dow Corning (SYLGARD 184), were manufactured using nanoimprint lithography (NIL) as described in [3]. The cores of the waveguides were filled with a different PDMS (LS-6257 - NuSil) which has a slightly higher refractive index than the surrounding cladding. Comparing to [3] a new method based on an approach shown by Missine et al. [4] is developed with enhanced repro-

ducibility of the cores. The waveguide carrier is cut in a way, that core trenches are opened on the two ends, generating an inlet and outlet for the core material to be filled into the trenches. The sensor carrier is then placed on a coated wafer with the core trenches being on the bottom side. This is done in a Cleanroom, to assure a dust particle free on surfaces. Even small particles would lead to enclosed air bubbles between the wafer and the carrier material, having a negative impact on light transmission in the waveguide subsequently. Next, core material is applied on the inlet side of the trenches to be soaked in due to capillary action forces. To ensure continuous supply of core material, a reservoir is necessary. It takes around 20 to 40 minutes for the trenches to be completely filled, dependent upon trench size. Lastly, the setup is baked to cure the core material and bond it to the cladding.



Fig. 1. Flexible PDMS mat with integrated curved waveguides (→).

Sensor units fabricated this way were then glued on a 3D printed support structure (Norland Optical Adhesive 68). To establish a link between the waveguide array and the light source and detector, glass fibers were used, which were aligned using a 3D printed v-groove adapter. After proper alignment, fibers were butt-coupled to the waveguide array. To ensure easy and fast replacement of the sensor unit, LED as light source and photodiode as detector were connected to the electronic unit by removable wire connectors. Figure (1) shows a flexible sensing unit glued to the support structure.

Experimental Setup

The system evaluation was performed using two different sensor designs. The first sensor includes an

array of four straight waveguides with a fixed core height of $230\mu\text{m}$ and a variable core width ($100\mu\text{m}$, $200\mu\text{m}$, $300\mu\text{m}$, $400\mu\text{m}$). This sensor was used to evaluate the effect of core width on the sensitivity and sensing range. The second sensor was designed with a single waveguide (width: $600\mu\text{m}$, height: $230\mu\text{m}$) splitting into two diverging waveguides (width: $600\mu\text{m}$, height: $230\mu\text{m}$) and being recombined at the end. The impact of splitting and uniting waveguides was investigated with this sensor. Measurements were performed placing the sensor unit including the support structure on a precision scale. Loads were exerted perpendicularly on the sensor surface using a metal rod with a spherical tip.

Results

To investigate the tunability of the system three measurements were performed with the source LED being at high, medium, and low intensity. Thus, the photodetector was fully saturated, just in saturation, and unsaturated. Figure (2) shows a shift of the measurement range to higher loads with increasing source intensity. Same is true for the linear range, shifting from 0 – 5 grams for low source intensity to higher values for high source intensity.

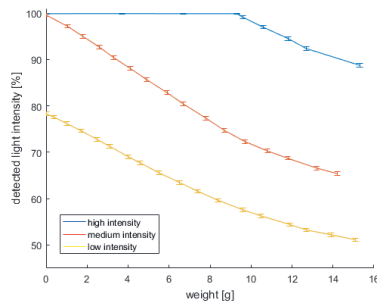


Fig. 2. Output light intensity as function of force exertion. Force is exerted three times at the same position but with different input intensities.

The impact of the channel width on the sensitivity and linear range was investigated using the first sensor. The light source of each channel was tuned to give all channels a matching starting value for the detected intensity at zero load. In Figure (3) the wider waveguides with $300\mu\text{m}$ and $400\mu\text{m}$ width responded linearly from the beginning while the waveguide with $200\mu\text{m}$ just behaved linearly after approximately 2 grams.

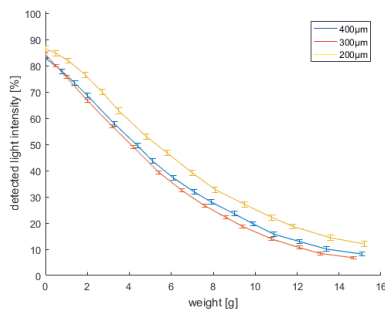


Fig. 3. Light intensity during force exertion. Force is exerted to straight waveguides with different width ($200\mu\text{m}$, $300\mu\text{m}$, $400\mu\text{m}$).

Figure (4) shows the impact of the Y-splitter and the curved waveguide geometry on the sensitivity and overall performance of the sensing unit. The load was applied at three sensor surface positions as indicated, with the light signal being transmitted from top to bottom. Position 1 and 2 showed slightly different sensitivity with loads > 5 grams, indicating that the source light was not split uniformly into the two channels by the Y-splitter. Also, the bending of the core seems to have a significant light loss as the curve for position 3 is shifted towards lower forces.

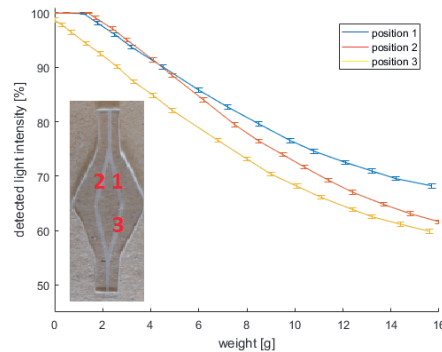


Fig. 4. Output light intensity as function of force exertion. Force is exerted at three different positions.

Conclusion

In this work we demonstrated a sensor system with a linear measurement range that is tunable within the limits of the detection range. Straight waveguides turned out to be the best waveguide design for this application since Y-splitters and curved waveguide geometries lead to falsified measuring results depending on the position of the load exertion. Furthermore, the whole measurement system is robust, transportable, flexible, and straightforward to produce, making the system simple to integrate in different settings.

References

- [1] Debus, E. S., and Gross-Fengels, W. (eds.): Operative und interventionelle Gefäßmedizin. Springer-Verlag, 2012.
- [2] Frölich, A. M. J. et al.: 3D Printing of Intracranial Aneurysms Using Fused Deposition Modeling Offers Highly Accurate Replications. *American journal of neuroradiology*, vol. 37 (1), 120–124, 2016.
- [3] Shojaei Khatouni, S. et al.: Faseroptisches Sensorarray aus PDMS zur Ermittlung lokaler Druckbelastung beim Coiling intrakranieller Aneurysmen. *Proceedings Mikrosystemtechnik Kongress 2017*. 2017.
- [4] Missinne, J. et al.: Stretchable optical waveguides. *Optics Express* 22 (4), 4168–4179, 2014.

Plastic Material Classification using Neural Network based Audio Signal Analysis

Sascha Grollmisch^{1,2}, David Johnson¹, Tobias Krüger¹, Judith Liebetrau¹

¹ Fraunhofer IDMT, Ilmenau, Germany

² TU Ilmenau, Ilmenau, Germany

jsn@idmt.fraunhofer.de

Summary:

Analyzing the acoustic response of products being struck is a potential method to detect material deviations or faults for automated quality control. To evaluate this, we implement a material detection system by equipping an air hockey table with two microphones and plastic pucks 3D printed using different materials. Using this setup, a dataset of the acoustic response of impacts on plastic materials was developed and published. A convolutional neural network trained on this data, achieved high classification accuracy even under noisy conditions demonstrating the potential of this approach.

Keywords: acoustic quality control, industrial sound analysis, neural network, material classification

Background, Motivation and Objective

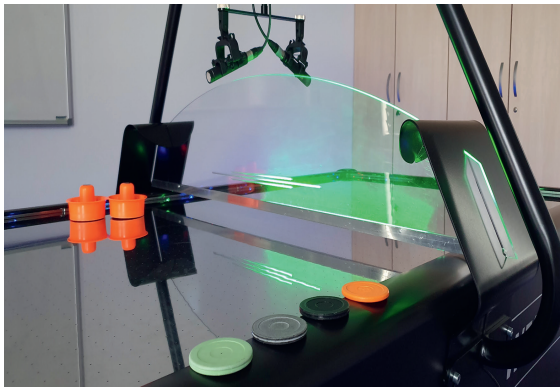


Fig. 1. Air hockey table with two microphones and pucks composed of different materials.

Analyzing acoustic signals in the human hearing range is often problematic due to the complex noise scenarios in factories. Industrial Sound Analysis (ISA) using low-cost microphones and neural networks was shown to be a potential solution for use-cases such as classifying metal surfaces or the operational state of electric engines [1]. Similarly, faults inside metal or plastic materials may only be identified through acoustic analysis because the faults are often not visible. Furthermore, applying structure-borne sensors to each product is often too costly. Analyzing the acoustic response of products such as metal screws was demonstrated to be a feasible solution for acoustic quality control [2]. Products are hit in a non-destructive way with the acoustic response being recorded. The recordings are then classified correctly under the noisy conditions of real-world production lines.

In this work, we evaluate if different plastic materials are distinguishable under noisy conditions by analyzing the acoustic response of the material on impact. Our proposed baseline system combines audio signal processing with a convolutional neural network (CNN) classifier. Additionally, we publish a novel dataset, *IDMT-ISA-PUCKS* (IIPD), alongside this paper for reproducibility and fostering further research [3].

Dataset

An air hockey table was used as a demonstration system for the simulation of difficult acoustic analysis conditions consistent with industrial manufacturing settings. Data collection was performed by equipping the air hockey table with two sE8 microphones, each recording one side of the table, as seen in Fig. 1, while a game is played. In addition to the standard pucks, several new pucks were 3D printed using one of three different materials. For each of the four materials, five three minute games were played, each with a different puck of the specific material. Further, each game was played with different sets of players. To mimic a real industrial setting, this scheme was repeated twice with industrial sounds at different loudness levels played in the background leading to a total dataset duration of 225 minutes.

Applied method

To detect the puck material during a game of air hockey, we propose a Convolutional Neural Network (CNN) classifier with five classes; four classes for each type of puck material and one class for the case when there is no puck in play.

We propose using a CNN over a fully connected neural network [1], because multiple hit events can occur in one analysis window. Since the CNN is invariant to time positions by applying pooling operations, generalization should improve. The proposed architecture should perform in near real-time and be robust to a variety of background noise.

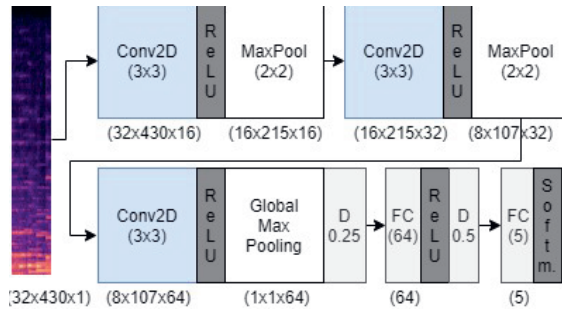


Fig. 2. CNN architecture with 3 convolutional layers, rectified linear unit (ReLU) activation, Dropout (D), a fully connected (FC) layer, and a final softmax classification layer.

To use a CNN with audio data, we prepare the data using the short-time Fourier transform (STFT) to generate a spectrogram as input to the classifier. For near real-time detection, we choose the maximum delay to be five seconds. Therefore, the analysis window is set to ten seconds with 50% overlap. For each ten second window, the raw data is downsampled to 22050 Hz and the STFT is applied with a window size of 512 samples and no overlap. We convert the spectrogram to mel-scale by applying a 32 band mel-scaled filter. This results in a 430 frame spectrogram with 32 frequency bins per ten second patch as input for the CNN. Additionally, per-channel energy normalization (PCEN) is applied to suppress background noise [5]. The CNN architecture, which was empirically designed, is shown in Fig. 2. Each CNN was trained for 1500 epochs using the Adam optimizer [5] with a learning rate of 0.001 and batch size of 256.

Experiments and Results

To validate the proposed method, we perform experiments evaluating puck material detection under different noise conditions. First, the model is trained using only recordings without background noise (nl1). This evaluates the general ability of the model to distinguish between materials. Additionally, to evaluate the robustness of the proposed method in real-world industrial scenarios with unknown background noises, the previously trained model is tested on recordings overlaid with background sounds at two different amplitudes (nl2 and nl3).

The results, evaluated using 5-fold cross validation, presented in Tab.1, show that materials are distinguishable with high accuracy

when there is no background noise (nl1). Adding background sounds decreases the performance to 89%. However, when PCEN is employed the accuracy only drops to 95% in the worst case, showing the potential of this preprocessing method to reduce unwanted signal components. The PCEN parameters have been kept to default, but for future work their optimization might improve the results. Using majority voting of the predictions over a time window of one minute (instead of ten seconds) improves the accuracy to 99.7%, even with the highest background noise level. A possible reason for the performance gap on short windows is a lack of hit events in some of the 10-second time frames. This could be avoided with systems where the product is directly hit and analyzed, eliminating frames with no events.

Tab. 1: Results showing accuracy for different noise levels (nl) with and without PCEN.

	nl1	nl2	nl3	nl3 1min
w/o PCEN	99.5	90.0	89.0	91.5
PCEN	96.1	96.6	94.9	99.7

Conclusion

A dataset and classification system were created to detect the material of plastic pucks. By applying preprocessing with PCEN high accuracies can be achieved, confirming our hypothesis that plastic materials can be distinguished by their acoustic response under noisy conditions. However, material type may have a bigger influence on sound than small faults inside the products. To test the capabilities of our proposed method, faults could be printed inside pucks or other products for future research aimed at improving automated quality control systems.

References

- [1] S. Grollmisch, et al., Sounding Industry: Challenges and Datasets for Industrial Sound Analysis, *EUSIPCO* (2019), A Coruna, Spain
- [2] J. Liebetrau, et al., Luftschallbasierte Rissdetektion von Metallteilen, *DAGA* (2018), Munich, Germany
- [3] IDMT-ISA-PUCKS dataset, Website: <https://www.idmt.fraunhofer.de/datasets>
- [4] Y. Wang, et al., Trainable frontend for robust and far-field keyword spotting, *ICASSP* (2017), New Orleans, USA
- [5] D. P. Kingma, et al.: A Method for Stochastic Optimization, *ICLR* (2015), San Diego, USA

This work has been partially supported by the German Research Foundation (BR 1333/20-1, CA 2096/1-1).

Measurement Uncertainty Assessment for Virtual Assembly

Manuel Kaufmann^{1}, Ira Effenberger¹, Marco Huber^{1,2}*

¹ Fraunhofer Institute for Manufacturing Engineering and Automation IPA,
Nobelstr. 12, 70569 Stuttgart, Germany

² Institute of Industrial Manufacturing and Management IFF, University of Stuttgart,
Nobelstr. 12, 70569 Stuttgart

*E-Mail: manuel.kaufmann@ipa.fraunhofer.de

Summary:

In dimensional metrology, a datum system is used for defining a coordinate system to enable the evaluation of geometrical tolerances of workpieces. With regard to function-oriented tolerancing representing the workpiece's function optimally, the physical workpiece contact has to be recreated by the datum system. Therefore, a new registration approach is used, where contact points of the acquired measurement point clouds determine the datums. In this paper, the propagation of the measurement uncertainty of contact points towards the registration result is discussed, having an impact on derived measurands.

Keywords: Virtual Assembly, Datum Definition, Geometrical Tolerancing, Dimensional Measurement, Uncertainty Assessment

Trends in Production and Metrology

Higher product requirements and smaller tolerances trigger an increasing attention on the geometrical assurance in manufacturing processes. A paradigm shift in the ISO system for Geometrical Product Specifications (ISO GPS) is the introduction of the Skin Model Shapes (SMS), where the part geometry is described by a holistic, discrete surface representation. By applying SMS, mainly the description of form tolerances could be improved. While deviations of size and location have decreased ten times every 50 years, form deviations remain at nearly constant level, and thus become an increasingly relevant field of research. Optical metrology systems and Computed Tomography (CT) enable the generation of SMS by capturing large measurement point sets (point clouds) in short acquisition time [1, 3].

Current method of datum definition

The main purpose of a datum system is to define a common coordinate system for measured point clouds of one or more workpieces. Tolerance zones are aligned according to the datum system, thus the derived tolerance value is sensitive to the datum system definition. The recent method for datum system definition is described in ISO 5459:2011 [2]. Here, the datum system is defined by approximated regular geometries like tangential planes (see Figure 1). However, it is disadvantageous that local form deviations are not considered, since approximated geometrical elements with ideal forms are employed [2, 3].

Method of Virtual Assembly

By the novel method of Virtual Assembly (VA), the holistic surface information is used for the datum definition. As shown in Figure 1 (right), surface 2 is aligned relatively to surface 1 by the minimization of their distances, avoiding a surface intersection. The registration of the datum is mathematically stated as an optimization problem [4].

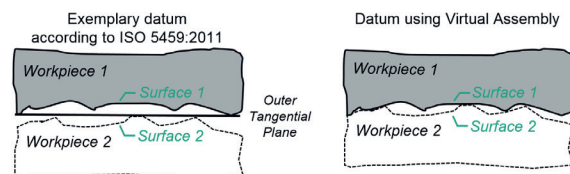


Fig. 1. Exemplary datum systems based on current ISO definition (left) and according to VA approach (right)

The signed Euclidean distance $d_{s,n}$ of N corresponding pairs of points $p_{1,n}$ and $p_{2,n}$, $n = 1 \dots N$, from point set P_1 of surface 1 and point set P_2 of surface 2 is used to compute the objective function (1).

$$f(T_x, T_y, T_z, \phi, \theta, \psi) = \sum_{n=1}^N d_{s,n}^2 = \min! \quad (1)$$

Here, the optimization variables T_x , T_y and T_z determine the translation and ϕ , θ , ψ are the Euler angles of the rigid transformation of P_2 to P_1 . The avoidance of surface intersection can be either formulated as a constraint, allowing $d_{s,n} \geq 0$ only, or by introducing a penalty term as summand to f in order to penalize intersection.

Concept for Uncertainty Assessment

A complete measurement result includes the associated measurement uncertainty. For the VA approach, the uncertainties of individual contact points of the acquired surfaces have a strong impact on the datum system. Hence, derived extrinsic measurands such as sizes or position tolerances are influenced by the uncertainty of the contact points. In this paper, the uncertainty is experimentally determined by *Type A* evaluation according to the *Guide to the Expression of Uncertainty (GUM)* [5]. The uncertainties $u_{q,n}$ considering the n -th point $p_{q,n,m}$ of a surface q and of repetition $m \in [1; M]$ are estimated according to (2) with $\bar{p}_{q,n}$ as mean value of M repetitions of $p_{q,n}$. In context of the VA approach, always two surfaces are registered, so that $q \in [1; 2] \mid q \in \mathbb{N}$.

$$u_{q,n} = \sqrt{\frac{1}{M-1} \sum_{m=1}^M (p_{q,n,m} - \bar{p}_{q,n})^2} \quad (2)$$

The general measurement model is described by q input estimates x_q and measurand $y = f(x_q)$ as output. Thus, the uncertainty of the measurand contains contributors of q input sizes [5]. Here, the uncertainty u_1 of surface 1 and the composed uncertainty $u_{2,c}$ of surface 2 are considered in the combined standard uncertainty u_c (3) of the measurement procedure [6]. Because the transformation uncertainty u_T propagates to uncertainty u_2 of the point cloud to register, the composed uncertainty $u_{2,c}$ (4) is considered. The uncertainty $u_{2,c}$ depends on the contact points determined by VA with their particular u_T and the uncertainty of the contact points in u_2 , so that all points in the point set are affected by these uncertainties. In (3), $\partial f / \partial x_q$ is the q -th sensitivity coefficient, equal to 1 here for all q , stated in [6].

$$u_c(y) = \sqrt{\left(\frac{\partial f}{\partial x_1}\right)^2 \cdot u_1^2 + \left(\frac{\partial f}{\partial x_{2,c}}\right)^2 \cdot u_{2,c}^2} \quad (3)$$

$$u_{2,c} = f(u_2, u_T) = f(u_2, u_x, u_y, u_z, u_\phi, u_\theta, u_\psi) \quad (4)$$

If the uncertainty $u_c(y)$ is computed considering more than one pair of points $\{p_{1,n}; p_{2,n}\}$, the propagated uncertainties have to be merged in a certain distribution model, e.g. the Fisher-Bingham-Kent distribution (FBK) in [7]. FBK describes the distribution on a sphere. Assuming an isotropic uncertainty $u_{q,n}$ here, meaning that $u_{q,n}$ is independent of the probing direction, the uncertainty representation in 3D is a sphere. According to [5, 6], the expanded uncertainty U is stated as $U = k \cdot u_c(y)$, with $k = 2$ as coverage factor.

Nonlinear uncertainty propagation

The uncertainty assigned to a point in 3D space can be described by the 3x3 covariance matrix. Due to orientation uncertainties u_ϕ, u_θ and u_ψ ,

the uncertainty propagation from the original to the transformed point cloud is nonlinear. Position uncertainties u_x, u_y and u_z propagate linearly. The propagation of orientation uncertainty considering the FBK distribution is described in [7].

Case Study

The uncertainty propagation of a linear guide including rail and slider is evaluated as shown in Figure 2. The measurement uncertainties are acquired by 20 repeated CT scans, the transformation uncertainties by 20 repeated VA registrations, where the initial point cloud position is varied by random numbers from a normal distribution with $\sigma_T = 0.05$ mm and the orientation is varied about $\sigma_R = 0.002^\circ$. Furtheron, the uncertainty U can be validated against the uncertainty acquired by repeated VAs. By doing so, the model for VA can be compared to the current ISO 5459 datum definition, allowing comparing uncertainty levels of both approaches quantitatively.

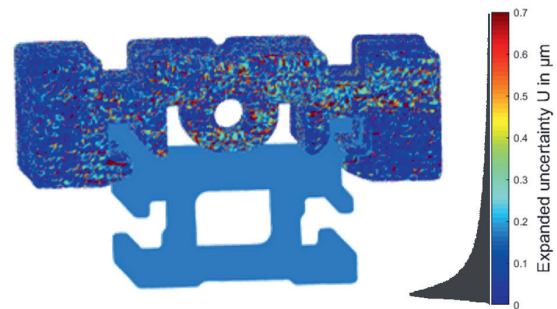


Fig. 2. Exemplarily propagated uncertainty U of the slider with respect to the rail including histogram of U

References

- [1] Nielsen, H.S., Recent developments in ISO GPS standards and strategic plans for future work. *J. Eng. Manuf.* 227 (5), 643–649 (2013); doi: 10.1177/0954405412466986
- [2] ISO 5459:2011, GPS – Datums and datum systems, Beuth, Berlin (2011)
- [3] Weißgerber, M. et al., Requirements for Datum Systems in Computer Aided Tolerancing and the Verification Process, *Procedia CIRP* 43, 238–243 (2016); doi: 10.1016/j.procir.2016.02.096
- [4] Keller, F.; Weißgerber, M., Datum Systems in Coordinate Measuring Technique. *XIth International Scientific Conf. on Coordinate Measuring Technique*, 77-81 (2014); ISBN 978-83-63713-88-1
- [5] ISO/IEC Guide 98-3:2008, Uncertainty of measurement – Part 3: Guide to the expression of uncertainty in measurement, Beuth, Berlin (2010)
- [6] ISO 15530-3:2011, GPS – Use of calibrated workpieces or measurement standards, Beuth, Berlin (2011)
- [7] Franaszek, M. et al., The axes of random infinitesimal rotations and the propagation of orientation uncertainty. *Measurement* 72, 68-76 (2015); doi: 10.1016/j.measurement.2015.04.020

Signal-to-Noise-Ratio Optimized Design of Rotating-Coil Magnetometers

Piotr Rogacki^{1,2}, Lucio Fiscarelli¹, Stephan Russenschuck¹, Kay Hameyer²

¹ CERN, Switzerland

² Institute of Electrical Machines (IEM), RWTH Aachen University, Aachen, Germany
ptrogacki@gmail.com

Summary:

The electronic acquisition chain of a rotating-coil magnetometer is analyzed to identify electromagnetic noise sources and the effective noise floor of the acquisition. This allows to optimize the system, and the layout and the support of the induction coils for the intended application. The influence of a built-in motor drive unit on the results is studied, in order to establish the minimum distance between the motor and the induction coils to avoid detrimental effects on the measurement accuracy. Two electronically commutated (EC) motors of different power ratings are studied.

Keywords: magnetometers, electromagnetic signal to noise ratio, electric motors

Introduction

Accelerator projects necessitate development of new measurement systems to keep up with the increasing accuracy and functional requirements on their accelerator magnets. An example of this is the Large Hadron Collider High Luminosity project (HL-LHC). The new magnets to be produced and installed in the framework of this project must be measured at ambient temperature with an accuracy that not only challenges the rotating-coil transducers, but approaches the limits of the acquisition electronics, such as the purpose-built digital integrator [1]. This is due to the low excitation-current levels that result in generated signals of tens of millivolts.

Moreover, the functionality of the magnetic measurement systems can be enhanced by adding a built-in motor unit that allows a longitudinal scan along the magnets. In this case it is important to ensure the absence of distortions in the magnetic measurements.

The test setup

The system used for the tests is the rotating-coil scanner [2] currently being developed for the HL-LHC magnets, together with its electronics rack. The main system components under study are integrators, induction coils, a patch panel, cables, slip rings and an encoder. In order to estimate the contribution of each system component to the overall noise of the acquisition chain, we characterized the background noise of various system configurations – starting with an integrator connected directly to an impedance equivalent

to a coil, through a bare coil, to the fully assembled system. The signals were acquired using the integrator at a sampling frequency of 2048 Hz. The integrator outputs the voltage integrated between two triggers, which is a measure for the flux linkage through the surface traced during this time interval, expressed in Vs.

The tests of the motor influence were conducted in an aperture of a powered magnet. Two motors were positioned at varying distances in front of the probe along its longitudinal axis, to test for the presence of distortions in the results of an ongoing magnetic field measurement. The first motor has an inner-rotor construction with a power rating of 80 W. Its dimensions are 32 mm in diameter and 130 mm length. The other, smaller motor has an outer-rotor construction, with 15 W power rating. It is 60 mm long with the same diameter of 32 mm. Both are equipped with a planetary gearbox.

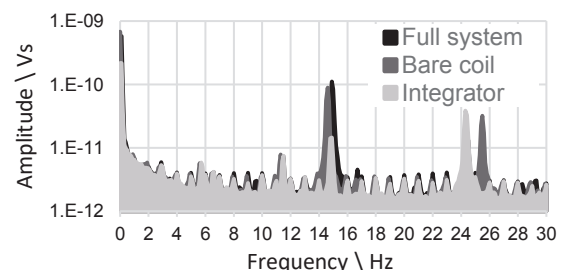


Fig. 1. Comparison of the spectra between a fully assembled system (non-rotating) and a bare coil with the integrator as a reference. The spectra were calculated from signals of 20480 samples and averaged over 50 acquisitions.

Noise evaluation results

The plot in Fig. 1 shows the noise spectra of three configurations. The cables, patch panel and slip rings add only minimal noise to the signal, which is obvious from comparing the coil connected directly to the integrator (bare coil) with the coil mounted in the transducer assembly. The bare coil is sensitive to the ambient electromagnetic interference, which represents the effective noise floor of the transducer itself. The system noise is at approximately 10 nVs RMS (root mean square) amplitude, where the integrator noise is at 1 nVs RMS amplitude.

Application example

This result can be used to design a cost-efficient transducer that provides the required signal-to-noise-ratio. The strength of the signal directly depends on the spanned surface of the coil. In a limited space, such as the bore of an accelerator magnet, the spanned surface can be enlarged only by increasing the number of coil turns, which results in additional (costly) layers when the coil is made in printed-circuit technology.

The test system has been designed for flux-density distributions with a peak of 4 mT. The precision requirements demand a SNR of at least 80 dB relative to the expected main signal. The surface necessary to generate a sufficient signal is approximately 2 m². With a safety margin, the coils were designed for 2.34 m².

The measurements with the test system indicate that the final precision is still limited by mechanical imperfections and vibrations. However, for the extracted field multipole coefficients [3], the system's precision approaches the precision of the integrator, thanks to the compensation (bucking) of the main component. This implies that for measurements that are less dependent on mechanical stability, such as fluxmeters, the acquisition electronics and signal transmission may become a limiting factor.

Influence of the motor drive

The long motor was first positioned 693 mm from the coil edge and moved by steps of 50 mm to a minimum of 93 mm, limited by the assembly. The measurements were taken in a 4.5 mT field. The only measured quantities that are noticeably affected by the motor are the multipole coefficients that are sensitive to 1 ppm levels. The effect of the motor on the measurement results is shown in Fig. 2. The distance at which first distortions above 1 ppm appear is approximately 300 mm.

The smaller motor was displaced in a similar range and in this case, the effects of the motor are only slightly discernible in the closest position, at 87 mm away from the coil edge. This means that a small motor can be placed as close

as 100 mm from an induction coil, without disturbing the measurement results. There was no significant difference in results between non-rotating and rotating motors.

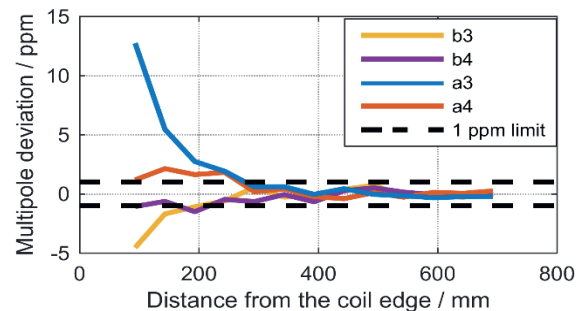


Fig. 2. Deviation of the multipoles measured in the presence of the motor from the reference measurement (without a motor). Only the affected multipoles are plotted.

Conclusions

A characterization of the noise in a rotating-coil acquisition system has been performed in order to establish the acquisition noise floor. It has been demonstrated that properly connected, screened and twisted signal cables do not add any significant noise to the acquisition chain. The limit that cannot be easily overcome is given by the background electromagnetic fields picked up by the coil. In any case, the known noise floor can be used to design a system to provide a required signal-to-noise-ratio in expected measurement conditions. It can also be used as a benchmark to evaluate the correctness of the system's assembly.

The study of the influence of the motor on the measurement results provided an estimation of a safe distance for using onboard motor units in precise rotating-coil magnetometers. The results show that it is possible to use EC motors for rotating-coil measurements inside low magnetic fields (<50 mT), if a minimal distance (depending on the motor size and power rating) is kept between the motor and the induction coil.

References

- [1] P. Arpaia, L. Bottura, L. Walckiers, and L. Fiscarelli, Performance of a Fast Digital Integrator in on-field Magnetic Measurements for Particle Accelerators, *Rev. Sci. Instrum.*, vol. 83, 2012, doi: 10.1063/1.3673000.
- [2] P. Rogacki, L. Fiscarelli, S. Russenschuck, and K. Hameyer, Development of a rotating-coil scanner for superconducting accelerator magnets in *Sensoren und Messsysteme 2019*, Nürnberg, Germany, doi: 10.5162/SEN-SOREN2019/3.4.3.
- [3] W. G. Davies, The theory of the measurement of magnetic multipole fields with rotating coil magnetometers, *Nucl. Instrum. Methods Phys. Res., Sect. A*, vol. 311, no. 3, pp. 399–436, 1992, doi: 10.1016/0168-9002(92)90637-J.

6 DoF Pose Estimation with $\mu\text{m}/\mu\text{rad}$ Accuracy Based on Laser Multilateration

Jan Nitsche¹, Matthias Franke¹, Nils Haverkamp², Daniel Heißelmann¹

¹ Physikalisch-Technische Bundesanstalt, Bundesallee 100, Braunschweig, Germany,

² Carl Zeiss Industrielle Messtechnik, Carl-Zeiss-Str. 22, Oberkochen, Germany

Jan.nitsche@ptb.de

Summary:

Laser multilateration is a well-established technology for 3D coordinate measurements. An extended multilateration setup using seven tracking laser interferometers and a triple-retroreflector target is described, which allows for the estimation of a full six degree of freedom pose of the observed target. In an experimental setup with four degrees of freedom, the concept was proved and shows promising results in comparison with a precision coordinate measuring machine.

Keywords: multilateration, six degrees of freedom, self-calibration, pose estimation

Introduction

The precise estimation of a six degree of freedom (6 DoF) pose (position plus orientation) of a given object in space plays an important role in robotics, automation and autonomous navigation. The pose of the end effector of industrial robots for example is essential for the precision of automated assembly processes. Different solutions for this problem are proposed, based on indoor gps systems [1], laser tracker measurements [2] or camera based sensors [3] and reach accuracies below 1 mm / 1 mrad.

Multilateration is a well-established technology to identify 3D coordinates of points in space [4,5]. Using laser interferometers for the distance measurement, accuracies of a few micrometers can be reached, depending on the size of the working space. By extending the multilateration principle from identifying 3D points to 6 DoF pose, higher precision of the pose estimation is expected.

6 DoF Multilateration

3D laser multilateration uses distances measured between three or more interferometric base stations and one retroreflector target to identify the 3D position of that target [5]. Results are achieved by minimizing the sum of squared residuals w_{ij} :

$$w_{ij} = \sqrt{(\Delta x_{ij})^2 + (\Delta y_{ij})^2 + (\Delta z_{ij})^2} - l_{ij} - l_{0j} \quad (1)$$

with $i = 1, \dots, n$ as the number of target positions $j = 1, \dots, m$ as the number of base stations, $\Delta x_{ij}, \Delta y_{ij}, \Delta z_{ij}$ representing the coordinate differences between target position i and base station

j . l_{ij} is the measured length change between target position i and base station j and l_{0j} is the dead path of each laser interferometer.

To extend the laser multilateration principle to identify a 6 DoF pose, an observed target requires three or more retroreflectors in a non-coplanar arrangement. The target is observed by at least 6 tracking laser interferometers in a non-coplanar setup. If the coordinates and dead paths of the interferometers need to be identified in a self-calibration process, at least seven interferometers are needed. Each retroreflector is observed by at least one interferometer. In addition to the residual functions (1), boundary conditions of the observed target are required:

$$w_{ik} = \sqrt{(\Delta x_{ik})^2 + (\Delta y_{ik})^2 + (\Delta z_{ik})^2} - l_k \quad (2)$$

with $k = 1, \dots, p$ as any set of two retroreflectors, $\Delta x_{ik}, \Delta y_{ik}, \Delta z_{ik}$ the coordinate differences between the two retroreflectors k and l_k the distance between the two retroreflectors. The resulting set of equations (1) and (2) contains $n \cdot (m + p)$ equations, $4 \cdot m$ unknowns for the interferometers, $3 \cdot n \cdot p$ unknowns for the retroreflector coordinates and p unknowns for the retroreflector distances. For a minimum required setup of seven interferometers and three retroreflectors, this results in $31 + 9 \cdot n$ unknowns and $10 \cdot n$ equations. Using a dataset of at least 32 measurement points results in an overdetermined equation system which can be used for self-calibration of the unknown system parameters. It is important however that the dataset contains target positions with different orientations.

Experimental Setup

An experimental setup was installed using a precision coordinate measuring machine (CMM) with additional rotational axis in the probing head. Three cat's eye retroreflectors are mounted to the probing head in a right-angled triangle with legs of 140 mm and 150 mm length. This setup provides a 4 DoF target. Seven tracking laser interferometers are installed along the short sides of the CMM working space in different z positions. For simultaneous data acquisition, six interferometers are triggered externally by one master interferometer. Reference positions of the CMM are acquired after a standstill period of 1 second. A grid of $3 \times 3 \times 3$ target positions is recorded in a measurement volume of 820 mm x 550 mm x 80 mm. Each position is measured two times in three target orientations of 0° , 120° and 240° respectively.

Data processing is performed in python. The overdetermined equation systems are solved using the Levenberg-Marquardt algorithm implemented in `scipy.optimize` package.

The limitation of the mover to 4 DoF requires a different approach for self-calibration as described in the previous section. In a first step, all seven interferometers are logged on to one retroreflector resulting in a classical 3D multilateration setup. This setup is used to calibrate the coordinates of the interferometers. In a second step the interferometers are split up to observe all three retroreflectors. In this step, dead paths of the interferometers and distances between the retroreflectors are calibrated.

First Results

The previously described setup was used to calibrate the multilateration system. Due to the delicate surfaces of the retroreflectors it was not possible to calibrate the position of the retroreflectors in relation to the CMM coordinate system. The residuals of the optimized equation system however are below $0.15 \mu\text{m}$.

For further evaluation of the multilateration setup, seven additional target positions in one orientation along a straight line through the measurement volume were evaluated. For this evaluation, the difference between the spatial distance resulting from the CMM readings and the multilateration system is calculated. The maximum deviation between the two independent systems over a measurement length of 460 mm is below $0.5 \mu\text{m}$.

The equation system used for optimization is based on cartesian coordinates for each retroreflector. From the given distances between the retroreflectors and the coordinate deviations, angular deviations of the pose estimation can be calculated. In the given setup of a shorter leg of 140 mm and coordinate deviations of $0.5 \mu\text{m}$ for each retroreflector, an angular deviation of $7.1 \mu\text{rad}$ is expected.

Conclusion

A multilateration setup for 6 DoF pose estimation using interferometric length measurement was developed and installed. In a reduced experimental setup with a 4 DoF positioning system, the setup could be implemented and calibrated. A first comparison to a precision CMM shows deviations of $0.5 \mu\text{m}$ for a measurement length of 460 mm.

As a next step, full 6 DoF pose estimation using an appropriate positioning system will be analyzed. Further evaluation of the measurement results by comparison measurements and a measurement uncertainty evaluation will be performed.

- [1] L. Stadelmann, T. Sandy, A. Thoma, J. Buchli, End-Effector Pose Correction for Versatile Large-Scale Multi-Robotic Systems, *IEEE Robotics and Automation Letters* 4(2), 546-553 (2019); DOI: 10.1109/LRA.2019.2891499
- [2] J. Yang, D. Wang, B. Fan, D. Dong, W. Zhou, Online absolute pose compensation and steering control of industrial robot based on six degrees of freedom laser measurement, *Optical Engineering* 56(3), 034111 (2017); DOI: 10.1117/1.OE.56.3.034111
- [3] P. Li, A. Ghasemi, W. Xie, W. Tian, Visual Closed-Loop Dynamic Model Identification of Parallel Robots Based on Optical CMM Sensor, *Electronics* 8(8), 836 (2019); DOI: 10.3390/electronics8080836.
- [4] T. Takatsuji, M. Goto, T. Kurosawa, Y. Tanimura, Y. Koseki, The first measurement of a three-dimensional coordinate by use of a laser tracking interferometer system based on trilateration, *Measurement Science and Technology* 9(1), 38-41 (1998); DOI: 10.1088/0957-0233/9/1/006.
- [5] K. Wendt, M. Franke, F. Härtig, Measuring large 3D structures using four portable tracking laser interferometers, *Measurement* 45(10), 2339-2345 (2012); DOI: 10.1016/j.measurement.2011.09.020.

Estimate the error of Offset Issue and Amplitude Mismatch of Atan2 Function

Jie Zhou¹, Markus Dietrich¹, Paul Walden¹, Johannes Kolb², Martin Doppelbauer³

¹ Schaeffler Automotive Buehl GmbH & Co. KG, Buehl, Germany

² Schaeffler Technologies AG & Co. KG – SHARE at KIT, Karlsruhe, Germany

³ Karlsruhe Institute of Technology, Karlsruhe, Germany
jie.zhou@schaeffler.com

Summary:

Atan2 function is widely used in most angular sensor nowadays. In order to increase the sensor accuracy, system errors must be compensated before the atan2 calculation. The offset issue and amplitude mismatch are two of the most significant system errors. Until today, different approximation methods are being used to estimate the maximum effects of them. However, these methods are not fully satisfying, especially in terms of high offset issue or angular mismatch, as mentioned. In this paper, a new method with Lissajous-figure is introduced to calculate this impact of those errors analytically and to provide an accurate solution, which can compensate the errors completely.

Keywords: angular sensor, atan2 function, offset issue, amplitude mismatch, Lissajous-figure

Introduction

Rotary position sensors such as resolvers and magnetic sensors are widely used for rotary positioning applications. The most popular method to calculate the angular position is using the atan2 function. In order to improve the sensor accuracy, systematic errors such as offset issue and amplitude mismatch should be compensated. The conventional solutions for them are given in [1]. However, they are not accurate because of the following two facts: a) imperfect sampling (e.g. noise, quantization); b) in some cases corrections are permitted only after atan2 calculation. Furthermore, a more accurate solution for the remaining error is required for sensor designing. Therefore, different methods have been studied: approximation methods for offset issue are introduced in [2] [3] [4] [5] [6]; approximation methods for amplitude mismatch in one-dimensional problem are explained in [5] [6] [7] [8]; a solution for the two-dimensional problem was given in [9]. Those methods base on approximation, so that, they are not accurate enough for precise applications. This paper presents solutions without approximation. Therefore, offset issue and amplitude mismatch can be compensated totally.

Estimate the Impact of Offset Issue

The effect of offset issue can be described using a Lissajous figure (see Fig.1). The circle with solid line represents the Lissajous figure of the ideal sinus and cosine signal, while the

circle with dashed line is regarded as the Lissajous figure for signals with offset issues.

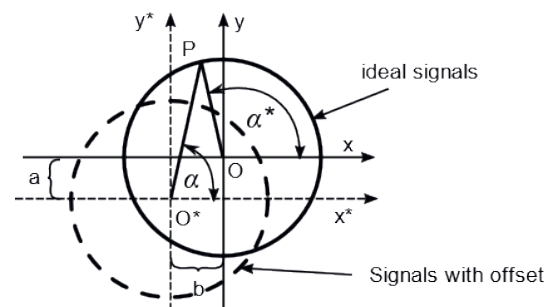


Fig. 1: Lissajous-figure with and without offset issue.

Moreover, the distance a and b represent the offset of sine and cosine signal. Furthermore, the angle α^* is equal to the target angle, while the angle α is known as the measured angle. In order to build the relationship between the angles α and α^* , both Lissajous-figures should be rotated around their own origins until the axis x and x^* are overlapped (see fig. 2a). The rotated angle can be proven as:

$$\varphi^* = \arctan\left(\frac{a}{b}\right) \quad (1)$$

As both of the x axes overlap, the angle error ε is then the difference between α and angle α^* :

$$\varepsilon = \alpha^* - \alpha \quad (2)$$

Furthermore, the angle ε can be calculated with the help of an auxiliary line OH, which is perpendicular to line PO^* (see fig 2b) and get:

$$\tan(\varepsilon) = \frac{OO^* \cdot \sin(\alpha)}{PO^* - OO^* \cdot \cos(\alpha)} \quad (3)$$

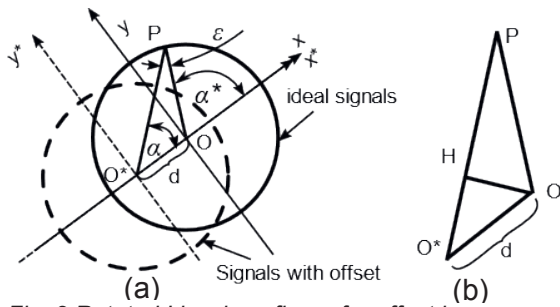


Fig. 2 Rotated Lissajous-figure for offset issue

The both Lissajous-figure must be standardized before the further mathematical deduction. Therefore, the radius O^*P is equal to 1, so that the eq. (3) can be simplified as eq. (4), with d being defined as eq. (5).

$$\tan(\varepsilon) = \frac{d \cdot \sin(\alpha)}{1 - d \cdot \cos(\alpha)} \quad (4)$$

$$d = \sqrt{a^2 + b^2} \quad (5)$$

Consequently, the maximum error can be calculated with the help of the eq. (6),

$$\frac{d\varepsilon}{d\alpha} = 0 \quad (6)$$

and get the eq. (7). That means also, if the error reaches its maximum, the edge OP should be perpendicular to OO^* .

$$\varepsilon_{max} = \arcsin(d) \quad (7)$$

Estimate the Impact of Amplitude Mismatch

The amplitude mismatch can also be illustrated with the Lissajous-figure (see fig. 3a). The Lissajous figure of a system with amplitude mismatch acts as an ellipse instead of a circle (see fig. 3a dashed line).

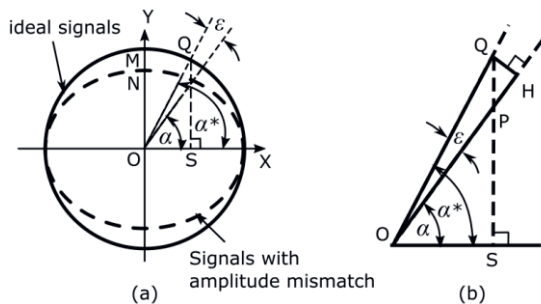


Fig. 3. Lissajous-figure for amplitude mismatch

The amplitude mismatch is formulated as:

$$\gamma = \frac{MO}{NO} \quad (8)$$

The angle α shows the measured angle, while α^* corresponds to the angle in an ideal system without amplitude mismatch. Moreover, the angle ε means the deviation between the measured angle and ideal angle. In addition an auxiliary line QH is required, which is perpendicular to OH (see fig. 3b). Observably, the triangle ΔQHP and the triangle ΔOSP are similar. Angle α can be measured and OQ represents the radius with value 1 (after standardization). Furthermore, the quotient of QP and QS is equal to the amplitude mismatch:

$$\frac{QP}{QS} = \gamma \quad (9)$$

Therefore, the edges of triangle OH and QH can be determined with eq. (10) and eq. (11):

$$Oh = Ph + OP = \frac{\sin^2(\alpha) + \gamma \cdot \cos^2(\alpha)}{\gamma} \cdot OP \quad (10)$$

$$Qh = \frac{1-\gamma}{\gamma} \cdot \sin(\alpha) \cdot \cos(\alpha) \cdot OP \quad (11)$$

Consequently, the angle error ε is defined as:

$$\tan(\varepsilon) = \frac{(1-\gamma) \cdot \sin(2\alpha)}{1 + \gamma + (\gamma-1) \cdot \cos(2\alpha)} \quad (12)$$

The maximum angle error at position α can be calculated as the first derivation. After a simplification the maximum angle is defined as:

$$\varepsilon_{max} = \arcsin \frac{\gamma-1}{\gamma+1} = \arcsin(\kappa) \quad (13)$$

Furthermore, that κ means the angle between the eigenvectors of the systems with/without amplitude mismatch (see fig. 4).

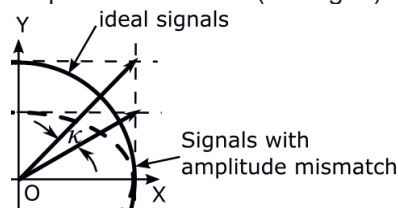


Fig. 4 correlation angle κ

Conclusion

To increase the sensor accuracy mathematical deduction was used. So that the impact of the offset issue and amplitude mismatch can be estimated. The eq. (7) and (13) can be used to estimate the maximum error of the offset issue and amplitude mismatch respectively. With the eq. (4), the offset issue can be compensated completely for each position α . Similarly, the amplitude mismatch can be corrected with the eq. (12) completely.

- [1] J.R.R. Mayer, High-resolution of rotary encoder analog quadrature signals 43, (1994)
- [2] D.C. Hanselman, Resolver signal requirements for high accuracy resolver-to-digital conversion
- [3] D.C. Hanselman, Techniques for improving resolver-to-digital conversion accuracy, (1991)
- [4] M. Blagojevic, M. Markovic, R. S. Popvic, Testing the Homogeneity of Magnets for Rotary Position Sensors, (2014)
- [5] J. Lara, J. Xu, A. Chandra, A Novel Algorithm Based on Polynomial Approximations for an Efficient Error Compensation of Magnetic Analog Encoders in PMSMs for EVs, (2016)
- [6] P.M. Drljaca, C. Schott; R. S. Popovic, Nonlinear effects in magnetic angular position sensor with integrated flux concentrator, (2002)
- [7] Q. Lin, Z. Zhou, Error Analysis and Compensation of the Orthogonal Magnetic Encoder, (2011)
- [8] R. Raja, T. Sebastian, M. Wang, A. Gebregergis; Effect of position sensor error on the performance of permanent magnet machine drives, (2013)
- [9] M. Demierre, Improvements of CMOS Hall microsystems and application for absolute angular position measurements, (2006)

Linear Regression Method for Measuring Characteristics of the ADC on Harmonic Test Signals

Sergey V. Sherstobitov¹, Maria V. Karpova¹

¹ *All-Russian Scientific Research Institute of Physicotechnical and Radio Engineering Measurements (VNIIFTRI), Mendeleevo, Moscow region, Russia, 141570
s_sherstobitov@rambler.ru; Lab-610@vniiftri.ru*

Summary:

Discusses the possibility of application linear regression methods and Josephson voltage standard for measurement characteristic harmonic signals or systems based on DAC/ADC in order to improve the accuracy of determination such parameters as amplitudes and phases of the fundamental tone and harmonics, effective number of bits, signal-to-noise ratio, harmonic distortion, and others.

Keywords: ADC, DAC, Josephson voltage standard, linear regression method, harmonic test signal.

Introduction

DAC ADCs are the main element of many measuring systems. The accuracy of the conversion and the accuracy of the measurements depend on their characteristics. In many methods, to determine the characteristics of the ADC, input voltage signals of a constant or step type are used. However, often such signals are not included in the class of ADC working signals, for example, due to the presence of an input filter that cuts off the DC component of the signal. Most ADCs work with harmonic sinusoidal signals of alternating voltage, in which the useful information is in the values of amplitudes, phases of fundamental tone and harmonic components. Until now, THRU RMS thermoelectric converters have been used at the top level of AC voltage metrology, but their use is limited by sinusoidal signals with low harmonic components. In the case of analog instruments, filters are used to measure signal harmonics contents. In the case of digital processing, FFT, DFT algorithms are often used, which have their own limitations on application and limit the measurement error. The construction of reference generators of test signals and the development of techniques for determining the characteristics of the ADC is an urgent task.

Description of the Method

Great metrology success was due to progress in the creation of AC voltage standards based on the Josephson effect [1, 2]. At the output of such a device, it is possible to obtain both a DC voltage output signal with an exact value and

almost zero non-linearity, and AC waveform signals with an exact value of the RMS value of a sinusoidal signal or an exact value of harmonic components. The value of the error in determining the characteristics of meters or ADCs depends on the applied algorithms for processing digital signal realizations. Authors developed algorithms for determining the characteristics of harmonic signals and the characteristics of the DAC/ADCs using the regression analysis method. Software was developed to generate digital implementations of test signals and to determine the characteristics of AC voltage signals or ADC. The process of obtaining the values of the ADC characteristics can be implemented in the following sequence: 1. Submission to the ADC input of an exemplary analog test signal included in the class of permissible signals with specified parameter values. 2. Recording a sequence of digital readings obtained in real-time operating mode in a digital storage device. 3. Recovery of signal parameter values by compute of the recorded sequence using software. 4. Comparison of the obtained parameter values with the given ones and calculation of the values of the ADC characteristics as signal conversion errors. The software consists of two blocks - a computer Generator of digital signals and a processing unit for digital implementations. The Generator creates sequences of digital samples of model implementations for digital-to-analog converters on Josephson binary array, and for other types of DACs. It is also used to generate digital test signals when characterizing signal processing software. The samples of the generated signal

consist of the values of the samples of the fundamental tone of the signal, the values of the samples of the harmonic components of the signal with frequencies that are multiples of the frequency of the fundamental tone, samples of additive white noise and the DC offset of the signal. For processing digital implementations, regression analysis method is used. The internal scale parameter of the implementation is the number of samples per period of the fundamental tone. With its known value, the task of reconstructing the parameters of a sinusoidal signal is formulated as a linear regression by the principle of least squares in the class of sums of trigonometric functions. Then, the algorithm calculates the amplitudes and phases of the fundamental tone and harmonics, the coefficient of nonlinear distortion, the effective number of bits of the ADC, the signal-to-noise ratio etc. The study of software characteristics was carried out by their direct determination by model implementations of signals with known values of the specified parameters. To obtain the uncertainty errors in determining the frequency and amplitude parameters, a statistical modeling process was used, consisting of cycles of modeling and processing realizations, statistical processing.

Results

The results obtained are presented below in the form of graphs.

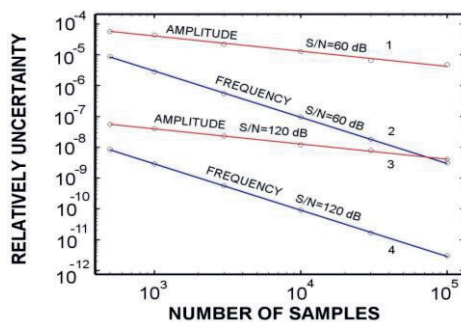


Fig. 1. The dependence of the relative errors in determining the frequency and amplitude on the length of the processed implementation N . Lines 1 and 2 are obtained with a signal-to-noise ratio of 60 dB; lines 3 and 4 at 120 dB.

Modeling and processing were carried out taking into account five harmonics with a harmonic coefficient equal to 0.01%. The noise model is normal white noise. The number of simulation-processing cycles (the number of sample parameter values for statistics) was 500 – 1000. The study of the graphs shows that the error in the amplitude of the fundamental tone is inversely proportional to the signal-to-noise ratio and the number of counts in the signal implementation. Implementation of the signal sam-

ples was loaded into the binary Josephson voltage converter.

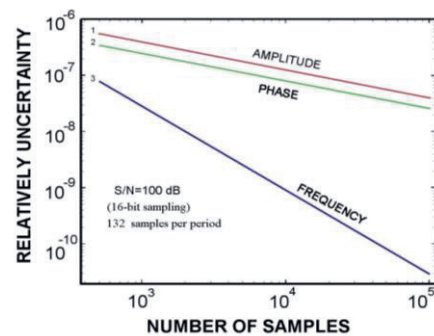


Fig. 2. A graph of the relative errors in determining the frequency, amplitude, and phase versus the implementation length for signal-to-noise ratios of 100 dB (16-bit sampling). Numbers of samples per period was 132.

The output signal from the Josephson setup was fed to 24-bit ADC. Signals with a number of samples from 30 to 4000 for the period of the fundamental tone of the generated signal were used. In the case of measuring purely sinusoidal signals, the minimum achieved error level of the amplitude or RMS value of the AC voltage was about 3.5 – 100 ppm.

Conclusion

The results of statistical modeling using this algorithm showed possible accuracy characteristics for measuring the parameters of the amplitude, phase, frequency of the fundamental tone of the signal and harmonics, which depend on the signal-to-noise ratio and the length of the processed implementation. The errors of the method when processing real signals will depend on the accuracy of the DAC/ADCs used, the accuracy and stability of the signal frequency and sampling frequency. Measurements with a Josephson setup, good results were obtained that were not achievable for other processing methods, such as FFT, DFT. The authors use these algorithms in the development of methods and instruments for measuring the characteristics of the ADCs and the characteristics of the Josephson setup to obtain uncertainty of amplitudes 1 ppm and less.

References

- [1] Hamilton C. A., Burroughs C. J., Kautz R. L., Josephson D/A converter with fundamental accuracy, *IEEE Trans. Instrum. Meas.* 1995, vol. 44, no. 2, p. 223–225; doi: 10.1109/19.377816
- [2] M. Sira, O. Kieler, R. Behr, A Novel Method for Calibration of ADC Using JAWS, *EEE Trans. Instrum. Meas.* 2019, vol. 68, no. 6, p. 2091–2099; doi:10.1109/TIM.2018.2888918

Mathematical Measures for Calibration and Evaluation of Gas Sensor Data

Rolf Seifert¹, Hubert Keller²

¹ *HybridSensorNet, Kaiserstraße 12, 76131 Karlsruhe, Germany*

² *Karlsruhe Institute of Technology, Hermann-von-Helmholtz-Platz 1, 76344 Eggenstein-Leopoldshafen, Germany
Corresponding rolf.seifert@partner.kit.edu*

Summary:

Economic online and in-situ field analyses wait for reliable and economic analytical solutions by sensor systems. This paper presents various innovative mathematical procedures to analyze data from gas sensor systems and gas sensor nets: ProSens - an efficient mathematical procedure for calibration and evaluation of tin oxide gas sensor data, SimSens – a Mathematical Procedure for Simultaneous Analysis of Gases and ProCal - a program for batch-wise calibration of multi gas sensors .

Keywords: Thermo cyclic operation, calibration and evaluation procedure, simultaneous evaluation, batch wise calibration, mathematical procedure

Introduction

There is a growing need of economic online and in-situ field analysis applications like online monitoring of volatile components in chemical and biochemical processes, quality monitoring in food processing, discriminated monitoring of toxic gas leakages, etc. In the last application, it is often necessary to find and locate the source of the leakage. In this context, isothermally operated metal oxide gas sensors (MOGs) with tin oxide as base material are manifold introduced due to their high sensitivity, long-term stability and low price. Their sensitivity to specific gas components, however, cannot be cultivated with high discrimination to others. Therefore, other approaches are necessary like a multi gas sensor array of MOGs [1][2] or thermo-cyclic operation of the MOG. With special chosen additives, the sensor can be adapted according to the gas composition to be measured.

For evaluation of the sensor data, powerful mathematical evaluation procedures for substance identification and concentration determination even in the case of variable environmental conditions like varying humidity are necessary. The calibration of sensor elements is very time consuming and expensive. Even sensor elements which are fabricated batch-wise have to be individually calibrated for good analysis performance. Therefore, economic mathematical calibration procedures are useful to reduce the costs and the scope of calibration measurements. Last not least to locate the source of

a leakage also mathematical procedures are needed.

At the Karlsruhe Institute of Technology (KIT) mathematical procedures are developed to meet the above mentioned requirements: ProSens – a mathematical procedure for calibration and evaluation, SimSens – a Mathematical Procedure for Simultaneous Analysis of Gases and ProCal – a mathematical procedure for batch-wise calibration of sensor elements. After some remarks to thermo-cyclic operation of the MOG these procedures will be briefly described in this paper and their performance will be demonstrated in applications with real data.

Thermo-Cyclic Operation

Thermo-cyclic operation means that the working temperature of the sensor element is periodically increased and decreased over the time in a triangular shape. Simultaneous sampling of the conductance values over the time leads to so-called Conductance over Time Profiles (CTP) [3][4][5]. These profiles give a fingerprint of the surface processes with the gas and represent the gas mixture under consideration.

Figure 1 shows the CTPs of some gases at a certain concentration level. It can be clearly seen that the shapes of the various gases are quite different and can be therefore used for substance identification using innovative calibration and evaluation procedures.

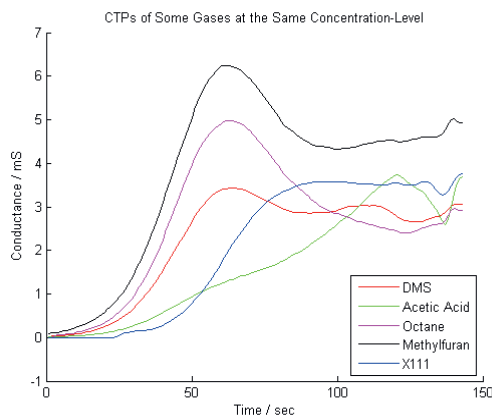


Fig. 1. CTPs of some gases at a certain concentration level

ProSens – a Mathematical Procedure for Calibration and Evaluation

As mentioned above MOGs can be used for ambitious analysis applications when they are thermo-cyclic operated. A mathematical procedure for data evaluation has to identify an unknown gas sample (classification) to avoid misleading results like false alarms and to determine the concentration of the components of the gas sample. Because often varying environmental conditions like varying humidity or varying environmental temperature influence the measurement results this must be incorporated in the evaluation model of the mathematical procedure.

The program ProSens, developed at KIT, was designed to meet the above mentioned requirements. [5].

SimSens – a Mathematical Procedure for Simultaneous Analysis of Gases

To meet the requirements of simultaneously analyzing a multitude of gases or gas mixtures of well-defined composition of components, the procedure SimSens (Program for Simultaneous Analysis of Gases) was developed. SimSens is an extension of ProSens, which was designed to analyze only one gas or one gas mixture. [6]

ProCal – a Mathematical Procedure for Batch-wise Calibration

To meet the requirements of simultaneously analyzing a multitude of gases or gas mixtures of well-defined composition of components, the procedure SimSens (Program for Simultaneous Analysis of Gases) was developed. SimSens is an extension of ProSens, which was designed to analyze only one gas or one gas mixture. [7]

Results

All above mentioned mathematical procedures, developed at the KIT, were tested in numerous

application scenarios with real measurement data and yield in all cases a very good performance. The technological transfer is supported by HybridSensorNet e.V. Assembling different new research results for forming a technological base at a higher level, the main goal is thereafter to realize new and innovative intelligent sensor systems.

References

- [1] P. Althainz, J. Goschnick, S. Ehrmann, and H.J. Ache, "Multisensor Microsystem for Contaminants in Air", *Sensors and Actuators B* 33 (1996) pp. 72-76.
- [2] V.V. Sysoev, I. Kiselev, M. Frietsch, and J. Goschnick, "Discrimination Power of a Metal- Oxide Thin-Film Sensor Microarray", *Sensors* 2004, 4, pp. 37-46.
- [3] A. Jerger, H. Kohler, F. Becker, H. B. Keller, and R. Seifert, "New applications of tin oxide gas sensors II. Intelligent Sensor System for Reliable Monitoring of Ammonia Leakages", *Sens. Actuators, B* 81, pp. 301-307 (2002).
- [4] K. Frank, A. Hetznecker, V. Schindler, H. Kohler, H.B. Keller, and R. Seifert, "Metal Oxide Gas Sensors: A new approach for high quality field analysis applications using a dynamically operated sensor array", 11th Internat.Meeting on Chemical Sensors (ICMS-11), Brescia, I, July 16-19, 2006.
- [5] R. Seifert, H. B. Keller, K. Frank, H. Kohler "ProSens - an Efficient Mathematical Procedure for Calibration and Evaluation of Tin Oxide Gas Sensor Data", *Sensor Letters*, Vol. 9/1, 7-10, 2011
- [6] H. B. Keller, R.Seifert, H. Kohler, „SimSens – a New Mathematical Procedure for Simultaneous Analysis of Gases with Resistive Gas Sensors”, *Sensors & Actuators: B. Chemical* (2015), pp. 203-207 DOI information: 10.1016/j.snb.2014.10.133
- [7] R. Seifert, H. B. Keller, K. Frank, H. Kohler, „Batch-wise Mathematical Calibration of Thermo-Cyclically Operated Tin Oxide Gas Sensors”, *Sensor Letters*, Vol. 9/2, 621-624, 2011

Expanded Uncertainty Evaluation Taking into Account the Correlation Between Estimates of Input Quantities

Igor Zakharov^{1,2}, Pavel Nevezhnikov¹, Olesia Botsiura²

¹National Scientific Centre "Institute of Metrology", 42, Myronosytska str., 61002, Kharkiv, Ukraine

²Kharkiv National University of Radioelectronics, 14, Nauky ave., 61166, Kharkiv, Ukraine

E-mail (I.P. Zakharov): newzip@ukr.net

Summary:

Cases of occurrence of correlation between estimates of input quantities are considered. An expression for the effective number of degrees of freedom and kurtosis of a measurand, taking into account the correlation between the estimates of the input quantities, is derived.

Keywords: expanded uncertainty, correlation, reduction method, effective degrees of freedom, kurtosis method

Introduction

When evaluating the measurement uncertainty, one has to deal with situations where estimates of input quantities are pairwise correlated. Correlation occurs in the following cases:

1) while observing both input quantities X_i and X_k entering the model

$$Y = f(X_1, X_2, \dots, X_N) \quad (1)$$

in one measurement experiment (observed correlation);

2) if there is a dependence of both input quantities X_i and X_k on the same variable Q , which appears when using the same measuring instruments, initial values or measurement methods (assumed or logical correlation):

$$X_i = \psi_i(\Theta); X_k = \psi_k(\Theta).$$

A measure of the correlation dependence is the correlation coefficient $r_{i,k}$, which for these two situations must be determined, respectively, by statistical (type A) and non-statistical (type B) methods [1].

When calculating the standard uncertainty $u(y)$ of the measurand Y , the correlation between the estimates is taken into account using the well-known formula [2]:

$$u(y) = \sqrt{\sum_{j=1}^N c_j^2 u_j^2 + 2 \sum_{i < k} r_{i,k} c_i c_k u_i u_k}, \quad (2)$$

where c_j , $j=1,2,\dots, N$ is the j -th sensitivity coefficient.

Difficulties in accounting for correlation arise

when evaluating expanded uncertainty U . The latter for linearized models is defined as the product of the standard uncertainty $u(y)$ by the coverage factor k :

$$U = k u_c(y). \quad (3)$$

The coverage factor k is determined in different ways with different approaches to estimating measurement uncertainty.

GUM approach

In GUM [2], the Student's coefficient $t_p(v_{eff})$ for the given confidence level p and the effective number of degrees of freedom v_{eff} is taken as the coverage coefficient k for repeated measurements.

The v_{eff} is obtained by the Welch–Satterthwaite formula [2]:

$$v_{eff} = \frac{u^4(y)}{\sum_{j=1}^N \frac{c_j^4 u_j^4}{v_j}}, \quad (4)$$

where v_j is the number of degrees of freedom of the j -th input quantity.

Expression (4) does not give a correct estimate of the number of degrees of freedom in the presence of a correlation between the input quantities.

Indeed, for a function of two correlated input quantities $Y=f(X_1, X_2)$ with an equal number of degrees of freedom $v_1=v_2=v$ and in the absence of uncertainties of type B, the effective number of degrees of freedom will be equal to

$$v_{\text{eff}} = v \frac{(c_1^2 u_1^2 + 2r_{1,2} c_1 c_2 u_1 u_2 + c_2^2 u_2^2)^2}{c_1^4 u_1^4 + c_2^4 u_2^4} \quad (5)$$

and when changing $-1 \leq r_{1,2} \leq 1$ will vary in the range from 0 to $8v$. On the other hand, to calculate the total standard uncertainty of the presence of correlation, the reduction method can be used [3]. It provides for bringing indirect measurements to direct ones by calculating the values of the measured value for each pair of correlated input quantities:

$$y_i = f(x_{1i}, x_{2i}), \quad i = 1, 2, \dots, n. \quad (6)$$

In this case, the measured value will be the arithmetic mean of the measured values obtained:

$$\bar{y} = \frac{1}{n} \sum_{i=1}^n y_i, \quad (7)$$

and the standard uncertainty of type A of the measured quantity is found as:

$$u_A(y) = \sqrt{\frac{1}{n(n-1)} \sum_{i=1}^n (y_i - \bar{y})^2} \quad (8)$$

and has the number of degrees of freedom $v=n-1$, which should be equal to the number of degrees of freedom v_{eff} , determined by the Welch–Satterthwaite formula (5).

This situation can be changed when taking into account that the correlated input quantities must be described by the joint PDF [4], which contributes $u_{i,k}(y)$ to the standard uncertainty of the measurand with the number of degrees of freedom $v=n-1$.

In this case, the expression for the combined standard uncertainty (2) can be rewritten as follows:

$$u(y) = \sqrt{\sum_{\substack{j=1 \\ j \neq k \neq l}}^N c_j^2 u_j^2 - u_{l,k}^2(y)}, \quad (9)$$

from which

$$u_{l,k}(y) = \sqrt{c_l^2 u_l^2 + 2r_{l,k} c_l c_k u_l u_k + c_k^2 u_k^2} \quad (10)$$

In this case, the Welch–Satterthwaite formula in the presence of correlated input quantities will have the form:

$$v_{\text{eff}} = \frac{u^4(y)}{\sum_{\substack{j=1 \\ j \neq k \neq l}}^N \frac{c_j^4 u_j^4}{v_j} + \frac{u_{l,k}^4}{n-1}}, \quad (11)$$

So, for a function of two correlated input quanti-

ties $Y=f(X_1, X_2)$ with an equal number of degrees of freedom $v_1=v_2=v$, the effective number of degrees of freedom will be equal to v , which coincides with the number of degrees of freedom for expression (8).

Bayesian approach. Kurtosis method

Expanded uncertainty:

$$U = k(\eta) \cdot u(y), \quad (12)$$

where the coverage factor $k(\eta)$ depends on the kurtosis η of the measurand, determined by the formula:

$$\eta = \frac{\sum_{j=1}^N c_j^4 u_j^4 \eta_j}{u^4(y)}, \quad (13)$$

where η_j is kurtosis of the j -th input quantity.

This expression also does not work in the case of correlated input quantities, however, it can be transformed for this case by analogy with expression (11):

$$\eta = \frac{\sum_{\substack{j=1 \\ j \neq k, j \neq l}}^N c_j^4 u_j^4 \eta_j + \eta_{l,k} u_{l,k}^4(y)}{u^4(y)}. \quad (14)$$

The coverage factor for a confidence level of 0.95 is calculated by the formula [5]:

$$k = \begin{cases} 0.1085\eta^3 + 0.1\eta + 1.96, & \text{when } \eta < 0; \\ t_{0.95; (6/\eta+4)} \cdot \sqrt{\frac{3+\eta}{3+2\eta}}, & \text{when } \eta \geq 0. \end{cases} \quad (15)$$

Examples of evaluation the expanded uncertainty of various measurements are considered, taking into account the correlation between estimates of input quantities.

References

- [1] EA-4/02 M: 2013 Evaluation of the Uncertainty of Measurement in Calibration
- [2] JCGM 100:2008 Evaluation of measurement data – Guide to the expression of uncertainty in measurement.
- [3] S.G. Rabinovich, Evaluating Measurement Accuracy: A Practical Approach, 3d ed., Springer (2017) 313.
- [4] JCGM 101:2008 Evaluation of measurement data – Supplement 1 to the “Guide to the expression of uncertainty in measurement” – Propagation of distributions using a Monte Carlo method.
- [5] I. Zakharov, O. Botsiura, Calculation of expanded uncertainty using the kurtosis method when implementing a Bayesian approach. *Measurement Techniques*. Volume 62 (2019), Issue 4, pp. 327-331; doi: 10.1007/s11018-019-01625-x.

Pillar

System of Units and Metrological Infrastructure

Innovative Mass Standards for the Worldwide Transfer of the Redefined Unit Kilogram

Katharina Lehrmann¹, Dorothea Knopf¹, Frank Härtig¹

*¹ Physikalisch-Technische Bundesanstalt (PTB), Bundesallee 100, 38116 Braunschweig, Germany
katharina.lehrmann@ptb.de*

Summary:

Manufacturing processes and handling procedures for new stable silicon mass standards with unprecedented accuracy have been developed and transferred to industry. The patented manufacturing process and the high precision calibration procedures were developed by PTB. Both the manufacturing process for the spheres and the handling of the spheres were extended to two small and medium-sized enterprises (SME). The transfer was part of the three-year transfer project "Si-kg" for industrial requirements and placed on the market with great success.

Keywords: Silicon, Kilogram, mass standard, sphere

I. Introduction

The Physikalisch-Technische Bundesanstalt (PTB) was significantly involved in the redefinition of the International System of Units [1]. In the field of mass, for example, the 130-year-old International Kilogram Prototype (IPK) was replaced by kibble balance methods and by several unique spheres with nominal mass of 1 kg made of monocrystalline isotopically enriched silicon (^{28}Si) [2]. In case of the silicon sphere, the unit kilogram is linked to the mass of its individual atoms and "traced back" to them [3]. A key challenge of this new approach has been to produce spheres with unprecedented accuracy in roundness and surface quality. In order to minimize measurement errors and the influence of undesirable environmental conditions, many physical barriers had to be overcome. For this purpose, PTB developed a manufacturing process for monocrystalline silicon. Since the high-cost and the complex enrichment process of the isotopically enriched material, only 12 spheres made of ^{28}Si will probably be available in the world.

Therefore, alternatives had to be developed for National Metrological Institutes, Calibration Laboratories and manufacturers of weighing instruments to reliably disseminate the unit kilogram via silicon spheres.

II. Know-How Transfer of Manufacturing Silicon Spheres to Industry

The manufacturing process was transferred to a small and medium-sized enterprises (SME) in order to produce spheres of natural monocrystalline silicon ($^{\text{nat}}\text{Si}$).

The patented manufacturing process of the purpose-built machine provides contaminant-free spheres showing only minor shape errors, low roughness and a very uniform and stable oxide-layer [4]. Despite the robust crystal structure, the polishing process enables due to the special composition of the polishing paste to physically remove atoms from the surface without scratches nor subsurface damage of the crystalline structure. The polishing process achieves very low roughness and achieves a defined thickness of oxide layers. As a result, mass standards made of silicon achieve a long-term stability that has not been achieved before.

The manufacturing partner is able to use the transferred process for the production of a large range of spheres. This includes spheres made of other materials as well as spheres that can be used as density standards.

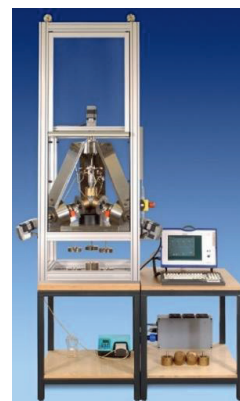


Figure 1 Polishing machine to manufacture high-precision spheres

III. Know-How Transfer of Handling, Transportation and Cleaning of Silicon Spheres

The know-how about handling silicon spheres and the necessary tools were passed on to a second company which has a long experience in manufacturing weights. In a series of trials and practical tests lasting several years, PTB has identified materials with which silicon spheres can be safely handled, stored and transported. In order to guarantee the extremely high mass stability, the silicon spheres are mounted on special rings which neither scratch the sphere nor leave any adhering to the surface of the sphere.

In contrast to other mass standards, silicon spheres can be cleaned in a simple, efficient and cost-effective way to remove all surface contamination. This cleaning procedure enables the high stability. Therefore, special cloths and handling equipment were developed and optimized with the industrial partner. In addition to the spheres, the cleaning and handling equipment, the sales partner offers training courses for silicon spheres handling.

In close cooperation a broad selection of accessories for silicon spheres like transport container and transport case, special tongs and fork (shown in Figure 2) and sphere holder for universal applications were designed [5].

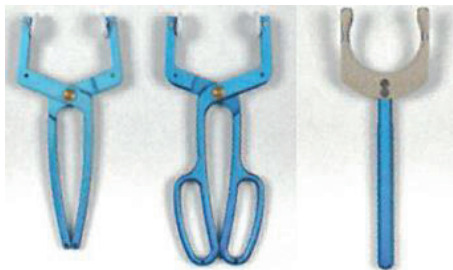


Figure 2 New designed special handling tools (tongs and fork) for silicon spheres

IV. Results

With the transfer of the sphere's manufacturing technique to an industrial company and the transfer of handling to a second SME, a worldwide unique ready to use infrastructure has been realised which allows highly stable and accurate mass standards to be delivered.

During the project period, the requirements for the high-precision manufacturing were even more than exceeded. Silicon spheres with form deviations (RONt) of less than 20 nm can now be manufactured by industry. Table 1 shows the achieved measurement uncertainties of the silicon spheres manufactured by the industrial cooperation partner [6]. All spheres are adjusted to 1 kg +/- 200 mg.

Tab. 1: Measurement uncertainties $U(k=2)$ of silicon spheres manufactured by manufacturing partner. All measurements are done by PTB

Parameter	$U(k=2)$
Mass in air	50 μg
Mass in vacuum	25 μg
Density (hydrostatic)	0.004 kg/m^3
Roughness S_a	< 0.5 nm
Form deviation RONt	10.2 nm
Average layer thickness	0.4 nm

The established infrastructure can meet the increasing global demand for stable high-precision mass standards. This is underlined by the sales of six silicon spheres, which were already sold to international customers during the project period. In addition, more than 12 spheres were distributed to leading national institutes worldwide for individual practice.

V. Summary

Processes for the production of mass standards made of highly enriched silicon with nominal mass of 1 kg have been developed in the preparation of the redefinition of the unit Kilogram. The methods and procedures were successfully transferred to industry for the manufacturing of spheres made of natural silicon. The transfer of the patented manufacturing process to two SMEs led to previously unattained small form deviation (RONt) of less than 20 nm in industrial production of spheres. An infrastructure which includes user-friendly handling tools and the needed accessories for the cleaning procedure was established. In future the procedures can be modified in order to manufacture spheres made of different materials and with different diameters.

References

- [1] F. Haertig, H. Bettin, R. Schwartz "The new Kilogram Materialized by Silicon Isotopes", Conference Paper Conference on precision electromagnetic measurements (CPEM) Jul 10-15, 2016, ISBN 978-1-4673-9134-4.
- [2] The International System of Units (SI); Bureau International des Poids et Mésures, 8th edition 2006
- [3] R. Wegge, H. Bettin, D. Knopf, F. Härtig „Dissemination of the kilogram via silicon spheres“; Euspen's 17 International Conference, Hannover 2017
- [4] Joint product flyer "Si-kg- the new kilogram made by natural silicon spheres", 2018
- [5] Internal calibration certificates and measurement reports, PTB, 2019

SI Realization of the farad at LNE

Almazbek IMANALIEV¹, Olivier THEVENOT¹, Kamel DOUGDAG¹, François PIQUEMAL¹
¹ LNE, 29 Rue Roger Hennequin 78197 Trappes, FRANCE
 almazbek.imanaliev@lne.fr

Summary:

This paper describes practical realizations of the farad in the revised SI at LNE. The latest developments on the new Thompson-Lampard calculable capacitor with target accuracy of one part in 10^8 for 1 pF are presented.

Keywords: impedance metrology, traceability, capacitance standard, Thompson-Lampard capacitor, precise mechanical positioning

I. Introduction

Within the revised SI and according to the Appendix 2 of the 9th SI Brochure (2019) [1], two practical realizations of the farad are indicated. The first method consists of using a calculable capacitor and the value of the electric constant $\epsilon_0 = 8.854\,187\,8128(13)$ pF/m [2]. On the other hand, the second method allows one to realize the farad by comparing the impedance of a known resistance, obtained using the quantum Hall effect (QHE) and the value of the von Klitzing constant $R_K = 25\,812.807\,459\,3045$ Ω , to the impedance of an unknown capacitance using, for example, a quadrature bridge. Fig. 1 illustrates the implemented chain of the two ways of realization of the farad at LNE [3] and their relation.

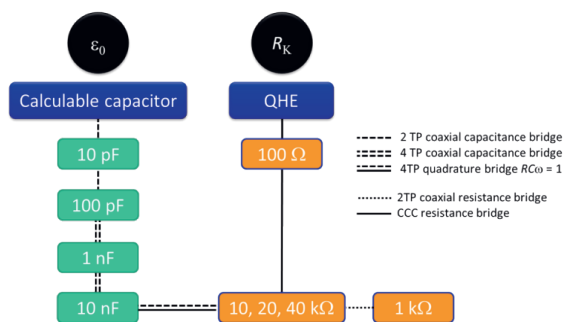


Fig. 1. Measurement chain linking ϵ_0 and R_K .

In practice, the two methods lead to measure 10 pF and 100 pF secondary capacitance standards. They are measured in terms of ϵ_0 using a 2-terminal-pair (TP) coaxial capacitance bridge or in terms of R_K by means of several other bridges and standards. This implies at first cryogenic current comparator (CCC) to measure in dc 100 Ω then 10 k Ω , 20 k Ω and 40 k Ω . The impedance of the resistors is then

compared to that of 10 nF capacitors at 400 Hz, 800 Hz and 1600 Hz by mean of a 4 TP quadrature bridge. The frequency dependences of the resistors are measured with a 1 k Ω calculable resistance standard. The 10 nF capacitances are finally used to measure 1 nF then 100 pF and 10 pF.

This measurement chain has allowed LNE to determine R_K with a standard uncertainty of 5.3 parts in 10^8 [3]. The previous developed calculable capacitor revealed the two prevailing uncertainty components among those due to the mechanical imperfections of the capacitor. The first one is related to the cylindricity defects of the cavity due to the deviation of the electrodes' shape from perfect cylinders and to their mispositioning with respect to each other (2.5 parts in 10^8). The second one is related to the coaxiality defect between the capacitor axis and the trajectory of the moving guard (3 parts in 10^8). The target uncertainty of one part in 10^8 requires LNE to develop a new standard calculable capacitor keeping the electrodes' cylindricity and positioning defects below 100 nm and that of the movable guard trajectory to 100 nm or less. Hereafter, are presented the results of some recent tests carried out on the alignment of the electrodes of a new calculable capacitor.

II. The LNE calculable capacitor

The new LNE calculable capacitor is a Thompson-Lampard calculable capacitor constituted of five cylindrical electrodes (bars) in vertical position arranged at the vertices of a regular pentagon. It generates a calculable capacitance variation, proportional to the length of the displacement of a movable guard in its cross section, allowing linking the farad to the meter as it is shown in Fig. 2.

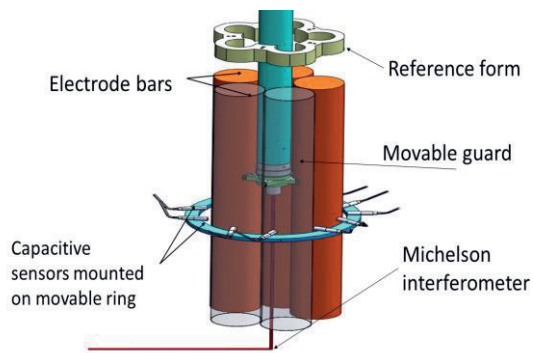


Fig. 2. LNE vertical five electrode-bar capacitor.

Cylindricity of new electrodes

Bars are made from non-magnetic stainless steel and are machined and grinded to obtain an initial cylindricity defect of about $1.5\ \mu\text{m}$. The surface roughness is then reduced to $100\ \text{nm}$ by lapping and polishing electrodes manually. The measurement of the straightness and parallelism of the electrodes are carried out with an on-purpose built measuring machine [4].

Aligning electrodes in parallel

The alignment procedure is carried out in two steps. In the first step, the top and bottom of the electrodes are positioned at the vertices of a regular pentagon with an accuracy of $5\ \mu\text{m}$ by aligning them with respect to the reference form (Fig. 2). The capacitive sensors mounted on a movable ring enable to measure the relative position of each electrode with a resolution of $20\ \text{nm}$ to the corresponding vertices of the reference form. However, the absolute positions of the capacitive sensors are not known sufficiently in horizontal plane (few μm of displacement depending on movable rings' vertical position). Therefore, alignment of electrodes in parallel is not guaranteed at this stage. In the next step, one of the bars is chosen as a reference and the four other bars are aligned with regard to it by measuring their relative tilt. In such a scenario, the relative position of sensors to the reference electrode and thus to the others is perfectly known at any moment due to the construction provided that capacitive measurements are taken simultaneously. The relative tilt of each electrode is estimated from a scan of capacitive measurements along the length of the electrodes at orthogonal horizontal axis. Firstly, the error introduced from sensors' positions is corrected and then linear regression is applied to the moving mean of the corrected data. In Fig. 3 an example of alignment for one electrode axis is shown. The achieved alignment has uncer-

tainty of $50\ \text{nm}$ ($k=1$) on average for four electrodes in accordance with initially defined target uncertainty.

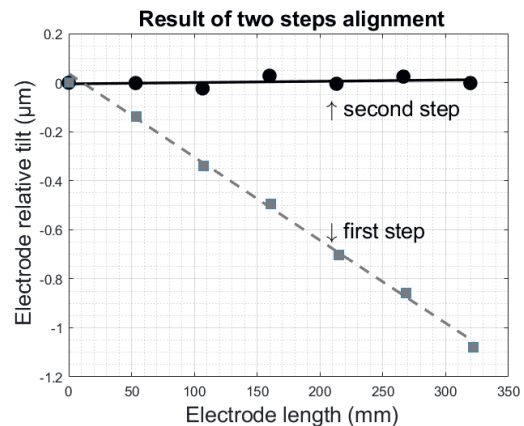


Fig. 3. Aligning an electrode in two steps.

III. Conclusion

The present status of the development of the new LNE calculable capacitor is briefly presented. The fabrication of the new set of electrodes and their sub-micrometric alignment system is finalized. Currently, tests related to the guard positioning is under progress. More details and results of these improvements will be given during the conference. In parallel to calculable capacitor development, improvements are made on the measuring chain linking the farad to the QHE to achieve an overall uncertainty lower than 1 part in 10^8 . In the context of European project JRP GIQS (*Graphene Impedance Quantum Standard, 2019-2022*), the implementation of AC quantum Hall effect in Graphene to realize the farad is in preparation at LNE for the future.

References

- [1] "Mise en pratique for the definition of the ampere and other electric units in the SI," *SI Brochure-Appendix 2*, 2019. [Online]. Available: <https://www.bipm.org/utis/en/pdf/si-mep/SI-App2-ampere.pdf>.
- [2] CODATA, "CODATA Recommended values of the fundamental physical constants: 2018," *NIST*, vol. 961, no. May, 2019.
- [3] G. Trapon, O. Thévenot, J. C. Lacueille, and W. Poirier, "Determination of the von Klitzing constant R_K in terms of the BNM calculable capacitor - Fifteen years of investigations," *Metrologia*, vol. 40, no. 4, pp. 159–171, 2003.
- [4] O. Thevenot, P. Gournay, L. Dupont, and L. Lahousse, "Realization of the new LNE Thompson Lampard electrode set," *CPEM Dig. Conference Precis. Electromagn. Meas.*, no. 1, pp. 418–419, 2010.

Studies on the Use of Bandgap References as a Voltage Standard

Bernd Schumacher¹, Christian Rohrig¹, Guido Weckwerth²

¹ *Physikalisch-Technische Bundesanstalt, Bundesallee 100, Braunschweig, Germany,*

² *wekomm engineering GmbH, Lena-Christ-Str. 46, Planegg, Germany
Bernd.Schumacher@ptb.de*

Summary:

The high precision of electrical direct current measurement technology is based on the traceability of the measured quantities to quantum standards, which are typically used in national metrology institutes such as the PTB. When calibrating voltage standards, the uncertainty of the transfer is limited by the inherent noise of the Zener diode used as transfer standard, which is based on an avalanche effect in a p-n transition. This noise is in the order of a few 100 nV. At PTB, studies were carried out to generate reference voltages by using alternative effects.

Keywords: electrical standards, voltage reference, Allan deviation, bandgap reference, calibration.

Introduction

The quantity voltage is one of the most important quantity in electrical metrology. For many decades, the international Weston element was used as physical representation of the Volt. In the 1970's, it was replaced by electronic voltage standards, based on stabilized Zener diodes [1]. In parallel, the Josephson voltage standard became the preferred reference at national metrology institutes and later also in high level calibration laboratories [2,3].

For the dissemination of the Volt, voltage references based on Zener-diodes are still important. A major disadvantage of these Zener references is their intrinsic noise level of about 100 nV. This noise is caused by the operation of the Zener diode in reverse mode by using the avalanche effect to stabilize the voltage. This noise limits the achievable calibration uncertainty compared to the noise level of a Josephson junction array voltage standard, which is of the order of a few nV. This has led to the development of a replacement for these Zener-based voltage references by other low-noise references of comparable stability.

Voltage standard based on a bandgap reference

A possible candidate as alternative type of voltage standard is the so-called bandgap diode [4]. Here, a p-n transition is operated in the forward direction. By choosing an appropriate operating point, voltage values in the order of 1 V can be achieved. The operation of these type of reference is less noisy than the Zener

diode. As proof of principle, a reference circuit with a commercial SMD-type bandgap diode was set up and the output voltage of the circuit was measured and compared to that of a calibrator. From the measured time series of voltages, the noise behavior can be determined [5,6]. For such a circuit, a RMS noise of approximately 3 μ V has been calculated, which is more than ten times higher than the corresponding noise of a Zener reference. This high noise of the commercial bandgap reference is probably caused by the high grade of integration of the SMD component.

Improvements of the reference

Therefore, a discrete circuit consisting of individual transistors, simulating a bandgap reference, was built (see Fig. 1).

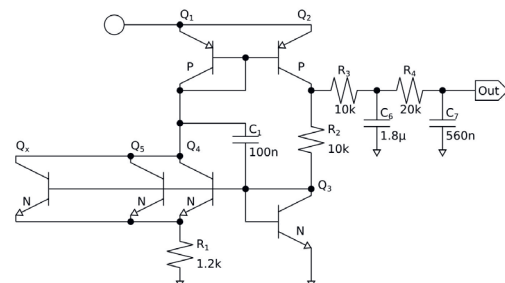


Fig. 1. Principle diagram of the discrete transistor circuit, operating as a bandgap reference.

The general idea is to reduce the noise by realizing a spacious p-n junction by connecting several transistors in parallel. Furthermore,

special attention was paid to an even temperature distribution among all components, i.e. the transistors as well as the resistors R_1 and R_2 , defining the operation point. They have to be of high quality (low temperature coefficient, high temporal stability).

The output voltage of this circuit was measured and compared to that of a calibrator and the time series of voltages was analyzed accordingly. With this circuit, an RMS noise floor of 100 nV could be achieved (see Fig. 2).

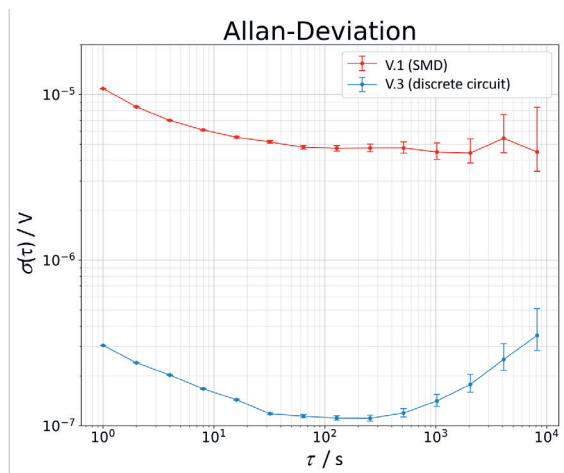


Fig. 2. Noise spectrum of the output voltage of a SMD bandgap diode compared to a discrete circuit consisting of transistors, shown as a plot of the Allan deviation versus measurement time τ .

The measurements also show that after 100 s the temporal drift of the circuit becomes the dominant noise component. This is due to the imperfect temperature stabilization of the transistors. Work is currently being carried out to further improve the temperature stability by means of a suitable structure, so that the basis for a future voltage standard can be achieved.

Conclusion and Outlook

It could be seen that in principle, the bandgap diode can be used as a low-noise voltage refer-

ence. Commercially available bandgap devices are of limited suitability due to their poor properties. It turns out that bandgap diodes with enlarged chip area (as simulated by paralleling several transistors) are a promising solution with respect to noise.

Due to the strong temperature dependence, additional measures with respect to temperature stability have to be taken. Nevertheless, we see a promising method to realize a new kind of low-noise voltage reference for the future.

Acknowledgements

The authors wish to thank Steffen Tunkel for carrying out the experiments.

References

- [1] F. Melchert, Zenerdioden als Spannungsnormale, *PTB Mitteilungen* 77, 289 (1967)
- [2] B.D. Josephson, Possible New Effects in Superconductivity Tunneling, *Phys. Letters* 1, 251-253 (1962)
- [3] R. Pöpel, The Josephson Effect and Voltage Standards, *Metrologia* 29, 153-174 (1992)
- [4] Z. Zhou, Y. Ma, X. Ming, B. Zhang, Z. Li, A 2.2-V 2.9-ppm/°C BiCMOS bandgap voltage reference with full temperature-range curvature-compensation, *Journal of Semiconductors* 31 (2010), doi: 10.1088/1674-4926/31/7/075004
- [5] T. Witt, Using the Allan Variance and Power Spectral Density to Characterize DC Nanovoltmeters, *IEEE Transactions on Instrumentation and Measurement* 50, 445 – 448 (2001)
- [6] T. Witt, Y. Tang, Investigations of Noise in Measurements of Electronic Voltage Standards, *IEEE Transactions on Instrumentation and Measurement* 54, 567 – 570 (2005); doi:10.1109/TIM.2004.843096

Photonic Thermometry at PTB – Challenges and Perspectives for Contact Temperature Metrology Utilizing Optical Sensors

Stephan Krenenk¹, René Eisermann¹, Georg Winzer², Tobias Habisreuther³, Steffen Rudtsch¹

¹ *Physikalisch-Technische Bundesanstalt, Abbestr. 2 - 12, 10587 Berlin, Germany*

² *Leibniz-Institut für innovative Mikroelektronik, Im Technologiepark 25, 15236 Frankfurt/O., Germany*

³ *Leibniz-Institut für Photonische Technologien, Albert-Einstein-Str. 9, 07745 Jena, Germany*

stephan.krenenk@ptb.de

Summary:

Photonic sensors offer new possibilities for the metrological temperature determination in specific applications including high electric fields or harsh environments. Within two EU projects the PTB develop and validate different kinds of photonic thermometers in a temperature range from 0 °C to over 1500 °C. The aim of this work is to develop and validate novel accurate photonic thermometers with uncertainties below 10 mK, and sensors for application within harsh environments at high temperatures. We show first results using silicon ring resonators and sapphire fiber Bragg gratings.

Keywords: photonic thermometry, temperature sensor, sapphire, fiber Bragg grating, whispering gallery resonator

Introduction

In the industrially most relevant temperature range from about –100 °C to 1000 °C temperature measurements are commonly based on the measurement of electrical resistance (e.g. Pt100) or voltage (thermocouple). Photonic sensors, in contrast, use the light-matter interaction to measure temperature. Usually the change of the refractive index and the resulting shift of the resonance wavelength of the corresponding optical resonator is utilized. Fiber sensors using fiber Bragg gratings (FBG) or systems using distributed methods based on scattering processes in optical fibers are industrially available. Nevertheless, the determination and reduction of temperature uncertainty is still a challenging task.

The Physikalisch Technische Bundesanstalt (PTB) is working on special photonic sensors for temperature measurement within two European research projects.

The first project "Enhancing process efficiency through improved temperature measurement 2" (EMPRESS 2) has the overall aim of improving the efficiency of key industrial manufacturing processes through improved temperature measurement and control. The project focuses on accurate and SI traceable temperature measurement with different stable, reliable, durable and robust sensors. One objective is the introduction of traceable fiber optic meas-

urements at high temperatures above 500 °C. PTB is working together with the Leibniz-Institut für Photonische Technologien (IPHT) on FBGs in sapphire fibers which can be used at temperatures exceeding 1500 °C.

The second project "Photonic and Optomechanical Sensors for Nanoscaled and Quantum Thermometry" (PhotOQuant) deals with fundamental research for high-precision or primary temperature sensors. Two micrometre-sized chip-based techniques are designed, manufactured, characterized and calibrated: optomechanical sensors, in which the temperature-dependent Brownian motion of nanostructures is optically detected, and photonic resonators, in which planar waveguides (e.g. ring resonators) allow very high-resolution measurements of the refractive index change. Together with the Leibniz-Institut für innovative Mikroelektronik (IHP), PTB investigates Si/SiO₂ structures which are manufactured by standardized masking processes.

Perspective and First Results

The well-established methodologies of the International Temperature Scale of 1990 (ITS-90) defines standard platinum resistance thermometers (SPRT) as the interpolating sensors between the defining fixed points (see Fig. 1, top). These thermometers are used in a large temperature range with superior reproducibility and uncertainties below 10 mK (see Fig. 1). Never-

theless, these sensors are mechanical fragile and principally unsuitable for harsh environments with strong electric fields.

Above approximately 1000 °C the ITS-90 is defined by radiation thermometers. These measure the spectral radiance of hot objects according to Planck's law. With ideal radiators (black bodies), uncertainties of less than 1 K can be achieved (see Fig. 1). For measurements on real objects, the emissivity of the surface is required, which here can only be determined with accuracies in the percentage range [5], thus increasing the overall uncertainty of the temperature measurement to about 10 K.

Approaches using photonic thermometers show great potential to reach comparable measurement uncertainties [1] with the additional advantage of a metal free, chemical inert and mechanical robust sensor design. Our efforts are concentrated in two directions, on the one hand the validation and improvement of photonic resonators (PhotoQuant) for moderate environments and temperatures up to 100 °C with measurement uncertainties below 10 mK (see Fig. 1). On the other hand, the metrological characterization of sapphire based fiber Bragg gratings (SFBG) for applications in harsh environments with temperatures above 1500 °C (EMPRESS 2).

Both photonic thermometer principles are mainly based on a determination of frequency (or wavelength) changes of an optical resonance. Using tunable laser for fiber Bragg grating (FBG) interrogation it has been shown, that peak wavelength tracking with an uncertainty below 1 pm is possible with stability better than 4 pm/year [2] and even lower for pre-annealed FBG [3]. Taking the temperature coefficient (≈ 12 pm/K) into account this yields to a temperature uncertainty below 100 mK in temperature range up to 600 °C.

Photonic ring resonators offer an even higher temperature coefficient (≈ 75 pm/K) and with improved quality factor of the resonant frequency. According to our results there are suitable for temperature uncertainty quite below 10 mK (see Fig. 1). The most challenging task and critical part to enable low uncertainties is the packaging of the planar photonic devices, due to the stabilization of fiber to chip coupling. Most approaches using for example glue are limited to temperatures up to around 250 °C. We actually are working on new package design to exceed this limitation up to approx. 600 °C.

Another solution suitable for even higher temperature above 1500 °C (probably up to 1900 °C) are SFBG's, which offer a temperature coefficient of 26 pm/K [4]. Since they are

intrinsically multimodal the corresponding resonance spectra is more complex compared to conventional singlemode FBG. Due to that, the precise determination of wavelength shift is the limiting factor for temperature uncertainties (1 K region, see Fig. 1). We therefore developing new methods for probing and signal processing to further reduce uncertainties.

In summary, photonic thermometer sensors are suitable to compete with conventional electrical sensors, however some effort and research have to be done in the future.

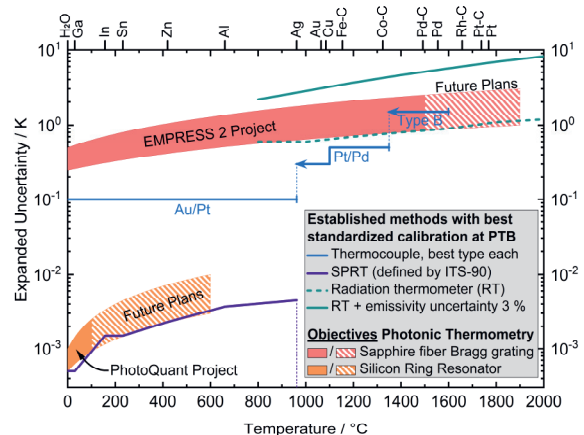


Fig. 1. Accuracy of different temperature measurement techniques: established electrical and radiance methods with the best possible standardized calibration at PTB in comparison to the target uncertainty ranges of the new photonic methods. (See text for details.)

Acknowledgment

This work has received funding from the EMPIR programme co-financed by the Participating States and from the European Union's Horizon 2020 research and innovation programme.

References

- [1] Z. Ahmed, et al., Proc. SPIE 10923, Silicon Photonics XIV, 109230L (12 April 2019), doi:10.1117/12.2505898
- [2] S. D. Dyer, et al., Proc. SPIE 5855, 17th International Conference on Optical Fibre Sensors, 88-93 (2005), doi:10.1117/12.623444
- [3] P. Mauron, et al., Scientific production and competences - EPFL Theses, EMPA (2001), doi:10.5075/epfl-thesis-2339
- [4] D. Grobncic, et al., Proc. SPIE 5855, 17th International Conference on Optical Fibre Sensors, (23 May 2005), doi:10.1117/12.623592
- [5] D. Urban, et al., Int J Thermophys 39, 10 (2018), doi:10.1007/s10765-017-2339-y

Special Session “Future topics in metrology”

Organizer: Sascha Eichstädt
Physikalisch-Technische Bundesanstalt, Braunschweig and Berlin, Germany
sascha.eichstaedt@ptb.de

Speakers: Tanja Dorst, Lara Hoffmann, Maximilian Gruber and Benedikt Seeger
Physikalisch-Technische Bundesanstalt, Braunschweig and Berlin, Germany

Summary:

Technological developments in industry and society result almost directly in novel requirements for metrology. This special session highlights a few of such *future topics*, presented by young scientists. The session focuses on novel developments and topics arising from the digital transformation in industry and society. This contains NMI-level calibration for and application of MEMS sensors; semantic data management and ontologies in sensor networks; deep learning for inverse problems in form metrology; uncertainty evaluation in machine learning.

Keywords: metrology; digitalisation; MEMS sensor; sensor network; deep learning; machine learning

Motivation

Many recent advances in industrial measurements can be related to digital transformation. An example is the increasing use of networks of sensors, so called “smart sensors” or MEMS sensors instead of single reference measuring instruments in industrial applications. The resulting large amounts of measured data, lack of calibration and complexity of the corresponding mathematical models require novel concepts from metrology regarding traceability and reliability. This session provides a brief look into some of the aspects, metrology institutes have to address in the very near future:

- 1) MEMS sensors and other sensors with digital-only output, as well as sensors with built-in pre-processing are challenging when it comes to calibration traceable to the SI.
- 2) Vocabulary, semantic data and ontologies are becoming much more relevant for metrology, when data and information is being processed by algorithms automatically.
- 3) Uncertainty evaluation in the area of machine learning is a topic of rapidly growing importance as such methods are increasingly applied in the analysis of measured data.
- 4) Deep learning for complex measurement tasks is becoming a standard tool in the data science toolbox, despite basic questions regarding reliability, transparency and confidence remaining an open topic of research.

These topics will be covered based on actual current research carried out at the German national metrology institute Physikalisch-Technische Bundesanstalt (PTB).

Topics and speakers

Semantic Information in Sensor Networks

Self-describing sensors and measurements are a key component to establish (semi-)automated data analysis in the context of Industry 4.0.

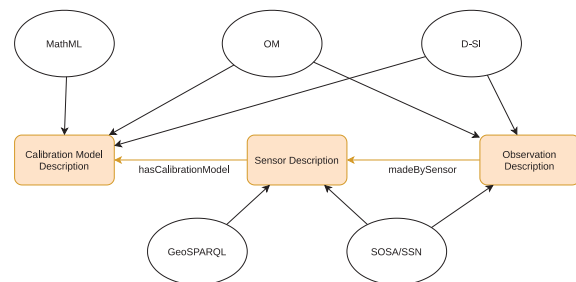


Figure 1 Outline of a concept to link different sources of semantic information

By mapping concepts from existing knowledge bases into a coherent ontology, metrological requirements of sensor and measurement descriptions are satisfied. Use cases considered for this ontology cover sensor networks, network topology, network robustness, information fusion, calibration models for dynamic uncertainty, correct metrological representation and implementation performance.

This topic will be presented by Maximilian Gruber, PhD student working in a research project with the aim to bring metrological principles into RAMI 4.0 and Industry 4.0.

Propagation of uncertainty for an Adaptive Linear Approximation algorithm

In machine learning, a variety of algorithms are available for feature extraction. To obtain reliable features from measured data, the propagation of measurement uncertainty is proposed

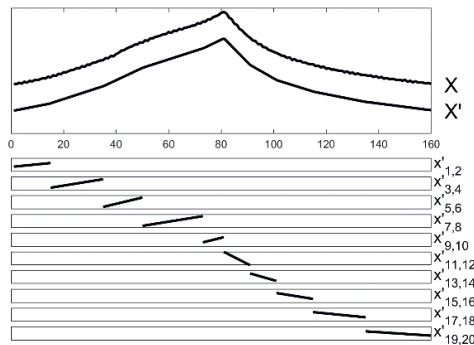


Figure 2 Approximation X' by mean values (uneven indices) and slopes (even indices) of ten segments determined by ALA.

here in line with the Guide to the Expression of Uncertainty in Measurement (GUM).

Recently, methods for the discrete Fourier and Wavelet transform have been published. Here, the Adaptive Linear Approximation (ALA) as a further complementary feature extraction algorithm is considered in combination with an analytical model for the uncertainty evaluation of the ALA features.

This topic will be presented by Tanja Dorst, PhD student working in a European metrology research project with the aim to provide measurement uncertainties for the complete data lifecycle in Industry 4.0.

Deep Neural Networks for optical form measurements

Deep neural networks have been successfully applied in many different fields like computational imaging, medical healthcare, signal processing or autonomous driving. We demonstrate in a proof-of-principle study that also optical form measurement can benefit from deep learning.

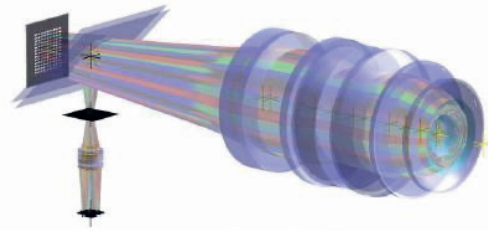


Figure 3 Schematic of the tilted-wave interferometer without reference arm.

Therefore, a data-driven machine learning approach is considered for solving an inverse problem in the accurate measurements of optical surfaces. The approach is developed and tested using virtual measurements (simulations) for the tilted wave interferometer with known ground truth.

This topic will be presented by Lara Hoffmann, PhD student working on the assessment of deep learning methods for solving complex measurement problems.

Dynamic calibration of digital sensors

For the processing of time-dependent data streams (e. g. dynamic measurement for monitoring vibration) an exact knowledge of the temporal relations is necessary. This is of particular importance when the measuring instrument is to be calibrated for dynamic measurements, because this requires traceable measurements of amplitude and phase values.

One approach is using a GPS signal for time stamping the calibration signals in the calibration experiment. To this end, a custom-designed microcontroller board with custom drivers have been developed at PTB. This enables traceable dynamic calibration for sensors with digital-only output.

This topic will be presented by Benedikt Seeger, PhD student working in a European metrology research project with the aim to provide traceable measurement data in Industry 4.0.

Semantic Information in Sensor Networks

Maximilian Gruber¹, Sascha Eichstädt¹

¹ *Physikalisch-Technische Bundesanstalt, Berlin, Germany
maximilian.gruber@ptb.de*

Summary:

Self-describing sensors and measurements are a key component to establish (semi-) automated data-analysis in the context of Industry 4.0. By mapping concepts from existing knowledge bases into a coherent new ontology, we fulfill metrological requirements of sensor and measurement descriptions. Use cases considered for this ontology cover sensor networks, network topology, network robustness, information fusion, calibration models for dynamic uncertainty, correct metrological representation and implementation performance.

Keywords: metadata, ontology, sensor network, information fusion, uncertainty

Introduction and Considered Use Cases

In order to automate the analysis of an ever-growing number of sensors in industrial plants, sensors must be able to self-provide information about themselves in an appropriate and machine-interpretable format [1-4]. To achieve these goals, developments of the semantic web group [5] and ontology engineers coming from diverse disciplines are taken into account [6].

Consider a use case with a set of calibrated dynamic sensors with topological and geometrical relations. A physical effect that is constant in its intensity moves relative to the array of sensors, leading to spatial and temporal dependent sensor observations. Multiple questions arise in this context: (1) estimation/location of the physical effect, (2) detect sensor failures and (3) recalibration of sensors through information redundancy. Answering these questions requires the raw sensor readings, but also meta information about sensor properties and their relations. A common, flexible and machine-interpretable approach is to use an ontology to represent the meta information.

Merge of Existing Data Schemes

Given the considered use cases, it is necessary to provide descriptions of the following three key components: (1) sensor, (2) observation and (3) calibration model. This can be achieved by merging and extending existing data schemes, vocabularies and ontologies, namely:

- Digital SI (D-SI, [7])
- Semantic Sensor Network (SSN, [8])
- Sensor, Observation, Sampling and Actuation (SOSA, [9])

- Ontology of Units of Measure and Related Concepts (OM, [10])
- Geographic Query Language (GeoSPARQL, [11])
- Mathematical Markup Language (MathML, [12])

Calibration model information is represented by a merge of OM, MathML and D-SI. These data schemes are used to define the concepts of `Parameter`, `Variable`, `Equation`, `EquationModel` and `CalibrationModel`.

General sensor information such as identifiers, manufacturing details, measurement principle and location is represented using the SO-SA/SSN ontologies. OM allows to specify the measurement quantity of the sensor. The location information is extended by GeoSPARQL for geometric and topological relations. A sensor is linked to its calibration model by the `hasCalibrationModel` attribute.

Observations are described by combining SO-SA, D-SI and OM. The OM concept of `om:Measure` is extended to cover uncertainties of values. An observation is then characterized by time aspects from SOSA and a result of type `dsi:MeasureWithUncertainty`, which follows the D-SI data model. Observations are connected to a sensor via the `sosa:madeBySensor` attribute.

A brief overview of the suggested combination is illustrated in figure 1.

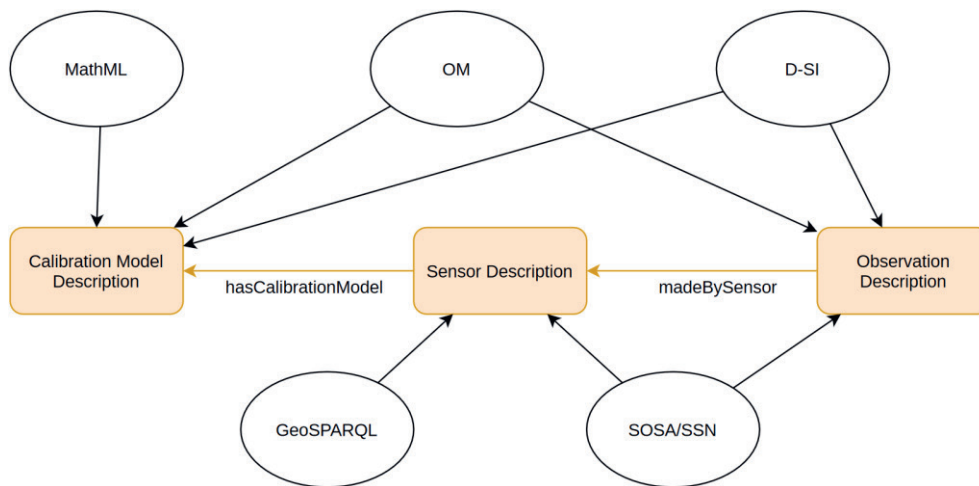


Figure 1: Overview of proposed merge

References

- [1] Plattform Industrie 4.0, and Federal Ministry for Economic Affairs. 2019. "Details of the Asset Administration Shell - Part 1."
- [2] Pfisterer, Dennis, Kay Romer, Daniel Bimschas, Oliver Kleine, Richard Mietz, Cuong Truong, Henning Hasemann, et al. 2011. "SPITFIRE: Toward a Semantic Web of Things." *IEEE Communications Magazine* 49 (11): 40–48. <https://doi.org/10.1109/MCOM.2011.6069708>.
- [3] Schütze, Andreas, and Nikolai Helwig. 2017. "Sensorik Und Messtechnik Für Die Industrie 4.0." *Tm - Technisches Messen* 84 (5): 310–19. <https://doi.org/10.1515/teme-2016-0047>.
- [4] Eichstädt, Sascha, and Björn Ludwig. 2019. "Metrologie Für Heterogene Sensornetzwerke Und Industrie 4.0." *Tm - Technisches Messen* 0 (0). <https://doi.org/10.1515/teme-2019-0073>.
- [5] Sheth, Amit, and Cory Henson. 2008. "Semantic Sensor Web." *Internet Computing, IEEE* 12 (August): 78–83. <https://doi.org/10.1109/MIC.2008.87>.
- [6] Padmavathi, Thimmaiah, and Madaiah Krishnamurthy. 2017. "Semantic Web Tools and Techniques for Knowledge Organization: An Overview." *KNOWLEDGE ORGANIZATION* 44 (4): 273–90. <https://doi.org/10.5771/0943-7444-2017-4-273>.
- [7] Hutzschenreuter, Daniel, Frank Härtig, Wiebke Heeren, Thomas Wiedenhöfer, Alistair Forbes, Clifford Brown, Ian Smith, et al. 2019. "Smart-Com Digital System of Units (D-SI) Guide for the Use of the Metadata-Format Used in Metrology for the Easy-to-Use, Safe, Harmonised and Unambiguous Digital Transfer of Metrological Data," November. <https://doi.org/10.5281/zenodo.3522631>.
- [8] Janowicz, Krzysztof, Armin Haller, Simon J. D. Cox, Danh Le Phuoc, and Maxime Lefrançois. 2019. "SOSA: A Lightweight Ontology for Sensors, Observations, Samples, and Actuators." *Journal of Web Semantics* 56 (May): 1–10. <https://doi.org/10.1016/j.websem.2018.06.003>.
- [9] Haller, Armin, Krzysztof Janowicz, Simon Cox, Maxime Lefrançois, Kerry Taylor, Danh Le Phuoc, Josh Lieberman, Raúl García-Castro, Rob Atkinson, and Claus Stadler. 2018. "The Modular SSN Ontology: A Joint W3C and OGC Standard Specifying the Semantics of Sensors, Observations, Sampling, and Actuation."
- [10] Rijgersberg, Hajo, Mark van Assem, and Jan Top. 2011. "Ontology of Units of Measure and Related Concepts." *Semantic Web – Interoperability, Usability, Applicability*.
- [11] Open Geospatial Consortium. 2012. "GeoSPARQL - A Geographic Query Language for RDF Data."
- [12] W3C. 2014. "Mathematical Markup Language (MathML) Version 3.0 2nd Edition."

Propagation of uncertainty for an Adaptive Linear Approximation algorithm

Tanja Dorst¹, Sascha Eichstädt¹, Tizian Schneider^{2,3}, Andreas Schütze^{2,3}

¹Physikalisch-Technische Bundesanstalt, Braunschweig and Berlin, Germany

²ZeMA – Center for Mechatronics and Automation Technology gGmbH, Saarbruecken, Germany

³Saarland University, Lab for Measurement Technology, Saarbruecken, Germany

E-mail (corresponding author): tanja.dorst@ptb.de

Summary:

In machine learning, a variety of algorithms are available for feature extraction. To obtain reliable features from measured data, the propagation of measurement uncertainty is proposed here in line with the Guide to the Expression of Uncertainty in Measurement (GUM). Recently, methods for the discrete Fourier and Wavelet transform have been published. Here, the Adaptive Linear Approximation (ALA) as a further complementary feature extraction algorithm is considered in combination with an analytical model for the uncertainty evaluation of the ALA features.

Keywords: measurement uncertainty, uncertainty propagation, feature extraction, Adaptive Linear Approximation, machine learning

Motivation

One of the most important advances in sensor technology has been the development of smart sensors. These sensors carry out internal signal processing, e.g. for machine learning, in addition to data acquisition. For data analysis with smart sensors, a fully automated machine learning toolbox (see Fig. 1) has been developed [1] which can be used without any expert knowledge and without knowledge of a physical model of the process. In this toolbox, five complementary algorithms for feature extraction (FE) and three for feature selection (FS) are combined and both classification based on the best combination of FE/FS and validation can be carried out. For the

FE, Adaptive Linear Approximation, Principal Component Analysis and the first four statistical moments are used to extract features in the time domain. For extracting features in the frequency domain, the Best Fourier Coefficient method is used and for the time-frequency domain the Best Daubechies Wavelet method is applied. In this unsupervised step, as many features as possible are extracted. After that, a supervised feature selection is performed either with simple Pearson correlation to the target or complex methods, i.e. Recursive Feature Elimination Support Vector Machine or RELIEFF. The objective of this step is to concentrate as much information as possible in as few features as possible and to remove

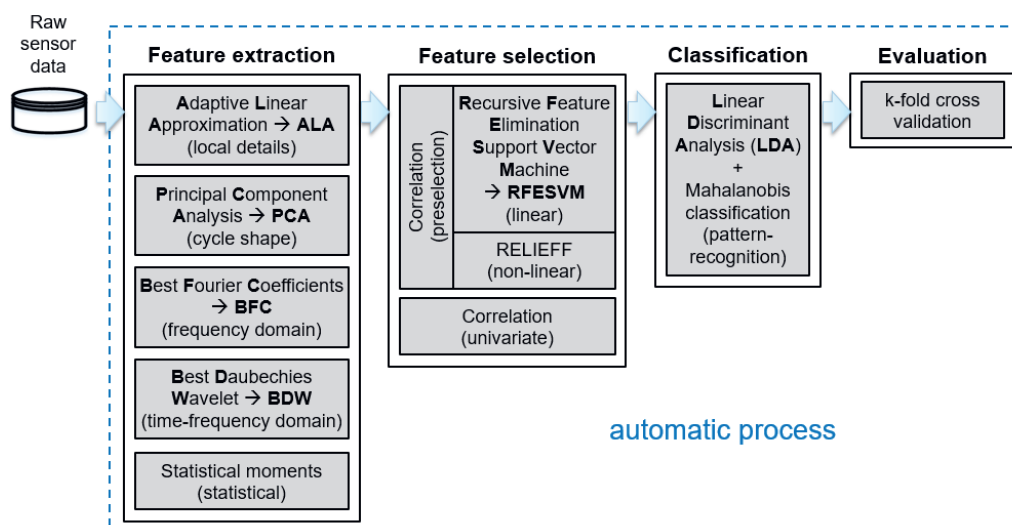


Fig. 1 Schematic of the algorithms implemented in the software toolbox [2]

features with low information content and redundant features from the set of features extracted in the previous step.

However, none of the methods within the toolbox so far consider measurement uncertainty. Recently, propagation of uncertainties for Discrete Fourier transform (DFT) [4] and Discrete Wavelet decomposition (DWT) [to be published soon] have been proposed. In this contribution, the propagation of uncertainties in line with the *Guide to the Expression of Uncertainty in Measurement (GUM)* [3] is applied to feature extraction with *Adaptive Linear Approximation (ALA)*.

Results

ALA approximates a certain time segment of sensor data or a measurement cycle [1] with linear segments of variable length. The mean and the slope of each segment are extracted as features. Dividing the cycle into many segments leads to many features together with a small approximation error and vice versa. When there is no significant decrease of the approximation error when performing an additional split, the algorithm stops automatically. In Fig. 2, the approximation of an original measurement cycle by ten segments is shown.

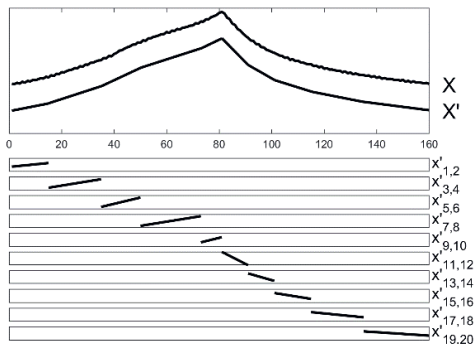


Fig. 2. Approximation X' by mean values (uneven indices) and slopes (even indices) of ten segments determined by ALA compared to the original cycle X (shifted for better clarity).

Since the calculations below are the same for every cycle, they are shown here for one cycle only. Let $Y = (y_1, \dots, y_n) \in \mathbb{R}^{1 \times n}$ denote the real-valued time-domain signal, i.e. one cycle. The result of the ALA for this cycle Y is given by

$$F = (\bar{y}_1, \dots, \bar{y}_{u_3+1}, b_1, \dots, b_{u_3+1}) \in \mathbb{R}^{1 \times 2(u_3+1)},$$

where \bar{y}_k denotes the mean value and b_k the slope of the k -th segment, respectively, of a cycle for $k = 1, \dots, u_3 + 1$. u_3 is the number of splits and therefore, $u_3 + 1$ the number of segments into which the cycle is split.

The mean value and slope for the k -th segment are determined by

$$\bar{y}_k = f(y_i) = \frac{1}{v_{k+1} - v_k} \sum_{i=v_k}^{v_{k+1}} y_i$$

and

$$b_k = h(y_i) = \frac{\sum_{i=v_k}^{v_{k+1}} (t_i - \bar{t}_k)(y_i - \bar{y}_k)}{\sum_{i=v_k}^{v_{k+1}} (t_i - \bar{t}_k)^2}.$$

For the propagation of uncertainties according to GUM, the sensitivities of the mapping $Y \mapsto F$ are given by

$$c_{k,j} = \frac{\partial \bar{y}_k}{\partial y_j} = \frac{1}{v_{k+1} - v_k + 1}$$

and

$$d_{k,j} = \frac{\partial b_k}{\partial y_j} = \frac{t_i - \bar{t}_k}{\sum_{i=v_k}^{v_{k+1}} (t_i - \bar{t}_k)^2},$$

for $j = v_k, \dots, v_{k+1}$. Thus, the sensitivity matrix has a block structure and is given by

$$\mathbf{J}_{\mathbf{y},\mathbf{b}}^m = \begin{pmatrix} \mathbf{C} \\ \mathbf{D} \end{pmatrix} \in \mathbb{R}^{2(u_3+1) \times n}.$$

In the sensitivity matrix, the matrix $\mathbf{C} \in \mathbb{R}^{(u_3+1) \times n}$ denotes the upper submatrix and has the entries $(c_{k,j})_{k=1, \dots, u_3, j=v_k, \dots, v_{k+1}}$. For the submatrix $\mathbf{D} \in \mathbb{R}^{(u_3+1) \times n}$, simply replace \mathbf{C} by \mathbf{D} in the statement above.

The given covariance matrix of the input quantities $\mathbf{U}_y \in \mathbb{R}^{n \times n}$ leads to the following expression for the covariance matrix $\mathbf{U}_F \in \mathbb{R}^{n \times n}$ associated with F :

$$\begin{aligned} \mathbf{U}_F &= \mathbf{J}_{\mathbf{y},\mathbf{b}}^m \cdot \mathbf{U} \cdot \mathbf{J}_{\mathbf{y},\mathbf{b}}^{mT} \\ &= \begin{pmatrix} \mathbf{C} \mathbf{U}_y \mathbf{C}^T & \mathbf{C} \mathbf{U}_y \mathbf{D}^T \\ (\mathbf{C} \mathbf{U}_y \mathbf{D}^T)^T & \mathbf{D} \mathbf{U}_y \mathbf{D}^T \end{pmatrix}. \end{aligned}$$

This block structure of the covariance matrix \mathbf{U}_F can be used to deal with computer memory issues. Since \mathbf{U}_F is symmetric, only three blocks must be stored, see also [4].

Acknowledgement

Part of this work has been developed within the Joint Research project 17IND12 Met4FoF of the European Metrology Programme for Innovation and Research (EMPIR). The EMPIR is jointly funded by the EMPIR participating countries within EURAMET and the European Union.

References

- [1] T. Schneider, N. Helwig, and A. Schütze, "Industrial condition monitoring with smart sensors using automated feature extraction and selection," *Meas. Sci. Technol.*, vol. 29, no. 9, 2018.
- [2] T. Dorst, B. Ludwig, S. Eichstädt, T. Schneider, and A. Schütze, "Metrology for the factory of the future: towards a case study in condition for the factory of the future: towards a case study in condition monitoring," 2019 IEEE International Instrumentation and Measurement Technology Conference (I2MTC), Auckland, New Zealand, pp. 439–443, 2019.
- [3] Joint Committee for Guides in Metrology, "JCGM 100: Evaluation of Measurement Data – Guide to the Expression of Uncertainty in Measurement," JCGM, 2008.
- [4] S. Eichstädt, and V. Wilkens, "GUM2DFT – a software tool for uncertainty evaluation of transient signals in the frequency domain," *Meas. Sci. Technol.*, vol. 27, no. 5, 2016.

Deep Neural Networks for optical form measurements

Lara Hoffmann and Clemens Elster

Physikalisch-Technische Bundesanstalt, Braunschweig and Berlin, Germany

E-mail (corresponding author): lara.hoffmann@ptb.de

Summary:

Deep neural networks have been successfully applied in many different fields like computational imaging, medical healthcare, signal processing or autonomous driving. We demonstrate in a proof-of-principle study that also optical form measurement can benefit from deep learning. A data-driven machine learning approach is considered for solving an inverse problem in the accurate measurements of optical surfaces. The approach is developed and tested using virtual measurements with known ground truth.

Keywords: machine learning, U-Net, inverse problem, virtual experiment, optical form measurement

Motivation

Deep neural networks and machine learning in general enjoy a rapidly growing impact on science and industry. Their application has proven beneficial in many different domains including medical image processing [1], anomaly detection in quality management [2], signal processing [3] or analysis of raw sensor data [4]. The great success of deep networks and machine learning is based on its ability to learn complex relations from data without knowing the underlying physical laws. In this study deep learning is applied to a novel field of applications – to optical form measurements.

Deep neural networks are artificial neural networks with ten and more hidden layers. A basic neural network with a single hidden layer is a nonlinear function $f_{\Phi}: \mathbb{R} \rightarrow \mathbb{R}$, with parameters $\Phi = \{\omega_i, b_i \in \mathbb{R} \mid i = 1, \dots, n\}$, where n is the number of neurons in the hidden layer. The univariate output of the network is modeled through:

$$f_{\Phi}(x) = \sum_{i=1}^n \sigma(\omega_i x + b_i), x \in \mathbb{R},$$

where σ is a nonlinear activation function. In general, input and output can be higher dimensional, and the architecture can get arbitrarily deep by adding more layers. An example deep network architecture is shown in Fig. 1, where two outputs are predicted from three given inputs after processing the information through several hidden layers. The network parameters can be optimized via backpropagation on given training data by minimizing a chosen loss function between the predicted and known output. It is crucial to have sufficiently many, representative training data in order that the trained net generalizes well. While such networks are viewed as

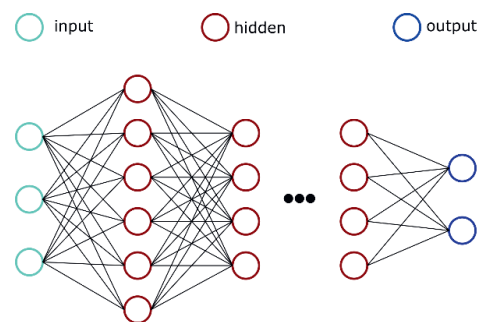


Fig. 1: Schematic of a deep neural network architecture.

black-box functions, techniques such as layer-wise-relevance-propagation [5] have been developed for understanding their behavior.

Accurate measurement techniques become more and more important as technology advances. Any object can be manufactured from a given design just as accurately as it can be measured. The novel deep learning application is based on the tilted-wave interferometer (TWI) [6]. It is a promising technique providing highly accurate reconstructions of optical aspheres and freeform surfaces using contact-free interferometric measurements. A scheme of the TWI is shown in Fig. 2. Multiple wavefronts are created from a 2D point source array. The rays pass

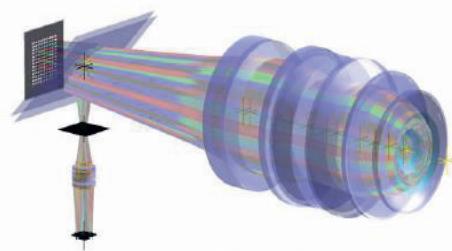


Fig. 2: Schematic of the tilted-wave interferometer without reference arm.

through various optical elements including the surface of the specimen under test and interfere at the CCD with rays from a reference arm. The test topography is then reconstructed by solving a numerically expensive inverse problem from the measured intensity images at the CCD.

Methods

The simulation toolbox SimOptDevice [7] has been used to construct a database of virtual measurement results. The test topographies were constructed by altering a specified design topography through adding random deviations. Fig. 3 shows some of these generated deviations. The simulation toolbox was applied to calculate the optical path length differences obtained for each test topography and for the design topography. In a real measurement, the optical path length differences for the specimen under test are measured by the CCD, while those of the design are calculated virtually. The constructed data base consists of 22.000 test topographies, together with the corresponding optical path length differences.

The data base was split into a training and test set. The latter contains 10% of randomly drawn samples from the data base. A U-Net [8] architecture with 69 layers was chosen to solve the inverse problem of reconstructing the test topography from the optical path length differences. A U-Net is a deep neural network with bottleneck structure and skip-connections. All data have been normalized prior to feeding the network. About two hours of training were carried out using the Adam optimizer, with an initial learning rate of 0.0005 with drop factor 0.75 every 5 periods and a mini batch size of 64. Training has been stabilized by applying a 2-norm regularization of the network parameters with a regularization parameter equal to 0.004.

Results and Conclusion

The trained network has been applied to predict the topographies from the optical path length differences for all cases in the test set. Note that none of the cases in the test set has been used for training. Fig. 3 shows some example results. The root mean squared error of the reconstructed topographies on the test set was 35 nm, compared with 560 nm root mean squared deviations between the test topographies and the design topography.

The obtained results are encouraging and suggest that deep learning can be successfully applied in the context of optical form measurements. The presented results are based on simulated data only and they constitute a proof-of-principle rather than a final method ready for application. Testing the approach on real measurements and accounting for fine-

tuning such as the calibration of the numerical model of the experiment are next steps. Nevertheless, these first results are encouraging and once trained, a neural network solves the inverse problem orders of magnitudes faster than currently applied conventional methods. We conclude from our findings that also optical form metrology can benefit from deep learning.

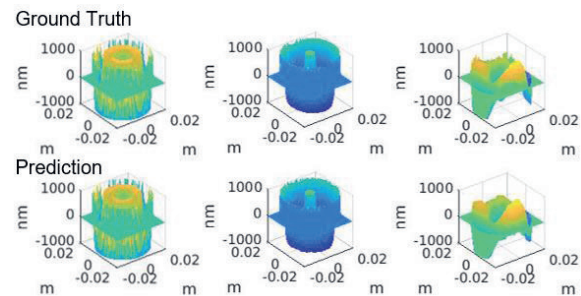


Fig. 3: Deep network results on random test data: ground truth and prediction.

Acknowledgement

The authors thank Manuel Stavridis for providing the software tool SimOptDevice and Ines Fortmeier and Michael Schulz for helpful discussions about optical form measurements.

References

- [1] A. Maier C. Syben, T. Lasser, C. Riess, "A gentle introduction to deep learning in medical image processing", *Zeitschrift für Medizinische Physik*, vol. 29, no. 2, pp. 86-101, 2019.
- [2] B. Staar, M. Lütjen, M. Freitag, "Anomaly detection with convolutional neural networks for industrial surface inspection", 2018 CIRP Conference on Intelligent Computation in Manufacturing Eng., Gulf of Naples, Italy, pp. 484-489, 2019.
- [3] A. Mousavi, R. Baraniuk, "Learning to invert: Signal recovery via deep convolutional networks", *IEEE Intern. Conf. on Acoustics, Speech and Signal Processing (ICASSP)*, pp. 2272-2276, 2017.
- [4] A. Moraru, M. Pesko, M. Porcius, C. Fortuna, D. Mladenic, "Using Machine Learning on Sensor Data", *J. of Computing and Information Technol.*, vol. 18, no. 4, 2010.
- [5] S. Bach, A. Binder, G. Montavon, F. Klauschen, K.-R. Müller, W. Samek, "On pixel-wise explanations for non-linear classifier decisions by layer-wise relevance propagation", *PLOS ONE*, vol. 10, no. 6, p. e0130140, 2015.
- [6] I. Fortmeier, M. Stavridis, A. Wiegmann, M. Schulz, W. Osten, C. Elster, "Evaluation of absolute form measurements using tilted-wave interferometer", *Optics Express*, vol. 24, no. 4, pp. 3393-3404, 2016.
- [7] R. Schachtschneider, M. Stavridis, I. Fortmeier, M. Schulz, C. Elster, "SimOptDevice: a library for virtual optical experiments", *J. Sens. Sens. Syst.*, vol. 5, pp. 105-110, 2019.
- [8] O. Ronneberger, P. Fischer, T. Brox, "U-Net: Convolutional Networks for Biomedical Image Segmentation", *MICCAI*, pp. 234-241, 2015.

Metrological support of VNIIFTRI for air ions measurements

Pavel N. Zubkov, Narine G. Oganyan,

*1All-Russian Scientific Research Institute of Physicotechnical and Radio Engineering Measurements (VNIIFTRI), Mendeleevo, Moscow region, Russia, 141570
zubkov@vniiftri.ru*

One of the parameters controlled in Russia that characterizes the cleanliness of the working space is the content of ions in a defined volume of air [1,2]. Air ions are the smallest complexes of atoms or molecules in the air that have a positive or negative charge. Under natural conditions, there are always positively and negatively charged light air ions in the open space air (air of forests, fields, seas and mountains). Scientists have detected a number of remarkable facts. The use of light air ions with negative polarity permits to reduce fatigability and tiredness, and accelerates rehabilitation from fatigue. However, constant presence of many people in a room, placement of equipment in small areas, increased electrostatic or electromagnetic field around the equipment, use of finishing materials that are not suitable for rooms with electronic equipment, leads to the degradation of air ion content in the air. Therefore, in production facilities and in offices it is necessary to control and maintain the ionic composition of the air. In addition, the content of ions in the air is the main quality indicator in aero onotherapy, where, in order to achieve a therapeutic effect, certain normalized concentration of negative ions in the air is necessary [2].

In order to provide metrological support in the field of measurement of air ions, the State Primary Standard for Volumetric Units of Volume Density of the Electric Charge of Ionized Air and the Number Concentration of air ions - GET 177-2010 has been developed [3-9] and has been successfully operated since 2010.

Metrological characteristics of the standard are:

- the range of units of polar volumetric density of the electric charge (number concentration) of air ions is from $1.6 \cdot 10^{-2}$ to $200 \text{ nC} \cdot \text{m}^{-3}$ (from 108 to $1.2 \cdot 10^{12} \text{ m}^{-3}$);
- expanded uncertainty $U_p = 7,5 \%$ with a coverage factor $k = 2$ and confidence level of $p = 0.99$.

In this field of measurement, VNIIFTRI provides metrological services for calibration and verification of measuring instruments, metrological expertise, tests for type approval, and develops working standards [10-12]. Over the past three years, on the basis of VNIIFTRI, two working standards ("REKLA-1" and "REKLA-1M") for units of polar volumetric density of electric charge and number concentration of air ions were developed to equip Federal regional metrological centers of metrological services (Nizhny Novgorod FMC and Novosibirsk FMC).

References

- [1] SanPiN 2.1.3.2630-10 "Sanitary and epidemiological requirements for organizations engaged in medical activities." (in Rus.)
- [2] SanPiN 2.2.4.1294-03 "Hygienic requirements for the aeroionic composition of air in industrial and public buildings. Sanitary and epidemiological rules and standards." (in Rus.)

- [3] Karpov, O.V., Kolersky, S.V., Zhuralev A.V., Kolerskaya, S.S. and Zubkov, P.N.: Measurement of air ions parameters by the integrated aspiration condenser method, Sci. sess. of NRNU MEPhI-2012. Abstracts, 2012, 225. (in Rus.)
- [4] Kolersky, S.V., Zhuralev A.V., Kolerskaya, S.S. and Zubkov, P.N.: Transfer of the unit of light air ions number concentration from the standard to the measuring instruments, Measur. Technique, 2013, 5, 47-49. (in Rus.)
- [5] Zubkov, P.N.: The application of dispersion analysis in the calibration of light aeroion counters, Metrology in the 21st cent. Abstracts of the sci. and tech. conf. of young scientists, graduate students and specialists, VNIIFTRI, 2014, 136-138. (in Rus.)
- [6] Kolersky, S.V. and Zubkov, P.N.: About a transfer the unit of the conductivity of air at small values, Sci. sess. Of NRNU MEPhI-2015, Abstracts, 2015, 279. (in Rus.)
- [7] Zubkov, P.N.: Study of the effect of atmospheric pressure and air temperature on the reproduction of the units of the light aeroions number concentration by the standard - GET 177-2010, Metrology in the 21st cent., Abstracts of the III sci. and tech. conf. of young scientists, graduate students and specialists, VNIIFTRI, 2015, 37-43. (in Rus.)
- [8] Zubkov, P.N.: The effect of atmospheric pressure and air temperature on the reproduction of a unit of the number concentration of light air ions by the radionuclide method, Measur. Technique, 2019, 7, 58-61. (in Rus.)
- [9] Dobrovolskiy, V.I., Kolersky, S.V., Zubkov, P.N. and Nechaev, N.V.: The effectiveness of the aspiration condenser method for verification and calibration of air conductivity meters, Measur. Technique, 2016, 4, 62-64. (in Rus.)
- [10] Zubkov, P., Kolersky, S. and Kolerskaya, S.: Evaluation of the effect of space charge on the accuracy characteristics of air-ionometric equipment. Scientific Session of NRNU MEPhI-2014. Abstracts, 2, 186. (in Rus.)
- [11] Zubkov, P., Dobrovolskiy, V.I., Kolersky, S.V. and Kolerskaya, S.S.: Testing installations - working standards of the number concentration of light air ions, Almanac of modern metrology, 2016, 6, 117-123. (in Rus.)
- [12] Nechaev, N., Kolersky, S. and Zubkov, P.: Light Air Ions Generators and Air Ion Concentration Working Standards, J. Phys: Conf. Ser., 1420, 012028, doi:10.1088/1742-6596/1420/1/012028.

Traceable Measurements of Harmonic (2 – 150 kHz) Emissions in Smart Grids

Daniela Istrate¹, Deepak Amaripadath¹, Etienne Toutain², Robin Roche³, Fei Gao³

¹ LNE, 29 av. Roger Hennequin, 78197, Trappes, France,

² EDF, Lab Les Renardières, 77250 Moret-sur-Loing, France,

³ Univ. Bourgogne Franche-Comté, 90010 Belfort, France

daniela.istrate@lne.fr

Summary:

The paper aims to study the supraharmmonic emissions in the frequency range of 2 to 150 kHz. The research applied the design of experience approach and a statistically based analysis method to identify the sources of the supraharmmonic emission from field measurements on a smart grid. A generic waveform platform was designed and metrological characterized both for the generation and for the acquisition part. The characterization was done in the French Electrical Metrology Laboratory, the obtained expanded uncertainty is $\pm 1\%$ for the harmonic amplitude.

Keywords: Supraharmmonic, Design of experience, Analysis of variance, Smart grids, Uncertainty

Harmonic emissions

The state-of-the art analysis indicates the supraharmmonic emissions (emissions from the grid equipment in the frequency range of 2 to 150 kHz) as one of the significant PQ issues in the smart grids appearing with the renewable energy sources [1], [2]. Two relevant challenging aspects emerged from this analysis: design the appropriate measurement system, create the measurement plan. The metrological characterization of the flexible measurement system based on 4 acquisition channels is described in this paper.

Identifying the sources of the supraharmmonic emissions in the electrical networks with multiple equipment is challenging due to interactions between the equipment. In this context, our approach relies on the Design of Experiment (DoE) and the Analysis of Variances (ANOVA) statistical method for the network analysis [3].

Measurement system: traceable calibration

The main challenges in the measurement of supraharmmonic emissions are: low amplitudes at high frequencies, non-invasive connections (sensors) for the public electrical networks, recording with high resolution and dynamic range to acquire even the smallest emissions.

The measurement system was designed [4] to be flexible and by considering safety aspects in the electrical network. Two channels are dedicated to voltage measurement and two other channels are used for the current measurement. These channels measure fundamental

and supraharmmonic components separately in order to maximize the dynamic range of the recording device.

The measurement and acquisition system was metrological characterized in the French Electrical Metrology Laboratory in a controlled environment and by means of the calibrated references. This guarantees the traceability of the measurement system and a low level of uncertainties. The linearity with the voltage, respectively the current levels and the frequency response were obtained for all 4 channels. These results lead to the implementation of the adequate corrections. The uncertainty components were estimated both for amplitude and time acquisitions. Repeatability, reproducibility, stability, average daily drift, resolution are evaluated both for fundamental and supraharmonics. In addition, the influences of the factors, such as Fast Fourier transform windows, noise, and cable length on the waveform platform are estimated. The expanded uncertainty ($k = 2$) of the waveform platform is obtained as $\pm 1\%$ for the amplitude of the studied harmonics.

Measurement principle

The supraharmmonic emissions are generated by the electronic converters used in the equipment, such as the PV inverters (PVI), electric vehicle chargers (EVC), heat pumps etc. The network measurement campaign with multiple factors and high sampling rate is challenging and time consuming due to the large amount of the measured data, and the required subsequent data analysis. Therefore, the Design of

Experience (DoE) approach was used. Four factors that influence the generation of supra-harmonic emissions are considered: the generation equipment: i) low power, PVI_R and ii) high power, PVI_I , iii) the load and iv) the measurement point location, MP. The applied DoE is a full factorial plan at two levels of operation. Once the factors and their position identified, an additive model with interaction effect is chosen. All possible combinations of the two levels of each factor are considered. The measurements are done on the Concept Grid platform according to the results of the chosen model. For each configuration, fundamental and supraharmonic components of both voltage and current waveforms were acquired simultaneously.

Results

The results of the measured data processing are available both in terms of harmonic amplitudes for the frequency components identified both in voltage and current signals and in terms of statistical table (Tab. 1) whose cells show the importance of the individual effects and of the interactions between factors. A color code indicates if a factor or the relationship between 2 factors is highly significant (red) or not (white).

Conclusions

The electrical network tests were carried out in the Concept Grid platform. The measurement and acquisition system is characterized and uncertainty budget is determined.

The voltage emissions are more prevalent at higher frequencies compared to the current

Tab. 1 ANOVA results

Waveform	Frequency (kHz)	Individual Effects				Interactions				
		PVI_R	PVI_I	Load	MP	PVI_R PVI_I	PVI_R MP	Load MP	PVI_I Load	PVI_I MP
Voltage	2-4									
	9-11									
	19-21									
	39-41									
	59-61									
	79-81									
	99-101									
	119-121									
Current	2-4									
	9-11									
	19-21									
	39-41									
	59-61									
	79-81									
	99-101									
	119-121									
139-141										

emissions. The load and MP are the main factors, which influence the higher voltage emissions in the frequency range of 2 to 150 kHz. The interactions between the Load and MP are highly significant for the voltage emissions in the frequency range of 9 to 11 kHz, and significant for the voltage emissions in the frequency range of 79 to 150 kHz.

Acknowledgment

This project has received funding from the European Union’s Horizon 2020 research and innovation programme under Grant Agreement No. 676042.

References

[1] S. Rönnerberg and M. Bollen, “Power Quality Issues in the Electric Power System of the Future,” *The Electricity Journal* 29, 49-61 (2016).

[2] M. Klatt, J. Meyer, P. Schegner, A. Koch, J. Myrzik, T. Darda, and G. Eberl, “Emission Levels Above 2 kHz - Laboratory Results and Survey Measurements in Public Low Voltage Grids,” *CIGRE*, 1-4 (2013) DOI: 10.1049/cp.2013.1102

[3] D. C. Montgomery, Design and Analysis of Experiments, 7th ed., New York, NY, USA: *John Wiley & Sons*, 12-13 (2008)

[4] D. Amaripadath and others, “Measurement and Analysis of Supraharmonic Emissions in Smart Grids”, *Proc. of UPEC* (2019)

Calibration Service as a Gateway to Sustainable Research and Development

Michael Melzer¹, Michael Fischer¹, Marcus Thomas¹, Andreas Subaric-Leitis¹, Matthias Bartholmai¹
¹ Bundesanstalt für Materialforschung und –prüfung (BAM), Unter den Eichen 87
 12205 Berlin, Germany

michael.melzer@bam.de

Summary:

Over decades, the German Federal Institute for Materials Research and Testing (BAM) has established a sophisticated calibration laboratory for force, temperature and electrical quantities. Since more than 15 years it is accredited, currently by the national accreditation body (DAkkS), and offers its service also to external entities on a global scale. As a public provider, we are furthermore committed to research and development activities that demand measurements with highest quality and low level of uncertainties. Two R&D examples are highlighted within this contribution.

Keywords: calibration of force, calibration of temperature, calibration of electrical quantities, measurement uncertainty, new sensor principles

Measurement and Calibration Capabilities

Calibration and testing are key elements in the field of activities of the Federal Institute for Materials Research and Testing (BAM), which is dedicated to safety in technology and chemistry. In order to ensure the reliable metrological traceability of its measuring equipment, BAM maintains its own calibration laboratory and optimized it over many years to achieve excellent conditions for highly precise measurements.

This particularly includes highly stable environmental conditions with minimum impact of perturbing thermal, mechanical, radiative or acoustic factors as well as a comprehensive inventory of high-end measuring equipment and calibration standards and facilities. Most of the reference standards in operation are directly linked to national standards, allowing small measurement uncertainties to be provided. Furthermore, we can rely on a profound expertise acquired over many years of dedicated operation. The BAM calibration lab is accredited to comply with the respective requirements of ISO/IEC 17025 since 2009 (ID: D-K-11075-08-00), confirming the effectiveness of its up-to-date quality management system and its competence in calibration. An extract from the scope of accredited calibrations, including its associated minimum measurement uncertainties, can be found in Table 1.

Tab. 1. Extract of the scope of accredited calibrations. Given are the best measurement capabilities ($k = 2$), the full scope can be found in [1].

Quantity	Range	Capability [1]
Force		
Tensile and compressive	10 N to 2 kN	0.01%
	0.4 kN to 5 MN	0.02%
Compressive	4 MN to 21 MN	0.1%
Temperature		
PRTs (e.g. Pt100)	-50°C to 160°C	0.03 K
Non noble TCs	-50°C to 160°C	0.25 K
Noble TCs	0°C to 160°C	0.5 K
Electrical		
DC current	>100 nA to 20 A	>1 nA
DC voltage	0 μ V to 1000 V	>1 μ V
DC resistance	100 $\mu\Omega$ to 1 G Ω	>4 ppm
Charge	5 pC to 100 nC	>0.1%
Voltage ratio	\pm [2 to 50] mV/V	>0.03 μ V/V

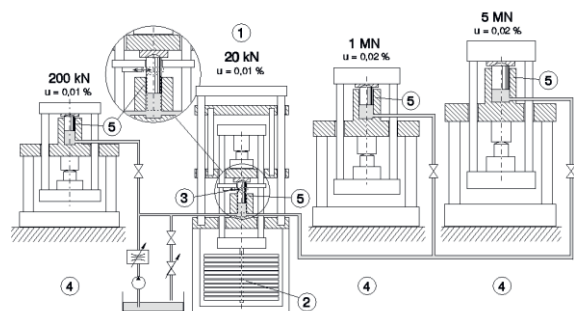


Fig. 1. Dead-weight force reference standard facility at BAM: (1) Dead-weight equipment and managing system, (2) Dead-weight stack up to 20 kN, (3) Hydraulic abutment, (4) Hydraulic connection, (5) Rotating pistons.

One of the core facilities at the BAM calibration lab is the hydraulically transmitted dead-weight force reference standard that provides a cascaded application of defined load up to 5 MN, as schematically depicted in Fig. 1.

Hydraulically Balanced Build-Up System for Load Measurements up to 25 MN

In order to satisfy the increasing demand for large force measurements, several high-load force transducers can be assembled in parallel to form a build-up system (BUS) [2]. In this way, five off-the-shelf 5 MN load cells can measure a compressive force of up to 25 MN. As such a system can also be operated with a lower number of cells, it represents a cost effective and versatile tool for a large range of precise high-load measurements, compared to a single custom-designed transducer for larger forces.

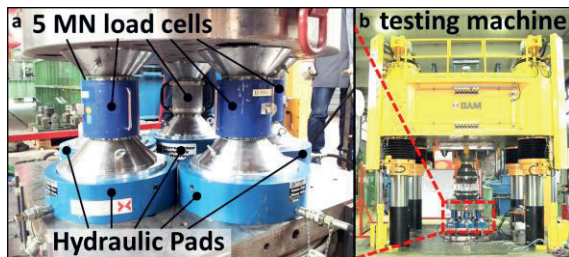


Fig. 2. 5x5 MN build-up system with hydraulic balancing (a), installed into the 25 MN testing machine at BAM (b).

BAM developed a coupled hydraulic balancing system for such BUS, as shown in Fig. 2a, which allows a homogeneous force distribution into the individual load cells, to achieve maximum load capacity also under unfavorable conditions. In addition, it allows generating defined off-axis loads on demand, without any retooling. Thorough traceable calibration of the single 5 MN load cells is necessary to achieve an expanded measurement uncertainty of down to 0.1% for the 25 MN BUS. Furthermore, the BAM calibration lab conducted comparative measurements of the entire system with static BUS: 3x7 MN from the Swiss Federal Laboratories for Materials Science and Technology (EMPA) [3] and 3x10 MN from the German National Metrology Institute (PTB), as depicted in Fig. 2b. As a result, the scope of our accredited calibrations for compressive force was extended to 21 MN.

In-situ Measurements of the Tension Robe Stress in Pretensioned Concrete

The life cycle of pretensioned concrete based infrastructure, particularly bridges, significantly depends on the condition of its tension robes. The impact of aging on the resilience of the buried metal tension robes is not fully understood, yet.

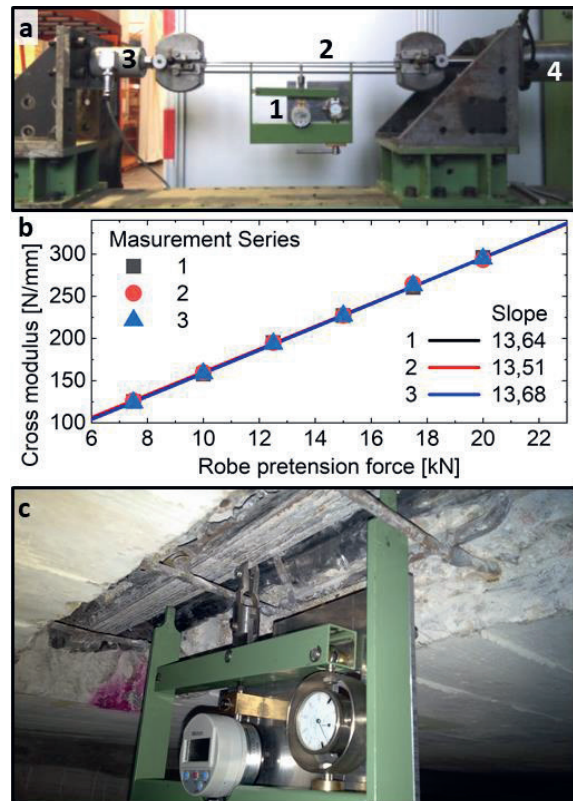


Fig. 3. Tension robe measuring bracket. a) mounted in the calibration setup with 1: the bracket, 2: pretension string, 3: tensile force transducer, 4: tensioner. b) response curve, c) mounted on Leinebridge for in-situ measurements.

BAM developed a specific measuring bracket to determine the prestress of a single partially excavated tensioning string via a perpendicular stress-strain test. [4] Comprehensive calibrations of the novel device in dependence of well-defined pretensions on a withdrawn real-aged string specimen were performed (Fig. 3a) in order to generate the characteristic response curve presented in Fig. 3b. By using the calibration parameters thus derived, measurements of individual tensioning robes were performed *in-situ* on an operating bridge, in a minimal invasive fashion, as shown in Fig. 3c.

References

- [1] www.dakks.de/as/ast/d/D-K-11075-08-00.pdf
- [2] A. Schäfer, Examples and proposed solutions regarding the growing importance of calibration of high nominal forces, *Proceedings of the IMEKO*, Pattaya, Thailand (2010).
- [3] B. Seiffert, C. Ullner; W. Honegger, W. Sennhauser, Investigation and Verification of Ultra-high Force Testing Machines, *Proceedings of the EUROLAB*, Dübendorf, Switzerland (2001).
- [4] A. Subaric-Leitis, Verfahrensvalidierung und Ergebnisunsicherheit am Beispiel der Spannkraftermittlung in Spannstählen, 4. VDI-Fachtagung Messunsicherheit, Erfurt (2008).

Calibration of Digital Dynamic Pressure Sensors

Recep Yilmaz¹, Yasin Durgut¹, Abdullah Hamarat¹

¹. TUBITAK UME, National Metrology Institute, Pressure Laboratory, Kocaeli, Turkey

Summary:

In dynamic pressure measurement phenomena, dynamic pressure calibration of the measurement chain including a pressure sensor, signal conditioning amplifier and data acquisition part is required. Some applications show time-invariant static characteristics, so certain types of transducers can be used to measure such static time-invariant value of pressure. The aim of this study is to modify and realise dynamic calibration methods for digital sensors inside calibration facilities and calibrating a dynamic digital sensor by using the newly developed dynamic calibration system

..

Keywords: Dynamic, pressure, calibration, digital, sensor, DTI

Introduction

Traceability for digital sensors in dynamic measurements and practical MEMS calibration services is currently completely lacking NMI-level or accredited calibration services. This is a consequence of the lack of adequate technical set-ups and procedures as well as normative standards [1]. If pressure value is changing by time or in other saying if it is time-dependent, it is defined as dynamic because it varies significantly in a short period of time demanding a dynamic calibration.

Dynamic Calibration System

National Metrology Institute of Turkey (TUBITAK UME) has developed a measurement standard based on dropping mass principle for dynamic calibration machine of pressure transducers. It uses conservation of energy which is the well-known basic physical law. (see Fig. 1). Drop mass system transfers the produced kinetic energy by free dropped mass to the sensor under test. The system can create a half-sinus signal with a width of around 5 ms for calibration of dynamic pressure transducers up to 500 MPa in hydraulic media with relative uncertainty 2% [2].

TUBITAK UME has a drop mass system with a measurement range from 50 MPa to 500 MPa. The distance between dropping mass and the piston is adjustable from 5 mm to 300 mm. There are piezoelectric based reference pressure sensors up to 500 MPa. The dynamic calibration system is able to produce a triggering signal from built-in PLC (programmable logic controller) for some purposes. In the measurement, it is planned to use the triggering signal to the trig DTI module.

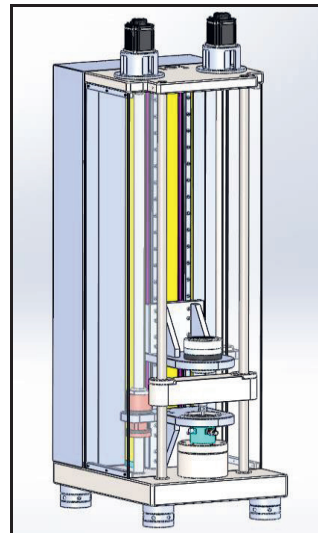


Fig. 1. Design of Dropping mass dynamic calibration system

In order to obtain testing pulse pressure, it uses a dropping mass on to a piston, increasing the pressure in the hydraulic medium by up to some hundreds of MPa in order to perform a quick and accurate check and calibration of high-pressure dynamic sensors. (see Fig. 1,2). The pulse amplitude level is adjusted by changing the dropping height of the dropping mass [3].

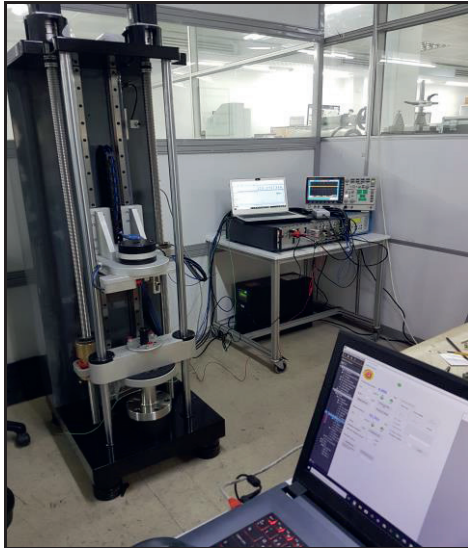


Fig. 2. Dropping mass dynamic calibration system

Calibration of Digital Pressure Sensors

The challenge in dynamic calibration is that traditionally, dealing with analogue signals, the timekeeping was managed by the calibration system. Such centralized time management was the enabling technology for synchronous sampling and hence, calibration of phase-response. The autonomous timing of digital sensors is currently impeding the phase response characterization and requires new concepts for the full characterization of the dynamic response of sensors with digitally pre-processed output are needed.

In the dynamic calibration system, there is a vessel equipped with a piston-cylinder unit, reference and test sensor. Glycerol is used as a pressure transmission media. The vessel has two ports usually used for the device under test DUT (port1) and reference pressure sensor (port 2). Pressure vessel and measurement set-up for calibration of the digital pressure sensor (see Fig. 3).

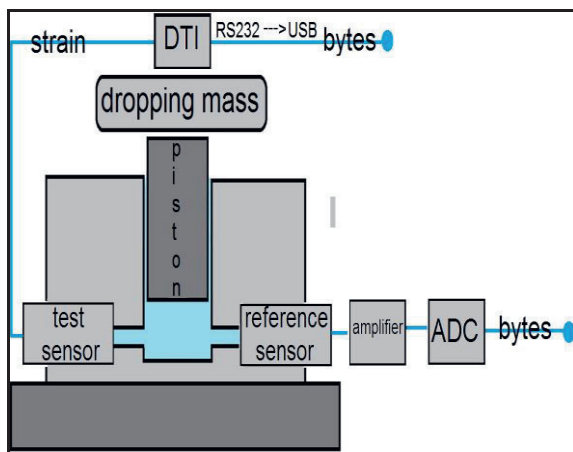


Fig. 3. Pressure vessel and measurement set-up for calibration of a digital pressure sensor

As DUT HBM P3TCP 10kbar transducer sensor together with the digital transducer interface (DTI) module.

Measurement intensities will be up to 500 MPa. One additional precondition for the DTI module is a trigger pulse/step provided by PLC on the dynamic pressure calibration system in order to start the acquisition. Since the transducer has a mounting thread of 20x1.5 mm we needed to modify our measurement system that is given in Fig. 2.

The DTI module is a very small circuit board which provides the equivalent to a bridge amplifier joint with an ADC. It needs an external trigger and once it receives that it starts sampling immediately with 20kS/s for 190 ms. After that, we read out the buffer and gather the samples. The trigger is a rising edge of ca. 3V which can be generated/adapted by an oscilloscope with an external trigger output. A measurement protocol is going to be used for the measurement. (see Tab. 1).

Tab. 1: Measurement protocol

Nominal pressure (MPa)	Reference pressure (MPa)	DUT pressure (MPa)
50	The output of the reference pressure sensor will be given for corresponding pressures	The output of the reference pressure sensor will be given for corresponding pressures
100		
200		
300		
400		

References

- [1] EMPIR 17IND12 Met4FoF Metrology for the Factory of the Future, Annex I-JRP Protocol, 2018
- [2] Bilgic, E., Durgut, Y. "Effects of Waveform Model on Sensitivity Values of Transducers Used in Mechanical Dynamic Measurements ", Acta Physica Polonica A, 128:2-B (2015): B-267-B-270
- [3] Durgut, Y., Bagci, E., Aksahin, E., Ince, A.T. "An Investigation on Characterization of Dynamic Pressure Transducers Using Material Impact Test Machine", Journal of the Brazilian Society of Mechanical Sciences and Engineering, 39:9 (2017): 3645–3655

Acknowledgement

This study was performed under the European joint research project named EMPIR 17IND12 Met4FoF Metrology for the Factory of the Future has received funding from the European Union. The EMPIR initiative is co-funded by the European Union's Horizon 2020 research and innovation programme and the EMPIR participating states.

Statistical Analysis of Nonlinear Time Series Based on Bearing Dynamic Response

Nicolas Meier¹, Bartłomiej Ambrożkiewicz², Grzegorz Litak², Anthimos Georgiadis¹
¹ *Leuphana University of Lüneburg, Universitätsallee 1, 21335 Lüneburg, Germany*
² *Lublin University of Technology, Nadbystrzycka 36, 20-618 Lublin, Poland*
 Corresponding Author's e-mail address: nicolas.meier@leuphana.de

Summary:

In the paper, the statistical analysis of nonlinear time series obtained from measurements of bearing vibrations is conducted. Data are collected from two different type and independent sensors, registering bearing vibrations in two axes. The measurements are mainly used to study bearing dynamic response with different radial internal clearance (RIC). In this paper time series of two different sensors are compared aiming to find correlations between mentioned design parameter and system's behavior.

Keywords: Ball Bearings, Bearing Clearance, Nonlinear Dynamics, Statistical Analysis, Statistical Measures

Introduction

One of the most important parameters in bearing design and exploitation is its radial internal clearance (RIC), which means the distance through which one ring can move to the other in the radial direction. From the bearing performance point of view, the radial clearance is one of the most influential parameters on the tribological phenomena and its proper setting ensures long-time, the maintenance free machine operation [1-2]. The bearing type used to the research is double row self-aligning ball bearing NTN 2309SK with tapered bore. In the bearing with such bore it's possible to change its radial clearance by fastening or loosening dedicated adapter sleeve. Such mounted bearing is taken under precise measurement of the distance between balls and raceways by automated system for measuring the radial clearance of rolling bearings [3-4]. Different value of clearance in the same type of ball bearing means the change in the dynamic response. In order to research bearing's behavior with different clearance, it is mounted in the bearing node. Two different kind of sensors, piezoelectric and MEMS are attached to the bearing's housing in two axes to measure bearing's vibrations. The experiment is performed for 6 different values of clearance and for 1 rotational velocity, in total we obtain 6 cases. In order to find correlation between considered parameter and dynamic response, statistical analysis of time series is performed using mean, standard deviation and kurtosis.

Experimental setup

Measurement procedure starts with setting radial clearance by fastening or loosening adapter sleeve dedicated to the bearing. Such axially loaded bearing is mounted on shaft's journal of automated system for measuring the radial clearance of bearing (see Fig. 1). On the setup, the clearance is measured 3 times and the final value is averaged. Bearing after measurements is mounted in the gearbox (see Fig.2 and Fig.3). The data are collected for only one fixed bearing. In the gearbox, 2 sensors are mounted to the housing (see Fig. 4) and acceleration's results are collected in plane perpendicular to the bearing's axis. Third component along bearing axis can be neglected in case its fixed, longitudinal displacement is very low in its amplitude.

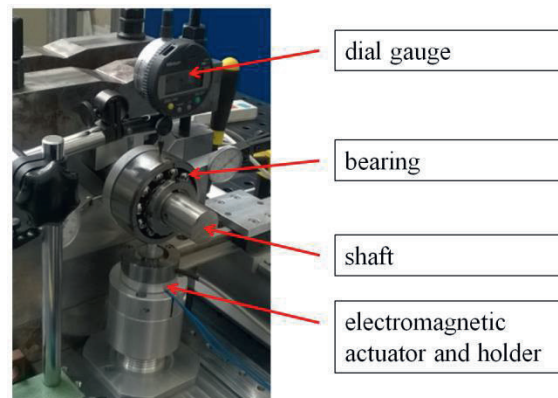


Fig. 1. Clearance measurement setup with a double row self-aligning ball bearing with tapered bore and adapter sleeve.

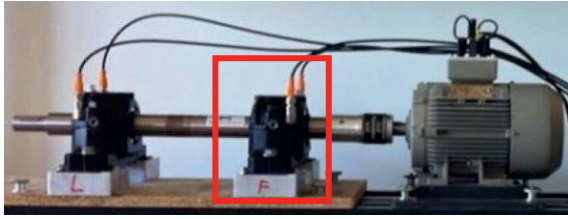


Fig. 2. Experimental gearbox. Red rectangle indicates tested bearing. Two accelerometers are mounted on the housing.

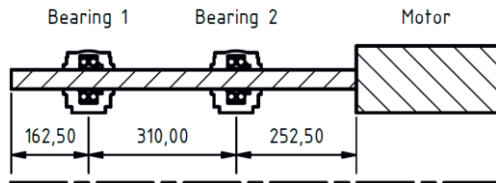


Fig. 3. Cross-section view of gearbox. In bearing node, bearing 1 is floating and bearing 2 is fixed.

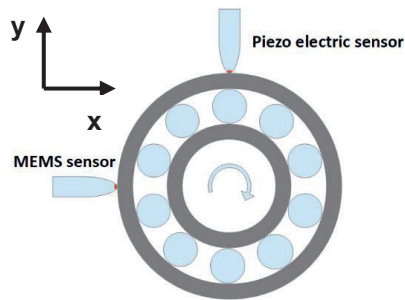


Fig. 4. Illustration of bearing with attached sensors. Data are collected from two axes.

Results

In this paper we consider only measurements by one rotational velocity $n = 10\text{Hz}$ and several values of radial internal clearance from different classes: $\text{RIC} = \{7; 20; 22; 34; 41; 46\} [\mu\text{m}]$. For the analysis of raw signal 15000 data points are taken into account (see Fig. 5) collected with sampling frequency $f_s = 392\text{Hz}$. Whole signal is analyzed both from x-axis and y-axis and they are evaluated separately. For the statistical analysis are used mean, standard deviation and kurtosis (see Fig. 6, Fig. 7 and Fig. 8).

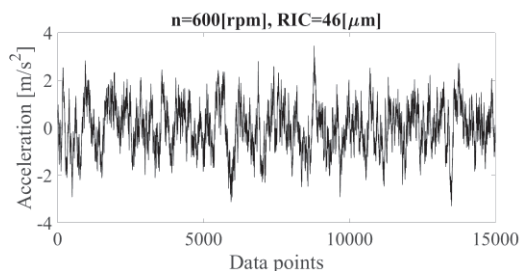


Fig. 5. Exemplary raw signal from x-axis.

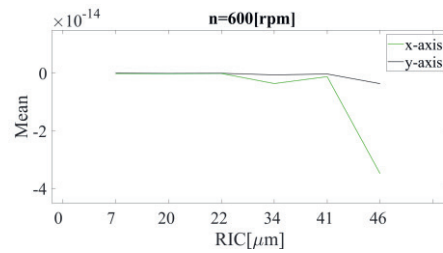


Fig. 6. Mean of the signal in RIC domain.

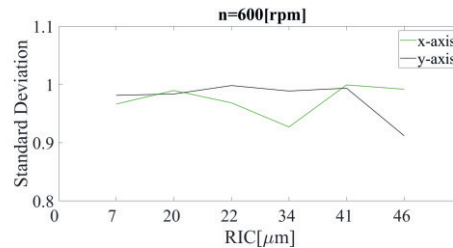


Fig. 7. Standard deviation of the signal in RIC domain.

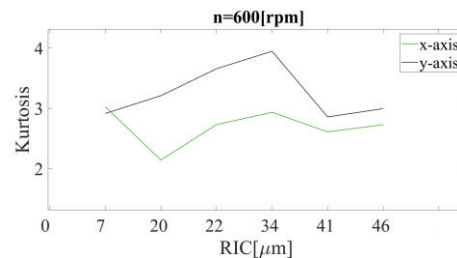


Fig. 8. Kurtosis of the signal in RIC domain.

Conclusions

The first results show that using this simple analysis the optimal value of RIC can be detected. The x-axis signal clearly shows the optimum clearance as given by the specification of the bearing ($16 \mu\text{m} - 22 \mu\text{m}$). Also the standard deviation detects this optimum. Accordingly, these methods could be used to monitor changes of RIC during application.

Bibliography

- [1] R. Ganesan, Dynamic response and stability of a rotor-support system with nonsymmetric bearing clearances, *Mechanism and Machine Theory* 31(6), 781–798 (1996).
- [2] M. Tiwari, et al., Effect of radial internal clearance of a ball bearing on the dynamics of a balanced horizontal rotor, *Journal of Sound and Vibration* 238(5), 723–756 (2000).
- [3] N. Meier, J. Papadoudis, A. Georgiadis, Automated system for measuring the radial clearance of rolling bearings, *Sensors and Measuring Systems; 19th ITG/GMA-Symposium* (2018).
- [4] N. Meier, B. Ambrożkiewicz, A. Georgiadis G. Litak, Verification of measuring the bearing clearance using kurtosis, recurrences and neural networks and comparison of these approaches, *18th IEEE Sensors Conference* (2019).

Outline for a radiometric unit of measure to characterize SWIR illumination

M. Hübner¹, A. Richards²

¹ HENSOLDT Optronics GmbH, Carl-Zeiss Strasse 22, 73447 Oberkochen, Germany,

² FLIR Systems, Inc. Wilsonville, OR USA
martin.huebner@hensoldt.net

Summary:

Imaging in the shortwave infrared (SWIR, 0.9-1.7 μm) is increasingly utilized in applications like security or military surveillance, industrial quality control, food and agricultural inspection and it is foreseen to be used in the fast developing market for advanced driver assistance systems (ADAS). All applications suffer from a lack of a standardized SWIR radiometric unit of measure, that can be used to definitely compare or predict SWIR camera performance with respect to SNR and range metrics. We outline the definition of a unit comparable to the photometric illuminance lux unit and show proposals for its implementation.

Keywords: SWIR, swux, InGaAs, radiometry, photometry

SWIR irradiance backgrounds do not consistently track visible-light illumination at all, [1] [2]. Nevertheless, in most system test reports of imaging devices relying on the short wave infrared spectral range, photometric units for the visible light are still used to characterize the illumination conditions. For the SWIR waveband we introduce the implementation of a new unit of illumination measurement, that is spectrally weighted to the standard lattice-matched InGaAs absorption, as proposed first in [1]. InGaAs is still the most commonly used material for SWIR camera sensors.

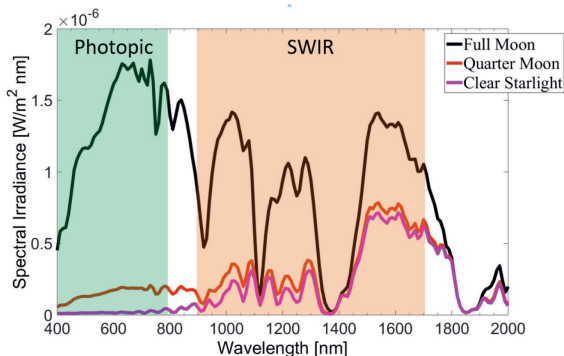


Fig. 1. Typical spectral irradiance levels for selected low light scene conditions, showing the weak correlation between photopic and SWIR specific integrated sensing levels.

This SWIR band specific irradiation unit is termed the swux, short for SWIR lux. The swux unit would be a good choice for characterization of ambient lighting conditions that exist during test trials of SWIR camera systems, particularly at night or limited sight conditions, where hu-

man observers tend to severely underestimate ambient SWIR backgrounds based on their subjective visual perception of lighting conditions, see e.g. Fig.1. We propose a method for measurement of ambient SWIR levels, a so-called “swux-meter” that can be constructed from COTS light measurement components and a COTS absorbing glass filter [3]. The intention of the new SWIR-specific spectroradiometric units (based on the idea of an analogous

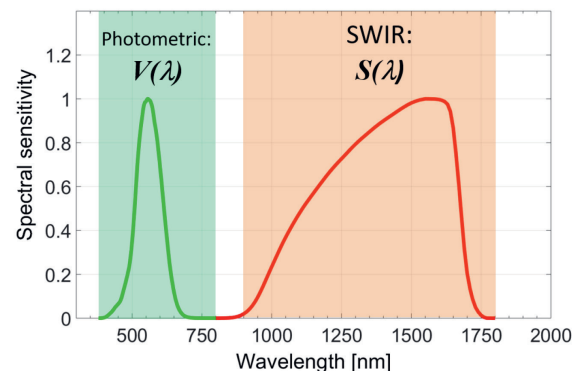


Fig. 2. Comparison of the well known photopic response curve $V(\lambda)$ used for photometric illumination unit and the proposed SWIR spectral radiant efficiency function for SWIR sensing called $S(\lambda)$, as defined in [1] and used for the definition of the SWIR specific irradiance unit as shown in Fig. 3.

source-independent SWIR-candela definition) is, to provide a practical integral measure for a unified quantification of SWIR scene illumination conditions that can standardize and improve the performance prediction and comparison of SWIR cameras, most of which have a

spectral sensitivity curve in the spectral band between 0.9 μm and 1.7 μm . For the definition of the SWIR specific radiometric units of measure we follow the framework for definition of detector-based photometric scales in Ref. [6]. First a source independent SWIR-candela is proposed as the radiant intensity, in a given direction, of a source that emits monochromatic radiation of frequency 193.413×10^{12} Hz ($\lambda = 1.55 \mu\text{m}$ in vacuum), with a radiant intensity in that direction of sc watt per steradian, where $sc = (1/210,000)$ by definition. Based on this scaling factor the SWIR-specific integral irradiance unit $swux$ can be defined as shown in the following Fig. 3, based on the weighting of the perceived irradiance $E_e(\lambda)$ with the $S(\lambda)$ curve. This constitutes an averaged response of standard lattice matched InGaAs which is shaped on the shortwave end of the band, to compensate for variations in backside substrate processing. A detailed listing of the $S(\lambda)$ values is provided in Ref.[1].

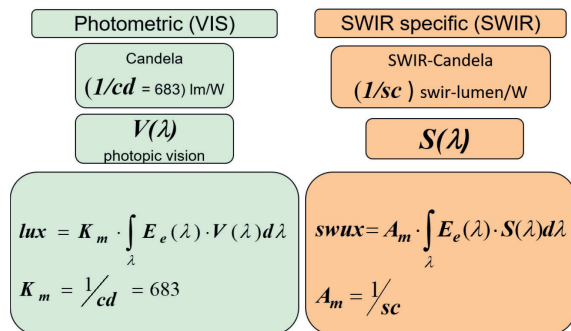


Fig. 3. Analog definition of the SWIR specific irradiance unit of measure compared with the photometric unit of illuminance. The SWIR spectral radiant efficiency function for SWIR sensing $S(\lambda)$ is shown in Fig. 2.

Based on the defined scaling factor $A_m = 2.1 \text{E}+5 \text{ (W/sr)}^{-1}$ resulting from the definition of the corresponding SWIR-candela unit in Fig. 3, the calculated $swux$ levels in Tab. 1 show that

Tab. 1: Selected reference spectral scene irradiance distributions from NVESD SSCamIP 2009.

illumination condition:	Swux level	Lux level
Overcast starlight	3.8	1.2E-4
Clear starlight	38	1.2E-3
Quarter Moon	44	1.1E-02
Full Moon	97	0.1
Overcast daylight	4.6E+04	900
Direct sunlight	2.8E+07	8.8E+4

a unity $swux$ irradiance level indicates the low light sensing limit for all currently available low light imaging technologies like Gen-3 image intensifier tubes, EMCCD, sCMOS and the highest grade of SWIR cameras. Up to 7 orders of magnitude in $swux$ level are covered from natural scene irradiance levels up to direct sunlight illumination.

We started several implementations of $swux$ -meters both as portable devices enabling field based scene measurements [3] and in radiometric test benches [4], [5], where the minimum receivable contrast of a SWIR camera can be measured in dependence of the corresponding $swux$ -level, thus making predictions on the field performance of the tested cameras in real life applications possible.

To become established among all users in the fields of relevant SWIR camera applications, the traceability of the new $swux$ unit would have to be established by relevant standardization institutions. An agreement on how to realize the proposed SWIR-candela is necessary. For these purposes it would be very useful to extend the definition of the broad band CIE standard Illuminant A [7] beyond 820nm, including the SWIR spectral range until at least 1800nm, as described in Ref. [1].

References

- [1] A. Richards, M. Hübner, "A new radiometric unit of measure to characterize SWIR illumination", *Proc. SPIE 10178, Infrared Imaging Systems: Design, Analysis, Modeling, and Testing XXVIII*, 101780C (2017)
- [2] M. Hübner et al., *Proc. SPIE 9819, Infrared Technology and Applications XLII*, 981905 (2016)
- [3] A. Richards, M. Hübner, M. Vollmer, "Measurements of SWIR backgrounds using the $swux$ unit of measure", *Proc. SPIE 10625, Infrared Imaging Systems: Design, Analysis, Modeling, and Testing XXIX*, 106250P (2018)
- [4] W. Büchtemann, S. Brückner, M. Hübner, H. Kampfl, "Advanced test station for imaging EO systems in the VIS to SWIR range", *Proc. SPIE 10795, Electro-Optical and Infrared Systems: Technology and Applications xV*, 107950Q (2018)
- [5] A. Richards, C. Durell, J. Jablonski, M. Hübner, "White Paper on SWIR Camera Test – The New $swux$ Unit", PHOTONCS MEDIA (2018)
- [6] C.L. Cromer, G. Eppeldauer, J.E. Hardis, T. C. Larason, and A. C. Parr, National Institute of Standards and Technology detector-based photometric scale, APPLIED OPTICS, Vol. 32. No.18, June 1993
- [7] ISO 11664-2:2007(en) Colorimetry — Part 2: CIE standard illuminants

Measurement Uncertainty Consideration of Electric Field Meters

Carola Schierding¹, Martin Thedens¹, Michael Beyer¹

¹ *Physikalisch-Technische Bundesanstalt, Bundesallee 100, Braunschweig, Germany
carola.schierding@ptb.de*

Summary:

The capability of electric field meters as traceable measuring devices in a static electrical field is investigated. For this purpose, the measuring method of the electric field meter is examined based on the influencing variables and possible conditions for application are derived. Based on the results, a model for the identification of measurement uncertainty according to the "Guide to the Expression of Uncertainty in Measurement" is developed.

Keywords: measurement uncertainty, electric field meter, traceability, electrostatics, surface charge

Introduction

In order to measure electrostatic charges on surfaces by means of an electric field meter (FM) with corresponding indication of the measuring accuracy, it is necessary to characterize metrologically the measuring method of a FM to obtain a traceable measuring instrument. By using a FM to determine the electrostatic field of the surface charges, a measurement without discharge can be obtained. This is possible due to the non-contact and discharge-free measuring method of a FM. The measuring method is based on the principle of electrostatic induction [1]. The FM used here [1, 2, 3] consists of a grounded measuring head and electronic measuring equipment in a grounded enclosure. With this measurement method, the FM does not directly influence the electrostatic charge. However, it is necessary to consider that the FM changes the shape of the E-field distribution. This is caused due to the characteristics of the FM, in particular, the edge of the grounded measuring head, which is not homogeneous (Fig. 1 left) [1]. This kind of distortion can be prevented by placing the measuring head into a grounded electrode. As a result of the homogenization, the measuring head causes no significant influence on the distribution of the E-field, see Fig. 1 right. That optimization is used by manufactures to indicate the measurement deviation of their FM. Hereby is the problem that the indication of the deviation applies for just one particular case, the so-called "one point calibration". For this one homogeneous E-field configuration: Measuring head placed centered in a ground electrode, a plate electrode as measuring object, both electrodes with the same diameter and are also placed

centered and parallel to each other in a set distance [2].

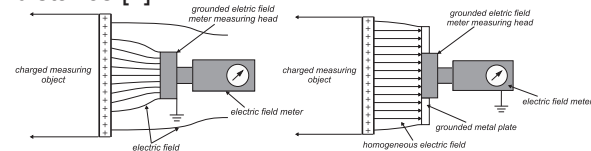


Fig. 1. Left: E-field distortion due to measuring head; Right: E-field homogenization by a grounded electrode (according to [1]).

However, no further indications on the measurement deviations for applications without a ground electrode, other measuring object sizes or shapes (homogenous and inhomogeneous E-field configurations) and measuring distances are provided. Establishing the FM as a measuring instrument requires precise knowledge of the measuring method, the characterization of influencing parameters and the traceability of the measured values to national standards. Therefore, a test setup was developed, which ensures correct and reproducible measurements [4]. Due to the investigation results [4], and additional considerations on the mode of operation of the FM within the E-field, it could be determined that measuring objects are detected by means of a measuring cone defined by a measuring angle (depending on the diameter of the measuring head) [5]. Thus, the influencing variables and conditions for the correct application of an FM could be identified [6]. Based on these results it is possible to develop a model for the indication of the measurement uncertainty according to GUM [7].

Modelling and Results

The GUM provides a consistent method for the determination and indication of the measure-

ment uncertainty. The determination of the influencing variables, the application conditions and the modelling are the main challenges and are discussed here for the measuring method FM. The influencing variables and conditions for the correct application of FM measurement are identified [6]. All other influences are considered as not relevant.

Conditions:

- Environmental conditions (temperature T , relative humidity rh)
- Optimal measuring distance depends on measuring object size, measuring angle and measuring range of FM.
- Tilting of FM to measuring object, indicated by tilt angle δ . Depends on optimal measuring distance and volume of measuring cone.

Influencing variables:

- Measuring distance (set distance, deviation according to calibration certificate, handling).
- FM measured value recording (accuracy recorder output, display output voltage FM).
- Voltage generation and measuring system (HV-divider, display voltage standard, nominal voltage deviation).
- Inhomogeneity of FM (correction factor of field distortion by measuring head for measurements without ground electrode).
- Inhomogeneity of the measuring objects (correction factor of field distortion by measuring real objects).

Fig. 2 shows the influencing variables for the measurement of the E-field caused by the measuring object and the symbol of the equation for the following consideration.

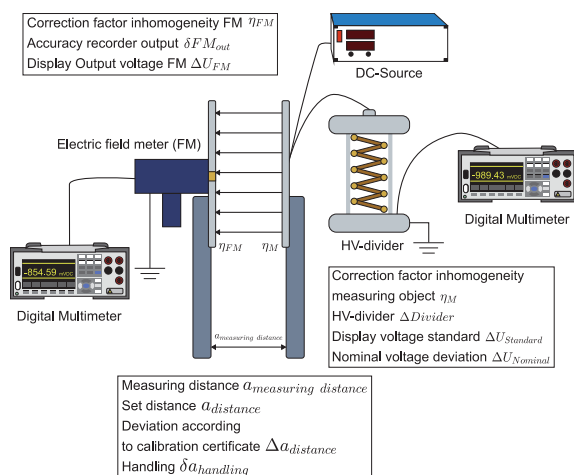


Fig. 2. Influences on the measuring method electric field meter by means of the schematic test setup.

The model equation is based on several analytical terms. In the equations, all quantifiable influences are indicated by Δ . The measurement result is corrected by these terms. All influences which cannot be quantified are indicated with δ . These do not change the meas-

urement result, but only contribute to the measurement uncertainty.

As a result, the model provides the value $\Delta E_{\%}$, which is the difference between the expected E-field E_h and the determined E-field $E_{h, measure}$ in percent. Here, the influence variables and the conditions on the measurement method as such, as well as the influences resulting from the specific measurement and measurement object after the measurement are considered according to the correction factors in the measurement uncertainty. With the measurement method, it is therefore possible to indicate the measurement deviation with extended uncertainty of the measurements with the extension factor $k = 2$ and a coverage probability of 95% (normal distribution), if the following applies:

- Environmental conditions:
 $T = 15\text{ °C}$ to 31 °C and $rh = 25\%$ to 65%
- Measurements with or without homogenizing electrode (η_{FM})
- Homogeneous measuring objects with a diameter $d_{HVe} = 100\text{ mm}$ to 400 mm
- Inhomogeneous measuring objects with round-, angle- or corner geometries (η_M)
- Depending on the respective optimal measuring distance $a_{optimal}$ and the acceptable tilt angle δ of FM

References

- [1] G. Lüttgens, et. al., "Statische Elektrizität begreifen - beherrschen – anwenden", 7. völlig neu bearbeitete Auflage, Expert Verlag, 2015.
- [2] J. N. Chubb, "Two New Designs of „Field Mill“ Type Fieldmeters not Requiring Earthing of Rotating Chopper", IEEE Transactions on industry applications, Vol.26, No. 6, 1990.
- [3] Eltex- Elektrostatik- GmbH, "Betriebsanleitung Influenz- Elektrofelmeter EMF58", Weil am Rhein, Germany, 1994.
- [4] C. Schierding, et. al., "Messtechnische Charakterisierung der berührungslosen Messung elektrostatischer Aufladungen mittels Feldmühlen", 13. Fachtagung Anlagen-, Arbeits- und Umweltsicherheit, Köthen, Germany, Nov 2017.
- [5] C. Schierding, et. al., „Further Developments of metrological and simulation-based characterization of the non-contact measurement of electrostatic charge by means of electric field meters", 21st International Symposium on High Voltage Engineering, Budapest, Hungary, Aug 2019.
- [6] C. Schierding, et. al., "Überblick zum aktuellen Stand der messtechnischen Charakterisierung der berührungslosen Messung elektrostatischer Aufladung mittels Feldmühlen", 14. Fachtagung Anlagen-, Arbeits- und Umweltsicherheit, Köthen, Germany, Nov 2019.
- [7] Guide to the Expression of Uncertainty in Measurement, ISO, Switzerland, corrected and reprinted 1995.

Higher Accuracy for Absolute Magnetic Position Measurement

Dr. Torsten Becker

*BOGEN Electronic GmbH, Potsdamer Str. 12-13, 14163 Berlin, Germany
Torsten.Becker@bogen-electronic.com*

Summary:

The shift to absolute magnetic measurement requires new solutions. Existing absolute measurement solutions are either too expensive or not accurate enough. With new approaches, the impact of new measurement principles on accuracy will be demonstrated and the effects of key parameters for improving the accuracy will be discussed in detail. A summary of achievable accuracies will give engineers recommendations, how to choose the right absolute magnetic measurement solution.

Keywords: Absolute measurement, magnetic sensors, accuracy

Absolute measurement for positioning

Absolute measurement means that the system will provide a defined position at startup. Absolute systems do not need to perform a reference run to a home position as in an incremental system that counts increments and will start at 0 at startup, regardless of the actual position. There are also pseudo-absolute systems available, which will identify a position after a short move, e.g. with distance coded references.

Several different measurement principles are used for absolute measurements of positions. Positions can be measured in rotary and linear applications. The key task is finding the right measurement principles. The different principles – Nonius, Pseudo-Random-Code, Bit patterns, selected special approaches – can be used.

The nonius principle has been widely adopted in magnetic measurement, because it offers a lot of flexibility, as it can be used for both linear and rotary with the same sensor, for different measurement lengths or diameters.

The pseudo random code, where interleaved binary patterns decode many positions, is mostly used for linear applications. The key differences to the nonius solution are coarser resolution and the need to adapt the sensors to different tasks and different geometries.

Absolute binary patterns are used for rotary applications, where different tracks are patterned with different multiples of two patterns. To avoid jumps due to inaccuracies,

the Grey pattern is used in many applications to provide a more fault tolerant approach.

Different other solutions are known, including an angle-based system.

Key parameters for absolute measurement

The first requirement is to understand, how many different positions need to be discerned. This is the resolution of the system. In many cases, this is based on the binary pattern, where the number of tracks describe the number of positions to be identified. A system with four binary tracks can identify 2^4 positions equal 16 positions. Therefore, the resolution of absolute measurement systems is described in a Bit number, in the example above a 4 Bit resolution. While low resolutions of up to 4096 have been the standard for rotary measurement for a long time, new solutions offer much higher resolutions, e.g. up to 20 Bit, meaning that a rotation can be discriminated in over 1 million different positions.

The next key parameter describing the application is the measurement length. Compared to incremental solutions, absolute solutions are built for a specific linear length and a rotary diameter.

The last parameter and most probably the most interesting for the end user is the accuracy. The accuracy denotes, how exact a system will achieve the required position. So, when the measurement system determines a position, this position is measured with other means, how well the measurement aligns with the reference measurement system. Depending on the application and requirements, linear accuracies are typically described in microns

while rotary solution may be measured in degrees, arc minutes or arc seconds.

Impact on accuracy

The accuracy of a magnetic measurement has several critical factors. The sensor and its reproducibility between different parts will provide clean input or not, that can either be improved during signal processing or not. This signal processing will delete noise out of the measurement. One other factor is the algorithm for position determination that will have different accuracies.

Geometric factors also impact the accuracy. Typically, absolute measurements require multiple sensors and the alignment of these impacts the performance of the system. The next geometric influence is the alignment of the sensor over the scale. Misalignments effect the results considerably. Especially for rotary measurement solutions, eccentricity of the rotating part may have a key impact on the accuracy that can be achieved.

The last factor influencing the accuracy is the scale. Scales cannot be produced without variations between the elements that will be used for measurement. The accuracy of the scale will impact the accuracy of the measurement solution directly. As most absolute systems require multiple tracks, not only the errors in one track, but also the differences between the tracks will impact the accuracy result.

Approach for improving accuracy

In order to achieve higher accuracy, the first key element is the scale accuracy. If a linear scale can be produced with a higher accuracy, than the overall system is more accurate.

There are scales with different accuracies. If better than 3 microns can be achieved in a scale, that is good performance in today's standards.

The accuracy of rotary scales is typically diameter dependent. The bigger the diameter, the higher the achievable accuracy.

Improving scale accuracy requires many different tasks depending on the scales production method, but translates directly to a higher measurement solution accuracy which puts a high emphasis on this.

In rotary applications, eccentricity is a key parameter to achieve highest accuracy. Some systems already provide eccentricity correction to overcome the impact of this difficult to master issue.

The second key parameter is the sensing principle. While a PRC system does not provide good resolution, it will identify a position easily and accurate. Typically the resolution of the PRC is quite big and the resolution to low. With an added incremental track that is aligned with the bit positions of the PRC, the resolution can be improved and accuracy will increase, if the alignment of the two tracks is closely controlled while the tracks each are written as precise as possible.

Results

While older absolute systems will only achieve an accuracy of roughly 50 μm , the new approaches achieve results of 10 μm . BOGEN is working on scales that will help to achieve less than 10 μm accuracy, which will improve the absolute performance significantly.

Study the Co-C/Re-C Eutectics Fixed Point Measurements For High Temperature Radiation Thermometer

Ko Hsin-Yi ¹, Liu Jun-Heng, Liao Shu-Chun, Yeh Chien-Chih, Chen Cheng-Hsien ¹
 Center for Measurement Standards, Industrial Technology Research Institute Bldg.16, no:321, Sec. 2,
 Kuang Fu Rd., Hsinchu, 30011, Taiwan, R.O.C,
 Shelley_ko@itri.org.tw

Summary:

CMS/ITRI study a relative primary radiation thermometer for realization and dissemination of thermodynamic temperature above the copper point. The measurements was carried out using the facility of the Co-C eutectic fixed point and Re-C eutectic fixed point. Research is focused on delivering study the measurement capability of the eutectic point. In this thesis, we describe the steps of analysis, the method and results of measuring the spectral radiance of the blackbody radiation of Co-C and Re-C, and to understand uncertainties associated with cells repeatability and reproducibility.

Keywords: radiation thermometer, thermodynamic, eutectic fixed point, blackbody, uncertainty

Background

CMS study the thermodynamic temperature indirectly through HTFPs whose thermodynamic temperatures have been assigned either a prior or through calibration. The relative method is elaborated in the text for the mise-en-pratique for the definition of the kelvin (MeP-K) [1, 2]. The implementation of relative primary radiometric thermometry requires the use of one or more fixed point blackbody sources. In this thesis, we describe the results of measuring the points of inflection of the melting transition curves of the metal-carbon eutectics Re-C, Co-C, and the same time understand associated with cells repeatability and reproducibility.

Description of Experimental Configuration

The primary radiometry measurements at CMS will be carried out using: A Si-based radiation thermometer - linear pyrometer LP4 which made from KE is used in the experiment. The wavelength setting of the interference filter in the linear pyrometer LP4 is 650 nm. A set of high quality fixed-point blackbody sources: the Co-C (1324 °C) eutectic fixed point cell and a Re-C (2474 °C) eutectic fixed point cell -- Commercial type made from CHINO. A PID-controlled furnace (CHINO model IR-R80) system which use graphite as the element of the heater has the ability to create a stable environment temperature range from 1000 °C to 2800 °C.

Measurement conditions

Melt and freeze steps will be presented below:

1. For a Re-C (2474 °C) eutectic fixed point cell: The furnace would be heat up at 2500 °C for melting, and go down from 2500 °C to 2412 °C for freezing.
2. For a Co-C (1324 °C) eutectic fixed point cell: The furnace would be heat up at 1340 °C for melting, and go down from 1340 °C to 1262 °C for freezing.

The measurement process is:

1. Repeatability: three melting plateau were realized in the same furnace on the same day
2. Reproducibility: three melting plateau were realized in the same furnace on 3 days

Results

The result of the points of inflection of the melting transition curves of the metal-carbon eutectics Re-C, Co-C is shown in Figure 1 and Figure 2 respectively.

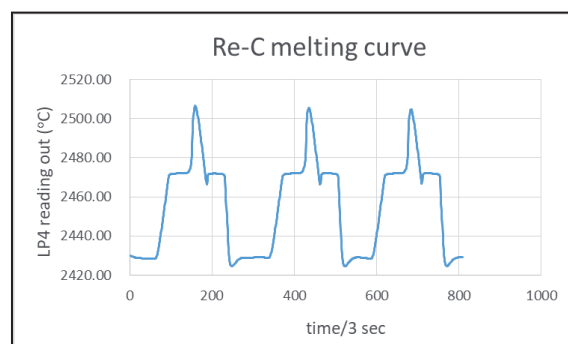


Fig. 1. . Re-C eutectic cell experimental result.

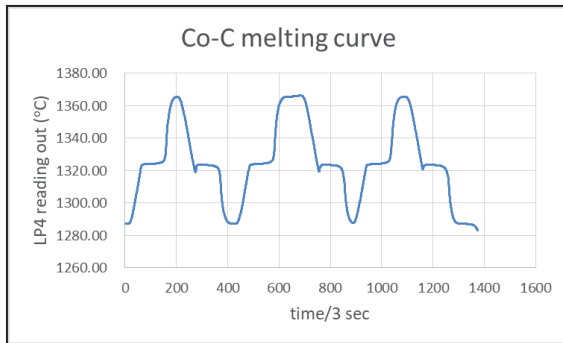


Fig. 2. . Co-C eutectic cell experimental result.

Analytic method is the third-order polynomial fit method [3]. A third-order polynomial is fitted (least-square method) to the data. Then, fitting coefficients can be used to calculate the time of point of inflection. Finally, the time of point of inflection is substitute back to the third-order polynomial to obtain the temperature. In order to fit the experimental result to the polynomial, it is necessary to select appropriate range of data. The data which we used for fitting is shown below. The fitting range of Re-C experiment is shown in Figure 3.

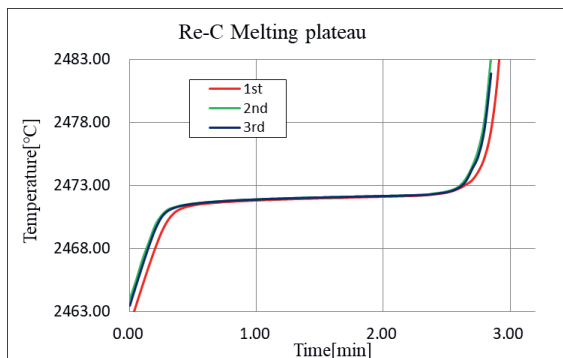


Fig. 3. . Re-C POI analytic result

The fitting range of Co-C experiment is shown in Figure 4.

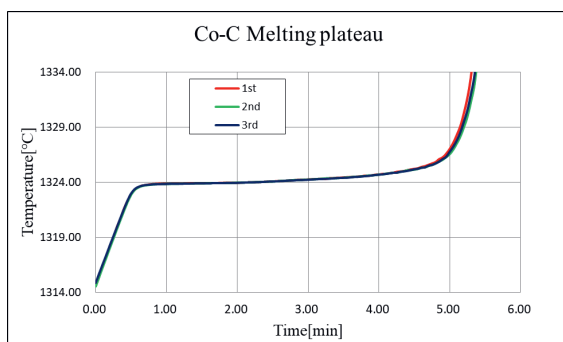


Fig. 4. . Co-C POI analytic result

Summary of the point of inflection uncertainty of the Re-C and Co-C cell is given in Table 1 and Table 2 respectively.

Tab. 1: Summary of Re-C cell uncertainty

Source of Uncertainty Re-C cell	U (k=1) /K
POI determination	1.39
POI Repeatability	0.06
POI Reproducibility	0.1857

Table. 2. Summary of Co-C cell uncertainty

Source of Uncertainty Co-C cell	U (k=1) /K
POI determination	0.96
POI Repeatability	0.015
POI Reproducibility	0.057

Conclusion

This paper has presented the results of the point of inflection of the melting transition of the metal-carbon eutectics Re-C and Co-C along with their cell effects uncertainties. In the near work, CMS will study the long-term stability tests on these cells and the uncertainties associated with furnace effects.

References

- [1] Machin G, Bloembergen P, Anhalt K, Hartmann J, Sadli M, Saunders P, Woolliams E, Yamada Y, Yoon H. 2010 Practical implementation of the mise-en-pratique for the definition of the kelvin above the silver point. *Int. J. Thermophys.* 31, 1779–1788. (doi:10.1007/s10765-010-0834-5)
- [2] Fellmuth B, Fischer J, Machin G, Picard S, Steur PPM, Tamura O, White DR, Yoon H. 2016 The kelvin redefinition and its mise en pratique. *Phil. Trans R. Soc. A* 374, 20150037 (doi:10.1098/rsta.2015.0037)
- [3] Lowe, Dave & Machin, Graham. (2012). Evaluation of methods for characterizing the melting curves of a high temperature cobalt–carbon fixed point to define and determine its melting temperature. *Metrologia.* 49. 189. 10.1088/0026-1394/49/3/189

Design and Implementation of Smart Multisensor Monitoring System for Safe Workplaces with LoRaWAN

Sergej Johann¹, Antoine Lapalus¹, Carlo Tiebe¹, Matthias Bartholmai¹

*¹ Bundesanstalt für Materialforschung und -prüfung, Unter den Eichen 87, 12205 Berlin, Germany
Sergej.Johann@bam.de, Antoine.Lapalus@bam.de, Carlo.Tiebe@bam.de,
Matthias.Bartholmai@bam.de*

Summary:

This project addresses the application of safe workplaces in offices and chemical laboratories where indoor air quality plays an important role. The LoRaWAN (Long Range Wide Area Network) is used as a communication interface to make important sensor data globally accessible. The goal of the development is to create a sensor node and an online and offline solution that collects the data from the sensor nodes and stores it on a local server or in a cloud. In cooperation with the companies WISTA GmbH and IONOS, a test sensor network is going to be established in the Berlin-Adlershof area.

Keywords: smart sensors, air quality monitoring, LoRaWAN, VOC, multisensor system

Idea

The idea of this project is based on developing a way to create a safe workplace. The implementation is based on the current technology LoRaWAN [1], which allows to cover a large area with a range of up to 15 km. Important parameters should be detected and measured to avoid endangering people. Both in the office and in the laboratory, limits for hazardous volatile gases can be exceeded [2-3]. The sensor network with the low power sensor nodes should continuously record all necessary data and issue a warning if the limit value is exceeded.

Concept and Implementation

The concept envisages the development of several sensor nodes and equipping them with different sensors to determine indoor air quality. Three sensors are implemented as a basis: volatile organic compounds (VOC) gas sensor, temperature and humidity sensor. The network can be operated in two ways to make the collected data available. Online via a cloud and via the associated network infrastructure, that is provided in cooperation with WISTA GmbH and IONOS and is implemented as the primary solution and the offline solution. This assures that the data can be retrieved even if there is no Internet connection. A local computer is configured as a server and provided with a user interface.

Figure 1 shows the overall concept of how the network should look like. The office or laboratory is equipped with sensor nodes, each sensor

node contains several sensors to determine the parameters for room air quality measurement.

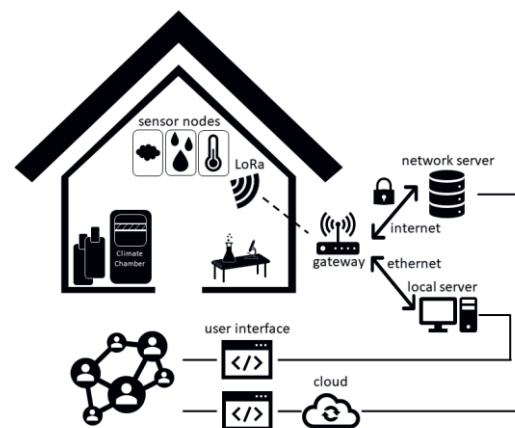


Fig. 1. Concept of the System Network.

Figure 2 shows the individual components of the sensor node. The system is powered by 3xAAA batteries to avoid the long charging times that occur with rechargeable batteries, so that the system is ready for use again more quickly. A Cortex M4 microcontroller controls the communication of the LoRa- and the GPS module. The sensors used to measure air quality parameters are commercially available, including the sensors for temperature, humidity, air pressure, and VOC concentrations (BME680 from bosch). The measured data is stored on a SD card as a storage medium. The BME680 was chosen because, unlike other sensors, its measuring range reaches the MAK value of ethanol, which was used as reference gas.

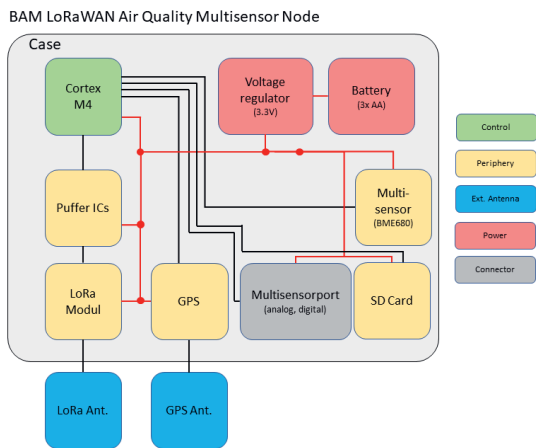


Fig. 2. Block diagram of the sensor node.

Figure 3 shows a 3D model of the electronic structure of the sensor nodes, with the components. Within the scope of a prototype development, the shape of the circuit board was developed for a standard housing.



Fig. 3. First functional model in 3D overview with the electronic components of the sensor node.

Optimization and extensions will be included in the design after the validation phase.

Results

In order to test the suitability of the sensor for this application, a laboratory test was carried out to show how the sensor reacts to different gas exposures. The setup was to validate the sensor under given conditions, the test gas was ethanol in synthetic air.

The validation of the BME680 was carried out in a closed measuring cells, a calibrated gas mixing system has introduced a previously specified ethanol in synthetic air concentration into the measuring cell. The validation was performed in two sequences, the environmental parameters were chosen according to application conditions, for the first sequence: 10 %rh and 25 °C and for the second sequence: 50 %rh and 25 °C. After a burn-in phase of the sensor (approx. 48 h), ethanol (C_2H_6O) in synthetic air with a concentration of 20 ppm, 40 ppm, 80 ppm, 100 ppm, 200 ppm and

300 ppm and an air flow rate of 1000 ml/min \pm 1 % was introduced into the measuring cell. Figure 4 shows the signal curves of the sensor response to the varying ethanol concentrations. First results show, that the sensor correlates well with the set concentrations but has a cross-sensitivity to moisture.

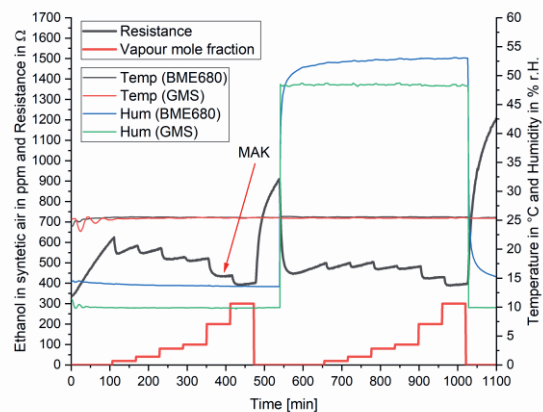


Fig. 4. Validation of the BME680 with ethanol in synthetic air in the climate chamber.

Outlook

The selected sensor shows promising result. Further tests are ongoing, e.g. to validate how robust and reliable the sensor nodes are. Another important aspect that should be investigated is the energy management of the LoRaWAN, where the runtime of the system and signal integrity up to shutdown is examined.

Furthermore, a user interface with sensor and value recognition is being developed for the local solution.

References

Text.

- [1] LoRa Alliance Inc., 2017, LoRaWAN Specification 1.1.
- [2] Technical instructions for keeping the air clean - TA Luft (in German) https://www.bmu.de/fileadmin/Daten_BMU/Download_PDF/Luft/taluft.pdf, 2020-01-23.
- [3] Directive (EU) 2016/2284 of the European Parliament and of the Council of 14 December 2016 on the reduction of national emissions of certain atmospheric pollutants, amending Directive 2003/35/EC and repealing Directive 2001/81/EC, <http://data.europa.eu/eli/dir/2016/2284/oj>, 2020-01-23.

2PP.....	A5.3	Bayesian analysis	D1.4
3d-coil.....	P3.5	Bayesian inference.....	D3.1
3D-integration.....	A5.1	Bearing Clearance	E4.1
3w-method.....	A5.2	bentonite	D4.4
absolute acidity.....	B6.1	bidomain structure.....	A2.4
Absolute measurement.....	E4.4	biochemical sensor	B3.3
absorption spectroscopy.....	B4.4, C2.2, C2.5, C4.4	biomarkers in sweat	B3.3
accuracy	E4.4, P1.10	bioprocess monitoring	B3.2
acoustic loss	A2.1, A2.3	blackbody	E4.5
acoustic quality control	D2.2, P3.11	blockchain	P3.1
acoustoelastic effect.....	D6.1	Body Detection.....	B4.5
active thermography.....	C4.2	brain imaging.....	C6.1
actuator	A2.5	bulk acoustic wave	A2.2, P1.9
adaptable system	P3.3	calibration.....	Plenary Talk 1
adaptive learning	D2.3	C3.1, C6.1, D1.1, E1.3, E3.4
Adaptive Linear Approximation.....	E2.3	calibration and evaluation procedure	P4.6
adaptive weight robust particle		calibration of electrical quantities	E3.3
swarm optimizer.....	D5.2	calibration of force	E3.3
adaptivity	P3.9	calibration of temperature.....	E3.3
AdBlue.....	A5.2	cantilever.....	A6.1
ADC.....	P4.5	capacitance standard	E1.2
Additive Manufacturing.....	A1.3, A5.3	Capacitive Sensor.....	B2.3
Adhesives.....	P1.12	carbon monoxide.....	P1.6
aerosol.....	P3.7	cargo safety.....	P2.8
AFM.....	D5.3	catalyst preselection.....	P1.4
air coupled ultrasound	D6.2	catalytic activity	P1.4
air gap	C5.4	catalytic combustion	B4.3
air ion.....	E3.1	catalytic gas sensor.....	P1.4
air ion composition.....	E3.1	catangasite.....	A2.1, A2.2
air pollution	P3.7	cavity perturbation technique.....	B2.4
air quality	B5.3, B5.4	cell capturing	A5.3
air quality monitoring	B5.2, E5.4	cell trap.....	A5.3
air-coupled ultrasound	D4.1	ceramic.....	P2.9, 2.10
ALD	A5.1	ceramic multilayer technology	B6.3
Allan deviation	E1.3	ceramics.....	D4.3
aluminum nitride	A2.3	cerium bromide	E6.2
ambient.....	B1.1	Characterization	C1.2
ammonium nitrate/fuel oil (ANFO).....	B4.2	chemical gas sensor	B5.2
amperometric chemical sensor.....	P1.8	Chemiresistor	B4.2
amplitude mismatch.....	P4.4	circular waveguide sensor.....	B2.4
Analysis of variance.....	E3.2	clamping force	P2.5
analytic method	A1.1	class interpolation	D5.1
Analytical spectroscopy	B6.4	classification.....	D5.1
angular sensor.....	P4.4	cleanliness of the working space.....	E3.1
antibiotic drug.....	P1.13	CMOS	C1.1
AOP.....	B6.2	CO2.....	B5.3
application	A3.1	coda wave	D4.1
Artificial Intelligence.....	D2.1	coil.....	P2.12
artificial neural networks	D2.4	cold-wire anemometry	P2.14
assembly preload	P2.5	color	P1.6
Asset-Tracking	A3.3	colorimetric.....	P1.6
atan2 function.....	P4.4	compact interro-gation unit.....	P1.14
atmospheric gas spectroscopy	C2.1	composite materials	C4.2
atomic force microscopy.....	A6.2	compressed sensing	C4.1
atomic layer deposition.....	P1.8	computational optics	C6.1
attenuation.....	A2.1	concentration measurements	B2.4
automotive.....	B1.1	condensing gas flow.....	B2.2
Au-ZnO.....	P1.8	Condition Monitoring	B2.1, D2.4, D4.2, D4.4
Ball Bearings	E4.1	E6.4, P3.4
bandgap reference	E1.3	conductive polymer	B4.2
batch wise calibration	P4.6	confocal chromatic sensor.....	C6.4

contact resonance	A6.2, A6.3	embedded sensor	B5.4
contact-free NDT	D4.1	embedded systems	D2.4
contactless	D2.3	Emissivity measurement	C4.3
correlation	P4.7	Energy-Autarchic	A3.3
coulometry	B1.3, B1.4	engine test bench	P3.3
crankcase	P1.1	enhanced thermal image	C5.3
Cryogenics	C3.2	environment	B5.4, P3.7
curing	P1.12	environmental awareness	B5.3
curvature measurement	D2.5	epitaxial graphene	B5.2
CUSUM Algorithm	P3.4	error state kalman filter	E6.1
DAC	P4.5	esophagus manometry	P1.14
Damage Detection	P3.4	estimated CO2 concentration	B5.1
data fusion	D5.3	eutectic fixed point	E4.5
Datum Definition	P4.1	exhaust	B1.1
definitions	D3.4	exhaust gas sensor	P1.7
degradation mechanism	D4.5	exhaust system	P2.14
density	A6.1	expanded uncertainty	P4.7
density	E6.3	experimental ray tracing	P3.8
Design of experience	E3.2	explosion pressure	P2.1
Detection	B4.1	Explosion safety	B2.3
detection limits	B1.2	Explosives	B4.1
detector calibration	C1.3	fast acquisition	B4.4
detectors	C1.4	fault detection	B3.2
Diesel exhaust fluid	A5.2	fault diagnosis	P3.3
differential pulse voltammetry	P1.13	feature extraction	E2.3
diffusion bonding method	A2.4	features	D5.1
digital	E3.4	FEM	P2.7
digital bee keeping	B3.1	FEM simulation	P3.9
Dimensional Management	P4.1	fiber Bragg grating	D2.5, E1.4, P1.14
distribution network	E6.4	fiber optic sensor	P1.14
diversified-redundant	B1.1	fiber optics	C6.2
DMP41	D1.2	fiber sensing	C6.2
Doppler interferometer	A2.4	Finite Element Method	A3.2, P2.13
drift correction	D5.3	FIR-imager	C3.3
DTI	E3.4	flameproof enclosures	P2.1
dual comb hyperspectral imaging	C2.3	flammable gas sensor	B4.3
dual-comb-spectroscopy	B4.4	flexible pressure sensor	P3.10
Dynamic	E3.4	flow sensor	B2.2
Dynamic pressure	A4.3	fluid dynamic	E6.1
Dynamic pressure sensor	A4.3	fluid sensing	B2.5
eddy current	D4.3, P2.12	fluid-structure interaction	B2.5
Eddy Current Testing	A1.3	Fluorescence	B4.1, P3.6
edge analytics	D2.4	food waste	P1.3
edge zone analysis	C4.2	force	D1.2
education	D3.4	Force calibration	A4.2
effective degrees of freedom	P4.7	force sensor	P2.8
effective elastic constants	D6.1	force tensions	P2.5
electric charge	E3.1	Force transfere standard	A4.2
electric field meter	E4.3	Foundry	D4.4
electric motors	P4.2	Fourier transform infrared spectroscopy	D4.5
electrical analysis	C5.2	freeform surfaces	P3.8
electrical conductivity	A5.4, P2.12	fruit storage	C2.5
electrical standards	E1.3	FTIR	C4.5
Electrochemical impedance spectroscopy	D4.5	fuel cell	B1.1
electrochemical sensor	P1.13	Functional Safety	P3.3
Electro-Magnetic Flowmeter	B2.1	galinstan	P1.15
Electromagnetic sensor	E6.4	galvanic isolation	P2.15
electromagnetic signal to noise ratio	P4.2	gas analysis	B4.4
Electromechanical Modeling	A3.2	gas chromatography	B1.3, B1.4
electromechanics	P3.9	gas chromatography/ mass spectrometry (GC/MS)	P1.3
electrostatics	E4.3		

gas monitoring.....	P4.3	InGaAs-Photodiode.....	C1.2
Gas sensing.....	B3.1, P2.11	in-hive measurement.....	B3.1
Gas Sensor.....	B4.5, C4.4, D3.2, P1.2, P1.6, P1.9	in-line.....	P1.2
Gas-Phase.....	B4.1	instrumentation.....	C1.4
GeoMetre.....	D3.3	Instrumentational amplifier.....	D5.2
Geometrical Tolerancing.....	P4.1	interconnection.....	P2.10
geometry detection.....	P2.6	interdigital electrodes.....	P1.7
geotextiles.....	A4.5	interdigital transducers.....	P2.13
glass.....	P2.2	interferometry.....	D6.4
glass electrodes.....	B6.1	Internet of Things.....	Plenary Talk 1, A3.3
Goniometer.....	C4.5	inverse method.....	D6.3
gradient method.....	D3.3	inverse problem.....	E2.4
Graphical Full Variability Program		Ion-sensitive electrodes.....	B6.3
ming Language.....	P3.3	IoT.....	D2.4, P3.1
Graphical Programming Language.....	P3.3	IoT Ecosystem.....	Plenary Talk 1
grip quality assessment.....	P2.4	ISO376.....	A4.2
guided waves.....	D6.3	Isotopic Composition Analysis.....	C4.4
H2O2.....	P1.8	ITS-90.....	Plenary Talk 3
H2-sensor.....	B1.1	iterative closest point (ICP) algorithm.....	D5.3
half-cells.....	B6.1	Jitter.....	A4.1
Hall constant.....	A5.4	Josephson voltage standard.....	P4.5
harmonic test signal I.....	P4.5	kelvin redefinition.....	Plenary Talk 3
harsh environment.....	P1.1	kilogram.....	D3.4, E1.1
harvester topology.....	A3.4	Knudsen effusion.....	P2.3
harvesting circuit.....	A3.4	kurtosis method.....	P4.7
hermetic sensor.....	B2.2	LabVIEW.....	P3.3
Heterodyning.....	A1.3	langasite.....	A2.1
Heterostructures.....	P1.8	langasite family.....	A2.2
HfO2.....	C1.1	langatate.....	A2.1
high humidity.....	B2.2	large gear.....	C6.4
High speed MWIR.....	C2.3	laser.....	C4.1, C5.1
high temperature.....	A2.1, A2.3, A2.5	laser excitation.....	D4.1
.....	A5.4, P2.9, P2.10, P2.11	Laser materials processing.....	D1.4
high-power laser.....	C5.1	LASSO.....	D1.1
high-temperature.....	P1.9	layer peeling.....	D6.2
humidity.....	P1.10	layer-wise relevance propagation.....	D2.2
humidity sensor.....	P1.10	leading edge erosion.....	C4.2
HVAC control.....	B5.1	LED array.....	D3.2
hydrogen cyanide.....	B4.4	LEL.....	P1.1
hydrogen sensor.....	B1.4	length measurement.....	D3.3
hydrogen sulfide.....	P1.3	light stimulation.....	D3.2
hydrophilicity.....	P1.11	Linear Guide Bearings.....	A4.4
Hygrometer.....	P1.10	linear measurement.....	D2.3
imaging.....	D5.4	linear regression method.....	P4.5
imaging spectroscopy.....	C2.3	liquid.....	P2.12
impedance.....	P1.11	liquid metal actuator.....	P1.15
impedance metrology.....	E1.2	lithium niobate.....	A2.4
impedance spectroscopy.....	D4.4, P2.3	lithium niobate-tantalate.....	A2.5
in situ.....	P3.6	Load cell.....	A4.2
inductive communication.....	P3.5	Load Determination.....	A4.4
inductive localization.....	P3.5	Load Distri-bution Model.....	A4.4
inductive sensor.....	P2.6	LoRaWAN.....	E5.4
Industrial sound analysis.....	D2.2, P3.11	low dielectric materials.....	B2.4
industrial thermometer.....	C5.4	low noise.....	C3.2
Industry 4.0.....	Plenary Talk 2, A4.4	low power.....	A3.1
Information fusion.....	E2.2	low-cost.....	A5.4
Information security.....	Plenary Talk 1	Low-Power and Harvesting.....	A3.3
Infrared.....	C1.4, C3.1, C4.5	low-power wireless.....	B4.3
Infrared Detector.....	C3.2	LTC3108.....	A3.4
infrared optical properties.....	C4.3	Machine Elements.....	D4.2
InGaAs.....	E4.2		

machine learning	A3.1, D2.1, D2.2	mold-ing compound.....	D4.5
.....	D2.5, E2.3, E2.4	Molecularly Imprinted Polymer	B3.4
Machine Vision	D2.1	monitoring	P1.12, P3.7
magnet	A1.2	MOS gas sensor	D5.1
magnet inspection	A1.2	motion tracking.....	E6.1
magnetic field camera	A1.2	multi-distance measurement	C6.4
magnetic field mapping.....	A1.2	multilateration.....	P4.3
magnetic nanocomposite.....	P1.13	multimode photonics	P3.10
magnetic position sensor systems.....	A1.1	multi-parameter sensing system	P1.14
Magnetic Sensors.....	D4.2, E4.4	multiphysics simulation.....	P2.11
Magnetic system design	A1.1	Multi-sensor.....	B4.1
magnetometer	A1.4, P4.2	multisensor system	D1.1, E5.4
Magnetoresistance	A1.3	multi-species	C2.5
magneto-resistive	D2.3	Murnaghan constants.....	D6.1
Magnetoresistive effect.....	D4.2	MWIR uncooled camera.....	C2.1
magneto-sensitive elastomer.....	P3.9	nanolayer	B5.2
Magnus effect.....	B2.2	nanomeasuring machine.....	C6.3
mass concentration	P3.7	nanometrology	D5.3
mass standard.....	E1.1	nanoscale.....	D6.4
material characterisation	D1.3, D6.2, D6.3,	Nanostructuring.....	B6.4
material classification	P3.11	nanotubes	C3.3
mathematical procedure.....	P4.6	neural network.....	D2.1, D2.2, P3.11
measurement	Plenary Talk 5	new sensor principles.....	E3.3
Measurement sensor.....	P2.12	Nitrogen vacancy	A1.4
measurement system.....	A5.4	NMR.....	P1.12
measurement uncertainty.....	E2.3, E3.3, E4.3	NO detection	P1.7
mechanical calibration systems.....	D1.2	non-destructive evaluation	D6.2
medium voltage cable.....	E6.4	nondestructive testing	C4.1
medium voltage switchgear.....	C5.3	Nonlinear Dynamics	E4.1
Membrane	A6.4	number concentration.....	E3.1
MEMS.....	A6.1, A6.2, A6.3, A6.4, P2.11	numerical modelling	D6.3
MEMS hydrogen sensor.....	B1.2	offset issue	P4.4
MEMS resonators.....	B2.5	Oil and Gas	B2.3
MEMS sensor.....	A3.1	oil sensor.....	E6.3
Metadata	E2.2	online measurements.....	B2.4
metal oxide	B5.2, P1.9	ontology.....	E2.2
metal oxide catalysts	P1.4	optical fiber sensors	C5.2
metal oxide gas sensor.....	B5.1	optical form measurement.....	E2.4
metal oxide semiconductor.....	P1.2	optical inspection.....	D4.3
meteorological sensors.....	D3.3	optical measurement.....	C6.4, P3.6
methane detection	P1.1	Optical Measuring System	C4.4
methanethiol.....	P1.3	Optical Measurement and Inspection	
metrological atomic force microscope	C6.3	Systems.....	D2.1
metrological characterization.....	C3.1	optical microphone	D4.1
Metrology.....	Plenary Talk 2, Plenary Talk 5	optical quartz glass fiber.....	B6.4
.....	D3.1, D3.4, D6.4, E2.1, P3.8	optical readout.....	P1.6
micro geometry.....	P3.6	optical synapse	P1.15
microbolometer.....	A6.4, C3.3	optical time domain reflectometry.....	A4.5
microgravity	P2.3	organic solvents	B6.1
microheater	P2.11	ozonation.....	B6.2
microprobe	A6.3	ozone	B6.2
Microvibration	A4.1	packaging.....	P2.9, P2.10
mid-infrared	C1.3, C2.2, C2.4, C2.5	Palladium optical hydrogen sensor	B1.2
mid-IR spectrometer	C2.1	parameter estimation	D6.2
mobile instrumentation	C2.4	particulate matter	B5.3
Mode analysis	P2.7	PDMS Waveguid.....	P3.10
model maintenance	B3.2	pellistor.....	A5.1
model selection	D1.1, D1.4	Penicillin V.....	B3.4
model-based diagnosis.....	P3.3	percolation network	B4.2
model-based evaluation	C6.4	permanent magnets	P2.6
modeling.....	Plenary Talk 5	pH-metry and bilimetry	P1.14

Photoacoustic detector	P1.5	radiometry	E4.2
photometer	P1.5	radio-over-fiber	C5.2
photometry	E4.2	Reaction Wheel	A4.1
photonic pressure sensor	P3.10	Recent Developments	P3.3
photonic thermometry	E1.4	Redefinition of the SI	Plenary Talk 2
photoreactor	P3.5	reduction method	P4.7
photothermal	C4.1	Reference Function	C1.2
photothermal imaging	C5.1	refractive index	D3.3
piezoelectric actuation	A6.1	refrigerants	P1.5
piezoelectric crystal	A2.2	regularization	D1.1
Piezoelectric Dynamometer	A4.1	reliability	P2.2
Piezoelectric Energy Harvesting	A3.2	remote phased array	C6.1
piezoelectric pressure sensor	P2.1	remotely powered sensors	P2.15
piezoelectric resonator	A2.1, A2.3	resistance welding	P2.10
piezoelectric sensing	A6.1	Resonant Frequency	B2.3
Piezoelectricity	A2.5, A3.3, P2.3	resonator	A6.1
piezoresistive	P2.5	response	B1.2
piezoresistive cantilever	A6.2, A6.3	response time	A6.4, C5.4, P1.10
Piezoresistive DLC	A4.4	RF modulated laser	C5.2
Planar capacitive sensors	P2.13	Robust optimization	D5.2
Plasmonics	B6.4	room temperature	A1.4
plates	B2.5	sand	D4.4
platinum thin film	A5.2, P2.11	sapphire	E1.4
PLTS-2000	Plenary Talk 3	SAW	A2.2
poisoning	P1.2	scalability	C3.3
poly (Ether Ether Ketone)	P1.11	scalar	A1.4
Polymer Nanoparticles	B3.4	scaled boundary finite element method	D1.3
polymer optical fiber	A4.5, P2.15	screen-printed electrode	P1.13
polymers	D1.3, D6.1	screw shaft	P2.5
pose estimation	P4.3	self-calibration	P4.3
positioning devices	A2.4	Self-x properties	D5.2
post-CMOS	A5.1	semiconductor lasers	C6.2
power over fiber	P2.15	semitransparent materials	C4.3
Preamplifier	C3.2	Sensitivity	P1.11
precise mechanical positioning	E1.2	sensitivity optimisation	D1.3
prediction	P1.12	sensor	A2.5, D4.1, E3.4, P3.1
Predictive Maintenance	B2.1, P3.4	sensor array	P1.1
Preparedness	E6.2	sensor faults	P3.3
pressure	D1.2, E3.4	sensor magnet	A1.2
pressure measurement	D2.5	sensor networks	E2.2, P2.15
pressure sensor	P2.2	sensor node	B4.3
primary thermometry	Plenary Talk 3	sensor particle	E6.1
Probability	D3.1	sensor responsivity	A6.4
process monitoring	D4.3	Sensorimotor device	P1.15
profile reconstruction	D6.4	sensors	D1.2, D4.2, P1.11, P3.7
Pt YSZ	P1.7	Sensory electronics	D5.2
pulsating flow	P2.14	ship fumes	C2.1
pulsed polarization	P1.7	SI	D3.4
pyroelectric sensor	C1.1	SI traceable	C1.3
pyrometers	C1.4	signal modeling	P3.6
quality monitoring	A5.2	silicon	C4.3, E1.1, P2.5
quantum	A1.4	siloxanes	P1.2
Quantum Cascade Laser	C4.4	simulation	B2.5, C3.2, D6.4
Quantum Revolution	Plenary Talk 2	simulation study	P2.6
Quartz Crystal Microbalance	B3.4	simultaneous evaluation	P4.6
QVGA	C3.3	Simultaneous Thermal Analysis (STA)	P1.4
R1234yf	P1.5	six degrees of freedom	P4.3
R134a	P1.5	smart contracting	P3.1
Radiation monitoring	E6.2	smart gas sensor	P1.3
Radiation Thermometer	C1.2, E4.5	Smart grids	E3.2
radiative transport	C4.3	smart ratchet tie-down strap	P2.8

smart sensors.....	E5.4	thermo-electric generator.....	A3.4
soft sensor.....	Plenary Talk 1, B3.2, E6.1	Thermographic camera.....	C3.1
Spatial Emission.....	C4.5	thermography.....	C4.1
Spectral Emission.....	C4.5	thermowell.....	C5.4
spectral responsivity.....	C1.3	thick-film technology.....	B6.3
spectro-dosimeter.....	E6.2	thin film.....	P1.9, P2.2
Spectrometry.....	D1.4	Thompson-Lampard capacitor.....	E1.2
spectroscopy.....	B5.4	time reversal.....	D5.4
specular surfaces.....	P3.8	time-resolved measurement.....	P2.14
sphere.....	E1.1	tin dioxide.....	D3.2
stability.....	P1.2	TOC.....	B6.2
Statistical Analysis.....	E4.1	torque.....	D1.2
Statistical Measures.....	E4.1	trace gas analysis.....	B1.3, B1.4
Statistics.....	Plenary Talk 5	trace gas sensing.....	C2.2, C2.5
stick-slip sensor.....	P2.4	traceability.....	E1.2, E4.3
Strain Gauges.....	A4.2, D1.2, P2.2, P2.5	Traceability of force measurements.....	A4.2
strain sensing.....	A4.5	True value.....	D3.1
stress.....	P2.5	tunable laser spectroscopy.....	C2.4
structural health monitoring.....	A4.5	tunable lasers.....	C6.2
subsurface defects.....	C4.2	tungsten oxide.....	D3.2
super resolution.....	C4.1	tuning fork.....	E6.3
supercontinuum.....	C2.1	tweezer.....	C6.1
Supraharmonic.....	E3.2	Two-phase flow.....	B2.3
surface characterization.....	P3.8	two-photon polymerization.....	A5.3
surface charge.....	E4.3	UAV.....	E6.2
surface roughness.....	A6.2	ultrapure water.....	B6.2
Surface-enhanced Raman scattering (SERS).....	B6.4	ultrasound.....	D5.4, D6.1, D6.3
sweat sensor.....	B3.3	ultrasound testing.....	D4.1
SWIR.....	E4.2	ultrasound transducer.....	D1.3
swux.....	E4.2	uncertainty.....	Plenary Talk 5
system design.....	A3.1	C1.3, D1.4, E2.2, E3.2
system identification.....	D5.4	Uncertainty Assessment.....	P4.1
tactile sensor.....	P3.9	Uncertainty in measurement.....	D3.1
tape casting.....	D4.3	uncertainty propagation.....	E2.3
technical specifications.....	C3.1	uncooled imager.....	C3.3
Technology Readiness.....	Plenary Talk 2	U-Net.....	E2.4
temperature.....	C1.4, C5.2, P1.10	unified pH.....	B6.1
temperature compensation.....	P2.6	vapour sensing.....	B4.2
temperature cycled operation.....	D5.1	varroa infestation level.....	B3.1
temperature measurement.....	D2.5, P1.10	vehicle safety systems.....	P2.13
temperature scales.....	Plenary Talk 3	velocity measurements.....	B2.4
temperature sensitivity.....	C1.1	Vibration Analysis.....	P3.4
temperature sensor.....	E1.4	Victim Recovery.....	B4.5
tension monitoring.....	P2.8	Virtual Assembly.....	P4.1
thermal actuator.....	A6.3	virtual experiment.....	E2.4
thermal contact.....	C5.4	viscosity.....	A6.1, E6.1
thermal imaging.....	C4.1	visualization.....	D2.2
Thermal monitoring.....	C5.3	VOC.....	E5.4
thermal protection.....	P2.1	volatile organic compounds.....	B5.3
thermal shock.....	P2.1	voltage reference.....	E1.3
Thermal Vision Camera.....	B4.5	washer.....	P1.9
thermal wave.....	C5.1	wavelength shift.....	C6.2
thermal wave fields.....	C5.1	wearable sensor.....	B3.3
thermal/IR camera.....	C5.3	wetness detection.....	P2.13
thermal-electrical model.....	C1.1	whispering gallery resonator.....	E1.4
Thermo cyclic operation.....	P4.6	wireless.....	P2.8
thermocatalytic sensor.....	A5.1	wireless sensors.....	P3.5
thermocouple.....	P2.9	working standard.....	E3.1
thermodynamic.....	E4.5	Ytria-stabilized zirconia (YSZ).....	B1.3, B1.4

Collaborating Institutions and Organizations

- AHMT German Working Group of Professors in Measurement Technology
- Federal Institute for Materials Research and Testing BAM (Germany)
- BIPM - Bureau International de Poids and Mesures (France)
- CETIAT - Centre Technique des Industries Aèrauliques et Thermiques (France)
- COOMET, Euro-Asian Cooperation of National Metrological Institutions
- EURAMET - The European Association of National Metrology Institutes
- Federal Institute of Metrology METAS (Switzerland)
- GMA - Society for Measurement and Automatic Control (Germany)
- IMEKO - International Measurement Federation (Hungary)
- INTI - Instituto Nacional de Teconología Industrial (Argentina)
- Italian National Agency for New Technologies, Energy and Sustainable Economic Development (Italy)
- MSC (USA)
- NCSLI - National Conference of Standard Laboratories International (USA)
- NIST - National Institute of Standards and Technology (USA)
- Physikalisch-Technische Bundesanstalt – PTB (Germany)
- RISE - The Swedish Research Institute (Sweden)
- ROSSTANDART (Russia)
- VNIIMS - All-Russian Scientific Research Institute of Metrological Service (Russia)

Supporting Institutions:

